

AD-A244 893



AGARD-CP-501

AGARD-CP-501

# AGARD

ADVISORY GROUP FOR AEROSPACE RESEARCH & DEVELOPMENT

7 RUE ANCELLE 92200 NEUILLY SUR SEINE FRANCE

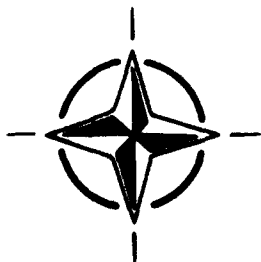
DTIC  
S  
C

AGARD CONFERENCE PROCEEDINGS 501

## Target and Clutter Scattering and their Effects on Military Radar Performance

(Diffraction par les Cibles et le Fouillis et ses  
Effets sur les Performances des Radars Militaires)

*Papers presented at the Electromagnetic Wave Propagation Panel  
Specialists' Meeting, held in Ottawa, Canada, 6th-9th May 1991.*



NORTH ATLANTIC TREATY ORGANIZATION

Published September 1991

Distribution and Availability on Back Cover

Document A

Not for release;

unclassified

# AGARD

ADVISORY GROUP FOR AEROSPACE RESEARCH & DEVELOPMENT

7 RUE ANCELLE 92200 NEUILLY SUR SEINE FRANCE

## AGARD CONFERENCE PROCEEDINGS 501

### Target and Clutter Scattering and their Effects on Military Radar Performance

(Diffraction par les Cibles et le Fouillis et ses  
Effets sur les Performances des Radars Militaires)

Accession For	
NTIS GRA&I	<input checked="" type="checkbox"/>
DTIC TAB	<input type="checkbox"/>
Unannounced	<input type="checkbox"/>
Justification	
By	
Distribution/	
Availability Codes	
Dist	Avail and/or
A-1	Special

91-16655



Papers presented at the Electromagnetic Wave Propagation Panel  
Specialists' Meeting, held in Ottawa, Canada, 6th-9th May 1991.



North Atlantic Treaty Organization  
*Organisation du Traité de l'Atlantique Nord*

91 11 27 057

# The Mission of AGARD

According to its Charter, the mission of AGARD is to bring together the leading personalities of the NATO nations in the fields of science and technology relating to aerospace for the following purposes:

- Recommending effective ways for the member nations to use their research and development capabilities for the common benefit of the NATO community;
- Providing scientific and technical advice and assistance to the Military Committee in the field of aerospace research and development (with particular regard to its military application);
- Continuously stimulating advances in the aerospace sciences relevant to strengthening the common defence posture;
- Improving the co-operation among member nations in aerospace research and development;
- Exchange of scientific and technical information;
- Providing assistance to member nations for the purpose of increasing their scientific and technical potential;
- Rendering scientific and technical assistance, as requested, to other NATO bodies and to member nations in connection with research and development problems in the aerospace field.

The highest authority within AGARD is the National Delegates Board consisting of officially appointed senior representatives from each member nation. The mission of AGARD is carried out through the Panels which are composed of experts appointed by the National Delegates, the Consultant and Exchange Programme and the Aerospace Applications Studies Programme. The results of AGARD work are reported to the member nations and the NATO Authorities through the AGARD series of publications of which this is one.

Participation in AGARD activities is by invitation only and is normally limited to citizens of the NATO nations.

The content of this publication has been reproduced directly from material supplied by AGARD or the authors.

Published September 1991

Copyright © AGARD 1991  
All Rights Reserved

ISBN 92-835-0633-2



*Printed by Specialised Printing Services Limited  
40 Chigwell Lane, Loughton, Essex IG10 3TZ*

# Theme

Radars have been used for target detection and identification for many years. Their performance is chiefly limited by clutter. New techniques in high resolution radars, millimeter wave systems, polarimetric analysis, bistatic radars, adaptive filtering are being developed. Recent advances in computing speed have enhanced enormously the radars' capability in differentiating targets from clutter. But ultimate performance of these new systems depends on more complex knowledge of clutter and target scattering.

Efforts for improving models and their experimental verification are underway concerning the clutter and target characteristics and their impact on radar systems. These issues were addressed during the symposium in the following topics:

## SCATTERING MODELS AND MEASUREMENTS:

- Models for surface scattering: ground and sea clutter.
- Models for volume scattering: atmospheric, ionospheric, chaff.
- Models for target scattering: RCS reduction or modification techniques.
- Methods of experimental characterization of clutter and targets; calibration procedures.
- Combined scattering and propagation effects on system performance.

## SIGNAL PROCESSING AND TECHNIQUES:

- Processing for target to clutter enhancement: coding and modulation, adaptive beam forming and nulling; polarimetric techniques, imaging, interferometric techniques.
- Processing for target identification.
- Practical signal processing implementation techniques.

# Thème

Les systèmes radar sont utilisés pour la détection, la poursuite et l'identification de cibles depuis longtemps. Le fouillis représente la principale limitation en ce qui concerne les performances de ces systèmes. De nouvelles techniques sont en cours de développement dans les domaines des radars à haute résolution, des systèmes à ondes millimétriques, de l'analyse polarimétrique, des radars bistatiques et du filtrage adaptatif. La vitesse de calcul élevée de la dernière génération d'ordinateurs a permis d'améliorer de façon très sensible la capacité de détection des cibles dans le fouillis. Cependant, toute définition des performances optimales de ces nouveaux systèmes passe par des connaissances plus approfondies du fouillis et de la diffusion de la cible.

Des efforts sont actuellement consacrés à l'amélioration des modèles du fouillis et des caractéristiques de cibles, ainsi qu'à leur vérification expérimentale, en vue d'évaluer les effets de ces deux éléments sur les systèmes radar. Ces questions furent examinées au cours de ce symposium qui traita les sujets suivants:

## LA MESURE ET LA MODELISATION DE LA DIFFUSION:

- Modélisation de la diffusion de surface: échos de sol et de mer.
- Modélisation de la diffusion de volume: fouillis atmosphérique et ionosphérique; paillettes.
- Modélisation de la diffraction des cibles: techniques de réduction ou de modification de la section équivalente radar.
- Méthodes expérimentales pour la caractérisation du fouillis et des cibles, procédures d'étalonnage.
- Effets combinés de la diffusion et de la propagation sur les performances des systèmes.

## LE TRAITEMENT DU SIGNAL ET SA MISE EN OEUVRE:

- Traitement du signal pour l'amélioration de la capacité de détection de la cible dans le fouillis: codage et modulation, formation adaptative des faisceaux; techniques polarimétriques, imagerie, techniques d'interférométrie.
- Traitement du signal pour l'identification des cibles.
- Techniques de mise en oeuvre du traitement du signal.



# Electromagnetic Wave Propagation Panel

**Chairman:** Ir H. Vissinga  
van Kempenstraat 30  
2252 VH Voorschoten  
Netherlands

**Deputy Chairman:** Dr Juergen H. Richter  
Head, Ocean and Atmospheric  
Sciences Division, Code 54  
Naval Ocean Systems Center  
San Diego, CA 92152-5000  
United States

## SYMPOSIUM – TECHNICAL PROGRAMME COMMITTEE

### CHAIRMEN

Mr F. Christophe  
Département Micro Ondes  
ONERA-CERT  
Boite Postale 4025  
31055 Toulouse Cedex  
France

Dr John L. Poirier  
Chief, Applied Electromagnetics Division  
RADC (EEC)  
Hanscom Air Force Base  
MA 01731-5000  
United States

Prof. K.C. Yeh  
Department of Electrical and  
Computer Engineering  
University of Illinois  
1406 W. Green Street  
Urbana, IL 61801-2991  
United States

### MEMBERS

Dr Joseph Cihlar  
Canada Center for Remote Sensing  
2464 Sheffield Road  
Ottawa, Ontario K1A 0Y7  
Canada

Prof. Prabhakar Pathak  
Ohio State University  
Electro Science Laboratory  
1320 Kinnear Road  
Columbus, OH 43212  
United States

Dr R. Klemm  
Forschungsinstitut für Funk und Mathematik  
FFM-FGAN  
Neuenahrer Strasse 20  
D-5307 Wachtberg 7  
Germany

Dr Walter A. Flood  
Director, Geosciences Division  
US Army Research Office  
PO Box 12211  
Research Triangle Park, NC 27709-2211  
United States

Mr G. Neiningner  
Standard Elektrik Lorenz AG  
Lorenzstrasse 10  
D-7000 Stuttgart 40  
Germany

Mr F. Le Chevalier  
L.C.T.A.R.  
6, rue Nieuport  
Boite Postale 16  
78143 Vélizy Villacoublay  
France

Dr L.C. Oldfield  
Royal Signals and Radar Establishment  
DP3 Division  
St Andrews Road  
Great Malvern, Worcs, WR14 3PS  
United Kingdom

### PANEL EXECUTIVE

**Mail from Europe:**  
AGARD—OTAN  
Attn: EPP Executive  
7, rue Ancelle  
92200 Neuilly sur Seine  
France

**Mail from US and Canada:**  
AGARD—NATO  
Attn: EPP Executive  
APO AE 09777

Tel: 33(1) 47 38 57 68  
Telex: 610176 (France)  
Telefax: 33(1) 47 38 57 99

# Foreword

The recent conflict in the Gulf brought realities of a war into living rooms of many world citizens. As people took their ringside seats daily to view the modern warfare on the screen they could not help but learn the importance played by the technology in this war. This became quite clear, even in the beginning few days, as the war unfolded before our very eyes.

The subject matter of Target Scattering and its associated detection problems was proposed almost two years earlier, before there was any inkling that there would be a war. At the time it was only thought that much scientific and technological progress on this subject had been made. It would be timely to review and report the latest work. Little did we know that there would be actual display of technological prowess for the world to see. Instantly, the subject matter was made timely and relevant. Early worries about travel restrictions evaporated with the unexpected speedy conclusion of the war. Accordingly, the symposium was well attended, better than any in recent memory, and all the scheduled papers were presented.

The symposium was organized into six sessions: two on Clutter Modeling and Measurements, one on Target Scattering, one on Signal Processing, one on Polarimetrics, one on Applications, and two on classified topics. Altogether there were fifty-two papers. It was indeed a very busy four-day meeting.

We wish to thank all members of the Symposium Technical Programme Committee for their help in soliciting papers and in organizing and arranging papers into coherent sessions. *There were a lot of communications among members, sometimes rather frantic in order to meet deadlines.* We would not know how these deadlines could be met before the age of fax. All the authors should be thanked for sharing their latest results with us. They had set high standards for others to emulate. We would also like to thank all the Session Chairmen and Round Table Participants for providing technical expertise. At Illinois, Mrs Belva Edwards transcribed the nonclassified Round Table Discussions from the tape, and she and Mrs Phyllis Dobney did a lot of typing. Finally the Office of EPP Executive was very helpful and cooperative in putting the Symposium in its final form. We wish to express our appreciation to these and other unnamed persons for making this symposium a success.

F. Christophe  
Toulouse, France

K.C. Yeh  
Urbana, Illinois

June 1991

# Contents

	Page
<b>Theme/Thème</b>	iii
<b>Electromagnetic Wave Propagation Panel and Technical Programme Committee</b>	iv
<b>Foreword</b>	v
	Reference
 <b>SESSION I – CLUTTER MODELS AND MEASUREMENTS – PART A</b> Session Chairman: Mr Christophe	
<b>Radar Ground Clutter Measurements and Models, Part 1: Spatial Amplitude Statistics</b> by J.B. Billingsley	1
<b>Radar Ground Clutter Measurements and Models, Part 2: Spectral Characteristics and Temporal Statistics</b> by H.C. Chan	2
<b>A Model of Coherent Radar Land Backscatter</b> by G.C. Sarro	3
<b>A Model for Bistatic Scattering of Electromagnetic Waves from Foliage Covered Rough Terrain</b> by R.J. Papa and D.T. Tamasanis	4
<b>Bistatic Scattering Statistics of Deciduous Trees</b> by K.V.N. Rao, W.G. Stevens and J. Mendonca	5
 <b>SESSION I – CLUTTER MODELS AND MEASUREMENTS – PART B</b> Session Chairman: Dr Vant	
<b>Altair UHF Observations of Backscatter Enhancement</b> by D.L. Knepp	6
<b>Parabolic Equation Modelling of Backscatter from the Rough Sea Surface</b> by M.F. Levy	7
<b>Experimental Characterization of Amplitude Distribution of Mediterranean Sea Clutter</b> by G. Corsini et al.	8
<b>Modeling and Measuring Millimeter-Wave Scattering from Snow-Covered Terrain</b> by F.T. Ulaby, Y. Kuga and R. Austin	9
<b>RENE, un Radar Aéroporté Simple à Haute Résolution pour l'Analyse des Caractéristiques du Fouillis en Bande X</b> (RENE, a Simple High Resolution Airborne Radar for Analyzing Clutter Characteristics at X Band) par N. Le Loch, D. Vidal-Madjar et J.P. Hardange	10†

---

† Not available at the time of printing.

## SESSION II — TARGET SCATTERING

Session Chairman: Dr Oldfield

<b>Analytical Prediction of EM Scattering by Complex Obstacles within Electrically Large Open Cavities</b> by P. Pathak	11
<b>RCS Prediction Models Based on PO and PTD and State of Validation</b> by V. Stein	12
<b>Aspects of Radar-Cross-Section Calculation for Targets of Complex Structure</b> by O. Weiland and J. Wendiggensen	13
<b>RCS Calculations of 3-Dimensional Objects Modeled by CAD</b> by I. De Leeneer, E. Schweicher and A. Barel	14
<b>Modèle de Calcul de Ser Haute Fréquence Basé sur des Techniques de CAO: SERMAT</b> (High-Frequency CAD Based Scattering Model: SERMAT) par D. Goupil et M. Boutillier	15
<b>Parametric Bicubic Spline and CAD Tools for Complex Targets Shape Modelling in Physical Optics Radar Cross Section Prediction</b> by A. Delogu and F. Furini	16
<b>Mesures de Surfaces Equivalentes Kadar en VHF/UHF</b> (Radar Cross Section Measurements in VHF/UHF) par J. Saget	17

## SESSION III — SIGNAL PROCESSING AND S.A.R.

Session Chairman: Dr Klemm

<b>Two-Dimensional Signal Processing for Airborne MTI</b> by R. Klemm and J. Ender	18
<b>The Application of Lattice-Structure Adaptive Filters to Clutter-Suppression for Scanning Radar</b> by C.J. Gibson	19
<b>Use of Target Spectrum for Detection Enhancement and Identification</b> by S. Pardini, P.F. Pellegrini and P. Piccini	20
<b>Classification d'Images SAR en Vue de Détection de Cibles</b> (SAR Image Classification for Target Detection) par A. Beaupère et G. Foulon	21
<b>Comparaison des Performances en Détection et Reconnaissance d'un Radar Imageur Bipolarisation HH-VV et d'un Polarimètre Total HH-HV-VH-VV</b> (Comparison of the Detection and Reconnaissance Capabilities of an HH-VV Bipolar Imaging Radar and an HH-HV-VH-VV Polarimeter) par J.M. Nasr	22
<b>Grazing Angle Dependency of SAR Imagery</b> by C.J. Baker, J.A.C. Beattie and R.G. White	23†
<b>Imaging Effects of Target Angular Motion on Spotlight Synthetic Aperture Radar Images</b> by A. Damini	24*

\* Published in Conference Proceedings Supplement — AGARD-CP-501 (Supp.).

† Not available at the time of printing.

**SESSION IV – POLARIMETRICS**

Session Chairman: Dr Flood

<b>Contribution de la Polarimétrie dans la Discrimination, la Classification et l'Identification de Cibles Radar</b> (Contribution of Polarimetry in Radar Targets Discrimination, Classification and Identification) par E. Pottier et J. Saillard	<b>25</b>
<b>Utilisation de la Polarisation pour l'Analyse Fine des Cibles Radar</b> (The Use of Polarization for Fine Analysis of Radar Targets) par C. Titin-Schnaider	<b>26</b>
<b>Polarimetric Covariance Matrix Analysis of Random Radar Targets</b> by E. Lüneburg, V. Ziegler, A. Schroth and K. Tragl	<b>27</b>
<b>Millimeter Wave Polarimetric Scatterometer Systems: Measurement and Calibration Techniques</b> by Y. Kuga, K. Sarabandi, A. Nashashibi, F.T. Ulaby and R. Austin	<b>28</b>
<b>Polarimetric Techniques and Measurements at 95 and 225 GHz</b> by J. Mead, R. McIntosh, P. Langlois and P. Chang	<b>29</b>
<b>Polarimetric Monopulse Radar Scattering Measurements of Targets at 95 GHz</b> by R.J. Wellman et al.	<b>30</b>

**SESSION V – APPLICATIONS**

Session Chairman: Mr Fuerxer

<b>Reduction of Target Scattering by Tropospheric Modification</b> by K.H. Craig	<b>31</b>
<b>Stochastic Model of Terrain Effects upon the Performance of Land-Based Radars</b> by S.P. Tonkin and M.A. Wood	<b>32</b>
<b>Measurements of Low Angle Tracking Errors Induced by Multipath at 95 and 140 GHz</b> by H.B. Wallace, S.R. Stratton and D.G. Bauerle	<b>33*</b>
<b>Overview of Weather Clutter Research at the Alberta Research Council</b> by C. Gibson and B. Kochtubajda	<b>34</b>
<b>Round Table Discussion – I</b>	<b>RTD-1</b>

**SESSION VI – CLASSIFIED SESSION – PART A**

Session Chairman: Dr Neininger

<b>Target Classification from Engine Modulated Signals</b> by Y.T. Chan and P.R. Jegard	<b>35*</b>
<b>Non-Cooperative Jet Aircraft Identification by Radar</b> by D. Faubert and F. Tremblay	<b>36*</b>
<b>Performance of Non-Cooperative Target Recognition Based on Jet Engine Modulation of Radar Echoes</b> by M.E. Hoffmann	<b>37*</b>
<b>Radar Identification of Helicopters</b> by H. Kuschel	<b>38*</b>

\* Published in Conference Proceedings Supplement – AGARD-CP-501 (Supp.)

	<b>Reference</b>
<b>Possible Polarimetric Techniques for the Enhancement of Targets in Clutter</b> by D. Bird	<b>39*</b>
<b>Optimal Polarimetric Processing for Enhanced Target Detection</b> by L.M. Novak	<b>40*</b>
<b>Signal Processing and Error Correction for a High Resolution Polarimetric Imaging Radar</b> by D. Mehrholz	<b>41*</b>
<b>"SOURSAR" Génération de Scènes Opérationnelles pour un Simulateur de Radar SAR</b> ( <b>"SOURSAR"</b> the Generation of Operational Scenes for an SAR Radar Simulator) par J.C. Motet et C. Cochin	<b>42*</b>
<b>Synthetic Target Scene Generation Using 35 GHz SAR Data</b> by J.C. Henry and D.E. Kreithen	<b>43*</b>
 <b>SESSION VI — CLASSIFIED SESSION — PART B</b> <b>Session Chairman: Mr Le Chevalier</b>  	
<b>Determination of Target Signatures with a Coherent, Frequency Agile Monopulse Radar at 94 GHz</b> by H. Schimpf, H. Essen and E.P. Baars	<b>44*</b>
<b>Broadening of the Doppler Spectrum of a Moving Target due to Rough Terrain</b> by H. Schimpf	<b>45*</b>
<b>Three Dimensional Radar Imaging of Targets and Clutter at W-Band</b> by H.B. Wallace, M.R. Zoll and R.L. Bender	<b>46*</b>
<b>Noncoherent, Frequency Agile 94 GHz Millimeter Wave Radar for the Detection of Targets in Clutter and Coarse Target Classification</b> by G. Neiminger and A. Strecker	<b>47*</b>
<b>UK Millimetre Radar Research for Anti-Armour Applications</b> by G.N. Crisp et al.	<b>48*</b>
<b>Sea Clutter under Low Angle Incidence at 94 GHz</b> by K. Makaruschka and H. Essen	<b>49*</b>
<b>Models for Surface Scattering and Signal Processing in a Pulsed Radar Altimeter</b> by G. Savini, P. Cassino and C. Svara	<b>50*</b>
<b>Radar Signature Analysis of a Low Observable Stand-off Configuration</b> by A. Nappi and F. Costa	<b>51†</b>
<b>Modélisation et Génération du Fouillis de Sol dans un Banc d'Essai Radar/Autodirecteur</b> (Modelling and Generation of Clutter on a Radar Homing Head Test Bench) par J.C. Auber et D. Passelaigue	<b>52*</b>
<b>Round Table Discussion — 2</b>	<b>RTD-2*</b>

\* Published in Conference Proceedings Supplement — AGARD-CP-501 (Supp.).

† Not available at the time of printing.

# **RADAR GROUND CLUTTER MEASUREMENTS AND MODELS PART 1: SPATIAL AMPLITUDE STATISTICS**

by  
J. Barrie Billingsley  
MIT Lincoln Laboratory  
P.O. Box 73  
Lexington, MA 02173  
USA

## **SUMMARY**

At MIT Lincoln Laboratory, we have collected a large multifrequency data base of radar ground clutter measurements from many sites. We employ our clutter data to develop clutter models. Of particular interest to us is the site-specific prediction of PPI ground clutter maps for ground-sited radars, that is, in simulating the spatial variation of ground clutter. This paper describes our measurements, and presents a statistical clutter model for spatial amplitude statistics based on depression angle, terrain type, RF frequency, and radar resolution.

## **1. INTRODUCTION**

MIT Lincoln Laboratory has collected a large data base of radar ground clutter measurements [1]. These measurements were conducted at 42 different sites in the United States and Canada. At each site, measurements were conducted in five different frequency bands from VHF to X-band. The various terrain types encompassed within these measurements include forest, farmland, urban, mountains, desert, and marshland. Lincoln Laboratory shares these data with Canada and the U.K., and coordinated analysis and clutter modeling activities are proceeding in all three countries.

The principal objective of our measurement program has been the development of a reliable model for the prediction of ground clutter spatial amplitude statistics for illumination angles near grazing incidence. Such low angles are of usual occurrence when ground-based air defense radars are operating against low-altitude targets. In this paper, we describe the multifrequency clutter model developed from our measurements which is currently in use in air defense studies at Lincoln Laboratory. The model captures all of the important trends that we have observed empirically in our measurement data. Many of these trends are discussed in this paper.

### **1.1 Measurement Program**

We refer to our multifrequency radar ground clutter measurement program as Phase One, in contrast to an earlier Phase Zero program. At each Phase One site, we measured all of the discernible ground clutter within the field-of-view through 360 degrees in azimuth and from one to 50 km or more in range, at five frequencies, two polarizations, and two range resolutions. The duration of time that our equipment spent at each site making these measurements was typically

two to three weeks. The amount of raw, digitally recorded, pulse-by-pulse measurement data collected at each site was usually such as to fill about 25 to 30 high-density magnetic tapes. Within the measurement program we included seven repeated data collection visits to a few sites at different times of the year to provide seasonal variations in our clutter measurement data base. Altogether we maintained our Phase One measurement equipment in the field for three years conducting this 49-site-visit measurement program.

### **1.2 Measurement Equipment**

Our Phase One clutter measurement equipment was self-contained and mobile, principally housed within three sixteen-wheeler tractor-trailer combination trucks and manned by a five-man crew. The equipment included a transportable antenna tower, expandable in six sections to a maximum height of 30 m. A photograph of the Phase One equipment erected at our Lethbridge West site in Alberta, Canada is shown in Figure 1.

Important Phase One system parameters are shown in Figure 2. Phase One operated in five frequency bands: VHF, UHF, L-, S-, and X-bands. These five bands shared three antenna reflectors. The large 3m by 9m reflector was a shared dual-frequency antenna between VHF and UHF with each band having its own set of crossed dipole feeds. The intermediate sized reflector was also a similar shared reflector between L- and S-bands, with a crossed dipole feed at L-band and a dual polarized waveguide feed at S-band. The L- and S-band feeds were protected by a radome. The small reflector was dedicated to X-band, which was fed with a dual polarized horn. The antenna beams were relatively wide in elevation and were fixed with boresight horizontal at zero degrees depression angle. Our measured clutter statistics were corrected for gain variations on the fixed elevation beam both within and beyond the 3 dB points, depending on the depression angle to the backscattering terrain point.

\*Three other papers in this Symposium, authored respectively by a) Dr. Chan, b) Dr. Sarno, and c) Dr. Tonkin and Dr. Wood are also based on the Lincoln Laboratory clutter data.

The Phase One radar was a computer controlled, instrumentation radar with high data rate recording capability (i.e., linear receiver, with 13 bit analog-to-digital converters in in-phase and quadrature channels), and maintained coherence and stability sufficient for 60 dB two-pulse-canceler clutter attenuation in postprocessing. The instrument had uncoded, pulsed waveforms, with two pulse lengths available in each band to provide high and low range resolution as is shown in Figure 2. Polarization was selectable as vertical or horizontal, with transmit and receive antennas always co-polarized (i.e., the cross-polarized component in the radar return signal could not be received). The Phase One system activated one combination of frequency, polarization, and pulse length at a time, for any particular clutter experiment. These three major radar parameters as well as other parameters (e.g., spatial extent in range and azimuth, number of pulses and pulse repetition rate, etc.) were selectable at the on-board computer console for each clutter experiment recorded. Internal calibration was provided for every clutter measurement. External calibration was provided through use of standard gain antennas and corner reflectors mounted on portable towers.

### 1.3 Measured Clutter Maps

Figure 3 shows measured ground clutter maps for all five Phase One frequencies at one of our sites high on the east bank of the Peace River in Alberta, Canada. In these maps, the maximum range is 23 km, and clutter is shown as being white where  $\sigma^0 F^4 \geq -40$  dB. To the west in each map is the well-illuminated river valley; to the east, level terrain is illuminated at grazing incidence. As patterns of spatial occurrence of ground clutter, all five clutter maps in Figure 3 are quite similar. The reason for this is that the relatively strong clutter being shown in Figure 3 largely comes from visible terrain. We predict these visible regions geometrically using digital terrain elevation data. Then we use the clutter model to provide clutter amplitudes within the visible regions.

At all five frequencies in Figure 3, the nature of the clutter tends to be granular and patchy. That is, the clutter is coming from discrete sources distributed over visible surfaces. However, the granularity is greater at grazing incidence to the east, less at the higher depression angles to the west. Such effects are principally due to depression angle as it affects microshadowing. Depression angle is the angle below the horizontal at which a clutter cell is observed at the radar. Also obvious in Figure 3 is the effect of increasing azimuth beamwidth with decreasing frequency causing increasing azimuthal smearing of the clutter.

### 1.4 Clutter Physics

The major elements that are involved in low-angle clutter are shown

in Figure 4. We focus our attention on directly illuminated clutter from large kilometer-sized regions of visible terrain. Our goal is to predict the distribution of clutter strengths over such regions. We use Weibull statistics, characterized by Weibull mean strength and Weibull spread parameter.

Within visible regions, at the low angles of ground-sited radar, clutter sources tend to be discrete vertical features, either objects associated with the land cover, or just high points of terrain. The discrete clutter cells are separated by microshadowed cells where the radar is at its noise floor. As depression angle rises, the amount of microshadowing decreases. As a result, mean strength rises with increasing angle, and the spread parameter falls with increasing angle. This is a fundamental effect.

We use depression angle to describe the geometry of illumination of the clutter cell. Depression angle is a quantity relatively simple and unambiguous to determine, depending as it does simply on range and relative elevation difference between the radar antenna and the backscattering terrain point. Our past attempts to use grazing angle (i.e., the angle between the direction of illumination and the tangent to the local terrain surface at the backscattering terrain point) have met with little additional success, partly due to difficulties associated with scale, precision, and accuracy in unambiguously defining local terrain slope, and partly due to the fact that many clutter sources tend to be vertical discrete objects associated with the land cover.

The terrain between the radar and the clutter region affects the measurement through propagation influences such as multipath which can change the effective gain at which the clutter is measured compared to free space. All such effects, both reflective and diffractive, are collected within the propagation factor  $F$ , which is defined to be the ratio of the incident field that actually exists at the clutter cell being measured to the incident field that would exist there if the clutter cell existed by itself in free space. What we measure as clutter strength is the product of the clutter coefficient itself,  $\sigma^0$ , defined to be radar cross section (RCS) per unit ground area in the resolution cell, and the fourth power of the propagation factor. Propagation effects cannot be separated from our measurements, and, particularly at low frequencies on open terrain, can dominate them.

## 2. CLUTTER MEASUREMENTS

### 2.1 Mean Strength

Figure 5 shows measured values of mean clutter strength versus frequency at 36 different rural sites. Results are shown for two pulse lengths, and for two polarizations. Each plotted point in



Figure 5 is the mean strength over a selected spatial macroregion, one such region per site. What we see in the data of Figure 5 is extreme variability. Variability is the most salient feature of ground clutter. We see about 20 dB of variability at X-band, increasing to almost 70 dB at VHF.

The scatter plot of Figure 5 is basically funnel shaped. We next specify the central or median position of this scatter plot in each frequency band. The results are tabulated in Table 1. In

Table 1  
Mean Clutter Strength (dB) vs Frequency  
(36 rural sites)

Frequency Band				
VHF	UHF	L-	S-	X-band
-29.6	-30.3	-27.8	-30.7	-27.5

overall terms, these results indicate that general mean ground clutter strength is remarkably invariant with RF frequency, VHF through X-band, at or about the -30 dB level, with no strong trend.

Besides characterizing the central level in our funnel plot, we also wish to quantify the spread whereby the funnel is wide at VHF and narrow at X-band. We do this by computing, for each band, the standard deviation or one-sigma range of variation of all the contributing mean strengths. The results are shown in Table 2. We see a strong clear monotonic

Table 2  
Standard Deviation in  
Mean Clutter Strength (dB)

Frequency Band				
VHF	UHF	L-	S-	X-band
16.6	13.6	9.7	7.1	5.8

trend in Table 2 where this one-sigma range of variation decreases with increasing frequency, from 16.6 dB at VHF to 5.8 dB at X-band. That is, mean clutter strengths in rural terrain vary much more at VHF than at X-band. The reasons are associated with VHF clutter strengths increasing in forest due to decreased vegetative absorption at VHF compared to the microwave bands, and with VHF clutter strengths decreasing in open level farmland because of multipath loss.

In what follows, we reduce the clutter variability shown in Figure 5 and move to a predictive capability by classifying terrain more finely than just "general rural".

## 2.2 Clutter Classifiers

Table 3 shows our major clutter classifiers. These are what need to be

Table 3  
Major Clutter Classifiers

Terrain:	
Urban	
Mountains	
Forest	
Farmland	
Desert, marsh, or grassland	
(few discretely)	
Relief (terrain slope):	
High	> 2°
Low	< 2°
Moderately low	1° to 2°
Very Low	< 1°
Depression Angle:	
High	1° to 2°
Intermediate	0.3° to 1°
Low	< 0.3°

known about terrain to predict clutter strength. First, gross terrain type requires specification. Table 3 shows five major categories. Second, terrain roughness requires specification. Table 3 shows two major categories, high-relief with terrain slopes greater than 2°, and low-relief with terrain slopes less than 2°. Sometimes we need to further distinguish low-relief as "moderately low" or "very low". Third, the depression angle at which the radar illuminates the ground requires specification. We shall see that small differences in depression angle cause large differences in clutter strength in ground-sited radar.

## 2.3 Forest and Farmland

Figure 6 is a three part figure showing mean clutter strength versus frequency for low-relief forest in three regimes of depression angle. The horizontal bars in these figures are the limits of the data in the funnel scatter plot of Figure 5. Figure 6(a) shows results for two sites at relatively high depression angles of 1° and 2°. In Figure 6(a), we see decreasing strength with increasing frequency. This is caused by the absorption characteristics of the forest, wherein with increasing frequency the foliage becomes increasingly absorptive and hence decreasingly diffuse reflective. Figures 6(b) and (c) show results at lower depression angles. In these three figures, we see at all frequencies a significant trend of increasing strength with increasing depression angle. Over the forest, the propagation factor is unity, so these are trends in intrinsic  $\sigma^0$ .

Figure 7 is a two-part figure showing mean clutter strength versus frequency for low-relief farmland sites in two regimes of relief. Figure 7(a) shows results for six very low-relief (i.e., level) farmland sites with terrain slopes less than 1°. For these level farmland sites in Figure 7(a), we see strongly increasing clutter strength with increasing frequency. This is an

opposite trend to that which we observed in Figure 6(a) for forest, which was a trend in intrinsic  $\sigma^0$ . The trend for level farmland in Figure 7(a), in contrast to forest, is entirely due to multipath loss entering through the propagation factor  $F$ . Thus, at low frequency, VHF, on level open terrain, strong forward reflections cause broad multipath lobes, and clutter returns are received well on the underside of the first lobe deep in the horizon plane null. As frequency rises, the multipath lobes become narrower, clutter strengths rise, until, in the microwave regime, multiple lobes play across typical clutter sources, and the effect averages out.

Figure 7(b) shows results for three moderately low-relief farmland sites with terrain slopes between  $1^\circ$  and  $2^\circ$ . In such terrain of slightly greater relief, terrain surfaces rise up into illumination by the first lobe, so clutter strengths remain high.

## 2.4 Spread in Amplitude Distributions

Figure 8 shows complete spatial amplitude distributions, cumulative probability versus clutter strength, for X-band data. It has been the mean strengths of such distributions that have thus far been under discussion in Section 2. Now we shall discuss spread in these distributions.

At low angles ( $< 0.25^\circ$ ), the distribution in Figure 8 is very broad because of discretely and microshadow. With increasing angle, the spread decreases, first with very small steps in angle in low-relief terrain, then with larger steps in angle in high-relief terrain. In the high-angle limit ( $6^\circ$  to  $8^\circ$ ) for a ground-sited radar, we have very close to Rayleigh statistics, because at such high airborne-like angles, we have floodlit illumination, no microshadowing, and less effect by discretely. So as angle increases, spread decreases, and we gradually transition from the spiky, low-angle Weibull regime to the better-behaved high-angle Rayleigh regime.

Figure 8 showed the effect of depression angle on spread. Figure 9 shows the effect of resolution on spread. In Figure 9 the Weibull spread parameter  $a_w$  is plotted versus the spatial resolution of the radar in square meters. What we observe in Figure 9 is decreasing spread with increasing cell size. As the cell size increases, the amount of averaging within the cell increases, and the variability from cell to cell decreases. These different cell sizes come about from our different range resolutions and beamwidths at different frequencies. Any dependence of  $a_w$  on frequency is also bound up in the results of Figure 9, but this is a secondary effect compared with the strong dependence of  $a_w$  on resolution. More specifically in Figure 9, in farmland at low depression angle large spread occurs

at high resolution because this process is so discrete dominated. In forest at low angle, less spread occurs because forest is a more homogeneous surface. And in forest at high angle, still less spread occurs as a result of the improved illumination.

## 2.5 Polarization

Polarization has very little general effect on clutter amplitude statistics. In the distribution of differences of vertically polarized mean clutter strength minus horizontally polarized mean clutter strength across all of our measurements, the median difference is only 1.48 dB. However, occasional specific measurements can show more significant variation with polarization. As one extreme example, at VHF in steep mountainous terrain, we have measurements from two different sites in which mean clutter strengths at VHF were 7 to 8 dB stronger at vertical polarization than at horizontal.

## 2.6 Weather and Season

General effects of weather and season on our measured clutter amplitude distributions are small and without apparent trend. On the basis of a repeated subset of measurements over the 2 to 3 week stay at every Phase One site, we specify the one-sigma day-to-day variability in mean clutter strength, largely due to changes in weather, to be 1.1 dB, with occasional variations (i.e., 10 percent) greater than 3 dB. The Phase One equipment made seven repeated visits to selected sites to investigate seasonal variations. On the basis of these measurements, we specify the one-sigma seasonal variability in mean clutter strength to be 1.6 dB, with occasional variations (i.e., 10 percent) greater than 4.8 dB. These variations are small because low-angle clutter is dominated by discrete sources which are usually little affected by weather and season.

## 3. MULTIFREQUENCY CLUTTER MODEL

### 3.1 Approach

Figure 10 compares terrain visibility with measured clutter visibility at our Katahdin Hill site in eastern Massachusetts. To the left in Figure 10, geometric line-of-sight terrain visibility is predicted using digital terrain elevation data. In the middle of Figure 10 is the measured clutter map at the same site thresholded for  $\sigma^0 F^4 > -40$  dB. In gross measure, these two patterns of terrain visibility and clutter visibility are quite similar. This similarity is borne out in the graph to the right in Figure 10, which shows percent circumference visible versus range in both maps.

Our approach to clutter modeling is as follows. First we use the terrain elevation data to deterministically predict where the clutter is. Then, depending on depression angle and terrain type, we use our statistical clutter

model to provide the strength of the clutter in each visible cell. This is what we mean by site-specific modeling.

### 3.2 Weibull Statistics

We engage in the empirical prediction of ground clutter spatial amplitude distributions using Weibull statistics. Weibull distributions provide the wide degree of spread appropriate to low-angle ground clutter amplitude distributions. The Weibull cumulative distribution function may be written as:

$$P(x) = 1 - \exp\left[-\frac{\ln 2 \cdot x^b}{(\sigma_{50}^b)^b}\right]$$

where

$\sigma_{50}$  = median value of  $x$ ,

$b$  =  $1/a_v$ ,

$a_v$  = Weibull spread parameter.

The mean-to-median ratio for Weibull statistics is

$$\frac{\bar{\sigma}_v}{\sigma_{50}} = \frac{\Gamma(1+a_v)}{(\ln 2)^{1/a_v}}$$

where  $\bar{\sigma}_v$  is the mean value of  $x$  and  $\Gamma$  is the Gamma function. Here, the random variable  $x$  represents clutter strength  $\sigma_v^4$ .

From these relationships, we see that a Weibull distribution may be characterized by  $\bar{\sigma}_v$  and  $a_v$ . Thus, our modeling objective becomes one of defining these coefficients as a function of the terrain type within the clutter patch, the depression angle at which the radar illuminates the clutter patch, and the radar parameters of RF frequency and spatial resolution.

### 3.3 Clutter Model

Multifrequency modeling information for predicting ground clutter amplitude statistics as they occur over macro-regions of geometrically visible terrain is presented in Figure 11. This information is provided in terms of the Weibull coefficients,  $\bar{\sigma}_v$  and  $a_v$ . Most terrain types in Figure 11 involve several depression angle regimes. The important general terrain types are threefold, namely: 1) rural/low-relief terrain, in which terrain slopes are usually less than two degrees; 2) rural/high-relief terrain, in which terrain slopes are usually greater than two degrees; and 3) urban terrain. A fourth general category comprising terrain observed at negative depression angle is included. Terrain observed at negative depression angle is usually relatively steep.

Within rural/low-relief terrain, our model further distinguishes the following specific important subclass terrain types: 1) continuous forest; 2) open

farmland; and 3) open desert, marsh or grazing land with very low incidence of large discrete vertical objects (e.g., farm buildings and machinery, transmission line poles and pylons, isolated trees, etc.). Within rural/high-relief terrain, we particularly separate out subclass terrain types of: 1) continuous forest; and 2) mountains. Within urban terrain, we separate out the subclass of urban terrain as observed on open low-relief terrain supportive of multipath. Concerning the several subcategories of terrain contained within each of the three general terrain types in Figure 11, the general category (i.e., category (a)) is applicable only if the terrain in question fails to meet the specification of any of the specific subcategories (i.e., category (b), (c), or (d)) within a group. That is, the general category applies to mixed or composite terrain that is neither completely open nor completely tree-covered. The subcategorization of terrain within each major group becomes increasingly important with decreasing frequency.

Altogether, the model of Figure 11 consists of 27 combinations of terrain type and depression angle. For each combination of terrain type and depression angle, the clutter model provides Weibull mean clutter strength as a function of radar frequency " $f$ ", VHF through X-band, as  $\bar{\sigma}_v(f)$ , and provides the Weibull spread parameter as a function of radar spatial resolution " $A$ " over the range between  $10^3$  and  $10^6$  m<sup>2</sup>, as  $a_v(A)$ . The spread parameter is obtained from linear interpolation on  $\log_{10}(A)$  between the values provided for  $A = 10^3$  m<sup>2</sup> and  $A = 10^6$  m<sup>2</sup>. The total matrix of information in Figure 11 codifies all important multifrequency trends that we have observed in our measured clutter amplitude distributions. Much of the  $\bar{\sigma}_v$  data of Figure 11 is plotted in Figure 12.

### 3.4 Model Validation

Our Weibull clutter model has now been in use at Lincoln Laboratory for several years in radar system studies involving clutter limited operation against various airborne targets. These studies have ranged from VHF surveillance and track to X-band fire control. Since the clutter model directly affects the outcomes of such studies, we have strong and ongoing interest in validating and improving the clutter model. In validating a clutter model, we hypothesize an air defense engagement to take place at one of our clutter measurement sites, and compute system performance in two ways: 1) using the actual measured clutter at that site; and 2) using the clutter model to simulate clutter at that site. Successful validation requires that the performance measure computed using modeled clutter be acceptably similar to that computed using the actual clutter. Model validation encompasses many measurement sites.

For X-band fire control in a surface-to-air missile system, the performance parameter we employ is the site-specific footprint of all points at which an intercept can be made. The Weibull model works well in predicting the site-specific intercept footprint. We then generalize system performance by computing the median intercept footprint of the system over many sites. A simple spherical earth, constant  $\sigma^0$  clutter model cannot deliver the same general performance as our more complicated model. That is, the constant  $\sigma^0$  required in the simple model is system dependent, whereas our Weibull statistical model works well for various systems.

For VHF track-while-scan surveillance radar, the performance parameter we employ is tracker coverage area. It is more difficult to predict VHF clutter than X-band clutter due to propagation effects. Still, our model is adequate in high-relief terrain where propagation effects are less dominant. However, in open low-relief terrain, we can improve our Weibull model by adding a deterministic computation of multipath propagation. We are engaged in this and other ways to improve our model.

### 3.5 Model Improvement

In the clutter model of Figure 11, clutter is represented as a Weibull statistical process occurring over visible terrain regions. The Weibull distributions aggregate the widely varying returns received predominantly from an infinity of discrete sources. Current studies to improve this model include the following:

- 1) separating the strongest discretely and introducing grazing angle dependence on the residual clutter background;
- 2) introducing clutter into shadowed regions;
- 3) utilizing improved land cover information as it becomes available;
- 4) improving propagation prediction at clutter source heights;
- 5) investigating non-site-specific clutter modeling.

Figure 11 conveniently represents the structure of our clutter model. Within this structure, we have an adaptive modeling capability resident on our computer. That is, we have on file 100,000 measured clutter spatial amplitude distributions together with their terrain descriptive parameters. The clutter model is the template by which we sort these data. Not only can we provide a general template (i.e., Figure 11), but we can also adjust the template to provide more detailed results specific to an individual user's particular interests.

## 4. CONCLUSION

At MIT Lincoln Laboratory, we have a large multifrequency data base of radar ground clutter measurements. Within this data base, we have different kinds of experiments suitable for different purposes. Some experiments provide cell-by-cell variation over wide spatial extent with relatively few (e.g., 125) pulses per cell. Other experiments constitute long-time-dwells (e.g., 30,720 pulses) on selected cells suitable for studies involving temporal statistics. All of our calibrated clutter data exist in pulse-by-pulse in-phase and quadrature format and thus are suitable for studies involving coherent processing.

We use our clutter data to develop clutter models. Of particular interest to us is the site-specific prediction of PFI ground clutter maps. This paper describes our approach to such prediction, wherein we employ Weibull distributed random numbers to represent cell-by-cell variations in clutter strength over visible regions of terrain viewed from the radar site. Validation of this modeling approach is based on simulated radar system performance in measured clutter matching that in modeled clutter. Our general clutter model continues to be developed and improved upon. The modeling information resident on our computer allows us to adapt our predictions more closely to particular situations as interest in them arises.

## REFERENCE

1. J. B. Billingsley and J. F. Larrabee, MIT Lincoln Laboratory, "Multi-frequency Measurements of Radar Ground Clutter at 42 Sites," 1991, Technical Report TR-916.

## ACKNOWLEDGEMENTS

The results of this paper are due to dedicated efforts by many people in measuring, reducing, and analyzing our ground clutter data. Many of our measurements were made in Canada within a joint program in which support was provided by the Canadian Department of National Defence. The Phase One measurement equipment was fabricated and operated by the General Electric Company. At Lincoln Laboratory, day-to-day assistance in managing and interpreting the large volume of analysis results has been provided by John F. Larrabee. Application of the clutter model in systems analysis and subsequent validation and improvement of the model has been under the jurisdiction of Dr. John C. Eidson. The skillful efforts of Ms. Pat DeCuir in preparing the manuscript are much appreciated.

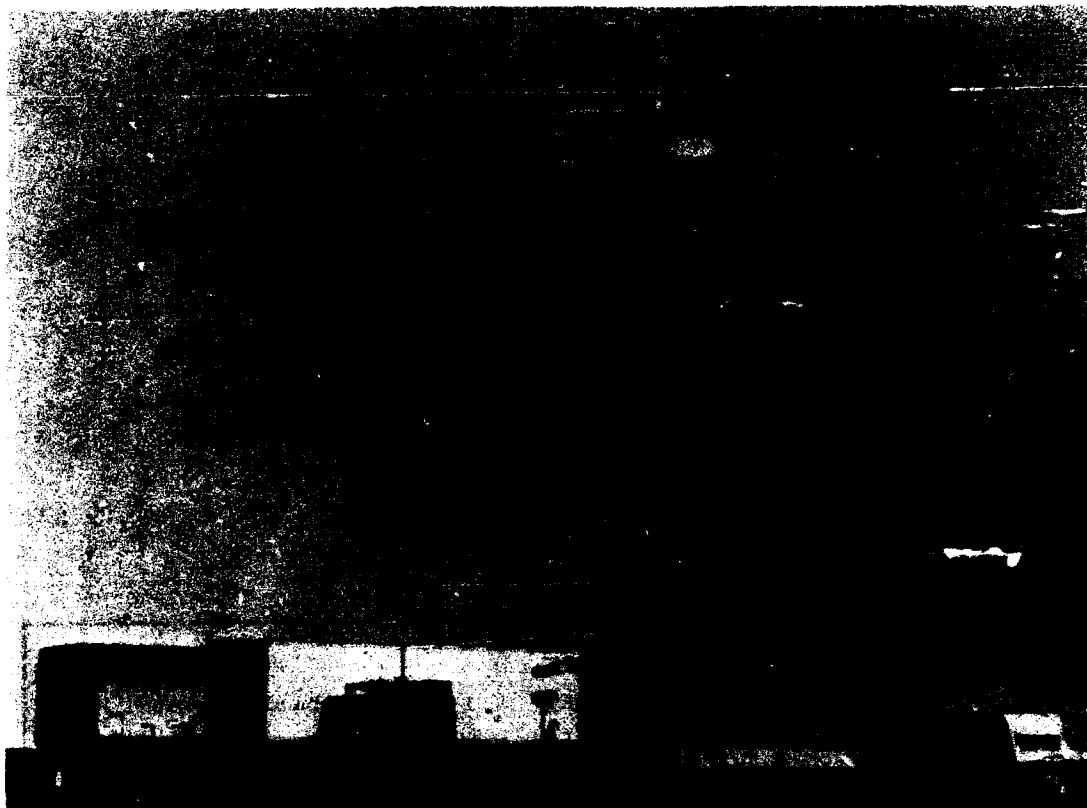


Figure 1. Phase One equipment at Lethbridge, Alberta.

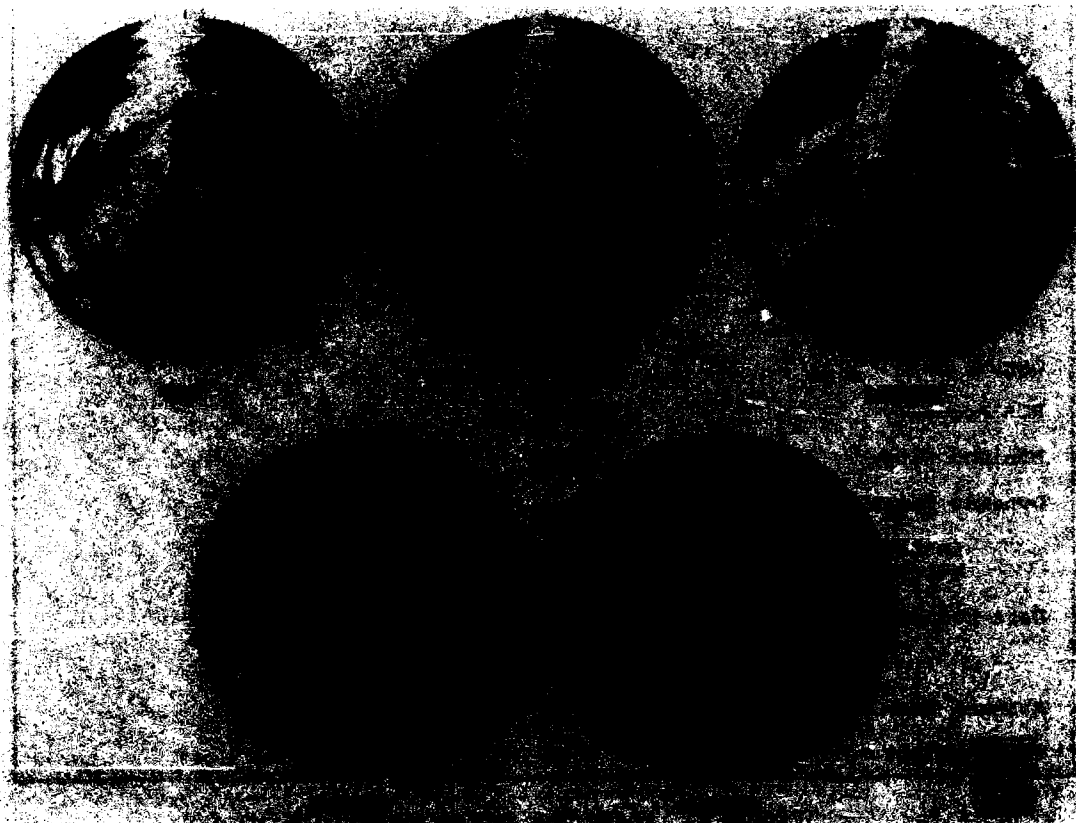


Figure 3. Measured multifrequency ground clutter maps at Peace River, Alberta.

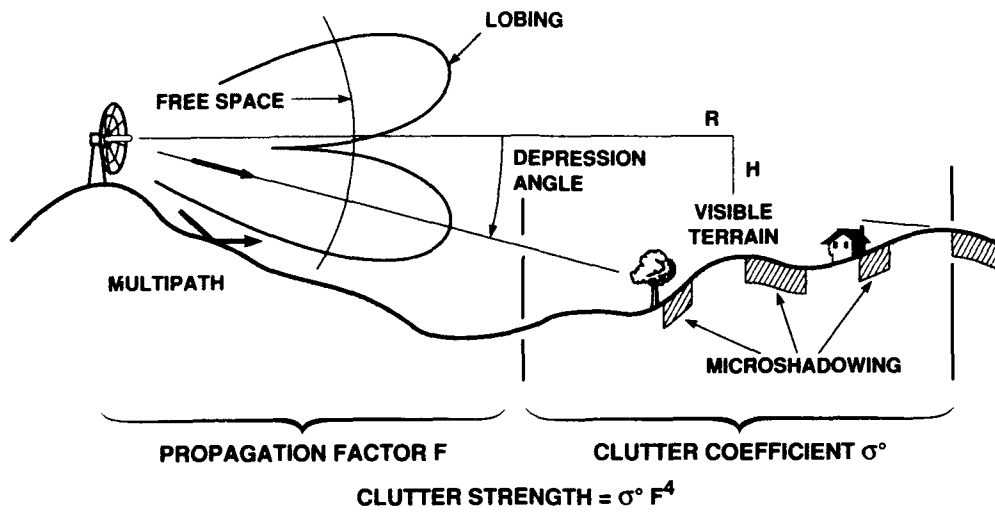


Figure 4. Clutter physics.

Frequency					
Band	VHF	UHF	L-band	S-band	X-band
MHz	165	435	1230	3240	9200
Polarization	VV or HH				
Range Resolution	36 or 150 m	36 or 150 m	15 or 150 m	15 or 150 m	15 or 150 m
Azimuth Beamwidth	13°	5°	3°	1°	1°
Elevation Beamwidth	39°	15°	10°	4°	3°
Antenna Gain (dBi)	13	25	28.5	35.5	38.5
Peak Power	10 kW (50 kW at X-band)				
10 KM Sensitivity	$\sigma^\circ F^4 = -60$ dB				
A/D Sampling Rate	1, 2, 5, or 10 MHz				
A/D Number of Bits	13				
Data Recording Rate	625K Bytes/sec				
Output Data	I and Q				
RCS Accuracy	2 dB rms				
Minimum Range	1 km				
Dynamic Range					
Instantaneous	60 dB				
Attenuator Controlled	40 dB				
Data Collection Modes	Beam scan Parked beam Beam step				
Azimuth Scan Rate	0 to 3 deg/sec				
Tower Height	9 m, 18 m, 30 m				

Figure 2. Phase One system parameters.

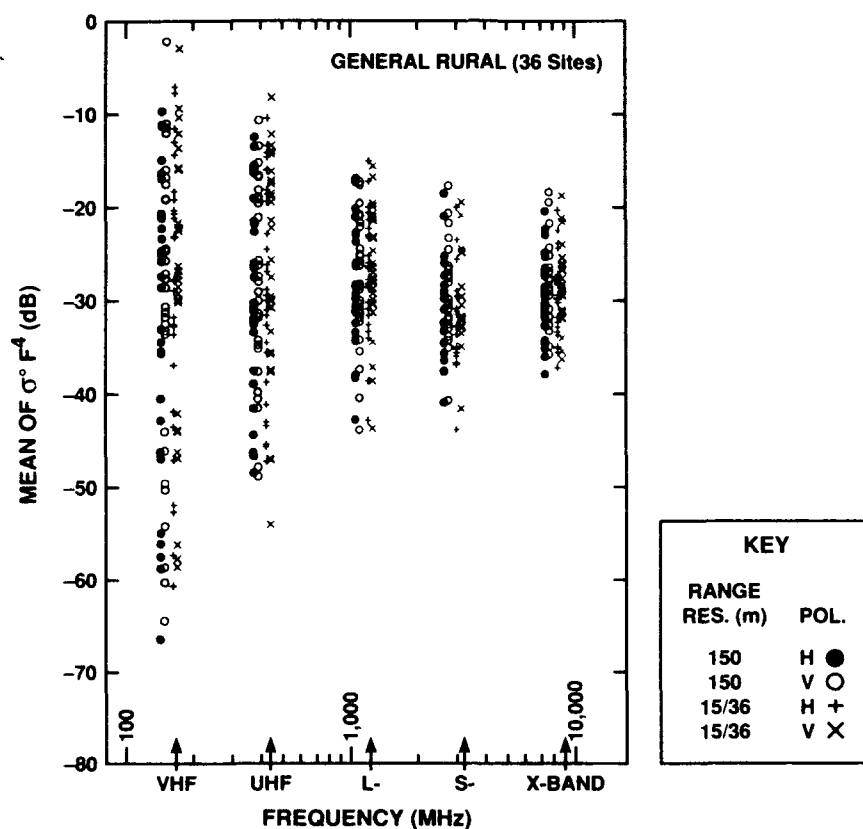


Figure 5. Mean ground clutter strength vs frequency at 36 rural sites.

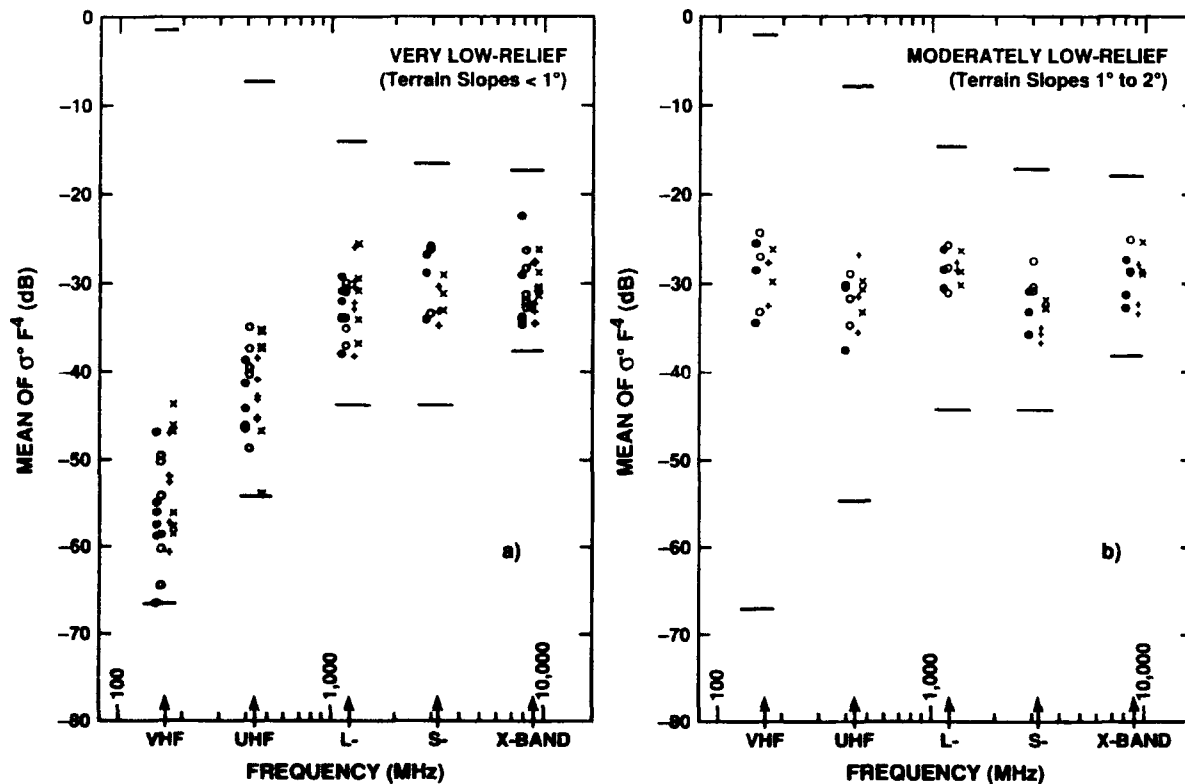


Figure 7. Mean ground clutter strength vs frequency in farmland terrain of a) very low-relief, and b) moderately low-relief.

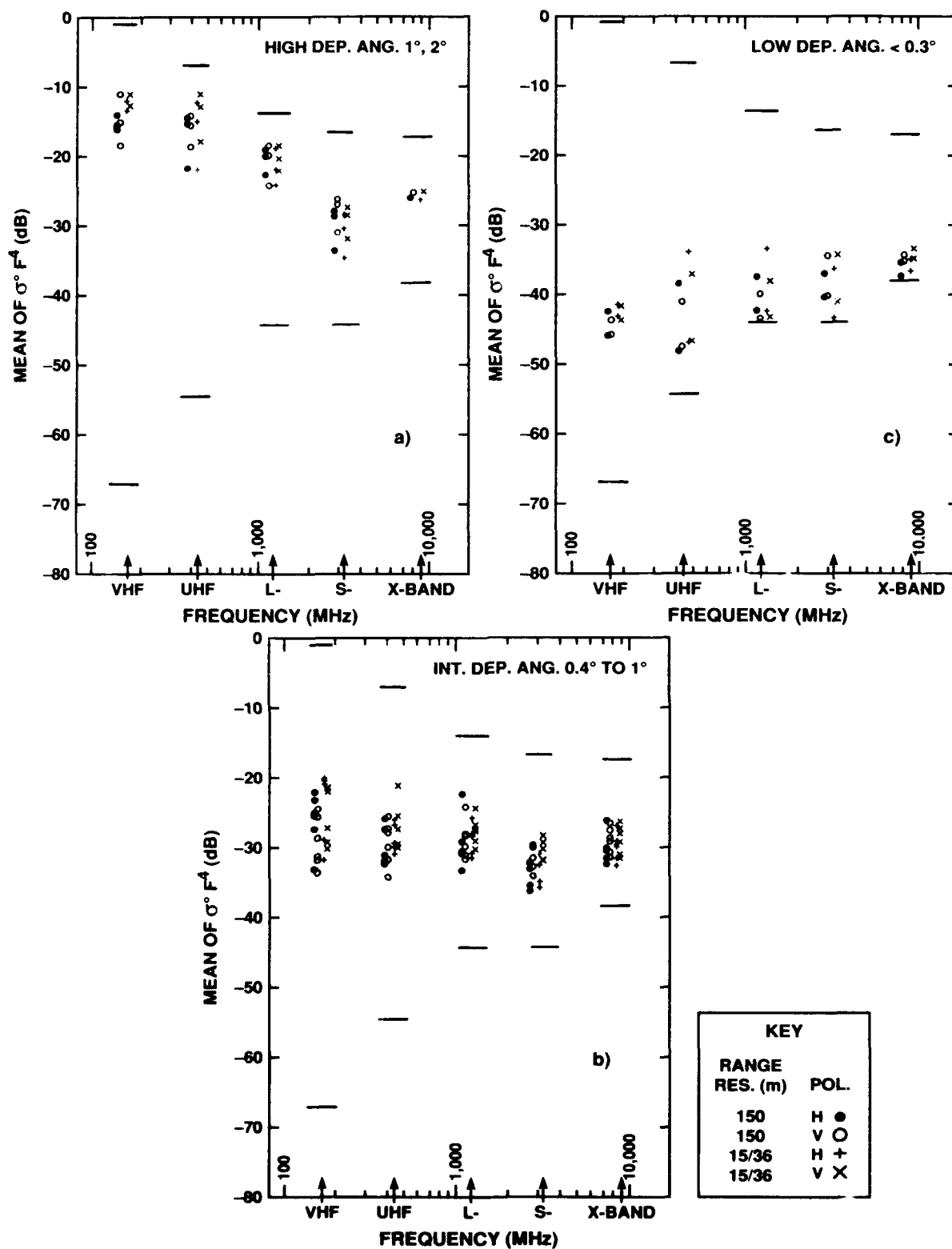


Figure 6. Mean ground clutter strength vs frequency in low-relief forest terrain at a) high depression angle, b) intermediate depression angle, and c) low depression angle.



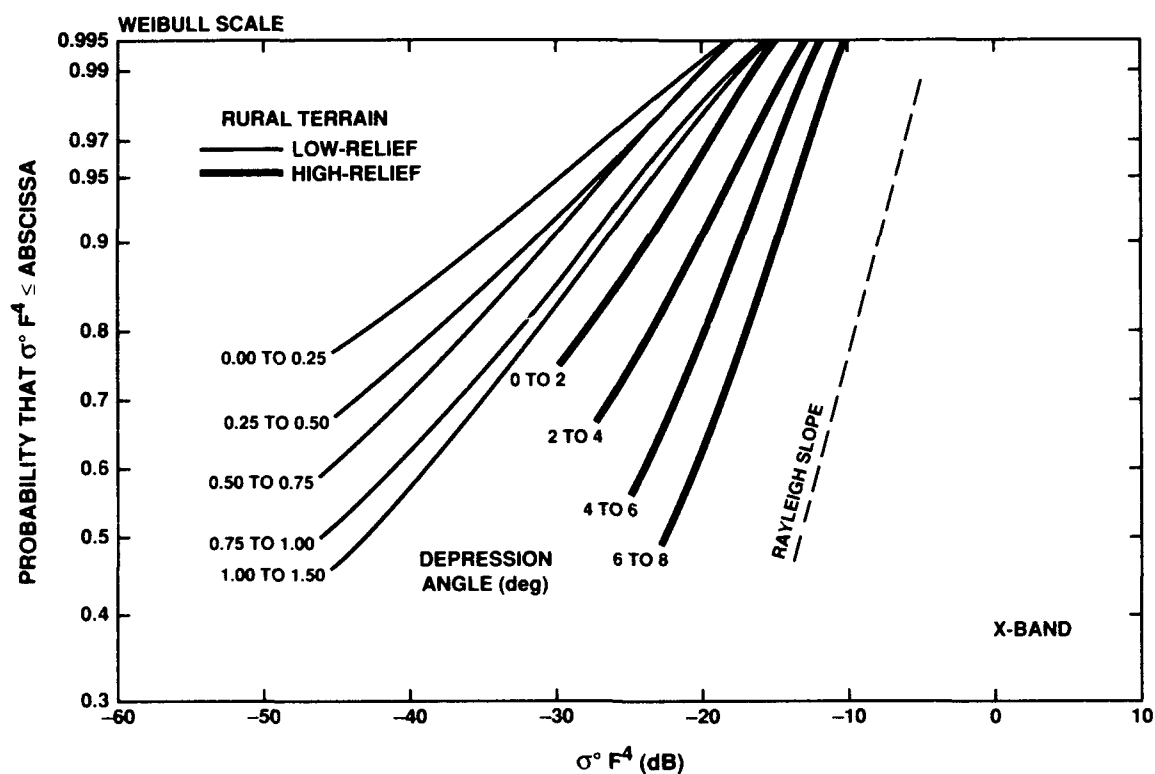


Figure 8. Cumulative ground clutter amplitude distributions by depression angle for rural terrain of low- and high-relief.

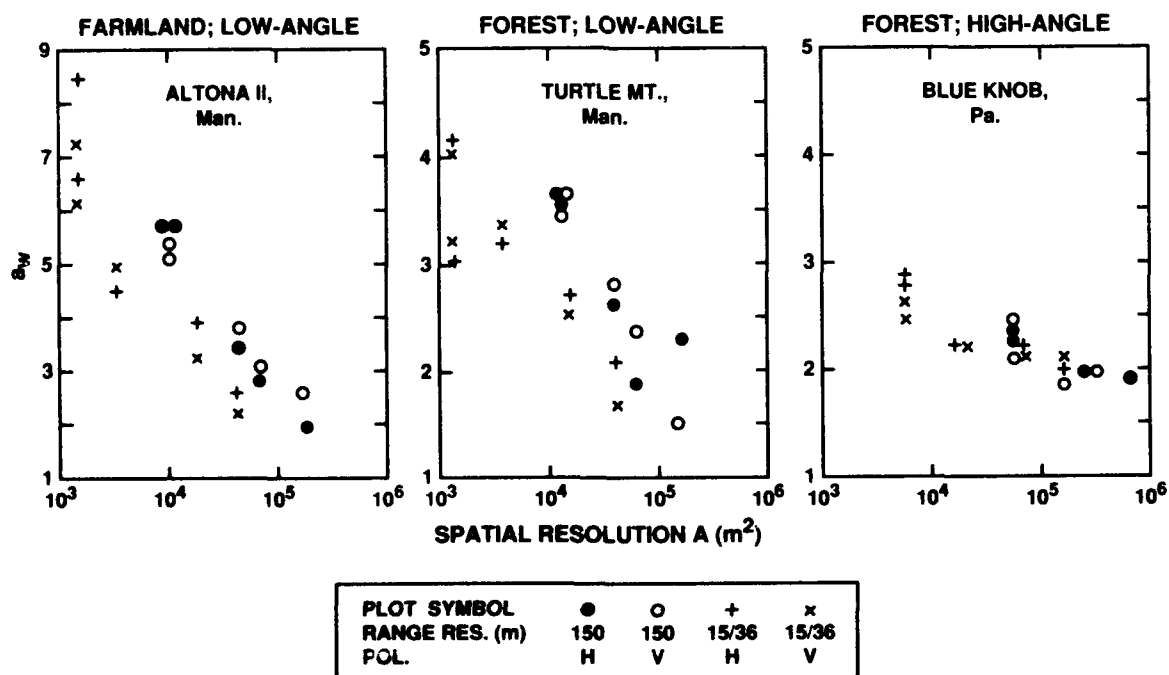


Figure 9. Weibull spread parameter  $a_w$  vs radar spatial resolution at three clutter measurement sites.

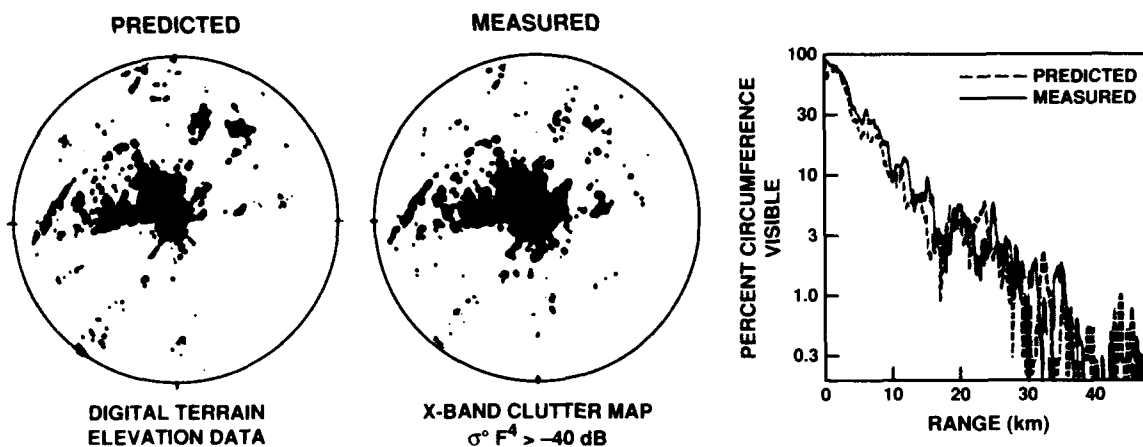


Figure 10. Ground clutter visibility at Katahdin Hill, Massachusetts.

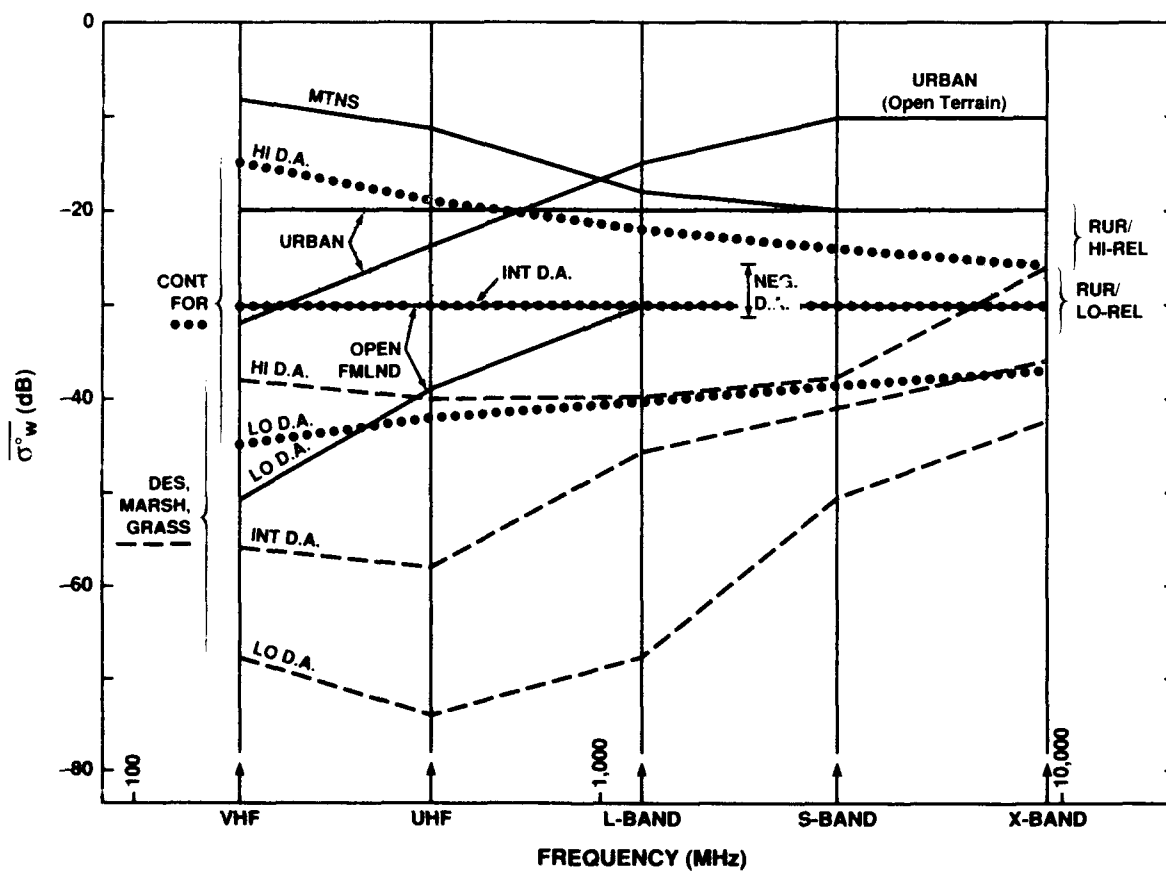


Figure 12. Weibull mean clutter strength  $\sigma_w^0$  vs frequency for various terrain types.

Terrain Type	Depression Angle (deg)	$\sigma_W^0$ (dB)					$\sigma_W$	
		Frequency Band					Resolution (m <sup>2</sup> )	
		VHF	UHF	L-	S-	X-BAND	10 <sup>3</sup>	10 <sup>6</sup>
<b>Rural/Low-Relief</b>								
a) General Rural	0.00 to 0.25	-33	-33	-33	-33	-33	3.8	2.5
	0.25 to 0.75	-32	-32	-32	-32	-32	3.5	2.2
	0.75 to 1.50	-30	-30	-30	-30	-30	3.0	1.8
	1.50 to 4.00	-27	-27	-27	-27	-27	2.7	1.6
	>4.00	-25	-25	-25	-25	-25	2.6	1.5
b) Continuous forest	0.00 to 0.30	-45	-42	-40	-39	-37	3.2	1.8
	0.30 to 1.00	-30	-30	-30	-30	-30	2.7	1.6
	>1.00	-15	-19	-22	-24	-26	2.0	1.3
c) Open farmland	0.00 to 0.40	-51	-39	-30	-30	-30	5.4	2.8
	0.40 to 0.75	-30	-30	-30	-30	-30	4.0	2.6
	0.75 to 1.50	-30	-30	-30	-30	-30	3.3	2.4
d) Desert, marsh, or grassland (few discrettes)	0.00 to 0.25	-68	-74	-68	-51	-42	3.8	1.8
	0.25 to 0.75	-56	-58	-46	-41	-36	2.7	1.6
	>0.75	-38	-40	-40	-38	-26	2.0	1.3
<b>Rural/High-Relief</b>								
a) General Rural	0 to 2	-27	-27	-27	-27	-27	2.2	1.4
	2 to 4	-24	-24	-24	-24	-24	1.8	1.3
	4 to 6	-21	-21	-21	-21	-21	1.6	1.2
	>6	-19	-19	-19	-19	-19	1.5	1.1
b) Continuous forest	any	-15	-19	-22	-22	-22	1.8	1.3
c) Mountains	any	-8	-11	-18	-20	-20	2.8	1.6
<b>Urban</b>								
a) General Urban	0.00 to 0.25	-20	-20	-20	-20	-20	4.3	2.8
	0.25 to 0.75	-20	-20	-20	-20	-20	3.7	2.4
	>0.75	-20	-20	-20	-20	-20	3.0	2.0
b) Urban, observed on open low-relief terrain	0.00 to 0.25	-32	-24	-15	-10	-10	4.3	2.8
<b>Negative Depression Angle</b>								
a) All, except mountains and high-relief continuous forest	0.00 to -0.25	-31	-31	-31	-31	-31	3.4	2.0
	-0.25 to -0.75	-27	-27	-27	-27	-27	3.3	1.9
	<-0.75	-26	-26	-26	-26	-26	2.3	1.7

Figure 11. Multifrequency Weibull parameters of ground clutter amplitude distributions.

## DISCUSSION

G. Neininger (GE) :

Have you taken into account the severe multipath problems at the lower frequency end of the measuring band ? How was the antenna configured ?

Author's reply :

In open terrain, our clutter measurements were often dominated by multipath propagation, particularly in our lower frequency bands. We present our results as  $\sigma^\circ F^4$  to emphasize this fact. Initially, one might suppose that the high theoretical ground would be to compute the propagation factor  $F$  and remove it as a contaminating influence in our data. However, it is our position that, using available digital terrain elevation data, it is not currently possible to compute the propagation factor  $F$  at clutter source heights sufficiently accurately to allow cell-by-cell separation of intrinsic  $\sigma^\circ$  in measured clutter data. Thus, our clutter model predicts the product  $\sigma^\circ F^4$  and separates very low-relief open terrain in which multipath loss is dominant from moderately low-relief open terrain in which multipath effects are more variable. Our antenna height was usually 18 m but we also made some measurements at 9 m and 30 m. These results showed that multipath loss was not strongly dependent on antenna height.

G. Crisp (UK) :

Why was your analysis based on a Weibull distribution rather than other 2 parameter statistical distributions ?

Author's reply :

Our measured distributions (of which we have about 100 000 on file) are usually more closely approximated by Weibull distributions than by other analytic distributions we have tried. For example, the lognormal distribution (another 2 - parameter distribution) usually overemphasizes the degree of spread required (i.e., our measured tails fall off more rapidly than do lognormal tails). Furthermore, the Weibull distribution provides decreasing spread with decreasing  $a$ -parameter and in the limiting case degenerates to a Rayleigh distribution when  $a = 1$ . This mimics the behavior of our measured distributions which, with increasing depression angle show decreasing spread and, in the limiting high-angle case for ground-sited radar (viz.,  $8^\circ$  or so) also often degenerate to approximately Rayleigh distributions.

G.H. Hagn (US) :

Have you considered the statistical confidence bounds on the measured distributions and can you use these bounds in the context of your model ?

Comment :

I have found it useful to use non-parametric (i.e., distribution free) statistics to put confidence bounds on sample cumulative distribution functions (CDFs) where only the sample size and level of significance (i.e., type 1 error,  $\alpha$ ) are needed to determine the confidence bound. For example, the Kolmogorov-Smirnoff statistic can be used to estimate the confidence bound and also to test for goodness of fit (see F.J. Massey, Jr., "The Kolmogorov-Smirnoff Test for Goodness of Fit" J. Amer. Statist. Assn., Vol. 46, pp.68 -78, March 1951 ; Z.W. Birnbaum, "Numerical Tabulation of the Distribution of Kolmogorov's Statistic for Finite Sample Size", J. Amer. Statis. Assn., Vol. 47, September 1952.

Author's reply :

Our measured distributions almost never pass rigorous statistical hypothesis tests (including the Kolmogorov-Smirnoff test) for belonging to Weibull, lognormal or any other analytic distributions we have tried. We are dealing with a messy statistical phenomenon in which we are collecting returns from all the discrete vertical scattering sources that occur at near-grazing incidence over real landscape. Rather than dwell on statistical rigor, we emphasize engineering approximations to our distributions using Weibull statistics. Working in this manner, we do not guarantee rigorous Weibull statistics within specified confidence bounds but we do, for example, provide the one-sigma variability of mean strength (an engineering indication of prediction accuracy) in our measured distributions within a given terrain type/relief/depression angle class which is often on the order of 3 dB. We are less concerned with the exact shape of the distribution than in getting its level (i.e. first moment) right.

F. Le Chevalier (FR) :

Don't you think a distinction between point-like scatterers and diffuse scattering could help in interpreting the differences between low frequency and high frequency statistics ?

Author's reply :

A classical ground clutter model consists of diffuse clutter emanating from area-extensive surfaces with a few large point-like discrete scatterers added in to account for objects like water towers. Our measurements reveal that, at the near grazing incidence of ground-sited radar, over ranges of many kms, a more realistic construct is to imagine clutter as arising from a sea of discretes. For example, over forest, it is a few projecting treetops in a resolution cell that cause the backscatter, with the in between shadowed areas of the canopy contributing much lower returns. Over agricultural terrain, it is the few projecting hillocks in the microtopography plus fence lines and other obvious cultural discretes that dominate the backscatter. All terrain types, open or forested, natural or cultural, are dominated by discretes. Thus our empirical clutter model for ground-sited radar is based on depression angle as it affects shadowing in a sea of patchy visibility and discrete scattering sources. As depression angle increases, we gradually begin to move from a discrete-dominated Weibull process towards more diffuse clutter and the accompanying Rayleigh process that exists in airborne radar. The differences between our low frequency and high frequency statistics are caused by frequency-dependent absorption and propagation effects. Our data are dominated by discretes at all our measurement frequencies.

Radar ground clutter measurement and models,  
Part II - Spectral characteristics and temporal statistics.

by  
Hing C. Chan  
Radar Division  
Defence Research Establishment Ottawa,  
3701 Carling Ave., Ottawa, Ontario, K1A 0Z4, Canada.

Summary

The performance of ground-based surveillance radars is affected by the spectral characteristics and the temporal statistics of ground clutter. Traditionally, ground clutter problems are treated by employing filtering techniques such as delay-line cancellers. These techniques result in a degraded detection performance of low-velocity targets. With the worsening congestion in air traffic, there is an increased demand for improved performance of low-velocity target detection.

To improve the detection performance of ground-based surveillance radars for low-velocity targets, signal processing algorithms which exploit ground-clutter characteristics must be developed. This requires a thorough understanding of ground-clutter behaviour. In this paper, we report the results of the spectral and statistical analyses of low-angle ground clutter, using data of the MIT Lincoln Laboratory Phase I program and S-band coherent ground-clutter data collected by the Radar Division of the Defence research Establishment Ottawa.

The results of the spectral analysis show that ground clutter, as observed by a coherent radar with a stationary antenna, comprises three components: (a) a coherent component, (b) a slow-diffuse component and (c) a fast-diffuse component. These components can be described by relatively simple models. The model parameters are functions of radar frequency, waveform resolution, land cover and wind speed.

The results of the statistical analysis show that the Ricean distribution and its limiting case, the Rayleigh distribution, are appropriate models for ground-clutter amplitude statistics in steady-state wind conditions. The relative frequency of fit of the ground-clutter statistics to each model depends on radar frequency, land cover and wind speed. However, at any given time, there is a significant proportion of resolution cells in a surveillance area which exhibits non-stationary statistics. This non-stationary statistical behaviour was a consequence of rapidly changing wind conditions.

The results presented in this paper are of use for the development of ground-clutter spectral and statistical models, CFAR processors, and algorithms for improved low-velocity target detection.

## 1 Introduction.

The performance of ground-based surveillance radars in areas within the radar horizon is largely ground-clutter-limited. Modern signal processing techniques such as moving target indicator (MTI) filtering and constant false alarm rate (CFAR) processors have improved the detection of moving targets to a level that is near-optimum. However, for targets with very low radial velocities, the detection performance is still very much dependent on the spectral characteristics and the temporal statistics of the clutter returns. Most signal processing algorithms designed to suppress ground clutter are Doppler sensitive. Processors designed to control false alarm rate are sensitive to changes in the amplitude statistics of the ground clutter.

The spectral behaviour of radar ground clutter has received less attention from radar researchers than other characteristics such as amplitude statistics and spatial distribution. Traditionally, clutter problems were treated by employing filters or cancellers. These filters usually have fixed bandpass characteristics. Targets with a Doppler shift which is close to that of the clutter are also attenuated, thereby reducing their detection probability in these so-called blind-speed regions. Staggered PRF or multiple PRF schemes must be employed to improve detection performance for targets with a speed that falls in the blind-speed regions. The design of a multiple PRF scheme is much simplified if the extent of the blind-speed regions is reduced. Signal processing techniques developed based on an incomplete knowledge of clutter spectral characteristics may not perform as expected. It is therefore essential that we identify the various spectral components of clutter and evaluate their relative significance in terms of signal processing.

The temporal statistics of ground clutter describe the statistical variation of the ground-clutter magnitude over time for a given resolution cell. A knowledge of these statistics enables one to set the detection threshold for an optimal probability of detection ( $P_d$ ) subject to the constraint of an acceptable probability of false alarm ( $P_{fa}$ ).

## 2. Ground-clutter data base.

To obtain accurate spectral and statistical information, ground clutter must be observed over a sufficiently long period of time. Preferably data should be available to allow for examination of the effects of radar frequency, resolution and polarization on clutter spectrum and amplitude statistics. For analyses using experimental data, a more practical constraint is the length of the recorded data. In this section we describe two ground-clutter data sources. The first was the MIT Lincoln Laboratory's Phase I ground clutter data base [1]. The second was the Defence Research Establishment Ottawa (DREO) S-band phased array radar. The advantages and limitations of these data are discussed.

### 2.1 The MIT Lincoln Laboratory Phase I data base

In the early eighties, the MIT Lincoln Laboratory Phase I program collected ground-clutter data from 33 Canadian and 9 American sites. The characteristics of the Phase I radar are summarized in Table 1.

Table 1: Characteristics of the Phase I Radar.

Frequency (MHz)	165	435	1230	3240	9100
Azimuthal Beamwidth (Deg)	13	5	3	1	1
Range Resolution (m)	36 m / 150 m		15 m / 150 m		
Polarization	Vertical Transmit/ Vertical receive Horizontal Transmit/ Horizontal Receive				
PRF	500 Hz to 4000 Hz				

The majority of the Phase I data was collected in the so-called SURVEY mode and the REPEAT mode. In the SURVEY mode, the antenna was mechanically scanned at a constant speed (less than  $3^\circ/\text{sec}$ ). The REPEAT mode employed a stationary antenna, but the dwell time was usually less than a second. These two modes were designed to collect spatial statistics of ground clutter which required a large ensemble of relatively short-time averages of the clutter magnitude from individual resolution cells. Data from the SURVEY and REPEAT modes are not suitable for spectral and temporal statistical analyses due to the high PRF and short dwell time. There was a small amount of long-dwell mode data from a few sites which are suitable. These data were recorded with a stationary antenna. Hence there was no antenna scanning modulation. The dwell time for these data was usually quite long, from 20 seconds to about a minute. Thus it was possible to obtain spectral resolution as low as a fraction of a Hz.

Unfortunately, the collection of long-dwell mode data is very time consuming and was performed only occasionally from a limited number of resolution cells. Consequently, there was not enough data from each site with sufficient diversity in land cover and a sufficiently wide range of wind speed to provide the necessary information for modelling. One exception was the Katahdin Hill, MA site where very detailed ground truth and a large amount of long-dwell data were collected from a small forested patch (about 2 km in range and  $1^\circ$  in azimuth). The analysis of some of these data has been reported by Billingsley and Larrabee [2].

The advantage of the Phase I data is that it permits the examination of ground clutter spectra and amplitude statistics over a wide range of radar frequency and wind speed. The limitation is that there is not enough variety in land cover.

## 2.2 The DREO S-band experimental phased array radar.

The Defence Research Establishment Ottawa (DREO) Radar Division's S-band coherent phased array radar facility was used to collect ground-clutter data specifically designed for detailed spectral and statistical analyses. The essential characteristics of the DREO S-band radar are summarized in Table 2

Table 2. Characteristics of the DREO Radar Division S-band Phased Array Radar.

Frequency .....	2970 MHz
Polarization .....	Horizontal
Range resolution.....	150 m
PRF .....	100 Hz
Azimuthal Beamwidth .....	$4^\circ$

For data collection, we used a dwell of 30720 pulses at a PRF of 100 Hz. The S-band phased array antenna can be electronically steered to cover an arc of  $80^\circ$ . We divided this arc into 20 look directions, each representing a  $4^\circ$  sector. The range extent for data collection was limited to about 10 km. With a 150m (1  $\mu\text{s}$  pulse) range resolution, there were 1200 resolution cells. Excluding those resolution cells located on the Ottawa River, ground-clutter data from approximately 600 resolution cells can be studied in detail. Three complete sets of clutter data were collected at winds speeds of 3, 12, and 25 mph respectively. The DREO data were not calibrated in terms of the equivalent radar cross section coefficient.

The 600 resolution cells were classified into three land-cover categories through interpretation of high resolution aerial photographs of the DREO site: type 1 - urban, type 2 - agricultural and type 4 - forested. Type 3 was designated as rangelands; however, there were no type 3 areas at the DREO site.

The urban land cover included residential and commercial buildings, highways, parking lots, terrain ridges and shore lines. The agricultural land cover included mostly fields with no visible trees but might include field boundaries and some farm buildings. The forested areas were primarily areas with trees. There were 108, 109 and 387 resolution cells classified as having urban, agricultural and forested land-covers, respectively.

The advantage of the DREO data is that it allows one to compare ground-clutter characteristics from three different land covers at different wind speeds. The limitation is that it can be done only at S-band and at horizontal polarization.

## 3. Spectral characteristics.

### 3.1 Spectral components of ground clutter.

Figure 1 shows a typical X-band ground-clutter spectrum obtained by averaging thirty periodograms. The periodograms were computed from contiguous 1024-point segments of a 30720-point clutter time series using a Blackman window. The radar parameters for the clutter time series are: radar frequency = 9100 MHz, H-POL, range resolution = 15 m, PRF = 500 Hz. The average wind speed at the time of the experiment was approximately 20 knots.

Similar spectral shapes were observed [3] in ground clutter at other frequencies. In most cases, the ground-clutter spectrum consisted of three components, (a) a coherent component, (b) a slow-diffuse component and (c) a fast-diffuse component.

(a) Coherent component.

Coherence factor and coherence interval.

When one speaks of coherence, it is necessary to specify the length of time interval over which a signal is coherent. Consider a radar which transmits a coherent pulse train of  $N$  pulses at a fixed direction with a pulse repetition interval (PRI) of  $t_p$ . The returns from a resolution cell are represented by a complex clutter time series  $\{x_n\}$   $n=0,1,\dots,N-1$ . We define the coherence factor (CF) of the clutter from a resolution cell as the ratio between the coherent component and the total clutter power computed over the coherence interval:

$$CF = \frac{\left[ \frac{1}{N} \sum_{n=0}^{N-1} x_n \right]^2}{\frac{1}{N} \sum_{n=0}^{N-1} |x_n|^2} \quad (1)$$

The number of pulses  $N$  together with the system PRI,  $t_p$ , determine the coherence interval ( $N \cdot t_p$ ).

The consideration of coherence interval is essential in assessing the feasibility of employing coherent clutter maps [4] at various frequencies. If the clutter remains coherent by the time the radar revisits the same resolution cell, the coherent component can be subtracted from the clutter returns of subsequent revisits, thereby removing a substantial amount of clutter without affecting the target signal that might be present.

(b) Slow-diffuse component.

The slow-diffuse component occupies a relative narrow region around zero Doppler. The spectral width of this component is a function of the radar frequency and wind speed. The magnitude of the slow-diffuse component relative to the coherent component usually decreases with decreasing radar frequency.

One significant result of the analysis was that the spectrum of the slow-diffuse component was approximately symmetrical around zero Doppler, and that its spectral density decreases (in dB scale) linearly with increasing absolute value of the Doppler shift.

A linearly decreasing spectrum in dB scale suggested that the spectral density may be modelled by a negative exponential function. This relationship was reported by Billingsley and Larrabee [2] in their analysis of spectrum from wind-blown trees. Our analysis of the clutter data in agricultural and urban areas indicated that the exponential model was also valid for other land covers.

At moderate wind speeds, the slow-diffuse component of ground clutter often exhibits a piecewise linear behaviour as a function of Doppler. That is, the spectral density decreases linearly (in dB scale) at a certain rate up to a certain Doppler, then decreases with a different rate. Figure 2 shows such a spectrum with the following parameters:  $f=3230$  MHz; polarization=V; range resolution=15m; land cover=forested; nominal wind speed=15 knots.

An inspection of the waveform of this clutter time series revealed that the clutter time series consisted of periods (which lasted for seconds) of fairly distinct rates of fluctuation. We computed the spectra using the portion of the time series that corresponded to these periods. These are shown in Figure 3. In each case, it can be seen that there is a dominant slow-diffuse component which decreases linearly with Doppler frequency. Thus in steady-state wind conditions the slow-diffuse component of ground clutter may be modelled as a symmetrically and exponentially decreasing function of Doppler frequency.

(c) Fast-diffuse component.

Figure 4 shows an S-band ground-clutter spectrum which contained a fast-diffuse component. The fast-diffuse component appeared in an averaged clutter spectrum like a band-limited noise; however, it actually consisted of many narrow band components occurring at different times. We examined the I-channel waveform together with the corresponding spectra of the S-band ground-clutter time series of Figure 4. These are shown in Figure 5. It can be seen that, besides the usual coherent and slow-diffuse components, there was a narrow spectral component on each side of zero Doppler. The Doppler shift of these components varied with time as can be seen from the corresponding spectra.

The fast-diffuse component could be localized, i.e., this component might be present in the clutter from one resolution cell while it was absent in the clutter of the neighbouring resolution cells during the same observation interval. The fast-diffuse component was evident only at relatively low wind speeds and its spectral extent had the same order of magnitude as the Doppler shifts that correspond to the prevailing wind speed.

### 3.1.2 Relative magnitudes of the spectral components.

The total clutter power included the coherent component and both the slow- and fast-diffuse components. To get a first order estimate of the relative significance of these three components, we integrated the spectral density of Figure 4 in three Doppler regions: (a) coherent component at zero Doppler, (b) slow-diffuse component from  $-8$  Hz to  $+8$  Hz, excluding the coherent component and (c) fast-diffuse component from  $-50$  Hz to  $-15$  Hz and  $+15$  Hz to  $+50$  Hz. We normalized the power of the diffuse components with respect to the coherent component. The slow- and fast-diffuse components were estimated to be  $-1.82$  dB



and -18.5 dB, respectively, below the coherent component. It should be emphasized, however, that the relative magnitudes of these components were dependent on the land cover and wind speed.

### 3.2 Low angle ground-clutter spectral model.

#### 3.2.1 Composite model for ground clutter spectrum

Based on the above observations, we can postulate that the spectrum of ground clutter comprised three components:

$$S(f) = C(f) + D^s(f) + D^f(f) \quad (2)$$

where  $f$  is the Doppler frequency and  $C(f)$ ,  $D^s(f)$  and  $D^f(f)$  are the spectral densities of the coherent, the slow- and fast-diffuse components, respectively. The spectral density of the coherent component may be modelled as a delta function at zero Doppler for steady-state wind conditions. The delta density yields the coherent clutter power,  $C$ , when it is integrated over the Doppler domain.

The slow-diffuse component may be modelled as a symmetrical negative exponential function:

$$D^s(f) = D_0^s \exp(-k_s |f|) \quad (3)$$

with the superscript  $s$  designating the slow-diffuse component.

The fast-diffuse component may be modelled as a constant density function over a limited region in Doppler.

$$\begin{aligned} D^f(f) &= D_0^f & |f| < f_c \\ &= 0 & |f| > f_c \end{aligned} \quad (4)$$

where  $f_c$  is the cutoff Doppler for the fast-diffuse component, usually slight less than the Doppler shift of the prevailing wind speed. We use the superscript  $f$  to designate the fast-diffuse component.

Since the partial spectra representing the coherent and slow-diffuse components dominate in different Doppler regimes, parameter  $k_s$  of the slow-diffuse component can be measured separately. Expressing Eqn (3) in dB scale, we have:

$$\begin{aligned} D_{dB}^s(f) &= 10 \log_{10}(D_0^s) - 10 \log_{10}(e) k_s |f| \\ &= D_0^s - k_s' |f| \end{aligned} \quad (5)$$

A symbolic diagram of the composite ground-clutter spectral model is shown in Figure 6. Since the fast-diffuse component is about two orders of magnitude lower than the slow-diffuse component, it will not be considered further.

#### 3.2.2 Model Parameters

For a simplified clutter spectral model which comprises only the coherent and slow-diffuse components, the pertinent model parameters are  $C$ ,  $D_0^s$  and  $k_s$ .

##### Spectral slope of the slow-diffuse component.

Parameter  $k_s$  is related to  $k_s'$  (Eq (5)) which is the slope of the slow-diffuse component and can be measured readily using linear regression with available clutter data for various radar frequencies as a function of wind speed. Figure 7 shows the slope  $k_s'$  of the slow-diffuse component at various frequency bands for the clutter from a small forested patch at Katahdin Hill as a function of wind speed. High resolution data were used (15m for X-, S- and L-bands; 36m for UHF and VHF). At each data point, the standard deviation computed over the sample space is also shown. The sample space in this case was 76 (resolution cells).

The spectral slope calculated above is in terms of changes in spectral density per unit Doppler shift (dB/Hz). It can be normalized with respect to the Doppler shift per unit velocity (1 m/sec) at each frequency so that the slope is in terms of changes in spectral density per unit velocity. If the clutter spectrum reflects accurately the distribution of scatterers at various velocities, then one would expect that the normalized curve would be similar for various frequencies.

This was observed to be the case for frequencies down to UHF; but a significant difference was observed for VHF. For example, since the ratio between the radar frequencies at UHF (435 MHz) and VHF (169 MHz) was about 2.57, we expected that the spectral slope at VHF is about 2.57 times steeper than that at UHF. At a nominal wind speed of 12 knots, the spectral slope at UHF was about -34 dB/Hz. One then expected to see a slope of -87 dB/Hz at VHF. But the value of the spectral slope at VHF obtained from Figure 7 at 12 knots was -51 dB/Hz which was significantly different.

There could be many explanations for this discrepancy. An important factor to be considered is the radar wavelength. For most objects on the ground, there is only a limited distance in which they can travel. Examples of this are tree leaves attached to a branches and small branches attached to a larger branch. At VHF the radar wavelength is in the order of 2 m. Thus the relative contribution to the clutter spectrum by objects with different limits of travel could be very different than those at higher frequencies.

### Coherence factor

Parameters  $C$  and  $D_0^s$  cannot be determined independently since there exists a complex interrelationship among these two parameters which depends on wind speed and the relative proportion of various land covers within a resolution cell. In general, the coherent component may include returns from fixed objects such as large buildings and heavy but flexible objects such as large tree branches and heavy hydro wires. Returns from buildings will remain coherent even at high frequencies over a long time interval. Returns from heavy but flexible objects will remain coherent at very low wind speeds. However, the returns become incoherent as the wind speed increases sufficiently.

For a resolution cell with high clutter-to-noise ratio, the CF gives an approximate ratio between the coherent component and the sum of the coherent component and the slow-diffuse component. Hence given the total power of the clutter from a resolution cell, one can determine  $C$  and  $D_0^s$  approximately through parameters CF and  $k_s$ :

$$CF \approx \frac{C}{C + \int_{-\infty}^{\infty} D_0^s \exp(-k_s |f|) df} \quad (6)$$

The CF, however, is a function of wind speed and can be considered only statistically. To obtain a reliable statistical profile for ground-clutter spectral modelling, a much larger data base with detailed ground truth data than available would be needed. However, we shall present two typical profiles of CF calculated from data of Katahdin Hill and those from the DREO sites. These results are not meant to provide modelling information for ground clutter spectra. They are presented to give some indication of the relative coherence of ground clutter from different land covers and at different radar frequencies.

The statistical profiles are presented in terms of the complementary cumulative distribution of the CF at various wind speeds. Each point on the complementary cumulative distribution curve of CF determines a pair of coordinates. The ordinate gives approximately the probability of finding a resolution cell with a clutter coherence factor greater than or equal to the value of the abscissa over the specified coherence interval. The result calculated from the Katahdin Hill data compares the profiles of CF at different frequencies but for forested land cover only. The DREO result compares the profiles of CF for three different land covers, but for S-band only.

Figure 8 shows the complementary cumulative distribution of the CF of clutter from the small forested patch of the Katahdin Hill site at various radar frequencies. The coherence interval was 10 seconds. Results are shown for moderate and high wind speeds for high resolution X-band, L-band, UHF and VHF data. It can be seen that for radar frequencies above L-band, the coherence factor of the clutter was very small, indicating that the clutter was essentially incoherent. However, at VHF, the clutter coherence factor remained high for most of the resolution cells even at relatively high wind speeds.

Figure 9 shows the complementary cumulative distributions of the CF for clutter from urban, agricultural and forested areas at the DREO site. The coherence interval was 10 seconds. At low wind speeds (3 mph), the probability of finding an urban resolution cell with a CF greater than or equal to 90% was 0.9. At moderate to high wind speeds (12 mph or higher), this probability dropped to 0.55, still very high.

For agricultural areas, the probability of finding a resolution cell with a CF of at least 90% was about 0.55 at low wind speeds. However, it reduced to values of 0.3 and 0.1 as the wind speed increased to 12 and 25 mph, respectively. Results for forested areas were similar to those for agricultural areas, except that the CF decreased more rapidly with increased wind speed compared with that in agricultural areas. At moderate to high wind speeds, the clutter from most forested and agricultural cells was essentially incoherent at S-band.

The results of Figure 8 and 9 are site-specific and cannot be used as accurate modelling information. In Section 5.2 we shall discuss means by which modelling information can be obtained.

#### 4. Temporal statistics

In subsequent discussions of temporal statistics of ground clutter, we shall be concerned with the probability distribution of the linear magnitudes of the clutter envelope.

##### 4.1 Experimental observation of temporal ground-clutter statistics.

Analyses of both the Phase I and DREO data [5] showed that the temporal statistics of ground clutter could be classified into three categories: (a) Rice, (b) Rayleigh, and (c) nonstationary. In the nonstationary category, there were two cases: (i) predominantly Ricean, with short periods of Rayleigh behaviour, and (ii) predominantly Rayleigh, with short periods of Ricean behaviour. Figures 10, 11 and 12 show an example of the above cases.

##### (a) The Ricean Model

The Ricean probability density function, derived by Rice [6] from the analysis of the statistical properties of a sine wave in additive noise, is given by:

$$p(z) = \frac{z}{\sigma^2} \exp\left\{-\frac{A^2 + z^2}{2\sigma^2}\right\} I_0\left[\frac{Az}{\sigma^2}\right] \quad (7)$$

where  $A$  is the amplitude of the sine wave,  
 $z$  is the envelope of a random variable representing the sum of the sine wave and a complex Gaussian noise process with power  $2\sigma^2$ ; and  
 $I_0(z)$  is the modified Bessel function of the first kind of order zero.

The first and second moments of a Ricean process are given by [6]:

$$\langle z \rangle = \left[ \frac{\pi}{2} \right]^{1/2} \sigma \exp \left[ -\frac{A^2}{4\sigma^2} \right] \left[ \left[ 1 + \frac{A^2}{2\sigma^2} \right] I_0 \left( \frac{A^2}{4\sigma^2} \right) + \frac{A^2}{2\sigma^2} I_1 \left( \frac{A^2}{4\sigma^2} \right) \right] \quad (8)$$

and

$$\langle z^2 \rangle = A^2 + 2\sigma^2 \quad (9)$$

respectively, where

$I_1(x)$  is the modified Bessel function of the first kind of order 1.

(b) The Rayleigh model.

If parameter A in Eqn (4) is set to zero, the Rayleigh pdf results:

$$p(z) = \frac{z}{\sigma^2} \exp \left\{ -\frac{z^2}{2\sigma^2} \right\} \quad (10)$$

The first and second moments of the Rayleigh distribution are:

$$\langle z \rangle = \left[ \frac{\pi}{2} \right]^{1/2} \sigma \quad (11)$$

and

$$\langle z^2 \rangle = 2\sigma^2 \quad (12)$$

respectively.

A Ricean process requires an estimate of both the first and second moments for a correct threshold setting. A Rayleigh process, on the other hand, requires only one parameter,  $\sigma$ , for its characterization. Hence it is attractive from the standpoint of determining the proper threshold setting for a specified  $P_{fa}$ . It is useful to have some information regarding the relative frequency of occurrence of these two types of clutter processes in a given surveillance area.

#### 4.2 A parameter for clutter statistical classification.

A convenient parameter which can be easily calculated from the clutter data and which can be used for classification of clutter statistics is the normalized second moment of a random process:

$$a = \frac{\langle z^2 \rangle}{\langle z \rangle^2} \quad (13)$$

For resolution cells with high clutter-to-noise ratio, parameters  $A^2$  and  $2\sigma^2$  may be approximated by the coherent and the slow-diffuse components, respectively. For a Ricean process, substitution of Eqn (8) and (9) into (13) and using:

$$y = \frac{\langle z^2 \rangle}{2\sigma^2} = \frac{A^2}{2\sigma^2} + 1 \quad (14)$$

yields:

$$\beta = \frac{1}{a} = \frac{\langle z \rangle^2}{\langle z^2 \rangle} = \frac{\pi \exp[-(y-1)] \left[ y I_0 \left( \frac{y-1}{2} \right) + (y-1) I_1 \left( \frac{y-1}{2} \right) \right]^2}{4y} \quad (15)$$

A plot of  $\beta$  as a function of  $y$  is shown in Figure 13. A value of  $y = 1$  represents the limiting case for a Rayleigh process ( $A=0$ ). In this case  $\beta=\pi/4$ . On the other hand, as  $y$  approaches infinity,  $\beta$  approaches unity. This represents the case of a large coherent component or a diminishingly small diffuse component.

Consider a Ricean process with a first moment  $\langle z \rangle = 1$  and a value of  $\beta = 0.8$ . From Eqns (12), (13) and (14) we obtain the following parameter values for the Ricean model:  $y = 1.5$ ,  $A = 0.6455$  and  $2\sigma^2 = 0.8333$ . If one wants to approximate this process by a Rayleigh process, one computes the Rayleigh parameter  $\sigma$  from Eqn (8) and obtains a value of  $\sigma_r = 0.79788$ . Using these values, the pdf's and the  $P_{fa}$  characteristic of the Ricean process and its Rayleigh approximation are plotted in Figure 14a and 14b, respectively.

It can be seen that the two pdf's are very close, and the  $P_{fa}$  characteristic predicted by the Rayleigh approximation is only slightly worse than that calculated from the correct (Ricean) model. For example, at a  $P_{fa}$  of  $10^{-4}$ , a threshold setting of  $V_T = 3.83$  is required for a Rayleigh model, while a value of  $V_T = 3.5$  is calculated for the Ricean model. In subsequent discussions, we shall classify a clutter process to be

predominantly Rayleigh if the value of  $\beta$  is less than 0.8, and the  $P_{fa}$  characteristic is close to that of the Rayleigh model. We shall call a Ricean process with a  $\beta \leq 0.8$  weakly Ricean.

#### 4.3 Statistical classification of DREO clutter data

In this section, we compare the statistics of three sets of S-band clutter time series recorded at progressively higher wind speeds. These data were recorded on separate days in February of 1989. The averaged wind speeds for the three sets of data were 3, 12 and 25 mph respectively.

The amplitude histograms of these sets of clutter data are classified against the Ricean and Rayleigh models, and the results are tabulated in Table 3.

Table 3: Classification of the clutter amplitude statistics for the DREO clutter data.

Land Cover	Wind Speed									Total No. of cells
	3 mph			12 mph			25 mph			
	Rice.	Rayl.	Others	Rice.	Rayl.	Others	Rice	Rayl.	Others	
1	63	0	45	40	9	59	35	23	41	108
2	78	3	28	43	28	38	24	45	40	109
4	238	4	145	175	92	120	94	185	108	387

This result shows the effects of wind speed and land cover on clutter amplitude statistics. For urban land cover (Land cover type 1), the majority of the resolution cells had clutter amplitude statistics approximately fitting the Ricean model. That is, for those resolution cells which had been classified as "others", the  $P_{fa}$  vs threshold curve is closer to the Ricean model than to the Rayleigh model, and the value of the parameter  $\beta$  was usually greater than 0.8. As the wind speed increased, the number of cells with Rayleigh and "nonstationary" amplitude statistics increased. Similar results were obtained for agricultural land covers (land cover type 2).

For forested land cover (land cover type 4), we observed a somewhat different result. The number of resolution cells classified as "others" actually decreased as the wind speed increased.

Figure 15 shows the value of  $\beta$  as a function of resolution cell number for land cover type 1 (urban) at the DREO site for three different wind speeds. At an averaged wind speed of 3 mph, the majority of the 108 resolution cells have a value of  $\beta$  close to unity. This indicates that most of the resolution cells in an urban area had clutter that was predominantly Ricean. At an averaged wind speed of 12 mph, a number of the resolution cells had  $\beta$  values less than 0.9, and some even approached the Rayleigh limit of  $\pi/4$ . However, for the majority of the resolution cells, the Ricean distribution was the best model. At an averaged wind speed of 25 mph, a slightly increased number of resolution cells with predominantly Rayleigh statistics was observed.

Figure 16 shows the value of  $\beta$  as a function of resolution cell number for land cover type 2 (agricultural). At low wind speeds, the majority of the resolution cells had clutter that was predominantly Ricean. At higher wind speeds, the majority of the resolution cells had clutter that was predominantly Rayleigh.

Significantly different results were observed for forested land covers. Figure 17 shows the value of  $\beta$  as a function of resolution cell number for type 4 (forested) land cover. At low averaged wind speeds, most of the resolution cells had clutter that could be classified as predominantly Ricean. However, there were still many resolution cells with a  $\beta$  value below 0.95 which indicated that the coherent-to-diffuse component ratio was low.

At moderate wind speeds, the number of resolution cells with  $\beta$  values close to unity decreased drastically, indicating that the clutter in more resolution cells was becoming incoherent. At high wind speeds (25 mph), most of the resolution cells had  $\beta$  values close to  $\pi/4$ , indicating that the distribution function for clutter in most of the resolution cells could be appropriately modelled as a Rayleigh process.

## 5. Conclusions.

### 5.1 Summary of results.

#### (a) Spectral characteristics.

(i) Clutter spectra observed by a ground-based radar comprised a coherent component, a slow-diffuse component and a fast-diffuse component. The coherent component was the result of radar returns from immovable objects such as buildings, highways, mountains, and those from movable objects (tree branches, etc) at rest. The slow-diffuse component was the consequence of motions of objects with moderate inertia such as tree branches. The fast-diffuse component occupies a Doppler region that was compatible with the Doppler shifts of the prevailing wind speed and was most likely the result of movements in light objects such as tree leaves and other vegetation.

(ii) The spectral shape of the slow-diffuse component may be modelled by a symmetrical negative exponential function.

(iii) The fast-diffuse component had a spectral density similar to a band-limited noise and was transient in nature. The magnitude of this component was usually small compared to the coherent component and the slow-diffuse component. At high wind speeds, the fast-diffuse component was generally not observable.

(iv) We did not observe any statistically significant effect of polarization on the clutter spectrum.

(v) Powers in the coherent and diffuse components could transfer back and forth from one another as the wind speed changes. This caused the coherence factor of ground clutter to vary with wind speed. The coherence factor was also a function of the radar frequency. At VHF, the coherence factor remained high for all land-covers and wind speeds. This means that coherent clutter map will be much more effective at lower frequencies than at higher frequencies.

(vii) Wind direction had only a marginal effect on the spectral slope of the slow-diffuse component. The spectral slope of the slow-diffuse component was slightly smaller in the up- and down-wind directions than in the cross-wind direction. The difference, however, was within the standard deviation that can be expected for clutter observed in resolution cells with the same wind direction.

(viii) Clutter spectra observed from various waveform resolutions ranging from 15 m to 150 m did not show significant differences. However, waveform resolution could affect the distribution of the coherence factor.

(b) Temporal amplitude statistics.

(i) The temporal statistics of ground clutter were best modelled by a Ricean distribution which sometimes degenerated into a Rayleigh distribution. The relative frequency of occurrence of fit of clutter data to the two models was a function of land cover, wind speed, radar frequency and resolution;

(ii) At any given time, there was a fraction of the resolution cells in a surveillance area whose clutter amplitude exhibited some degree of nonstationarity. Occurrence of nonstationary statistical behaviour was more likely in forested areas and was associated with sudden changes in wind speed.

(iii) The clutter coherence factor was an important parameter in ground-clutter temporal statistics. A high CF value is associated with Ricean statistics, and a low CF value is associated with Rayleigh statistics.

## 5.2 Modelling information requirements.

The results of this analysis indicated that both the spectrum and the temporal amplitude statistics of ground clutter can be described very well by relatively simple models. In both cases, the coherence factor played an important role. What is not yet available is the statistical information which relates the model parameters to physical parameters such as land covers and wind speeds. Besides wind speed, the principal parameters which affect both the spectral and temporal statistical characteristics of ground clutter are radar frequency, waveform resolution, and land cover. The distribution of the clutter coherence factor over an area was site-dependent on account of the mixing of data from different categories. For example, trends of the CF obtained from resolution cells with mixed agricultural and forested land covers would be significantly different from those from areas of pure forested land cover. The distribution of CF could also change with seasons. For example, in winter most deciduous trees would be stripped of leaves, and the effect of wind on the motion of the tree branches could be different from that in the summer. Consequently, modelling information should be categorized according to these parameters and collected over many sites.

## 5.3 Applications

Although information for the modelling of temporal characteristics of ground clutter is still incomplete, some of the results can already be utilized.

(a) Adaptive clutter filter.

Using the spectral model, the spectral extent of the ground clutter can be estimated once the wind speed is known. This permits the use of adaptive clutter filters which have a variable cutoff frequency depending on the prevailing wind speed. Improved sub-clutter visibility may be obtained for targets with low but non zero radial velocities.

(b) Coherent clutter maps

The coherent clutter map is the simplest way to utilize a priori spectral information of ground clutter to improve detection performance in resolution cells with a high coherence factor. A high coherence factor permits the coherent cancellation of large ground clutter returns without affecting the target signal even for targets with zero radial velocity. The coherence factor of clutter from urban areas is high for most radar frequencies. Since the clutter coefficient for resolution cells with predominantly urban land covers (buildings) is usually much higher than those of other land covers, cancelling the coherent component in clutter returns from these resolution cells will substantially improve detection performance for applications such as civil airport surveillance.

From the results of this analysis, the coherent clutter map will not be effective for X- and S-bands for land cover other than pure urban areas. At lower frequencies, the coherent clutter map concept becomes practical even for land covers other than pure urban areas. The coherent clutter map should be implemented with a non-mechanically scanned antenna such as a phased array.

(c) Predictive coherent clutter map

An extension of the coherent clutter map concept is the predictive coherent clutter map. That is, we analyze the ground-clutter spectra for various land covers and wind conditions. Predictive models are then derived and catalogued from the observed clutter spectral characteristics. The model will be used to estimate the ground clutter amplitude and phase from each resolution cell for the next revisit time, based on past observed samples. The estimate would be subtracted coherently from the actual return. If the estimate is accurate, the residual clutter should be significantly lower than the original clutter sample without affecting target components that may be present. A good candidate is the autoregressive model [7] which has many of the attributes that characterise radar ground clutter.

The prediction of a random process requires adequate sampling (at Nyquist rate) of the process. This could require that the time of revisit to a resolution cell be reduced. Again a electronically scanned antenna will offer more flexibility. More research is needed to determine the feasibility of the predictive clutter map approach, the achievable performance improvement and the operational requirements.

## 6. References

- [1] Billingsley, J.B., "Phase one master directory file", MIT Lincoln Laboratory CMT project memorandum no.45 PM-CMT-0003, September 1985.
- [2] Billingsley, J.B. and Larrabee, J.F., "Measured spectral extent of L- and X-band radar reflections from wind-blown trees", Lincoln Laboratory Project Report No. CMT-57, February 1987.
- [3] Chan, H.C., "Spectral characteristics of ground clutter", DREO Report No. 1020, Defence Research Establishment Ottawa, Ottawa, Ontario, Canada, December 1989.
- [4] Bird, J.S., "Coherent processing of ground clutter to improve low-Doppler target detection and identification", NATO AGARD Symposium on target signatures, London, U.K., October 1984, pp. 3-1 to 3-10.
- [5] Chan, H.C., "Temporal statistics of low-angle ground clutter", DREO Report no. 1021, Defence Research Establishment Ottawa, Ottawa, Ontario, Canada, December 1989.
- [6] Rice, S.O., "The mathematical analysis of random noise", Bell System Technical Journal, vol.23, pp.282-332, July 1944.
- [7] Akaike, H., "Fitting autoregressive models for prediction", Ann. Inst. Stat. Math., vol. 21, 1969.

## 7. Acknowledgement.

The author thanks the U.S. Defense Advanced Research Projects Agency and the personnel of Group 45 of the MIT Lincoln Laboratory for furnishing the clutter data used in this study. Special thanks are due Mr. J. Barrie Billingsley and Mr. J. Larrabee of Lincoln Laboratory for useful discussions.

## 8. Illustrations.

Note: Since not all clutter data were calibrated (in terms of  $m^2$ ), the spectral densities are shown relatively in dB scale.

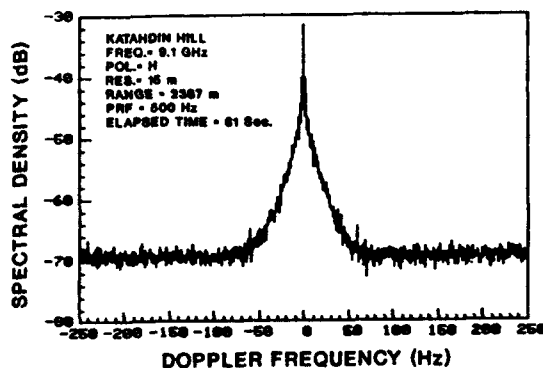


Figure 1. A typical X-band ground-clutter spectrum.

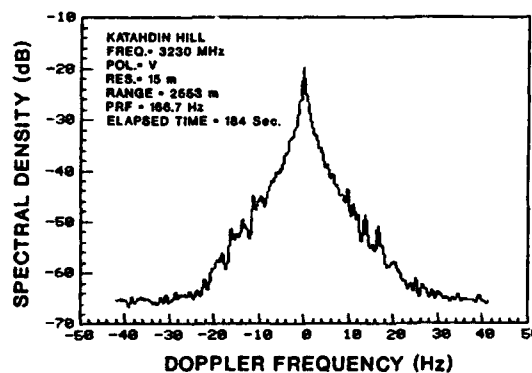


Figure 2. A typical S-band ground-clutter spectrum.

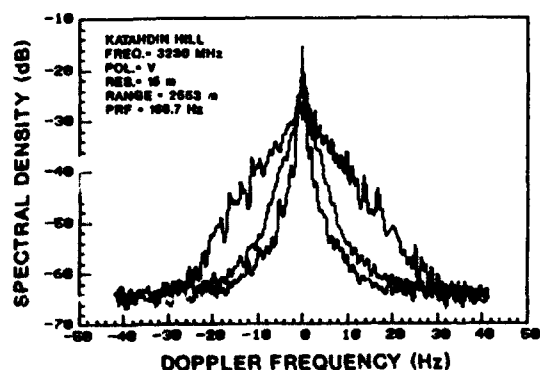


Figure 3. Variation of the spectral slope of the slow diffuse component over an observation interval.

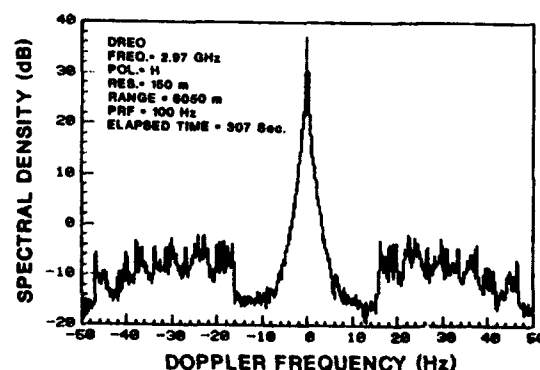


Figure 4. Averaged spectrum of an S-band ground-clutter time series containing fast-diffuse component.

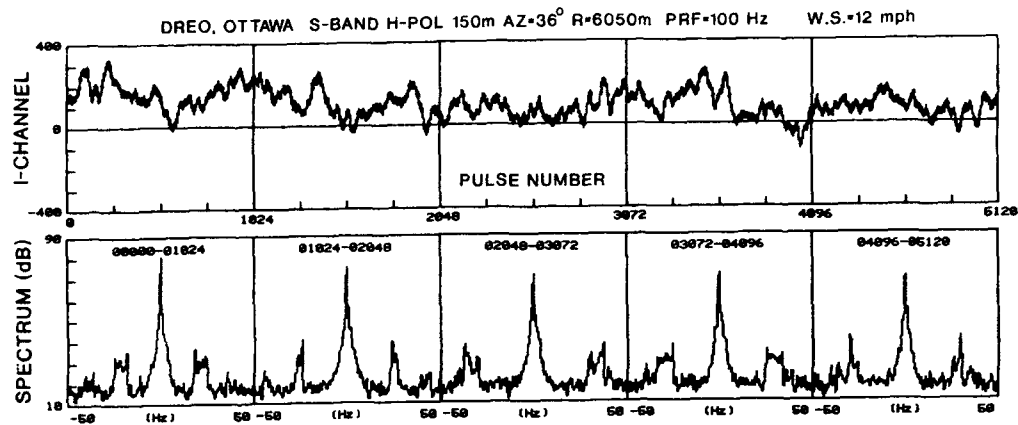


Figure 5. Waveform and sectional spectra of the S-band ground-clutter time series of Figure 4.

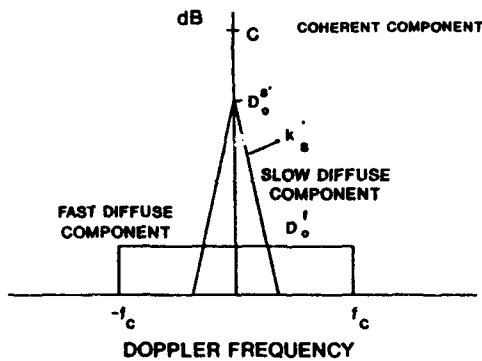


Figure 6. Symbolic diagram of a ground-clutter spectral model.

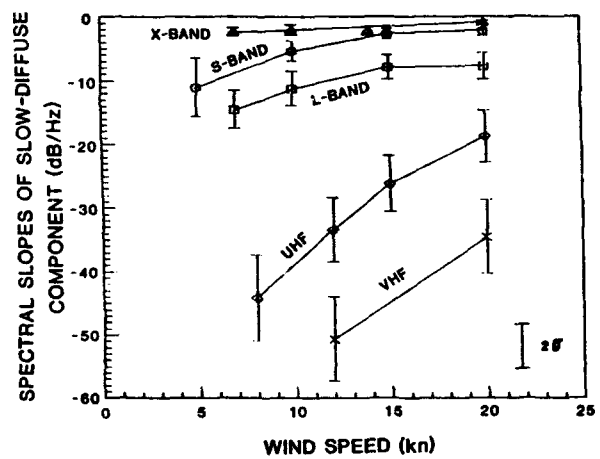


Figure 7. Spectral slopes of the slow-diffuse component at various frequency bands - from a small forested patch at Katahdin Hill.

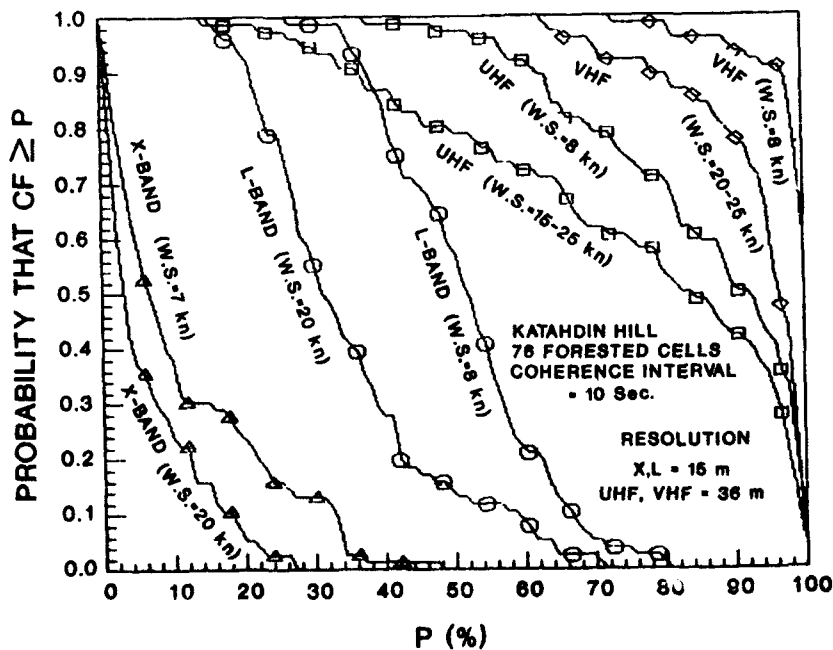


Figure 8. Complementary cumulative distribution of CF for clutter from a small forested patch at Katahdin Hill.

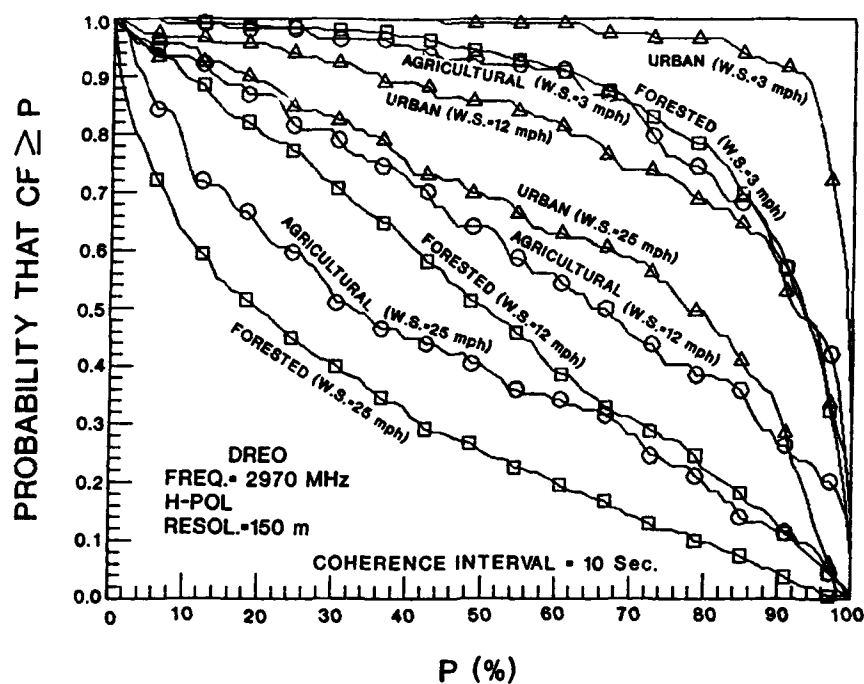


Figure 9. Complementary cumulative distributions of CF for S-band clutter at the DREO site.

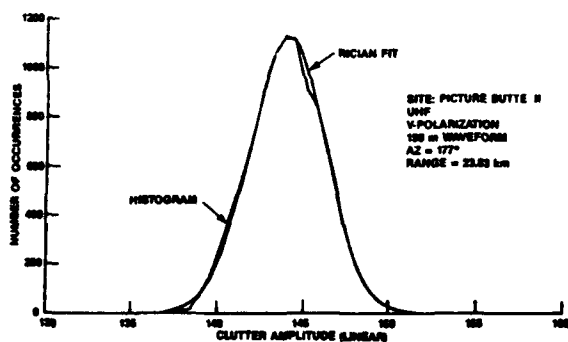


Figure 10. An example of ground-clutter temporal statistics fitting the Ricean model.

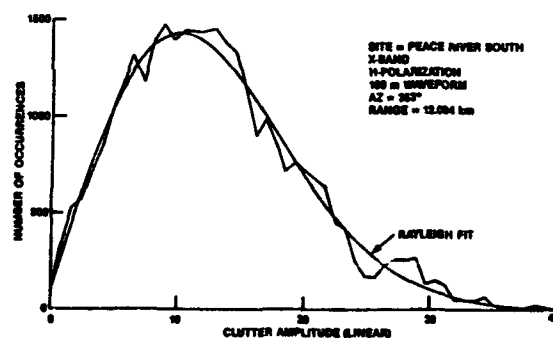


Figure 11. An example of ground-clutter temporal statistics fitting the Rayleigh model.

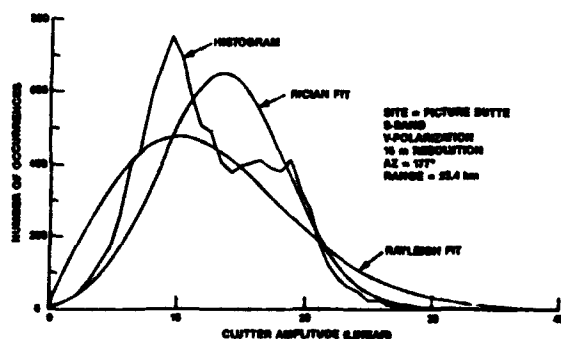


Figure 12. An example of non-stationary ground-clutter statistics.

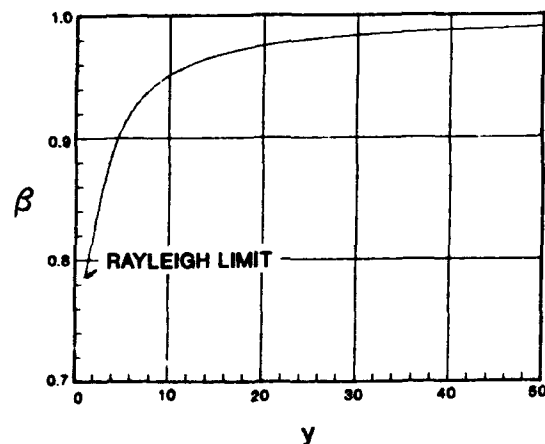


Figure 13. Parameter  $\beta$  as a function of  $y$ .



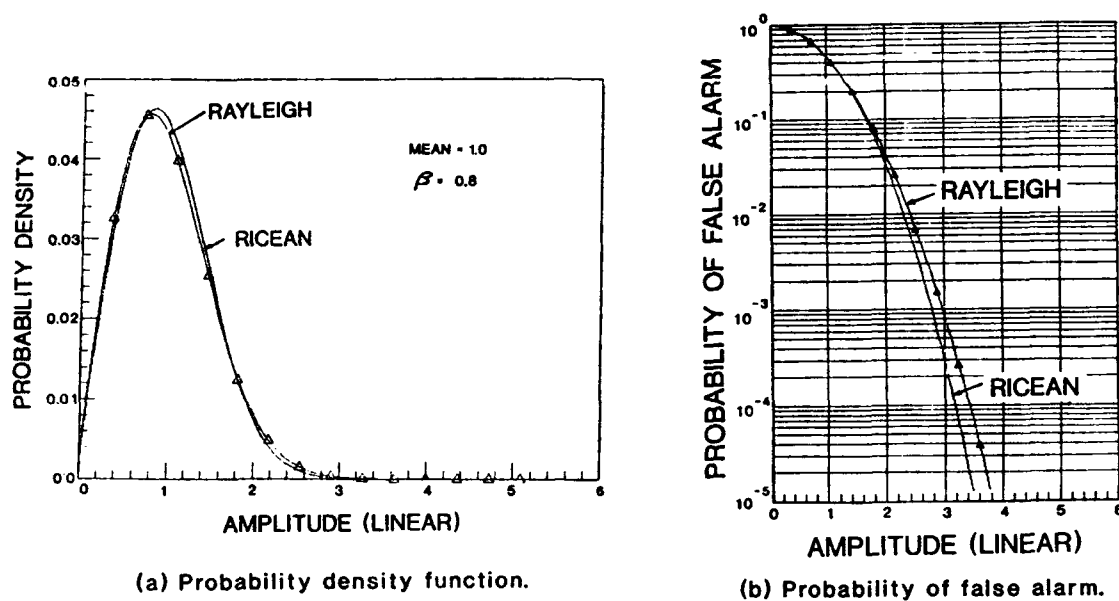


Figure 14. Comparison of a weakly Ricean process with a Rayleigh approximation.

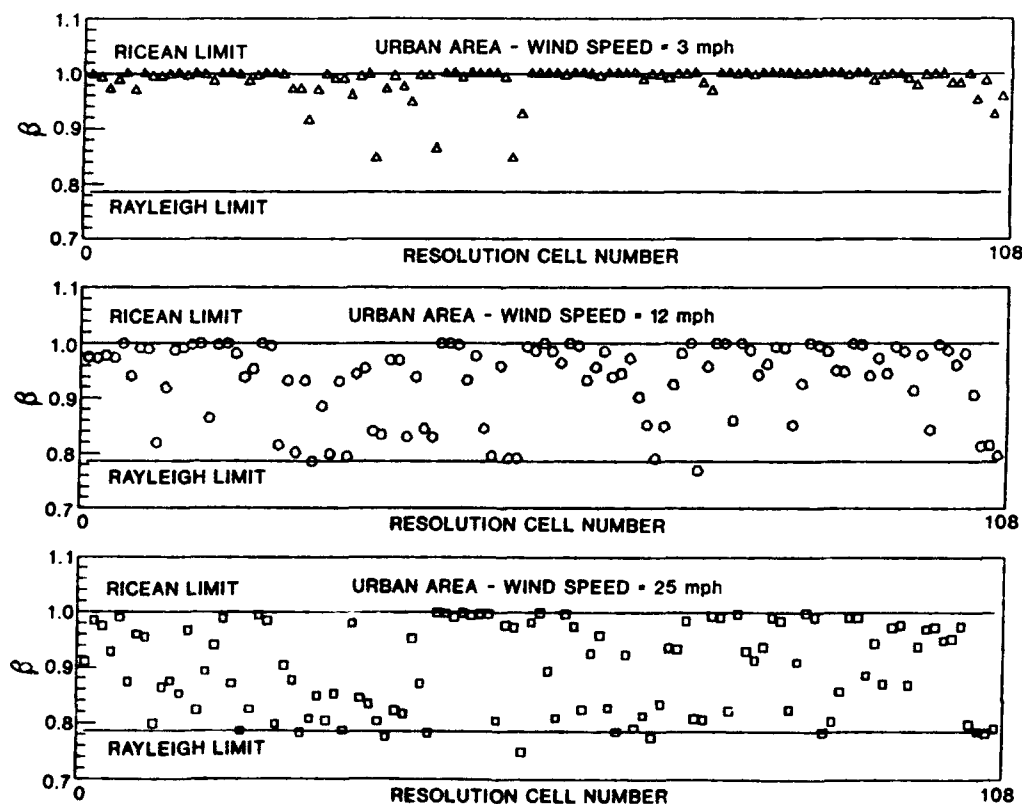


Figure 15. Scatter plots of parameter  $\beta$  for S-band clutter from urban areas at the DREO site.

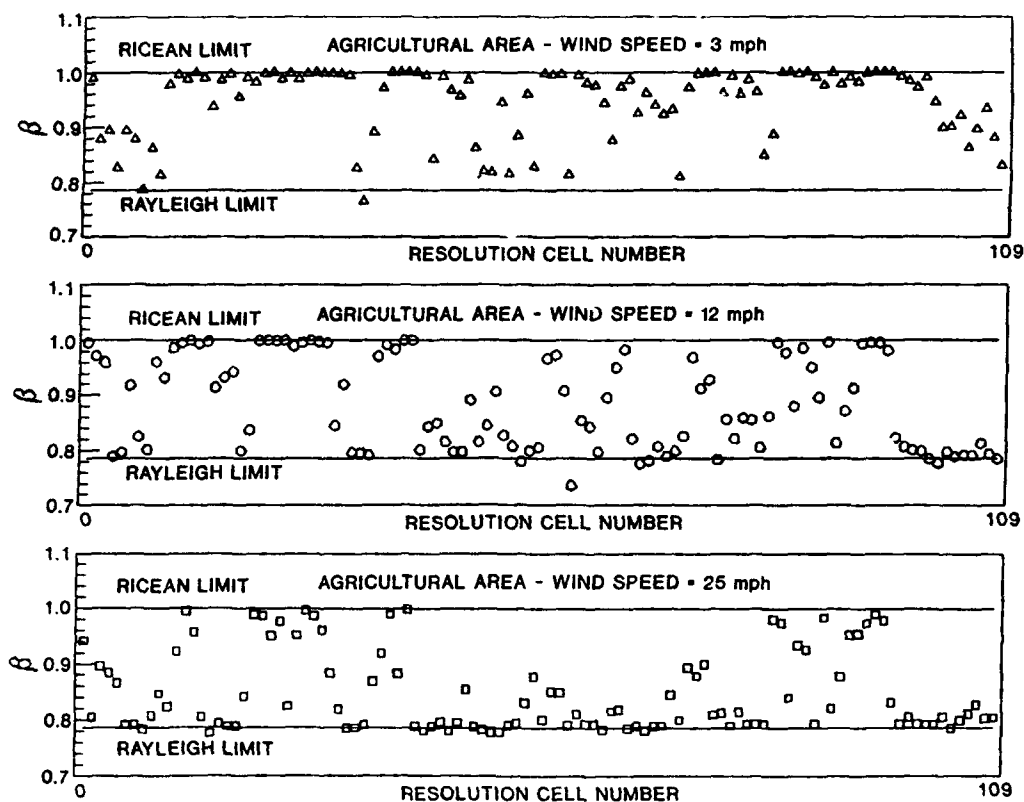


Figure 16. Scatter plots of parameter  $\beta$  for S-band clutter from agricultural areas at the DREO site.

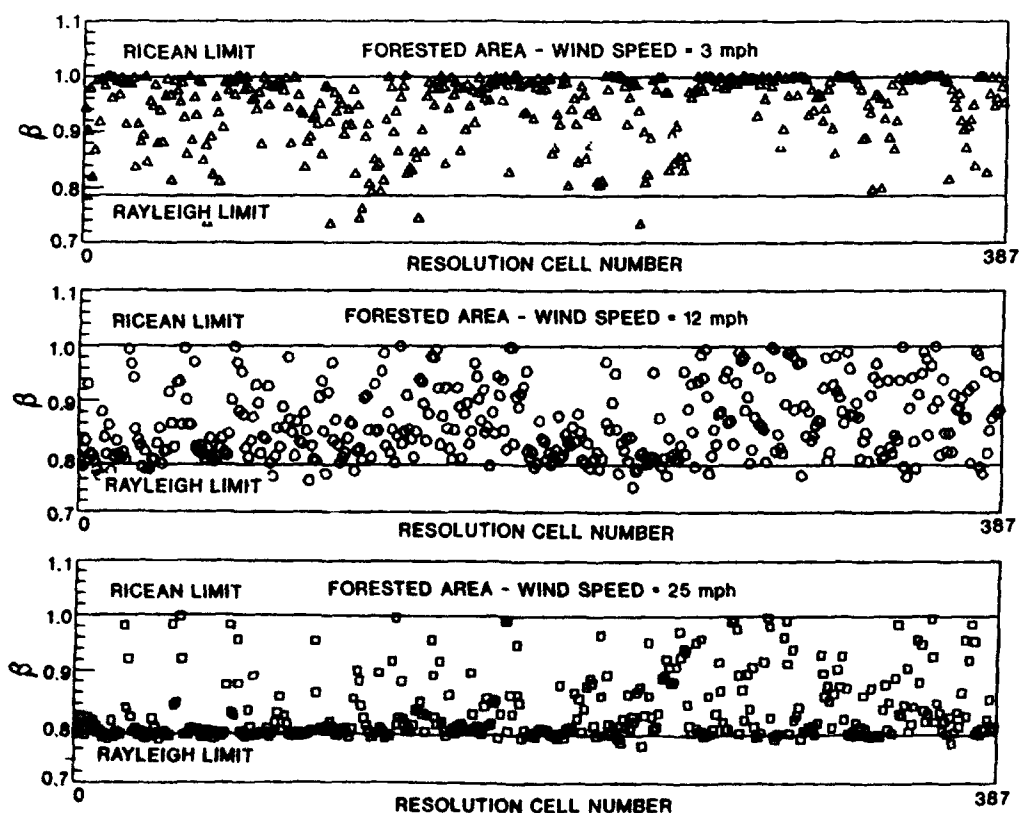


Figure 17. Scatter plots of parameter  $\beta$  for S-band clutter from forested areas at the DREO site.

## **DISCUSSION**

**G. Neininger (GE) :**

Concerning spectral distribution diagrams (which are excellent also at the near carrier range ! ) : what was the phase noise behaviour of the used measuring equipment ? Was it taken into account ?

**Author's reply :**

Both the phase I and the DREO's S-Band radars were coherent radars. The phase noise characteristics for both radars were very good ; however, I do not have the precise technical data concerning phase noise of the equipment. If the bandwidth of the phase noise is wider than the PRF, then it can be considered as white noise. The inter-pulse stability of the phase was improved by taking a sample of the transmit pulse phase and using it to correct for any drift from pulse to pulse.

**G. Brown (US) :**

Do you see any sensitivity to polarization in the coherency factor data ?

**Author's reply :**

There is some sensitivity but it seems to be of second order and less important compared to effects caused by changes in wind speed.

**U. Lammers (US) :**

1 - What distinguishes calibrated from non-calibrated data ?

2 - Most Lincoln Lab data were taken in Canada. Could you say what is peculiar about these data : type of vegetation, frozen ground, etc... ?

**Author's reply :**

1 - We used the term "calibration" to describe the process of transforming the raw clutter data which were sampled from the radar's analog - to - digital converter, into the equivalent radar cross section in  $m^2$ . The process involves the two-way radar equation which accounts for system parameters such as gain, transmit power and range, etc... The MIT Lincoln Labs' phase II data were calibrated, while the DREO data were not.

2 - When the phase I experiment was planned at Lincoln Laboratory, there was a variety of land covers which was of particular interest. These areas were more readily available in Canada because the country is still sparsely populated and negotiation with property owners for the use of their land could be more easily arranged.

# A MODEL OF COHERENT RADAR LAND BACKSCATTER

By

G.C. Sarno

GEC-Marconi Research Centre

West Hanningfield Road

Great Baddow

Chelmsford

Essex

CM2 8HN

ENGLAND

**Summary :** The detection of targets in a land clutter background is a problem for most ground-based and airborne pulse-Doppler radars. Understanding how land clutter behaves can lead to modified clutter suppression techniques for improving radar target detection performance. This paper presents a model of land clutter which has been validated against a number of different land types observed at different frequencies. The characteristics of the clutter which limit target detection are discussed.

## 1 INTRODUCTION

The modelling of the clutter environment is of critical importance to the radar designer who has to ensure that the detection capabilities of the radar system designed are maintained in all foreseeable scenarios. A coherent pulse-Doppler radar, which uses Doppler processing to extract target radial velocity and to suppress clutter, requires knowledge of the statistics of the clutter fluctuations in each Doppler channel. By anticipating the behaviour of the clutter background, thresholds may be set at the outputs of these Doppler channels so that design false-alarm rates can be achieved.

Backscatter from the ground presents problems to ground-based or look-down airborne radar systems that attempt to detect targets of interest submerged in such a background.

Models of the clutter environment allow investigation of signal processing architectures and algorithms for determining their clutter suppression capabilities and, hence, detection performance. Improvements to current suppression techniques can then be suggested.

This paper outlines a statistical model of land backscatter as applied to a coherent pulse-Doppler radar. The model has been based on recorded data provided by Lincoln Labs. of MIT. The recordings, acquired at numerous sites in North America, were collected as part of a study undertaken by Lincoln Labs. to characterise land backscatter measurements at low grazing angles. The recordings covered a number of distinct landcover and landform types. Also, certain radar operational parameters, such as carrier frequency, range

resolution and polarisation, were varied from recording to recording to determine how these affected the clutter characteristics.

The clutter model, presented in the next section, regards individually the statistical behaviour of the temporal and spatial fluctuations of the clutter, as was the approach taken by [4] for sea clutter. This approach has led to a compound model for sea clutter from which detection probabilities can be readily calculated. A compound model of ground clutter is given here. The implications of this model on target detection is then discussed.

## 2 CLUTTER MODEL

The clutter model presented in this paper has been developed based on low-grazing angle clutter measurements taken at a number of sites in Canada. The sites analysed in the study are tabulated below in Table 1 :

Site	Landcover	Landform
Beiseker	Cropland	Undulating to Hummocky
Big Grass Marsh	Wetland	Level
Brazeau	Forest	Undulating to Ridged
Picture Butte	Cropland	Undulating
Wainwright	Forest	Undulating

Table 1

The measurements were calibrated to give absolute values of RCS. Measurements were acquired at sites over a number of range-azimuth cells. They were recorded using a number of transmitter wavelengths, ranging from VHF (170 MHz) to S-band (3.24 GHz) and X-band (10 GHz), as well as either vertical or horizontal polarisation. In addition, the pulse duration varied so that range resolutions of 15 m, 36 m and 150 m were available.

Marked differences in the clutter characteristics resulting from the use of VHF frequencies as opposed to S or X-band frequencies were observed and these are discussed in the following sections.

In the measurements used for the temporal and spatial analysis of the clutter the number of pulses recorded per range gate, available for processing, was of the order of 1000, with an effective PRF of 15.625 Hz. This gives high quality information on the temporal behaviour of the clutter in each of a small number of range gates.

For the validation of the model via Doppler processing (section 2.4), measurements with 32 pulses transmitted in each of a larger number of range gates were made, with PRFs varying from 62.5 Hz to 93.75 Hz. This gives good spatial description of the clutter, together with realistic Doppler resolution.

For both analysis and validation, range cells from a single azimuth direction were chosen.

The temporal and spatial characteristics of land clutter have been separately modelled using the clutter measurements. They are separately discussed below.

### 2.1 Temporal Behaviour

Various sources, e.g. [1], have attempted to describe the contributions of scattering energy from a typical resolution cell illuminating a patch of land as coming from two distinct sources: energy being received from a large number of small moving scatterers with dimensions of the order of a wavelength (i.e. those that fall in the Resonance region) and energy from a number of larger, relatively stationary, scatterers with dimensions greater than a wavelength. These two components shall be called the random component and the steady component respectively.

The energy from the random component fluctuates within a train of pulses (dwell) as the scatterers are displaced, by turbulence for example. There is usually pulse-to-pulse correlation of the returns relating to the internal motion of the clutter, the degree of which, as received by the radar, is dependent on the radar wavelength and the PRF.

A proportion of the scatterers observed in a resolution cell will, generally, be stationary over the dwell duration (in fact over several dwell durations). The returns are specular, that is the radar waveform is reflected back from these scatterers with a random phase which remains constant over the dwell. The amplitude of the scatterers within the dwell is assumed to be completely correlated from pulse-to-pulse.

Statistically, the random component behaves in the classical fashion of a Gaussian process where there are a large number of independently fluctuating scatterers within a resolution cell. This comes from the Central Limit Theorem [6]. This constraint may be broken if the number of scatterers in a cell becomes small, as may be the case when small resolution cell sizes are used. For the resolution sizes used in the clutter recordings, this constraint is not expected to be broken. For a coherent pulse-Doppler radar the statistics of the random component received in each of the Inphase and Quadrature channels are Gaussian.

Supplementary to the returns from these two clutter components is uncorrelated complex-Gaussian system noise.

Mathematically, the total interference return from a resolution cell may be given by:

$$z = z_r + z_s + z_n \quad \dots (1)$$

where  $z_r$ ,  $z_s$  and  $z_n$  are the complex returns from the random component, steady component and system noise respectively

Each of these terms may be individually defined:

$$\text{random: } z_r = \frac{\alpha_r}{\sqrt{2}} v_I^{(c)} + j \cdot \frac{\alpha_r}{\sqrt{2}} v_Q^{(c)} \quad \dots (2)$$

$$\text{steady: } z_s = \alpha_s e^{j\theta} \quad \dots (3)$$

$$\text{noise: } z_n = \frac{\alpha_n}{\sqrt{2}} v_I^{(n)} + j \cdot \frac{\alpha_n}{\sqrt{2}} v_Q^{(n)} \quad \dots (4)$$

where  $v_I^{(c)}$ ,  $v_Q^{(c)}$  are Gaussian random variables describing the random component in the I and Q channels, respectively

$v_I^{(n)}$ ,  $v_Q^{(n)}$  are Gaussian random variables describing the system noise in the I and Q channels, respectively

$\alpha_r$  and  $\alpha_s$  are the mean amplitudes of the random and steady component scattered energy in a pulse, respectively

$\alpha_n$  is the mean system noise amplitude

$\phi$  is the phase of the steady scatterers, constant over a dwell

The mean amplitudes of the scattering components and the phase of the steady component each vary spatially, from range gate to range gate. The characteristics of this, and other, spatial behaviour will be discussed in detail in the next section.

The temporal correlation in the random component may be exhibited by examining its Power Spectral Density (PSD). The amount of correlation is reflected in the width of the PSD as measured at some defined level below the peak. Commonly held theory states that the PSD of ground clutter best fits a Gaussian function [7]. From the clutter recordings analysed this has not been found to be generally true. It has been found to obey consistently a double-sided exponential function :

$$S(f) = \frac{1}{2w} e^{-\frac{|f|}{w}} \quad \dots\dots(5)$$

where  $f$  is frequency

$w$  is the (power) spectrum width

The wavelength affects not only the RCS of the scatterers and, hence, the total scattered energy, but also the spectral spread  $w$  of the scattered energy. Moving scatterers impart phase modulation on the reflected RF carrier. With large displacements relative to the wavelength, this produces a broad Doppler spectrum of the form described by equation (5). For displacements less than a wavelength the spectrum width and amplitude decreases in proportion to the displacement to wavelength ratio. The RCS of steady scatterers, on the other hand, is generally independent of wavelength.

The RCS of typical moving scatterers, such as leaves and crops, is wavelength dependent. For wavelengths greater than the scatterer dimensions the scatterers are in the Rayleigh region and their RCS diminishes in proportion to the wavelength. At microwave frequencies (e.g. S and X-band) both the dimensions and the displacements of moving scatterers are comparable to a wavelength and, hence, broad Doppler spectra with significant energy are expected. Conversely, at VHF, where dimensions and displacements are less than a wavelength, narrow, low energy spectra are expected.

Figure 1 presents examples of forest clutter PSDs evaluated for a number of data-sets acquired at Wainwright at four different radar frequencies : VHF, L, S and X-bands. The PSD of returns in each of a number of range gates were estimated using a 70 dB weighted 256-pulse FFT and then averaged spatially. The frequency (horizontal) axis is normalised to the PRF whilst the power (vertical) axis is in dBW.

Clutter at the short wavelengths display broad Doppler spreading as expected. As the wavelength increases the spread and energy decreases, so that at VHF there is purely a spike at zero relative Doppler. The PSD of the random component is found to be of the double-sided exponential form (5). The contribution from the steady component is observable from the spike at zero Doppler. Thermal noise is present in varying levels in each recording.

The total single-pulse statistics of the interference power, where the complex return is given by (1), can be shown to be described by a squared-Rice distribution :

$$f_x(x) = \frac{1}{\alpha_r^2 + \alpha_n^2} e^{-\frac{x + \alpha_r^2}{\alpha_r^2 + \alpha_n^2}} I_0\left(\frac{2\alpha_r}{\alpha_r^2 + \alpha_n^2} \sqrt{x}\right) \quad \dots\dots(6)$$

where  $x = |z|^2$  is a random variable describing the interference power statistics.

$I_0$  is a modified Bessel function

Strictly speaking, this pdf (6) is conditional on the mean clutter power which, as discussed later, is spatially varying.

As the radar beam illuminates clutter in different range-azimuth cells the statistics will change from cell to cell since the contribution of each scattering type to the total backscatter will vary. The change in the distribution (6) can be shown by plotting the moments of the distribution from each range gate and observing the variation. The two simplest moments that can be estimated are the mean and standard deviation. The standard deviation, however, is highly dependent on the scale, so a more sensible measure is the normalised standard deviation, called by [6] the "coefficient of variation" and in this paper the "shape parameter",  $V$ :

$$V = \frac{S_x}{\mu_1(x)} \quad \dots\dots(7)$$

where  $S_x$  is the Standard Deviation of the sample set  $\{x\}$

$\mu_1(x)$  is the mean value of  $\{x\}$

The statistical distribution described by (6) has the property that as the steady power diminishes (i.e. as  $\alpha_r^2 \rightarrow 0$ ) the shape parameter tends to a value of 1, denoting an exponential-power distribution, i.e. a Rayleigh-amplitude distribution. On the other hand, as the random component disappears (i.e. as  $\alpha_r^2$  and  $\alpha_n^2 \rightarrow 0$ ) the shape parameter tends to a value of 0.

Figure 2 plots the shape parameter for each range cell of a VHF and S-band forest clutter data-set acquired at Brazeau. By observing the variation in shape parameter values with range we can deduce that the contribution of each component of the clutter to the total, or equally the ratio of the two, changes. This implies that the statistics of the clutter in each range cell are changing, so emphasising the spatial variation of the clutter which is discussed in the next section.

The squared-Rice distribution (6), which is a general model of the temporal statistics of the clutter power, has been found to be violated in some experimental data. This may occur when few scatterers are illuminated in a resolution cell, although this has not been fully investigated.

## 2.2 Spatial Behaviour

Although Figure 2 depicts the spatial behaviour of the clutter power it conceals the spatial variation in each of the random and steady components which are not immediately available from the shape parameters plotted.

Clutter power varies within a dwell, from pulse to pulse, because of the internal motion of the clutter. To investigate the spatial behaviour of the clutter this temporal variation may be ignored by observing the mean power in each dwell. Naturally, the physical distribution and the number of scatterers in a range cell varies from range cell to range cell so that adjacent cells have different mean power. This is particularly accentuated if the dimensions of the range resolution cells are small in relation to the scatterers.

Empirical observations of the spatial variation in mean clutter power has been observed in sea clutter ([2],[3]), both in coherent and non-coherent radars. Statistical modelling of the spatial behaviour in sea clutter has resulted in a compound model of the overall clutter statistics involving both temporal and spatial behaviour, giving the well-known K-distribution model. From this, thresholds for maintaining a design

false-alarm rate and the related detection loss as compared to using Rayleigh-amplitude thresholds have been determined.

In ground clutter there is a spatial variation in the returns due to the natural variation in the physical form of the terrain as well as due to the distribution of scatterers in the radar coverage. Even analysing clutter data taken at the long 150 m range resolution some spatial variation has been observed. This variation has been observed in the Lincoln Labs. clutter data-sets studied as well as in other land clutter measurements, e.g. [5].

The spatial variation in the mean power of each component of land clutter can be seen for each data-set by examining range profiles which show the estimated mean powers for each of a number of range gates. This has been performed on a number of data-sets as shown in Figures 3a and 3b. Range profiles of the mean steady and random power are shown for two X-band data-sets, one from Big Grass Marsh (marshland) and one from Wainwright (forest).

Several observations can be made. The power in each component is seen to vary significantly from range cell to range cell as the landcover and landform varies. The extent of this variation is different for each data-set. In addition to this there is a well-defined empirical relationship between the mean power in the steady component and the mean power in the random component in each range cell:

$$A_r = k A_s \quad \dots (8)$$

This coupling may be better visualised by scatter plots of steady power vs random power, as shown in Figures 3c and 3d, for the profiles of Figures 3a and 3b. Each point signifies a particular range cell. Linear relationships may be ascertained from the scatter plots. These illustrate that the ratio of steady power to random power remains roughly constant over all range gates considered.

This is somewhat predictable since, in nature, the distribution of slowly-moving or stationary scatterers and rapid moving scatterers are generally related. This is because the smaller moving scatterers are likely to be anchored to the stationary scatterers. An example is a forest where the number of leaves illuminated depends on the number of tree trunks present. The argument can equally be applied to other landcover types as implied by Figure 3. Indeed it also applies at different radar frequencies as observed in the measurements. In fact, the linear coupling has been observed qualitatively in most of the clutter data-sets analysed. This phenomenon obviously fails at VHF frequencies

where the RCS of the random component is negligible, so that system noise, alone, is present with the steady component.

In Figures 3a and 3b range profiles of the mean power in the steady and random components were plotted and shown to vary with range. The spectrum width, which depicts the degree of temporal correlation of the random component within a dwell, can also be estimated from returns in each range cell. Range profiles of spectrum width can, hence, be plotted and its spatial behaviour observed in the same way as with the mean clutter power. Figures 3e and 3f display range profiles of spectrum width for the data-sets of Figures 3a and 3b. The range variation is evident in these examples, as well as in others studied (except at VHF where spectrum width is indeterminable).

Modelling of the spatial statistics of these three clutter parameters - mean random power, mean steady power and spectrum width - requires insight into the distribution of values that may be observed. Sample histograms facilitate this by providing a picture of the distribution of values observed in a collection of data-points. These are also called sample probability density functions (sample pdfs). The data-points in this context are the parameter values estimated for each range cell.

Figure 4 plots the sample distribution of the three clutter parameters for the forest clutter data-set of Figure 3. Qualitatively the distribution of random and steady powers show a similar statistical law whilst that of the spectrum width is markedly different.

These curves suggest a generic statistical model which can encompass the spatial statistics of the mean power and spectrum width, namely the Gamma distribution:

$$f_p(p) = \frac{p^{\nu-1} e^{-\frac{p}{\gamma}}}{\gamma^{\nu} \Gamma(\nu)} \quad \dots\dots(9)$$

$$f_w(w) = \frac{w^{\alpha-1} e^{-\frac{w}{\lambda}}}{\lambda^{\alpha} \Gamma(\alpha)} \quad \dots\dots(10)$$

where  $f_p(p)$  is the pdf of the random or steady power

$f_w(w)$  is the pdf of the spectrum width

$\nu$  and  $\alpha$  are order parameters

$\gamma$  and  $\lambda$  are scale parameters

The sample pdfs of the mean random and steady powers suggest that a Gamma Distribution with order parameter  $\nu < 1$  is an appropriate model for the spatial statistics of these parameters. In fact, because of the coupled nature of these parameters as previously discussed, the order parameter for both should be identical, whilst the scale parameters will generally differ. In practice, as shown by the spread of points in the scatter plots of steady power vs random power, the estimated steady and random shape parameters will not, in general, be the same.

The sample pdfs of the spectrum width suggest that a Gamma Distribution with order parameter  $\alpha > 1$  is more appropriate to describe its spatial statistics.

Supplementary to the stochastic processes which describe the spatial variation of the clutter there are underlying correlation processes which affect these statistics. As shown by the range profiles in Figure 3 the clutter varies with range. However the profiles are not range independent. There is a degree of correlation between contiguous range cells. This is because local clutter scatterers have similar behaviour, especially when high radar range resolution is used.

This aspect of the clutter can affect the performance of spatial non-coherent integration processes, such as CFAR processing, which requires the range samples being integrated to be independent over the extent of the processing interval.

The degree of correlation observed in most of the ground clutter data-sets analysed is small enough to be largely ignored. This is obviously qualified by the statement that other clutter types and resolution cell sizes may alter this fact.

## 2.3 Detection performance

The implications of the Non-Rayleigh models of sea clutter on target detection is well documented. The spatial variation is such that, to maintain design false-alarm rates, thresholds need to be set higher than is necessary for classical Rayleigh-amplitude clutter. This implies that there is a detection loss imposed by the higher thresholds.

Non-Rayleigh models can be applied to coherent radars that employ Doppler processing for clutter suppression and target separation. In ground clutter, the spatial variation of spectrum width implies that the clutter statistics are not the same in each Doppler channel because different Doppler channels will exhibit different degrees of clutter power variation.



The effect of the spatial variations in the clutter on the statistics of each Doppler channel may be shown by the "shape spectrum". The shape spectrum is similar in concept to a mean power spectrum which displays estimates of the power in a number of Doppler channels, averaged in range. A shape spectrum displays the estimate of the shape parameter in each Doppler channel, where the shape parameter is evaluated from the channel outputs in range. The shape spectrum provides a simple and succinct means of determining which channels have greater spatial variation in power output and, hence, which require greater thresholds to maintain an overall design false-alarm rate.

The form of the shape spectrum is dependent on the characteristics of the clutter. Before discussing this it is necessary to understand how the shape spectrum attains its form. The coupling of the mean power of the steady and random component causes the clutter shape parameters, as due to mean power variation, to be the same in each Doppler channel (i.e. the statistical distributions are the same, notwithstanding the differences in scale). The spectrum width variation, on the other hand, has a more complex effect on the variation in each channel. This is best shown by an idealised picture which depicts what happens to the outputs of Doppler channels when the spectrum width varies spatially.

Figure 5 shows that, as the spectrum width varies, the power levels in the Doppler channels in which the tails of the PSDs are located display greater variation than do those in channels closer to dc. Shape parameters can clearly be seen to be greatest in the channels where the tails of the individual PSDs dominate. Unquestionably the degree of spatial variation of the spectrum width plays an important role in this as too does the level of the noise floor since this determines where the tails of the clutter PSD in each range cell are defined. Both the magnitude of the channel shape parameter values and the location of the maximum shape parameters are determined by these, and other, factors.

#### 2.4 Validation with Recorded Clutter Data

The model described in this paper has been encapsulated in software which allows complex land backscatter returns to be simulated. By performing identical coherent Doppler processing it is possible to validate the model against recorded clutter data.

The stochastic nature of the clutter means that only ensemble behaviour can be observed for comparisons. In the previous section the mean power spectrum and shape spectrum obtainable from a clutter data-set proved to give a concrete

picture of the understanding of the problem of setting thresholds in a ground clutter environment to maintain desired false alarm rate.

Consequently these have been used extensively to provide means of comparisons of the model with recorded data and, hence, to provide the necessary validation. The measurements used for this purpose are different in nature to those hitherto analysed. These have been recorded with 32 pulses per dwell over a large number of range gates. This gives more accurate estimation of the spectra. Moreover, they reflect the realistic Doppler resolutions that most operational pulse-Doppler radars employ.

Numerous clutter measurements have been Doppler-processed, using a 50 dB Dolph-Chebyshev weighted 32-pulse FFT. From this, mean power spectra and shape spectra have been evaluated. For each such data-set a number of parameters characterising the clutter, as required by the model, have been estimated, via numerous techniques. Consequently, simulated clutter returns have been generated which have been processed identically to the associated recorded data.

Figure 6 displays comparisons of mean power and shape spectra for some X-band forest and cropland clutter. Discussing initially the forms of the spectra, the mean power spectra can clearly be seen to accord with (5). The shape spectra exhibit the characteristic form as described in the previous section with higher power level variations in those channels dominated by the tails of the clutter PSDs.

Comparing the spectra of recorded and simulated returns one can see that qualitatively as well as quantitatively the power spectra and the shape spectra match well so implying that these characteristics of the clutter, which affect detection performance, are effectively modelled.

### 3 CONCLUSIONS

A general statistical model of land backscatter, which models the temporal and spatial fluctuations of the clutter, has been developed, and has been shown to accommodate different clutter types acquired by radars employing different operational parameters. By comparisons of the mean power spectra and shape spectra of recorded data and simulated data the model has been shown to emulate the characteristics of ground clutter that limit pulse-Doppler radar detection performance.

In addition to the effect of the spatial variation of the mean power of the clutter, spatial variation of the spectrum width has been observed. It may play an important part in limiting target detection, especially in those Doppler channels where there is

little clutter-to-noise. Compensation for this, in terms of setting thresholds higher than the classical Rayleigh-amplitude thresholds required to maintain the same overall false-alarm rate, therefore signifies that some detection loss must be accepted.

#### REFERENCES

- [1] M.W. Long, "Radar Reflectivity of Land and Sea", Ch. 5, 2nd Edition, Artech House, 1983
- [2] S. Watts, "Radar Detection Prediction in Sea Clutter using the Compound K-Distribution Model", Proc. IEE, vol. 132, Pt. F, no. 7, pp 613-620, Dec. 1985
- [3] K.D. Ward, C.J. Baker and S. Watts, "Maritime Surveillance Radar Part 1, Radar Scattering from the Sea Surface", Proc. IEE, vol. 137, pt. F, no. 2, pp 51-62, April 1990
- [4] E. Jakeman, P.N. Pusey, "A Model for Non-Rayleigh Sea Echo", IEEE Trans-AP, vol. AP-24, no. 6, pp 806-814, Nov. 1976
- [5] J.K. Jao, "Amplitude Distribution of Composite Terrain Radar Clutter and the K-Distribution", IEEE Trans-AP, vol. AP-32, no. 10, pp 1049-1062, Oct. 1984
- [6] M.G. Kendall, A. Stuart, "The Advanced Theory of Statistics", vol. 1, 3rd Edition, 1969
- [7] F.E. Nathanson, "Radar Design Principles", p.243, McGraw-Hill, 1969

#### ACKNOWLEDGEMENTS

The radar ground clutter measurement data referred to in this paper were collected by Lincoln Laboratory, a centre for research operated by Massachusetts Institute of Technology. This work was sponsored in the United States by the U.S. Defense Advanced Research Projects Agency and the U.S. Department of the Air Force under Air Force Contract F19629-85-C-0002 (ARPA Order 3724). Many of the measurements were conducted in Canada under a Memorandum of Understanding between the U.S. Department of Defense and the Canadian Department of National Defense.

The author would like to gratefully acknowledge the assistance of R. Miller of the GEC-Marconi Research Centre, Chelmsford in the development of the model, to J.B. Billingsley of MIT, Mass. and Dr. H. Chan of DREO, Ottawa for their involvement in the supply of their Phase 1 ground clutter measurement data, and to the Procurement Executive of the MoD for funding the study.

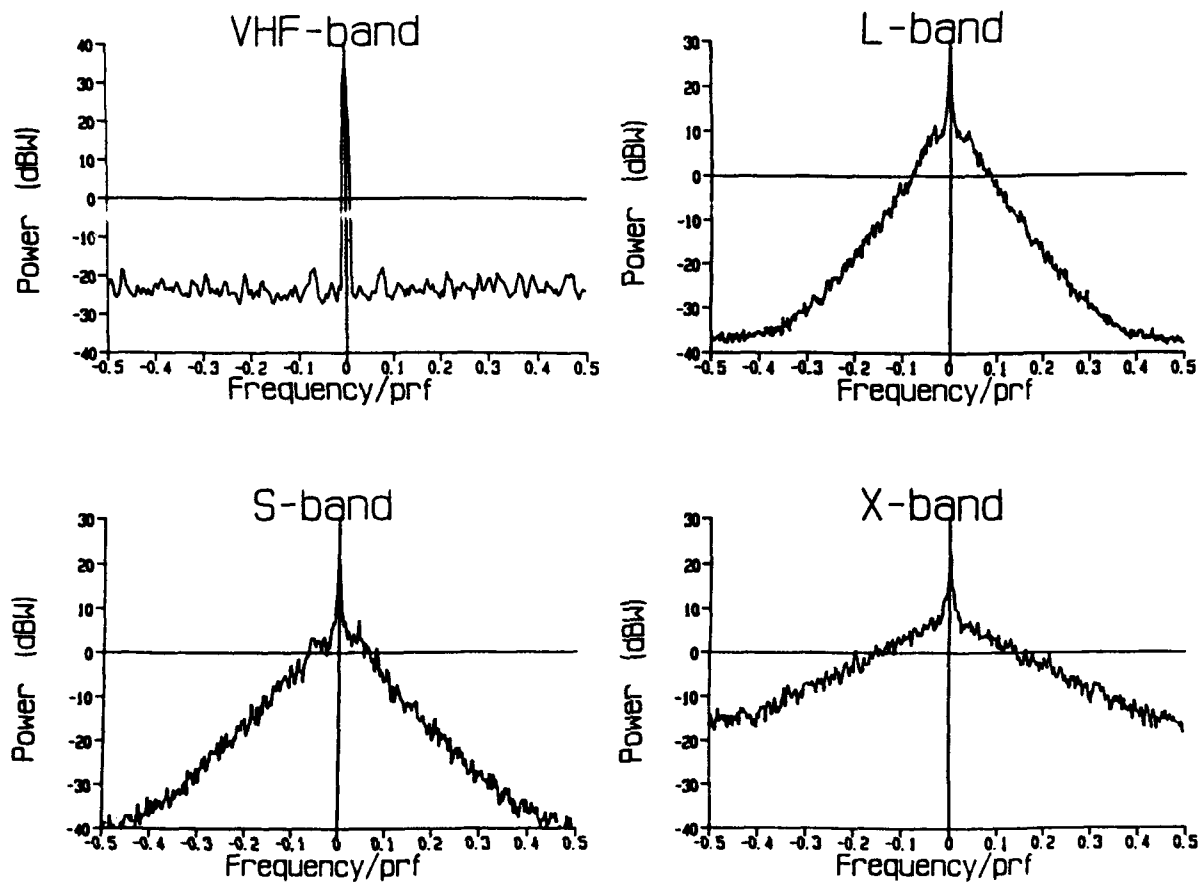


Figure 1 Mean power spectral density for forest clutter at four different radar frequencies, as a function of normalised frequency.

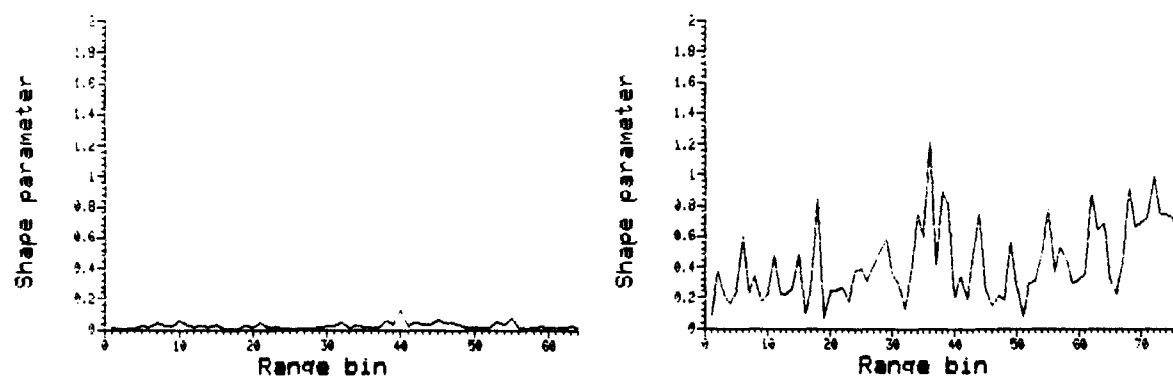
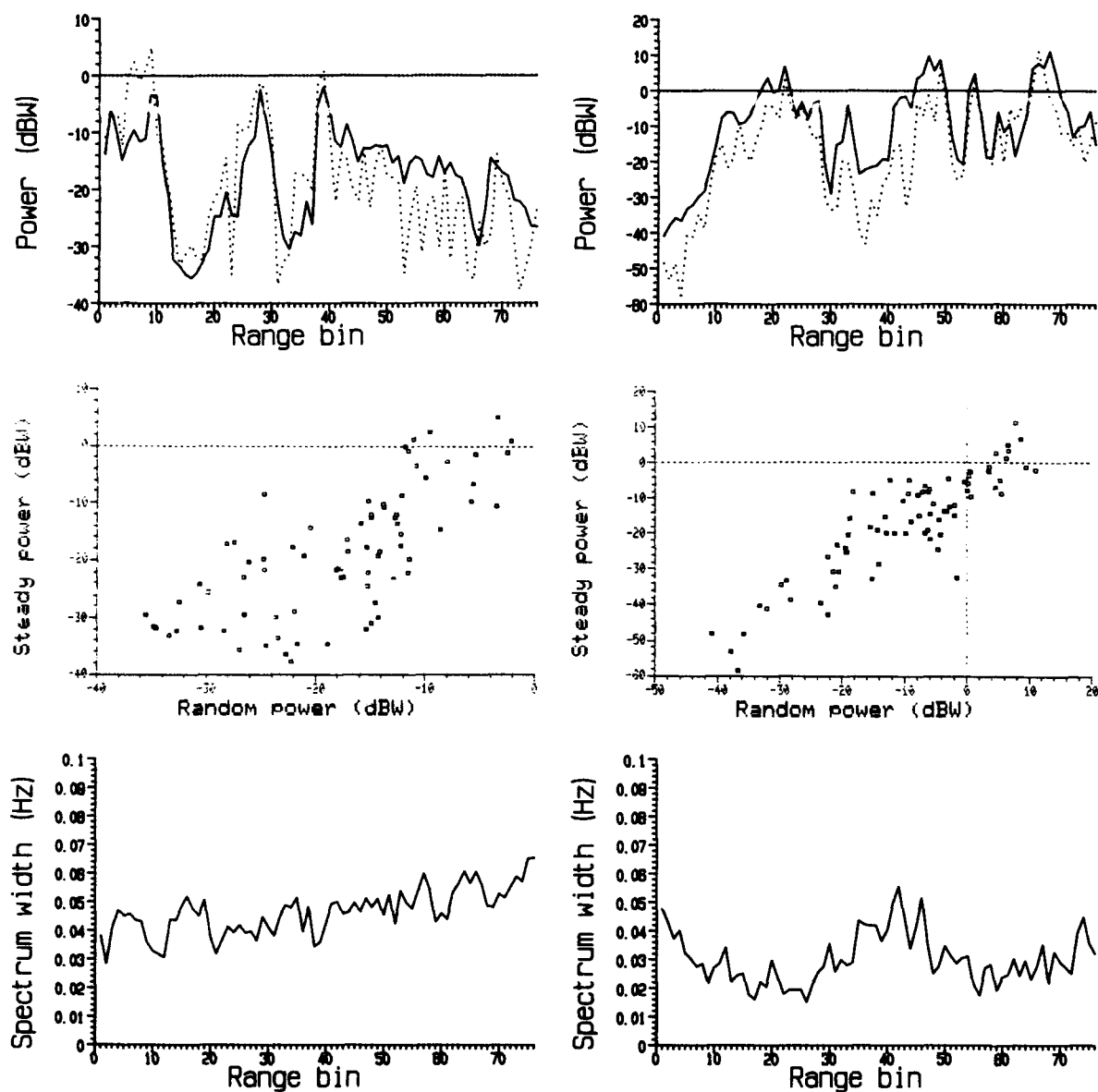


Figure 2 Shape parameter for forest clutter at two different radar frequencies, as a function of range.



**Figure 3** Random (solid line) and steady (dotted line) power for a) Wetland and b) Forest clutter at X-band, as a function of range.  
 c) and d) are scatter plots of steady power vs random power for a) and b) respectively.  
 e) and f) are plots of spectrum width as a function of range for the wetland and forest clutter of a) and b) respectively.

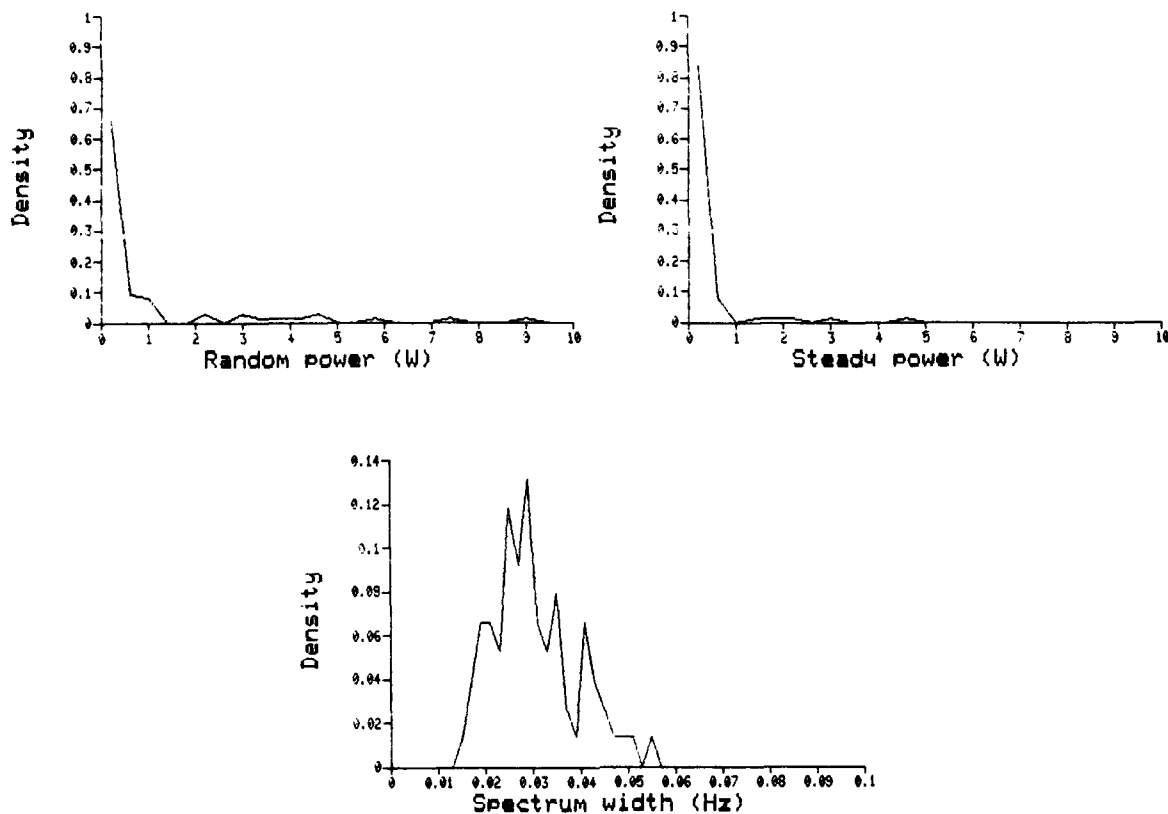


Figure 4 Sample distribution of  
 a) Random power  
 b) Steady power  
 c) Spectrum width  
 for the forest clutter data-set in Figure 3.

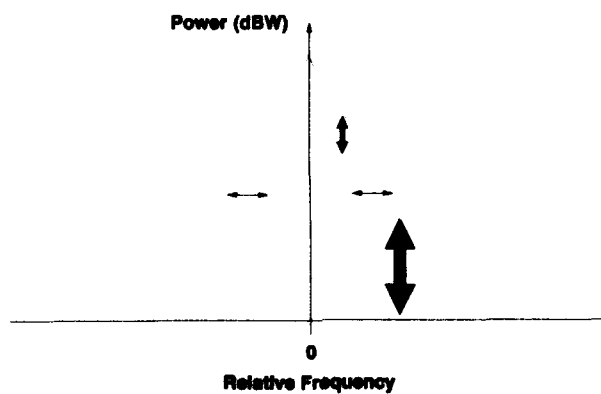
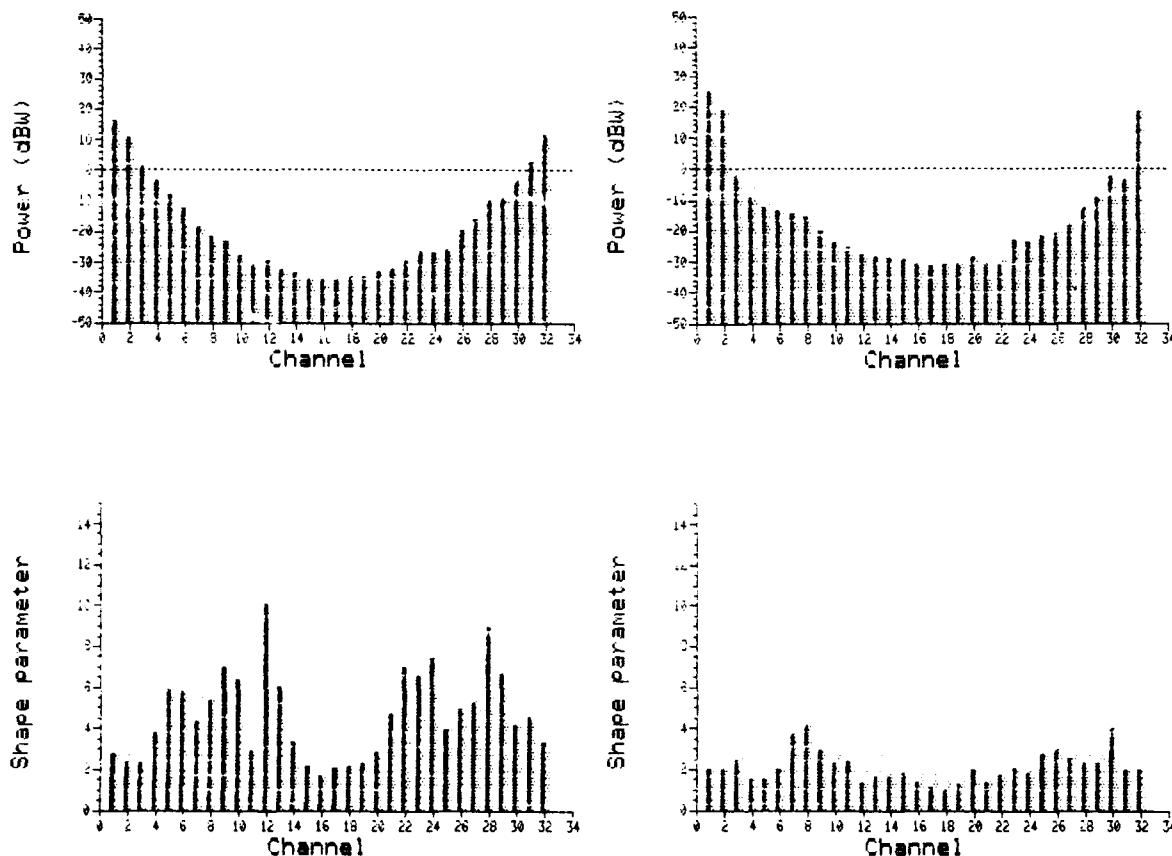


Figure 5 Idealised diagram showing the effect of spectrum width variation on Doppler channel power levels.



**Figure 6** Comparison of mean power spectral density of recorded data (dark bars) with simulated data (light bars) for a) Forest and b) Cropland clutter at X-band. c) and d) give comparison of shape spectra for the forest and cropland clutter of a) and b) respectively.

## DISCUSSION

**H. Chan (CA) :**

What insights led you to choose the Gamma distribution to represent the variation of mean power and the spectral width ?

**Author's reply :**

I chose the gamma distribution for three reasons. One, it is a mathematically tractable model to use. Secondly, it suitably models non-negative random variables which is necessary for modelling near powers and spectral widths. Thirdly, it offers a tie-in with the K-distribution model of sea clutter, of which much work has been done relating to radar detection performance.

# A MODEL FOR BISTATIC SCATTERING OF ELECTROMAGNETIC WAVES FROM FOLIAGE COVERED ROUGH TERRAIN

by

Dr. Robert J. Papa  
Rome Laboratory  
Hanscom AFB, MA 01731

and

Mr. Douglas T. Tamaskanis  
ARCON Corporation  
260 Bear Hill Road  
Waltham, MA 02154

## SUMMARY

The problem of determining the electromagnetic (EM) power received by an antenna located over foliage covered rough terrain in a bistatic scattering geometry is important and quite complex. A model has been developed which can quantitatively determine the effect of a foliage layer on EM waves scattered from rough terrain. The theoretical approximations obtained from this model are compared with data at two levels; the loss in penetrating the foliage and the total normalized scattering cross section  $\sigma^0$ .

In the model, a transmitting antenna and receiving antenna are located at arbitrary heights and locations over a surface with two scales of roughness covered by a foliage layer. Both the coherent and incoherent power scattered into the receiver are calculated. It is assumed that the foliage is sufficiently sparse that the coherent field is dominant over the incoherently scattered waves within the medium. The propagation of the coherent field in the foliage is characterized by an "effective" complex dielectric constant,  $\epsilon^*$ . Explicit expressions for  $\epsilon^*$  have been determined from several multiple scattering formalisms and are based on the dielectric properties of the scattering elements comprising the foliage, i.e. wood, leaves, blades of grass.

The coherent field from the transmitting antenna is ray traced through the foliage layer down to the underlying surface. The waves which are scattered from the rough surface are then ray traced upward through the foliage layer into the receiving antenna. It is assumed that there are no multiple interactions between the waves scattered from the two layers, that the scattering processes for the two media are statistically independent, and that only amplitude (no phase) information is needed for the incoherent waves scattered from the rough surface upward through the foliage.

The results of this theoretical modeling are compared with experimental data at two levels. First, the effective dielectric constants for a foliage environment were used to calculate the attenuation

constants of coherent waves propagating through a dense forest. The attenuation constants given by the model were compared with data taken at 200MHz, 500MHz and 800MHz, resulting in good agreement. Then, the entire bistatic scattering model was used to calculate an effective normalized scattering cross section  $\sigma^0$  for a sod field, grass and forest covered terrain. This was compared with L-band data resulting in excellent agreement between theory and experimental data.

## 1. INTRODUCTION

There have been numerous investigations of the scattering of electromagnetic (EM) waves from foliage and foliage covered rough surfaces [1 through 16]. One of the earliest models [10] for scattering from foliage covered rough surfaces consisted of the simple addition of the scattering cross sections of the vegetation layer and the rough surface. This model suffers from the inadequacy of accounting for the influence of the vegetation layer on the rough surface scattering process. Another early model for describing EM scattering from vegetation was developed by Peake [10]. In this model, the vegetation is represented by long, thin dielectric cylinders, arranged randomly, but having preferred vertical orientation. This model does not account for multiple scattering and scattering from a rough surface lying underneath the vegetation.

In almost all of the models which consider propagation through and scattering from vegetation alone, use is made of the experimental fact that the volume fraction occupied by the foliage is usually less than 5%, i.e. the foliage is sparse [1,12,14]. Another assumption made in the modeling of the propagation through and scattering from foliage is that the scattering from the interconnects between leaves and branches and leaves and stalks is neglected. As pointed out by Brown [11], this is a good assumption since the component elements of foliage are much better absorbers of EM energy than scatterers of EM energy in the frequency range of interest here (500MHz to 3GHz).

Based upon the assumptions mentioned above, there have been numerous attempts to solve for the EM fields scattered from foliage. References [9], [12], and [15] give extensive lists of relevant work. Most of these studies treat the foliage as a continuous medium, with the propagation of the waves governed by an effective dielectric constant,  $\epsilon^*$  [12,14]. This approach, which is used in this paper, is limited by the low frequency constraint that

$$\frac{2\pi}{\lambda} \cdot (\sqrt{\epsilon^*} - 1) \cdot L \leq 0.5 \quad (1)$$

where  $\lambda$  is the free space EM wavelength and  $L$  is the characteristic dimension of a foliage element (leaf or branch).

The continuous medium approach, characterized by an effective dielectric constant, may be analyzed by solving the wave equation with a fluctuating (random) dielectric constant using various approximation techniques. Some of these techniques, whose results will be used in this paper, include the average T-matrix approximation (ATA), the coherent potential approximation (CPA), the effective medium approximation (EMA), and the self-consistent approximation (SCA). These methods will be briefly summarized in Section 2, and are discussed in detail in references [12] and [15].

It will be mentioned that there have been at least two notable attempts to overcome the low frequency limitations of the continuous medium approach: the work of Lang and Sidhu [9] and Brown's investigation [11]. Lang and Sidhu used the Foldy-Twarsky [7] scattering theory to model the scattering from a foliage layer over a flat earth. However, it is not clear how Lang and Sidhu's work would be extended to include a rough earth surface. In Brown's [11] analysis, the field incident on a foliage layer is converted, inside the foliage, to a mean field and a (small) fluctuating field. The mean field is calculated using the Foldy-Twarsky [7] scattering theory and the fluctuating field is calculated from an exact integral equation using a distorted wave Born approximation. These fields are then incident upon a rough surface, giving rise to surface currents. The surface currents are determined by solving the Magnetic Field Integral Equation using iterative techniques. After determining these surface currents, the fields which propagate back up through the foliage layer may be calculated by again splitting them into a mean field component and a fluctuating component. Multiple reflections within the foliage layer are neglected, only a single up-and-down passage is considered. The foliage and rough surface are assumed to be statistically independent physical entities.

In this paper, following Blankenship [12], multiple scattering between different foliage elements is not neglected, i.e. between different leaves and between leaves and branches. The analysis is somewhat similar to Brown's [11] approach, with the exception that the propagation of EM waves through the foliage is characterized by an effective dielectric constant given by the coherent potential approximation (CPA). A transmitting antenna and receiving antenna are located over a surface with two scales of roughness that is covered by a foliage layer. Both the coherent and incoherent power scattered into the receiver are calculated. The model assumes, for this paper, only in-plane scattering; there is no out-of-plane azimuthally dependent scattering. Waves are launched from the transmitting antenna down to the foliage covered terrain. Each ray from the transmitting antenna is treated as a plane wave whose amplitude is weighted by the pattern factor of the transmitting antenna. Each wave in the angular spectrum of plane waves emanating from the transmitter is ray traced through the foliage layer down to the rough surface, is reflected, and then ray traced back up through the foliage layer and into a bistatic receiving antenna. Only the mean value of the electric field (coherent part) is ray traced down through the foliage layer. The coherent wave reflected from the rough surface is ray traced back up through the foliage layer and is amplitude weighted by the pattern factor of the receiving antenna. Also, the diffuse EM energy reflected from the rough surface is composed of an angular spectrum of waves, each of which is ray traced up through the foliage layer, suffers some attenuation, and is then amplitude weighted by the pattern factor of the receiving antenna. The bistatic system may also be studied in a monostatic scattering mode. In this investigation, the theoretical model, with appropriate rough surface parameters, is used to predict an effective normalized cross section  $\sigma^0$  which is then compared with some experimental data. This comparison is made for four terrain types: a sod field, a grass covered field, a forest and a flooded forest. The agreement between the theoretical model and the data is, in general, quite good.

## 2. THEORETICAL MODELS FOR EFFECTIVE DIELECTRIC CONSTANTS OF FOLIAGE

This section presents a brief review of the theoretical models which lead to expressions for an effective dielectric constant  $\epsilon^*$  of foliage media, as discussed in Blankenship [12] and Tamaskanis [14]. Subject to the constraints stated in the introduction, the use of an effective dielectric constant  $\epsilon^*$  permits a heterogeneous mixture of random scattering elements to be treated as a homogeneous medium.



The transition operator  $T$  is used as a basis for the various approximations in multiple scattering formalisms. Maxwell's equations are written as,

$$\nabla \cdot (\epsilon_0 \vec{E}) + \sum_{i=1}^m (\epsilon_i - \epsilon_0) \sum_{j=1}^{N_i} \nabla \cdot (\chi_{ij} \vec{E}) = 0, \quad (2)$$

and,

$$\nabla \times \vec{E} = 0, \quad (3)$$

where (3) is a quasi-static approximation. There are  $m$  constituents and  $N_i$  is the number of scatterers of the  $i^{\text{th}}$  type. Here,  $\rho_i$  is the volume fraction of the  $i^{\text{th}}$  type of scatterer,  $x$  is a spatial parameter and  $\chi_{ij}$  is the support of the  $j^{\text{th}}$  scatterer of type  $i$ , where,

$$\chi_{ij}(x) = \begin{cases} 1 & x \text{ in } j^{\text{th}} \text{ scatterer of type } i \\ 0 & \text{otherwise} \end{cases} \quad (4)$$

The two relationships,

$$\vec{D}(x) = \epsilon(x) \vec{E}(x), \quad (5)$$

and,

$$\langle \vec{D}(x) \rangle = \epsilon^* \vec{E}, \quad (6)$$

define  $\epsilon^*$  where  $\langle \cdot \rangle$  denotes ensemble average.

Expressing Eq. (2) in operator form,

$$(L_0 + M) \vec{E} = 0, \quad \nabla \times \vec{E} = 0, \quad (7)$$

where,

$$L_0 = \nabla \cdot (\epsilon_0 \cdot), \quad (8a)$$

$$M = M_1 + \dots + M_m,$$

with,

$$M_i = \sum_{j=1}^{N_i} V_{ij}, \quad (8b)$$

and,

$$V_{ij} = (\epsilon_i - \epsilon_0) \cdot \nabla (\chi_{ij}(\cdot)) \quad (8c)$$

The  $T$  matrix may be defined as,

$$T = (L_0 + M)^{-1} M. \quad (9)$$

After considerable algebraic manipulation, and expanding the  $T$  matrix in a power series and neglecting higher order multiple interaction terms, an expression for  $\epsilon^*$  may be determined in terms of expectation values of the  $T$  operator and the dielectric constant (Lax [5], Blankenship [12]). In addition, if it is assumed that there is only a single

class of embedded scatterers ( $m=1$ ) and the scatterers are spherical in shape, the following approximation for  $\epsilon^*$  may be obtained [12,14]:

$$\epsilon^*(\epsilon_0; \epsilon_1, \rho_1) \simeq \frac{\langle \epsilon \rangle + \rho_1 \epsilon_1 \left( \frac{\epsilon_0 - \epsilon_1}{2\epsilon_0 + \epsilon_1} \right)}{1 + \rho_1 \left( \frac{\epsilon_0 - \epsilon_1}{2\epsilon_0 + \epsilon_1} \right)}. \quad (10)$$

where,

$$\langle \epsilon \rangle \triangleq (1 - \rho_1) \epsilon_0 + \rho_1 \epsilon_1. \quad (11)$$

For low volume fractions, the average  $T$ -matrix approximation (ATA) may be written,

$$\epsilon^*(\epsilon_0; \epsilon_1, \rho_1) \simeq \epsilon_0 \left( 1 + 3\rho_1 \left( \frac{\epsilon_1 - \epsilon_0}{2\epsilon_0 + \epsilon_1} \right) + 3\rho_1^2 \left( \frac{\epsilon_1 - \epsilon_0}{2\epsilon_0 + \epsilon_1} \right)^2 \right). \quad (12)$$

This approximation is good only for small volume fractions  $\rho \leq 0.01$  and neglects interparticle scattering interactions.

In the coherent potential approximation (CPA), the difference between the field exciting the medium and the average field is neglected [12,14,15,16]. A reference dielectric constant  $\epsilon_r$  is introduced into Maxwell's equations, and is later chosen to simplify (optimize) the equations for  $\epsilon^*$ :

$$\begin{aligned} \nabla \cdot (\epsilon_r \vec{E}) + \sum_{i=1}^m \sum_{j=1}^{N_i} \nabla \cdot ((\epsilon_i - \epsilon_0) \chi_{ij} \vec{E}) + \\ \sum_{i=1}^m \sum_{j=1}^{N_i} \left( \frac{\epsilon_0 - \epsilon_r}{m N_i} \right) \nabla \cdot \vec{E} = 0, \end{aligned} \quad (13)$$

In operator notation, this is written as,

$$(L_r + M_r) \vec{E} = 0, \quad (14)$$

where,

$$L_r = \nabla \cdot (\epsilon_r \cdot), \quad (15a)$$

$$M_r = \sum_{i=1}^m \sum_{j=1}^{N_i} V_{ij}^r, \quad (15b)$$

and,

$$V_{ij}^r = \nabla \cdot ((\epsilon_i - \epsilon_0) \cdot \chi_{ij}) + \left( \frac{\epsilon_0 - \epsilon_r}{m N_i} \right) \nabla \cdot. \quad (15c)$$

The  $T$  matrix in this approximation is defined as,

$$T_{ij}^r = (L_r + V_{ij}^r)^{-1} V_{ij}^r. \quad (16)$$

After much algebraic manipulation, an expression for  $\epsilon^*$  may be determined in terms of  $\epsilon_r$ , and expectation values of the dielectric constant and the  $T^r$  matrix. This expression for  $\epsilon^*$  greatly simplifies if  $\epsilon_r$  is chosen so that [12,14,15,16],

$$\left\langle \sum_{i=1}^m \sum_{j=1}^{N_i} T_{ij}^r \right\rangle = 0 \quad (17)$$

This CPA model requires that,

$$\frac{\epsilon_0 - \epsilon_r}{3\epsilon_r} = \sum_{i=1}^m \rho_i \cdot \left( \frac{\epsilon_0 - \epsilon_i}{3\epsilon_r + \epsilon_i - \epsilon_0} \right) \quad (18)$$

The general expression for  $\epsilon^*$  obtained by solving the operator equation (14) is,

$$\begin{aligned} \epsilon^* \simeq & \epsilon_0 + \left( \sum_{i=1}^m \rho_i \epsilon_i - \rho \epsilon_0 \right) \cdot (1 - \rho) \epsilon_0 \left( \frac{\epsilon_0 - \epsilon_r}{3\epsilon_r} \right) + \\ & \left( \sum_{i=1}^m \rho_i \epsilon_i \cdot \frac{\epsilon_0 - \epsilon_i}{3\epsilon_r + \epsilon_i - \epsilon_0} \right) \cdot \\ & \left( \sum_{i=1}^m \rho_i \epsilon_i \right) \cdot \left( \frac{\epsilon_0 - \epsilon_i}{3\epsilon_r + \epsilon_i - \epsilon_0} \right) \end{aligned} \quad (19)$$

where,

$$\rho = \sum_{i=1}^m \rho_i$$

When only one class of embedded scatterer is considered ( $m=1$ ) and the scatterers are very small, Eqs. (18) and (19) combine to give the CPA for  $\epsilon^*$ ;

$$\begin{aligned} \epsilon^*(\epsilon_0; \epsilon_1, \rho_1) \simeq & \epsilon_0 \left( 1 + 3\rho_1 \left( \frac{\epsilon_1 - \epsilon_0}{2\epsilon_0 + \epsilon_1} \right) + \right. \\ & \left. \rho_1^2 \left( \frac{(\epsilon_1 - \epsilon_0)^2 (\epsilon_1^2 + 13\epsilon_0 \epsilon_1 - 5\epsilon_0^2)}{\epsilon_0 (\epsilon_1 + 2\epsilon_0)^3} \right) \right) \end{aligned} \quad (20)$$

In the effective medium approximation (EMA), proposed by Elliot et al [13], a two-phase material was considered in which the two phases fill all of space and there is no distinction between a host medium and embedded particles. In the EMA model, the equation for  $\epsilon^*$  may be written [12];

$$\begin{aligned} \epsilon^*(\epsilon_0; \epsilon_1, \rho_1) \simeq & \epsilon_0 \left( 1 + 3\rho_1 \left( \frac{\epsilon_1 - \epsilon_0}{2\epsilon_0 + \epsilon_1} \right) + \right. \\ & \left. 9\rho_1^2 \left( \frac{\epsilon_1 - \epsilon_0}{2\epsilon_0 + \epsilon_1} \right)^2 \left( \frac{\epsilon_1}{\epsilon_1 + 2\epsilon_0} \right) \right) \end{aligned} \quad (21)$$

The Self-Consistent Approximation (SCA) is readily derived from the CPA by letting the reference dielectric constant  $\epsilon_r$  in Eq. (19) be equal to the effective medium dielectric constant  $\epsilon^*$ .

Then, an implicit functional relationship may be obtained for  $\epsilon^*$  [12,14,16]:

$$\begin{aligned} \epsilon^*(\epsilon_0; \epsilon_1, \rho_1) \simeq & \frac{\langle \epsilon \rangle + \rho_1 \epsilon_1 \left( \frac{\epsilon_0 - \epsilon_1}{3\epsilon^*(\epsilon_0; \epsilon_1, \rho_1) + \epsilon_1 - \epsilon_0} \right)}{1 + \rho_1 \left( \frac{\epsilon_0 - \epsilon_1}{3\epsilon^*(\epsilon_0; \epsilon_1, \rho_1) + \epsilon_1 - \epsilon_0} \right)} \end{aligned} \quad (22)$$

Numerical evaluation of Eq. (22) requires the use of an iterative algorithm which has not yet been developed. Therefore, results from the SCA are not presented in this paper but may be the subject of future efforts. There are theoretical reasons to conclude that the SCA method will give the most accurate representation for  $\epsilon^*$  [12].

It is possible to extend the case of one embedded scatterer in a host medium ( $m=1$ ) to the case of several embedded scatterers in a host medium ( $m \geq 2$ ) by using an iterative procedure. When a background medium  $\epsilon_0$  contains two classes of embedded scatterers  $\epsilon_1$  and  $\epsilon_2$ , the effective dielectric constant of the medium can be defined as  $\epsilon^*(\epsilon_0; \epsilon_1, \rho_1 / (1 - \rho_2))$ . This recursive technique is found to work well for two embedded scatterers when the volume fractions  $\rho_1$  and  $\rho_2$  are small,

$$\begin{aligned} \epsilon^*(\epsilon_0; \epsilon_1, \rho_1; \epsilon_2, \rho_2) \simeq & \epsilon^* \left( \epsilon^*(\epsilon_0; \epsilon_1, \frac{\rho_1}{1 - \rho_2}); \epsilon_2, \rho_2 \right) \end{aligned} \quad (23)$$

Figures (1) and (2) are plots of the real part and imaginary part of  $\epsilon^*$  versus the volume fraction occupied by wood ( $\rho_2$ ) for a hardwood (oak) forest and a softwood (fir) forest, respectively. The volume fraction of leaves  $\rho_1$  was taken to be 10% of the total volume fraction of a typical density forest [14], which is consistent with what has been reported in the literature, i.e.  $\rho_1 = 0.1\%$ . The conditions correspond to summer with an ambient air temperature of 25°C. The signal frequency is 1.3GHz (L-band). Because of the relatively low volume fractions  $\rho_1$  and  $\rho_2$ , the ATA, CPA and EMA models all agree to within a few percent. Also, as noted by Tamaskanis [14], these values agreed with the experimental data reported in the literature when the volume fractions are less than 5%. Fortunately, volume fractions of foliage above 5% do not often occur in nature.

### 3. SIMULATION OF BISTATIC SCATTERING FROM FOLIAGE COVERED TERRAIN

In the introduction, it was explained how the scattering model consists of a transmitting antenna and receiving antenna located at arbitrary

heights over a surface with two scales of roughness covered by a foliage layer (Fig. 3). In the angular spectrum of plane waves emanating from the transmitter, each coherent wave is ray traced down through the foliage layer, is reflected from the rough surface, and the coherent wave is ray traced back up through the foliage layer and into the receiver. The incoherent power scattered from the foliage is neglected because the foliage is sparse. There is an angular spectrum of plane waves due to the diffuse power (partially coherent) reflected from the rough surface. From each of these waves is ray traced back up through the foliage layer and into the receiver (see Fig. 4). The numerical procedure consists of breaking up the foliage free-space interface into  $\frac{1}{5}\lambda$  patches, where  $\lambda$  is the EM free space wavelength. The model also includes the reflection of the coherent incident rays from the top of the foliage layer and the reception of those reflected waves by the receiving antenna, using Fresnel's plane wave reflection coefficients.

In the ray tracing technique, each ray in the foliage layer is represented as,

$$\vec{E} = \vec{E}_0 \cdot \exp\left(j \cdot \frac{2\pi}{\lambda} \cdot \sqrt{\epsilon^*} \cdot z\right), \quad (24)$$

where  $\vec{E}_0$  is the amplitude of the incident electric field and  $z$  is the path length in the foliage. At the foliage-free space interface, Snell's law is used to determine the direction of the refracted ray:

$$\sin\theta_i = \text{Re}(\sqrt{\epsilon^*}) \cdot \sin\theta_r, \quad (25)$$

for an air-foliage interface where  $\theta_i$  is the angle of incidence and  $\theta_r$  is the angle of refraction.

The model used in this report considers only in-plane bistatic scattering, with no azimuthally dependent scattering processes (this model will be extended to include these cases in future work). The transmitter may be either horizontally or vertically polarized. According to the previous discussions, the diffuse power coming into the receiver is then calculated from the equation (see Fig. 4):

$$P_r = \sum_j \frac{|E_i|^2 \cdot G_t^2}{4\pi R_{1j}^2} \cdot |1 + F_{rj}|^2 \cdot \left| \exp\left(ik\sqrt{\epsilon^*} Z_{1j}\right) \right|^2 \cdot \left( \sigma_{pq}^0 A_j \right) \cdot \left| \exp\left(ik\sqrt{\epsilon^*} Z_{2j}\right) \right|^2 \cdot |1 + F_{rj}|^2 \cdot \frac{G_r^2 \cdot \lambda^2}{(4\pi R_{2j})^2}. \quad (26)$$

Here,

- $E_i$  is the intensity of the transmitting antenna.
- $G_t$  is the angular dependent gain (E-Field) of the transmitting antenna.
- $R_{1j}$  is the distance from the transmitting antenna

to a small  $(\lambda/5)$   $j^{\text{th}}$  patch on the ground.

$F_{rj}$  is the Fresnel reflection coefficient of the  $j^{\text{th}}$  patch of the foliage layer above the ground for either vertical or horizontal polarization.

$k = 2\pi/\lambda$ .

$Z_{1j}$  is the path of the incident ray in the foliage from the  $j^{\text{th}}$  patch.

$Z_{2j}$  is the path of the reflected ray in the foliage towards the  $j^{\text{th}}$  patch.

$\sigma_{pq}^0$  is the normalized cross section of the rough surface where;

$p$  is the transmitter polarization and,

$q$  is the receiver polarization.

$A_j$  is the area of the  $j^{\text{th}}$  small patch on the ground.

$G_r$  is the angular dependent gain (E-Field) of the receiving antenna.

$R_{2j}$  is the distance from the receiving antenna to a small  $(\lambda/5)$   $j^{\text{th}}$  patch on the ground.

The sum in Eq. (26) is over all the small patches on the foliage free-space interface where the transmitting antenna patterns and receiver antenna patterns have significant contributions.

The two-scale normalized cross section  $\sigma_{pq}^0$  is written as the sum of a large scale physical optics (PO) cross section and a small scale perturbation method (PM) cross section (Ruck et al [10]):

$$\sigma_{pq}^0 = \sigma_{pq}^0(\text{PO}) + \sigma_{pq}^0(\text{PM}), \quad (27)$$

which is valid when  $\sigma_L/T_L \ll 1$ . Here,  $\sigma_L$  and  $T_L$  are the standard deviation in height and correlation length for the large scale roughness,  $p$  is the polarization of the transmitter and  $q$  is the polarization of the receiver. Also,

$$\sigma_{pq}^0(\text{PO}) = |\beta_{pq}|^2 \cdot J \cdot S, \quad (28)$$

where,

$$J = \left(\frac{8\pi^2}{\lambda^2}\right) \int_0^\infty J_0(v_{xy}\tau) \cdot [\chi_2 \chi_1 \chi_1^*] \tau \cdot d\tau, \quad (29)$$

and  $v_{xy}$  is a function of  $\lambda$  and angles of incidence and scattering,  $\beta_{pq}$  is a scattering matrix element [10],  $\chi_1$  and  $\chi_2$  are the univariate and bivariate Gaussian characteristic functions, and  $S$  is Sancer's [17] shadowing function. For the small scale cross section,

$$\sigma^0(\text{PM}) = \frac{4}{\pi} k^4 \sigma_s^2 \cos^2 \theta_r \cos^2 \theta_s \cdot |\alpha_{pq}|^2 \cdot I \cdot S, \quad (30)$$

where  $\alpha_{pq}$  is a scattering matrix element and for a Gaussian surface correlation function [10]:

$$I = \pi \cdot T_s^2 \cdot \exp\left(-\frac{v_{xy}^2 T_s^2}{4}\right), \quad (31)$$

and  $\sigma_s$  and  $T_s$  are the small scale roughness parameters.

#### 4. COMPARISON OF MODEL PREDICTION WITH SOME EXPERIMENTAL DATA

The first data set demonstrates the ability of the effective medium model to simulate the propagation of EM waves through foliage. Results of recent experimental measurements of the attenuation of EM waves through vegetation media are reported in Tewari [20]. A comparison of the attenuation coefficients ( $\alpha$ ) at various frequencies, calculated using values of  $\epsilon^*$  from the coherent potential model above, and the Tewari data are summarized in Table 1. The theoretical model estimations of the attenuation coefficients describing EM wave propagation in foliage media show good agreement with the experimental data [14].

Frequency (MHz)	Calculated $\epsilon^*$	Model $\alpha$ (dB/m)	Tewari $\alpha$ (dB/m)	Variation (%)
50	(1.03,7.3e-4)	0.0033	-	-
200	(1.03,4.6e-4)	0.0082	0.0110	-25.5
500	(1.03,2.8e-4)	0.0125	0.0138	-9.1
800	(1.03,2.1e-4)	0.0151	0.0152	-0.9
1300	(1.03,2.0E-4)	0.0233	-	-

Table 1. Comparison of experimental attenuation constants with calculated values.

Experimental data was taken over some bare fields with a synthetic aperture radar SAR at L-Band (Larson et al [18]). Both HH and VV polarization data were taken for these sod fields as shown in Figs. 5 and 6 ( $\sigma^\circ$  vs.  $\theta_i$ ). For the theoretical model calculations, the surface parameters were taken as follows:  $\sigma_L = 1.22$  m,  $T_L = 5.0$  m,  $\sigma_s = 3.16 \cdot 10^{-2}$  m,  $T_s = 4.0 \cdot 10^{-2}$  m, while  $\epsilon(\text{ground}) = 30.0 + j0.6$  and  $\epsilon(\text{grass}) = 1.2 + j0.005$ . Fig. 5 shows excellent agreement between the three sets of data and the theoretical model (the two-scale model) for HH polarization. In Fig. 6, the data for VV polarization for the three sod fields shows appreciable variability, with good agreement with the theoretical model for one data set only. The variability is due to different surface conditions; variations in surface roughness parameters having more effect on  $\sigma^\circ$  than variations in  $\epsilon$  (due to moisture content).

Figures 7 and 8 show L-Band scattering data ( $\sigma^\circ$  vs.  $\theta_i$ ) for a 1-meter grass field taken with a SAR [18]. The theoretical model calculations were performed with the following surface parameters:  $\sigma_L = 1.22$  m,  $T_L = 5$  m,  $\sigma_s = 3.16 \cdot 10^{-2}$  m,  $T_s = 4.0 \cdot 10^{-2}$  m, where  $\epsilon(\text{ground}) = 30.0 + j0.6$  and  $\epsilon(\text{grass}) = 1.2 + j0.005$ . Figure 7 shows the excellent agreement between the SAR data and the theoretical model for HH polarization for the grass covered field. Figure 8 shows moderately good agreement between theory and data for the VV

polarization for the grass covered field. The 5 dB discrepancy may be due to some depolarization for the VV polarization (the vertically polarized incident EM waves are partly scattered into horizontally polarized waves).

Figure 9 shows two data points ( $\sigma^\circ$ ) for a sparse softwood forest ( $\approx 22$  m trees) from a SAR with HH polarization. One data point (the circle) corresponds to a normal forest [18], and falls exactly on the theoretical model curve (perfect agreement). The surface parameters used in the theoretical model curve are given as follows:  $\sigma_L = 1.22$  m,  $T_L = 10.0$  m,  $\sigma_s = 3.16 \cdot 10^{-2}$  m, and  $T_s = 4.0 \cdot 10^{-2}$  m, while  $\epsilon(\text{ground}) = 30.0 + j0.6$  and  $\epsilon(\text{forest}) = 1.03 + j0.0002$ . The second data point (the triangle) in Fig. 9 corresponds to  $\sigma^\circ$  for the same forest ( $\approx 22$  m trees) flooded. The theoretical model surface parameters are the same as for the normal forest, but with  $\epsilon(\text{ground}) = 80.0 + j0.6$  (corresponding to lake water). The agreement of the data [18] with the theoretical model is quite good (within 3dB). The theoretical model also shows the same trend as the data points, the  $\sigma^\circ$  for the flooded forest is several dB higher than  $\sigma^\circ$  for a normal forest.

In Fig. 10, several L-Band data points for  $\sigma^\circ$  from softwood 10m trees are shown versus incidence angle  $\theta_i$  for HH polarization [19]. The surface parameters used in the theoretical calculations are as follows:  $\sigma_L = 1.22$  m,  $T_L = 10.0$  m,  $\sigma_s = 3.16 \cdot 10^{-2}$  m,  $T_s = 4.0 \cdot 10^{-2}$  m, where  $\epsilon(\text{ground}) = 30.0 + j0.6$  and  $\epsilon(\text{forest}) = 1.03 + j0.0002$ . The agreement of the data with the theoretical model is again quite good. The most statistically significant point of the measured data corresponds to the value of  $\sigma^\circ$  at an incidence angle of  $55^\circ$ . This is also where the theoretical model curve nearly intersects the data curve.

#### 5. CONCLUSIONS

The general agreement of the L-Band  $\sigma^\circ$  versus  $\theta_i$  data with the theoretical model for four different terrain types is very good for the HH polarization. The agreement between theory and experimental data for the forest terrain shown in Figs. 9 and 10 should be particularly noted. The agreement between the  $\sigma^\circ$  vs.  $\theta_i$  data and the theoretical model shown in Figs. 6 and 8 for an L-Band SAR with VV polarization is not quite as good as the corresponding HH polarization cases. This discrepancy is most likely due to the fact that the theoretical model does not account for out of plane scattering (no azimuthal variation). Some of the vertically polarized incident EM radiation can be scattered into horizontally polarized waves. This depolarization would result in experimental  $\sigma^\circ$  values being lower than what would be predicted by the theoretical model. This trend is shown

clearly in Figs. 6 and 8. Because of the physical mechanisms involved in the scattering processes, this effect is more pronounced for vertically polarized incident waves compared to horizontally polarized incident waves.

## REFERENCES

1. Brown, G.S. and Curry, W.J., "An Analytical Study of Wave Propagation Through Foliage," Rep. RADC-TR-79-359, Rome Air Development Center, Hanscom, AFB, Mass., *Final Technical Report*, January (1980). AD A084348
2. Keller, J.B. and Karal Jr., F.C., "Effective Dielectric Constant, Permeability, and Conductivity of a Random Medium and the Velocity and Attenuation coefficient of coherent Waves," *J. Math Phys.*, 7 (4), (1966).
3. Twersky, V., "Multiple Scattering of Electromagnetic Waves by Arbitrary Configurations," *J. Math Phys.*, 8 (3), (1967).
4. Twersky, V., "Interference Effects in Multiple Scattering by Large, Low-Refracting, Absorbing Particles," *J. Opt. Soc. Am.*, 60 (7), (1970).
5. M. Lax, "Multiple Scattering of Waves", *Rev. Mod. Phys.*, 23 (4), (1951).
6. Varadan, V.K., Bringi, V.N. and Varadan, V.V., "Coherent Electromagnetic Wave Propagation Through Randomly Distributed Dielectric Scatterers," *Phys. Rev. D*, 19, (1979).
7. Ishimaru, A., *Wave Propagation and Scattering in Random Media*, Vols. I and II, Academic Press, New York, (1978).
8. Brown, G.S., "Coherent Wave Propagation Through a Sparse Concentration of Particles," *Radio Science*, 15 (3), (1980).
9. Lang, R.H. and Sidhu, J.S., "Electromagnetic Backscattering From a Layer of Vegetation: A Discrete Approach," *IEEE Trans. Geoscience & Remote Sensing*, GE-21 (1), (1983).
10. Ruck, G.T., Barrick, D.E., Stuart, W.D., and Krichbaum, C.K., *Radar Cross Section Handbook*, Vol. 2, Plenum press, (1970).
11. Brown, G.S., "A Theoretical Study of the Effects of Vegetation on Terrain Scattering,, Rep. RADC-TR-88-64, Rome Air Development Center, Hanscom, AFB, Mass., (1988). AD A198781
12. Blankenship, G.L., "Stochastic Modeling of EM Scattering From Foliage," Rep. RADC-TR-89-22, Rome Air Development Center, Hanscom, AFB, MA, (1989). AD A213118.
13. Elliott, R., Krumfronl J.A., Leath, P.L., "The Theory and Properties of Randomly Disordered Crystals and Related Physical Systems," *Rev. Mod. Phys.*, 46, (1974).
14. Tamaskanis, D., "Effective Dielectric Constants of Foliage Media," Rep. RADC-TR-90-157, Rome Air Development Center, Hanscom AFB, MA, (1990). AD A
15. Tsang, L., Kong, J.A., Shin R.T., "Theory of Microwave Remote Sensing," John Wiley and Sons, (1985).
16. Chow, P.L., Kohler, W.E., and Papanicolaou, G.C., *Multiple Scattering and Waves in Random Media*, North-Holland, New York, (1980).
17. Sancer, M.I., "Shadow-Corrected Electromagnetic Scattering From a Randomly Rough Surface," *IEEE Trans. on Antennas and Propagation*, AP-17, No. 5, (1969).
18. Larson, R.W., Kasischke, E.S., and Maffett, A.L., "Calibrated L-Band Terrain Measurements and Analysis Program - Results," RADC-TR-88-49, (1988) AD A196573.
19. Ulaby, F.T., and Dobson, M.C., "Handbook of Radar Scattering Statistics for Terrain," Artech House, (1989).
20. Tewari, R.K., Swarup, S., Roy, M.N., "Radio Wave Propagation Through Rain Forests of India," *IEEE Trans. Antennas and Propagation*, AP-38, No. 4, (1990).

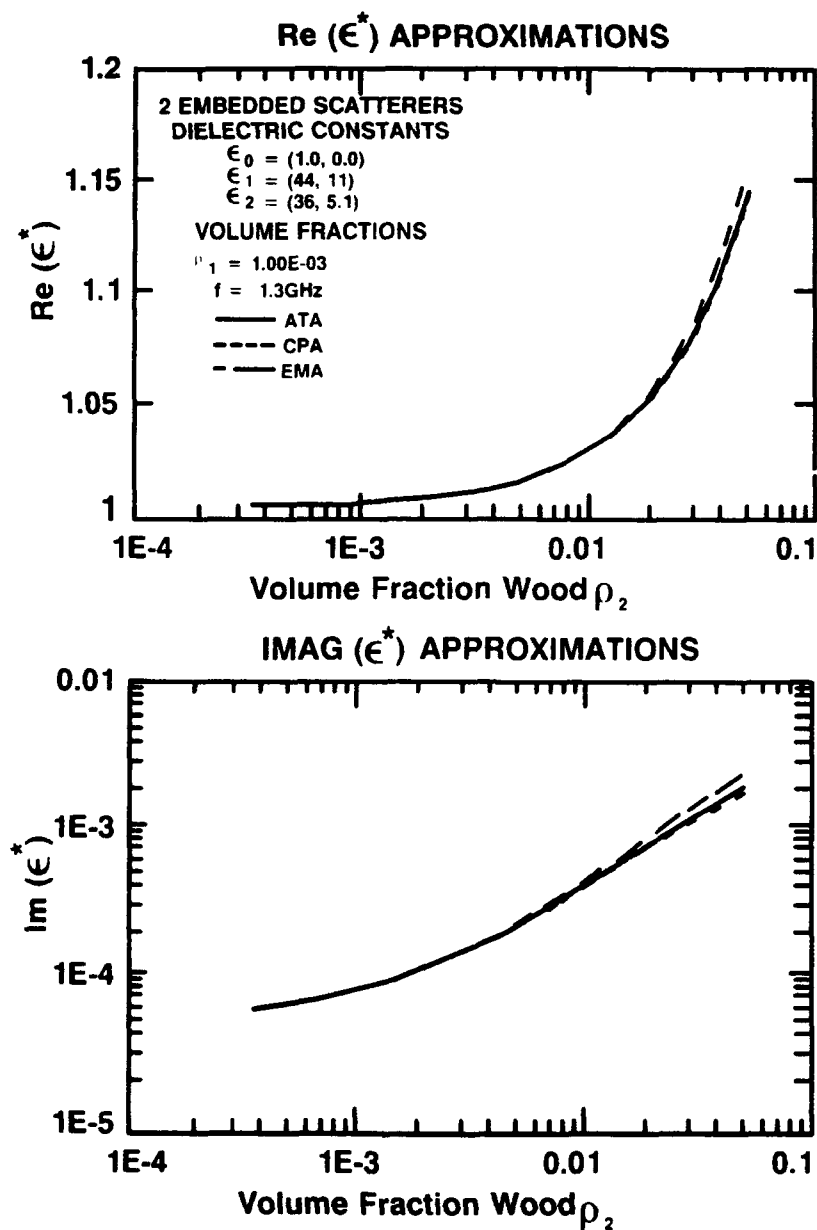
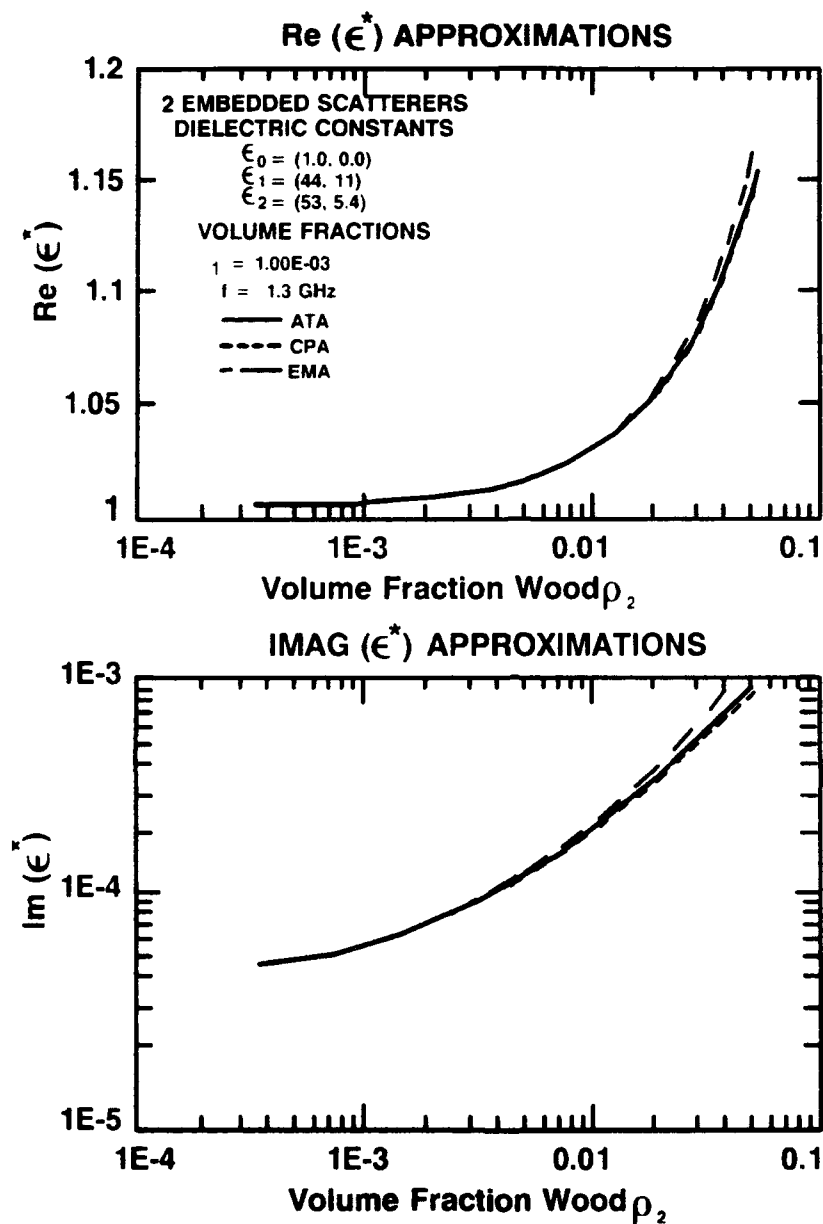


FIGURE 1.

REAL AND IMAGINARY PARTS OF  $\epsilon^*$  OF HARD WOOD VEGETATION  
 (OAK) MEDIA. WOOD GRAIN IS RANDOMLY ORIENTED  
 TO THE E-FIELD POLARIZATION



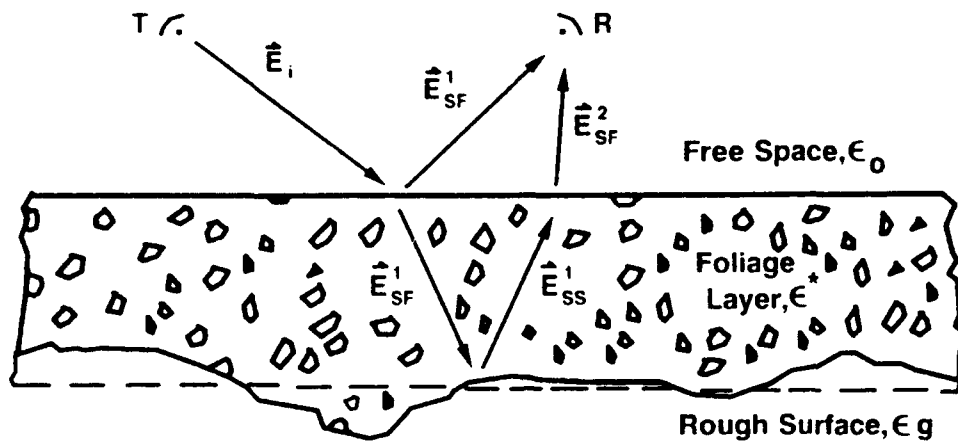


FIGURE 3. SCATTERING MODEL GEOMETRY

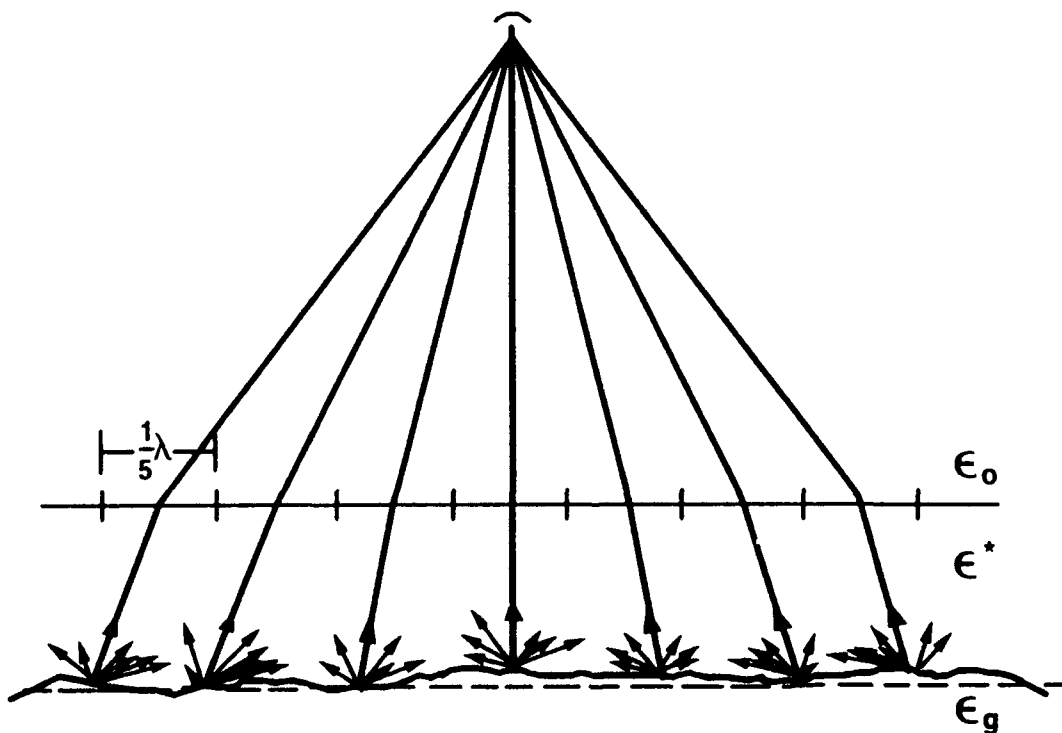


FIGURE 4. ANGULAR SPECTRUM OF PLANE WAVES DUE TO DIFFUSE POWER SCATTERED FROM ROUGH SURFACE, MONOSTATIC DIRECT DOWNLOOK CASE



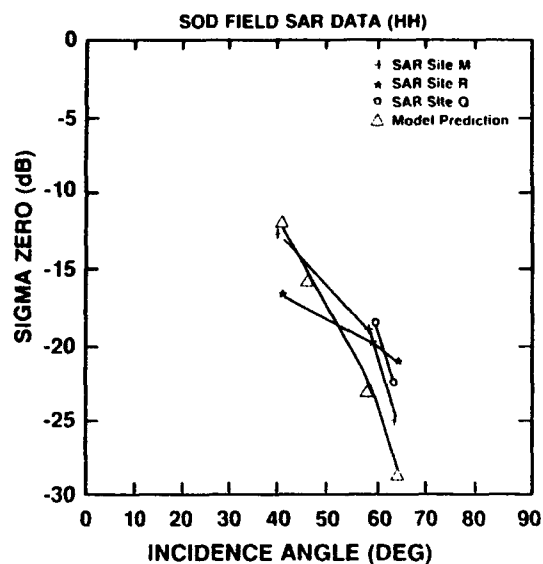


Figure 5.  
COMPARISON OF MODEL PREDICTED  $\sigma^0$  VALUES WITH  
MEASURED SAR DATA FOR A SOD FIELD AT L-BAND

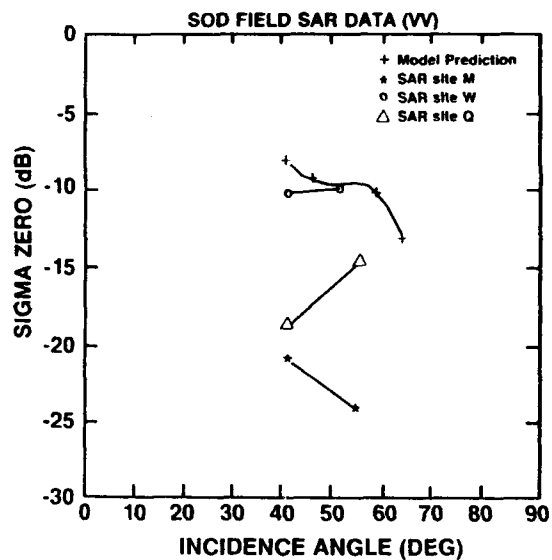


Figure 6.  
COMPARISON OF MODEL PREDICTED  $\sigma^0$  VALUES WITH  
MEASURED SAR DATA FOR A SOD FIELD AT L-BAND

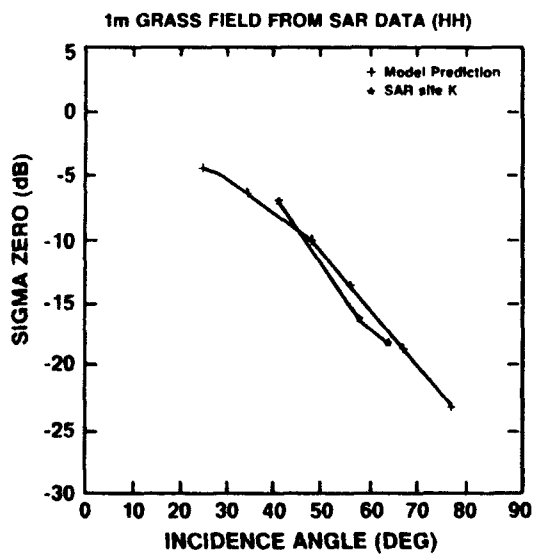


FIGURE 7.  
COMPARISON OF MODEL PREDICTED  $\sigma^0$  VALUES WITH  
MEASURED SAR DATA FOR A 1 METER GRASS FIELD AT L-BAND

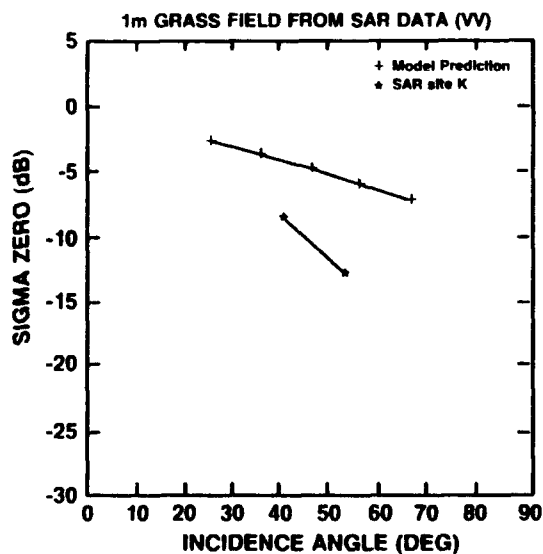


FIGURE 8.  
COMPARISON OF MODEL PREDICTED  $\sigma^0$  VALUES WITH  
MEASURED SAR DATA FOR A 1 METER GRASS FIELD AT L-BAND

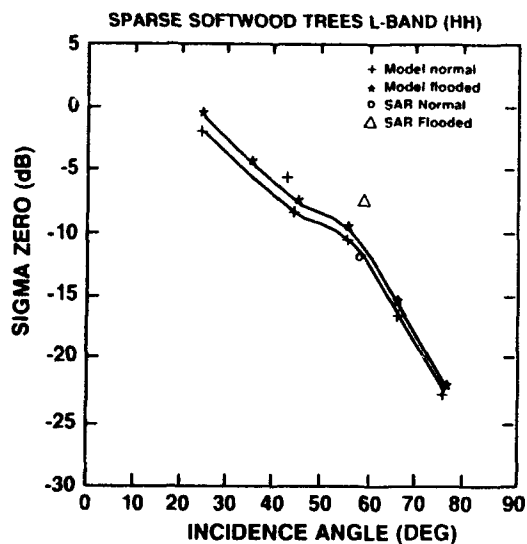


FIGURE 9.  
COMPARISON OF MODEL PREDICTED L-BAND  $\sigma^0$  VALUES OF A SOFT  
WOOD FOREST (22 METER TREES) AND SAR MEASURED VALUES  
FOR BOTH NORMAL AND FLOODED FOREST FLOOR

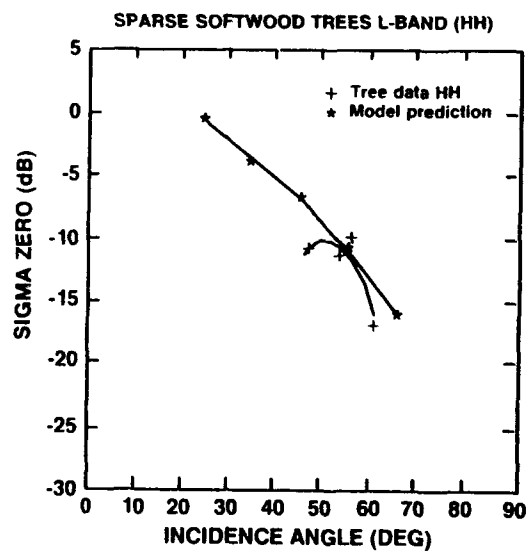


FIGURE 10.  
COMPARISON OF MODEL PREDICTED L-BAND  $\sigma^0$  VALUES OF A  
SOFTWOOD FOREST (10 METERS TREES) AND SAR  
MEASURED DATA

## DISCUSSION

G. Hagn (US) :

How were the values for the dielectric constant for the trees determined for use in the computations as a function of volume fraction of wood ?

Author's reply :

Although scarce, experimental measurements of the dielectric constants of vegetation components at specific frequencies and moisture contents are available in the literature. The results from these measurements were used to verify the validity of specific models which were in turn used to determine the dielectric constants of the vegetation components for the desired conditions. A detailed review of the methods used and specific papers referenced can be found in the paper by Tamassanis listed in the reference section of the paper.

# BISTATIC SCATTERING STATISTICS OF DECIDUOUS TREES

by

K.V.N. Rao, W.G. Stevens, J. Mendonca

Rome Laboratory

Hanscom AFB, MA 01731

## SUMMARY

Theoretical predictions have shown that significant variations in the power scattered by a rough surface exist when the orientation of a linearly polarized bistatic receiver is changed with respect to the transmitter polarization. Experiments conducted at laser frequencies have verified the existence of these polarization variations. This present work was performed to determine if this behavior could be observed at microwave frequencies at a field test site. In this report the experimental results on the polarization dependence of bistatic scattering from deciduous trees are described. The bistatic scattered power from foliage (mixture of Birch, Maple, Ash and grass) at 3.2 GHz was measured as a function of the receiver polarization angle. This paper reports on data for one configuration: incidence angle of 80°, elevation scattering angle of 84°, and one azimuthal scattering angle of 105°. The scattering surface size was approximately 4.5 square meters. A wide band (200 MHz) S-band radar system was used to conduct these measurements. Both vertically and horizontally polarized signals were transmitted. The receiver antenna polarization was varied from 0° to 360° in each case. As the receiver polarization was varied, the scattered power levels changed considerably. In the course of the tests polarization nulls 7 to 20 dB below peak level of the scattered power were observed, depending on the geometrical configuration. The location of these nulls was compared with theoretical predictions, which are based on estimates of surface roughness and complex dielectric constant. A brief discussion on the dependence of the location and depth of polarization nulls on the complex permittivity and roughness characteristics of the scattering surface is also given. Results of experiments show that measured theoretical null locations are in reasonable agreement. Further measurements at additional azimuthal scattering angles will be made. Future plans include phase and amplitude measurements with a dual orthogonal-polarized receiving antenna to determine the ellipticity of scattered signals.

## 1. INTRODUCTION

The scattering of electromagnetic waves from various types of terrain at microwave frequencies has been investigated during the last three decades for several scattering and remote sensing applications. The scattering phenomena is

dependent on frequency, polarization, angles of incidence and scattering, the type of surface, its roughness and its dielectric properties. A brief review of the aforementioned literature indicates that very little emphasis has been placed on polarization dependent bistatic scattering from terrain. However, polarimetric techniques have been developed and investigated in somewhat greater detail to observe the co and cross-polarization of scattering from objects with canonical shapes. Recently investigators have initiated studies on the polarization dependent scattering of electromagnetic waves from randomly oriented objects and surfaces.

## 1.1 OBJECTIVE

The variation of the bistatic rough surface scattering has been discussed in several publications. In particular Papa, Lennon and Taylor examined the general behavior of the rough surface scattering cross section as a function of incident and scattering angles, surface roughness, dielectric constant and polarization using a physical optics model. For some conditions, these authors have predicted that deep nulls occur in the variation of the copolarized bistatic cross section sigma-zero as a function of the scattering angle. For the case where the incident signal polarization is fixed, they showed that varying the linear polarization of the receiving antenna can optimize (either maximize or minimize) the diffuse power scattered by a rough surface. In the general case of bistatic scattering from rough surfaces, the polarization state of the signals entering the receiver is elliptical (Papa and Woodworth). Thus, it is necessary to measure simultaneously the amplitudes and phases of the co and cross polarized signals to demonstrate the absolute null location and its depth. However, in this report we describe the results obtained from measurements of the magnitude of the signal as a function of the receive polarization angle. This restricts the results to those for a linearly polarized receiver.

## 1.2 SCOPE

In section 2 of this report a brief description of the bistatic geometry is given, where we show the relative locations of the transmitter, the illuminated clutter patch and the receiver. The bistatic measurement system and data acquisition techniques are also discussed in this section. Section 3 contains an overview of the theoretical models and the predicted plots of the received

power as a function of the receiver polarization state. Section 4 shows the experimental results obtained when the clutter patch was illuminated with vertically and horizontally polarized signals for two azimuthal scattering angles. The results consist of the magnitude of the signal in the receiver as a function of the receiver's polarization state. The comparison of the experimental observations with the analytical predictions is described in section 5. The summary is contained in section 6.

## 2.0 SYSTEM CONSIDERATIONS

Two critical factors in this experiment are the bistatic geometry in which the behavior is to be observed and the measurement techniques used to acquire the data. Both of these topics will be discussed before the results are presented.

### 2.1 BISTATIC CONFIGURATION DETAILS

The bistatic scattering clutter geometry is shown in figure 1. It is assumed the terrain is in the x-y plane and the transmitter and receiver are located at positions T and R respectively.  $\theta_i$  is the incident elevation angle,  $\theta_s$  is the scattering elevation angle and  $\phi_s$  is the azimuthal scattering angle. The incident and scattering planes shown are designated as I and S. The origin is taken to be the center of the scattering surface clutter cell of interest. The incident electric field is restricted to be either parallel or perpendicular to the plane of incidence "I", whereas the receiving antenna (a 6' parabolic dish) can be rotated through 360 degrees about the boresight axis from the receiver antenna to the origin. This rotation allows us to vary arbitrarily the receive signal polarization. The illuminated terrain is a combination of grass, brush, pine, ash, birch and poplar trees. The grass is approximately 3" to 4" high. The brush is about 2 to 3 feet high, and the height of trees varied between 6 and 15 feet.

### 2.2 DESCRIPTION OF THE EXPERIMENTAL CONFIGURATION

An artist's sketch of the various components of the transmitter, receiver are shown in figure 2. The transmitter van has a pneumatic telescopic mast which can be raised 50 feet above the ground level. A standard gain horn is used as a transmitting antenna mounted on top of the mast and is adjustable so that the clutter patch can be illuminated either with vertically or horizontally polarized signals. Azimuthal rotation of the mast as well as the elevation angle of the horn is possible to illuminate the desired clutter patch at the incidence scattering angle. The 6' parabolic dish mounted on a three-axis positioner served as the receiving antenna. The parabolic dish is fed from a standard gain horn with linear polarization. This

dish is located on the roof of a building at Rome Laboratory's Ipswich Site. Appropriate adjustment of the three axes of the parabolic dish allows us to aim the receiver's boresight to the center of the desired clutter cell.

### 2.3 THE MEASUREMENT SYSTEM AND DATA ACQUISITION TECHNIQUES

The original design of this system was described by Price and Green, as a communication technique for multipath channels and by Linfield et. al for transmission channel characterization by impulse response measurement. We found that this system, suitably modified as shown in figure 3, can be used to make terrain scattering measurements with extremely high range resolution. In both the transmitter and receiver assemblies, all frequencies are derived from a stable 5 MHz crystal oscillator via a series of varactor amplifiers. A pseudo-noise sequence is used to BPSK (Binary Phase Shift Key) modulate the S-Band transmitter, which has a center frequency of about 3.2 GHz. The pseudo-noise sequence is generated by a 10-stage shift register with selectable frequencies of 50, 100, or 200, Mbits/sec. Thus, the bit length can be selected to 20, 10, or 5 nanosecond duration (the shift registers produce a 1023-bit code), resulting in range resolutions of 6 meters, 3.0 meters, and 1.5 meters, respectively.

The pseudo-noise code length in the receiver is of the same length as that in the transmitter. However, the clock frequency in the receiver is offset by a specific value of  $\Delta f$ . The effect of this offset is that the reference code blocks (1023-bit sequence) are continuously "sliding" past those signals entering the receiver. Whenever the reference code in the receiver matches with the code of the signal entering into the receiver the analog correlator in the receiver produces an output.

Figure (3) illustrates the four types of signals entering the receiver. The first one is a reference signal injected into the receiver via a direct cable link between the transmitter and the receiver, thereby eliminating both the antennas. The second signal which enters the receiver is that which is coupled directly via the sidelobes of the antennas along a path which is in the direct line of sight. The third type of signal is that which enters into the receiver via various multipath directions. The fourth type of signal is that which is emanating from the calibration horn. The output of the analog correlator consists of the in-phase and quadrature components as well as the magnitudes of the correlated signals. The auto-correlation function of the pseudo-noise maximal length sequence used provides a high level of discrimination between the correlated and uncorrelated codes such that the four types of signals are individually resolved if their differences

in times of arrival are greater than the code clocking interval  $1/f$  (5 nanoseconds for 200 Mbits/sec). The auto-correlation time sidelobes are about -30 dB. The repetition period of the correlation function (in effect, the data interval of the measurement system) is  $1023/\Delta f$ . Via appropriate choice of  $\Delta f$ , the data intervals are selectable from 10 milliseconds to 2 seconds. This limits the system collecting temporal variations of the clutter fluctuations between 0.5 and 100 Hz. However, all of the data presented in this report are taken with a data collection interval of 200 milliseconds and 200 MHz bandwidth. As mentioned earlier the outputs of the analog correlator consist of in-phase (I), quadrature (Q), and magnitude  $\sqrt{I^2 + Q^2}$ . Thus, by coherent processing of I and Q signal amplitudes, in principle, it is possible to calculate the amplitude and phase of the scattered signal from each range-resolvable clutter cell or time-resolvable signal entering the receiver.

### 3.0 BRIEF OVERVIEW OF THE ANALYTICAL MODELS AND PREDICTION OF THE BISTATIC POLARIZATION NULLS

In this section we will give a brief overview of the analytical models and the prediction of the amplitude of the received power as a function of the scattering angles and the receiver's polarization state. The reader who is interested in the details of the derivation should refer to Papa et al.

#### 3.1 ANALYTICAL MODEL

We summarize here briefly the necessary equations to describe the dependence of the received power on the polarization angle, as well as the scattering angles. For conditions of physical optics, the scattering cross section as defined by Barrick including the shadowing factor S as given by Sancer is,

$$\sigma^0 = |\beta_{pq}|^2 J \cdot S \quad (1)$$

$$\beta_{vv} = \frac{a_2 a_3 R_{\parallel}(i) + \sin \theta_i \sin \theta_s \sin^2 \phi_s R_{\perp}(i)}{a_1 a_4} \quad (2)$$

$$\beta_{hv} = \sin \phi_s \frac{-\sin \theta_i a_3 R_{\parallel}(i) + \sin \theta_s a_2 R_{\perp}(i)}{a_1 a_4} \quad (3)$$

$$\beta_{vh} = \sin \phi_s \frac{\sin \theta_s a_2 R_{\parallel}(i) - \sin \theta_i a_3 R_{\perp}(i)}{a_1 a_4} \quad (4)$$

and,

$$\beta_{hh} = \frac{-\sin \theta_i \sin \theta_s \sin^2 \phi_s R_{\parallel}(i) - a_2 a_3 R_{\perp}(i)}{a_1 a_4} \quad (5)$$

Here, the angles  $\theta_i$ ,  $\theta_s$ , and  $\phi_s$  are defined in Fig. 1,

and  $R_{\parallel}(i)$ ,  $R_{\perp}(i)$  are the Fresnel reflection coefficients for vertical (V) and horizontal (H) polarizations, respectively. The angle  $i$  is defined as

$$\cos i = \frac{1}{\sqrt{2}} \cdot \sqrt{1 - \sin \theta_i \sin \theta_s \cos \phi_s + \cos \theta_i \cos \theta_s} \quad (6)$$

with,

$$a_1 = 1 + \sin \theta_i \sin \theta_s \cos \phi_s - \cos \theta_i \cos \theta_s \quad (7)$$

$$a_2 = \cos \theta_i \sin \theta_s + \sin \theta_i \cos \theta_s \cos \phi_s \quad (8)$$

$$a_3 = \sin \theta_i \cos \theta_s + \cos \theta_i \sin \theta_s \cos \phi_s \quad (9)$$

and,

$$a_4 = \cos \theta_i + \cos \theta_s \quad (10)$$

The quantity J in (1) is proportional to  $\rho(\xi_x, \xi_y)$ , the probability density function for the slopes. The quantities  $\xi_{xsp}$  and  $\xi_{ysp}$  are the surface slopes necessary to give rise to specular reflection of the incident field into the scattering direction:

$$\xi_{xsp} = \frac{\sin \theta_i - \sin \theta_s \cos \phi_s}{\cos \theta_i + \cos \theta_s} \quad (11)$$

and,

$$\xi_{ysp} = \frac{\sin \theta_s \sin \phi_s}{\cos \theta_i + \cos \theta_s} \quad (12)$$

Implicit in the above derivation are the assumptions that  $T \gg \lambda$ ,  $\xi_x \ll 1$ ,  $\xi_y \ll 1$ .  $\xi_x$  and  $\xi_y$  are the local slopes in x and y directions at the local surface point. T is the surface height correlation length and  $\lambda$  is the wavelength. Papa et al give the dependence of scattered power intensity on receive polarization as:

$$I_R \propto (\beta_{VV}^R \cdot \cos \psi + \beta_{VH}^R \cdot \sin \psi)^2 + (\beta_{VV}^I \cdot \cos \psi + \beta_{VH}^I \cdot \sin \psi)^2$$

The scattered power is dependent on the incident elevation angle, receive elevation angle, the azimuthal scattering angle, the Fresnel reflection coefficient and the complex dielectric constant. This leads to an explicit expression for the polarization state (angle) of the receiver which optimizes the received power (either a maximum or a minimum). This expression is given by:

$$\tan \psi_0 = \frac{-B_1 \pm \sqrt{B_1^2 - 4A_1C_1}}{2A_1} \quad (13)$$

where,

$$A_1 = -\beta_{VV}^R \beta_{VH}^R - \beta_{VV}^I \beta_{VH}^I \quad (14)$$

$$B_1 = (-\beta_{VV}^R)^2 + (\beta_{VH}^R)^2 - (\beta_{VV}^I)^2 + (\beta_{VH}^I)^2, \quad (15)$$

$$C_1 = \beta_{VH}^R \beta_{VV}^R + \beta_{VH}^I \beta_{VV}^I. \quad (16)$$

The angle  $\psi_0$  defines the direction of (linear) polarization the receiver should have to optimize the received power scattered from the rough surface. Note that this polarization direction depends only on the dielectric constant (complex) of the surface and the bistatic incidence scattering angles. It is independent of the surface roughness for a single scale of roughness model. When a composite scattering model is used that considers small as well as large scale roughness parameters, the optimum polarization direction may change slightly but the magnitude of the scattered power can vary by several decibels. Thus, if the surface roughness can change with time (as is the case with windblown trees) the clutter polarization minimum and maximum may change in magnitude without a significant shift in their relative locations.

### 3.2 PREDICTIONS FOR EXPERIMENT CONDITIONS

Using the analytical algorithm given by Papa, Lennon and Taylor we computed the intensity of the received power as a function of the polarization state (angle) for our experimental conditions. The plots showing the received intensity as a function of the polarization angle are shown in figures (4a) and (4b) for two correlation lengths. Figure (4a) is for the incident signal on the clutter patch being vertically polarized and the plot shown in figure (4b) is that for the case when the incident signal is polarized horizontally. Implicit in the algorithm is that a linearly polarized receiver is used. It is clear that the depth of the null and the magnitude of the scattered power are dependent on the surface conditions. These results will be related to the experimental data in section 6.

### 4.0 EXPERIMENTAL RESULTS ON POLARIZATION NULLS

In this section we present some results obtained from the bistatic polarimetric experiment conducted at Rome Laboratory's Ipswich Field Site. We measured the power reflected from the deciduous trees using the bistatic geometrical configuration shown in figure (2) for various receiving antenna polarizations. Although our system can resolve 1023 range bins, we recorded only a small percent of this number because relatively few range bins were intersected by both transmitter and receiver antenna patterns for this bistatic configuration. For each polarization state of the receiving antenna we collected data from 100 frames for statistical analysis. Figure (5a) shows

the mean value of the observed power from a typical cell as a function of the receiver polarization angle. As indicated in the figure the data were collected when the patch was illuminated with a vertically polarized signal. Figure 5b shows the results for horizontal polarization. The angles  $\theta_i$ ,  $\theta_s$ , and  $\phi_s$  were 80°, 84°, and 105° respectively. The power from the particular cell is averaged over the 100 data collection frames for each polarization state. The received power is normalized with respect to the maximum power received at polarization angle which is scanned through 360 degrees. The receiving antenna was rotated in incremental steps of 10 degrees. It took approximately ninety minutes to collect the data over the entire 360 degrees.

Figures 6a and 6b show plots of the 90th, 50th, and 10th percentile of the magnitude of the received power for the same bistatic geometry and range bin of figures 5a and 5b. Figure 6a is for vertical and figure 6b is for horizontal transmit polarization. These plots are more revealing than those of just the mean power. It can be seen from these figures that the receiver polarization for which the scattered power is a maximum or minimum does not change whether it is observed from the mean, median, 90th or 10th percentiles. Another interesting feature shown in these plots is that there are variations in the separation of the 90th, 50th, and 10th percentiles for different receiver polarizations. This is discussed in greater detail later in the paper.

Figures 7 and 8 are histograms showing the differences in temporal fluctuations of scattered power from deciduous trees in one range resolution cell as the receiver antenna is oriented to produce the maximum and minimum scattered power. The data in figure 7 were obtained with the transmitting horn antenna vertically polarized, while those of figure 8 were for horizontal transmit polarization. The solid bars of the histogram represent data obtained when the receiving dish antenna was oriented to the polarization of maximum terrain reflectivity for this bistatic geometry. The cross-hatched bar data were obtained when the receiving dish antenna was oriented for minimum reflectivity. For vertical incident polarization, the maximum clutter power occurred at receiver polarization angles of -150 and +30 degrees while the minima occurred at -80 and 100 degrees. For the horizontal incident case, clutter maxima occurred at receiver polarization angles of -60 and +120 degrees while the minima occurred at -140 and +40 degrees. In each of these histograms, the data are normalized to their respective mean values. This allows direct comparison of features of the individual distributions such as shape, spread, and power contained in the distribution tails.

Figures 9 and 10 are histograms of the received power at the two polarization angles at which the minima occur, and are presented to illustrate the differences in distribution. Figure 9 is for vertical incident polarization and figure 10 is for horizontal. Again, the data in these histograms are normalized to their respective mean values. As both of these histograms show, for each incident transmit polarization the two minima have different spreads in their distributions. The difference in spread (or dispersion) between the data obtained at the four polarization angles can be obtained quantitatively by comparing the standard deviations of the normalized data, or equivalently, the ratio of the standard deviation of the unnormalized data to the mean value of the unnormalized data. This standard of comparison is called the relative dispersion, or coefficient of variation.

For vertical incidence, the coefficient of variation of the data at the polarization maximum was 0.192. Values at the polarization minima -80 degrees and +100 degrees were 0.313 and 0.716 respectively. For horizontal incident polarization, the coefficient of variation at the maximum was 0.152 while the minima were 0.372 at -140 degrees and 0.550 at +40 degrees. Two observations can be made from these calculations: First, the relative dispersion of the maxima for each incident polarization is less than that of the respective minima; and second, for each incident polarization case the relative dispersions of the minima data at the two receiver polarization angles are different.

Figures 11 and 12 show more general polarization trends for these results. They show the mean power and coefficient of variation vs. receiver polarization for both transmit polarizations. The results illustrate the trend of falling coefficients with rising mean power and vice versa. Analysis of data for other nearby range cells produced similar findings. Not only do the relative dispersions change with receiver polarization, but that a time dependence is also present. We feel that this time dependence could be attributed to motion of the trees in the very high range resolution cells of our system and to the approximately 40 minutes between data collections at the polarization angles corresponding to the two minima. At present, no attempt has been made to fit a theoretical distribution to these data. But these results show that the shape parameter estimate, if not the fitted distribution type, would change with receiver polarization angle.

## 5.0 DISCUSSION OF EXPERIMENTAL RESULTS AND ANALYTICAL PREDICTIONS

Comparison of the experimental data with analytical predictions would be exact if all the assumptions made in the predictions were met by

the experiments. It is, however, difficult to construct a perfectly linearly polarized antenna for either transmission or reception. It is possible, though, to measure and/or calculate the isolation between co-and cross-polarized components of any given antenna. The antennas used in this experiment have an isolation of 20 dB for the transmitting horn and an isolation of approximately 26 dB for the receiving dish. A second source of error is in the measurement of the exact scattering angles. The incident elevation scattering angle, the receiver elevation scattering angle and the azimuthal angles are exactly measured in the boresight directions. However, the variations in these angles in the intersection of the transmit antenna and receive antenna footprint can only be conjectured. A third source of error is in estimating the rms surface slopes of the surface canopy of the trees and the depth of penetration of the signals into the volume of the deciduous trees.

Emphasis was placed more on identifying the differences in statistics of the scattered power as the receiver polarization was varied. As was seen in plots of measured power vs. polarization angle, the magnitude of the null depth was different for the two polarization minima conditions, while the separation of the nulls remained at 180°. We attribute these results to changes in the rms surface slopes of the range cell of interest over time. Even with mild wind, the surface roughness parameters could change, while the net permittivity of the terrain may remain steady. As shown in the analytical results, calculations made of the scattered power at the two polarization minima for two different surface roughness but similar permittivities produced findings that were similar to experimental results, i.e., nulls that were separated by 180° but were different in magnitude.

## 6.0 SUMMARY

In summary, for our limited data set we have confirmed the existence of polarization nulls in the energy scattered by terrain for bistatic geometries. We have found that there exist differences in the temporal statistical distributions of the scattered power when the receiving antenna is oriented to different polarizations. Our measurements of the power scattered by deciduous trees as a function of receiver polarization angle exhibited minima for two different azimuthal scattering angles. These minima were of different magnitudes and had different coefficient of variation statistics. A physical optics model using the same azimuthal and elevation angles as those in the experiment, and an estimated value of the terrain dielectric constant and surface rms slope was used to predict the scattered power versus polarization angle. Locations of minima predicted by the model were in close agreement with measurements.

## REFERENCES

1. D. E. Kerr, "Propagation of Short Radio Waves", Massachusetts Institute of Technology Radiation Laboratory Series, Vol. 13, McGraw-Hill Book Company, Inc., New York, New York 1951.
2. M. I. Skolnik, "Radar Handbook", McGraw-Hill Book Company, Inc., New York, New York 1970.
3. F. E. Nathanson, "Radar Design Principles", McGraw-Hill Book Company, Inc., New York, New York 1969.
4. M. W. Long, "Radar Reflectivity of Land and Sea", Lexington Books, D.C. Heath and Company, Lexington, MA 1972.
5. N. C. Currie, "Techniques of Radar Reflectivity Measurements", Artech House, Dedham, MA 1984.
6. P. Beckmann and A. Spizzichino, "The Scattering of Electromagnetic Waves from Rough Surfaces", Pergamon, New York, New York 1963.
7. G. T. Ruck, D. E. Barrick, W. D. Stuart and C. K. Krickbaum, "Radar Cross Section Handbook", Vols. I and II, Plenum, New York, New York 1970.
8. S. R. Clonde, "Polarization Techniques in Radar Signal Processing", Microwave Journal, July 1983.
9. A. P. Agrawal, H. J. Eom and W. M. Boerner, "Use of Dual Polarization Radar Polarimetric Clutter Suppression" in Proc. IEEE Intl. Symposium AP-2-2, Vol. II, June 1985.
10. R. J. Papa, J. F. Lennon and R. L. Taylor (1985) "A Technique for Terrain Clutter Suppression on Bistatic Radars with Polarization Diversity", RADC-TR-85-200, AD B100814.
11. D. E. Barrick and W. H. Peake, "Scattering from Surfaces with Different Roughness Scales" Analysis and Interpretation: Battele Report, AD 662751, November 1967.
12. R. J. Papa, J. F. Lennon and R. L. Taylor, "The Variation of Bistatic Rough Surface Scattering Cross Section for a Physical Optics Model", IEEE AP-S, Trans., Vol. 34, 1986.
13. R. J. Papa, Personal Communication.
14. A. K. Fung and H. J. Eom "Effects of a Rough Boundary Surface on Polarization of the Scattered Field from an Inhomogeneous Medium", IEEE Trans. Geo. Sci Remote Sensing, Vol. GE-21, 23, July 1983.
15. R. J. Papa and M. B. Woodworth "Optimization of the Incoherent Power Scattered from a Rough Surface Using Polarization Diversity", Digest of the Radio Science Meeting, (URSI) San Jose, CA., June 1989.
16. R. Price and P. E. Green, "A Communication Technique for Multipath Channels", Proc. IRE 46, (1958).
17. R. F. Linfield, R. W. Hubbard L. E. Pratt, "Transmission Channel Characterization by Impulse Response Measurement", Department of Commerce, Office of Telecommunications, OT Report 76-96, 1976.
18. J. A. Austin, MIT Lincoln Laboratory, Lexington, MA 1985. Personal Communication.
19. K.V.N. Rao, James W. Coffey and John Austin, "Use of Wideband Channel Probe for Clutter Cross Section Measurement", Digest of the Radio Science Meeting (URSI Boulder, CO., January 1984.
20. K.V.N. Rao, John F. Lennon and W. G. Stevens, "Near Real-Time Terrain Clutter Cross Section Measurements, Analysis and Graphical Display", Digest of the Radio Science Meeting (URSI) Philadelphia, PA., June 1986.
21. M. I. Sancer, "Shadow-corrected Electromagnetic Scattering from Randomly Rough Surfaces", IEEE Trans. Antenna Propagation, Vol. AP-19, No. 5, pp 577-585, Sept. 1969.
22. F. I. Ulaby, R. K. Moore, and A. K. Fung (1982) Microwave Remote Sensing. Vols. II Addison-Wesley, Reading, MA



# BISTATIC CLUTTER SCATTERING GEOMETRY

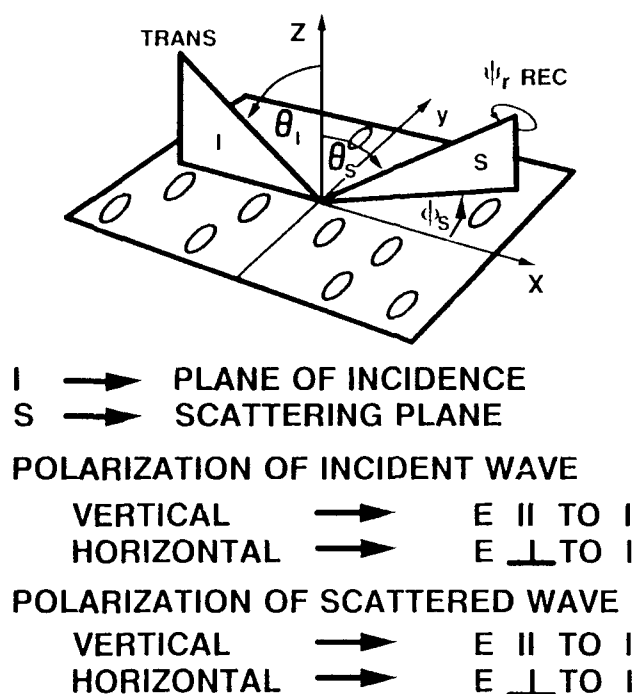


FIGURE 1

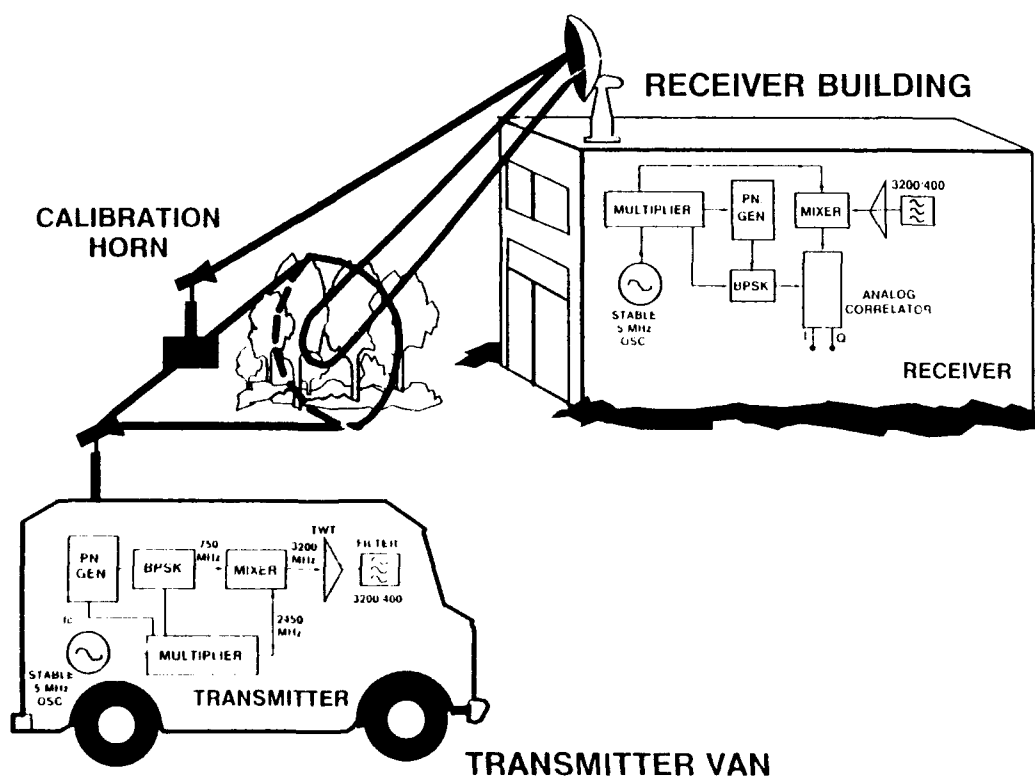
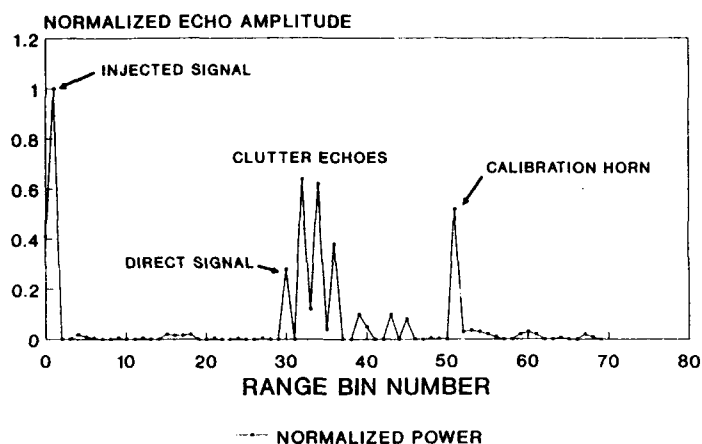
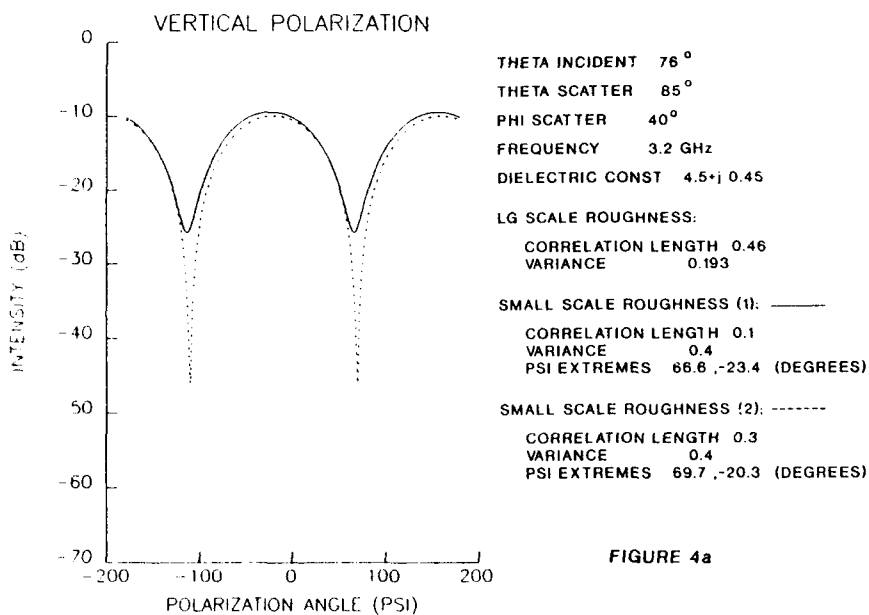


FIGURE 2

# ECHO AMPLITUDE vs RANGE S - BAND DECIDUOUS TREES



VV POLARIZATION; SINGLE FRAME **FIGURE 3**



**FIGURE 4a**

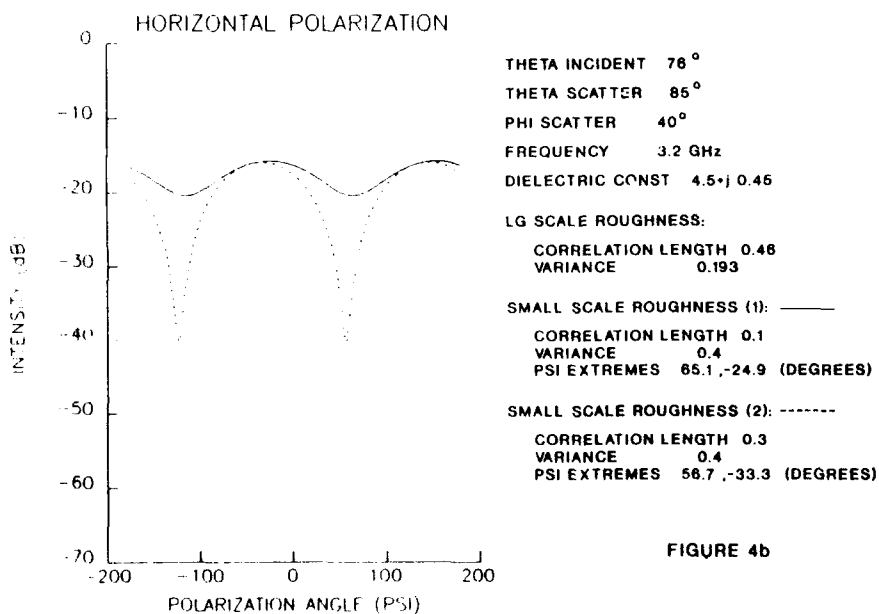
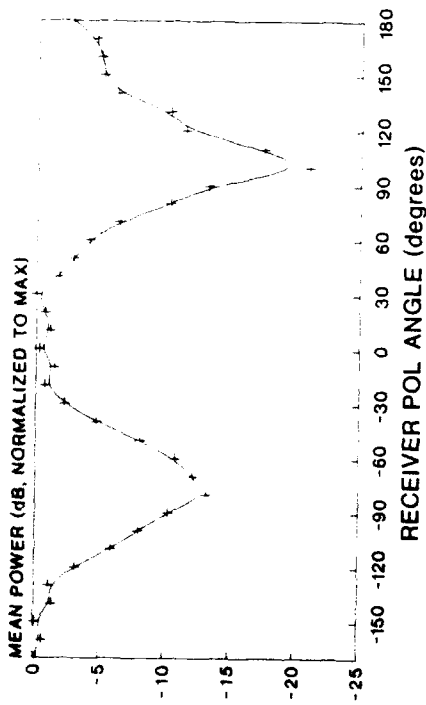


**FIGURE 4b**

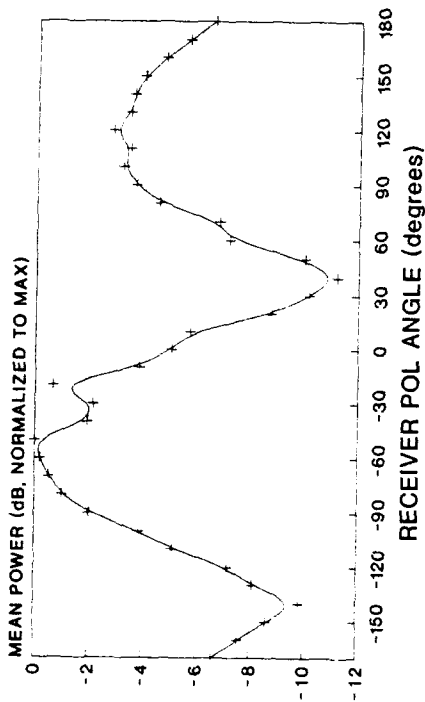
# RECEIVED POWER VS POL ANGLE



VERTICAL TRANS POL

FIGURE 5a

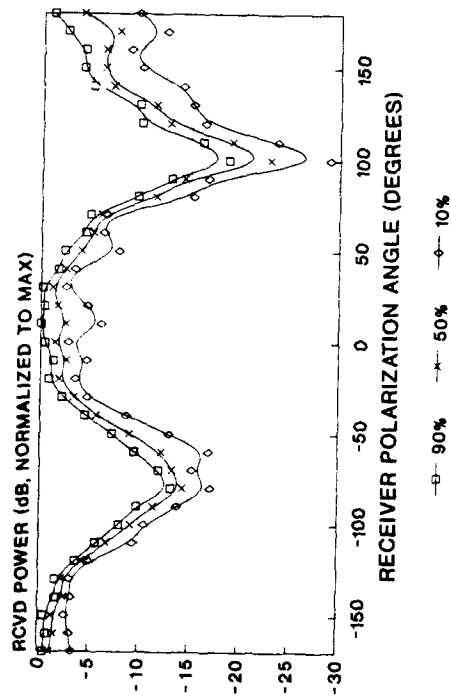
# RECEIVED POWER VS POL ANGLE



HORIZONTAL TRANS POL

FIGURE 5b

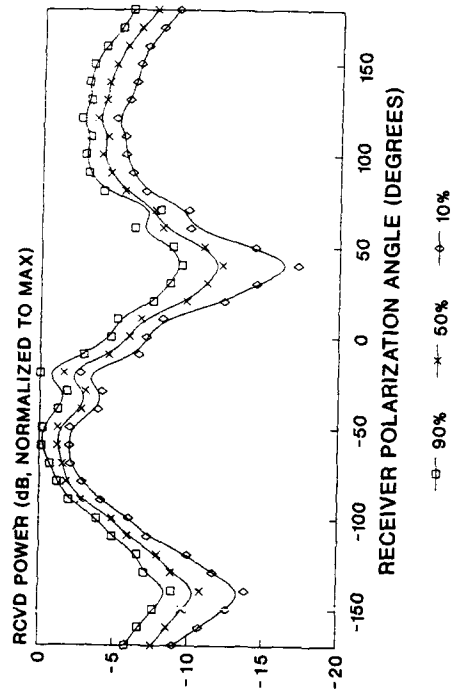
# RCVD POWER vs RCVR POL ANGLE 90, 50, 10 PERCENTILES



VERTICAL XMIT POL

FIGURE 6a

# RCVD POWER vs RCVR POL ANGLE 90, 50, 10 PERCENTILES



HORIZONTAL XMIT POL

FIGURE 6b

# HISTOGRAMS OF RECEIVED POWER VERTICAL TRANSMIT POLARIZATION

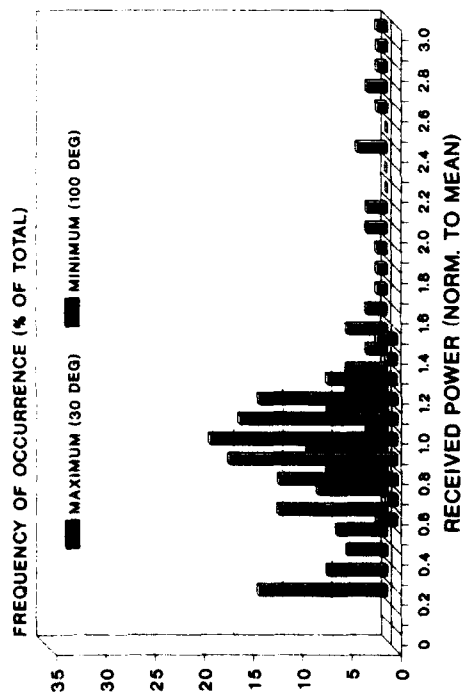


FIGURE 7.

# HISTOGRAMS OF RECEIVED POWER HORIZONTAL TRANSMIT POLARIZATION

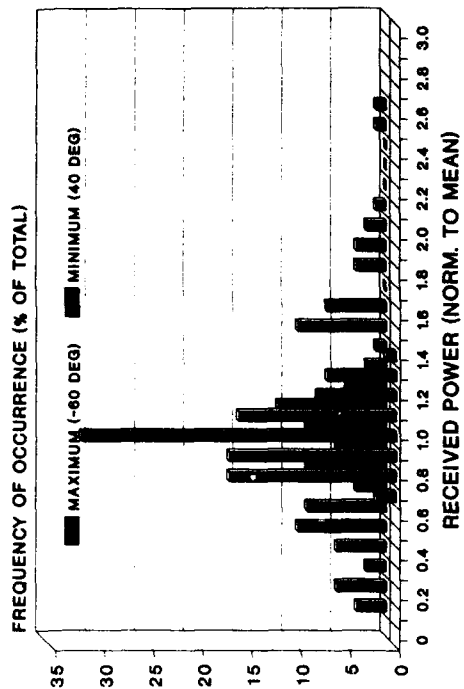


FIGURE 8.

# HISTOGRAMS OF RECEIVED POWER VERTICAL TRANSMIT POLARIZATION

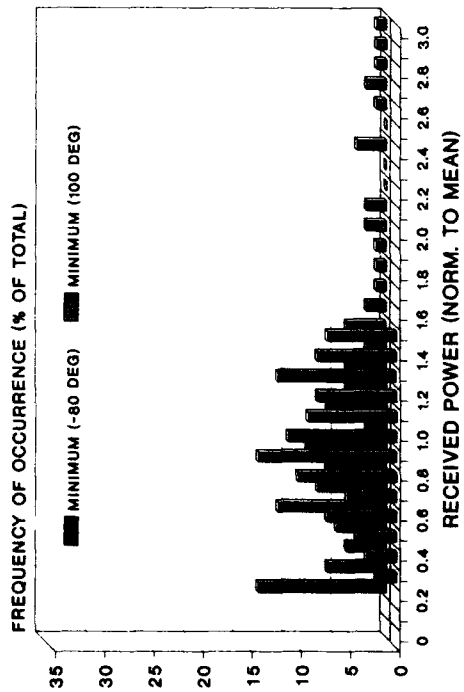


FIGURE 9.

# HISTOGRAMS OF RECEIVED POWER HORIZONTAL TRANSMIT POLARIZATION

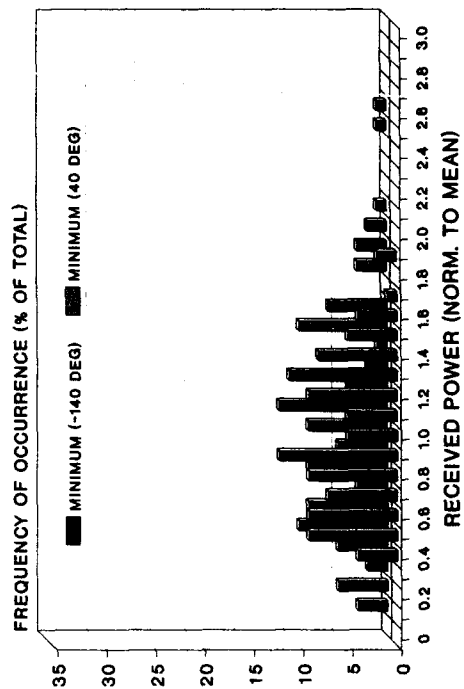
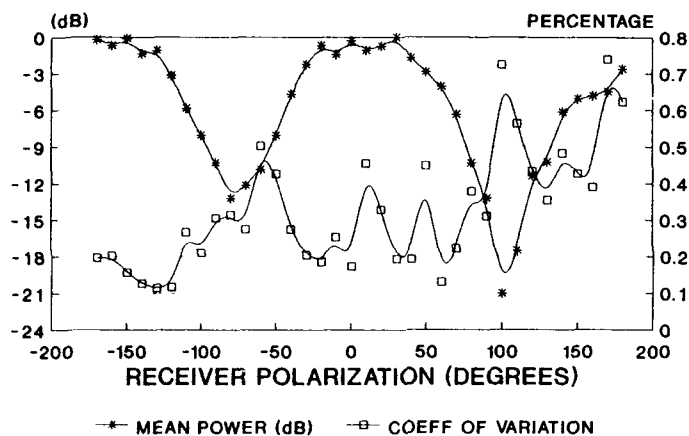


FIGURE 10.

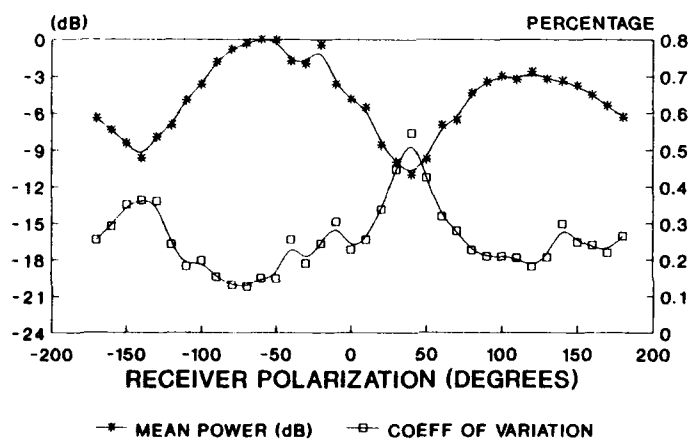
### MEAN POWER AND COEFF OF VARIATION vs RECEIVER POLARIZATION ANGLE



VERTICAL XMIT POL

FIGURE 11.

### MEAN POWER & COEFF OF VARIATION vs RECEIVER POLARIZATION ANGLE



HORIZONTAL XMIT POL

FIGURE 12.

## DISCUSSION

F. Le Chevalier (FR) :

Since level distribution is wider for polarizations states where mean clutter level is lower, do you think there remains interest in making use of polarization effects to improve the probability of detection ?

Author's reply :

These measurements were taken using an S-band 200 MHz bandwidth transmitter illuminating a clutter patch. The data indicate that the temporal spreads about the mean are dependent on the polarization angle of the receiver. Further experiments for coarser resolution cell behavior would have to be carried out prior to determining whether probability of detection could be significantly altered. In addition, the dependence would have to be constantly updated, depending on the bistatic configuration and type of clutter environment.

## ALTAIR UHF OBSERVATIONS OF BACKSCATTER ENHANCEMENT

Dennis L. Knepp  
Mission Research Corporation  
2300 Garden Road, Suite 2  
Monterey, California 93940-5326

### SUMMARY

During the Defense Nuclear Agency (DNA) PEAK (Propagation Effects Assessment - Kwajalein) experiment in August 1988, the ALTAIR VHF/UHF wide bandwidth radar was used to track spherical satellites in low-earth orbit. The purpose of the experiment was to obtain radar data during the most severe propagation disturbances available naturally. The PEAK experiment has been quite successful, giving many measurements of strong scintillation as well as the first measurements of frequency-selective fading on propagating radar pulses.

In this paper the experimental results are used to demonstrate an enhancement, due to scattering, in the average received power that is observed during severe scintillation. The observed statistics of the enhancement are compared to analytic calculations using the Nakagami- $m$  distribution with very good agreement. This enhancement is predictable on the basis of the first-order amplitude statistics for two-way radar propagation in a monostatic propagation geometry as well as by a more thorough analysis using reciprocity; both analytic approaches are presented here. The enhancement is important for both ground and space-based radars that have to operate during scintillation, since as much as a 3 decibel increase in the target (and clutter) signal-to-noise ratio is possible, depending on the severity of the scintillation and on the radar transmit/receive geometry.

### INTRODUCTION

It is well-known that a propagating signal in the frequency range from VHF to L-band can experience disturbances due to naturally occurring F-region ionization. Disturbances due to mean or average ionization consisting of dispersion, refraction, Faraday rotation, and phase shift have been the subject of research work over the last several decades and are well understood [Lawrence, *et al.*, 1964]. Disturbances due to smaller scale electron-density irregularities that produce scintillation of propagating waves are the subject of current research [Basu, *et al.*, 1987; Kumagai, 1987].

Scintillation consists of the rapid variation of signal phase, amplitude, angle-of-arrival, time-of-arrival and other signal properties. Intense signal scintillation is often observed over satellite links and in radar measurements [Towle, 1980] through the ambient ionosphere at VHF and UHF. Strong equatorial scintillation is even observed at frequencies as high as C-band, but rarely [Franke, *et al.*, 1984].

The DNA PEAK experiment was developed with the major goal of using the severely disturbed ionospheric propagation channel to measure and record worst-case propagation effects. The primary experiment utilized ALTAIR, a high-performance long range VHF/UHF tracking radar. The ALTAIR VHF signal is of prime interest since the lower frequency experiences the greatest degree of scintillation. The goal of the DNA program is to measure radar signal propagation effects, determine the irregularity structure, measure the radar performance degradation, and then to relate the performance degradation to the measured propagation disturbances and to the in-situ irregularity structure.

### ALTAIR WAVEFORM DESCRIPTION

ALTAIR utilizes a circular antenna with a diameter of 150 feet. The 3 dB beamwidths are 2.8 degrees at VHF (155.5 MHz) and 1.1 degrees at UHF (422 MHz). In the PEAK experiment, independent range tracks were maintained at both frequencies, but the UHF angle information was used to steer the antenna. During the satellite track portion of PEAK, the VHF and UHF waveforms chosen were those with the maximum bandwidth available. This selection gives an LFM (linear frequency modulated) waveform with a chirping bandwidth of 7.05 MHz at VHF and 18 MHz at UHF. Because of duty cycle limitations the maximum pulse repetition frequency is 372 Hz. Note that the actual PRF is determined by the radar control system to avoid eclipsing of pulses (i.e., to avoid reception of a pulse when the radar is transmitting).

The analysis that follows is based, for the most part, on data taken during several tracks of the Soviet satellite Cosmos 1427. Cosmos 1427 is a 2-meter diameter calibration sphere in a near circular orbit at an altitude of about 420 km. The use of spherical satellites eliminates the problem of target glint that causes fluctuation in the received signal due to interference from multiple target scatterers. Figure 1 (top) shows an example of severe UHF scintillation measured during the evening of August 20, 1988, on a pass starting at 9:18 pm, referred to as PEAK 9C.

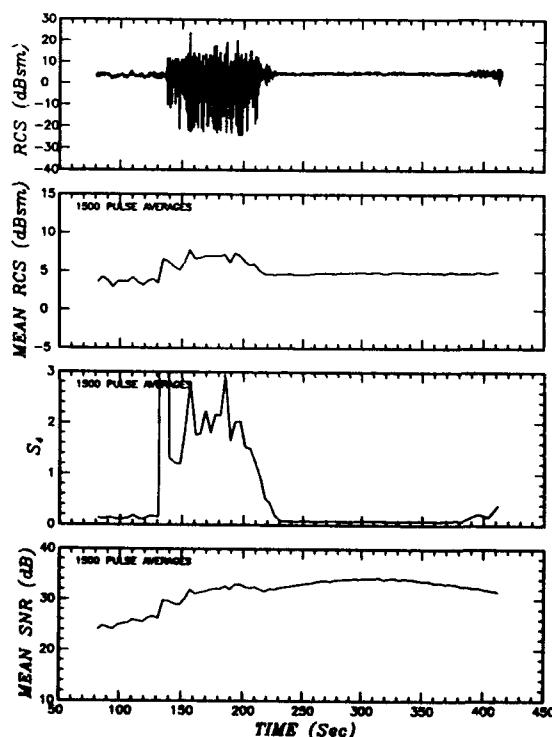


Figure 1. UHF RCS, average RCS,  $S_4$ , and average signal-to-noise ratio for Cosmos 1427, PEAK 9C, 8/20/88, 9:18 PM.

The figure shows the measured UHF radar cross section in decibels below a square meter as a function of ALTAIR tag time, which is time measured from the start of track. Notice the abrupt onset of a patch of severe scintillation starting at a time of 135 seconds and ending at 220 seconds. The elevation at 140 seconds is  $7.5^\circ$  and is increasing slowly until about 300 seconds when the satellite begins to descend. This high elevation angle rules out ground multipath as the source of the observed signal fluctuations.

The lower three frames in Figure 1 show computed quantities obtained by averaging the UHF data over 1500 consecutive received pulses. The second frame gives the average RCS. The average is obtained by summing 1500 values of RCS, dividing the sum by 1500, and then converting to decibels. The third frame gives the values of  $S_4$  discussed below. The bottom frame shows the average signal-to-noise ratio (SNR) computed by averaging the ratio of the power in the track gate to the power in the last recorded range gate. Time-samples of the received UHF pulse are recorded corresponding to a spatial separation of 15 m; the track gate (where the radar tracker attempts to place the peak of the return signal) corresponds to sample number 4, the last recorded sample is number 12. Note that our SNR measurements could be corrupted by range sidelobes, but are not here since the range sidelobes are 35 dB below the peak and, therefore, below the noise, for the most part. Unfortunately, we do not have available for analysis the radar's actual noise power measurement.

An enhancement in received average RCS during scintillation is clearly visible in the second frame of Figure 1. If one uses the period between 250 to 300 seconds to measure the mean RCS without scintillation, increases in RCS due to scintillation approaching 3 dB are apparent in the period 140-210 seconds.

Figures 2-5 present all the data that we were able to analyze to measure this enhancement in the average received power (or RCS) during scintillation. Figures 1-5 each consist of four frames showing single-pulse measurements of the received RCS, and values of the average RCS, the  $S_4$  scintillation index (defined below), and values of the average SNR. The average quantities were calculated by averaging 1500 consecutive samples of recorded data, or about 4 seconds of consecutive data during the satellite pass. Figures 1-2 and 4-5 show data taken during four tracks of COSMOS 1427. The data shown in Figure 3 was taken during a pass of LCS-4, a MIT Lincoln Laboratory calibration satellite. LCS-4 is smaller than COSMOS 1427 and at a higher altitude of 770 km.

In each figure we see that there is a distinct correlation between the severity of the scintillation and an increase in the measured average SNR. We will show in the following that this enhancement in measured average RCS and power is due to focusing.

**Scintillation Index ( $S_4$ ).** The level of amplitude scintillation is often measured by the  $S_4$  scintillation index defined as the normalized standard deviation of the RCS obtained from a constant-RCS target.

$S_4^2 = ((P^2) - \langle P \rangle^2) / \langle P \rangle^2$ , where  $P$  is the apparent radar RCS (the fluctuations in  $P$  are due to scintillation) and the angle brackets denote a stochastic average. Values of  $S_4$  on a one-way path generally range from a minimum of zero signifying no scintillation to a maximum of unity indicating worst-case Rayleigh fading where the quadrature components of the received (one-way) signal are uncorrelated Gaussian variates.

To measure a single value of  $S_4$ , 1500 values of sampled RCS measurements (corresponding to about 4 seconds of data during the satellite pass) were averaged. Note that the measurements of  $S_4$  exceed in many cases the maximum value  $\sqrt{5} = 2.24$ , valid for saturated scintillation in the two-way radar geometry [Knepp and Reinking, 1989]. This is the result of focusing caused by large scale irregularities "close to" the radar location.

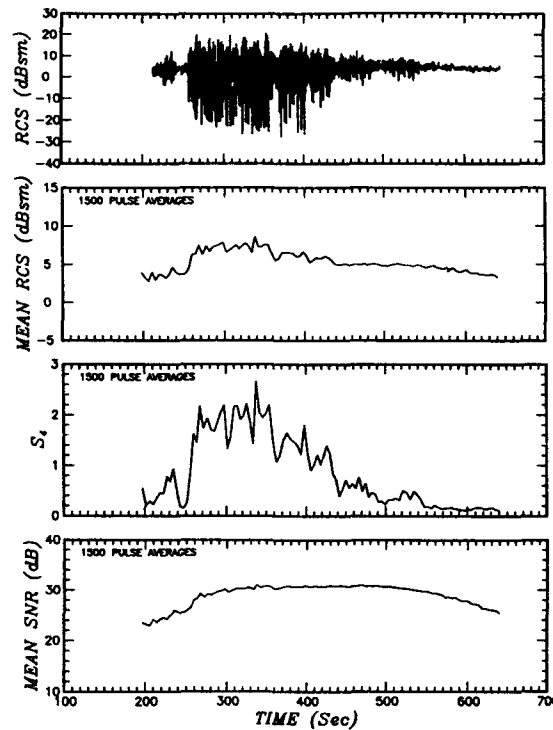


Figure 2. UHF RCS, average RCS,  $S_4$ , and average signal-to-noise ratio for Cosmos 1427, PEAK 2G, 8/7/88, 1:14 AM.

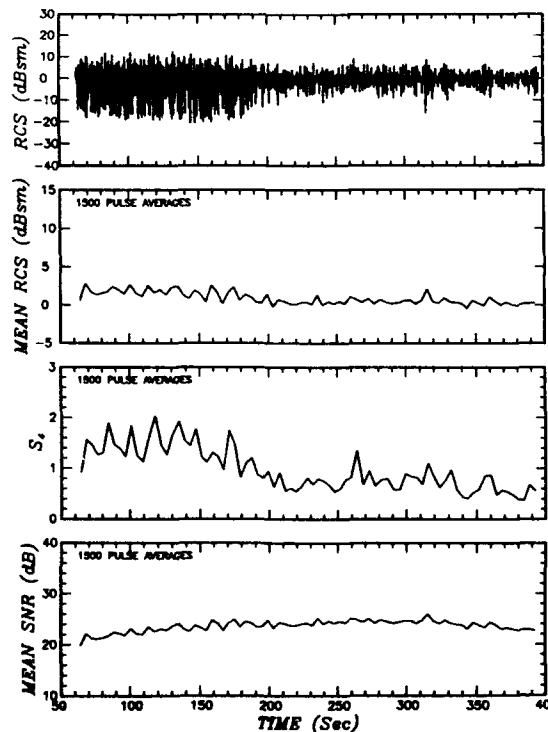


Figure 3. UHF RCS, average RCS,  $S_4$ , and average signal-to-noise ratio for LCS-4, PEAK 6G, 8/15/88, 12:53 AM.



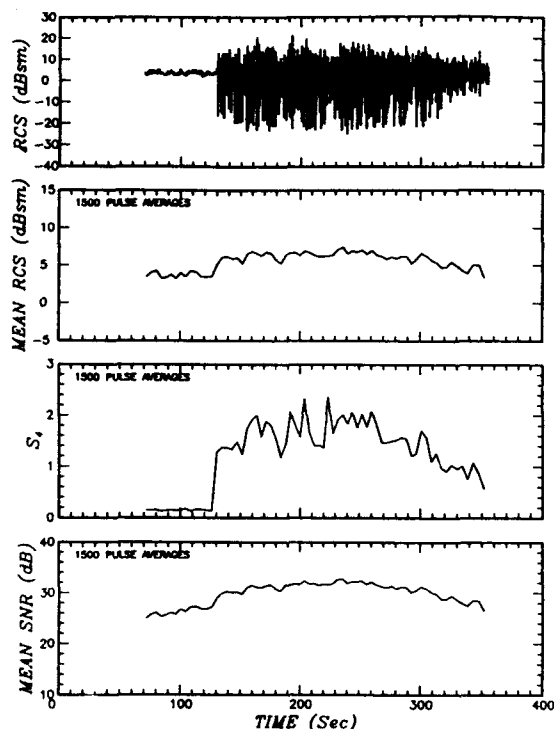


Figure 4. UHF RCS, average RCS,  $S_4$ , and average signal-to-noise ratio for Cosmos 1427, PEAK 7C, 8/17/88, 9:56 PM.

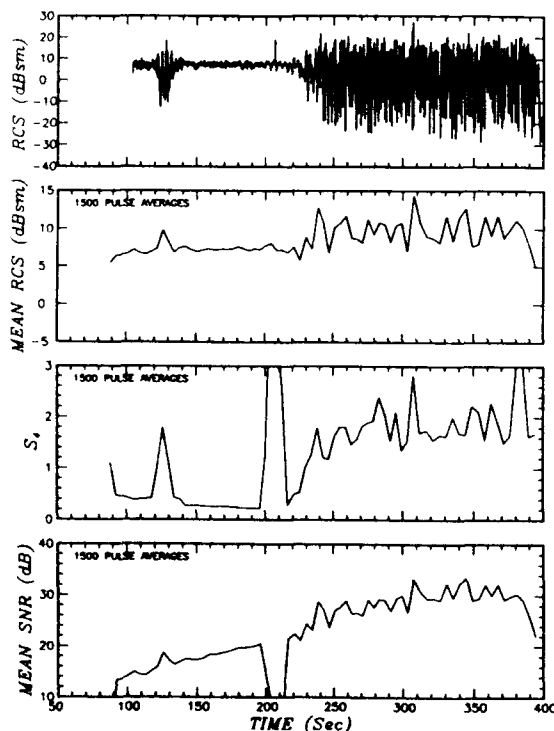


Figure 5. UHF RCS, average RCS,  $S_4$ , and average signal-to-noise ratio for Cosmos 1427, PEAK 6F, 8/15/88, 12:07 AM.

Equivalently, the Fresnel zone size is larger than the freezing scale of the irregularities.

### THEORY OF POWER ENHANCEMENT

In the following a simple expression is obtained for the two-frequency, two-position, two-time mutual coherence function (MCF) for the case of two-way propagation from a radar antenna to a point target and back to the antenna. The result is given in terms of products of the one-way MCFs for propagation from the radar target to the radar transmit and receive locations and is valid for saturated scintillation where the quadrature components of the signal, after one-way propagation, are uncorrelated Gaussian variates. This result explains the observed enhancement as caused by correlation of the wave that propagates from the radar location to the target with the wave that propagates from the target to the radar.

The backscatter enhancement appears to have first been noticed by Watson in 1969. Several authors [de Wolf, 1971; Fante, 1973] have predicted enhancements of a factor of two in the case of backscatter from a turbulent plasma. Yeh [1983] calculated the two-position, two-frequency MCF for the case of radar backscatter from a target located within a random medium, which is similar to the present calculation. Our calculation differs from Yeh's in that it also includes the effects of possible temporal decorrelation due to changes with time in the propagation medium or propagation geometry as well as temporal changes during the time of travel of the propagating signal. More recent work has concentrated on the backscatter enhancement from rough surfaces and from media consisting of randomly distributed particles [Kuga, et al., 1989].

Consider the problem illustrated in Figure 6 of a wave transmitted at time  $t$  at a center radian frequency of  $\omega$  with time dependence  $\exp(i\omega t)$  from an aperture antenna located in the  $\rho_x$ -plane at  $\bar{\rho}_T$ . Fante [1985], gives the received field using the Huygens-Fresnel Principle under two important assumptions. First, the transmitted signal must be narrow-band about the center radian frequency  $\omega$ , and second, the time rate of change of the index-of-refraction fluctuations and of the transmitted temporal envelope must be slow in comparison to the radian frequency  $\omega$ . These conditions are generally satisfied in modern pulsed radars. In this case the field received after propagation from the antenna to a location in the plane of the scattering layer,  $\bar{\rho}_\xi$  is

$$E_{\text{inc}}(\bar{\rho}_\xi, \omega, t + \frac{Z_\xi}{c}) = \int d\rho_x^2 A(\bar{\rho}_x - \bar{\rho}_T) G_1(\bar{\rho}_x \rightarrow \bar{\rho}_\xi; \omega; t) E_0(\bar{\rho}_x, \omega) \quad (1)$$

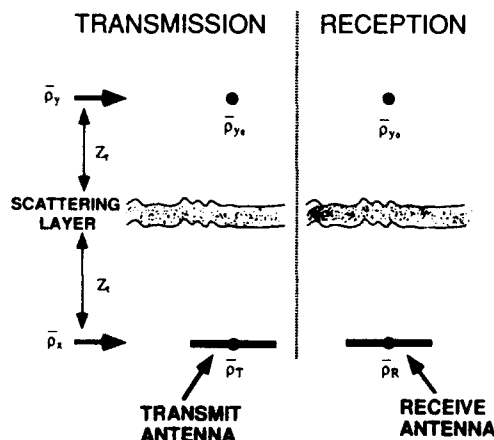


Figure 6. Two-way scattering geometry.

From the figure  $Z_t$  is the distance along the direction of propagation from the transmitter plane to a scattering layer. The quantity  $Z_r$  is the distance from the scattering layer to the target location,  $E_0(\bar{\rho}_s, \omega)$  is the frequency-domain representation of the signal transmitted from location  $\bar{\rho}_s$  and  $A(\bar{\rho}_s - \bar{\rho}_T)$  is the aperture weighting function for the transmit antenna located at position  $\bar{\rho}_T$ . For example, the choice  $A(\bar{\rho}) = \text{constant}$  for  $|\bar{\rho}| \leq \rho_0$  and zero otherwise is appropriate for a circular antenna. The time dependence  $t$  in the propagator  $G_1$ , given by Equation 3, signifies that the transmission occurs at time  $t$ . The signal arrives at the scattering layer at a later time,  $t + Z_t/c$  as included in the expression for  $E_{\text{inc}}$ . The propagator is given as

$$G_1(\bar{\rho}_s \rightarrow \bar{\rho}_t; \omega; t) = \frac{k}{i2\pi Z_t} \exp \left\{ -ikZ_t - \frac{ik}{2Z_t} (\bar{\rho}_t - \bar{\rho}_s)^2 \right\} \quad (2)$$

Now the signal in the target plane may be written by propagating in the same manner from the scattering layer up to the target. The result can be expressed as

$$E_{\text{tar}}(\bar{\rho}_y, \omega, t + \tau) = \int d\bar{\rho}_t^2 E_{\text{inc}} \left( \bar{\rho}_t, \omega, t + \frac{Z_t}{c} \right) G_2 \left( \bar{\rho}_t \rightarrow \bar{\rho}_y; \omega; t + \frac{Z_t}{c} \right) \quad (3)$$

where the propagator,  $G_2$  accounts for propagation of a wave starting from the layer at time  $t + Z_t/c$ , and includes the phase term  $\phi$  which gives the scattering layer contribution to the phase in the Huygens-Fresnel principle.

$$G_2 \left( \bar{\rho}_t \rightarrow \bar{\rho}_y; \omega; t + \frac{Z_t}{c} \right) = \frac{k}{i2\pi Z_r} \exp \left\{ -ikZ_r - \frac{ik}{2Z_r} (\bar{\rho}_t - \bar{\rho}_y)^2 + i\phi \left( \bar{\rho}_t, \omega, t + \frac{Z_t}{c} \right) \right\} \quad (4)$$

For simplification, the above three equations can be combined as

$$E_{\text{tar}}(\bar{\rho}_y, \omega, t + \tau) = \int d\bar{\rho}_s^2 A(\bar{\rho}_s - \bar{\rho}_T) G_{\text{up}}(\bar{\rho}_s \rightarrow \bar{\rho}_y; \omega; t) E_0(\bar{\rho}_s, \omega) \quad (5)$$

which represents upward propagation of a wave from the  $\rho_s$ -plane starting at time  $t$ , to the  $\rho_y$ -plane or target plane, arriving at time  $t + \tau$  where  $\tau = (Z_t + Z_r)/c$ . The quantity  $G_{\text{up}}$  is a time-variable (varying with  $t$ ) transfer function for a sinusoid of radian frequency  $\omega$ .

Now let the target be a point scatterer with unity reflectivity and located at  $\bar{\rho}_{y0}$ . Then the field received at time  $t + 2\tau$  after downward propagation from the target back to the radar location is given as

$$E_{\text{rev}}(\bar{\rho}_R, \omega, t + 2\tau) = \int d\bar{\rho}_s^2 B(\bar{\rho}_s - \bar{\rho}_R) G_{\text{down}}(\bar{\rho}_{y0} \rightarrow \bar{\rho}_s; \omega; t + \tau) E_{\text{tar}}(\bar{\rho}_{y0}, \omega, t + \tau) \quad (6)$$

Equations 5-6 can be combined to yield a simplified expression

$$E_{\text{rev}}(\bar{\rho}_R, \omega, t + 2\tau) = \int d\bar{\rho}_s^2 d\bar{\rho}_t^2 A(\bar{\rho}_s - \bar{\rho}_T) B(\bar{\rho}_s - \bar{\rho}_R) G_{\text{down}}(\bar{\rho}_{y0} \rightarrow \bar{\rho}_s; \omega; t + \tau) G_{\text{up}}(\bar{\rho}_s \rightarrow \bar{\rho}_{y0}; \omega; t) E_0(\bar{\rho}_s, \omega) \quad (7)$$

where the quantity  $B(\bar{\rho}_s - \bar{\rho}_R)$  specifies the aperture weighting function for the receive antenna which is located with its phase-center at  $\bar{\rho}_R$  at time  $t + 2\tau$ . Now simplify by letting both transmit and receive apertures be point antennas so  $A(\bar{\rho}_s - \bar{\rho}_T) = \delta(\bar{\rho}_s - \bar{\rho}_T)$  and similarly for  $B$ .

Then the expression for the desired autocorrelation function after two-way propagation is obtained as

$$\Gamma_2(\bar{\rho}_{R1} - \bar{\rho}_{R2}; \omega_1 - \omega_2; \Delta) = \langle E_{\text{rev}}(\bar{\rho}_{R1}, \omega_1, t + 2\tau + \Delta) E_{\text{rev}}^*(\bar{\rho}_{R2}, \omega_2, t + 2\tau) \rangle \quad (8)$$

where the angle brackets denote stochastic average.  $E_{\text{rev}}(\bar{\rho}_{R1})$  is the voltage received at  $\bar{\rho}_{R1}$ , due to a transmitter at  $\bar{\rho}_{T1}$ ;  $E_{\text{rev}}(\bar{\rho}_{R2})$  is the voltage received at  $\bar{\rho}_{R2}$  due to a transmitter at  $\bar{\rho}_{T2}$ . To proceed further, reciprocity must be invoked to relate upward and down-going waves through the expression

$$G_{\text{up}}(\bar{\rho}_s \rightarrow \bar{\rho}_y; \omega; t) = G_{\text{down}} \left( \bar{\rho}_y \rightarrow \bar{\rho}_s; \omega; t + \frac{Z_t - Z_r}{c} \right) \quad (9)$$

The above equation states reciprocity as follows. In propagating upward, starting at time  $t$ , the wave arrives at the layer at time  $t + Z_t/c$ ; in downward propagation starting at time  $t + (Z_t - Z_r)/c$ , the wave arrives at the screen at time  $t + (Z_t - Z_r)/c + Z_r/c = t + Z_t/c$ , i.e., the same time. Thus the scattering layer is in the same position for upward as it is for downward propagation, so reciprocity holds.

Application of reciprocity allows one to replace the upward-going transfer functions with their equivalent downward-going transfer functions.

Now, if scintillation is saturated on a one-way propagation path so that  $G_{\text{down}}$  is a complex Gaussian variate, then one can write the fourth-order moment using the well-known expression

$$\langle x_1 x_2 x_3 x_4 \rangle = \langle x_1 x_2 \rangle \langle x_3 x_4 \rangle + \langle x_1 x_3 \rangle \langle x_2 x_4 \rangle + \langle x_1 x_4 \rangle \langle x_2 x_3 \rangle.$$

In the application of this expression for the fourth-order moments, the term  $\langle G_{\text{down}} G_{\text{down}} \rangle \langle G_{\text{down}}^* G_{\text{down}}^* \rangle$  is found to be of the form  $(\langle Re^2 \rangle - \langle Im^2 \rangle)^2$  where the variances of real and imaginary parts are equal, giving zero. The other two terms are written in Equation 10 as the products of MCFs valid for the downward path ( $\Gamma_{\text{down}}$ ) from the target to the various transmitter and receiver locations.  $\Gamma_{20}$  is the two-way MCF in the absence of a scattering layer.

$$\begin{aligned} \Gamma_2 = & \Gamma_{20} \left\{ \Gamma_{\text{down}}(\bar{\rho}_{R1} - \bar{\rho}_{R2}; \omega_1 - \omega_2; \Delta) \right. \\ & \Gamma_{\text{down}}(\bar{\rho}_{T1} - \bar{\rho}_{T2}; \omega_1 - \omega_2; \Delta) \\ & + \Gamma_{\text{down}} \left( \bar{\rho}_{R1} - \bar{\rho}_{T2}; \omega_1 - \omega_2; \Delta - \frac{2Z_r}{c} \right) \\ & \left. \Gamma_{\text{down}} \left( \bar{\rho}_{T1} - \bar{\rho}_{R2}; \omega_1 - \omega_2; \Delta + \frac{2Z_r}{c} \right) \right\} \\ & E_0(\bar{\rho}_{T1}, \omega_1) E_0^*(\bar{\rho}_{T2}, \omega_2) \end{aligned} \quad (10)$$

where  $\Delta = \omega_1 - \omega_2$  and  $\delta = 2Z_r/c$ .

The quantity  $\bar{\rho}_{T1}$  is the transmitter location at time  $t + \Delta$ ;  $\bar{\rho}_{T2}$  is the transmitter location at time  $t$ ;  $\bar{\rho}_{R1}$  and  $\bar{\rho}_{R2}$  are the receiver locations at times  $t + 2\tau + \Delta$  and  $t + 2\tau$ , respectively. The quantity  $2Z_r/c$  is the time required for the wave to propagate from the scattering layer to the target, and then back to the scattering layer. Changes in the medium that occur more rapidly than  $2Z_r/c$  can act to decorrelate the up and down-going waves and reduce or eliminate the backscatter enhancement. Equation 10 is in agreement with Yeh [1983].

Expressions for  $\Gamma_{\text{down}}$  and  $\Gamma_{20}$  for this geometry are given in Knepp [1983; 1985].

If transmitter and receiver are far from one another, the second term in Equation 10 is zero, since each  $\Gamma_{\text{down}}$  is separately zero. If transmitter and receiver are collocated

and  $2Z_r/c$  is small, the second term is equal to the first term and thereby represents the enhancement. The enhancement depends on the relative positions of transmitter and receiver at two different times. It is therefore important in the evaluation of the performance of space-based radar, particularly displaced phase center antenna (DPCA) wherein the transmit and receive phase-centers have complicated relative motion.

For the case of no scattering, the resulting expression for the MCF is  $\Gamma_2(\text{no scint}) = \Gamma_{20} E_0(\beta_{T1}, \omega_1) E_0^*(\beta_{T2}, \omega_2)$ . For the case of a monostatic radar geometry with small values of the order  $2Z_r/c$ , so that  $\Gamma_{\text{down}} = 1$  in all cases in Equation 10, one obtains  $\Gamma_2(\text{monostatic radar}) = 2\Gamma_2(\text{no scintillation})$  or a 3 dB increase in average received power above that measured with no scintillation.

**Measurements of the Enhancement.** Now if one restricts consideration to only the first-order or signal amplitude statistics, it is possible to relate the amount of the enhancement to the severity of the signal fluctuations. At its simplest the enhancement can be derived using reciprocity which states that, if the propagation environment is unchanging, a signal with a single frequency component traverses the same path in traveling from the radar to the target and back.

In that case the voltage after two-way propagation is proportional to the square of the one-way voltage. Now if the one-way signal experiences saturated scintillation in which the quadrature components are uncorrelated Gaussian variates, then it is easy to show that the MCF for two-way propagation is twice the square of the one-way MCF. Equation 10 is the result of a more detailed derivation which similarly predicts the factor of two enhancement for the case of a monostatic radar geometry and the special case of small  $Z_r/c$ .

The Nakagami- $m$  [Nakagami, 1960] probability distribution is a simple, one-parameter distribution that correctly describes both the weak and strong scatter limits of ionospheric scintillation and has been found to give a very good fit to observed scintillation data [Fremouw, et al., 1980] over a wide range of scintillation conditions. Under the assumption of Nakagami- $m$  statistics for the one-way power, the probability density function (pdf) of received RCS is given by Equation 3.4 of Knepp and Reinking [1989].

If reciprocity holds, the radar measures the two-way RCS,  $Q = S^2$  which then has the pdf given by

$$p_2(Q)dQ = \frac{m^m Q^{m/2-1}}{2\Gamma(m)\langle S \rangle^m} \exp\left\{-\frac{m\sqrt{Q}}{\langle S \rangle}\right\} dQ, \quad Q \geq 0, \text{ (two-way)} \quad (11)$$

where  $m = 1/S_4^2(\text{one-way})$ .

We have compared our measurements of the cumulative power distribution function with Equation 11 and have obtained good agreement for all values of measured  $S_4$ . This agreement with a well-known distribution is useful since it removes the possibility of statistics as a possible cause of the observed enhancement in average power.

From Equation 11 the mean received two-way power can be computed in terms of the square of the one-way power as  $\langle Q \rangle = \int_0^\infty p_2(Q) Q dQ = \frac{(m+1)}{m} \langle S \rangle^2$ . In the case of a constant signal with no fading,  $S_4$  is zero,  $m$  is infinity and one obtains  $\langle Q(\text{no scint}) \rangle = \langle S \rangle^2$  which can be combined with the above expression to yield a relationship between average RCS and  $m$  where  $m$  is appropriate to the one-way propagation path.

$$\frac{\langle \text{RCS} \rangle}{\text{RCS (no scint)}} = \frac{m+1}{m} \quad (12)$$

Table 1. Summary of Data Analyzed to Measure Enhancement Statistics.

Satellite Pass Designation	Total Time Interval Analyzed	Time Interval for RCS(no scint) Measurement
PEAK 2G 8/7/88; 1:14 AM	200-600 sec	590-630 sec
PEAK 6G 8/15/88; 12:53 AM	70-400 sec	380-390 sec
PEAK 7C 8/17/88; 9:56 PM	80-360 sec	90-110 sec
PEAK 6F 8/15/88; 12:07 AM	160-400 sec	160-180 sec
PEAK 9C 8/20/88; 9:18 PM	130-380 sec	250-300 sec

Table 1 calls out the data intervals that were analyzed from the five satellite passes of Figures 1-5. For each pass, we first determined the average RCS without scintillation. This measurement was necessary because the ALTAIR RCS calibration was not constant during the month-long experimental campaign. The average RCS under conditions of no scintillation was obtained for each pass by averaging all the RCS measurements during the time intervals shown in the third column of the table.

Measurements of the average RCS and  $S_4$  during scintillation were obtained using 1500 point averages over the time extent shown in the second column of the table.

In Figure 7 the UHF measurements of  $S_4$  and average RCS are combined in a format to check the relationship given above. By using the ALTAIR data similar to that shown in Figure 1 it is possible to measure all the values in Equation 12 to check this relationship. For example, for PEAK 9C, take the average RCS during undisturbed propagation conditions as the average of the received RCS over the interval 250-300 seconds. Then consider the other measurements of average power and  $S_4$  with (and without) scintillation during the time period 130-380 seconds. These measurements of  $S_4$  are used to obtain the  $m$ -parameter through the expression  $S_4^2(\text{two-way}) = (4m^2 + 10m + 6)/(m(m+1)^2)$  [Knepp and Reinking, 1989].

The resulting data is then presented in the form of a scatter plot shown in Figure 7 where the ratio of the average RCS measurements with and without scintillation are plotted as a function of the ratio  $(m+1)/m$ . A straight line with unity slope corresponds to the enhancement theory described above.

Figure 7 shows similar UHF data for three additional passes of Cosmos 1427 of (PEAK 2G, 7C, 6F) and a pass of a smaller U.S. calibration sphere, LCS-4 (PEAK 6G).

There is good agreement between the data collected in Figure 7 and the theory; the value of the standard deviation of the data points from the straight line with unit slope through the origin is 0.17. The minimum SNR for the UHF data is 22 dB, so noise effects on the measurements are minimal. The major cause of variation from the theory is the measurement of the undisturbed RCS, which is difficult during some satellite passes without noticeable regions of undisturbed returns. Radar calibration problems preclude the use of a single value for undisturbed RCS. The UHF data agrees well with the theory; the VHF data (not shown) exhibits much more erratic behavior, most likely due to dispersive pulse spreading that causes loss in peak power not accounted for

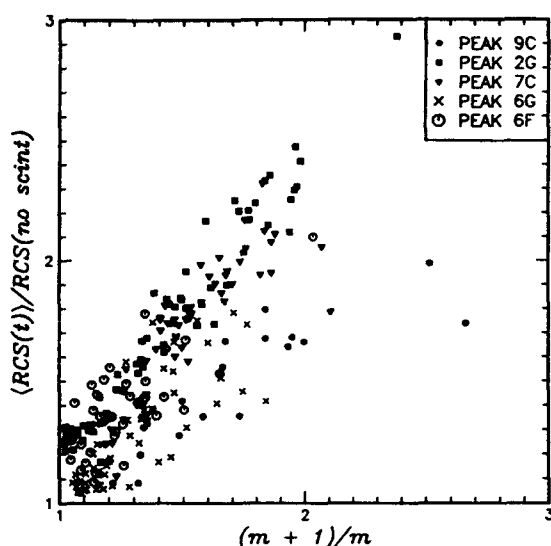


Figure 7. Comparison of ALTAIR UHF measurements of the enhancement versus theory, PEAK 9C (8/20/88; 9:18 pm), 2G (8/7/88; 1:14 am), 7C (8/17/88; 9:56 pm), 6F (8/15/88; 12:07 am), 6G (8/15/88; 12:53 am).

in the scattering theory, and possibly due to the reduced SNR available at VHF.

### CONCLUSIONS

This paper has presented ALTAIR data illustrating the effects of severe ionospheric multipath on the received VHF wideband chirp waveform. Data for the received cumulative distribution function after two-way propagation supports the use of the Nakagami- $m$  distribution for calculations of the probability of detection [Knepp and Reinking, 1989]. The work of Yeh [1983] has been extended to include temporal variation (which is important for long-range radars) and convincing experimental proof of the backscatter enhancement due to scintillation is presented.

### ACKNOWLEDGEMENT

The authors are indebted to the ALTAIR staff and to Dr. Robert Stagat of Mission Research Corporation, Mr. Warren Dickinson of the U.S. Army Strategic Defense Command, and Dr. Leon Wittwer of the Defense Nuclear Agency for useful discussions regarding this work. The work was supported under DNA Contract No. DNA001-87-C-0169 and NRL Contract No. N00014-87-C-2336.

### REFERENCES

- Basu, S. E. MacKenzie, S. Basu, E. Costa, P. F. Fougere, H. C. Carlson and H. E. Whitney, "250 MHz/GHz Scintillation Parameters in the Equatorial, Polar and Auroral Environments," *IEEE Journal on Selected Areas in Communications*, Vol. SAC-5, No. 2, 1987.
- de Wolf, D. A., "Electromagnetic Reflection From an Extended Turbulent Medium: Cumulative Forward-Scatter Single-Backscatter Approximation," *IEEE Transactions on Antennas and Propagation*, Vol. AP-19, No. 2, pp. 254-262, 1971.
- Fante, R. L., "Propagation of Electromagnetic Waves Through Turbulent Plasma Using Transport Theory," *IEEE Transactions on Antennas and Propagation*, Vol. AP-21, No. 5, pp. 750-755, 1973.
- Fante, R. L., "Wave Propagation in Random Media: A Systems Approach," in *Progress in Optics XXII*, E. Wolf, Ed., Elsevier, 1985.
- Franke, S. J., C. H. Liu and D. J. Fang, "Multifrequency Study of Ionospheric Scintillation at Ascension Island," *Radio Science*, Vol. 19, pp. 695-706, May-June 1984.
- Fremouw, E. J., R. C. Livingston and D. A. Miller, "On the Statistics of Scintillating Signals," *Journal of Atmospheric and Terrestrial Physics*, Vol. 42, pp. 717-731, 1980.
- Knepp, D. L. and J. T. Reinking, "Ionospheric Environment and Effects on Space-based Radar Detection," in *Space-Based Radar Handbook*, L. J. Cantafio, Ed., Artech House, 1989.
- Knepp, D. L., "Aperture Antenna Effects After Propagation Through Strongly Disturbed Random Media," *IEEE Trans. Antennas and Propagation*, Vol. AP-33, No. 10, pp. 1074-1084, October 1985.
- Knepp, D. L., "Analytic Solution for the Two-Frequency Mutual Coherence Function for Spherical Wave Propagation," *Radio Science*, Vol. 18, No. 4, pp. 535-549, July-August 1983.
- Kuga, Yasuo, A. Ishimaru and Q. Ma, "The Second-order Multiple Scattering Theory for the Vector Radiative Transfer Equation," *Radio Science*, Vol. 24, No. 2, pp. 247-252, 1989.
- Kumagai, H., "Spatial correlations in intense ionospheric scintillations: Comparison between numerical computation and observation," *Radio Science*, Vol. 22, No. 3, pp. 439-448, May-June 1987.
- Lawrence, R. S., C. G. Little and H. J. A. Chivers, "A Survey of Ionospheric Effects Upon Earth-Space Radio Propagation," *Proceedings of the IEEE*, pp. 4-27, January 1964.
- Nakagami, M., The  $m$ -distribution - A General Formula of Intensity Distribution of Rapid Fading, in *Statistical Methods in Radio Propagation*, edited by W. C. Hoffman, pp. 3-36, Pergamon, New York, 1960.
- Towle, D. M., "VHF and UHF Radar Observations of Equatorial F Region Ionospheric Irregularities and Background Densities," *Radio Science*, Vol. 15, No. 1, pp. 71-86, January-February 1980.
- Watson, K. M., "Multiple Scattering of Electromagnetic Waves in an Underdense Plasma," *Journal of Mathematical Physics*, Vol. 10, No. 4, pp. 688-702, 1969.
- Yeh, K. C., "Mutual Coherence Functions and Intensities of Backscattered Signals in a Turbulent Medium," *Radio Science*, Vol. 18, No. 2, pp. 159-165, 1983.

## DISCUSSION

E. Schweicher (BE) :

On the viewgraph entitled "Backscatter enhancement : general theory", you mentioned that the "Transmission Frequency" was the carrier frequency. Is it not rather the PRF ?

Author's reply :

In order to make the narrow-band approximation, it is necessary that the variation in the signal envelope be slow with respect to the radar transmission frequency, also referred to the carrier frequency in the communication literature. Fante discusses this on page 344 of Progress in Optics XXII, Elsevier, 1985, edited by Wolf.

C. Goutelard (FR) :

Avez-vous examiné l'influence du champ magnétique qui n'est pas négligeable à 155 MHz notamment. Dans les statistiques que vous présentez en fonction du paramètre m de la distribution de Nakagami, la distribution des points de part et d'autre de la première bissectrice ne peut-elle être interprétée à partir de ces considérations ?

Author's reply :

The major effect of the earth's magnetic field at 155 MHz is Faraday rotation. However ALTAIR is circularly polarized on both transmission and reception, so there is no impact on our results. Incidentally, all the enhancement data and statistical analysis of its relationship to the Nakagami-m distribution is based on the ALTAIR UHF (422 MHz) data.

C.J. Baker (UK) :

Can you comment on whether your experimental results can be used to predict the reduction in coherency of space based radars particularly those operating at high resolutions which employ long (many seconds) integration times.

Author's reply :

The experimental results would be ideal to measure space based radar coherent processing degradation at VHF and UHF. However the theory needs to be applied to assess radar performance at other frequencies or for complicated antennas, such as displaced phase center antennas (DPCA).

## PARABOLIC EQUATION MODELLING OF BACKSCATTER FROM THE ROUGH SEA SURFACE

M.F. Levy

Radio Communications Research Unit  
Rutherford Appleton Laboratory  
Chilton, Didcot, OX11 0QX  
United Kingdom

### SUMMARY

This paper presents a physically based numerical method for calculating sea clutter at low grazing angles for microwave frequencies. Sea clutter is modelled as a two-scale phenomenon: at low grazing angles, the backscattered energy is generated by ripples on the sea surface. A first order perturbation method gives the backscatter from a small patch of surface, as a function of the angle of incidence and of the magnitude of the incident field. Returns from a clutter cell are obtained by incoherent summation of these echoes. Shadowing and tilting effects due to the larger scale components of the sea surface are modelled using a finite difference implementation of the parabolic equation method, which also deals with atmospheric refraction effects. Realizations of the sea surface with the desired spectral characteristics are generated with a Monte Carlo method. Results are presented at S-band and X-band for a variety of propagation conditions.

### 1. INTRODUCTION

The performance of maritime surveillance radars is greatly affected by backscatter from the sea surface. The most commonly used sea-clutter models are empirical, based on clutter measurements, and are not readily applicable to near horizontal propagation geometries. The reason for this is firstly that shadowing effects become important for small grazing angles, and secondly that the propagation factor at these angles deviates significantly from its  $4/3$  Earth value because of refractive effects which are present most of the time in the air/sea boundary layer. Parabolic equation techniques have been used to improve empirical models [4,14] by taking the propagation factor into account. However the resulting models are still empirical in nature, as the sea reflectivity is derived from a limited set of measurements.

The technique presented in this paper is based almost entirely on the physics of electromagnetic scattering

from a rough surface, although it ultimately relies on a semi-empirical description of the sea surface. We assume that backscatter from the sea surface at low grazing angles is caused by Bragg scattering from capillary waves. Well-known formulae of perturbation theory may be used to calculate the backscatter from the ripples on a small patch of the sea surface, knowing the incident field on that patch. If the shape of the sea surface is known, together with the forward propagation factor on the surface, a first order approximation of the backscattering cross-section of a given clutter cell may be obtained by incoherent summation of the echoes of the small patches which compose that cell.

The idea of using a two-scale model is not new (see for example [1,16,17], or more recently [15]). However we believe that no previous investigator has been able to determine accurately the propagation factor on the sea surface. The problem resides in the modelling of the interaction of atmospheric refraction effects with diffraction and shadowing from the ocean surface. This difficulty is removed by the finite difference implementation of the parabolic equation technique.

The parabolic equation approximation to the Helmholtz wave equation was introduced by Fock [5] to treat the problem of diffraction of radiowaves by the Earth. Many years later, it was realized that this approximation provided an elegant numerical solution to propagation problems where the propagation directions of interest remain within a narrow angular sector.

Several investigators developed FFT algorithms to solve the parabolic equation for electromagnetic propagation problems in the troposphere (see for example [3,10]). These techniques are most appropriate when atmospheric refraction is the dominant phenomenon. For cases when diffraction by irregular terrain has to be modelled as well, a finite difference implementation provides a very flexible tool. Finite difference codes were first developed in the underwater acoustics community [11], and then adapted for electromagnetic

propagation in the troposphere [12].

The finite difference implementation of the PE allows the specification of an arbitrary sea surface together with arbitrary atmospheric refractive index profiles. The main problem is now the specification of the sea surface. In this paper we use simple sea spectra to demonstrate the power of the two-scale PE method.

Our technique provides the usual advantages of numerical methods, as it allows a variety of parametric studies. It also permits the visualization of striking forward scatter effects, as well as the simulation of realistic snapshots of clutter returns.

## 2. REFRACTION EFFECTS

The main mechanism of non-standard atmospheric refraction over the sea is the evaporation duct which is caused by the strong humidity gradient just above the sea surface. This phenomenon has been extensively studied, and good radio-meteorological models of the evaporation duct are available, as well as statistics of evaporation duct height [14]. Although our method can cope just as well with more general ducting structures, in this paper we shall limit our investigation of propagation effects on sea clutter to the case of the evaporation duct, which is the dominant one in practice.

Figures 1 and 2 illustrate the effects of evaporation duct height on clutter returns at S-band and X-band: the variation of the 2-way propagation factor with range is shown for various evaporation duct heights, assuming an effective clutter height of 1 m. The antenna is located at a height of 25 m.

The main effect of the evaporation duct is to extend detection ranges and hence to raise clutter levels at longer ranges. Generally the propagation factor decreases with distance and increases with duct height, but the situation becomes more complex at X-band for strong ducting, as interference patterns appear when several lobes become trapped into the duct.

## 3. MODELLING BACKSCATTER

We use a two-scale approach to backscatter modelling: the sea surface is seen as a collection of facets on which ride small scale ripples. At very low grazing angles, backscatter from the sea surface is caused mainly by Bragg scattering from these short capillary waves. The components of the sea spectrum for large wavenumbers have the effect of tilting the facets: this results in shadowing effects, and also in increased backscatter from the steeply tilted facets in a rough sea.

Following [9], we define the normalized radar cross-

section per unit area  $\sigma_0(R)$  for the clutter cell at range  $R$  by the clutter power equation

$$P_c = \frac{P_t G^2 \lambda^2 f^4}{(4\pi R)^3} \left( \sigma_0(R) \Phi \frac{c\tau}{2} \right) \quad (1)$$

where  $f$  is the two-way antenna pattern at the sea surface,  $\Phi$  is the azimuthal beamwidth and  $\tau$  is the pulse width.

We can rewrite  $\sigma_0(R)$  in terms of the two-scale model: for a clutter cell located between ranges  $R - c\tau/4$  and  $R + c\tau/4$ , the cross-section of the cell is obtained by incoherent summing of the cross-sections of the scatterers in the cell

$$\frac{c\tau}{2} \sigma_0(R) = \int_{R-c\tau/4}^{R+c\tau/4} \sigma_0^l(r) F^4(r) dr \quad (2)$$

where  $F^4(r)$  is the 2-way propagation factor on the sea surface at range  $r$  and  $\sigma_0^l(r)$  is the local cross-section per unit area at range  $r$ . The idea here is to use the finite difference implementation of the PE to calculate  $F^4$  for a realistic description of the large scale features of the sea surface. Then  $F^4$  includes atmospheric refraction effects as well as shadowing effects. The local backscattering cross-section per unit area  $\sigma_0^l(r)$  depends on the small-scale roughness produced by capillary waves.

For a given large scale facet of the sea surface, backscatter from the small-scale roughness is modelled using the first order perturbation method [8]. The local backscattering cross-sections per unit area for horizontal and vertical polarization are given respectively by

$$\sigma_H = 16\pi k_1^4 \cos^4 \theta \Psi(2k_1 \sin \theta, 0) \quad (3)$$

$$\sigma_V = 16\pi k_1^4 (1 + \sin^2 \theta)^2 \Psi(2k_1 \sin \theta, 0) \quad (4)$$

where  $\Psi$  is the sea spectrum,  $k_1$  is the wave number of the incident wave and  $\theta$  is the angle of incidence on the facet.

Realizations of a random sea surface with the desired spectral characteristics can be generated by standard Fourier transform techniques [13]. The basic ingredient is the wavenumber spectrum of the sea surface. This topic has been extensively treated in the literature. A bibliography can be found in [7].

Here we have used the approximation of the Phillips spectrum given in [6]

$$\Psi(k) = \frac{B}{\pi} k^{-4} \exp(-k_0/k) \quad (5)$$

in the half-space into which the wind is blowing, where  $v$  is the wind speed and  $k_0 = g/v^2$ . We take  $B = 0.005$ .

**Angle of incidence:** For each facet of the sea surface, the angle of incidence depends on the facet tilt, but also on propagation conditions. For this first attempt at a physical model of sea clutter for very low grazing angles, we decided to neglect propagation effects on the angle of incidence: our grazing angle is just the angle of the local horizontal with the facet under consideration. Obviously the assumption of horizontal propagation is wrong at very short ranges, but is justified for the situations of interest here which involve relatively long ranges and low antennas.

At the ranges of interest, this approximation will have very little effect on the results for vertical polarization, but it could affect horizontal polarization calculations. However atmospheric refraction effects do not affect propagation angles by more than a fraction of a degree [14], even for very strong evaporation ducts. By comparison, the sea slopes are usually of the order of a few degrees so that the error on  $\sigma_H$  is small except for very low sea states.

**Polarization dependence:** With this formulation, the polarization dependence of sea clutter at low grazing angles is easy to understand: at microwave frequencies, the electrical characteristics of the sea are very similar for the two polarizations, so the propagation factor is independent of polarization. The difference in clutter returns is due to the behaviour of the local cross-section, which is always larger for vertical polarization. As wind speed increases and the sea gets rougher, the sea slopes increase and the ratio of the two cross-sections gets closer to 1. This topic is examined in more detail in the next section.

**Look direction:** There are two ways in which the radar look direction relative to the wind and swell can influence clutter returns: first the directional sea-spectrum itself is generally much more complex than the isotropic Phillips model we have used here. Secondly the angle of incidence on the facets is a function of their azimuthal tilt as well as of their elevation from the horizontal. The results we present here are valid for upwind conditions, assuming that the upwind and upswell directions coincide.

#### 4. EXAMPLES

In all the examples that follow, the antennas are located at a height of 25 m above mean sea level. We present results at S-band (3 GHz) and X-band (10 GHz).

Figure 3 shows path loss contours at X-band for a 10 m evaporation duct for sea state 0, sea state 4 and sea state 6. The large scale roughness of the sea surface has a noticeable effect on the lobing pattern, as it perturbs specular reflection: as the sea gets rougher, the lobes are pushed upwards and start to disappear

as coherent reflection becomes weaker.

For the clutter calculations, we present the results in terms of the reflectivity  $\sigma_0$  defined in Equation 1. Although the dependence is not explicit, the reflectivity values are influenced by the pulse width, which determines the integration bounds in Equation 2, and hence the amount of averaging that takes place. Here we have taken  $\tau = 0.66 \mu s$ , corresponding to a clutter cell of 100 m.

Figure 4 shows reflectivity against range at S-band for a wind speed of 5 m/s (sea state 2) and several evaporation duct heights, for a vertically polarized antenna. Similar results at X-band are shown in Figure 5. At S-band, reflectivity closely follows the variations of the 2-way propagation factor, increasing with evaporation duct height, and generally decreasing with distance. An interesting feature of these graphs is the similarity of the small scale variations for the four duct heights. This indicates that it might be possible to write the backscattering cross-section in terms of the propagation factor and of a shadowing function.

The X-band results show similar trends, except for the large variations obtained for the 30 m duct. This stems from the fact that as more energy is trapped in the duct close to the sea surface, interference effects due to the large scale roughness of the sea become more important.

**Influence of sea state:** Figure 6 shows reflectivity against range at S-band for an evaporation duct height of 10 m and sea states 2, 4 and 6, corresponding to wind speeds of 5 m/s, 10 m/s and 15 m/s. The antenna is vertically polarized. The trend certainly shows the expected increase of reflectivity with sea state. This is accompanied by an increase of spatial variability with sea state which is clearly due to the stronger irregularity of the sea surface.

**Influence of polarization:** The results of simulations carried out for both vertical and horizontal polarizations show that the ratio  $\sigma_0^V/\sigma_0^H$  is not sensitive to atmospheric refraction conditions and depends essentially on frequency and sea state. Figure 7 shows  $\sigma_0^V/\sigma_0^H$  against range at S-band for sea states 2, 4 and 6. As discussed in the previous section, the reflectivity ratio is large for moderate sea and decreases for rougher seas.

Figure 8 shows  $\sigma_0^V/\sigma_0^H$  for sea state 2, at S-band and X-band. The polarization dependence is larger for the larger wavelength. This has been noted by several investigators [2,16]. We know from Equations 3 and 4 that large polarization ratios occur for backscatter from facets making a small angle with the horizontal. We conjecture that at X-band, these facets are almost always obscured from the transmitter and contribute



very little to the total backscatter, whereas more energy can reach small slope facets by diffraction over the waves at lower frequencies.

Although we have not done it here, it is possible to investigate cross-polarization effects by introducing the azimuthal tilt of the facets into Equations 3 and 4. The difficulty is then to obtain a realistic model for the spectrum of the azimuthal tilts along a given direction.

**Variability of the results:** All the results presented here are derived from a single realization of the sea surface, and are not necessarily representative of the mean clutter returns for a given sea state. Figure 9 shows the variation of  $\sigma_0$  for two realizations of sea state 2, at S-band and X-band, with a 20 m evaporation duct. The S-band results are very similar for the two runs, while quite large differences appear at X-band. We have already noted that interference effects are bound to be strong when large quantities of energy reach the surface. The resulting variability is likely to be large at X-band in strong ducting situations.

Here we have used two uncorrelated realizations of the sea surface. The method can be taken one step further to provide a tool for the study of the spatial and temporal fluctuations of sea clutter, since successive snapshots can be simulated by using an appropriate sequence of sea spectra.

## 5. CONCLUSIONS

The two-scale parabolic equation technique provides a rigorous numerical solution of the backscattering problem for propagation close to the horizontal over the rough sea surface. As a consequence, the difficulties now lie with the modelling of the sea surface rather than with the electromagnetic scattering.

Simulations with simple sea spectra extend previous work on polarization and frequency dependence of sea clutter to the case of very low grazing angles. More generally, reflectivity values can be obtained for any combination of radar parameters, sea spectrum and atmospheric refractivity profile.

## 6. REFERENCES

- [1] Bass, F.G.I. et al, Very high frequency radiowave scattering by a disturbed sea surface, *IEEE Trans.*, **AP-16**, 554-568, 1968.
- [2] Chan, H.C., Radar sea-clutter at low grazing angles, *IEE Proc. F*, **137**, 102-112, 1990.
- [3] Craig, K.H. and Levy, M.F., Parabolic equation modelling of the effects of multipath and ducting on radar systems, *IEE Proc. F*, **138**, 153-162, 1991.
- [4] Dockery, G.D, Method for modelling sea surface clutter in complicated propagation environments, *IEE Proc. F*, **137**, 73-79, 1990.
- [5] Fock, V.A., *Electromagnetic diffraction and propagation problems*, Pergamon Press, 1965.
- [6] Holliday, D. et al, A radar ocean imaging model for small to moderate incidence angles, *Int. J. Remote Sensing*, **7**, 1899-1934, 1986.
- [7] Hurtaud, Y., Millimetre wave propagation over the sea, Nato Defence Research Group, Technical Report AC/243 TR/3, 1990.
- [8] Ishimaru, A., *Wave propagation and scattering in random media, Vol.2, Multiple scattering, turbulence, rough surfaces, and remote sensing*, Academic Press, New York, 1978.
- [9] Kerr, D.E. (Ed.), *Propagation of short radio waves*, McGraw Hill, New York, 1951.
- [10] Ko, H.W. et al, Anomalous microwave propagation through atmospheric ducts, *Johns Hopkins APL Tech. Dig.*, **4**, 12-16, 1983.
- [11] Lee, D. and McDaniel, S.T., Ocean acoustics propagation by finite difference methods, *Comput. Math. Applic.*, **14**, 305-423, 1987.
- [12] Levy, M.F., Parabolic equation modelling of propagation over irregular terrain, *Elec. Lett.*, **56**, 1153-1155, 1990.
- [13] Macaskill, C. and Ewart, T.E., Computer simulation of two-dimensional random wave propagation, *IMA Journal of Appl. Math.* **33**, 1-15, 1984.
- [14] Reilly, J.P. and Dockery, G.D., Influence of evaporation ducts on radar sea return, *IEE Proc. F*, **137**, 80-88, 1990.
- [15] Robinson, I.S. and Ward, N., A numerical, phase-summation model of radar backscatter from a rough sea surface, *IEE Digest*, No **37**, 7/1-7/6, 1990.
- [16] Wright, J.W., Backscattering from capillary waves with application to sea clutter, *IEEE Trans.*, **AP-14**, 749-754, 1966.
- [17] Wright, J.W., A new model for sea clutter, *IEEE Trans.*, **AP-16**, 217-223, 1968.

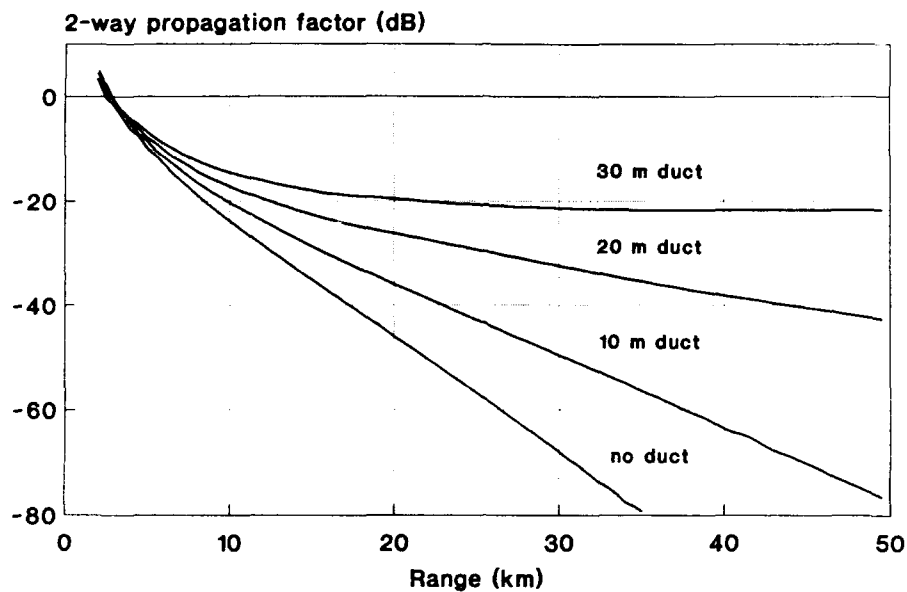


Figure 1. Two-way propagation factor at S-band for various evaporation duct heights  
Antenna height: 25 m Effective clutter height: 1 m

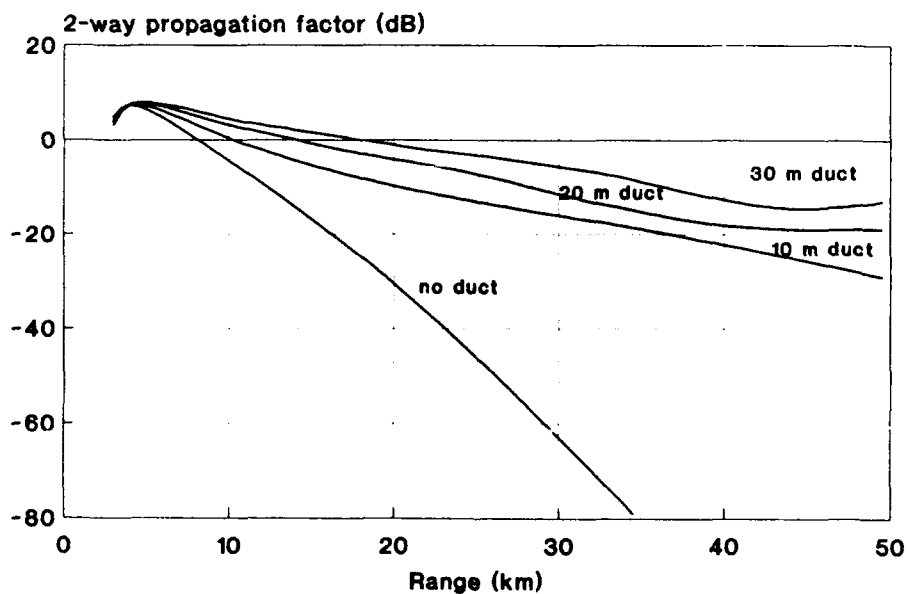


Figure 2. Two-way propagation factor at X-band for various evaporation duct heights  
Antenna height: 25 m Effective clutter height: 1 m

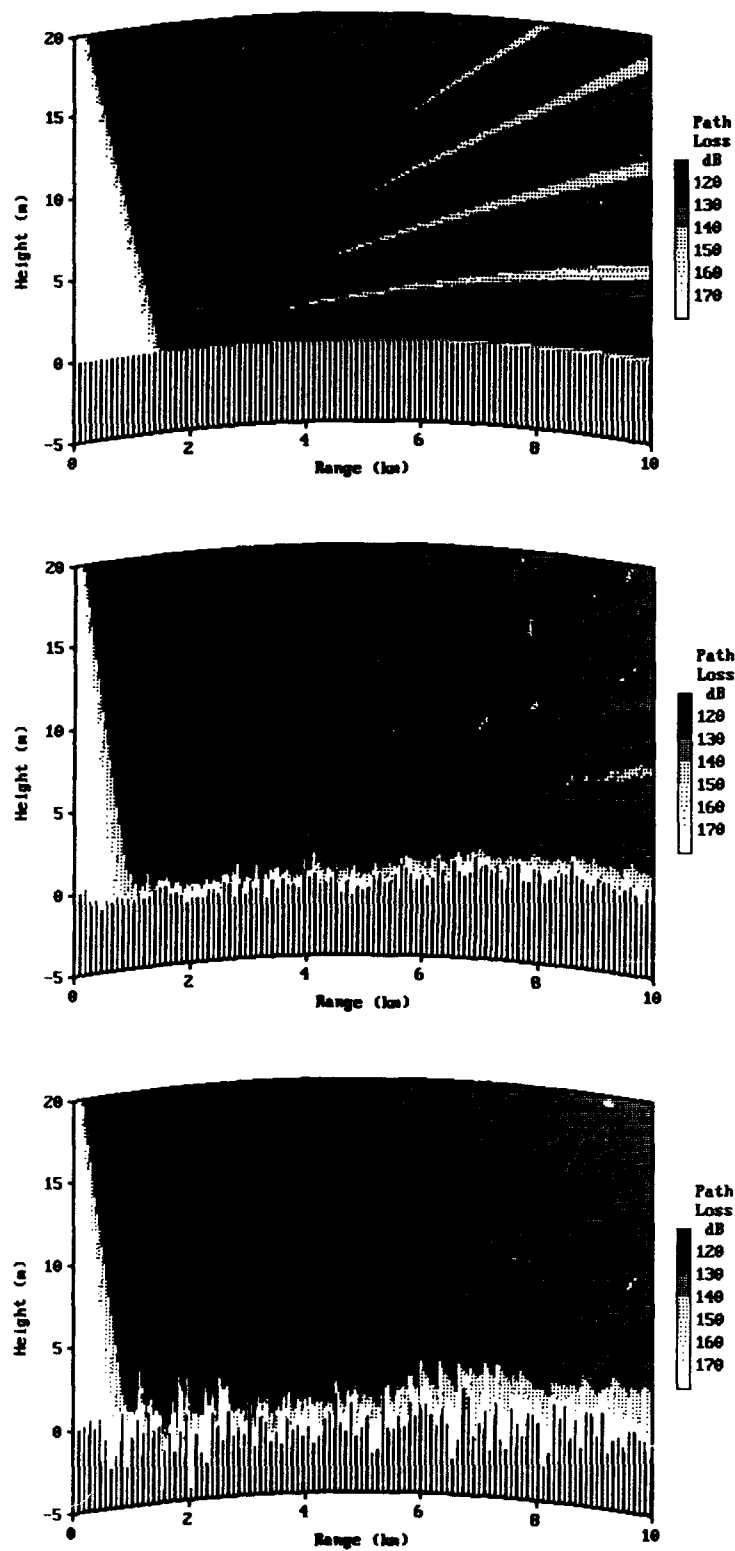


Figure 3. Path loss contours at X-band for various sea states  
a) sea state 0 b) sea state 4 c) sea state 6

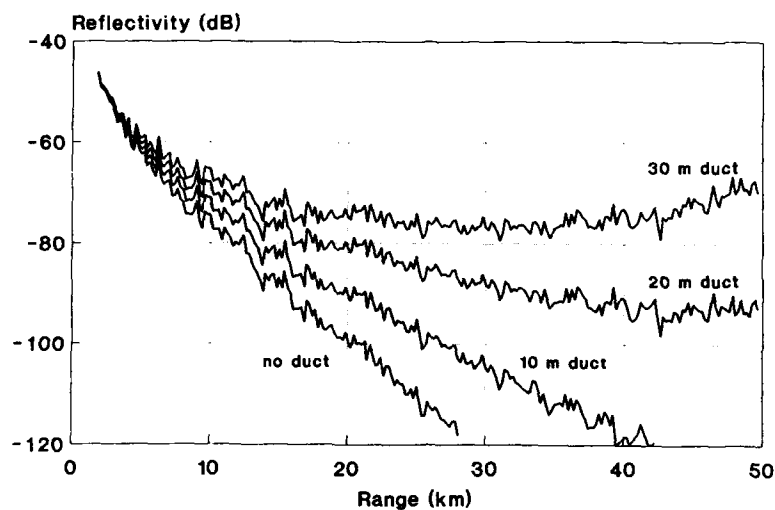


Figure 4. Reflectivity at 3 GHz for various evaporation duct heights  
Sea state 2

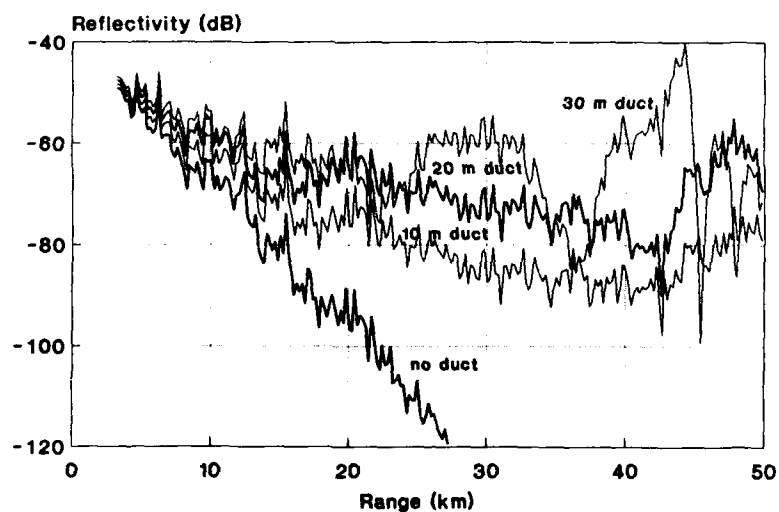


Figure 5. Reflectivity at 10 GHz for various evaporation duct heights  
Sea state 2

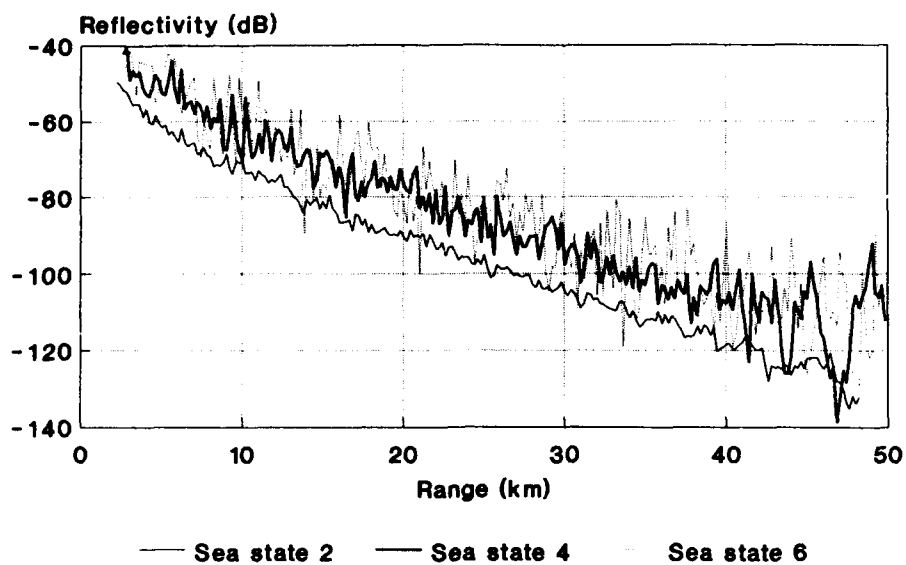


Figure 6. Reflectivity at 3 GHz for various sea states  
Evaporation duct height: 10 m

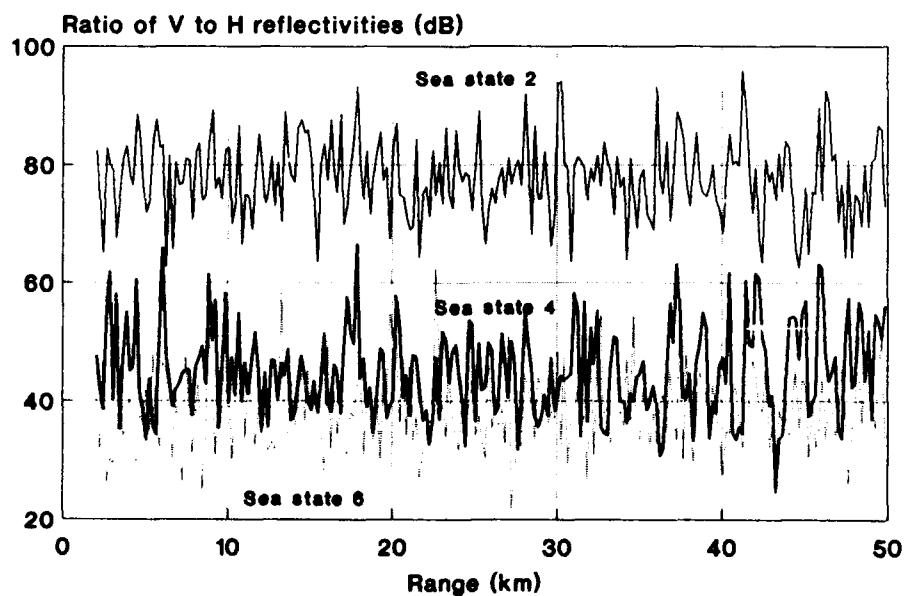


Figure 7. Ratio  $\sigma_V/\sigma_H$  (dB) at S-band for various sea states  
Evaporation duct height: 10 m

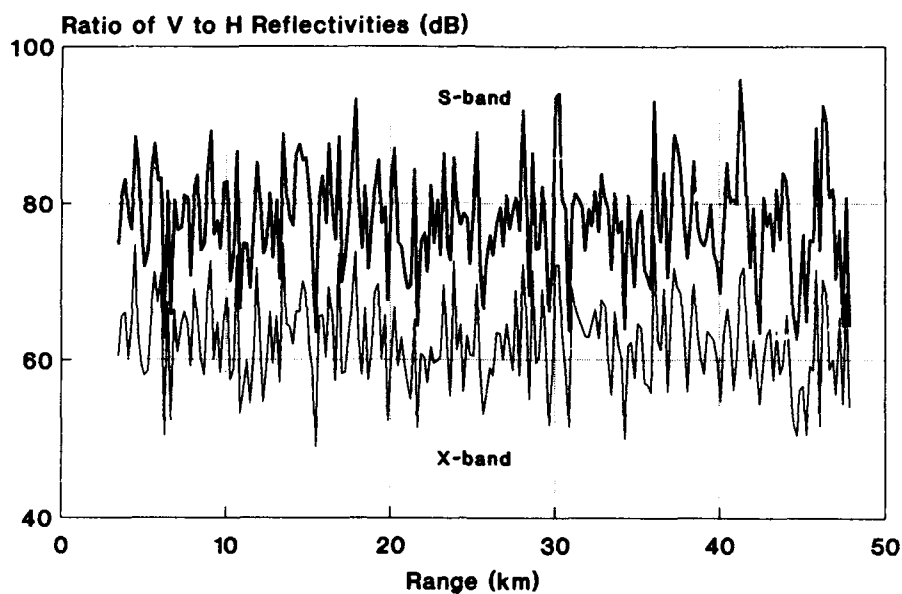


Figure 8. Comparison of  $\sigma_V/\sigma_H$  (dB) at S-band and X-band  
Evaporation duct height: 10 m Sea state 2

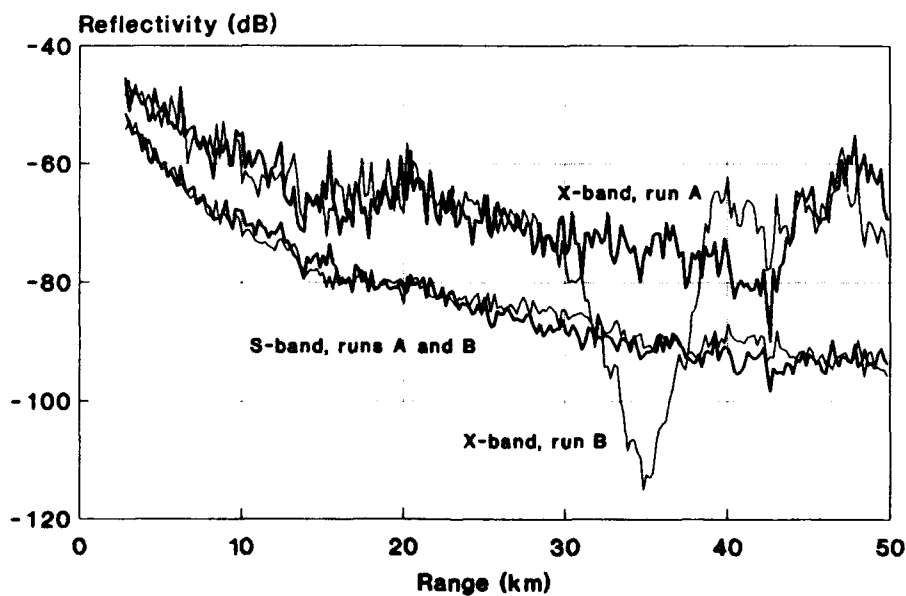


Figure 9. Comparison of clutter returns for two realizations of the sea surface  
Evaporation duct height: 10 m Sea state 2

F. Jouailllec (FR) :

What type of boundary condition is applied on the upper surface of the grid and does it affect the result in the duct ?

Author's reply :

An absorber is applied in a safety region above the domain of interest, in order to eliminate spurious reflections. This does not affect results in the domain of interest.

## DISCUSSION

A. Altintas (TU) :

As far as I can see your parabolic equation analysis is scalar and limited to two dimensions. Can you elaborate on the generalization to three dimensions to get the cross-polarization reflection ?

Author's reply :

A first approximation of 3 D situations may be obtained by considering tilted facets on the sea surface. Full 3 D parabolic equation codes are available and could be used for a more exact solution.

U. Lammers (US) :

One of your viewgraphs showed differences in reflectivities for horizontal and vertical polarization up to 80 dB. Is this correct ?

Author's reply :

I believe this is correct for low sea-states, when clutter returns come from capillary waves on near horizontal facets. I would be glad to compare these results to measurements.

(See also reply to K. Rao).

K. Rao (US) :

1 - What is the isolation ratio of V and H components ?

2 - What is the dynamic range of the receiver ?

Author's reply :

My results are obtained from numerical simulations. The large difference between V-V and H-H clutter returns cannot be compared to measurements at this stage, since no published results are available at very low grazing angles. However the trend shown by measurements at higher angles is compatible with the simulations (See H.C. Chan, "Radar sea-clutter at low grazing angles", IEE Proc. F, Vol 137, pp 102-112). I cannot comment on experimental parameters.

G. H. Hagn (US) :

At very low angles of arrival (near grazing),  $\theta$ , the backscatter reflection coefficient ( $\Pi$ ) as a function of arrival angle drops rapidly below a critical angle,  $\theta_c$ . This phenomena has been observed for both vertical and horizontal polarization, from both sea and land and it has been discussed by P. Beckmann and A. Spizzichino. Can you comment on this critical angle phenomena, in the context of your Parabolic Equation modeling of rough sea backscatter ?

Author's reply :

I think the very low angle of arrival region is precisely the one that can be treated with the 2-scale Parabolic Equation technique : at angles below the critical angle  $\theta_c$ , backscatter must come from small scale roughness caused by capillary waves. Above the critical angle, diffuse reflection from intermediate facets comes into play and this is not taken into account in my model.

# EXPERIMENTAL CHARACTERIZATION OF AMPLITUDE DISTRIBUTION OF MEDITERRANEAN SEA CLUTTER

G. Corsini \*, E. Dalle Mese \*, M. De Palo \*, A. M. Ricci \*, L. Vanni \*, L. Verrazzani \*

\* Department of Information Engineering - University of Pisa - Via Diotisalvi, 2 - I-56026 - Pisa - Italy

\* Institute of Electronics and Telecommunications "G. Vallauri" of the Italian Navy - Viale Italia - I-57100 - Livorno - Italy.

\* Naval Academy - Viale Italia - I-57100 - Livorno - Italy

## Abstract

In this paper, some results relevant to experimental characterization of Mediterranean sea clutter are presented. The data were collected by using a X-band coastal radar sited on an Italian Navy area in Livorno. The aim of this research activity is the collection of clutter samples in different conditions (weather conditions, carrier frequency, polarization and radar site) for clutter models validation, performance assessment and optimization of the radar processor.

## 1. Introduction

In this paper, some results relevant to experimental characterization of Mediterranean sea clutter are presented. The data was collected during the first step of a measurement activity performed in cooperation between the Institute of Electronics and Telecommunications "G. Vallauri" of the Italian Navy (MARITELERADAR) and the Department of Information Engineering of the University of Pisa. The aim of this research activity is the collection of clutter samples in different conditions (weather conditions, carrier frequency, polarization and radar site) for clutter models validation, performance assessment and optimization of the radar processor. In the paper, the experimental set-up is presented. The data were collected by using a X-band coastal radar sited on an Italian Navy area in Livorno. This first set of measurements were obtained in different weather conditions and for different angles between antenna bearing and wind directions. After a brief review of the sea clutter model proposed in the literature [1], [2], [3], [4], the methods used for the experimental characterization of the amplitude distribution of the echoes are presented and discussed. In particular, the analysis of the moments of the intensity fluctuation [5] and some extrapolative estimators of probability tails based on the generalized extreme value theory (GEVT) [6] has been applied on the experimental data. The condition under which the experiment was performed gives rise to results which show a sub-Rayleigh or super-Rayleigh behaviour of the intensity fluctuation. In the first case a K-distribution of the intensity is a good approximation of the cumulative distribution of the experimental data, while in the second case a law with smaller second order moment is required. Thus the Weibull distribution seems to fit well experimental data in all the situations.

## 2. A review of sea clutter models

When the grazing angle is small and the resolution cell dimensions are comparable with the sea swell wavelength, the amplitude distribution of the sea clutter is not a Raleigh-type distribution and the sea clutter radar returns show up as spikes. These spikes have a decorrelation time of several seconds, which is much longer than the decorrelation period of some milliseconds which is typically observed using low-resolution radars. The formal solution of the scattering problem, exhibiting the correct dependence of the probability distribution of the echo envelope on the properties of the scattering centres and on the fluctuations of the number  $N$  of scatterers contributing to the field, has been developed by E. Jakeman [5]. In his approach the received field is represented by a two-dimensional random walk consisting of a fluctuating

number  $N$  of steps whose lengths  $\{a_i\}$  and orientations  $\{\phi_i\}$  are statistically independent random variables. The random phases  $\{\phi_i\}$  are assumed to be uniformly distributed over  $(0, 2\pi)$ . The normalized second moment of the radar cross section is then

$$M_2 = \frac{\langle |E(r)|^4 \rangle}{\langle |E(r)|^2 \rangle^2} = 2 \left( 1 + \sigma_N^2 \right) \cdot \langle N \rangle^{-1} \left( 1 - \sigma_A^2 \right) \quad (2.1)$$

where  $E(r)$  represents the scattered field from the resolution cell at the distance  $r$  from the radar,  $\langle N \rangle$  is the average number of scatterers per cell and  $\sigma_N^2 = \frac{\text{Var}(N)}{\langle N \rangle^2}$  is the normalized variance of the r.v.  $N$  and  $\sigma_A^2 = \frac{\text{Var}(a^2)}{\langle a^2 \rangle^2}$  is the normalized variance of the cross section of a single scatterer.

Eqn. (2.1) emphasizes the effect of the fluctuations of  $N$ , because it can significantly increase  $M_2$ , which entails a longer tail in the amplitude distribution. If  $N$  is distributed according to the negative binomial distribution

$$P_N = \binom{N+\alpha-1}{N} \frac{(\langle N \rangle / \alpha)^N}{(1 + \langle N \rangle / \alpha)^{N+\alpha}} \quad \alpha > 0 \quad (2.2)$$

where  $\alpha$  is a free parameter measuring the "degree of the bunching" in a time sequence of events, a K-distribution of the amplitude results, whatever the properties of the individual steps.

Note that the variance of the negative binomial distribution is  $\sigma_N^2 = \langle N \rangle (1 + \langle N \rangle / \alpha)$  and tends to  $\langle N \rangle$  when

$\alpha \rightarrow \infty$  (Poisson distribution).

In this case eqn.(2.1) becomes

$$M_2 = 2(1 + \alpha^{-1}) + \frac{\langle a^4 \rangle}{\langle a^2 \rangle^2 \langle N \rangle} \quad (2.3)$$

The concept of bunched scatterers is well justified by observing that, if the large-scale sea structure is resolved, the mean level of the clutter fluctuates reproducing the sea swell structure.



Many experimental data, referred in the literature, fit quite well the K-distribution in the range of  $M_2$  of practical interest, i.e.  $2 < M_2 < 10$ .

In the previous model both the distribution of the number of scatterers and the distribution of sea clutter returns for a given number of steps  $N$  are of fundamental importance. Particularly, eqn.(2.1) shows that if the cross sections  $\{\alpha_i^2\}$  are spatially uniform ( $\sigma_A^2 \rightarrow 0$ ) and  $\sigma_N^2 \rightarrow 0$  then the second moment decreases with  $\langle N \rangle$ . This effect can be enhanced if the assumption of randomness in the phases  $\{\phi_i\}$ , which is plausible in confused short-crested sea, fails because of a well-developed long-crested swell, so that sub-Poisson fluctuations occur. In this case the scatterers are antibunched and simulate a specular effect (Rician distribution). The conditions under which our experiments were performed give rise to results which show a sub-Rayleigh or super-Rayleigh behaviour of the amplitude. In the first case a K-distribution of the intensity is a good approximation of the cumulative distribution of the experimental data, while in the second case a law with smaller second-order moments is required. Thus the Weibull distribution seems to fit experimental data well in all situations. The birth-death process used to derive the K-distribution allows modeling the short-term and long-term temporal correlation properties of the clutter. In fact the intensity correlation function is given by

$$\frac{\langle I(t)I(t+\tau) \rangle}{\langle I(t) \rangle \langle I(t+\tau) \rangle} = 1 + (1 + \alpha^{-1}) |g(\tau)|^2 + \alpha^{-1} \theta(t) \quad (2.4)$$

with:

$$g(\tau) = \frac{\Delta \exp(-\mu\tau) \langle a(0) \cdot \tau \rangle \langle \exp[j(\phi(0) - \phi(\tau))] \rangle}{\langle a^2 \rangle} \quad (2.5)$$

$$\theta(t) = \exp[(\lambda - \mu)t] \quad (2.6)$$

$\lambda$  and  $\mu$  are the birth rate and the death rate of the scatterers. Thus in sub-Rayleigh conditions two contributions to the autocorrelation function with quite different time scales can be foreseen. The first contribution is due to the interference effect described by the function  $|g(\tau)|$ , depending on the "fine structure" fluctuations produced by the motion of the scatterers within the patch. The second contribution is due to the fluctuations of the number of scatterers described by  $\theta(t)$  which depends on the lifetime of the scatterers. The first contribution is fast varying and its correlation time can be of the order of 10 ms; the second contribution, which can be associated with the clustering effect, is slow varying and its correlation time can be of the order of seconds. In the absence of the bunching effect (Rayleigh conditions) the long-time term contribution vanishes, while in super-Rayleigh conditions a long periodic time term, apparently connected with the swell, must be observed.

### 3 Radar and Instrumentation System.

The measurement system consists essentially of four main units: the radar, two digitizer and acquisition sets and one host computer. The block diagram of the measurement system is reported in Fig. 3.1.

The data were taken using a fixed antenna of a X-band radar with a frequency of 8.94 GHz, vertical linear polarization,

a pulse width of 0.3  $\mu$ s, a pulse repetition frequency of 2000 Hz, a beamwidth of 4.7° and a transmitted peak power of 100KW.

The receiver is tuned on an intermediate frequency (IF) of 60 MHz. The IF signal is detected by a logarithmic detector and then is sampled.

The IF amplifier gain is 75 dB for the weak signals and 46 dB for the strong signals; its dynamic range is about 70 dB. A calibrated attenuator (0-10dB), placed between the mixer and the IF amplifier, prevents the saturation in the case of particularly strong echoes as could be obtained for sea state 5-7.

The output signal from the log-detector is checked by an oscilloscope for a first qualitative analysis. It is digitized and acquired or by the EG&G model 4420 system or by Tektronix 7612D system. The EG&G model 4420 acquisition and processing unit permits to sample a signal with a maximum rate of 3 Ksamples/s. The RAM memory can store 8192 data points, coded on 12-bit words. An external trigger pulse sets the sampling frequency.

The trigger pulse frequency was changed in order to enlarge the observation time, for any cell, from 4s to 160s.

The other digitizer, the Tektronix 7612D, is faster than the EG&G, but the maximum number of samples that can be stored is 2048. The maximum sampling rate is 200 Megasamples/s and each sample is coded as a 8-bit word. With this system was possible to obtain data in adjacent resolution cells. In our experiment we obtained one sample in each of 256 consecutive range cells, enough to characterize the spatial autocorrelation function of the clutter.

The host computer controls via IEEE-488 interface both acquisition units and allows to record data on a magnetic memory support.

### 4 Data analysis methods

Two types of distribution have gained interest for the modelization of amplitude fluctuation of sea clutter returns: the Weibull distribution and K-distribution. The Weibull distribution of sea clutter was proposed by Fay, Clarke and Peters in 1977 [4]. It has the characteristic of changing the size of the tail by varying the shape parameter.

Consider the backscatter coefficient  $\sigma_o$  of the clutter (it is proportional to the instantaneous power of the output of detector) and assume the Weibull distribution as a model of the clutter returns we have:

$$f(\sigma_o) = \frac{1}{\sigma_o} c \sigma_o^{c-1} \exp \left( - \frac{\sigma_o^c}{\bar{\sigma}_o^c} \right) \quad (4.1)$$

where  $c$  is the shape parameter and  $\bar{\sigma}_o$  is the average backscatter coefficient.

The normalized moments of  $\sigma_o$  are given by:

$$M_m = \frac{E[\sigma_o^m]}{\{E[\sigma_o]\}^m} = \frac{\Gamma\left(\frac{m}{c} + 1\right)}{\left[\Gamma\left(\frac{1}{c} + 1\right)\right]^m} \quad (4.2)$$

Fig. 4.1 shows the plot of the second order moment as a function of the shape parameter  $c$ .

For  $c=1$  eqn.(4.1) reduces to the exponential distribution so that  $M_2=2$ . A distribution with  $M_2$  larger than 2 exhibits a longer tail of the exponential and a smaller

value of the shape parameter  $c$ . The probability tail  $Q(\sigma_0)$  can be easily obtained by integrating eqn.(4.1):

$$Q(\sigma_0) = \exp\left(-\frac{\sigma_0^c}{\bar{\sigma}_0^c}\right) \quad (4.3)$$

Eqn.(4.3) suggests a simple heuristic method [4] to estimate the shape parameter. In fact, taking

$10\log\left(\ln \frac{1}{Q(\sigma_0)}\right)$  it is obtained:

$$10\log\left(\ln \frac{1}{Q(\sigma_0)}\right) = c \cdot 10\log \sigma_0 - 10\log \bar{\sigma}_0 \quad (4.4)$$

from which we have that the shape parameter represents the slope of the straight line obtained by plotting  $10\log(\ln[1/Q(\sigma_0)])$  against the value of the backscatter coefficient  $\sigma_0$  in units of dB.

To check if the clutter distribution is Weibull the experimental histogram of the data was evaluated and the shape parameter  $c$  was estimated by fitting the histogram represented according to the above mentioned technique, with the straight line drawn by the least-squares method. The root means square error RMSE of the linear fit was assumed as a parameter indicating the departure from the Weibull distribution.

Finally, the moments up to the fourth order obtained by eqn.(4.2) for the estimated value of  $c$  were compared with the moments estimated from the data.

The second model that we assumed was the K-distribution. This class of distributions was proposed by Jakeman and Pusey [1] for the sea clutter model and is given by:

$$f(\sigma_0) = \frac{b}{\sqrt{\sigma_0}} \frac{\Gamma(v)}{\Gamma(v)} \left(\frac{b\sqrt{\sigma_0}}{2}\right)^v K_{v-1}\left(b\sqrt{\sigma_0}\right) \quad (4.5)$$

for  $v \geq 1$ , where  $K_v(\cdot)$  is the modified Bessel function of  $v$ -th order,  $b$  is the scale parameter and  $v$  is the shape parameter. The normalized moments of  $\sigma_0$  are:

$$M_m = \frac{m! \Gamma(m+v)}{v^m \Gamma(v)} \quad (4.6)$$

For  $v$  approaching the infinity, eqn.(4.6) reduces to the exponential function and the second order moment  $M_2$  is equal to 2. By using eqn.(4.6) the following expression of the shape parameter as a function of  $M_2$  can be easily derived:

$$v = \frac{2}{M_2 - 2} \quad (4.7)$$

The experimental data were checked by evaluating the shape parameter from the estimated second order moment and comparing the higher order moments calculated by eqn.(4.6) with the estimated ones.

A realistic clutter model represents the fundamental tool for the performance prediction of the radar detector and for the design of optimised processor as CFAR detector. However, a different approach can be followed to give an estimate of the false alarm rate of occurrence of rare events as the spiky returns. In fact, the problem can be approached by

extrapolative techniques based on the generalized extreme value theory GEVT. According to this method the unknown underlying probability tail is approximated by a curve defined by three parameters.

Let  $X_i$  ( $i = 1, 2, \dots, n$ ) be  $n$  i.i.d. random variables with distribution  $F_X(x)$ , so that the exact distribution of the maximum  $Y = \max(X_1, \dots, X_n)$  is given by:

$$F_Y(y) = F_X^n(y) \quad (4.8)$$

From the stability postulate of the generalized extreme value theory (GEVT) and the theorem of Gnedenko follows that if  $F_X(x)$  is a member of the class of exponential

distributions then  $F_X^n(y)$  converges to an asymptote:

$$\lim_{n \rightarrow \infty} F_X^n\left[\left(a_n^v + \frac{u}{d_n}\right)^{1/v}\right] = \exp[-\exp(-u)] \quad (4.9)$$

with  $v > 0$ , if and only if

$$\lim_{n \rightarrow \infty} n\left\{1 - F_X\left[\left(a_n^v + \frac{u}{d_n}\right)^{1/v}\right]\right\} = \exp(-u) \quad (4.10)$$

$$\text{where } F_X(a_n) = 1 - \frac{1}{n} \quad (4.11)$$

$$F_X\left(a_n + \frac{1}{c_n}\right) = 1 - \frac{1}{ne} \quad (4.12)$$

$$\text{and } a_n = \frac{c_n}{v a_n^{v-1}} \quad (4.13)$$

Lognormal, Weibull and K distributions are members of the exponential class. From eqn.(4.10) the following approximation of the probability tail is easily derived:

$$Q_X(x) \approx \frac{1}{n} \exp\left\{-d_n \left(x^v - a_n^v\right)\right\} \quad (4.14)$$

where  $d_n, v, a_n$  are evaluated from eqn.(4.11- 4.13).

Note that the coefficient  $v$  must be regarded as an independent parameter and then, for a fixed  $n$ , we obtain a set of curves depending on  $v$  that can be used to approximate the probability tail. The value of  $v$  for which the convergence of eqn.(4.9) is fastest can be chosen as the optimum. For a Weibull distribution with shape parameter  $c$  it is easy demonstrated that the maximum convergence rate is obtained for  $v = c$  [6]. Fig.4.2 shows the approximations of a Weibull distribution with parameter  $c = 0.7$  and  $\sigma_0 = 0.003$  obtained by using eqn.(4.14) with  $v=1$  and  $v=0.7$  respectively. Note that the curve for  $v=0.7$

is a good approximation of  $Q(x)$  for very low values (in the order of  $10^{-6}$ ) of the probability tail. Assuming that the underlying unknown distribution of the clutter amplitude  $F_X(x)$  belongs to the exponential class it is possible to derive from eqn.(4.10) a heuristic procedure to approximate the probability tail  $Q_X(x)$ . Consider a sample consisting of  $nN$  independent observations from a population having the distribution  $F_X(x)$ . Partitioning the observations in  $N$  groups of  $n$  elements and determining the maximum of each group, a  $N$ -valued extremes sample of the distribution  $F_X^n(y)$  is formed. For sufficiently large  $n$ , we can approximate the distribution of the maximum value of  $n$  i.i.d. random variables with the expression derived from eqn.(4.9):

$$F_X^n(y) = \exp \left\{ -\exp \left[ -d_n \left( y^v - a_n \frac{v}{n} \right) \right] \right\} \quad (4.15)$$

Hence, an estimate of the parameters  $d_n$ ,  $a_n$  and  $v$  of the asymptotic probability distribution of the maximum  $Y$  can be found by fitting the empirical distribution of the  $N$ -valued extremes sample with the curve given by eqn.(4.15). In this way, a large saving in the number of observations necessary to estimate the probability of rare events can be achieved. An extensive empirical examination of the properties of the GEVT estimator is presented in [6], where several factors characteristic of the method are considered. In particular the problem related to the sample partition in order to obtain a sample of extremes is addressed.

## 5. Experimental results

A first data set was taken from sea state 3-5 in a range interval of 3-10Km with a sampling frequency equal to the pulse repetition frequency of the radar. Each value of the output from the detector, for a fixed range bin, was recorded as a 12-bit signal. The number of data points was 8192 for each record. This is equivalent to 4.096s according to 2000Hz repetition frequency. The measurements were performed at very low grazing angle and for different wind direction and velocity. The radar was installed on a platform site and the antenna height was about 10m above the mean sea level. A record of the data obtained upwind and in the range bin located at 4.5Km and for a wind velocity of 50 Km/h is shown in Fig. 5.1. The data were preprocessed in order to compensate the non linearity of the detector and then the instantaneous power was calculated so that values proportional to  $\sigma_0$  were obtained. It can be seen in Fig. 5.2 that the normalized backscatterer coefficient  $\sigma_0$  distribution can be fitted with a Weibull distribution with shape parameter  $c = 0.66$  and RMSE = 0.29. In Table 1 the estimates  $\hat{M}_n$  of the normalized moments up to the fourth order compared with the moments  $\bar{M}_n$  of the Weibull distribution having the estimated shape parameter  $c$ . The experimental results are in good agree with the Weibull model. For a fixed range, as the sea state increased, the shape parameter  $c$  decreased. Table 2 shows the results obtained assuming the K- distribution as the model of the clutter fluctuations. The values of  $v$  are in the range 2-25 and decrease as the sea state increase for a fixed range. Also in this case, the result show a behaviour very similar to the K-distribution. This is not surprising, in

fact, for  $M_2$  ranging in the interval 2 - 6 Weibull and K distributions are very close.

The data were collected during a 48 hours period where the sea state varied considerably. In particular, several variations on the direction and velocity of the wind occurred. During the periods on which a developed swell of the sea can be assumed we noted some data set exhibiting a second order moment less than 2. Although the data are characterized by low value of the amplitude the mean power is considerable higher than the estimated noise power collected by the system. Hence, this behaviour (i.e.  $M_2 < 2$ ) could be explained by the theoretical model relevant to the Super-Rayleigh conditions discussed in Section 2.

A second data set was taken on longer time intervals by reducing the sampling rate down to 50Hz. The data were collected during a 4 hours period from a sea state 6. Each record consists of 2048 data points corresponding to 40.96s. Values of  $M_2$  in the order of several tens corresponding to a shape parameter of a Weibull distribution in the range 0.3-0.4 were obtained.

The GEVT extrapolative method was considered. At first, a simulation test was performed in order to establish the way of partitioning the data. Table 3 shows the root mean square errors normalized with respect to the true probability tail obtained for different data partitions. The results have been obtained on 100 independent runs by simulating random sequences with Weibull distribution having the shape and scale parameters close to the experimental ones. A possible partition of 8192 data points (8192 is the maximum record length of the experimental data) is given by  $n=16$  and  $N=512$  or  $n=8$  and  $N=1024$ . Hence, in this case, a good approximation of the probability tail in the range  $10^{-3} - 10^{-4}$  can be obtained with small values of  $n$ . The result obtained by using the GEVT extrapolative method on a 8192 data record are reported in Fig. 5.3. The data, characterized by  $M_2 = 3.331$ , were partitioned in 1024 groups of 8 elements. The empirical distribution of extrema was used to estimate the parameter of asymptotic probability tail.

## 6. Conclusions

In this paper some results relevant to experimental characterization of the temporal distribution of the Mediterranean sea clutter are reported and discussed. A short time analysis of the data shows that sub-Rayleigh or super-Rayleigh behaviour of the amplitude fluctuation can be obtained. In the first case a K-distribution of the intensity is a good approximation of the cumulative distribution of the experimental data, while in the second case a law with smaller second order moment is required. Thus the Weibull distribution seems to fit well experimental data in all the situations. The analysis of longer temporal sequences shows that very higher second order moments can be obtained for sea state 6. The application of GEVT extrapolative methods of probability tail of the sea clutter data has been considered. At the end of 1991 data will be available from a coherent radar in the band 1-18 GHz with pulsewidth down to 5 ns, arbitrary polarization and pulse by pulse frequency agility and it will be possible a more accurate analysis of the phenomenon.

## 7. References

- [1] E. Jakeman, N. Pusey, "A model for Non-Rayleigh Echo", IEEE Trans. on Antennas and Propagation, Vol. AP-24, No. 6, pp.806-814, November 1976.

[2] K.D.Ward, S. Watt, "Radar Sea Clutter", Microwave Journal, pp. 109-186, June 1985.

[3] K.D. Ward, "Compound representation of high resolution sea clutter", Electronics Letters, Vol. 17, No. 16, pp. 561-563, 6th August 1981.

[4] F.A. Fay, J. Clarke, R.S. Peters, "Weibull distribution applied to sea clutter", IEE RADAR 77, pp. 101-103, 1977.

[5] E. Jakeman, "Speckle statistics with a small number of scatterers", Optical Engineering, Vol.23, No. 4, pp. 453-461, July-August 1984.

[6] M. Guida, D. Iovino, M. Longo, "Comparative performance analysis of some extrapolative estimators of probability tails", IEEE Journal on Selected Areas on Communications, Vol. 6, No.1, pp. 76-84, January 1988.

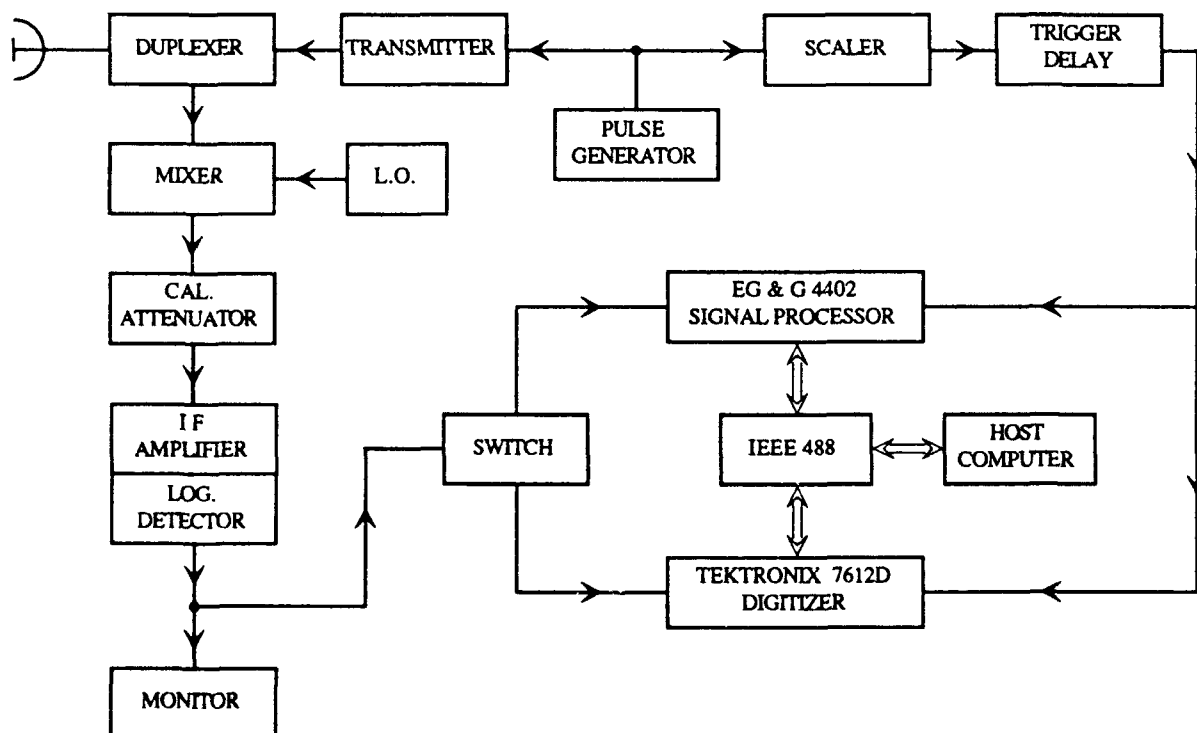


Fig. 3.1 Block diagram of the radar and acquisition system

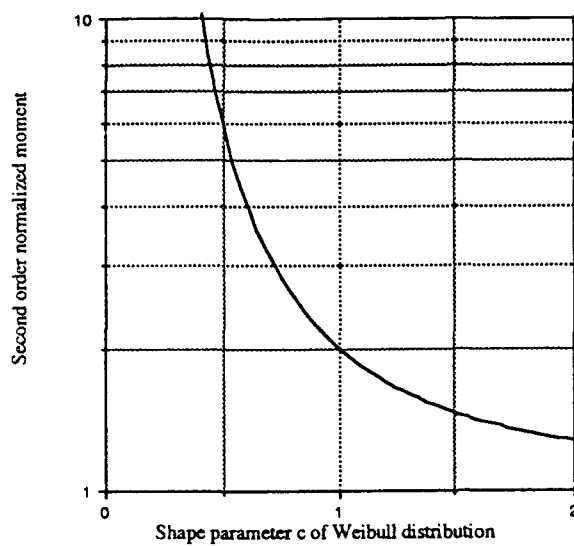


Fig. 4.1 Plot of the normalized second order moment of the Weibull distribution against the shape parameter.

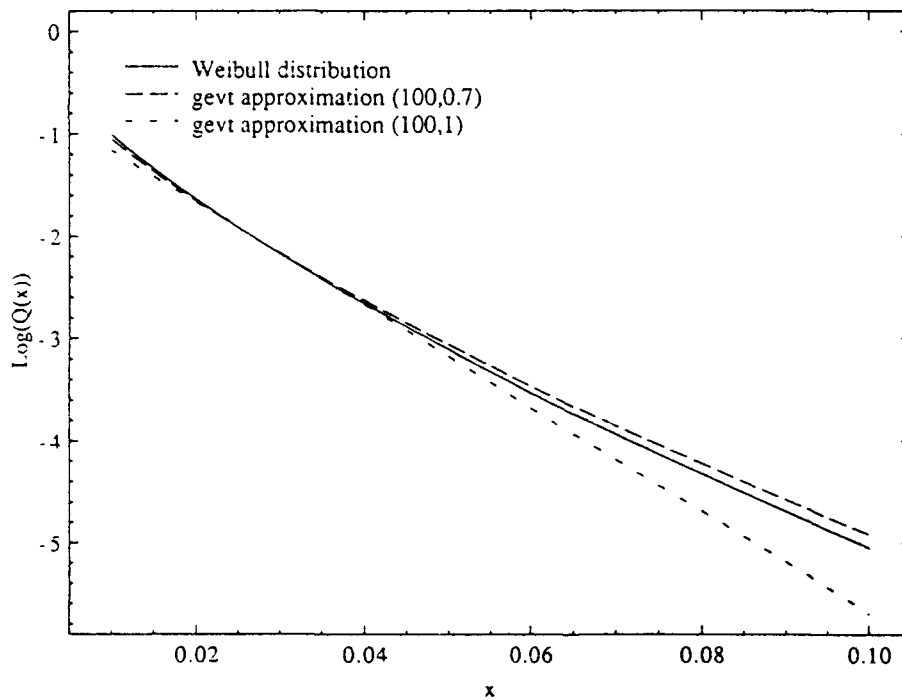


Fig. 4.2 Approximation of a Weibull probability tail with parameters  $c=0.7$   $\sigma_0 = 0.003$  by GEVT extrapolation method with  $n=100$ ,  $v=1$  and  $\nu=0.7$

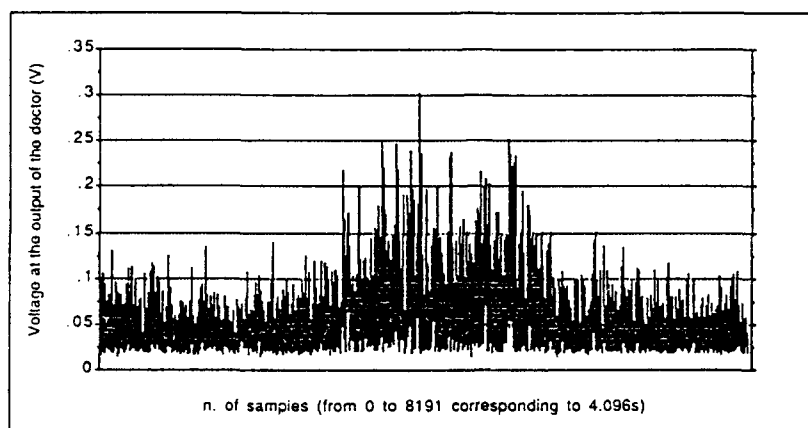


Fig. 5.1 A record of clutter data for a fixed range bin located at 4.5 Km; wind speed of 40 Km/h, upwind, 8192 samples corresponding to 4.096s.

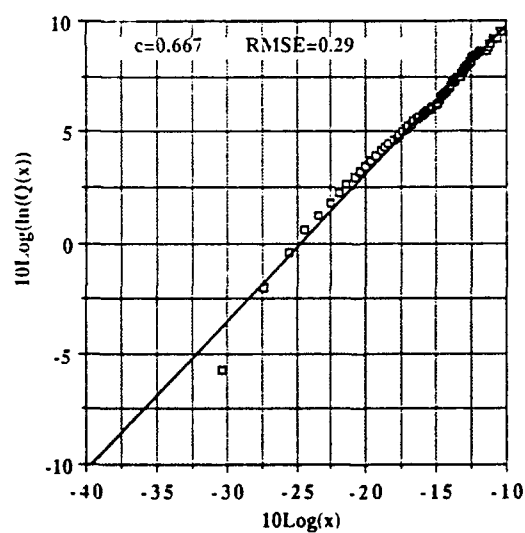


Fig. 5.2 Fitting of the empirical distribution of clutter data with a Weibull distribution ( $M_2 = 3.31$ ,  $c = 0.67$  and mean value of  $4 \cdot 10^{-3}$ )

range Km	sea state	c	$\hat{M}_2$	$\overline{M}_2$	$\hat{M}_3$	$\overline{M}_3$	$\hat{M}_4$	$\overline{M}_4$
3	2-3	0.775	2.55	2.7	12.72	12.69	86.53	87.57
3	2	0.95	2.14	2.1	7.82	6.76	38.33	29.56
4.5	4-5	0.68	3.31	3.39	22.64	22.18	225	228
4.5	3	1.02	2.082	1.93	6.7	5.5	28.25	20.52
6	4-5	0.72	3.786	3.05	18.25	16.49	159.4	137.4
6	4	0.76	2.705	2.756	12.99	13.31	89.94	95.05
10	4	0.73	2.23	2.9	16.54	15.18	141.4	119.2

Table 1 Comparison between experimental data and the Weibull distribution

range Km	sea state	n	$\hat{M}_2$	$\hat{M}_3$	$\overline{M}_3$	$\hat{M}_4$	$\overline{M}_4$
3	2-3	3.64	2.55	12.72	11.85	86.53	86.43
3	2	14.18	2.14	7.82	7.32	38.33	35.53
4.5	4-5	1.5	3.31	22.64	23.29	225	279
4.5	3	24.26	2.082	6.7	6.72	28.25	30.39
6	4-5	2.012	3.786	18.25	17.91	159.4	178.5
6	4	2.83	2.705	12.99	13.83	89.94	113.4
10	4	2.32	2.23	16.54	15.99	141.4	146.6

Table 2 Comparison between experimental data and the K-distribution.

$Q(x)$	$n=8; N=1024$	$n=16; N=512$	$n=32; N=256$	$n=64; N=128$
$10^{-2}$	0.06476	0.06503	0.07411	0.09834
$10^{-3}$	0.24153	0.25444	0.25474	0.24219
$10^{-4}$	0.64620	0.73425	0.80872	0.70316
$10^{-5}$	1.47523	1.82632	2.20209	1.88693
$10^{-6}$	3.21232	4.44497	5.94729	5.45013
$10^{-7}$	7.05832	11.19384	16.88716	17.43900
$10^{-8}$	16.10191	29.88144	51.54015	61.99307

Table 3

Empirical investigation of the effects due to different partitions of the 8192 data set.  
 The estimated normalized mean square errors were obtained by simulating random sequences with Weibull distribution having parameters  $c=0.67$  and mean value 0.003.

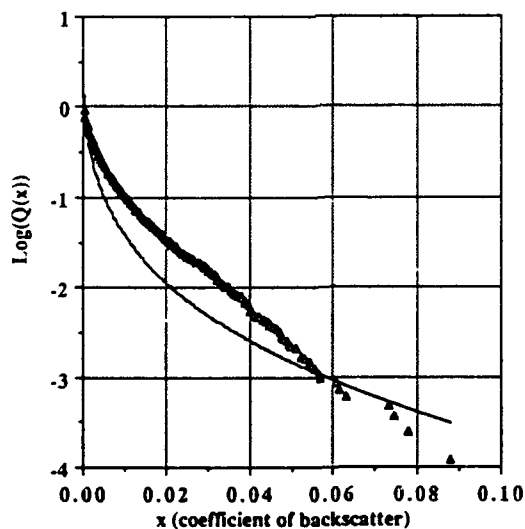


Fig. 5.3 GEVT extrapolation of the Probability tail of a 8192 data set with  $M_2 = 3.31$  and mean level of 0.003.  
 The result was obtained partitioning the data in 1024 groups of 8 elements.



## **DISCUSSION**

**J. Tunaley (CA) :**

Why was the chi-squared test not used to compare theoretics and experimental frequency distribution ?

**Author's reply :**

The results presented in this paper were obtained following a method commonly used in literature (see for example reference 4 in the paper). The hypothesis that the Weibull distribution fits the data is tested by computing the RMSE between distribution of the experimental data and the assumed distribution. However, to have a better statistical inference, we are going to use Kolmogorov-Smirnoff test.

**C.J. Baker (UK) :**

Although you conclude that the data fits best to the Weibull distribution, would it not be better to use the compound form of the K-distribution. This allows clutter correlation properties to be incorporated into any prediction calculations which are more significant than any difference in the amplitude statistics described by these two models ?

**Author's reply :**

The Weibull distribution seems to be a more general model for the distribution of clutter measured data because it can represent with a *suitable choice of the shape parameter*, a large number of different situations [ $M_2$  ranging in the interval  $(1, + \infty)$ ]. This adaptability of the model to these different conditions is not possible with the K-distribution. Furthermore, short time temporal sequences could have a super Rayleigh behaviour due to specular effects and in this case the K-compound model could not be applicable directly.

# MODELING AND MEASURING MILLIMETER-WAVE SCATTERING FROM SNOW-COVERED TERRAIN

Fawwaz T. Ulaby and Yasuo Kuga, and Richard Austin  
University of Michigan  
The Radiation Laboratory  
Department of Electrical Engineering and Computer Science  
3228 EECS Building  
Ann Arbor, Michigan 48109-2122

## SUMMARY

A radiative transfer model was developed for characterizing radar backscatter from snow-covered ground at millimeter wave-lengths. The model was used to evaluate the radar response to incidence angle, snow depth, snow surface roughness, and snow liquid water content, for both like- and cross-polarization configurations. The model behavior was compared with experimental observations made at 35, 95, and 140 GHz, including observations over diurnal cycles. The experimental data were acquired during the 1989 and 1990 winter seasons in Michigan using a truck-mounted millimeter-wave scatterometer system capable of observing the ground surface over a wide range of incidence angles for all linear combinations of transmit and receive antenna polarizations.

Comparison of the measured data with model calculations revealed excellent agreement for dry snow as well as when the surface layer of the snowpack was wet. However, when the surface layer was dry and lower layers were wet, the model results were inconsistent with the radar observations. To deal with the general case wherein the liquid water content exhibits a nonlinear profile with depth, a hybrid numerical-first order solution of the radiative transfer model was developed. This hybrid model provided excellent agreement with the diurnal observations of radar backscatter.

## 1 INTRODUCTION

Although several papers have appeared recently documenting the results of millimeter-wave (MMW) radar observations of snow-covered terrain [1-9], the interaction mechanisms responsible for the observed radar response are not well understood at the present time. At millimeter wavelengths, snow is a highly lossy medium, particularly when wet; consequently, the penetration depth is only on the order of a few centimeters [4, 10, 11]. For dry snow, the attenuation is dominated by scattering because the ice particles are comparable to the wavelength in size, and for wet snow both absorption and scattering are important.

The physical parameters that exhibit the strongest importance on the radar backscatter from snow are snow surface roughness, crystal size, snow depth, and the liquid-water profile with depth. This paper provides a radiative transfer model for characterizing MMW scattering from snow. It uses experimental data in conjunction with the quasi-crystalline approximation [12] to compute the extinction coefficient of the snow medium. The results of experiments conducted at 35, 95, and 140 GHz are compared with theoretical calculations.

## 2 SNOW MODEL

In our snow model, we assume ground snow to consist of spherical ice particles embedded in a background medium. Liquid water, when present, is included as part of the background medium. The size of the water inclusion is usually much smaller than the wavelength for millimeter-wave remote sensing. Therefore, it is reasonable to assume that the water is uniformly distributed in the snow and the dielectric constant of water can be included as a part of the background.

From ground-truth data, we know that the ice particles have an average diameter on the order of 0.1-2 mm and their shapes are round but non-spherical. In our model we treat the snow ice particles as spheres with a normal-size distribution with an average diameter of 1 mm and a standard deviation of 0.2 mm. The values of the dielectric constant of the ice particles needed in this study were obtained from Mätzler and Wegmüller, [13] and are listed in Table 1. Also from the ground-truth data measured in conjunction with the experimental observations, the volume concentration of snow is approximately 40% and the snow depth is 0.45 m. These values are used in our model calculations.

## 2.1 Background Absorption by Water Inclusions

The imaginary part of the background dielectric constant is directly related to the background absorption coefficient. We use a dielectric mixing formula to calculate the background dielectric constant, and we assume that scattering by the water particles to be much smaller than absorption. The absorption coefficient  $\kappa_{ag}$  of the background medium is given by

$$\kappa_{ag} = 2\text{Im}\{k_b(1-f)\} \quad (1)$$

$$= 2k_o(1-f)\text{Im}\{\sqrt{\epsilon_b}\} \quad (2)$$

where  $k_o$  is the free space wavenumber,  $\epsilon_b$  is the background dielectric constant, and  $f$  is the volume fraction of ice particles. To obtain the dielectric constant of the background, which is a mixture of air and water, we use the Van Santen mixing formula [10],

$$\epsilon_b = 1 + \frac{m_w}{3}(\epsilon_w - 1) \sum_{u=a,b,c} \left[ \frac{1}{1 + A_u(\frac{\epsilon_w}{\epsilon_b} - 1)} \right] \quad (3)$$

where  $\epsilon_w$  is the dielectric constant of water,  $m_w$  is the volumetric snow wetness, and  $A_u$  is the depolarization factor which depends on the shape of the water droplet.

If the water droplet is spherical,  $A_u$  is constant and given by  $A_u = 1/3$ , but the water particles in snow are usually non-spherical and they change shape with the amount of liquid water present [11]. If the liquid water content is low, known as the pendular regime, the values of  $A_u$  are close to those for a needle. On the other hand, if the liquid water level is high, known as the funicular regime, the values of  $A_u$  are close to those for a disk. Hallikainen et al. [11] provide plots for  $A_u$ ,  $A_b$  and  $A_c$  as a function of  $m_w$ , which show that the transition from the pendular to funicular regime occurs at around  $m_w = 2.5$ . These plots are used in all calculations of  $\epsilon_b$  in this paper (see Table 1).

## 2.2 Scattering Characteristics of Ice Particles

The scattering characteristics of ice particles are calculated using the Mie solution. The background dielectric constant is assumed to be the real part of  $\epsilon_b$  listed in Table 1. The average total and absorption cross-sections are shown in Table 1.

## 2.3 Extinction Coefficient of Dry Snow

When snow is dry, the attenuation at millimeter wavelengths is due mainly to scattering by the snow particles. In a sparsely distributed medium in which the correlation between particles can be neglected, the effective field approximation (EFA) can be applied and the extinction coefficient is linearly proportional to the concentration of particles [12]. Ground snow, however, has an ice volume fraction of 10 to 40% and the dielectric constant of ice is much larger than that of the background medium. Hence, the independent-scatterers assumption is inappropriate for snow, which means that correlation between adjacent ice particles should be considered [12]. An additional important phenomenon that must be considered when treating propagation in a dense medium like snow is the fact that the extinction coefficient ceases to vary linearly with density. When the volume fraction of particles is more than 1%, the extinction coefficient is no longer linearly proportional to the number density. The deviation from the linear relationship applicable at low densities is related to the size parameter, the dielectric constant and volume fraction of the particles. Extensive experimental and theoretical studies on the extinction coefficient in a dense medium have been conducted in recent years [12, 14]. The theoretical models include Twersky's model, the perturbation solution with hole-correction, the quasi-crystalline approximation (QCA) with Percus-Yevick pair

correlation function, and the quasi-crystalline approximation with coherent potential (QCA-CP). Twersky's model is simple but it is applicable only for small particles. The formula based on the hole-correction is valid if the volume fraction is much less than 10%. For higher concentrations, QCA and QCA-CP with the Percus-Yevick pair correlation function have been shown to be effective [12].

In the millimeter-wave region where the size parameter is close to 1, we cannot use a small-particle approximation. We need to solve the QCA numerically. We calculated the extinction coefficient of snow using the QCA with the Percus-Yevick pair distribution function at 35, 95 and 140 GHz. The results are listed in Table 1. When the volume fraction  $f$  is 0.4, the extinction coefficients given by QCA are only 6.5 % of those calculated according to the EFA at 35 GHz and similar percentages apply at 95 and 140 GHz. The optical distance, which is defined as  $\tau = (\kappa_e + \kappa_{ag})d$ , is shown in Fig. 1 as a function of liquid water content for both EFA and QCA.

According to recent extinction measurements conducted for dry snow at 35 and 95 GHz [4], the extinction coefficient was found to exhibit a strong dependence on snow type. The reported values of the extinction coefficient covered the range between 0.96 and 15.4  $\text{m}^{-1}$  at 35 GHz and between 1.0 and 30.7  $\text{m}^{-1}$  at 95 GHz, with estimated median values of about 3.7  $\text{m}^{-1}$  at 35 GHz and 19  $\text{m}^{-1}$  at 95 GHz. The median value at 95 GHz is close to that computed using the QCA method, but the median extinction coefficient at 35 GHz is much higher than that computed according to the QCA method.

If the optical distance is greater than 5, the backscattering coefficient of dry snow becomes essentially independent of the optical distance (in the millimeter-wave region). For a snow thickness of 0.45 m and extinction coefficient of 19  $\text{m}^{-1}$ , the optical distance is already more than 8 at 95 GHz. Therefore, the exact value of extinction coefficient is not important at 95 and 140 GHz. However, an accurate estimate of the extinction coefficient is important at 35 GHz because  $\tau$  is smaller. In our model calculations with a volume fraction  $f = 0.4$ , we used extinction coefficients of 3.7  $\text{m}^{-1}$  at 35 GHz and 19  $\text{m}^{-1}$  at 95 GHz, which seem to offer the best fit to the experimental data. For snow with other values of  $f$ , the extinction coefficient is scaled in proportion to the change in the QCA model. This method is chosen because the extinction coefficient is a non-linear function of  $f$  and the density dependence curve given by QCA has been confirmed experimentally [14]. With this correction, for example, the extinction coefficient at 35 GHz becomes 5.18  $\text{m}^{-1}$ , 4.45  $\text{m}^{-1}$ , and 3.7  $\text{m}^{-1}$  when the snow density  $f$  is 20, 30, and 40%, respectively. Due to the lack of measured extinction-coefficient data at 140 GHz, we will use the value calculated by the QCA model.

### 3 RADIATIVE TRANSFER MODEL

Microwave remote sensing of ground snow has been studied by many researchers in the past [10]. The model usually used is based on the radiative transfer theory, with the Rayleigh phase function used for modeling the ice particles. This is a good approximation at microwave frequencies because the ice-particle size is much smaller than the wavelength. At millimeter wavelengths, where the ice particle size is comparable to the wavelength, the Mie phase function must be used instead.

In a dense medium like snow, we need to modify the conventional radiative transfer theory to take into account the correlation between particles. A dense-medium radiative transfer theory was recently developed using the Dyson equation with QCA-CP and the Bethe-Salpeter equation under the ladder approximation of correlated scatterers [15]. The form of the dense-medium radiative transfer theory is the same as the conventional radiative transfer theory and, therefore, the same numerical techniques can be used for its solution. The difference between the conventional radiative transfer theory and the dense-medium radiative transfer theory is the extinction rate, which can be obtained by the QCA-CP and the new form of the albedo. This dense-medium modeling approach was further modified by Kuga et al. [16] to incorporate contributions due to scattering by the snow surface. They used the Kirchhoff model with the stationary-phase approximation to compute the co-polarized backscattering coefficient of the snow surface

$$\sigma_{ss} = \frac{|r(0)|^2 \exp(-\frac{\tan^2 \theta_o}{2m^2})}{2m^2 \cos^4 \theta_o} \quad (4)$$

where  $\theta_o$  is the incidence angle,  $m$  is the rms slope, and  $r(0)$  is the Fresnel reflection coefficient evaluated at normal incidence. The Kirchhoff approximation does not produce depolarization in the backscatter direction. Therefore, the total-snow backscattering coefficient is

$$\begin{aligned} \sigma_{ss}^{vv} &= \sigma_{ss}^{vv} + \sigma_{ss} \\ \sigma_{ss}^{hh} &= \sigma_{ss}^{hh} + \sigma_{ss} \\ \sigma_{ss}^{hv} &= \sigma_{ss}^{hv} = \sigma_{ss}^{vh} = \sigma_{ss}^{vv} \end{aligned} \quad (5)$$

where the superscripts denote the receive/transmit antenna polarizations, and the subscript  $sv$  refers to the backscattering coefficient of the snow medium. Details of the model formulation and solution are given in Kuga et al. [16].

### 4 SNOW EXPERIMENTS

The measurements reported in this paper were acquired by the University of Michigan's truck-mounted millimeter-wave scatterometer [17, 18]. A summary of the system's specifications is given in Table 2. Ground-truth observations were made for the following parameters: (a) air temperature, (b) near-surface snow temperature, as well as the temperature at deeper locations in the snow layer, (c) snow density  $\rho_s$  ( $\text{g}/\text{cm}^3$ ), (d) height profile of the snow surface using a graded metal plate inserted edgewise into the snow, from which the rms height  $s$  is calculated, (e) depth of the snow layer, (f) volumetric liquid water content of the surface 5-cm layer,  $m_v$  (%), measured using the freezing calorimeter technique and (g) microscope photographs of thin snow samples, from which the ice crystal-size is estimated.

The standard measurement procedure consisted of measuring the backscattered power for  $hh$ ,  $hv$ ,  $vh$ , and  $vv$  polarizations at each of 30 or more spatial locations. The backscattering coefficient was obtained by averaging the measurements for the different spatial locations. In addition to spatial averaging, frequency averaging was used to further improve measurement precision [7]. The estimated uncertainty associated with the values reported in this paper is  $\pm 0.5$  dB. Analysis of the data shows that the  $hv$ - and  $vh$ -measurements are essentially identical (within a fraction of 1 dB), which is expected from the reciprocity relation. In almost all cases, the co-polarized responses,  $\sigma_{hh}^0$  and  $\sigma_{vv}^0$ , were within 1–2 dB of each other.

Two sets of experiments were conducted. In the winter seasons of 1989 and 1990, the focus of the experimental observations was to evaluate the response of the backscattering coefficient at 35, 94, and 140 GHz to snow surface roughness and liquid water content. In 1991, measurements were conducted using a 35-GHz polarimetric system to investigate the diurnal response of the degree of polarization.

### 5 EXPERIMENTAL OBSERVATIONS

#### 5.1 Angular Response

The data shown in Figure 2 were measured for a 12-cm thick layer of dry, freshly fallen, unmetamorphosed snow composed of ice crystals with diameters on the order of 1 mm. The measured rms height was 1.4 mm. Only  $hv$ - and  $vv$ -polarized data are shown because the difference between  $\sigma_{hh}^0$  and  $\sigma_{vv}^0$  is 1 dB or less across the entire angular range at all three frequencies. The curves shown in the figure were calculated according to the theoretical model described in Section 3. For  $vv$  polarization, theory and experiment are in good agreement at 35 and 95 GHz. At 140 GHz, however, the level predicted by theory is lower than the experimental observations for  $vv$  polarization by about 4 dB. We attribute the difference to the backscattering enhancement effect, which the model does not take into account.

A typical example of the angular dependence for wet snow is shown in Figure 3. The theoretical curves were computed assuming a mean ice crystal diameter of 1 mm and a rms slope of 0.07. Reasonable agreement between theory and experiment is obtained except for  $vv$  polarization of 140 GHz; we again attribute the difference to the backscattering enhancement effect, although no strong evidence exists to support this contention.

## 5.2 Effect of Snow Surface Roughness

According to the model results presented in the previous paper, snow surface roughness should have a minor effect on the level of  $\sigma^0$  (except at normal incidence) when the snow is dry. For wet snow, however,  $\sigma^0$  should increase by as much as 5 dB at 35 GHz if the surface is made rough relative to the wavelength, but the increase should not be significant at 95 GHz or higher frequencies [16]. There is plenty of experimental evidence to support the model expectations with regard to dry snow, both at 35 GHz [1] and 95 GHz [6]. Additional support is provided by the data shown in Figure 4. A detailed examination of the effect of surface roughness on the radar response from snow was conducted by observing the radar backscatter as a function of time for three sections of a 71-cm deep snowpack with different surface roughnesses. Twelve sets of observations were made, all at  $\theta_0 = 40^\circ$ , for each surface roughness, starting at 6:30 am and ending at 10:00 pm; each set consisted of measurements at 35 and 95 GHz for all linear polarization combinations. The measured rms heights of the three surfaces were  $s_1 = 0.49$  cm,  $s_2 = 0.89$  cm, and  $s_3 = 1.98$  cm, and the liquid water content of the 5-cm surface layer exhibited a Gaussian like variation with a peak value of 4.8% (Figure 4).

Figure 4 shows a sample of the measured data, specifically the cross-polarized diurnal responses of all three roughnesses at both 35 GHz and 95 GHz. According to the 35 GHz data, increasing the rms height from 0.49 cm to 0.88 cm (which corresponds to increasing  $s/\lambda$  from 0.57 (slightly rough) to 1.02 (rough)) causes  $\sigma^0$  to increase by 1–3 dB, but increasing the roughness further to  $s_3 = 1.98$  cm does not seem to have much of an impact on  $\sigma^0$ . At 95 GHz, even the least rough surface (with  $s_1/\lambda = 1.5$ ) is electromagnetically very rough. Hence,  $\sigma^0$  exhibits approximately the same diurnal pattern for all three surface roughnesses. A similar behavior was observed for vv polarization.

## 5.3 Diurnal Response

Because the numerical solution of the radiative transfer model described briefly in Section 3 (and in more detail in ([16]) takes into account all orders of multiple scattering in the snow volume, its implementation requires a substantial amount of computer processing time, in spite of the fact that the snow medium is assumed to have uniform properties throughout. If we were to formulate the solution for a multilayer structure in order to accommodate a nonuniform depth profile for the liquid water content  $m_w$ , the complexity of the numerical approach would make the solution computationally impractical. On the other hand, the first-order solution is perfectly amenable to computing the backscatter from a medium with nonuniform properties in the depth dimension, but it does not account for multiple scattering. Ulaby et al. [19] developed a hybrid model that takes advantage of the more accurate feature of the numerical solution and the easier structure of the first-order solution. Their procedure was applied to a measured wetness profile, and the results are shown in Figure 5 for hh polarization at 35, 95, and 140 GHz. The plots compare the measured diurnal variation of  $\sigma^0$  (relative to its value for dry-snow conditions) with the variation computed using the hybrid solution outlined above. Very good overall agreement is observed at all three frequencies, and similar agreement was obtained for the other polarizations and for other diurnal experiments.

## 5.4 Polarimetric Response

To investigate the polarimetric radar response of snow at millimeter wavelengths, 35 and 94 GHz coherent-on-receive polarimetric radar systems were constructed in 1990 and used in 1991 at test sites near Ann Arbor and Pellston, Michigan. Only part of the 35-GHz results are ready for presentation in this paper. The coherent-on-receive polarimetric systems measure the Mueller matrix directly by transmitting six different polarizations and receiving the magnitude and phase of the horizontally polarized and vertically polarized components of the wave backscattered in response to each transmitted polarization. The technique is described in [20].

From the measured Mueller matrix, we can compute the backscattering coefficient for any combination of transmit and receive antenna polarizations, as well as the degree of polarization  $m$ :

$$m = \frac{\text{polarized power}}{\text{total power}} \quad (6)$$

where total power includes both the polarized and unpolarized components of the scattered energy. The degree of polarization represents the average fraction of the backscattered power that maintains coherence between the  $h$  and  $v$  polarized components. If the scattered wave is perfectly polarized, as is the case with scattering from any point target, then  $m = 1$ . For a perfectly unpolarized wave,  $m = 0$ .

An experiment was conducted in February, 1991 to examine the response of  $m$  to the liquid water content  $m_w$  and the snow surface roughness. Figures 6-8 show plots of the vv and hv backscattering coefficients, the liquid water content  $m_w$ , and the degree of polarization  $m$ , all as a function of time over a 16-hour period, for three snow surface roughness conditions. The accuracy of the liquid-water-content measurements is about  $\pm 0.5\%$ . Although the overall diurnal response of the backscattering coefficient is driven by the liquid water content of the surface layer,  $\sigma^0$  appears to lead  $m_w$  during the melting cycle, which is attributed to changes in  $m_w$  in the very surface layer that are not detectable by the freezing colorimeter (which measures  $m_w$  of the top 5-cm layer), and it lags  $m_w$  during the freezing cycle, which is attributed to the presence of liquid water in layers deeper than the 5-cm surface layer. The overall response of  $\sigma^0$  is approximately the same for all three surface roughness conditions.

The degree of polarization increases with increasing  $m_w$ , indicative of less multiple scattering, which is consistent with theoretical expectations. Two plots are shown for the degree of polarization, one corresponding to a vertically polarized transmitted wave, and the other for a circularly polarized transmitted wave (right-hand circular polarization and left-hand circular polarization gave approximately identical responses). For dry snow, the smooth surface data of Fig. 6 shows the lowest values for the degree of polarization. As the surface gets rougher (Figs. 7 and 8), the degree of polarization of dry snow increases because the backscatter has comparable contributions from the snow surface and volume. Although the degree of polarization is a good indicator of liquid water in the snow, its relative sensitivity is not as large as that exhibited by the backscattering coefficient.

The results of an interesting experiment that was conducted in March, 1991 are shown in Fig. 9. The highest daytime temperature was below  $-3^\circ\text{C}$ , and the freezing calorimeter did not detect the presence of any liquid water over the entire experiment duration. Yet, the backscattering coefficient exhibited a change of 8 dB for vv polarization and 10 dB for hv polarization. This change is attributed to the presence of liquid water in the very surface layer, generated in response to solar illumination. This behavior is indicative of the strong sensitivity of radar to liquid water content, suggesting that a millimeter-wave radar is perhaps a much more sensitive indicator of the presence of liquid water in snow than available *in-situ* devices.

## 6 CONCLUDING REMARKS

The radiative transfer model with the quasi-crystalline approximation, together with the hybrid first-order numerical solution, provide an excellent tool for examining the radar response of snow at millimeter wavelengths. This conclusion is supported by comparisons of theoretical predictions with experimental observations made at 35, 95, and 140 GHz.

The degree of polarization provided by polarimetric observations exhibits a dependence on liquid water content and snow surface roughness, but its relative sensitivity to liquid water content is not as great as that exhibited by the backscattering coefficient  $\sigma^0$ , particularly for hv polarization.

## REFERENCES

- [1] Stiles, W. H., and F. T. Ulaby, The active and passive microwave response to snow parameters: Part I: Wetness, *J. Geophys. Res.*, 85, 1037-1044, 1980.
- [2] Ulaby, and F. T., W. H. Stiles, The Active and Passive Microwave Response to Snow Parameters, Part II: Water Equivalent of Dry Snow, *J. Geophys. Res.*, 85, 1045-1049, 1980.
- [3] Hayes, D. T., U. H. W. Lammers, and R. A. Marr, Scattering from snow backgrounds at 35, 98, and 140 GHz, RADX-TR-84-69, Rome Air Development Center Report, 1984.

- [4] Hallikainen, M., F. T. Ulaby, M. Abdelrazik, Dielectric properties of snow in the 3 to 37 GHz range, *IEEE Trans. Antennas and Propagation*, 34, 1329-1340, 1986.
- [5] Baars, and E. P., H. Essen, Millimeter-wave backscatter measurements on snow-covered terrain, *IEEE Trans. Geoscience and Remote Sensing*, 26, 282-299, May 1988.
- [6] Williams, L. D., J. G. Gallagher, D. E. Sugden, and R. V. Birnie, Surface snow properties effects on millimeter-wave backscatter, *IEEE Trans. Geoscience and Remote Sensing*, 26, 300-306, May 1988.
- [7] Ulaby, F.T., T.F. Haddock, and R.J. Austin, Fluctuation Statistics of Millimeter-Wave Scattering From Distributed Targets, *IEEE Trans. on Geoscience and Remote Sensing*, 26, 268-281, 1988.
- [8] Currie, N. C., J. D. Echard, M. J. Gary, A. H. Green, T. L. Lane, and J. M. Trostel, Millimeter-wave measurements and analysis of snow-covered ground, *IEEE Trans. Geoscience and Remote Sensing*, 26, 307-318, 1988.
- [9] Narayanan, R.M., and R.E. McIntosh, Millimeter-Wave Backscatter Characteristics of Multilayered Snow Surfaces, *IEEE Trans. on Antennas and Propagation*, 38, 693-703, 1990.
- [10] Ulaby, F. T., R. K. Moore, and A. K. Fung, *Microwave Remote Sensing*, Vol. III, Artech House, 1986, p. 1608.
- [11] Hallikainen, M., F. T. Ulaby, and M. Abdelrazik, Dielectric properties of snow in the 3 to 37 GHz range, *IEEE Trans. Antennas and Propagation*, 34, 1329-1340, 1986.
- [12] Tsang, L. J., A. Kong, and R. T. Shin, *Theory of Microwave Remote Sensing*, Wiley, New York, 1985, pp. 461-469.
- [13] Mätzler, and C., U. Wegmüller, Dielectric properties of fresh water ice at microwave frequencies, *J. Phy. D: Applied Physics*, 20, 623-630, 1987.
- [14] Ishimaru, A., and Y. Kuga, Attenuation constant of coherent field in a dense distribution of particles, *J. Opt. Soc. Am.*, 72, 1317-1320, 1982.
- [15] Tsang, L., and A. Ishimaru, Radiative wave equations for vector electromagnetic propagation in dense nontenuous media, *J. of Electromagnetic Waves and Applications*, 1, 52-72, 1987.
- [16] Kuga, Y., F.J. Ulaby, T.F. Haddock, and R. DeRoo, "Millimeter-Wave Radar Scattering from Snow: Part I - Radiative Transfer Model," *Radio Science*, 1991.
- [17] Ulaby, F.T., T.F. Haddock, J.R. East, and M.W. Whitt, A millimeterwave network analyzer based scatterometer, *IEEE Transactions on Geoscience and Remote Sensing*, 26, 75-81, 1988.
- [18] Haddock, T.F., and F.T. Ulaby, 140-GHz scatterometer system and measurements of terrain, *IEEE Transactions on Geoscience and Remote Sensing*, 28, 492-499, 1990.
- [19] Ulaby, F.T., R. Austin, T. Haddock, Y. Kuga, Millimeter-Wave Radar Scattering from Snow: Part II - Comparison of Theory with Experiment, *Radio Science*, 1991.
- [20] Kuga Y., K. Sarabandi, A. Nashashibi, and F.T. Ulaby, "Millimeter-Wave Polarimetric Scatterometer Systems: Measurements and Calibration Techniques," AGARD Symposium, Ottawa, Canada, 6-10 May, 1991.

$$35 \text{ GHz } \epsilon_{ice} = 3.15 + i0.003, \sigma_t = 1.2 \times 10^{-8}, \sigma_a = 5 \times 10^{-10}, \kappa_e(EFA) = 8.24 \text{ m}^{-1}$$

$m_v$ (%)	$\epsilon_b$		$\kappa_{ag}(\text{m}^{-1})$	$K(QCA)$		$\text{Re}[n(QCA)]$	$\kappa_e(QCA), \text{m}^{-1}$
	Real	Imag.		Real	Imag.		
0	1	0	0	930	0.269	1.268	0.538
1	1.0427	0.0129	5.56	942	0.267	1.285	0.534
2	1.104	0.0532	22.2	958	0.264	1.307	0.528
3	1.1776	0.0869	35.2	977	0.262	1.332	0.524
4	1.2405	0.1268	50.0	992	0.259	1.353	0.518
5	1.3046	0.1723	66.2	1007	0.257	1.373	0.514

$$95 \text{ GHz } \epsilon_{ice} = 3.15 + i0.0085, \sigma_t = 5.89 \times 10^{-7}, \sigma_a = 4.28 \times 10^{-9}, \kappa_e(EFA) = 402 \text{ m}^{-1}$$

$m_v$ (%)	$\epsilon_b$		$\kappa_{ag}(\text{m}^{-1})$	$K(QCA)$		$\text{Re}[n(QCA)]$	$\kappa_e(QCA), \text{m}^{-1}$
	Real	Imag.		Real	Imag.		
0	1	0	0	2562	11.35	1.2884	22.69
1	1.0296	0.0138	16.2	2582	10.91	1.298	21.82
2	1.0626	0.0397	45.9	2604	10.43	1.3095	20.86
3	1.1055	0.0697	78.7	2632	9.84	1.323	19.68
4	1.141	0.0961	107.2	2654	9.39	1.335	18.78
5	1.1765	0.1244	136.6	2676	8.95	1.346	17.9

$$140 \text{ GHz } \epsilon_{ice} = 3.15 + i0.012, \sigma_t = 1.95 \times 10^{-6}, \sigma_a = 2.33 \times 10^{-8}, \kappa_e(EFA) = 1331 \text{ m}^{-1}$$

$m_v$ (%)	$\epsilon_b$		$\kappa_{ag}(\text{m}^{-1})$	$K(QCA)$		$\text{Re}[n(QCA)]$	$\kappa_e(QCA), \text{m}^{-1}$
	Real	Imag.		Real	Imag.		
0	1	0	0	3876	56.58	1.32	113.15
1	1.0254	0.0115	20	3891	54.95	1.326	109.9
2	1.0534	0.0307	52.67	3909	53.94	1.331	107.9
3	1.0883	0.0540	91.15	3933	53.36	1.339	106.7
4	1.1181	0.0741	123.38	3955	53.2	1.347	106.4
5	1.1482	0.0953	156.54	3977	53.1	1.354	106.3

$m_v$ : liquid water content by volume,  $\epsilon_b$ : background dielectric constant,  $\kappa_{ag}$ : background absorption coefficient,  $K(QCA)$ : propagation constant in the snow layer obtained by QCA,  $\text{Re}[n(QCA)]$ : real part of the effective index of refraction obtained by QCA,  $\kappa_e(QCA)$ : extinction coefficient of ice particles obtained by QCA,  $\kappa_e(EFA)$ : extinction coefficient of ice particles obtained by EFA,  $\sigma_t$  and  $\sigma_a$ : total and absorption cross-sections of ice particles obtained by EFA.

Table 1. Dielectric and propagation properties of a snow medium with ice volume fraction  $f = 0.4$ , average ice particle diameter of 1 mm, and number density  $N = 7.64 \times 10^8$ .

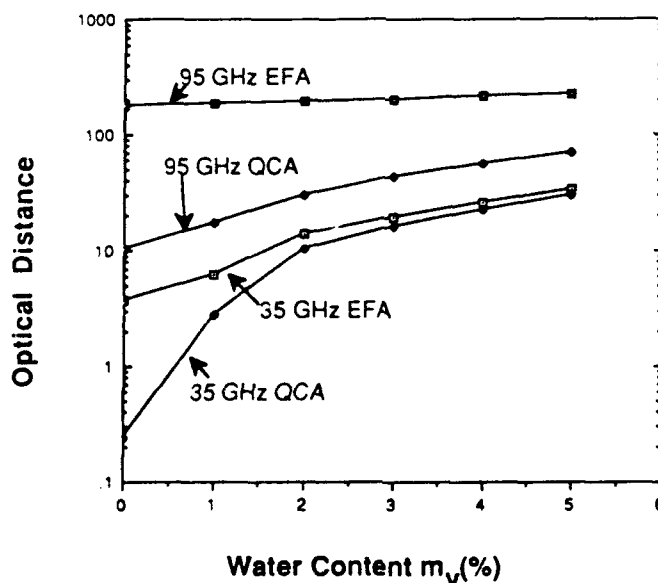


Figure 1. Optical distance  $\tau$  versus liquid water content  $m_v$  at 35 and 95 GHz. Snow depth is 0.45 m, the ice volume fraction is 0.4, and average ice particle diameter is 1mm. EFA is the effective field approximation and QCA is the quasi-crystalline approximation.

FREQUENCIES:	35, 94, 140 GHz		
IF BANDWIDTH:	0 to 2.0 GHz		
TRANSMIT POWER:	35 GHz:	+3 dBm	
	94 GHz:	0 dBm	
	140 GHz:	-4 dBm	
SWEEP RATE:	1 m-sec/freq., 51, 101, 201, 401 freq./sweep		
POLARIZATION:	HH, HV, VV, VH		
INCIDENCE ANGLES:	0 to 70 degrees		
PLATFORM HEIGHT:	3 meters minimum, to 18 meters maximum		
NOISE EQUIV. $\sigma^\circ$ :	35 GHz:	-22 dB	
	94 GHz:	-28 dB	
	140 GHz:	-21 dB	
CROSSPOL ISOLATION:	35 GHz:	23 dB	
	94 GHz:	20 dB	
	140 GHz:	10 dB	
PHASE STABILITY:	35 GHz:	~1 degree/hour	
	94 GHz:	~1 degree/minute	
	140 GHz:	~10 to 50 degrees/second	
NEAR FIELD DIST:	35 GHz:	2.7 m	
	94 GHz:	7.3 m	
	140 GHz:	2.7 m	
BEAMWIDTH:	35 GHz:	R: 4.2 deg	T: 4.2 deg
	94 GHz:	R: 1.4 deg	T: 2.8 deg
	140 GHz:	R: 2.2 deg	T: 11.8 deg
ANTENNA DIAMETER:	35 GHz:	R: 6 inches	T: 6 inches
	94 GHz:	R: 6 inches	T: 3 inches
	140 GHz:	R: 3 inches	T: 0.36 inches
SIGNAL PROCESSING:	HP 8510A/8511A based		
OUTPUT PRODUCTS:	-received power verses range -received power verses frequency (at fixed R) -phase and amplitude for each frequency		

Table 2 Millimeter wave Polarimeter system parameters

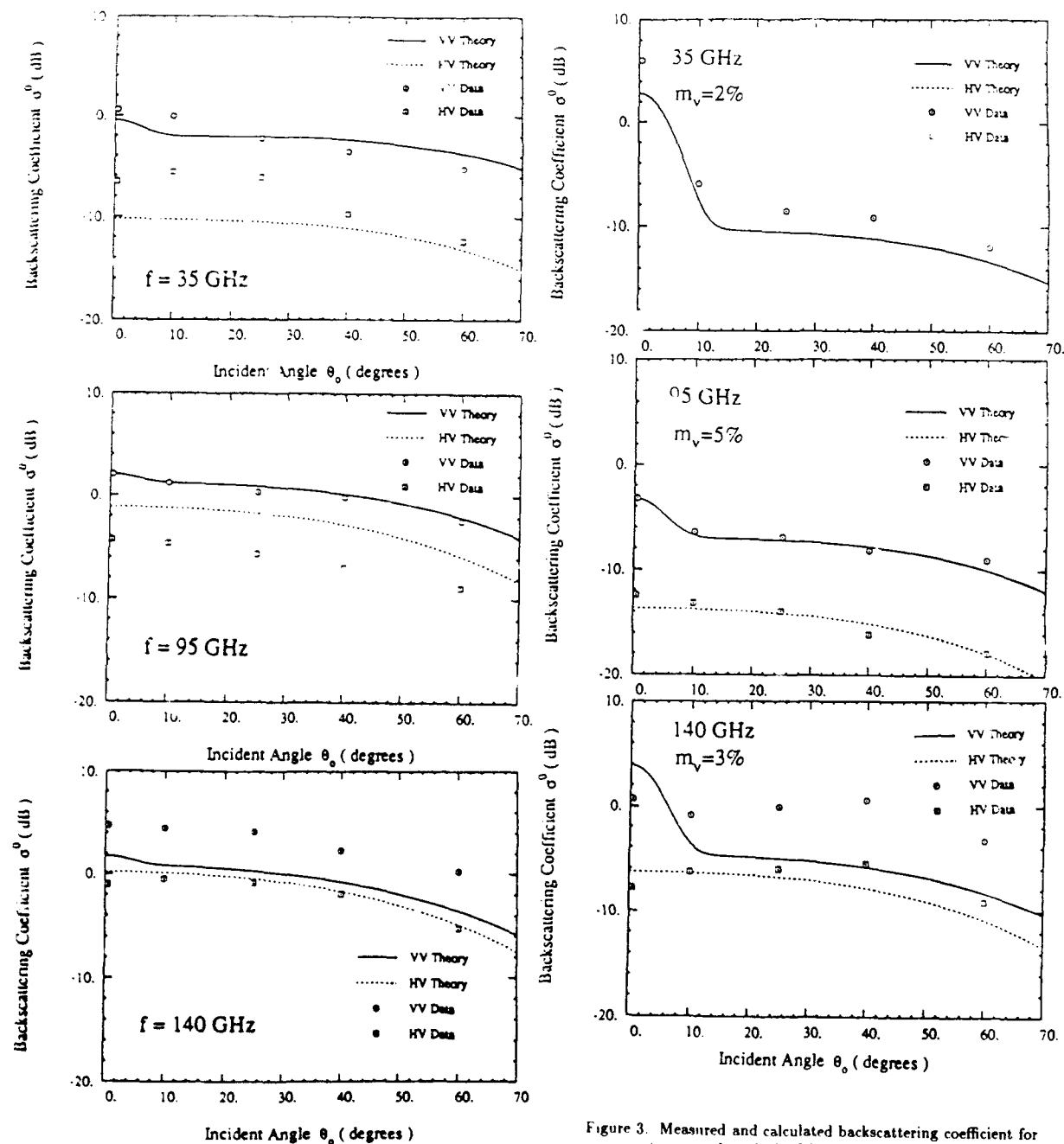


Figure 2. Measured and calculated backscattering coefficient for a dry snowpack with the following parameters: depth = 12 cm, snow density =  $0.2 \text{ g/cm}^3$ , mean crystal diameter = 1 mm, and rms surface slope = 0.07.

Figure 3. Measured and calculated backscattering coefficient for a wet snowpack with the following parameters: depth = 27 cm, snow density =  $0.4 \text{ g/cm}^3$ , mean crystal diameter = 1 mm, rms surface slope = 0.07.



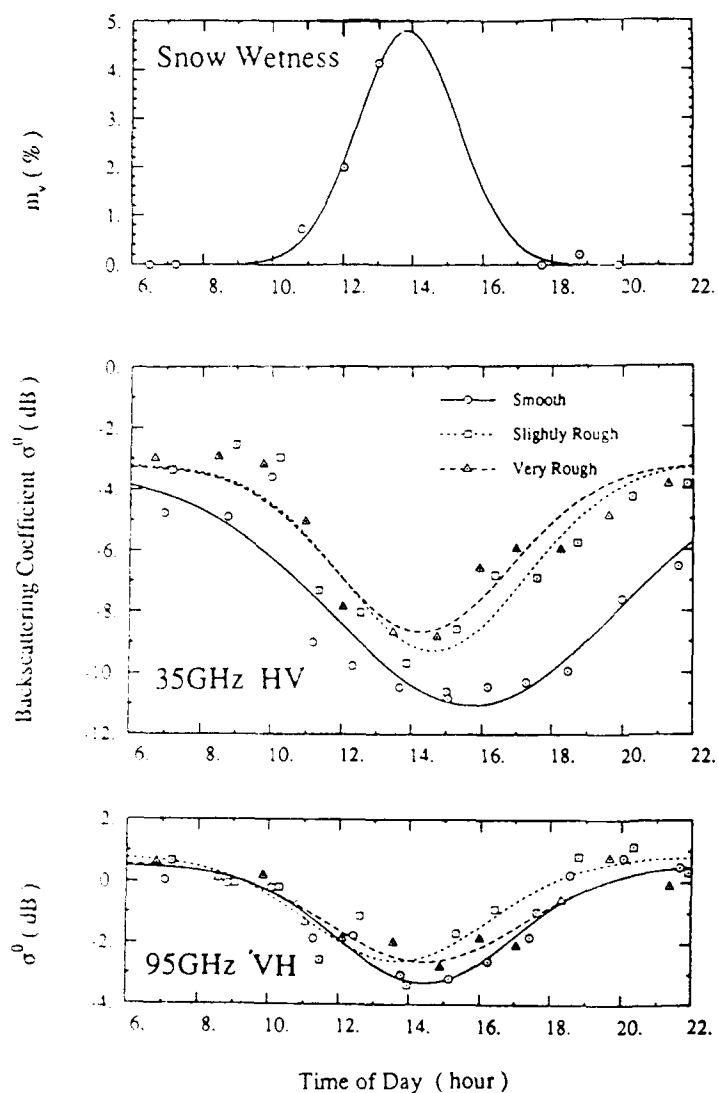


Figure 4. Observed diurnal variation of  $m_v$ , the liquid water content of the top 5-cm layer, and  $\sigma^0$  at 35 and 95 GHz for cross polarization. The snowpack was 28-cm deep, had a mean crystal diameter of 0.6 mm, and a density of 0.4 g/cm<sup>3</sup>. The measured rms heights of the surfaces were:  $s_1 = 0.49$  cm (smooth),  $s_2 = 0.89$  cm (slightly rough), and  $s_3 = 1.98$  cm (very rough).

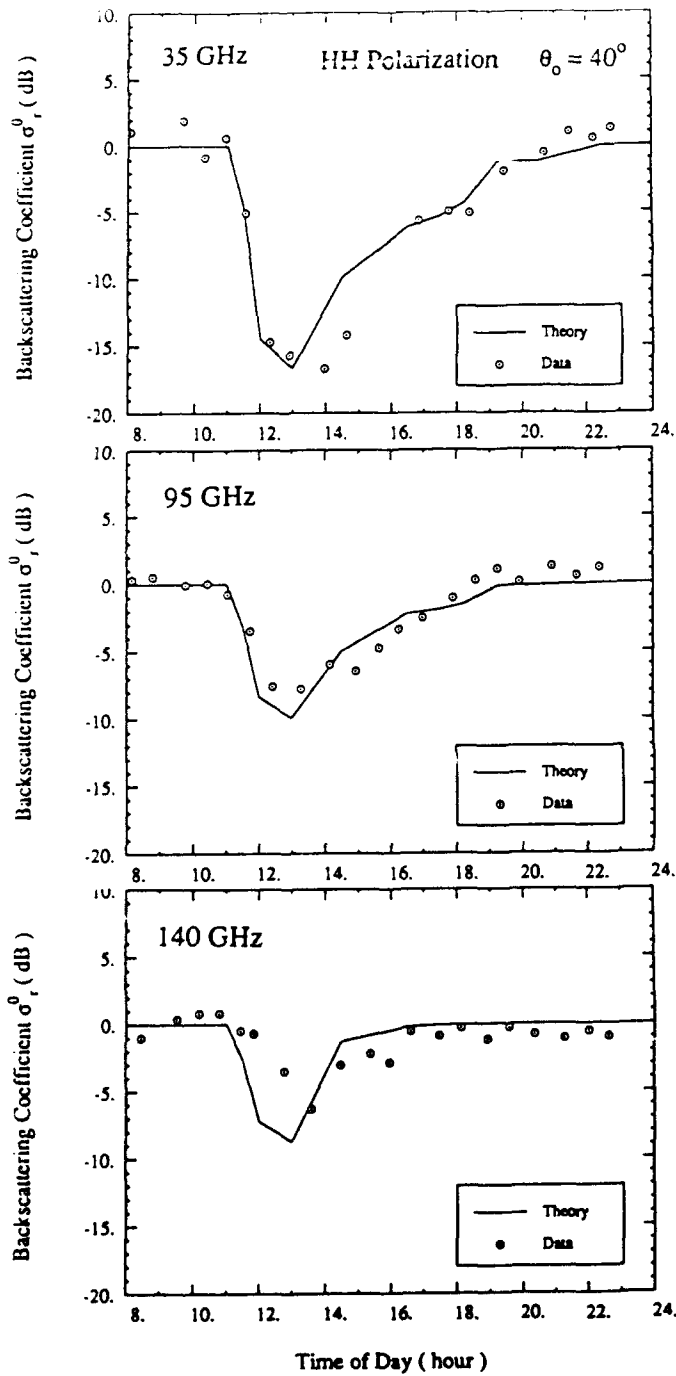


Figure 5. Comparison of the diurnal variation of the measured backscattering coefficient (relative to dry snow) with that using the hybrid first-order numerical model.

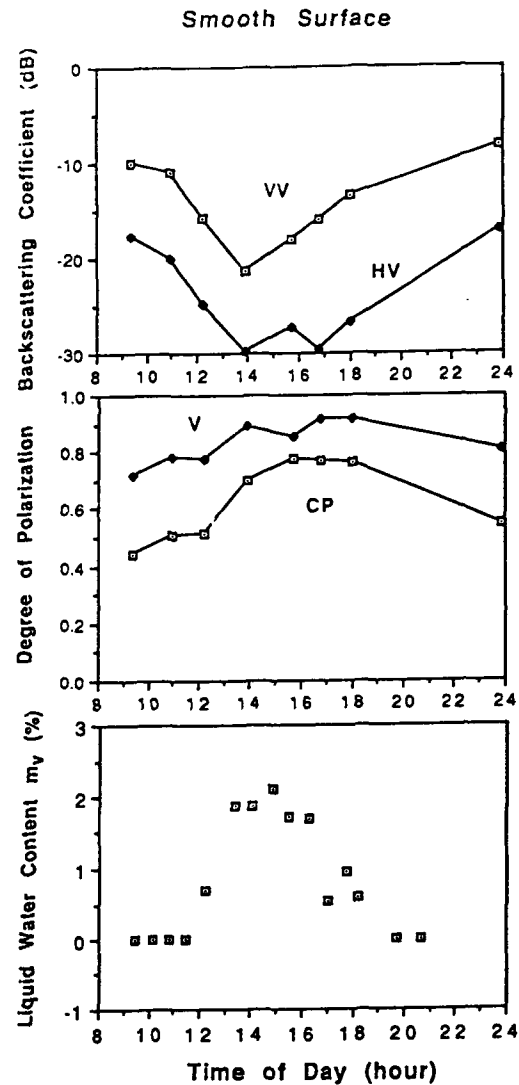


Figure 6. Diurnal response of snow at 35 GHz measured in Ann Arbor, MI in Feb. 1991. The surface is smooth with *rms* height of 0.7 mm. The snow characteristics: new snow, depth = 13cm, crystal shape = 1mm long needle, snow density = 0.27.

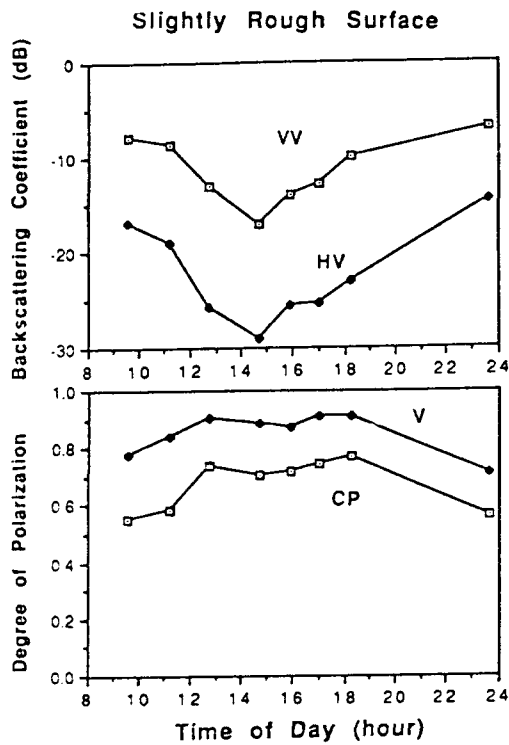


Figure 7. The surface is slightly rough with *rms* height of 3.64 mm. The snow characteristics are the same as those listed in Fig. 6

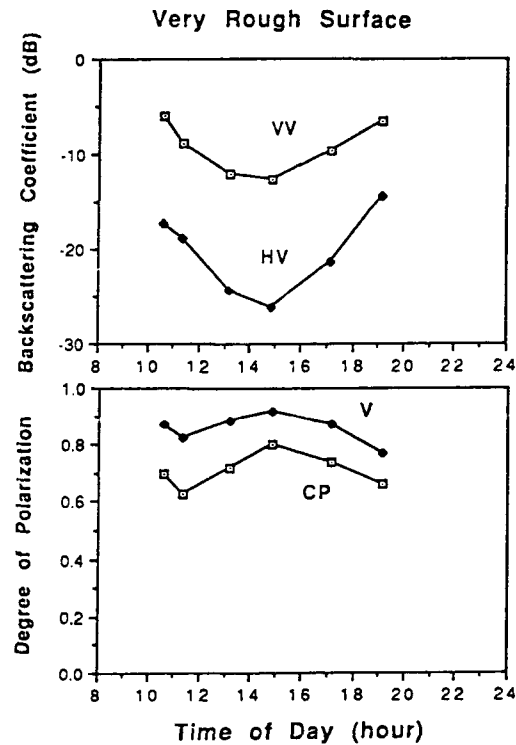


Figure 8. The surface is very rough with *rms* height of 18.6 mm. The snow characteristics are the same as those listed in Fig. 6.

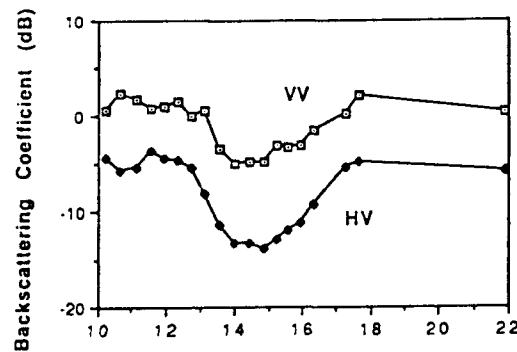


Figure 9. Diurnal response of snow at 35 GHz measured in Pellston, MI in March 1991. The surface is smooth with *rms* height is 1 mm. Snow characteristics: metamorphic snow, snow depth is 10 cm and 10 cm of ice below it, crystal size - 0.5 mm diameter, snow density = 0.34. Air temperature was below -3°C throughout the measurement period.

## **DISCUSSION**

**U. Lammers (US) :**

How did you roughen the snow surface artificially for the 35 GHz measurements ?

Also, to what accuracy could you measure liquid water content of snow as a function of depth ?

**Author's reply :**

The snow surface was roughened with a rake. We could not measure liquid water content as a function of depth. Our liquid water measurements are very laborious, requiring 30 minutes for a single measurement. We kept two people busy doing nothing but liquid water content measurements continuously. Each measurement used a snow sample from the entire top 5 cm. We would very much like to be able to measure liquid water with depth.

The moisture profiles shown were based on a model of the snowpack melting from the top then refreezing from the top. They were numerically constrained, so that the average moisture in the top 5 cm was equal to the measured value at that time.

**H. Schimpf (GE) :**

Do you have a physical explanation for the relation between "degree of polarization" and the diurnal variation of  $\sigma_0$  and liquid water content ?

**Author's reply :**

Yes, as liquid water content during the course of the day varies generally, the more liquid water, the more surface reflexion and a higher degree of polarization.

**J. Mead (US) :**

Was the degree of polarization for backscatter from snow found to vary with frequency ?

**Author's reply :**

Only the 35 GHz data has been processed at present.

# ANALYTICAL PREDICTION OF EM SCATTERING BY COMPLEX OBSTACLES WITHIN ELECTRICALLY LARGE OPEN CAVITIES

P.H. Pathak

The Ohio State University ElectroScience Laboratory  
1320 Kinnear Road, Columbus, Ohio 43212, U.S.A.

## I. INTRODUCTION

The object of this paper is to describe an analytical technique for predicting the electromagnetic (EM) scattering by complex obstacles within electrically large open waveguide cavities. This topic is of relevance to EM scattering and EMC type applications. Figure 1(a) illustrates a general open-ended cavity configuration of interest in the present work. The fully three dimensional open waveguide cavity in Figure 1(a) is assumed to be relatively arbitrarily shaped, and the open front end of the cavity is illuminated by an arbitrarily polarized external plane wave field. The interior obstacle is assumed to be located within the cavity near the back end, and it generally contributes significantly to the fields scattered into the exterior by the entire cavity configuration. The scattering from the external features of the cavity, excluding the scattering from just the rim at the open front end, is not of interest in the present analysis. Hence, the present scattering analysis is restricted to within approximately  $70^\circ$  from boresight with respect to the open front end; outside of this region, the scattering by the external features of the cavity are generally more significant than from the interior of the cavity. It is also assumed in the present work that the incident wave always directly illuminates the open front end.

The present scattering analysis is composed of two main parts. The first part, deals with the analysis of the coupling of the incident plane wave field, via the open front end, into the arbitrarily shaped waveguide cavity using the high frequency ray or beam shooting methods as discussed in [2]-[9]. Also, the scattering of the incident wave back into the exterior region by the rim at the open end is included in this part of the analysis. It is assumed that the rays (or beams) launched into the cavity interior from the open front end propagate to the plane  $S_T$  (shown in Fig. 1) chosen conveniently near the obstacle, but with the obstacle removed and with the back end of the waveguide cavity extended to infinity as shown in Fig. 1(b). Only the ray shooting procedure for evaluating the interior cavity fields at  $S_T$  is discussed here. A corresponding Gaussian beam shooting procedure can also be employed as mentioned above; however, it is not discussed here for the sake of brevity, but it may be found in [2,8,9,10]. Actually, two different ray shooting procedures, namely the shooting and bouncing ray (SBR) method [2,3,4] as well as the generalised ray expansion (GRE) approach [9,10], will be described. After being launched from the open front end, the rays evolve within the cavity via the rules of geometrical optics; thus, the rays undergo multiple reflections at the interior walls of the waveguide cavity which are assumed to be impenetrable. For the sake of being specific, the interior waveguide cavity walls and the rim at the open front end are taken to be

perfectly-conducting. It is further assumed that the interior diffracted fields are negligible in comparison to the internal multiply reflected geometrical optics ray fields, so that the geometrical optics ray approach remains accurate. It is noted, of course, that modes cannot be defined in the usual sense for an arbitrarily shaped (non-separable) waveguide cavity geometry; therefore, this is one of the main reasons for the choice of asymptotic high frequency ray (or beam) procedures for performing the present coupling analysis. The numerical solution techniques such as those based on the integral equation or the finite element (or difference) formulations are expected to be extremely cumbersome and inefficient as compared to the ray (or beam) techniques for computing the fields coupled into an electrically large waveguide cavity. For later purposes, when combining the results of the first and second steps so as to find the external EM scattering arising from the interior obstacle, it is also necessary to break the problem configuration at  $S_T$  into two separate parts as shown in Figs. 1(c) and (d). The field coupled into the cavity via the open front end, as discussed above, is then allowed to radiate from the cavity which is now assumed to be suddenly terminated at  $S_T$  as in Fig. 1(c) and made to exist without the portion of the cavity containing the obstacle. The field radiated from the resulting open end at  $S_T$  is found by using the unperturbed field arriving there (i.e., by using the field at  $S_T$  as if the cavity was not abruptly truncated at  $S_T$  as in Fig. 1(b)) to constitute the equivalent sources of the radiated field in Fig. 1(c). This then essentially constitutes the first part of the analysis.

The second part of the analysis deals with separately obtaining the plane wave scattering characteristics of the interior obstacle. The part of the waveguide cavity structure beyond  $S_T$  which contains the obstacle is now assumed to be separated from the rest of the structure, as in Fig. 1(d); next, this configuration of Fig. 1(d) is illuminated in its forward region by a discrete but sufficiently large number of incident plane waves from different directions. The field scattered from the obstacle section of the cavity beyond  $S_T$  (in Fig. 1(d)) in sufficiently large number of discrete directions, again in the forward half space of this section, then provides the relevant plane wave scattering matrix.

The final step involves combining the results of the two main steps described above, through a reciprocity integral, to provide the field scattered into the exterior by the interior obstacle within the original entire waveguide cavity configuration of Fig. 1(a).

Thus, the present analysis represents a hybrid combination of an asymptotic high frequency ray/beam method for tracking the fields through the cavity as in the first part, together with any suitable method for obtaining a plane wave characterisation of the interior

obstacle as in the second part. The advantage of dealing with the analysis in two parts is that it allows one to separately estimate the effect on the overall scattering as the waveguide cavity geometry is changed for a given interior obstacle, and as the interior obstacle is changed for a given waveguide cavity geometry, without having to analyze the complete problem each time this happens.

The two parts of this analysis as well as their hybrid combination is summarized briefly next in Section II. Finally, some numerical results indicating the utility of the present hybrid analysis are presented in Section III.

## II. BRIEF SUMMARY OF THE ANALYTICAL STEPS

In Section I, a general introduction to the approach for analyzing the electromagnetic scattering from electrically large, open ended cavities containing an interior obstacle (Fig. 1(a)) was presented. The various steps involved in this approach are briefly summarized below.

The major contribution to the total field scattered into the exterior, within the range of angles of incidence and scattering of interest here, is due to the field scattered directly by the rim at the open front end, the field scattered by the interior obstacle, and the part of the field scattered from the interior cavity region which turns around without reaching the interior obstacle. The remaining contribution arising from the rest of the external features of the cavity are ignored for reasons indicated earlier in Section I, and the contribution resulting from all the multiple wave interactions is also ignored in this analysis. The multiple wave interactions across the aperture contribute weakly if the aperture is sufficiently large electrically, and the multiple wave interactions between the obstacle and the open end are likewise negligible for an electrically large aperture and obstacle; it is assumed that such conditions are true in the present analysis. It is also assumed that the waveguide cavity is perfectly-conducting, and that the medium surrounding this cavity configuration of Fig. 1(a) is free space. Finally, the illumination of the cavity in Fig. 1(a) is assumed to be an EM plane wave which is incident from an arbitrary direction.

The contribution to the external scattered field arising from just the rim at the open end can generally be found by employing the geometrical theory of diffraction [1] used in conjunction with the equivalent current method [11].

The contribution to the external scattering arising from the interior obstacle is found in two parts as indicated in Section I. The first part requires one to track the portion of the incident field which is coupled into the cavity via the open front end using a high frequency ray or beam shooting technique. The ray technique is chosen in this analysis as mentioned earlier. At least two different ray shooting approaches are possible for tracking the fields from the open front end to the plane  $S_T$  in the absence of the obstacle as in the configuration of Fig. 1(b). The two different ray shooting approaches are referred to as the shooting and bouncing ray (SBR) method [2,3,4], and the generalized ray expansion (GRE) [9,10]. The SBR method requires one to break up the part of the incident wave captured by the open front end into a dense grid of ray tubes

which are launched within the cavity. These incident ray tubes reflect from the cavity walls according to the rules of geometrical optics (GO) as they propagate into the cavity; this is illustrated in Fig. 2. On the other hand, the GRE requires the aperture at the open front end to be discretized (into subapertures) as shown in Fig. 3, and then the rays are launched radially from the phase centers of each subaperture. The initial launching amplitudes of the GRE rays are weighted by the subaperture far field pattern with the waveguide cavity walls absent. Once launched, the GRE rays propagate within the cavity via reflections at the interior cavity walls as in the SBR case; this is seen in Fig. 3. It is noted that the ray paths in the GRE method are unchanged for a given waveguide cavity geometry; only the initial ray launching amplitudes depend on the direction of the incident plane wave. Furthermore, the GRE implicitly includes the effects of rays entering the cavity via diffraction of the incident wave by the edges at the open front end.

Let  $(\vec{E}^g, \vec{H}^g)$  denote the electromagnetic fields coupled into the cavity as shown in Fig. 1(b). For the case of bistatic scattering, a similar set of fields  $(\vec{E}_t^g, \vec{H}_t^g)$  need to be tracked within the cavity of Fig. 1(b); these fields are launched into the cavity by a plane wave incident in a direction reciprocal to the bistatic scattering direction of interest. If GRE is employed, no new rays need to be tracked to find  $(\vec{E}_t^g, \vec{H}_t^g)$  for reasons given above and hence only the initial ray launching amplitudes are different for computing  $(\vec{E}_t^g, \vec{H}_t^g)$  than they are for computing  $(\vec{E}^g, \vec{H}^g)$ .

Next, the unperturbed fields  $(\vec{E}^g, \vec{H}^g)$  of Fig. 1(b) are allowed to radiate from  $S_T$  if the section of the cavity beyond  $S_T$  containing the obstacle is removed as in Fig. 1(c); this radiation field, which is required essentially in the forward half space of  $S_T$  in Fig. 1(c), is found via a Kirchhoff approximation which is accurate for an electrically large aperture  $S_T$ . This essentially completes all of the computations necessary for the first step.

In the second step, it is necessary to find the fields  $(\vec{E}^{sg}, \vec{H}^{sg})$  which are scattered by the interior obstacle to the plane  $S_T$  in Fig. 1(a) when the unperturbed fields  $(\vec{E}^g, \vec{H}^g)$  are incident on the obstacle. In this step,  $(\vec{E}^{sg}, \vec{H}^{sg})$  are found approximately but quite accurately as follows. A discrete, but sufficiently dense, set of unit amplitude plane wave fields are made to illuminate the forward half space of the isolated section of the cavity beyond  $S_T$  which contains the obstacle as in Fig. 1(d). The field scattered by the obstacle-cavity section of Fig. 1(d), when it is illuminated by each of the unit amplitude incident plane waves, is found by using analytical methods, or by numerical methods if the obstacle is too complex to be treated analytically. In particular, the fields in the aperture  $S_T$  of Fig. 1(d) are of interest. If these cannot be found directly via the analytical or numerical methods mentioned above, they can still be found indirectly by these methods which do provide the fields scattered in all bistatic directions for each unit amplitude incident plane wave. Indeed, if these fields scattered in bistatic directions are sampled at a discrete but sufficiently dense number of aspects, then a spectral inversion (from aspect angle to the spatial domain) of these values via a fast Fourier

transform (FFT) provides the fields at  $S_T$  in Fig. 1(d). This information is then stored for each unit amplitude incident plane wave thereby essentially completing the computations necessary for the second step.

Finally, the results of the first and second steps discussed above are combined to provide a hybrid solution for the fields scattered into the exterior by the obstacle within the original cavity configuration of Fig. 1(a). In this combination, one modifies the results of the second step by weighting the unit amplitude incident plane waves therein by the radiation pattern of the fields which are radiated from  $S_T$  by  $(\bar{E}^{sg}, \bar{H}^{sg})$  in Fig. 1(c), corresponding to the final part of the first step. This then directly furnishes the fields in the aperture  $S_T$  which are scattered by the portion of the cavity containing the obstacle as in Fig. 1(d). To a very good approximation, these fields at  $S_T$  in Fig. 1(d) are the same as  $(\bar{E}^{sg}, \bar{H}^{sg})$  at  $S_T$  in the original configuration of Fig. 1(a). The electric field  $\bar{E}_o$  which is scattered into the exterior by the interior obstacle in Fig. 1(a) is then given approximately, but accurately by the generalized reciprocity integral [2,9,10]; namely,

$$\hat{u} \cdot \bar{E}_o \approx \int \int_{S_T} (\bar{E}_t^{sg} \times \bar{H}_t^{sg} - \bar{E}_t^{sg} \times \bar{H}_t^{sg}) \cdot d\bar{s} \quad (1)$$

It is noted that  $(\bar{E}_t^{sg}, \bar{H}_t^{sg})$  are the fields coupled into the cavity with the interior obstacle absent (see Fig. 1(b)) when a  $(-\hat{u})$ -polarized plane wave is incident at the open front end.

Finally, the contribution to the external scattering due to waves coupled into the cavity which then turn around without reaching the obstacle is found by tracking the associated ray tubes by SBR or GRE back to the open front end where they are made to define equivalent sources. Incorporating these equivalent sources into the radiation integral thus provides the necessary fields.

### III. NUMERICAL RESULTS

Figure 4 illustrates the echo area patterns (backscatter, in decibels relative to a square wavelength) of an open ended semi-infinite waveguide cavity with a rectangular open end transitioning to an elliptical cross section. A planar short circuit is placed as an obstacle inside the cavity where its cross-section becomes elliptic. The echo area is calculated using both the SBR and the GRE approaches, respectively. These two ray approaches compare reasonably well with each other. Figure 5 illustrates the backscatter patterns of a perfectly conducting circular waveguide containing a conical obstacle placed on a planar interior termination. The solid line in these plots is a measured result for the complete geometry of length  $L + L_1$ . The dashed line is calculated using the two step hybrid procedure discussed above, however it assumes that the external portion of the cavity is not rounded as for the measured case but is semi-infinite in the present two step procedure. Both of these approaches show close agreement. Since the circular waveguide modes are known, a modal representation is employed for describing the interior waveguide cavity fields instead of the SBR or GRE representations. The short obstacle section of length  $L$  was analyzed via the numerical moment method (corresponding to the second step)

while the front section of length  $L$ , corresponding to the first step was analyzed by the modal procedure in conjunction with the Kirchhoff approximation for the fields in the aperture at the open front end to find the fields coupled into the circular waveguide.

### REFERENCES

- [1] J.B. Keller, Geometrical theory of diffraction, *Journal Opt. Soc. Am.*, 52:116-130 (1962).
- [2] P.H. Pathak and R.J. Burkholder, "Modal, Ray and Beam Techniques for Analyzing the EM Scattering by Open-Ended Waveguide Cavities," *IEEE Trans. Antennas Prop.*, Vo. AP-37, No. 5, pp. 635-647, May 1989.
- [3] S.W. Lee, H. Ling and R-C. Chou, "Ray-Tube Integration in Shooting and Bouncing Ray Method," *Microwave and Optical Tech. Letters*, Vol. 1, No. 8, October 1988.
- [4] H. Ling, R-C. Chou and S.W. Lee, "Shooting and Bouncing Rays: Calculating the RCS of an Arbitrary Cavity," *IEEE Trans. Antennas and Prop.*, Vol. AP-37, No. 2, pp. 194-205, February 1989.
- [5] H. Shirai and L.B. Felsen, "Rays, Modes and Beams for Plane Wave Coupling into a Wide Open-Ended Parallel-Plane Waveguide," *Wave Motion*, 9, pp. 301-317, 1987.
- [6] H. Shirai and L.B. Felsen, "Rays and Modes for Plane Wave Coupling into a Large Open-Ended Circular Waveguide," *Wave Motion*, 9, pp. 461-482, 1987.
- [7] J. Maciel and L.B. Felsen, "Systematic Study of Fields Due to Extended Apertures by Gaussian Beam Discretization," *IEEE Trans. Antennas and Prop.*, Vol. AP-37, No. 7, pp. 884-892, July 1989.
- [8] J. Maciel and L.B. Felsen, "Gaussian Beam Analysis of Propagation from an Extended Plane Aperture Distribution Through Dielectric Layers, Part I — Plane Layer, Part II — Circular Cylindrical Layer," *IEEE Trans. Antennas and Prop.*, Vol. AP-38, No. 10, pp. 1607-1624, October 1990.
- [9] P.H. Pathak and R.J. Burkholder, "High Frequency EM Scattering by Open-Ended Waveguide Cavities," *J. Radio Science*, Vol. 26, No. 1, pp. 211-218, January-February 1991.
- [10] P.H. Pathak, P.H. Law and R.J. Burkholder, "High Frequency EM Scattering by Non-Uniform Open Waveguide Cavities containing an Interior Obstacle," *Invited Paper presented at the International Conference on Directions in EM Wave Modelling sponsored by Weber Research Institute Polytechnic University, N.Y., New York, N.Y. October 22-24, 1990.*
- [11] P.H. Pathak, "Techniques for high frequency problems," in *Antenna Handbook - Theory, Applications, and Design*, Van Nostrand Reinhold, New York (1988).

## ACKNOWLEDGEMENTS

Special thanks are due to Drs. R.J. Burkholder, P. Law and R-C. Chou for their assistance in obtaining the numerical results shown in this paper. Also, the ray tracing subroutines used to compute both the GRE and SBR results in Fig. 4 are based on a super ellipse geometry modelling package provided by Prof. S.W. Lee (Univ. of Illinois). The work reported here was supported in part by the General Electric Company, the Joint Services Electronics Program (Contract N00014-89-J-1007), and the NASA/Lewis Research Center (Grant NAG3-476).

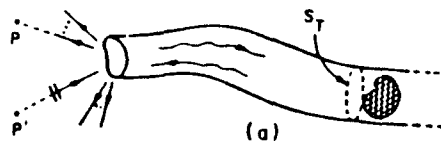


Figure 2: GO ray tubes launched into an open-ended cavity demonstrating a ray caustic and a shadow region.

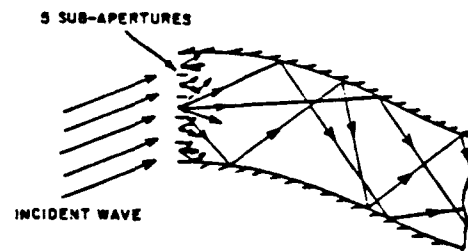
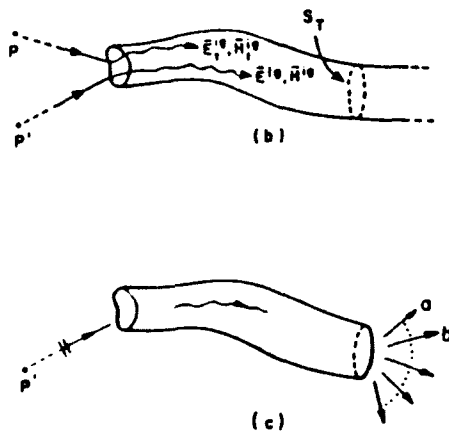


Figure 3: Ray tubes launched in the GRE method.

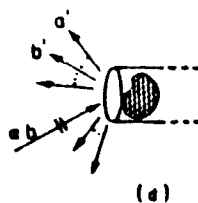
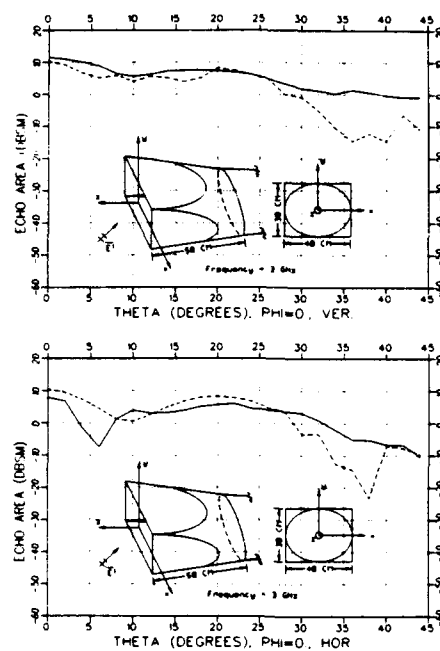
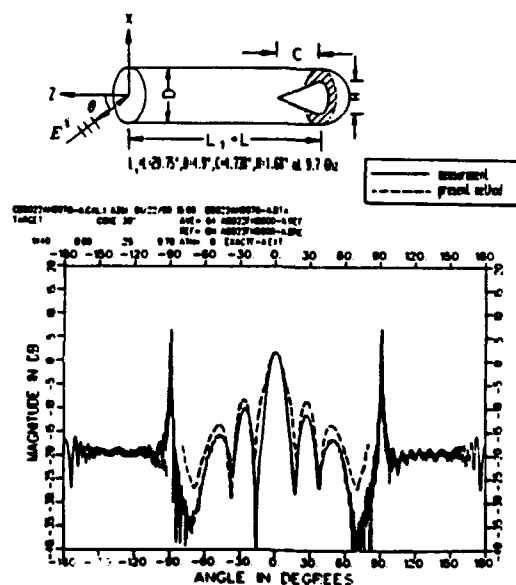


Figure 1: The scattering by an open-ended waveguide cavity.





**Figure 4: Backscatter patterns in the  $x-z$  plane of an open ended rectangular waveguide whose cross-section changes continuously into an ellipse. An interior planar short circuit is placed where the cross-section just becomes an ellipse. Note: in the above figures, VER  $\rightarrow$  VERTICAL POLARIZATION CASE and HOR  $\rightarrow$  HORIZONTAL POLARIZATION CASE.**



**Figure 5: Backscattered horizontally polarized  $E$  fields for a conical hub termination inside an open ended circular waveguide.**

## DISCUSSION

G. NEININGER, (GE)

Have you made investigations concerning an array of waveguides; for example, a slotted waveguide array antenna?

AUTHOR'S REPLY

No, i.e., not by ray methods. Presently we only have a pure moment method solution of an integral formulation for the problem involving a finite array of waveguide-fed slots.

# RCS PREDICTION MODELS BASED ON PO AND PTD AND

## STATE OF VALIDATION

by

V. Stein

Deutsche Forschungsanstalt für Luft- und Raumfahrt e.V.  
Institut für Hochfrequenztechnik  
8031 Oberpfaffenhofen  
Germany

### SUMMARY

In the microwave case the scattering matrix of complicated targets is often evaluated on the basis of physical optics (PO). In cases where edge diffraction effects become relevant, the physical theory of diffraction (PTD) is used to correct the PO-field. Both methods are applied in the following paper to determine the radar cross-section (RCS) of a series of perfectly conducting structures: a thin flat plate, a thin cylinder, a cone-cylinder-half-sphere, a double dihedral and a periscope-like object. Since the geometric model of each object consists of panels, internal and external tests were made to estimate the deviations between the true surface and the model surface which can be tolerated to guarantee sufficient accuracy. All predicted RCS values are compared either with measurements or with independent theoretical results as references. Conclusions for the accuracy of PO and PTD are drawn and further work is discussed.

### INTRODUCTION

The physical-optics method (POM) has been used widely in the past for the prediction of the RCS of perfectly conducting basis structures like spheres, flat plates, cylinders, circular disks, cubes, cones, dihedrals, etc. see e.g. [1, 2]. These basis structures can often be found as sub structures within more complicated objects like cars, ships and airplanes. So conclusions over the range of application can be drawn in analyzing these basis structures. Specially the flat plate plays a dominant role since basis and complicated structures can be modeled by a unifying concept with flat plates. Thereby panels of triangular and quadrangular shape are preferred. Depending from the special shape a panel model can agree perfectly with the original structure or show some differences due to the size of the panels. In modeling a smooth surface by panels artificial edges are introduced. In general panels of very different sizes, with dimensions ranging from a fractional of a wavelength to many wavelengths, are needed. Since the computer time to solve for the PO-field depends directly on the number of the panels, one tries to create the model with panels of a maximum admissible size.

Since the experience shows that in special cases POM alone does not lead to sufficient accurate results an edge diffraction term is introduced which is based on the method of equivalent currents (ECM) and was derived by Mitzner [3] and independently by Michaeli [4, 5]. It takes into account edge diffraction effects of first order for arbitrary aspect angles and is, therefore, more general than the solution of Ufimtsev [6] who has introduced the term physical theory of diffraction (PTD). Both terms are used in the report synonymously.

It is the intention of this paper to show the influence of modeling accuracy and the efficiency of POM and ECM by means of a series of test objects.

### THEORETICAL BACKGROUND

The polarization dependent RCS is computed from

$$(1) \quad \sigma_{ij} = \lim_{r \rightarrow \infty} (4\pi r^2 t_{ij} t_{ij}^*), \quad i = x, y; j = x, y,$$

where  $r$  is the distance between the radar observer and the test object.  $t_{ij}$  are the elements of the scattering matrix

$$(2) \quad [T] = \begin{bmatrix} t_{xx} & t_{xy} \\ t_{yx} & t_{yy} \end{bmatrix},$$

which relates the cartesian components of the scattered field  $\vec{E}_s$  propagating in  $z$ -direction to those of the incident field  $\vec{E}_i$  by

$$(3) \quad \begin{bmatrix} E_{sx} \\ E_{sy} \end{bmatrix} = [T] \begin{bmatrix} E_{ix} \\ E_{iy} \end{bmatrix}.$$

The RCS referred to 1 square meter (sq.m) and expressed in decibels yields the quantity which in general is used to compare theoretical and experimental results for the selected transmitting/receiving polarizations. In the case of basis structures the RCS is sometimes normalized by the square of the wavelength or by a characteristic area of the structure under test. If no calibration measurements are available, the experimental results are referred to any internal value, mostly the measured peak value. In these cases theoretical and experimental curves are shifted against each other till the peak values will coincide.

The scattered electric field of a perfectly conducting panel with zero thickness is as follows:

$$(4) \quad \vec{E}_s(\vec{r}) = \frac{j k}{4\pi} \frac{e^{-j k r}}{r} Z \cdot \int_{F_P} (\vec{s} \times (\vec{s} \times \vec{J}_F(\vec{r}')) e^{j k \vec{s} \cdot \vec{r}'} df',$$

where

- $\vec{r}$  = vector of the observation point,
- $\vec{r}'$  = vector of the integration point,
- $\vec{s}$  = unit vector pointing from the origin 0 toward the observation point, propagation direction of the scattered wave,
- $F_P$  = surface of the panel,
- $k$  =  $2\pi/\lambda$  = wave number,
- $\lambda$  = wavelength,
- $\vec{J}_F(\vec{r}')$  = electric surface current density at the integration point,
- $\vec{E}_s(\vec{r})$  = scattered electric field at the observation point,
- $Z$  = wave impedance of the propagation medium.

The geometric parameters are explained in Fig. 1.

According to the principle of PO the current density at the integration point is computed from the incident magnetic field  $\vec{H}_i$  as follows:

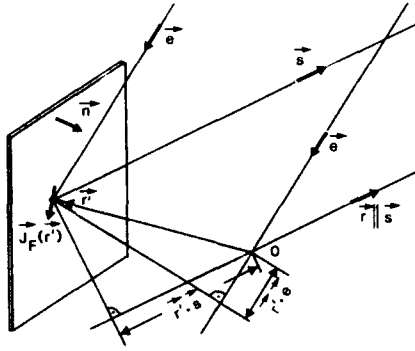


Fig. 1 Geometric sketch for the interpretation of the radiation integral;  $\vec{s} = \vec{e}$  in the monostatic radar case.

$$(5) \quad \vec{J}_p^o(\vec{r}') = \left\{ \begin{array}{l} 2\vec{n} \times \vec{H}_e(\vec{r}') \\ \text{(illuminated)} \\ \text{(hidden)} \end{array} \right\} \text{ on the surfaces of the panels.}$$

$\vec{n}$  represents the unit normal vector of the panel and is a constant for each panel face.

Expressing the incident magnetic field by the incident electric field  $\vec{E}_e = \vec{p}_e E_o$  with polarization vector  $\vec{p}_e$  and introducing (5) in (4) one receives the PO-scattered field of a panel with zero thickness as follows:

$$(6) \quad \vec{E}_s(\vec{r}) = -\frac{jk}{2\pi} \frac{e^{-jk r}}{r} \vec{p}_e E_o (\vec{n} \cdot \vec{s}) \cdot \int_{F_p} e^{j2k\vec{s} \cdot \vec{r}'} df'.$$

The polarization of the scattered field is identical with that of the incident field. From expression (6) the scattering matrix can be derived as

$$(7) \quad [T^{PO}] = -\frac{jk}{2\pi} \frac{e^{-jk r}}{r} (\vec{n} \cdot \vec{s}) \int_{F_p} e^{j2k\vec{s} \cdot \vec{r}'} df' \cdot \begin{bmatrix} 1 & 0 \\ 0 & 1 \end{bmatrix}.$$

One observes that no cross-polarization effects, nor any differences between xx- and yy-polarization are predicted by PO in cases where the structure is perfectly conducting and no double or multiple reflections occur.

The phase integral in (7) can be solved analytically, see [2]. Independent from the size of the panel it takes about 0.13 ms on a computer of the type IBM 3091 to evaluate the scattering matrix of a panel for each aspect angle, including the solution of geometric problems.

There are several methods to treat edge diffraction effects. The most appropriate is the ECM, since the PO-field is corrected by an additive fringe diffracted field. ECM is based on electric and magnetic fringe currents  $I^f$ ,  $M^f$  flowing along an edge:

$$(8) \quad I^f(\psi_e, \beta_e) = -\frac{j2(\vec{r} \cdot \vec{E}_e)}{kZ \sin^2 \beta_e} D_{\theta}^f(\psi_e, \beta_e) - \frac{j2(\vec{r} \cdot \vec{H}_e)}{k \sin^2 \beta_e} D_{\phi}^f(\psi_e, \beta_e),$$

$$(9) \quad M^f(\psi_e, \beta_e) = \frac{j2Z(\vec{r} \cdot \vec{H}_e)}{k \sin^2 \beta_e} D_{\phi}^f(\psi_e, \beta_e).$$

Denotations:

$\beta_e$  = angle between the incident ray and the edge,  
 $\psi_e$  = angle between the plane of incidence and a reference face of the wedge (face 1 in Fig. 2),  
 $\vec{t}$  = unit tangent vector parallel to the edge,  
 $\vec{t} = (t_x, t_y, t_z)^T$ ,  $t_z = -\cos \beta_e$ .

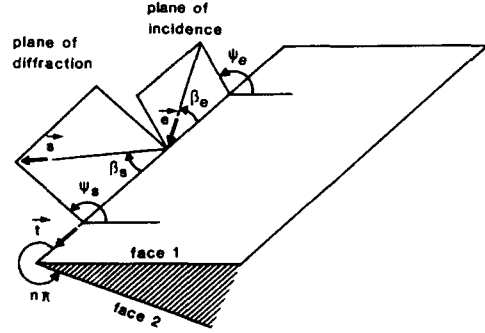


Fig. 2 Wedge geometry;  $\beta_s = \beta_e$ ,  $\psi_s = \psi_e$  in the monostatic radar case.

The coefficients  $D_{\theta}^f$ ,  $D_{\phi}^f$  and  $D_{\phi m}^f$  are constructed from the difference between the total equivalent current, responsible for the total field and the PO-equivalent current, generating the PO-field. They depend from  $\psi_e$ ,  $\beta_e$  and the outer wedge angle  $n\pi$  and are given in the appendix for first order diffraction processes.

From expressions (8) and (9), given by Michaeli, the edge diffracted fields of Ufimtsev and Mitzner can be derived, see [7].

The fringe diffracted field for an edge of length  $L$ , see Fig. 3, is expressed by

$$(10) \quad \vec{E}_s^f(\vec{r}) = \frac{jk}{2\pi} \frac{e^{-jk r}}{r} \cdot \int_L (Z I^f(\vec{r}') (\vec{s} \times (\vec{s} \times \vec{t})) + M^f(\vec{r}') (\vec{s} \times \vec{t})) e^{j2k\vec{s} \cdot \vec{r}'} dl'.$$

Introducing (8) and (9) into (10) one receives

$$(11) \quad \vec{E}_s^f(\vec{r}) = -\frac{1}{2\pi} \frac{e^{-jk r}}{r} E_o \int_L e^{j2k\vec{s} \cdot \vec{r}'} dl' \cdot \frac{1}{|\vec{r} \times \vec{s}|^2} ((\vec{p}_e \cdot (\vec{s} \times \vec{t})) D_{\theta}^f(\vec{s} \times \vec{t}) - ((\vec{p}_e \cdot \vec{t}) D_{\theta}^f + (\vec{p}_e \cdot (\vec{s} \times \vec{t})) D_{\phi}^f) (\vec{s} \times (\vec{s} \times \vec{t}))).$$

From the last expression the scattering matrix  $[T^f]$  of an edge is derived:

$$(12) \quad [T^f] = -\frac{1}{2\pi} \frac{e^{-jk r}}{r} \int_L e^{j2k\vec{s} \cdot \vec{r}'} dl' \cdot \begin{bmatrix} D_{\theta}^f t_x^2 + D_{\phi}^f t_y^2 - D_{\phi m}^f t_x t_y & (D_{\theta}^f - D_{\phi}^f) t_x t_y + D_{\phi m}^f t_x^2 \\ (D_{\theta}^f - D_{\phi}^f) t_x t_y - D_{\phi m}^f t_y^2 & D_{\phi}^f t_x^2 + D_{\theta}^f t_y^2 + D_{\phi m}^f t_x t_y \end{bmatrix}.$$

One observes that the edge scattering matrix in contrary to the PO-scattering matrix predicts

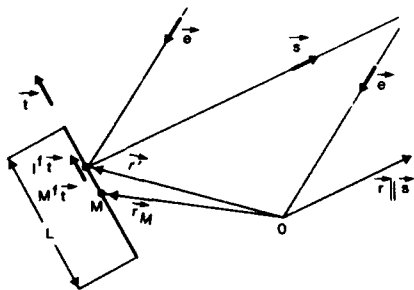


Fig. 3 Geometry to evaluate the radiation integral;  $\vec{s} = \vec{e}$  in the monostatic radar case.

differences between VV- and HH-polarization and also cross polarization effects. However, the cross-polarization terms are different from another besides the specular case where  $D_{em}^s = 0$ . The physical reason for the violation of reciprocity is that the fringe current model employed ignores the effect of corner diffraction.

The phase integral again can be evaluated analytically. Due to the more complex expressions as in the PO-case it takes about 0.55 ms to compute the scattering matrix for one aspect angle. This time is a mean value resulting from the analysis of an object with several hundred edges and includes the time for the search of the edges.

The scattering matrix  $[T]$  of a complicated structure is the sum of a matrix  $[T^N]$ , which again is the sum of the scattering matrices based on PO of the  $N$  visible panels, and the scattering matrix  $[T^M]$  which sums up the scattering matrices of  $M$  visible edges:

$$(13) \quad [T] = [T^N] + [T^M],$$

where

$$(14) \quad [T^N] = \sum_{n=1}^N [T_n^N], \quad (15) \quad [T^M] = \sum_{m=1}^M [T_m^M].$$

#### SQUARE FLAT PLATE

The square plate under test had an edge length of  $5.08 \lambda$  and a thickness of  $0.044 \lambda$ . The wavelength was  $17.995 \text{ mm}$ . In a series of figures the results of experiment (EX), POM, POM + ECM and integral equation method (IEM) are compared. Since this plate has very similar dimensions as the plate analyzed by Ross [9], a further cross check with the results of the geometrical theory of diffraction (GTD) and independent measurements can be made, however, only for the principal plane.

Fig. 4 presents experimental results for the principal plane and the diagonal plane, each for VV- and HH-polarization. Off-diagonal cuts are not available. Since the aspect angles range from  $-90^\circ$  to  $+90^\circ$  from broadside one can estimate the measurement accuracy by means of the unsymmetries which arise at low energy levels. Especially from the diagonal cut one can conclude that levels lower than about 35 dB under the peak are not very reliable. The results are given by relative values, the peak value amounts to about 4.33 dB over 1 sq.m.

Fig. 5 compares in the first row the results of POM for the main plane, assuming zero thickness (left side) and  $0.044 \lambda$  thickness (right side) for the test plate. PO-results for plates are presented in the literature very often only for panels with zero thickness and compared with measurements which only can be carried out for panels

with non zero thickness. It is very often stated that PO is not allowed to be applied on objects whose dimensions are small compared to the wavelength. However, one can see from Fig. 5, first row, that the contribution of the very small side faces leads to an improvement of the result for the zero thickness panel near and at the grazing angle. In the second row the results for a diagonal cut and an off-diagonal cut including an angle of  $30^\circ$  with an edge, are presented. The peak of the third sidelobe ( $-37 \text{ dB}$  under 1 sq.m) of the diagonal cut agrees well with that of the measurement. The computer time for each aspect angle amounts to about 0.8 ms.

Fig. 6 shows the polarization dependent results of POM corrected by ECM for the plate with its actual thickness of  $0.044 \lambda$ . The first row presents the results for the principal plane. For VV-polarization one can state a perfect agreement with the experimental results. For HH-polarization also an improvement can be observed, the characteristic null at grazing incidence, however, is not reproduced. Since ECM is used for the contribution of all edges, one could object in a similar way as in the case of the application of PO on small faces, that ECM is not allowed to treat edges with a distance of only a fractional of a wavelength. Assuming a plate with zero thickness where only four edges with wedge angles of  $360^\circ$  are present one obtains identical results for the two polarizations which is not in agreement with physical reasons. The consideration of the natural wedge angle of  $270^\circ$  effects practically no changes in the VV-polarization but influences the HH-polarization in the right manner. The second row in Fig. 6 shows the RCS for the diagonal plane. One observes that ECM changes the results of POM in a negligible manner. Small differences between VV- and HH-polarization occur, but for HH-polarization the peak before grazing incidence again is not reproduced. In summary for the diagonal plane one can state a good agreement for near broadside aspect angle (from the peak value down to the third sidelobe whose level is about  $-35 \text{ dB}$  under the peak). Row three presents results for the off-diagonal plane. In this case cross-polarization effects are indicated by ECM, represented in row four. No measurements are available for this plane.

Therefore, the IEM (electric field integral equation, wire grid model with about 3436 wires and a mesh width of about  $0.125 \lambda$ ) was used to fill this gap. The results are shown in Fig. 7 and seem to agree for the principal plane and the diagonal plane somewhat better with the measurements than the PO- and EC- results. This improvement, however, must be paid with a higher computer effort. POM and ECM together need about 5.4 ms per aspect angle. Under the assumption that the matrix inversion is considered separately one has to assume 1760 ms on a Cray-computer for one aspect angle which is 2000 times the value using POM alone and 176 times the value using POM and ECM together. The matrix fill in and inversion work must be done only once. It is independent from aspect angle and polarization for a fixed frequency. It amounts to about 2800 s. Under these circumstances one can state that the use of POM and ECM is a good compromise between accuracy and economy.

#### THIN CYLINDER

The cylinder under test had a length of  $5.0 \lambda$  and a radius of  $0.5 \lambda$ . Since the wavelength was chosen to be  $1128 \text{ mm}$  the circular cross section has an area of 1 sq.m. The cylinder is closed by flat end caps. The broadside RCS value amounts to 20 dB over 1 sq.m, the front face RCS amounts to 9.9 dB over 1 sq.m.

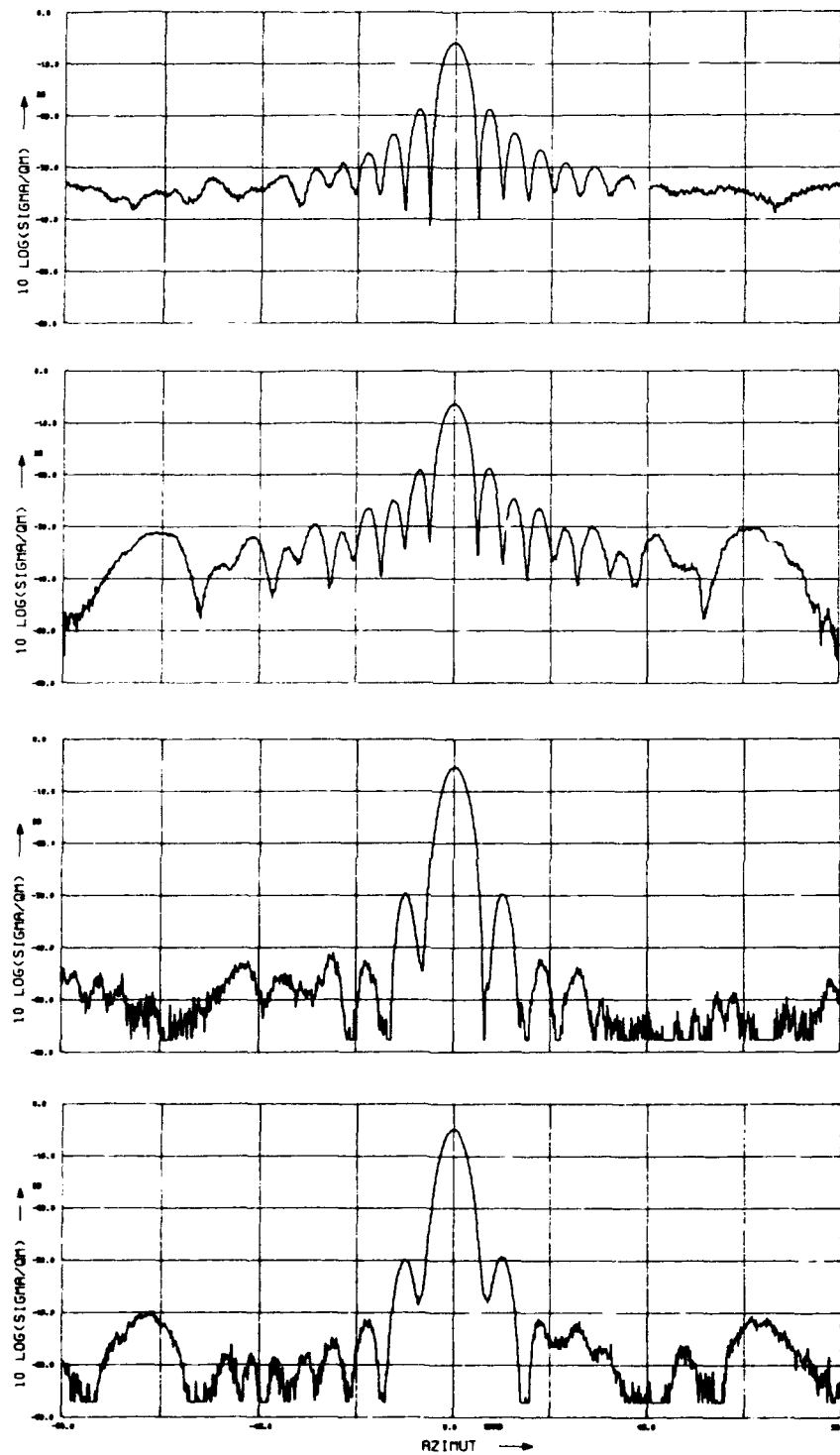


Fig. 4 Experimental RCS values of a square test plate with edge length  $5.08 \lambda$  and thickness  $0.044 \lambda$ ,  $\lambda = 17.995$  cm;

first row: principal plane VV-polarization;  
 second row: principal plane, HH-polarization;  
 third row: diagonal plane, VV-polarization;  
 fourth row: diagonal plane, HH polarization.

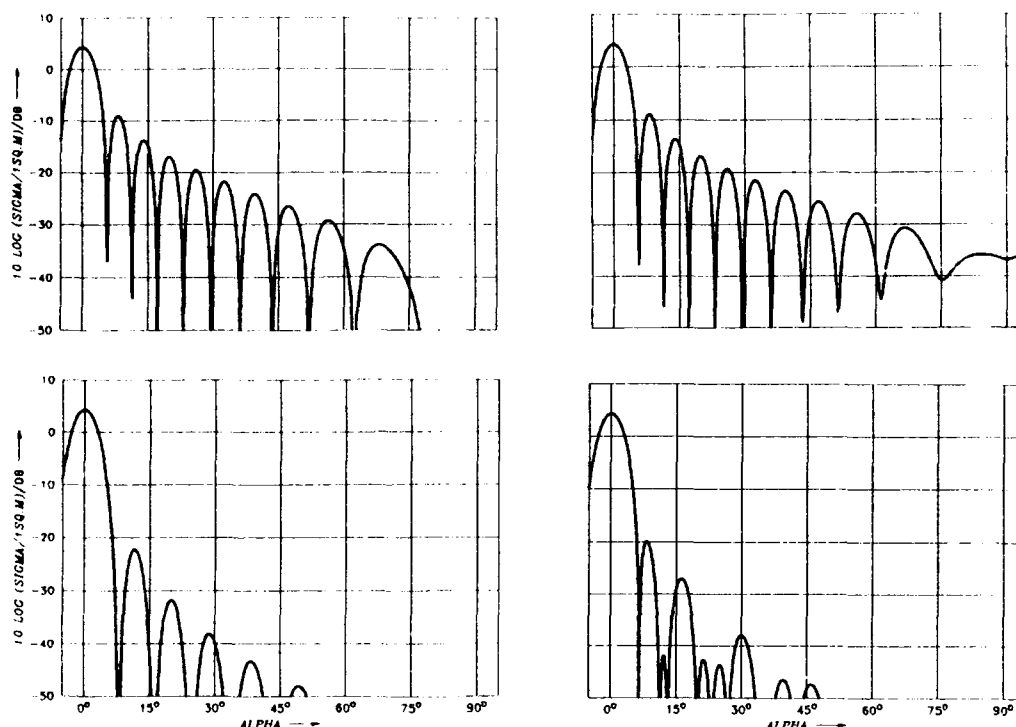


Fig. 5 RCS results of POM for the test plate;  
first row: principal plane, left side: panel with zero thickness, right side: panel with  $0.044 \lambda$  thickness;  
second row: panel thickness =  $0.044 \lambda$ ; left side: diagonal plane ( $45^\circ$ ), right side: off-diagonal plane ( $30^\circ$ ).

In the case of the flat plate the PO-model consisting of 6 panels agreed perfectly with the original object. By modeling general objects by panels differences between the original surface and the model surface arise, whose magnitude depends from the number of panels used. In order to find out the minimum number of panels an internal experiment is arranged: the cylinder is modeled by panels of varying number and turned around its own axis. Observing the variation of the RCS one can estimate the maximum admissible deviation. The results of this study are presented in Fig. 8.

The cylinder barrel and the two front faces are modeled by rectangular and triangular panels resp. At first 7 panels were used for the barrel and each front face. This results in a width of the barrel panels of  $b = 0.43 \lambda$  and a difference of  $\delta = 0.05 \lambda$  ( $\lambda/20$ ) between the model and the original object. The fluctuation of the broadside RCS amounts to about 4 dB (see first row, left side) which is much more than can be tolerated. In the next step the model is refined consisting now of 14 panels which yield  $b = 0.22 \lambda$  and  $\delta = 0.013 \lambda$  ( $\lambda/80$ ). The fluctuations (see first row, right side) now amount to about 0.5 dB, which in general is acceptable.

The original cylinder has only two natural edges between the barrel and each of the front faces. The outer wedge angle has a value of  $270^\circ$  ( $n = 1.5$ ). Artificial edges between the panels of the barrel are introduced by the modeling technique. The outer wedge angle for the 7-panel model is  $231^\circ$  ( $n = 1.29$ ) and for the 14-panel model  $206^\circ$  ( $n = 1.14$ ). Taking into account the natural and the artificial edges by ECM one obtains the RCS-results of the second row for the 14-panel model. While for HH-polarization a further improvement against the PO-result is obtained, one observes a slight degradation for VV-polarization. Therefore,

in order to serve computer time it seems to be useful to decide whether natural or artificial edges occur within the panel model. The third row presents the results of POM and ECM, the latter applied only on natural edges.

RCS-results in dependence from the aspect angle are presented in Fig. 9. The PO-results and the polarization dependent PO + EC-results are presented in the first and in the third row resp. Measurements [9] are shown in the second row by the dashed lines. The solid lines in the second row present the results of PTD (see also [9]) which in this special case should yield the same results as ECM. One observes a good agreement between all diagrams for angles between  $0^\circ$  and about  $45^\circ$  as well as around and at  $90^\circ$ . Only for HH-polarization some remarkable differences between POM and the experimental results become evident, while POM + ECM generate results which are in good agreement with the experiment. One can conclude (under the assumption that the cylinder is modeled with sufficient accuracy) that POM can be applied for the analysis also of thin cylinders with radii of about a wavelength within a wide range of aspect angles around broadside while correction by ECM becomes efficient within a small range around the cylinder axis. In the literature one can find so-called PO-results which are based on the integration over the currents of an infinite long cylinder, thus neglecting the contribution of the front faces. These results, therefore, differ significantly from the results presented here.

#### CONE-CYLINDER - HALF-SPHERE

In order to have a further estimation of errors which are introduced by the differences between an actual surface and a panel model, in this section an external test by measurements is arranged as follows. The results presented here are restricted

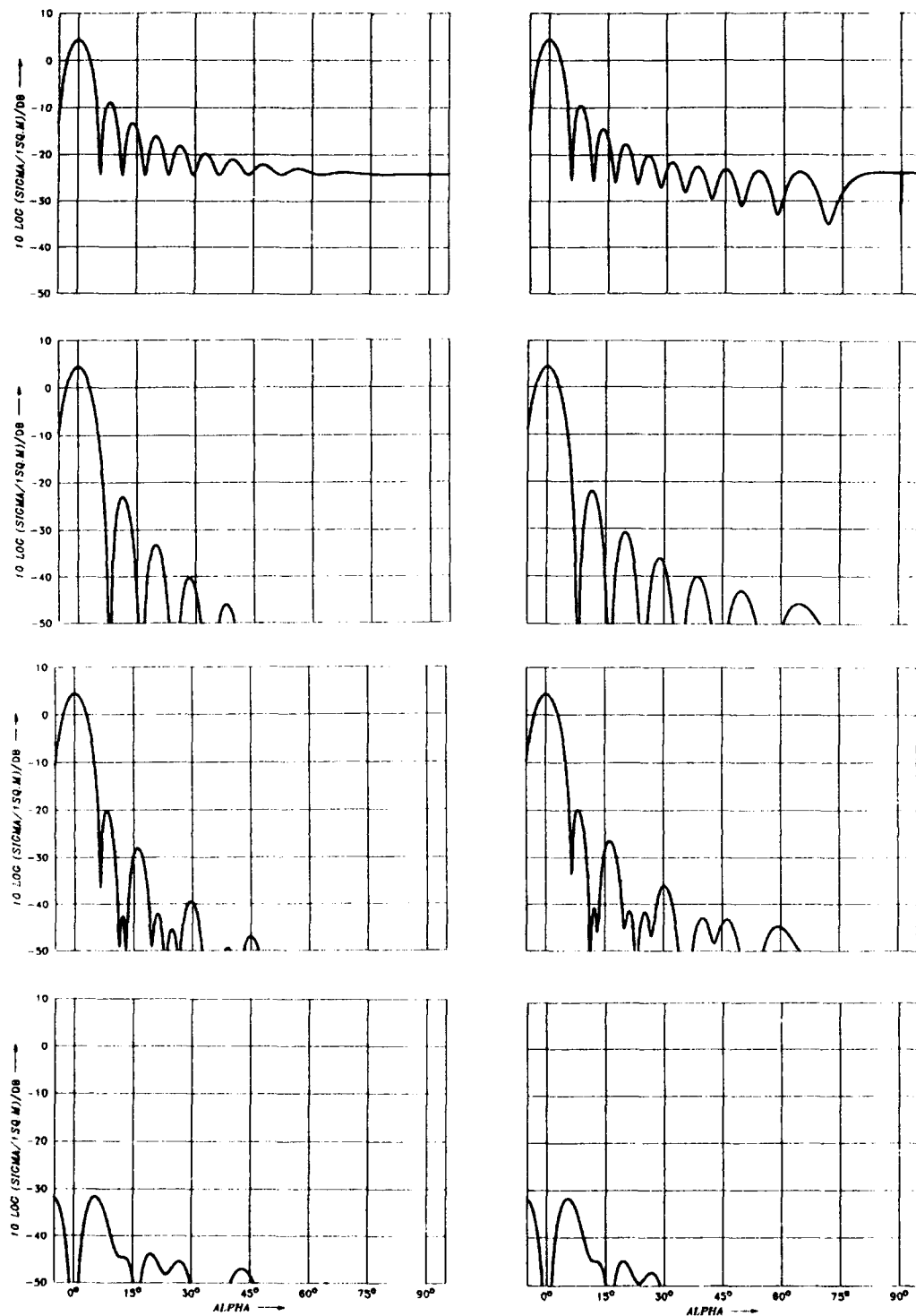


Fig. 6 RCS results of POM and ECM for the test plate;

first row: principal plane, left side: VV-polarization, right side: HH-polarization;  
second row: diagonal plane, left side: VV-polarization, right side: HH-polarization;  
third row: off-diagonal plane, left side: VV-polarization, right side: HH-polarization;  
fourth row: off-diagonal plane, left side: VH-polarization, right side: HV-polarization.



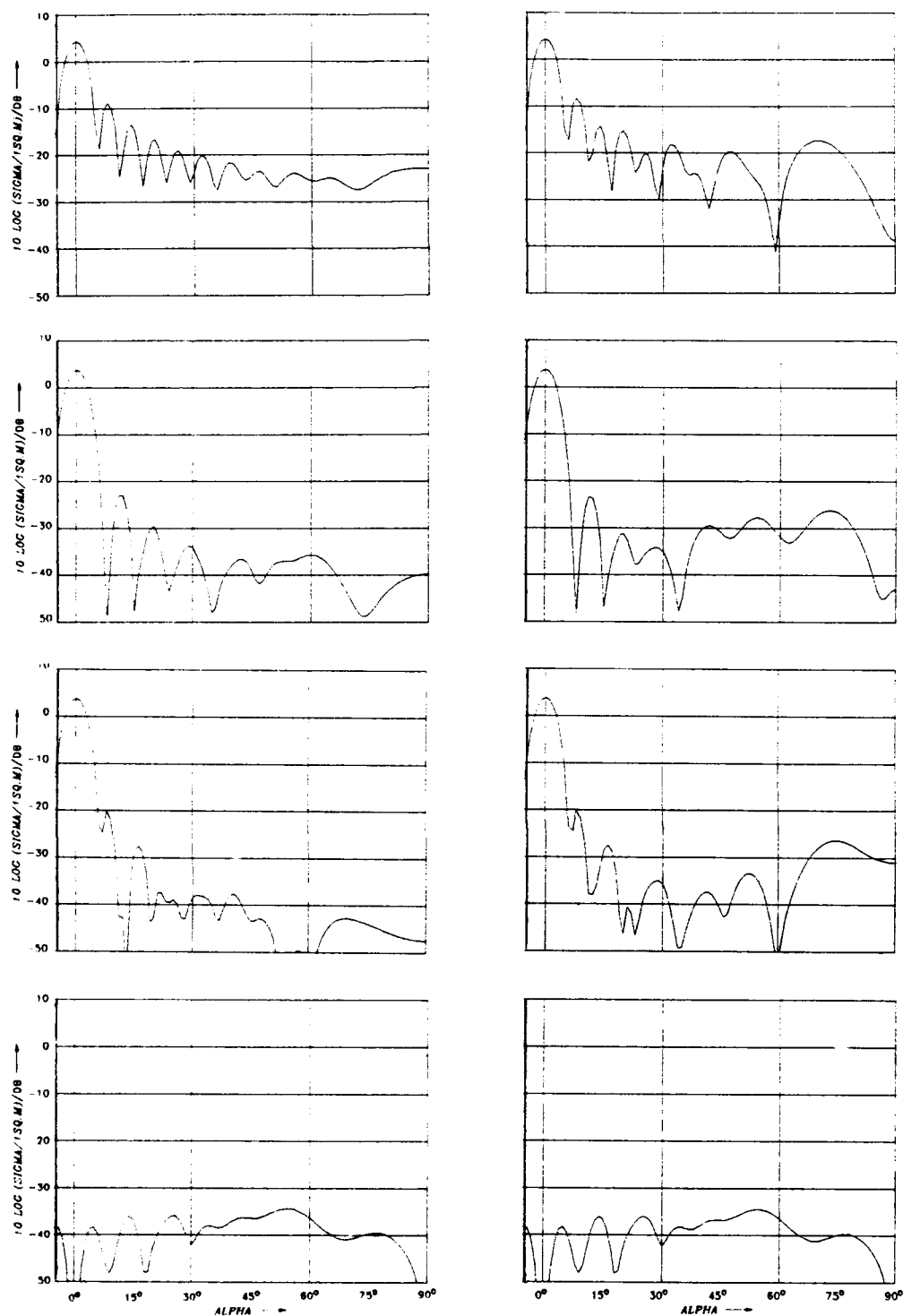


Fig. 7 RCS results of IEM for the test plate;

first row: principal plane, left side: VV-polarization, right side: HH-polarization;  
second row: diagonal plane, left side: VV-polarization, right side: HH-polarization;  
third row: off-diagonal plane, left side: VV-polarization, right side: HH-polarization;  
fourth row: off-diagonal plane, left side: VH-polarization, right side: HV-polarization.

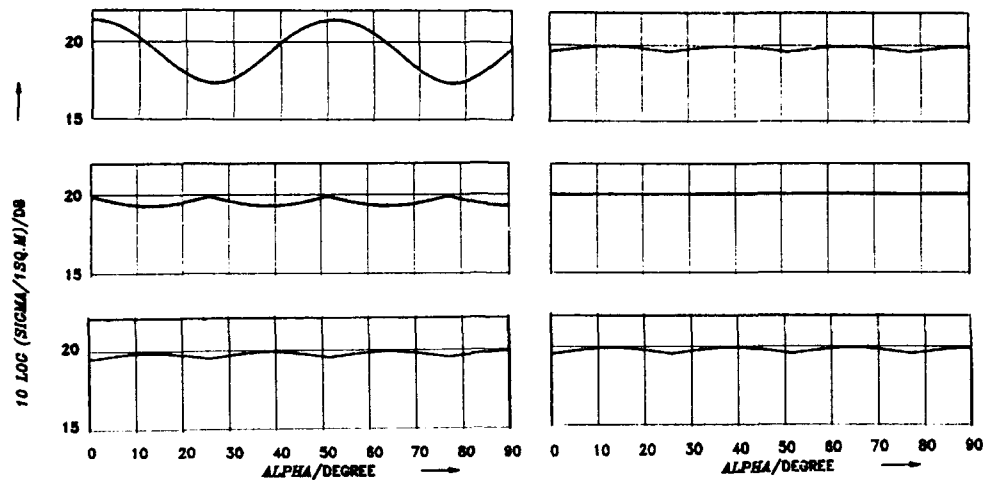


Fig. 8 Modeling accuracies influencing the broadside peak of the test cylinder rotating around its own axis. Length =  $5\lambda$ , radius =  $\lambda/2$ ,  $\lambda = 1128$  mm, peak value: 20 dB;

first row: left side: cylinder barrel and front faces each modeled by 7 panels, POM right side: cylinder barrel and front faces each modeled by 14 panels, POM  
second row: cylinder casing and front faces, each modeled by 14 panels, POM + ECM for artificial and natural edges; left side: VV-polarization, right side: HH-polarization;  
third row: cylinder barrel and front faces, each modeled by 14 panels, POM, ECM only for natural edges; left side: VV-polarization, right side: HH-polarization.

to HH-polarization.

The test object consists of a cone, a cylinder and a half-sphere. It is manufactured twice: one configuration with smooth surfaces and the other with facets corresponding to the panels of the geometric model. The latter is shown in Fig. 10. The dimensions were as follows:



Fig. 10 Cone-cylinder - half-sphere with facets as surface.

overall length: 950 mm  
diameter of cylinder and sphere: 170.6 mm  
interior cone angle: 30°  
length of the cylinder: 546.4 mm

24 rectangular panels were used for the cylinder and 24 triangular panels for the cone. This leads in case of the cylinder to a panel width of 44.3 mm and to a maximum difference of 0.73 mm. Since the frequency was 15.5 GHz ( $\lambda = 19.4$  mm) this corresponds to a difference of about  $\lambda/26$ .

Fig. 11 shows in the first row the experimental results for the smooth object on the left and for the objects with facets on the right. The PO-results are given in the second row on the left while the results of POM + ECM are presented on the right. The peak at 90° is due to broadside incidence for the cylinder while the peak at 75° arises at broadside incidence for the cone. For 0° the radar observer sees the tip of the cone, for 180° the sphere alone is seen.

One realizes that all results agree nearly perfectly with the only exception near and around 180° where the sphere is seen. The measurements indicate differences between the results for the smooth object and the object with facets which are due to oscillations of the RCS around the well-known value of a sphere. The PO-results, however, show also differences against the experimental results for the facet model. The same is true for the results obtained by POM + ECM. The oscillations predicted by the theories occur with comparable magnitude but with opposite sign as in the measurements. This effect is not yet clarified but a detailed comparison between the manufactured facet model and the mathematical model revealed differences for the sphere.

#### DOUBLE DIHEDRAL

A double dihedral constructed on the basis of a cube with additional shadowing surfaces, see Fig. 12, is rotated in an unconventional way so that its edges include an angle of 45° with the axis of rotation, see Fig. 13. The reason is to generate a strong depolarizing back-scatter. Previous

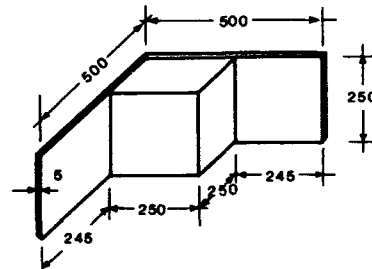


Fig. 12 Cube with additional shadowing surfaces forming a double dihedral, dimensions in mm.

PO-results are published for the main cut in [1] and for the diagonal cut within a restricted range of aspect angles in [2]. Figs. 14 and 15 present the results of experiment, POM and POM + ECM for the full range of aspect angles and a frequency of 15.5 GHz ( $\lambda = 19.4$  mm). The measurements had to be arranged with great care since a wide dynamic range was needed. In addition the exact positioning

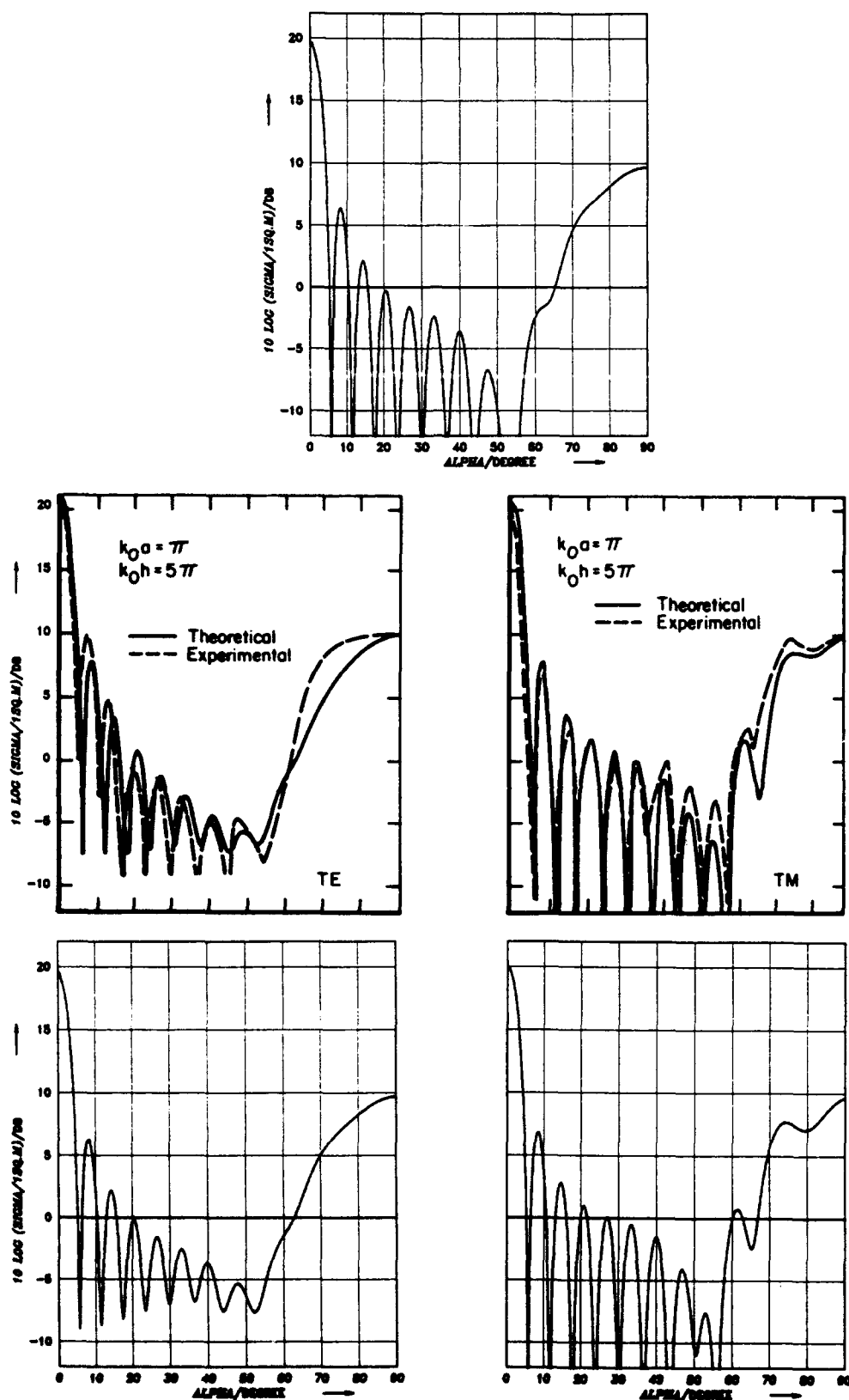


Fig. 9 RCS of the test cylinder;  
first row: PO-solution;  
second row: experiment (---) and PTD-solution [9]; left side: VV- (TE-) polarization, right side: HH- (TM-) polarization;  
third row: POM and ECM, left side: VV-polarization, right side: HH-polarization.

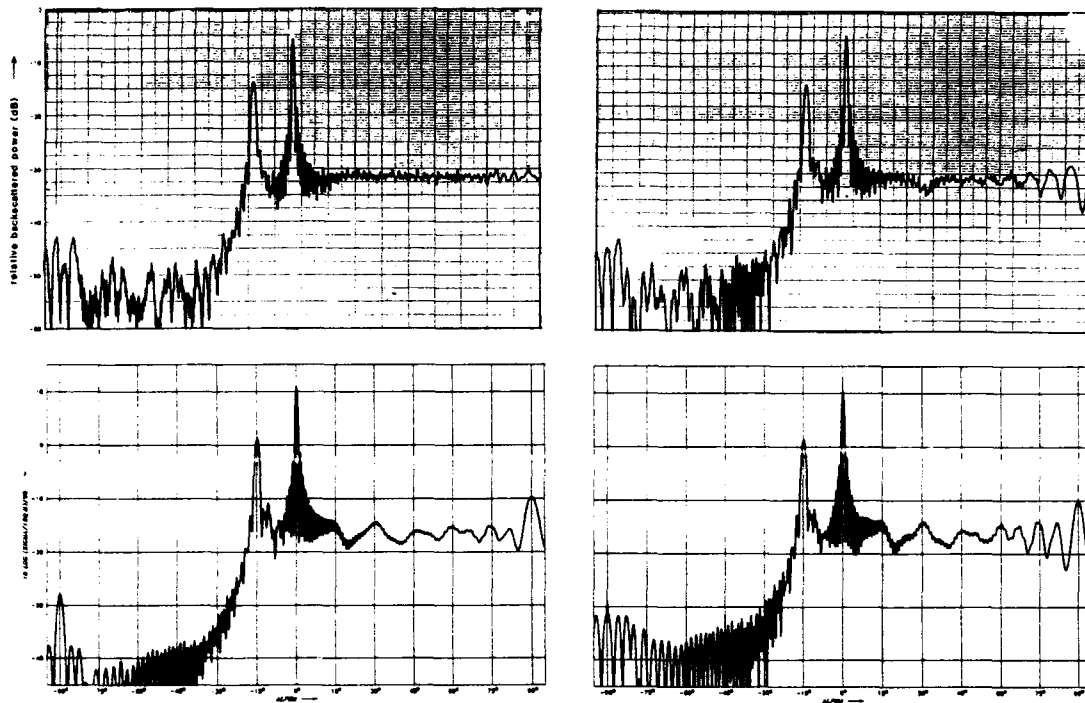


Fig. 11 EX- and PO/EC-results for the cone-cylinder-half-sphere; HH-polarization;  
first row: left side: EX-result for the smooth object; right side: EX-result for the object with facets;  
second row: left side: PO-result; right side: PO+EC-result.

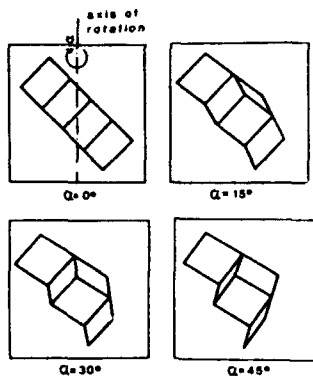


Fig. 13 Geometry and axis of rotation which cause strong depolarized backscatter.

of the double dihedral according Fig. 13 caused major problems.

The PO-results agree quite well with the EX-results for the two copolar diagrams. In the cross polar case the structure of the pattern around  $0^\circ$  is well represented but the decrease is too rapid with increasing aspect angles. In addition the spikes at  $-234^\circ$ ,  $-180^\circ$ ,  $-54^\circ$  and  $+54^\circ$  are not predicted by PO. This, however, is the case when the EC-field is added to the PO-field. The spikes, therefore, are due to edge diffraction only. It must be emphasized that the double dihedral has edges with exterior wedge angles  $270^\circ$  and  $90^\circ$ . Only the first type of edges is considered by ECM.

#### PERISCOPE

In order to study the capability of POM and ECM by means of a more complex object a 1:1 scale model of a periscope-like structure, whose surface was

coated with conductive silver, was manufactured. The dimensions of the structure were as follows:

overall height:	1255 mm
distance between the collar and the top of the radome:	590 mm
diameter of the collar:	800 mm
thickness of the collar:	65 mm

The lower part of the periscope was constructed as an ogival cylinder with a radius of 412 mm and a height of 600 mm. Two pairs of swell deflecting plates with dimensions of about 530 mm  $\times$  150 mm are fixed at opposite positions under the collar. The surface of the optical and infrared windows above the collar was also metallized. Fig. 16 shows on the left a picture of the 1:1 scale model and on the right the panel model consisting of 1059 panels.

In a first step the RCS of the periscope was measured and computed under free space conditions. The EX- and PO-results are presented in Fig. 17 for the main cut with the turn axis coinciding with the axis of the collar. The frequency was 9.375 GHz ( $\lambda = 32$  mm). The radar field was HH-polarized. Between HH- and VV-polarization only negligible differences exist. The first main peak arises at an aspect angle of  $90^\circ$  which describes a view normal to the plates opposite to the window side. The second main peak occurs at  $270^\circ$ . The level of both peaks is determined nearly alone by the scattered fields of the plates and of the ogival cylinder.

The PO-result fits very well to the EX-result. The use of ECM influences the PO-result only in a negligible manner for this special cut. The computer time for each aspect angle is 0.14 s on an IBM 3091.

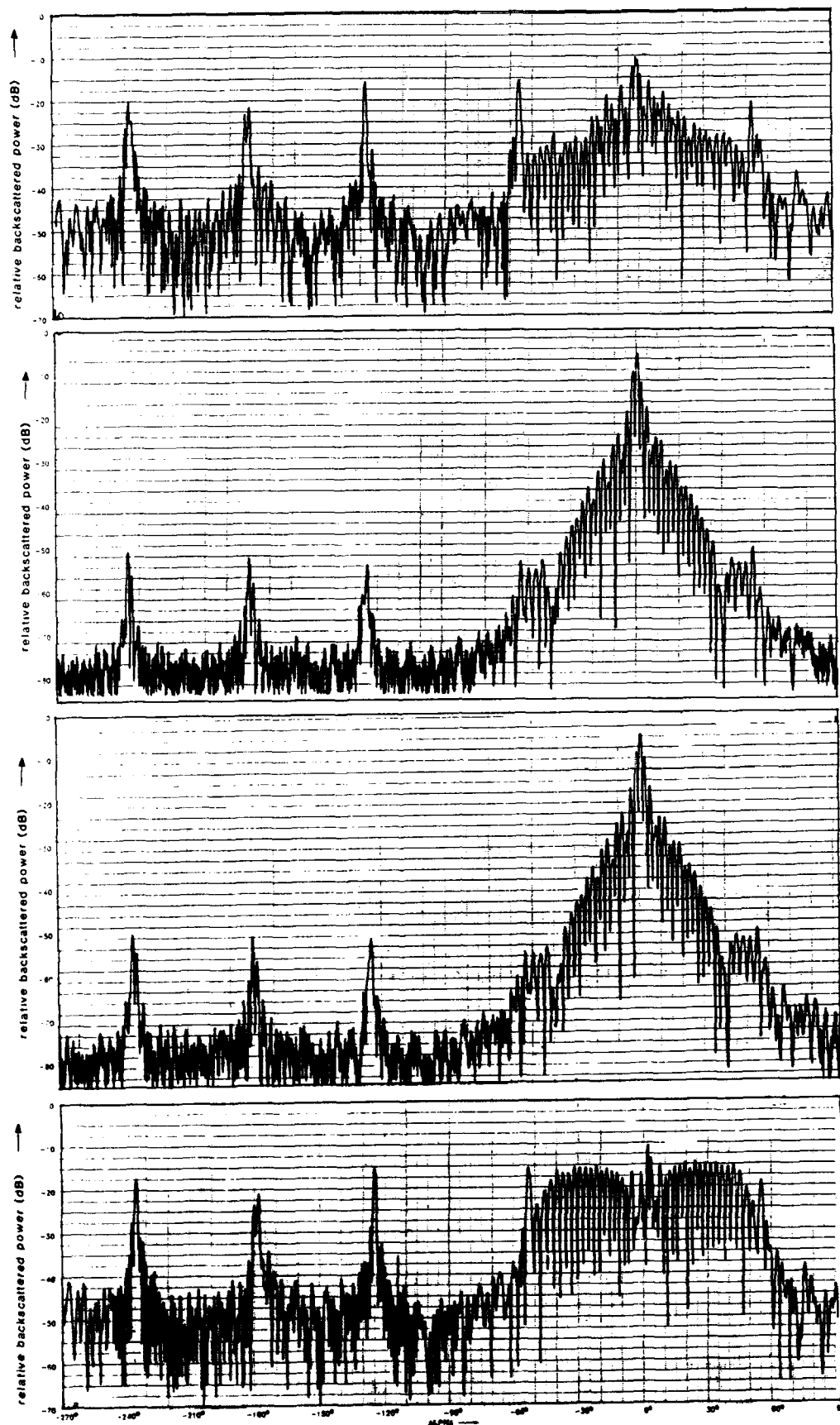


Fig. 14 EX-results for the double dihedral;  
first row: VV-polarization;  
second row: VH-polarization;  
third row: HV-polarization;  
fourth row: HH-polarization.

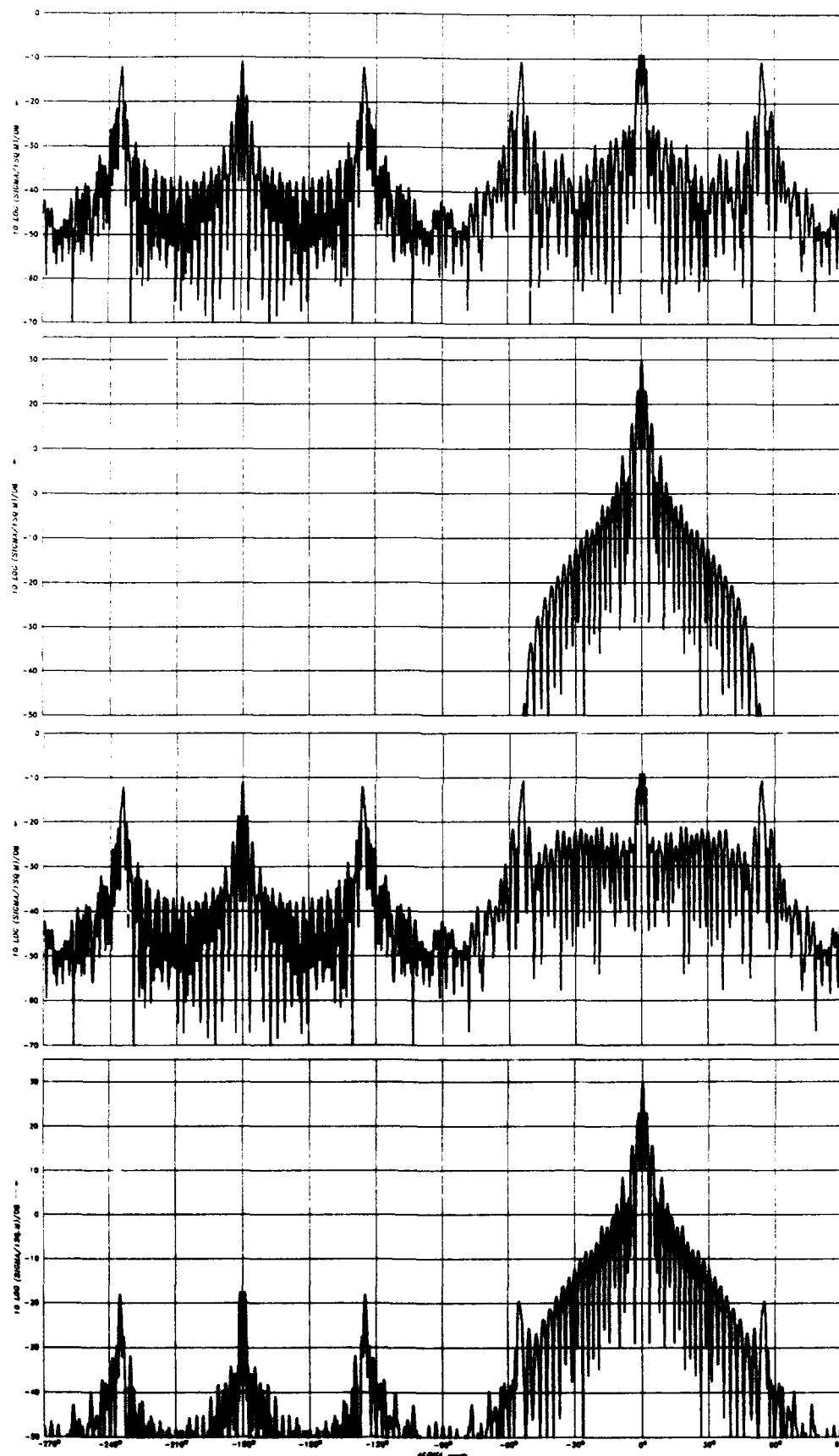


Fig. 15 PO/EC-results for the double dihedral;  
first row: VV-polarization PO;  
second row: VH-polarization PO;  
third row: HV-polarization PO;  
fourth row: HV-polarization PO + EC.

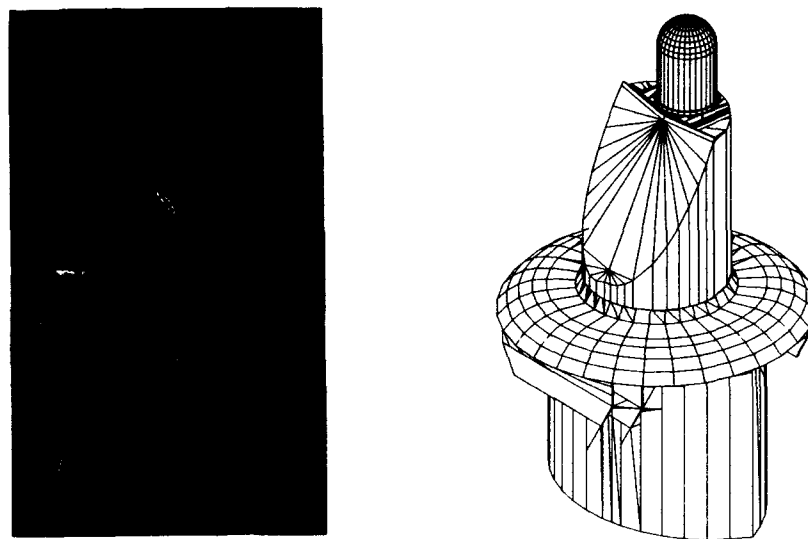


Fig. 16 Picture of the 1:1 scale model and panel model of the periscope.

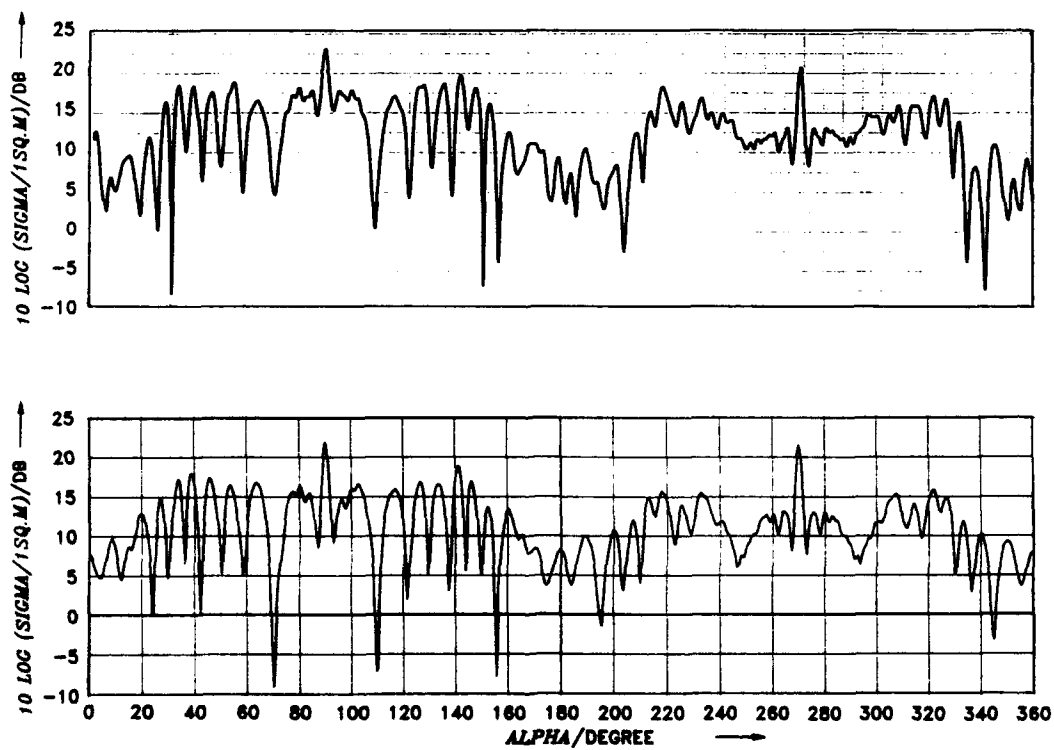


Fig. 17 Comparison between EX- and PO-results for the periscope, HH-polarization; top: EX, bottom: PO.

## CONCLUSION

POM and ECM have been used to determine the RCS of a thin plate, a thin circular cylinder, a cone-cylinder-half-sphere, a double dihedral and a periscope-like structure. All objects were perfectly conducting and modeled by panels. All theoretical results were compared with experimental results or the results of other independent theories.

POM and ECM based on a panel model have been proved to be a useful tool for the RCS analysis not only of basis structures but also of more complex objects. It could be shown by means of the flat plate that PO predicts good results even in cases where the dimensions are only a fraction of a wavelength. The same is true for the application of ECM in the case where the distance between edges is very small compared to the wavelength. The obtained accuracy by POM alone and in special cases by the combination with ECM is a good compromise to the computer effort which is very low compared to other more rigorous methods.

In case of perfectly conducting bodies the next step of validation of the PO- and EC-theory should extend to the treatment of higher order edge diffraction effects, interior edge effects, structures over a large plane surface, quasi near-field and bistatic problems.

## ACKNOWLEDGEMENT

This paper could not be prepared without the support of and the discussion with many colleagues. The author wishes to thank Dieter Klement and Rolf Schwemmer for modeling all of the objects presented and for a series of PO-calculations, Dr. Erich Kemptner for the IE-computation of the flat plate, Dr. Bernd Röde and Dr. Karl Heinz Bethke for nearly all RCS precision measurements, Mrs. Margaretha Malchow for preparing the manuscript, Mrs. Gertraud Jacob for the line illustrations and Mrs. Alice Bastian for the pictures and viewgraphs. This work has been supported in part by the Bundesamt für Wehrtechnik und Beschaffung of the German Ministry of Defense under the contractual direction of Mr. M. Heuel.

## APPENDIX

The coefficients of the backscattering matrix (12) are given by

$$(A1) \quad D_v = D_{1v} - D_{1v}^{PO} + D_{2v} - D_{2v}^{PO}, \quad v = e, m, em,$$

$$(A2) \quad D_{1e} = \frac{\sin \frac{v_e}{n}}{n} \frac{1}{\cos \frac{\pi - \alpha_1}{n} - \cos \frac{v_e}{n}},$$

$$(A3) \quad D_{1m} = \frac{\sin \frac{v_e}{n}}{n} \frac{\sin \frac{\pi - \alpha_1}{n}}{\sin \alpha_1} \frac{1}{\cos \frac{v_e - \alpha_1}{n} - \cos \frac{v_e}{n}},$$

$$(A4) \quad D_{1em} = \frac{1}{n} \cos \beta_e (\mu_1 + \cos v_e) \frac{\sin \frac{\pi - \alpha_1}{n}}{\sin \alpha_1} \cdot \frac{1}{\cos \frac{\pi - \alpha_1}{n} - \cos \frac{v_e}{n}},$$

$$(A5) \quad D_{1e}^{PO} = -U(\pi - v_e) \frac{\sin v_e}{\mu_1 + \cos v_e},$$

$$(A6) \quad D_{1m}^{PO} = -U(\pi - v_e) \frac{\sin v_e}{\mu_1 + \cos v_e},$$

$$(A7) \quad D_{1em}^{PO} = 0.$$

$$(A8) \quad \mu_1 = \cos v_e - \frac{2}{\tan^2 \beta_e},$$

$$(A9) \quad \alpha_1 = \arccos \mu_1,$$

$$(A10) \quad U(x) = \begin{cases} 1 \\ 0 \end{cases} \quad \text{for} \quad \begin{cases} x > 0 \\ x < 0 \end{cases}.$$

The coefficients  $D_{1v}$ ,  $D_{2v}^{PO}$  result from  $D_{1v}$ ,  $D_{1v}^{PO}$  by the following transformations:  
 $v_e \rightarrow \pi - v_e$ ,  $\beta_e \rightarrow \pi - \beta_e$ .

## REFERENCES

- [1] Klement, D. Computation of the Scattering Preissner, J. Matrix of Radar Targets: Concept of the Method and First Results. AGARD Conference on Target Signatures, London, Oct. 1984, Conference Print CP 364, pp. 20-1 to 20-22 (unclassified).
- [2] Klement, D. Special Problems in Applying the Preissner, J. Physical Optics Method for Backscatter Computations of Complicated Objects. IEEE Trans. on Ant. and Prop., Vol. 36, No. 2, Febr. 1988, pp. 228-237.
- [3] Mitzner, K.M. Incremental Length Diffraction Coefficient. Aircraft Division Northrop Corp., Tech. Rep. No. AFAL-TR-73-236, 1974.
- [4] Michaeli, A. Equivalent Edge Currents for Arbitrary Aspects of Observation. IEEE Trans. on Ant. and Prop., Vol. AP-32, No. 3, March 1984, pp. 252-258.
- [5] Michaeli, A. Elimination of Infinities in Equivalent Edge Currents, Part I: Fringe Current Components. IEEE Trans. on Ant. and Prop., Vol. AP-34, No. 7, July 1986, pp. 912-918.
- [6] Ufimtsev, P.Y. Method of Edge Waves in the Physical Theory of Diffraction. Foreign Technology Division, FTD-HC-23-259-71, Translation, AD 733203, Reproduced by National Technical Information Service, Springfield, Va. 22151, 1962.
- [7] Stein, V. Beziehungen zwischen bekannten Theorien zur Behandlung der Beugung an der Kante im Hochfrequenzfall. DLR-FB 89-49 (1989).
- [8] Ross, R.A. Radar Cross Section of Rectangular Flat Plates as a Function of Aspect Angle. IEEE Trans. on Ant. and Prop., Vol. AP-14, No. 3, 1966, pp. 329-335.
- [9] Ruck, G.T. Radar Cross Section Handbook, Vol. 1. Plenum Press, New York, London, 1970, p. 310.



## DISCUSSION

G. Neininger, GE

1. To what lower frequency end could the method be used?
2. What is the frequency sensitivity of the periscope characteristic?

Author's Reply

1. The efficiency of the method is only limited by the object's dimension related to the wavelength. The analysis of the thin cylinder shows that even in the case where the diameter of the cylinder amounts to one wavelength, good results are obtained.

2. The analysis of the periscope is not yet finished; measurements require a high effort. The results are presented for the first time in this session.

U. Lammers, US

Referring to your periscope model: 1. How much computer time did it require, and 2. Why did the physical optics solution suffice?

Author's Reply

1. The computer (IBM 3091) time is about 0.14 sec per aspect angle.

2. The main contribution to RCS is due to the ogival cylinder and the swell deflecting panels. Both structures are very large compared to the wavelength, so edge diffraction effects play a minor role.

# Aspects of Radar-Cross-Section Calculation for Targets of Complex Structure

KKpt Dr.-Ing. O. Weiland, Dipl.-Ing. J. Wendiggensen  
University of German Armed Forces Hamburg  
Institute of Automation  
Holstenhofweg 85  
D-2000 Hamburg 70  
F.R.G.

## Abstract

Minimizing the Radar Cross Section (RCS) of a new warship, it is important to determine the expected RCS in the phase of design because of high development costs. Furthermore it is desirable to identify design dependent scattering centers and analyse their mode of action. This is probably done most effectively by a graphical representation of the scattering mechanisms on a 3-dimensional drawing of the target itself. The paper summarizes the development of a computer code that combines graphical representation methods with well established theoretical techniques to predict the RCS for targets of complex structure. The tool is based on physical optics, physical theory of diffraction, ray tracing and it accounts for multiple shadowing and scattering up to triple bounce. The method of component technique using primitives is applicable to electrically large bodies and the calculation is limited to the monostatic case for perfectly conducting surfaces. Object coherence is used to reduce computation time during the solution of the hidden surface problem.

## List of symbols

$\vec{E}_I$	incident electric field vector
$\vec{E}_S$	scattered electric field vector
$F_S$	surface
$F_S^*$	illuminated surface
$\vec{H}_I$	incident magnetic field vector
$\vec{H}_S$	scattered magnetic field vector
$H_0$	magnetic field strength
$\vec{J}_{F_S}$	induced surface current
$\vec{J}_{F_S}^*$	induced surface in the illuminated area wavenumber
$\hat{k}$	propagation unit vector

$\hat{k}$	pointing vector
$\hat{l}_H$	magnetic polarisation vector
$\hat{n}$	unit normal vector
$\hat{n}$	unit normal vector at the point of integration
$\hat{n}^*$	unit normal vector at the integration point in the illuminated area
$R$	range
$\vec{r}$	position vector to the observation point
$\vec{r}'$	position vector to the integration point
$\vec{r}^*$	position vector to the integration point in the illuminated area
$\sigma$	radar cross section
$\phi$	free space Green's function

## 1. Introduction

Induced by the development of more and more sensitive radar systems, stealth is seen as one of the key military technologies of the nineties and has attracted a high level of defence funding. Predicting the radar signature of military vehicles has become an important top in every stealth program, because of the ability to prove the expected RCS in an early state of design. Compared with scale measurements, where every change in design forces a new model, theoretical modelling of the target seems to be a more attractive solution.

In addition to the modelling, this way requires the calculation of the expected RCS by a well established technique like Physical Optics (PO). Therefore the theoretical foundations have been developed in the past, permitting the calculation of RCS-signatures, based on a range of asymptotic formulations of electromagnetic scattering, for well-shaped targets [1-2]. In most cases the prediction of the RCS is limited to simple geometries not more than a hundred wavelengths long, neglecting multiple interaction and shadowing effects. With large complex tar-

gets, up to thousands of wavelengths, this is no longer true. For increasing amounts of individual scatterers and interactions, the main problem is to separate visible and effective components from those which do not contribute to the target's RCS at a given aspect. To investigate solutions to this problem, a computer program has been developed at the German Armed Forces University, Hamburg.

The program is divided into two parts; the first one creates a data-based new structure of the model, (a priori database) including structure properties independent of the radar line of sight, using object coherence. The second part solves the hidden surface problem, using the a priori database to reduce computing time during the variation of the aspect. Different graphic features are included to explain the scattering mechanisms on a perspective drawing of the target itself.

## 2. Target Modelling and Presentation

The program is based on the method of components technique using primitives. This technique is applicable to electrically large bodies, that is,  $k \cdot L \gg 1.0$ , where  $k = 2\pi/\lambda$  is the wavenumber and  $L$  the maximum dimension of the component. The designer can break the complex target into a set of components. The shape of each component is then approximated by one or more of the following primitives:

- triangular and quadrangular flat plates,
- cylinders,
- cones and truncated cones,
- elliptical cylinders,
- elliptical cones and truncated cones.

Consider, for example, the funnel of a ship. This component is usually modelled using two cylinders, describing the front and aft curvature, and a few flat plates representing the port, starboard and top faces [Fig. 1]. If the component's length is too large, or its shape may not be approximated sufficiently correctly, a description in terms of triangular and quadrangular flat plates only, is preferred. Therefore the flat plate is the primitive used most.

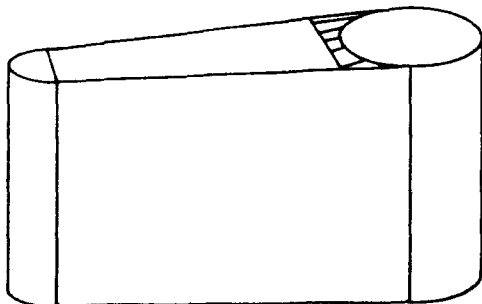


Fig. 1: Funnel of a ship, modelled in terms of plates and cylinders only.

Each primitive is defined by his own characteristics. A flat plate is defined by three or four points and their order to form the outward unit normal  $\hat{n}$ . A singly curved surface like a truncated cone, is defined by the top and bottom central points and the related radii  $r_t$  and  $r_b$ .

There are some restrictions concerning flat plates, if it is a quadrangular one, the four points have to lie in a plane creating a convex polygon. This is because there is some comfort in solving the hidden surface problem for convex structures. Straight wedges, which represent a new primitive, may be extracted automatically by the program, thus there is no need to model them explicitly. The program takes as its primary input a digital description of the target geometry from six databases. The first one contains all defined points, represented by their location in x-, y-, and z-direction of a global system. The remaining five refer to these points and offer additional information like radii, separate for each primitive.

During the creation of the a priori database, the description of the primitives is not changed. As we will see, singly curved primitives are replaced by polygons, representing the outer envelope, during the hidden-surface and shadowing algorithm. The errors induced by this approximation do not justify the increased cost solving the hidden surface problem for curved lines.

Solving the hidden surface problem at a given aspect forces a new description of the primitives. Partially shadowed primitives have to be substituted by their visible rest, to get the remaining area for PO integration. Induced by successive checking the shadowing effect for a primitive, it might occur that the visible rest of this primitive is partially shadowed again by another primitive. This repeating process leads to a successive substitution of the visible rest. No matter how often the primitive is shadowed, only the visible rest of a primitive (rest-polygon) has to be checked for shadowing. In general this rest-polygon is a non-convex polygon. To avoid code extensions and using the advantage of convex polygons, the rest-polygon is splitted into convex polygons, called sub-polygons. Instead of the rest-polygon the related sub-polygons have to be checked for shadowing in the next step. To handle this successive process it is useful to apply terms like 'mother' to the original primitive and 'child' to the sub-polygon. Thus every generation with no descendant has to be checked in the next step. Once the hidden surface problem for a primitive is solved, their might be a tree of generations behind the mother, describing the visible rest in terms of convex polygons in his 'youngest' child generation.

The outer envelope of a singly curved primitive is a convex polygon, because of the convexity of the original description. The only difference from the description of a flat plate is the higher number of points, used to form the envelope. As described in section 3, all tests to extract the rest polygons or the common areas of two polygons are performed in a

plane, thus everything is reduced to a 2-dimensional point of view. The only exception is a test, which determines the position of a polygon with regard to another polygon in the third dimension.

### 3. Scattering calculations

As they are well established, optics-based RCS-prediction methods were chosen for the code. Physical optics is one of the most robust calculation techniques for scattering problems and represents a solution to Maxwell's equations at high-frequency, where the accuracy should improve as the target size increases. In specular and near-specular direction the prediction is good, but disintegrates as the scattering direction moves away from this region [3], [4]. In regions outside specular directions the neglect of higher order effect, such as diffraction and the creeping wave effect, is no longer true. Fortunately, targets of complex structure are dominated by specular effects, this can be proved by RCS-distribution techniques. Thus PO is sufficient for complex targets. Analyzing small components or single scattering centers, other prediction techniques are required to overcome the weakness of physical optics.

One method, the physical theory of diffraction (PTD) has been developed by Ufimtsev [5], who improved the physical optics prediction for a flat plate by adding a non uniform current, located to a flat plate's edges, to the uniform surface component in the PO. Mitzner [6] extended Ufimtsev's theory in 1974 by the concept of his incremental length diffraction coefficient (ILDC), giving the field of the edge alone [7]. The other one, the method of equivalent currents (MEC), suggested independently by a number of authors [4], [8-9], has been extended by Michaeli to arbitrary aspects of observation [10]. The integrative technique MEC describes the source of the diffracted field in terms of fictitious equivalent electric and magnetic currents along the edge. The fact that only line integrals are involved tend to make the MEC more suitable for practical calculations than the PTD. To analyze scattering centers in detail one of the described methods is currently implemented, together with a preprocessing algorithm to extract the wedges automatically. Thus the presentation is limited to complex structures.

The usual definition of the radar cross section is

$$\sigma = 4\pi \lim_{R \rightarrow \infty} R^2 \frac{|E_S|^2}{|E_I|^2} = 4\pi \lim_{R \rightarrow \infty} R^2 \frac{|H_S|^2}{|H_I|^2}, \quad (1)$$

where  $R$  is the distance between the radar and the target,  $E_I$  and  $E_S$  are the incident and scattered electric fields, and  $H_I$  and  $H_S$  are the magnetic fields respectively. The scattered magnetic field for a perfectly conducting surface is given by [11]

$$\vec{H}_S(\vec{r}) = \frac{1}{4\pi} \int_{F_S} [\vec{J}_F(\vec{r}') \times \nabla' \cdot \phi(\vec{r}', \vec{r})] \cdot d\vec{r}', \quad (2)$$

where

$$\phi(\vec{r}', \vec{r}) = \frac{e^{-j \cdot k \cdot |\vec{r}' - \vec{r}|}}{|\vec{r}' - \vec{r}|} = \frac{1}{R} e^{-j \cdot k \cdot R}$$

is the scalar free-space Green's function, and

$$\vec{J}_F(\vec{r}') = \hat{n}' \times \vec{H}(\vec{r}') \quad (3)$$

is the induced surface current. Applying the farfield approximation to the Green's function and replacing  $\vec{J}_F$  with the geometric optic current

$$\vec{J}_F(\vec{r}') = \begin{cases} 2 \cdot \hat{n}' \times \vec{H}_I(\vec{r}'), & \text{on } S \text{ illuminated} \\ 0, & \text{otherwise} \end{cases}$$

yields to

$$\vec{H}_S(\vec{r}) = \frac{2j \cdot k \cdot e^{-j \cdot k \cdot r}}{4\pi r} \int_{F_S} \left[ \hat{n}' \times \vec{H}_I(\vec{r}') \right] \times \hat{r} \cdot e^{j \cdot k \cdot \vec{r} \cdot \vec{r}'} \cdot d\vec{r}' \quad (4)$$

The integration is to be carried out over the illuminated part  $F_S^*$  of  $S$ . Replacing the incident magnetic field with

$$\vec{H}_I(\vec{r}, t) = H_0 \cdot \hat{H} \cdot e^{j \cdot (\omega \cdot t - \vec{k} \cdot \vec{r})}, \quad (5)$$

suppressing time harmonic terms and examining the monostatic case with

$$\vec{r} = -\vec{R} = -|\vec{R}| \cdot \hat{k},$$

yields to

$$\vec{H}_S(\vec{r}) = -H_0 \cdot \hat{H} \cdot \frac{2j \cdot k \cdot e^{-j \cdot k \cdot r}}{4\pi r} \int_{F_S^*} \left[ \hat{k} \cdot \hat{n}' \right] \cdot e^{-2j \cdot k \cdot (\hat{k} \cdot \vec{r}')} \cdot d\vec{r}' \quad (6)$$

The integral in (6) is calculated following Gordon's method [12], for every illuminated polygon, and the total RCS from  $N$  illuminated polygons is thus

$$\sigma = 4\pi \lim_{R \rightarrow \infty} R^2 \frac{\left| \sum_{n=1}^N \vec{H}_S \right|_n^2}{|H_I|^2} \quad (7)$$

RCS calculation of singly curved primitives is based on the method of stationary phase, for totally illuminated primitives near vertical incidence with respect to

the main axis. Partitionally illuminated primitives or non vertical incidences are treated in a more complicated way, by substituting the original primitives with a paneled equivalent. Each panel is calculated like a flat plate. The substitution is done automatically with a tolerance of  $\lambda/16$  to the original figure.

If the hidden surface problem is solved the illuminated part of a primitive is represented by a polygon, as described in section 2. To calculate the double- and triple bounce contribution, geometric optics (GO) ray tracing is applied. Therefore the area of both polygons involved is projected onto a plane formed normal to the reflected propagation (projection plane) vector [Fig. 2]. The common area is found using the algorithm in [13]. This area is projected back onto the final plates' plane. For triple bounce this process is repeated. Once the effective illuminated area has been found for the final plate, the integration is carried

out by substituting  $H_i(\vec{r}^*)$ ,  $\hat{l}_H$ ,  $\hat{k}$  in (4) with

$$H_{I,i}(\vec{r}^*) = H_0 \cdot \hat{l}_{H,i} \cdot e^{-j \cdot \vec{k} \cdot [\vec{k} \cdot \vec{r}_i + \vec{k}_i \cdot (\vec{r}^* - \vec{r}_i)]},$$

$$\hat{l}_{H,i} = \hat{l}_H - 2 \cdot (\hat{l}_H \cdot \hat{n}_i) \cdot \hat{n}_i,$$

$$\hat{k}_i = \hat{n} - 2 \cdot (\hat{k} \cdot \hat{n}_i) \cdot \hat{n}_i, \text{ where } i$$

indicates the  $i$ -th reflection.

#### 4. Structure immanent properties

For a complex structure, consisting of  $N$  primitives, the hidden surface problem has to be solved  $N(N-1)$  times, after fixing the aspect. This is directly related to a quadratic rise in computation time, with an increasing number of primitives. Several methods to reduce computation time, after fixing the aspect, have been developed in the past (see [14] for example).

A fundamentally different way is to analyze the structure independent of the line of sight. The goal is to extract structure immanent properties and define them in statements like: "primitive  $a$  is never shadowed by primitive  $b$ , independent of the aspect." Those constant properties are called object coherence. Consider a convex polyhedron consisting of  $N$  faces, the primitive representation would be a set of  $N$  flat plates, as described in section 2. After fixing the aspect the primitives are sorted according to their normals, having a non vanishing component in the backscatter direction. This simple test solves the hidden surface problem completely. No plate with a non vanishing component of the normal in the backscatter direction is shadowed by another plate, because of the convex structure. If this is recognized, further tests would not be required and the efficiency of the a priori-test is maximal.

Unfortunately complex structures are not convex, but they include convex components. For components consisting of a set

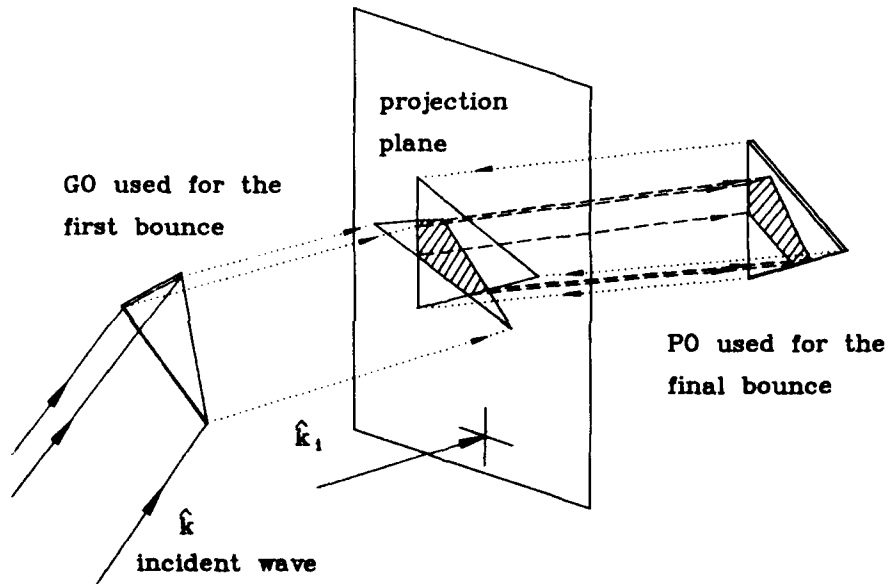
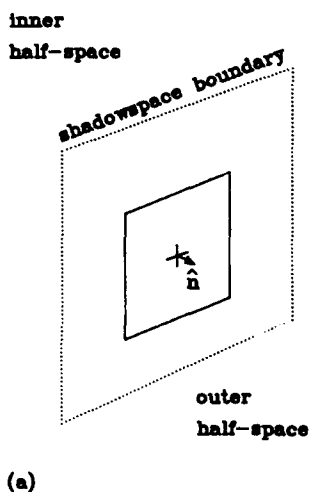
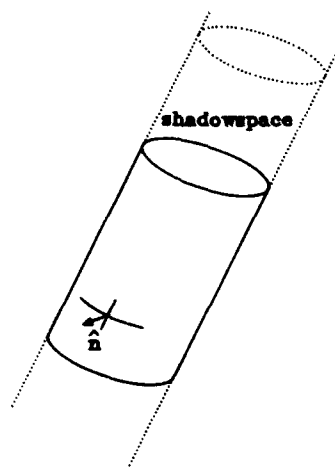


Fig. 2: Area projection method, finding the common area of two triangular plates.

of primitives, the same assertion as for the polyhedron is valid. The reasonable view could be replaced by the statement: "a primitive could never be shadowed by another primitive, if this is located within the shadowspace of the first". A shadowspace is the infinite half-space located at the flat plates' inner side; the infinitely long inner side cylinder is the shadowspace of a material cylinder, which is in fact only a cut of the shadowspace, [Fig. 3].



(a)



(b)

Fig. 3: Shadowspace, inner and outer half-space for a flat plate (a), and a cylinder (b).

The possible combinations of primitives lead to a number of tests, related to their describing geometric properties. Consider a target consisting of cylinders and plates only, like the funnel of a ship above, following tests have to be done.

describing geometric property	shadowspace	
	half space	infinitely cylinder
point	point-plane-test (PP)	point-cylinder-test (PCY)
circular arc	circle-plane-test (CP)	circle-cylinder-test (CCY)

The location of a point relative to the shadowspace leads to one of three possible statements:

1. The point is not located in the shadowspace.
2. The point is located in the shadowspace.
3. The point is located at the shadowspace-boundary.

Within the meaning of the a priori test, 1. defines a negative, 2. and 3. a positive conclusion of the test. The combination of two primitives determines how many times which test has to be performed. Describing the tests is not within the scope of this paper, but it is worth knowing that a complex geometric description of a primitive is related to an increasing test routine. The shadowspace-test reduces the number of required operations at a given aspect to about 10 % of the original value without a priori tests.

Up to now invariable properties have been extracted; furthermore it is of great use to extract properties being invariable within certain aspect boundaries, called frame-to-frame coherences. This permits checking the visibility of the boundary primitives, instead of every primitive, of a convex component only. This is not described here.

Concerning multiple scattering and shadowing, there are certain properties independent of the radar line of sight. The multiple scattering contribution is primarily expressed in terms of facet-facet interaction. The most simple interaction is the double-bounce effect, with two flat plates being involved. Furthermore it is the base for higher order interactions. The plate pairs that might contribute to multiple scattering are sorted according to a simple test, concerning the scalar product of their normals. Pairs of plates may illuminate each other if the normal test,

$$\hat{n}_1 \cdot \hat{n}_2 > 0$$

is true.

The output of this test is a list of pairs, which may illuminate each other, independent of the line of sight. The rays between the two plates may be obstructed by another primitive, thus there is a secondary hidden surface problem in the reflected radar line of sight. Since the aspect is not fixed, all possible reflected rays have to be taken into account. This is done by constructing a convex polyhedron between the two plates and testing the location of all primitives, in the outer half-space of both, with regard to their location to the polyhedron.

For every pair of plates exists an intersection line of their planes, after carrying out the normal test. The location of a plate relative to this intersection line leads to one of the following two statements:

- one plate of the pair is cut by the intersection line, thus one part of the cut plate is located in the

outer half-space, the rest in the shadowspace of the other plate,

- the intersection line does not cut the plate and the plate is located in the outer half-space of the other plate.

In the first case only the part located in the outer half-space is of interest. The polyhedron is built up between this part, the whole plate in the second case, and the other plate following the algorithm described in [13]. In any case the polyhedron is convex, because only convex ground plates are used. Now every primitive, located in the outer half-space of both plates, is tested in a minmax-routine against the outermost coordinates of the polyhedron. This reduces the number of primitives for the following tests. In a second step it is checked whether one plate cuts the polyhedron totally or not. If this is true, no interaction between the two plates is possible and the pair of plates can be deleted. If not, the location of every remaining primitive is tested in relation to the faces of the polyhedron. This test is very similar to the shadowspace-test, because of the convexity of the polyhedron. Every primitive projecting into the polyhedron might obstruct the raypath and is stored in an obstruction list, related to the pair of plates being checked.

Calculating the double bounce contribution after fixing the aspect leads to the following procedure. At first, the visibility of the pairs of plates is tested. Both plates have to be visible, to get a double bounce contribution, thus all other combinations are rejected. The rejection includes a normal incidence on one of the two plates. In a second step the common area in the projection plane is determined, as described in section 3. Then every primitive in the obstruction list of the pair is projected onto the projection plane to determine the shadowing of the common area. The number of primitive pairs and obstructing primitives which have to be regarded at fixed aspects is reduced to ~ 0.2 % of the theoretical value.

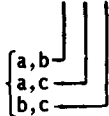
Once the list of possible pairs and the related obstruction list is found, the next a priori test is to extract possible triples of pairs contributing to triple bounce effects. It is easy to understand, that this is done, using the list of pairs as a base for the test. The list is searched for three pairs with one or two equal plate(s) in two of the three pairs. Those pairs form a triple with their different plates, permutations of a triple are only stored once. The triples are marked, whether double bounce is possible between two plates or not. For example:

list of pairs	extracted pairs	triples	marking
⋮			
(5,6)	(5,6)	} → (5,6,8)	1 1 1
(5,7)	(5,8)		
(5,8)	(6,8)		
⋮			

$$\begin{matrix} (6,1) & (5,6) \\ (6,8) & (5,7) \end{matrix} \} \rightarrow (5,6,7)$$

$$\vdots$$

indicating double bounce between



In a next step open cavities formed by two plates are extracted from the list of pairs. This is done by testing the scalar product of their normals, being greater than zero.

Triple bounce calculation, after fixing the aspect, is retracted to a recurrence double bounce calculation. Therefore all possible permutations, which represent the six different raypaths of a triple are determined. The related double bounce marking of a triple is permuted, too. The relationship between the visibility for each plate of a triple and the double bounce marker determines, which of the six raypaths have to be taken into account. For a full visible trihedral corner-reflector, all six raypaths contribute to the backscatter RCS.

##### 5. Graphical presentation techniques

The final areas, the common areas in the case of double and triple bounce and the partially shadowed or visible primitives in the case of single bounce, build up the base for a graphical representation of the scattering mechanisms. These areas are projected onto the viewing plane, figuring the target as a parallel projection viewed from the infinity. Single, double and triple bounce effects are treated separately to avoid confusion.

Single bounce contributing areas are filled solid, if they are shadowed and striped, if not. The color depends on the direction of the scattered field. For partially shadowed singly curved surfaces the region of specular return is marked. Double and triple bounce effects are analyzed by projecting the common area onto the final plate (Fig. 4). The difficult raytracing for triple bounce effects may be plotted separately for small components (Fig. 5a-f).

The final areas do not represent the scattered field, because of possible overlapping of the areas. A false color image of the scattered field is generated by determining the overlapping areas and calculating new RCS values for this areas. This has to be done for the remaining areas also. The total RCS of an overlapping area is found by summing all contributions within this areas.

Other graphical features like radial and cumulative distribution of the scattering centers are included. The total amount of graphical presentation offers the unskilled user an easy understanding of the scattering mechanisms. The ability to identify scattering centers and analyze their mode of action, makes it easier changing the design to get a 'low observable' target.

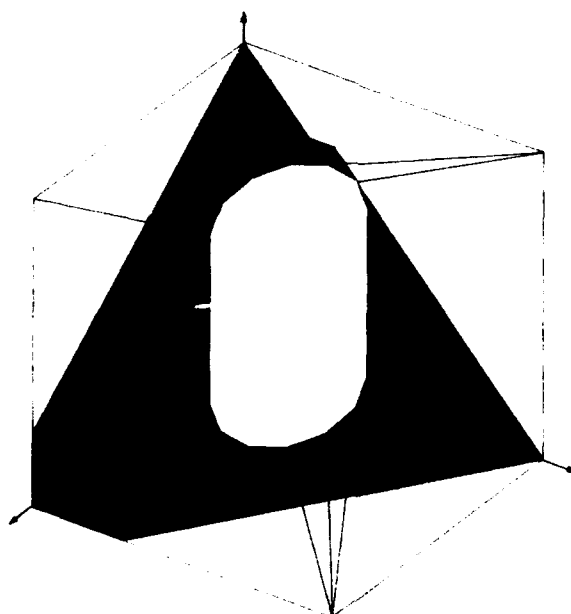
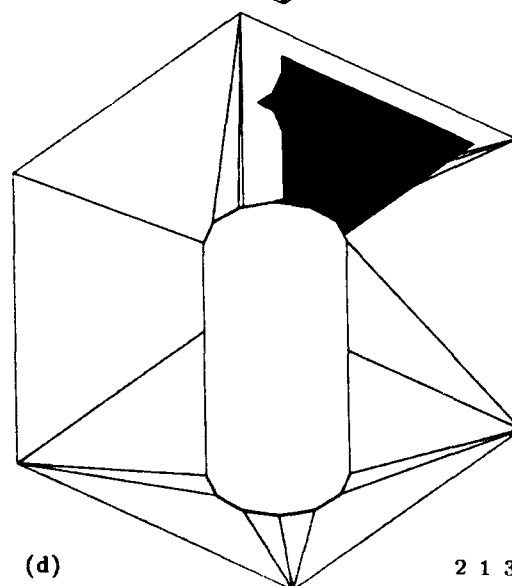
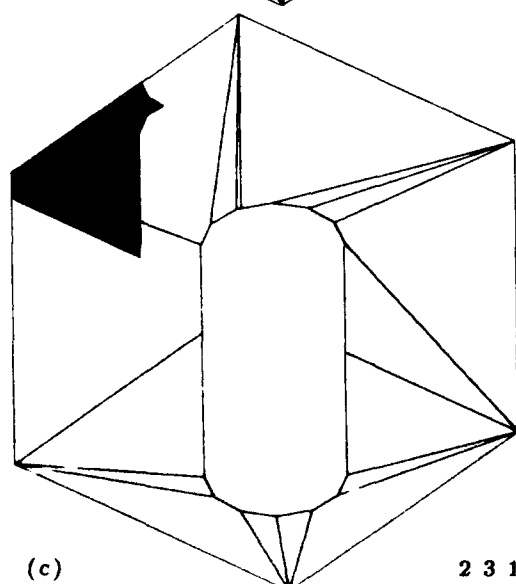
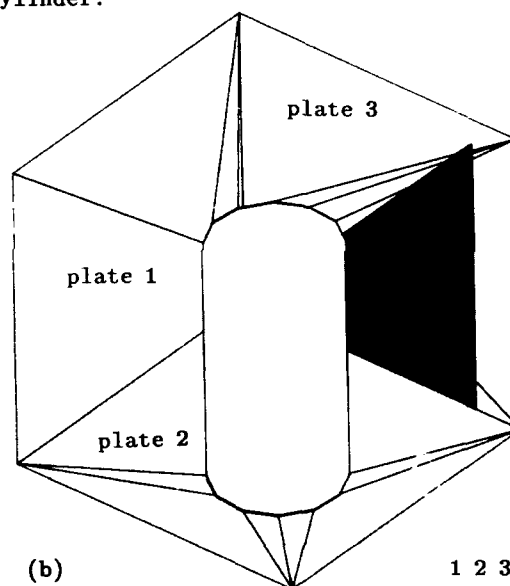
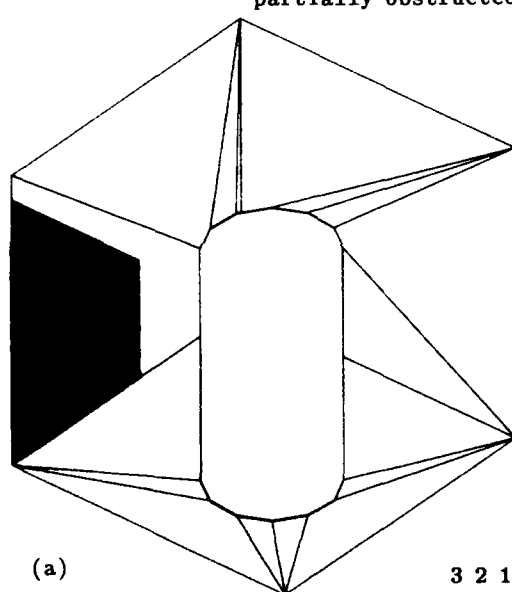


Fig. 4: Final PO integration areas for a trihedral corner, partially obstructed by a cylinder.





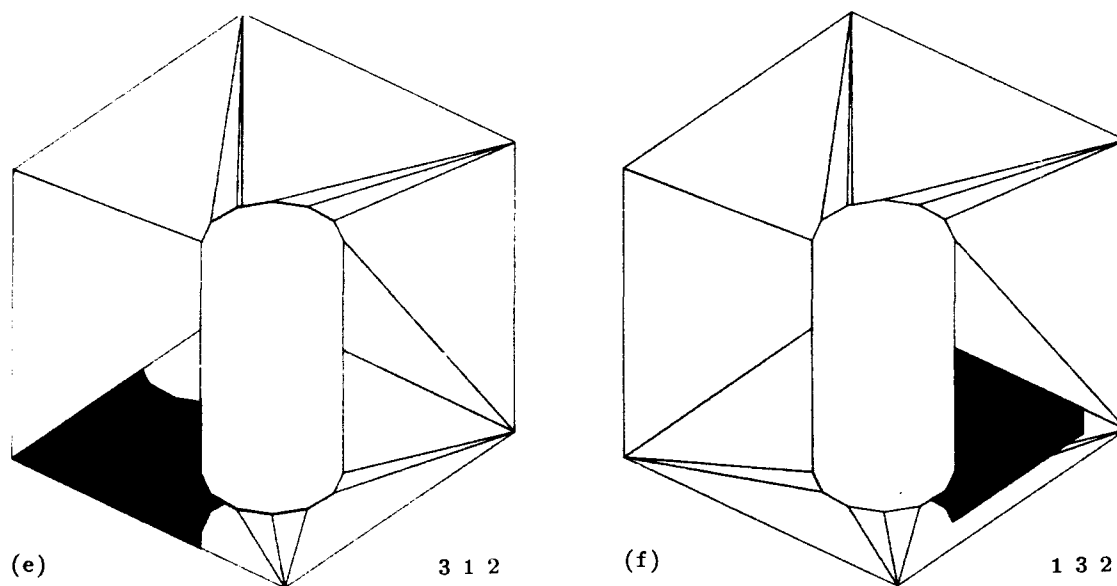


Fig. 5: Separated ray tracing. The order of the plate numbers indicates first, second and final bounce.

## 6. Results

This section presents some results obtained using the computer RCS prediction program described above. A flat plate model of the new frigate F 123 has been chosen to illustrate the capabilities of this approach [Fig. 6]. The model is viewed from  $-16.0^\circ$  azimuth and  $6.0^\circ$  elevation. The representation is limited to 652 flat plates. Partially shadowed primitives are substituted by sub-polygons as described in section 2. Those plates may be identified by additional lines from one edge to the intersection point(s) of the shadowing primitive.

A single bounce graphical representation of the model is shown in Fig. 7. The main contributions to the total RCS are marked with horizontal stripes. Within this group of scatterers, the triangular flat plate of the port funnel is identified to give the main contribution. 402 convex sub-polygons are needed to extract the visible rest of partially shadowed flat plates.

Fig. 8 shows the double bounce representation for two aspects. The PO integration areas are filled solid. Some parts of the superstructure deck are illuminated from different plates in the same area. Thus there are different PO integration areas that have to be taken into account. The viewing position in (b) offers a good understanding of the double bounce scattering mechanism. Because of the oblique

arrangement of the hangar gate, the illumination is only in the direction from the hangar deck to the hangar gate. The illuminated area in the upper right corner of the top component is projected from the port funnel's top face. Several corners, formed by the deck buildings, are identified by the program to give the main contribution to the total RCS. In comparison to the single bounce case this corners are the dominant scatterers. Not assumed dihedral corner reflectors are identified to lie at the maneuver deck.

Azimuthal sweeps from  $0^\circ$  to  $180^\circ$  at an elevation angle of  $7^\circ$  are shown in Fig. 9. The prediction is calculated for a frequency of 3 GHz with horizontal polarization of transmitter and receiver. The solid line is corresponding to the relative phase method, the plus sign markers are corresponding to the random phase method. The single bounce sweep (a) and the double bounce sweep (b) are calculated in intervals of  $0.25^\circ$ . The distinct difference between single and double bounce contribution is shown, particularly for rear aspects of observations. The CPU time taken by the program, when running on a SUN 4/330, to calculate the RCS at each aspect angle is 4.57 seconds for the frigate F 123 model in the case of single bounce and 10.2 seconds for double bounce. This is related to a computation time of 0.007 seconds for a single facet at a given aspect for one frequency and polarisation.

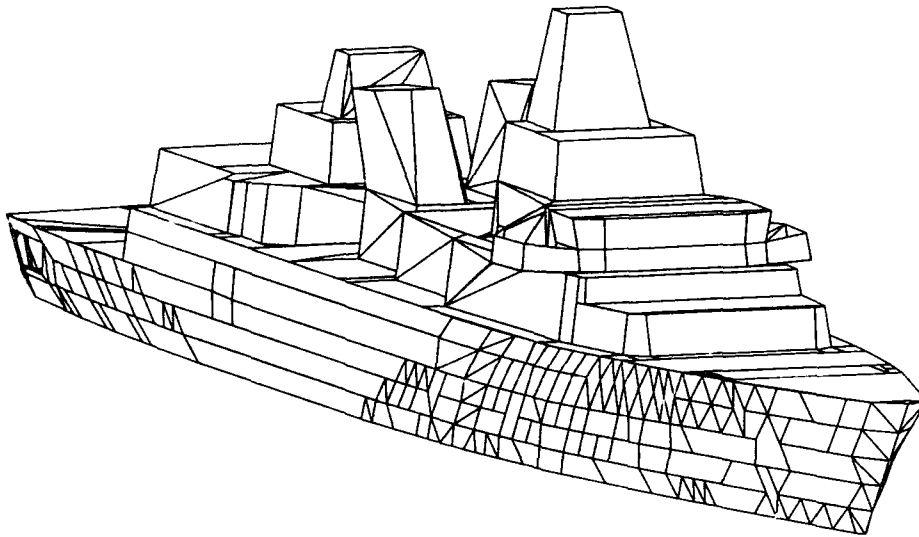


Fig. 6: Fregate F 123 model, represented in terms of flat plates only.

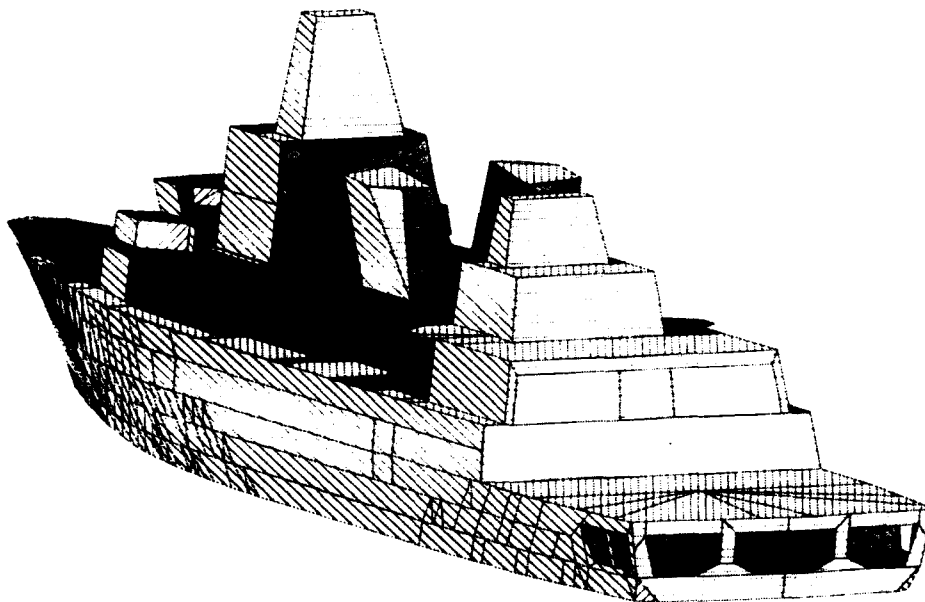
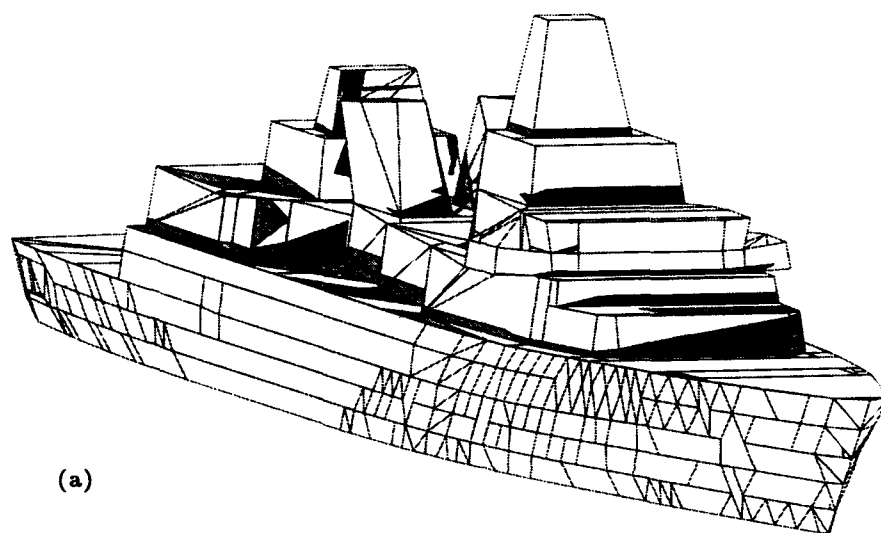
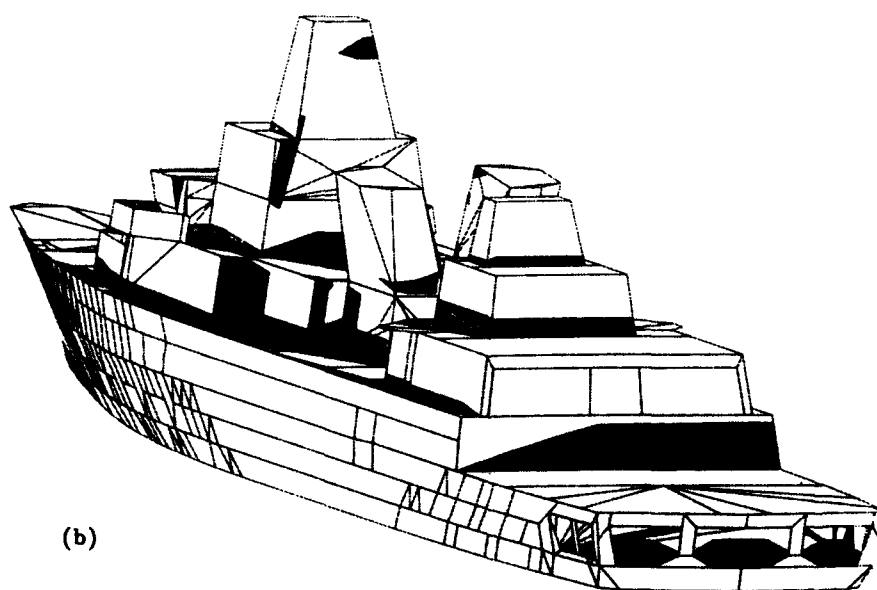


Fig. 7: Single bounce graphical representation of the fregate F 123 model. Viewed from 165° azimuth and 5° elevation.



(a)



(b)

**Fig. 8:** Double bounce graphical representation of the frigate F 123. Viewed from -15° azimuth and 5° elevation (a). Viewed from 165° azimuth and 5° elevation (b).

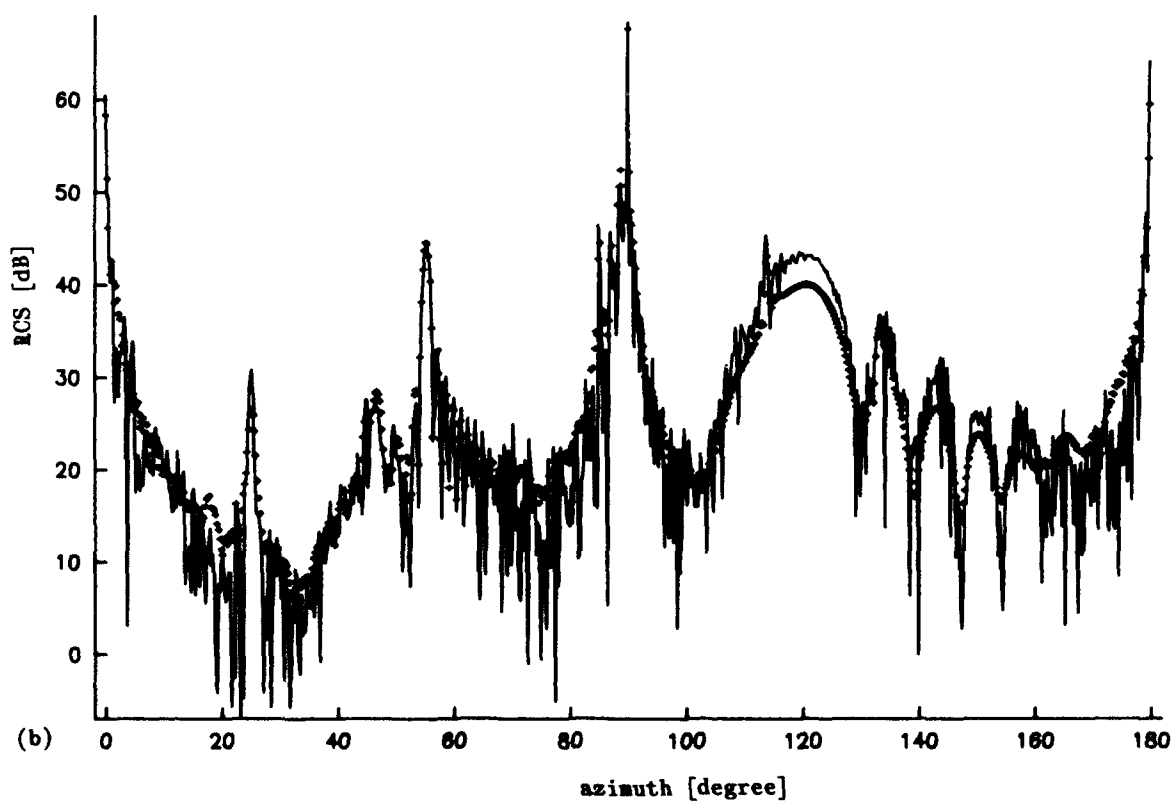
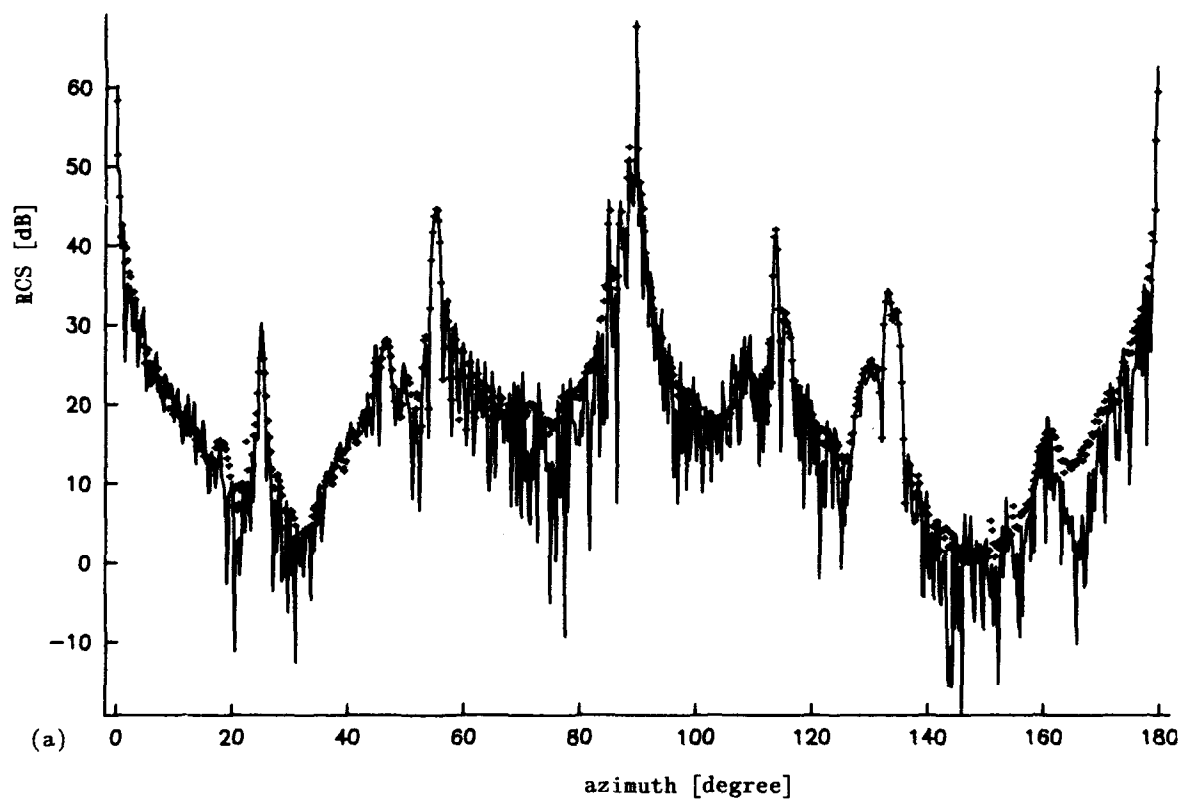


Fig. 9: RCS diagrams for an azimuthal sweep from 0°-180° at an elevation of 7°. Single bounce (a). Double bounce (b).

## 7. Conclusion

The a priori test method described above is presented as a possible solution to reduce computing time during the variation of the aspect for RCS predictions. Structure immanent properties are used to reduce the number of primitives to be checked. These properties are extracted for single, double and triple bounce independent of the radar line of sight. The GO-PO prediction technique combined with graphical presentation techniques offers the unskilled user a good understanding of different scattering mechanisms. The user can extract a local scattering center and study it in detail separately. This allows him to determine the effects of design changes within a few minutes, allowing an interactive approach.

## References

- [1] Ruck, G.T. et al.: Radar Cross Section Handbook. Vol. 1 + 2, New York, Plenum 1970.
- [2] Crispin, J.W.; Maffet, A.L.: Radar cross section estimation for simple shapes. Proc. IEEE Vol. 53, August 1965, pp. 833-848.
- [3] Ross, R.A.: Radar cross section of rectangular flat plates as a function of aspect angle. IEEE Trans. Antennas Propagat. Vol. AP-14, No. 8, May 1966, pp. 329-336.
- [4] Ryan, C.E. and Peter, L.: Evaluation of edge diffracted fields including equivalent currents for the caustic regions. IEEE Trans. Antennas Propagat., Vol. AP-17, No. 3, May 1969, pp. 292-299.
- [5] Ufimsev, P.Y.: Method of edge waves in physical theory of diffraction. Trans. by U.S. Air Force Forgein Tech. Div., Wright-Patterson, AFB, OH, 1971.
- [6] Mitzner, K.M.: Incremental length diffraction coefficients. Aircraft Div. Northrop Corp. Tech. Rep. No. AFAL-TR-73-296, April 1974.
- [7] Knott, E.F.: The relationship between Mitzner's ILDC and Michaeli's equivalent currents. IEEE Trans. Antennas Propagat. Vol. AP-33, No. 1, January 1985.
- [8] Clemmow, P.C.: Edge currents in diffraction theory. IEEE Trans. Antennas Propagat. Vol. AP-4, July 1956, pp. 282-287.
- [9] Millar, R.F.: An approximate theory of the diffraction of an electromagnetic wave by an aperture in a plane screen. Proc. IEE Vol. 103, March 1956, pp. 177-185.
- [10] Michaeli, A.: Equivalent edge currents for arbitrary aspects of observation. IEEE Trans. Antennas Propagat. Vol. AP-23, No. 2, March 1984, pp. 252-258.
- [11] Stratton, J.A.: Electromagnetic Theory. New York, McGraw-Hill, 1941.
- [12] Gordon, W.B.: Far-field approximation to the Kirchhoff-Helmholz representations of scattered fields. IEEE Trans. Antennas Propagat. Vol. AP-23, No. 5, July 1975, pp. 864-876.
- [13] Weiland, O.: Ein Algorithmus zur Berechnung des Radarquerschnittes von Schiffen auf der Grundlage einer Modellierung mit verschiedenen Basiskörpern. Dissertation 1990, University of the German Armed Forces.
- [14] Galimberti, R.; Montanari, U.: An algorithm for hidden line elimination. Communications of the ACM, Vol. 12, No. 4, April 1969, pp. 206-211.

## DISCUSSION

### A. Altintols, TU

Since you are using physical optics for the scattering calculation, it seems to me that on a parallel computer, the computations can be made faster. Can you make a comment on that?

### Author's Reply

Most of the time is used to solve the hidden surface problem. Depending on the approach we have to do this primitive after primitive. Thus parallel computing could only be used after the hidden surface problem is solved.

### L. Oldfield, UK

The use of large simply curved surfaces to construct your model ship may yield falsely low values of RCS. Do you plan to extend your method to include perturbations of the surfaces to give improved representation of a real ship?

### Author's Reply

Yes, we plan to do this, and then we have to include all the effects Dr. Stein spoke about. This has been the first step to get and analyze the specular effects only.

### U. Lammers, US

Do you use experimental imaging to verify your computation models?

### Author's Reply

No, we only use geometric optics.

## RCS calculations of 3-dimensional objects, modeled by CAD

I. De Leeneer  
Royal Military Academy  
Dept of Mathematics  
30, Renaissance Avenue  
1040 BRUSSELS - Belgium

E. Schweicher  
Royal Military Academy  
Dept of Opto-Electronics and Microwaves  
30, Renaissance Avenue  
1040 BRUSSELS - Belgium

A. Barel  
Vrije Universiteit Brussel  
Applied Sciences-dept ELEC  
Pleinlaan 2  
1050 BRUSSELS-Belgium

### 1 Summary

The aim of this work is to detail all the steps, that one has to perform to enable efficient Radar Cross Section calculation for objects with a complex and general shape. Only cavities are supposed to be non existent at this state of the work. Before the actual Radar Cross Section calculations, preliminary treatments like systematic modeling, Hidden Faces removal, and automatic recognition of reflection and diffraction centres are realised. After the creation of the object's geometry, and its adaptation to the direction of the observator, we use Physical Optics (PO) to determine the backscattered field, and Geometrical Theory of Diffraction (GTD) to evaluate the diffracted fields. Only monostatic scattering (i.e back-scattering) will be considered.

### 2 General

If RCS measurements are impossible or too expensive, or if shaping is investigated for stealth purposes, computer simulation becomes a very interesting alternative to RCS determination. To perform this latter, several methods were developed. Briefly summarized [5, 6, 7, 8], we have on one hand the Method of Moments (MoM), which is too time and memory consuming if large objects are studied, but gives correct results in "near field" situations, and on the other hand Physical Optics (PO) and Geometrical Optics (GO), two high frequency approximation methods which allow fast calculations with acceptable results, assuming the object is in far field conditions. If plane surface patches (triangles) are used for the modeling of the object, Physical Optics becomes the most interesting method. The Radar Cross Section of the complete three-dimensional body is obtained by summing up the complex amplitudes of the RCS of each triangle. To validate the obtained results, comparison between measurements and calculations are performed, using test bodies of relatively simple shapes like cones, spheres, dihedral corners .... The modeling of those bodies can be performed manually, and their shapes are sufficiently simple to avoid complicated geometrical tests.

If Radar Cross Section calculations have to be performed on bodies of much more complex shapes, several additional problems arise:

- modeling has to become systematic, being too complicated to be handled manually.
- Hidden faces have to be removed, for each angle of observation.

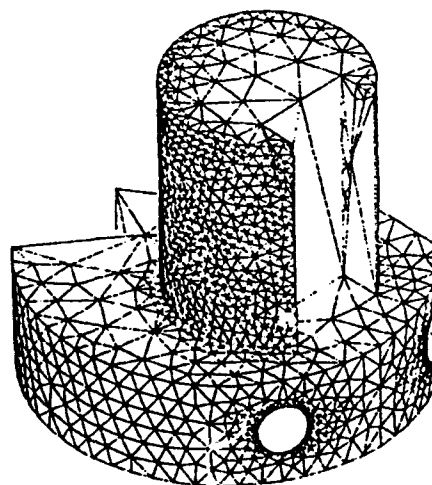


Figure 1: Complex object introducing different reflection and diffraction cases

- Tests for finding double and triple reflections, or for the determination of diffraction centres (tips, wedges,...) become more complicated.

In the following sections, we will develop those items, which will enable us to apply well known RCS calculation methods to objects of arbitrary geometries.

### 3 Modeling

Having chosen to describe the objects by triangular patches, we looked for existing software, which would enable us to create a triangular surface mesh, and to save the results in two files, one containing the coordinates of the nodes (or triangle points), and one containing the triangles. We found the answer in the graphical interface of SYSTUS, a tool to perform finite elements calculations on Apollo stations. The introduction of the three-dimensional bodies is based on the principle that each surface can be defined by the rotation, translation or transformation of specific edges, and that every edge can be defined by a number of its points. So, the creation of the object's surface requires the following steps: define the points, define the edges going through those points, and finally define the surfaces by specific actions on the edges.

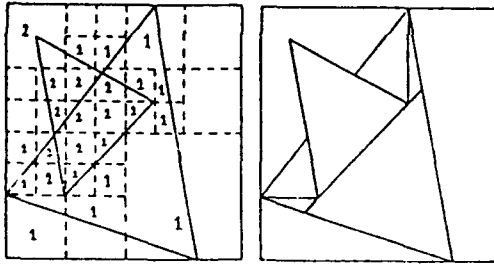


Figure 2: Warnock's determination of hidden triangles.

Next, the different surfaces are put together and the triangular mesh is created. The size of the triangles is optional, so we could fix their *minimal* size at about  $5\lambda$  ( $\lambda$  is the free space wavelength of the incident field), this to satisfy the tangent plane approximation for each individual triangle. Fig 1 shows an example of an object defined with this software. The minimal size of the triangles can be insufficient for the modeling of parts of the object with an important curvature (one should keep in each point of the object, the distance between the real surface and the triangle within a  $\lambda/16$  limit [10]). In this case, the MoM can be applied locally to solve the problem for this particular part of the object. This hybrid approach needs again a geometrical analysis of the object, to find out automatically where such high curvature centres are localized. This problem is to be solved in the future.

#### 4 Removing Hidden triangles

This operation needs to be performed for each possible reflection (see point 5.2) and direction of observation. To eliminate the hidden triangles from the file describing the object, one has to work in different steps, which could be summarized as follows:

- Perform simple tests to remove obvious hidden faces from the file describing the object.
- For the simplified object, select the totally seen, partially seen or completely hidden triangles, for a given position of the observer.
- Divide the partially seen triangles in little triangles, that are completely hidden or completely seen.
- Create a new file, describing the object, but containing only the visible triangles.

Before applying a complicated algorithm to a great amount of little triangles, one should try to reduce their number by a fast elimination of obviously hidden ones using as much *simple tests* as possible. No doubt this will significantly reduce the computation time of the Hidden Faces program. A standard test is the comparison of the orientation of the normal of the plane of each triangle, to the direction of observation. One could also characterize some parts of the object by a special code, like {UP, DOWN, LEFT, RIGHT}. If the observer is located upwards, one certainly can eliminate all its triangles located DOWN, even if the faces are oriented towards the source.

Once simple tests have simplified the object, an algorithm for hidden faces elimination is required. Because RCS calculations are using approximation methods, full precision

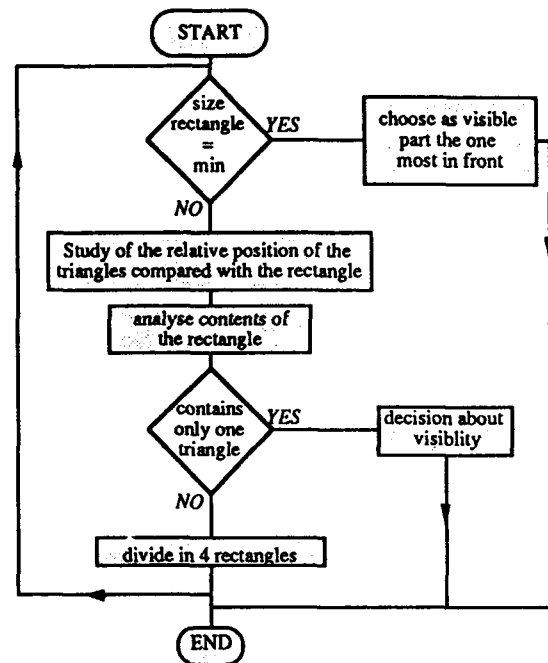


Figure 3: Organigram of the Hidden Faces Algorithm.

is not necessary, and we chose the WARNOCK's method[3]. This method projects all triangles on a plane perpendicular to the line of sight, and divides successively the obtained scene, which is contained in a "big" rectangle, in smaller and smaller rectangles, until *one* rectangle contains only information of *one* triangle, or until the precision of the screen is reached. In fact, we are working in two steps:

1. For each triangle, determine (in %) the fraction of its surface which is really seen (Warnock)
2. For the partially seen triangles, divide the resting surface in new little triangles.

In fig 2, the rectangles are divided according to the complexity of the scene that they contain. In each rectangle, a number indicates if it is triangle 1 or triangle 2 that is considered as the one which is seen. In this particular case, triangle 1 is partially hidden by triangle 2. The resulting file contains 6 visible triangles, because some parts of triangle 1 had to be adapted by dividing them in new triangles.

By each next division of a rectangle, one has to keep track of precedent informations, and store new data. Indeed, every part issued from a triangle, will inherit some of its characteristics (for example, if another triangle is completely hiding one, it will also hide every part issued from it), and insert some characteristics of its own (is the little part completely visible or not). Each new division will simplify the observed scene, so that once a *simple* feature is encountered (only one piece of triangle in the considered rectangle) a conclusion can be made for this specific part (hidden or not). This information has to be added to the summarizing description of the triangle we are studying. Eventually, the surface of this little part is added to the visible surface of the original triangle. The organigram on fig 3 shows the general idea of the Hidden Faces program we developed. To enable

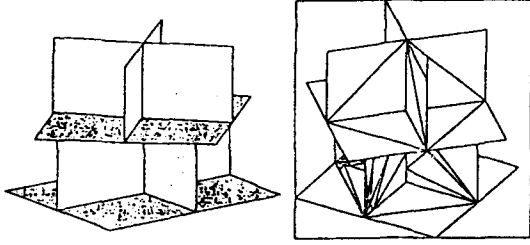


Figure 4: Decoy: how it looks, and resulting visible triangles.

the adaptation of the calculation effort to the complexity of the object, we made the "precision" of the screen optional, so that the size of the minimum rectangle can depend on the relative size of the triangles compared to the total dimension of the object (which determines the starting rectangle). The algorithm allows us to treat non convex objects, like the following configuration on fig 4. As one can see on this figure, the resulting triangles do not always have ideal dimensions (one size much smaller than the two others). If this is influencing the computer effort, or the results, will be analysed in the future.

## 5 Reflections

### 5.1 Physical Optics in simple and double reflections

One of the advantages of Physical Optics (PO) lies in the fact that this high frequency method enables Radar Cross Section calculations for plane surfaces. The restrictions of the method are :

- The illuminating wave is a plane wave, the target must be in the far field of the source (radar).
- The dimension of the triangles must be such that they are small enough to keep close to the real object shape, but large enough to satisfy the tangent plane approximation, and to reduce the calculation time .

As the method is based on the assumption that the tangential magnetic fields are equal to twice the incident magnetic field at the surface, and non existent elsewhere, it supposes a sudden discontinuity in the field at the shadow boundaries. Diffraction calculations will treat this problem in section 6.

To perform RCS calculations for simple reflections on each one of the triangles constituting the object, we used the general formula, obtained in [10, 11]:

$$\begin{aligned} \vec{E}_s &= \begin{pmatrix} E_{sx} \\ E_{sy} \end{pmatrix} \\ &= \frac{-jke^{-jkr}}{2\pi r(1-n_z^2)} \int_F e^{2jky} dx dy \\ &\quad \cdot \begin{pmatrix} R_H n_z^2 - R_E n_y^2 & (R_H + R_E) n_z^2 n_y^2 \\ (R_H + R_E) n_z^2 n_y^2 & R_H n_y^2 - R_E n_z^2 \end{pmatrix} \cdot \begin{pmatrix} E_{ix} \\ E_{iy} \end{pmatrix} \end{aligned} \quad (1)$$

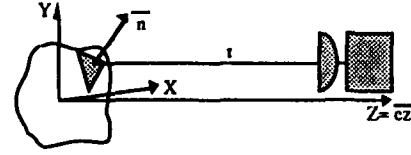


Figure 5: Geometry for monostatic scattering (after [10]).

Here,  $r$  is the distance of the triangle to the source,  $n_x, n_y, n_z$  are the components of the normal vector  $\vec{n}$ ,  $R_H$  and  $R_E$  are the Fresnel Reflection Coefficients,  $z(x,y)$  expresses the equation of the plane of the considered triangle,  $F$  is the triangular integration domain,  $\vec{E}_s$  is the electric field backscattered by the triangle, and  $\vec{E}_i$  is the incident electric field. The expression (1) is derived from the Stratton-Chu equations [5], which express the field present in a volume, when all the sources are localized outside this volume. If the sources are assumed to be localized at an infinite distance, one gets the expression of the scattered field [8]. The coordinate system giving the Stratton-Chu equations and their derivatives, is local to the reflecting surfaces and determined by the unit vectors  $\vec{n}$  which is the normal to the plane, and  $\vec{e}_{\parallel}, \vec{e}_{\perp}$  the unit vectors respectively parallel and perpendicular to the plane of incidence, which is defined as the plane containing  $\vec{n}$  and  $\vec{e}_i$  ( see fig 5). Transforming this local coordinate system into an absolute OXYZ system finally gives eq.(1).

If one considers perfectly conducting surfaces ( $R_H = -R_E = 1$ ), (1) simplifies considerably, and the Radar Cross Section, given by:

$$\sigma = 4\pi \lim_{r \rightarrow \infty} r^2 \cdot \frac{|\vec{E}_s|^2}{|\vec{E}_i|^2}$$

depends only on the phase integral. If non ideally conducting surfaces are treated, one can use the complex Fresnel Reflection Coefficients for multilayered object [11, 6]:

$$R_H = \frac{Z^{(1)} \cos \alpha^{(1)} - Z_{IH}^{(2)} \cos \alpha^{(2)}}{Z^{(1)} \cos \alpha^{(1)} + Z_{IH}^{(2)} \cos \alpha^{(2)}} \quad (2)$$

$$R_E = \frac{Z_{IE}^{(2)} \cos \alpha^{(1)} - Z^{(1)} \cos \alpha^{(2)}}{Z_{IE}^{(2)} \cos \alpha^{(1)} + Z^{(1)} \cos \alpha^{(2)}} \quad (3)$$

and substitute them in (1) . Here  $Z^{(n)} = \sqrt{\frac{\mu_0}{\epsilon_0}} \cdot \sqrt{\frac{\epsilon^{(n)}}{\epsilon^{(1)}}}$  is the impedance of the  $n$ -th layer, with  $n=1$  indicating the first layer (in our case air). To obtain the  $Z_{IE}^{(2)}$  and  $Z_{IH}^{(2)}$  values of the second layer, one has to use the recursive expressions [11] to determine the intermediate values  $Z_{IH}^{(n)}$  and  $Z_{IE}^{(n)}$  of all the layers present, the last one ( $n=N$ ) being in our case a perfect conductor. In the case of double reflections, if one uses virtual panels [10], these should be supplied with a "virtual" reflection coefficient. In the case that the normals to the reflecting panels have a zero  $n_x$  or  $n_y$  coefficient (triangles in the OYZ or in the OXZ plane) eq.(1) reduces to (take for example  $n_x = 0$ ) :

$$\begin{aligned} \vec{E}_s &= \begin{pmatrix} E_{sx} \\ E_{sy} \end{pmatrix} = \frac{-jke^{-jkr} n_y^2}{2\pi r(1-n_y^2)} \int_F e^{2jky} dx dy \\ &\quad \cdot \begin{pmatrix} -R_E & 0 \\ 0 & R_H \end{pmatrix} \cdot \begin{pmatrix} E_{ix} \\ E_{iy} \end{pmatrix} \end{aligned} \quad (4)$$



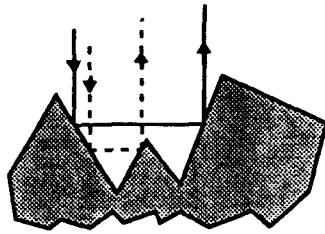


Figure 6: Complex object with some double reflection candidates.

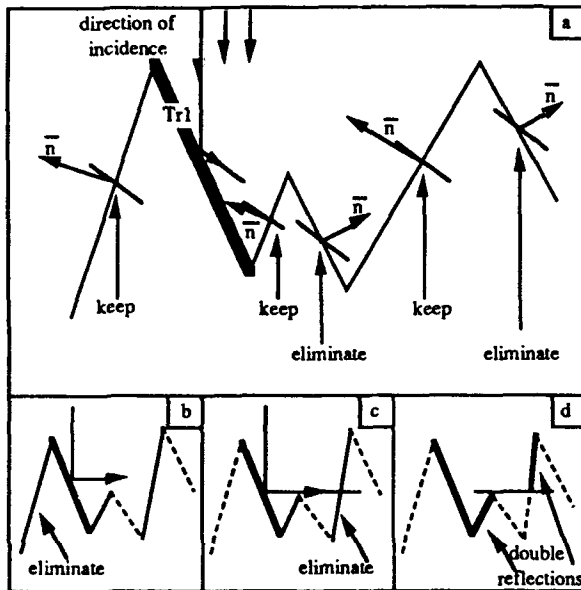


Figure 7: selecting the actual double reflecting parts.

which means that in this case, in order to obtain the "virtual" reflection coefficient, one needs only to successively multiply the respective complex reflection coefficients  $R_E$  or  $R_H$ . In other, more general cases however, one should carefully examine if such a simple solution is still possible.

## 5.2 Finding the double reflections

Every field which is reflected by a triangle, could meet another triangle and give rise to a double reflection. As already said in the beginning of section 4 and as is pointed out in fig 6, if the object is complex, several parts of existing triangles can be active in this double reflection problem. One has to look through the complete collection of triangles constituting the object, to find the candidates for double reflections, but can restrict himself to the triangles kept after the elimination of the hidden faces. Indeed, a hidden triangle will never reflect anything back towards the observer. Cavities are an exception to this rule, and work is done to find a simple method to detect them.

To constitute the collection of triangles, which actually lead to double reflections, the faces, not visible from a

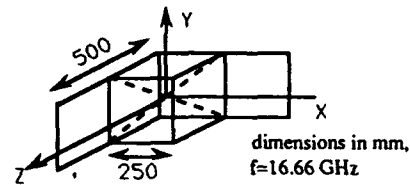


Figure 8: geometry of the cube with additional faces, after [10]

"reflected wave" point of view should be eliminated. Again, the Hidden Faces program can be used, although this involves the assumption of a reflection of the incident field in the GO sense. The following preliminary treatments are required, because the Hidden Faces algorithm supposes the observer to be located at an infinite distance of the considered object, and not inside (more specifically, on the reflecting triangle) the object like here.

- A first test on the triangles selects those, oriented towards the "reflecting triangle" which we will note Tr1 (fig 7a). This is done by the evaluation of the angle between the rays (GO) reflected by Tr1 and the normal to the triangles.
- Next, we eliminate from this new list all the triangles not being "in front" of the ray reflected by Tr1 (fig 7b).
- Finally, the hidden faces algorithm is applied to the resting triangles (fig 7c). In this last step, the limitation of the starting rectangle (for the Warnock algorithm) to the size of Tr1 reduces the time for hidden surfaces treatment.

The resulting triangles effectively giving rise to double reflections are finally shown in (fig 7d).

## 5.3 Calculations of the reflections

To compare our results to examples given in literature, we have chosen the cube with additional surfaces [10], because it makes use of double reflections, hidden faces and wedges (see next section), and still remains a simple shape.

Two types of calculations were performed with this object. First, the incident field was parallel to the OXZ plane (see fig 8), and a variation of the horizontal aspect angle was performed. We obtained the curve on fig 9, exhibiting a good agreement with well known curves [10].

Next, we tried to obtain, for the same cube with additional faces, but in the position given in fig 10, the curves given in [10]. The curve we obtained (see fig 12) has the same general shape as in [10] (see fig 11). The maxima and minima seem to agree, but still there are some differences, and work is done to explain them. Maybe the rotation of the object was not identical to that performed in [10].

## 6 Diffractions

### 6.1 Geometrical Theory of Diffraction

To treat the influences of the edges, and the unacceptable field discontinuity imposed by Physical Optics, diffracted fields have to be determined. Physical Theory of Diffraction (PTD) and Geometrical Theory of Diffractions (GTD)

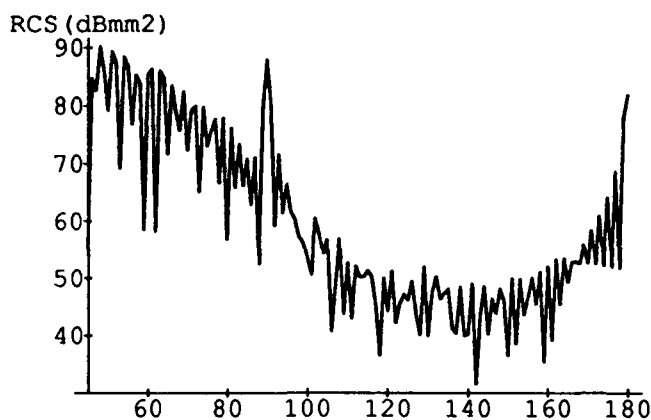


Figure 9: Cube with additional faces, RCS in function of aspect angle in degrees, rotation of observer in horizontal plane

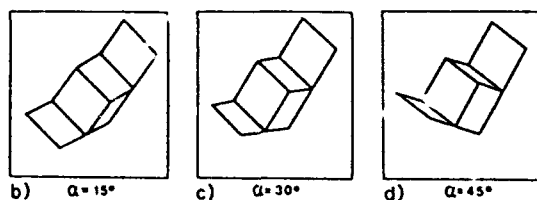
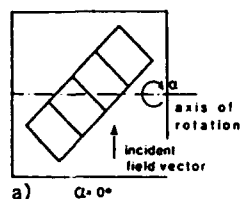


Figure 10: Special orientation of the cube with additional faces, after [10]

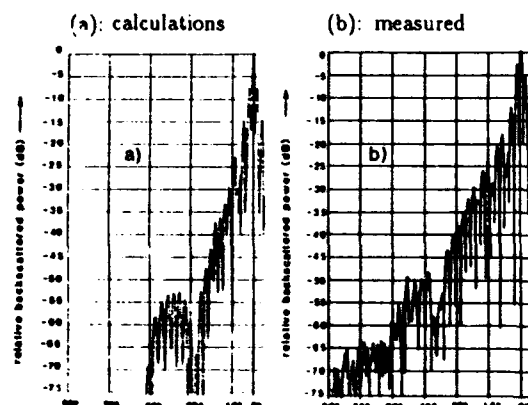


Figure 11: Cube with additional faces, RCS in function of aspect angle in degrees, rotation in vertical plane, after [10]

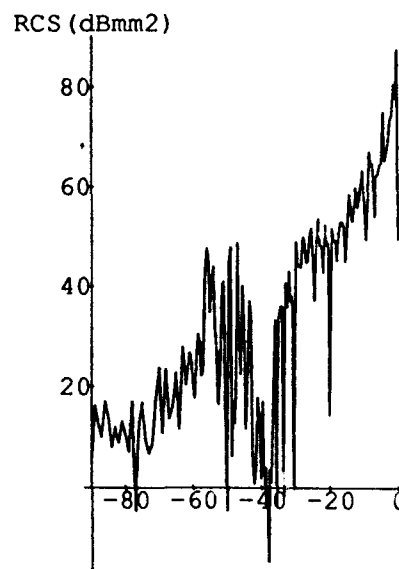


Figure 12: cube with additional faces, rotation in vertical plane

are two methods treating this problem. Both use diffraction coefficients to relate the diffracted field to the incident field, and use as reference the two-dimensional solution proposed by Sommerfeld [12] for the diffraction by a wedge. Moreover, both methods are quite similar in their shortcomings. They give acceptable results only for diffracting directions lying on the Keller cone [7], and progressively fail as the scattering direction moves further from the specular direction. The major advantage of PTD concerns the continuity of its diffraction coefficients near shadow and reflection boundaries, where the GTD coefficients fail, although in the monostatic case, this problem can be overcome (see section 6.2) without too much difficulties.

Being an extension of Physical Optics, PTD seems more indicated to our problem, but we preferred to illustrate the detection of the diffraction centres using Geometrical Theory of Diffraction, because of its simplicity in only invoking two rather simple scalar diffraction coefficients. The principles of the determination of the different variables (section 6.3) can be applied without problems to PTD which in fact uses similar parameters.

In Geometrical Theory of Diffraction, one brings the diffracted field in relation to the incident field by means of diffraction coefficients, in the same way reflected fields can be expressed using reflection coefficients. The edge diffracted field is given by: [13]

$$\vec{E}_d(r) \sim \vec{E}_i \cdot \vec{D} \cdot \sqrt{\frac{\rho}{r(r+\rho)}} e^{2\pi j k r} \quad (5)$$

where  $\vec{E}_d$  and  $\vec{E}_i$  are respectively the diffracted and incident electric fields,  $r$  is the distance from the edge caustic to the observer,  $\vec{D}$  is the dyad counting for the diffractions, and  $\rho$  depends on the radius of curvature of the incident wavefront and on the radius of curvature of the illuminated edge [13].

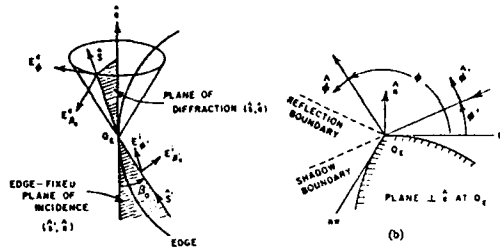


Figure 13: geometry for diffraction by an edge (after [13]).

In the case of a straight edge and of a plane wave, the variable  $\rho$  equals infinity, so that eq.(5) becomes:

$$\bar{E}_d(r) \sim \bar{E}_i \cdot \bar{D} \cdot \sqrt{\frac{1}{r}} \exp^{-jkr} \quad (6)$$

The dyad  $\bar{D}$  in eq.(6) for a perfect conductor can be expressed by: [13]

$$\bar{D} = -\bar{\beta}'_0 \bar{\beta}_0 D_s - \bar{\phi}'_0 \bar{\phi}_0 D_h$$

(see figure 13 for the orientation of the vectors) or in matrix form:

$$\begin{pmatrix} -D_s & 0 \\ 0 & -D_h \end{pmatrix}$$

In the case that the field point is not too close to a shadow or reflection boundary, the scalar diffraction coefficients  $D_s$  and  $D_h$  are:

$$D_{s,h}(\phi, \phi', \beta_0) = \frac{\exp(-j\pi/4) \sin(\pi/n)}{n \sqrt{2\pi k} \sin \beta_0} \quad (7)$$

$$\left[ \frac{1}{\cos \pi/n - \cos[(\phi - \phi')/n]} \mp \frac{1}{\cos \pi/n - \cos[(\phi + \phi')/n]} \right]$$

with the upper sign referring to  $D_s$ , and the lower to  $D_h$ .

To determine the Radar Cross Section related to the diffractions, one can observe in (6) that the obtained diffracted field is in  $1/\sqrt{r}$  (and not in  $1/r^2$  like we would expect), because in our case the problem is reduced to a two-dimensional one. To transform this result into a three-dimensional expression, the influence of the finite length of the wedge needs to be introduced. In the case of a dihedral corner, Ross [15] solved this problem by the following transformation of the two-dimensional results:

$$\sigma_d = \frac{2L^2}{\lambda} \sigma_{1d}$$

where  $\sigma_{1d}$  is the *echoing width*:

$$\sigma_{1d} = 2\pi \lim_{r \rightarrow \infty} r \cdot \frac{|\bar{E}_d|^2}{|\bar{E}_i|^2}$$

and  $\sigma_d$  the equivalent three-dimensional Radar Cross Section. This could enable the determination of an independent Radar Cross Section contribution of the diffracted field, but the integration of the obtained  $\sigma_d$  in the RCS calculations remains a problem. Simply adding this diffraction contribution to the reflection bounded RCS seems too unprecise to

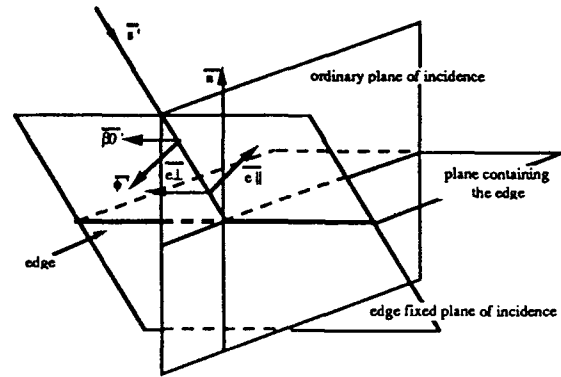


Figure 14: Monostatic diffraction on a wedge.

be acceptable. A better treatment should consist in immediately adding the diffracted field to the PO field of the triangles constituting the wedge, but then a three-dimensional diffracted field should be used. This is possible if one uses PTD, because with this method, an integration is performed along the wedge [16] to obtain the diffracted field, which means that the influence of the finite length of the wedge is automatically taken into account.

In any case, PTD and GTD require the same preliminary geometrical treatments, and our purpose is to give a description of the actions to be taken.

The determination of the diffracted field requires the following steps:

1. Determine (see figure 13) the exterior angle  $n\pi$ , and the values of the angles  $\phi$ ,  $\phi'$  and  $\beta_0$ .
2. Bring the edge fixed coordinate systems  $\bar{\beta}'_0$ ,  $\bar{\beta}_0$ ,  $\bar{\phi}'_0$  and  $\bar{\phi}_0$  in relation with the absolute coordinate system OXYZ.
3. Determine the resulting Radar Cross Sections.

These topics will be treated in the following sections, but before that, a prior problem has to be solved, namely the *localisation* of the wedges.

## 6.2 Finding the wedges

To find the wedges, certain preliminary considerations have to be done. We are working with "specular" methods, and we know that the diffracted rays are localized on the Keller cone. Moreover, we are only treating monostatic scattering. This means that (see fig 13) the angles  $\phi$  and  $\phi'$  are equal, and that only edges perpendicular to the plane of incidence (fig 14) will be treated.

A second consideration concerns the domains in which the Geometrical Theory of Diffraction fails. Indeed, the diffraction coefficients become infinite at the reflection and shadow boundaries. Being in the monostatic case ( $\phi' = \phi$ ), the conditions for an observer located near the shadow boundary ( $\phi' - \phi = \pi$ ) will never be satisfied. Concerning the reflection boundary ( $\phi' + \phi = \pi$ ), only when  $\phi' = \phi = \pi/2$ , thus for a wave incident in the direction of the normal to the considered plane (total reflection), an infinite result for the diffraction coefficients will be obtained. A way to circumvent this problem is to try to treat the "other" plane constituting the wedge as the reference plane, if this is possible.

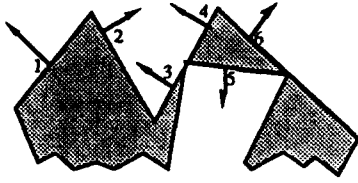


Figure 15: Ambiguity in finding the wedge.

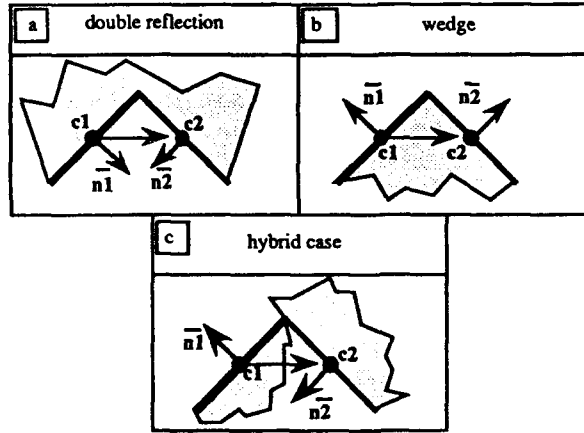


Figure 16: 3 different relative positions of triangles.

Finally, one should not forget to keep track of the treated wedges, to avoid double treatments.

Consider the same starting situation as for the reflection calculations: we have a triangle (Tr1) receiving the initial incident field  $\vec{E}_i$ . To find the wedges, two options can be chosen [16]: do we only consider the actual wedges (those effectively present on the illuminated object), or do we treat all the wedges we created by our modeling, which most of the time are fictitious, but which could count for the influence of the curvature of the surface in the backscattering process. We chose the second option, which enjoins us to find all the possible wedges existing for each triangle, or, with other words, to analyse the 3 neighbouring triangles.

First of all, one should analyse carefully whether what is found really is a wedge! Indeed, fig 15 shows three configurations that could satisfy simple wedge detection tests: double reflection (faces 2 and 3), wedge (faces 1 and 2 or 4 and 6) and a hybrid case (faces 3 and 5). This ambiguity is treated by a simple comparison of the orientation of the normals of the planes containing the triangles, with the vectors connecting the two centres of gravity of the triangles. To simplify the calculations, we will first project these vectors in a plane, perpendicular to the intersection line between the two planes containing the triangles. Doing this, one gets the three cases shown in fig 16. Here the indicated normals are already projected. The vector from c1 to c2 will be called c12, and the vector from c2 to c1 (not drawn) c21. For those configuration, one can conclude that

- if  $\vec{n}_1 \cdot \vec{c}_{12} > 0$  and  $\vec{n}_2 \cdot \vec{c}_{21} > 0$  then one has a double reflection (fig 16a),

- if  $\vec{n}_1 \cdot \vec{c}_{12} < 0$  and  $\vec{n}_2 \cdot \vec{c}_{21} < 0$  a wedge is encountered (fig 16b),
- if the signs of  $\vec{n}_1 \cdot \vec{c}_{12}$  and  $\vec{n}_2 \cdot \vec{c}_{21}$  are different, we have a hybrid case (fig 16c).

By this way, a wedge is easily detected.

### 6.3 Determination of the diffracted fields

If we are sure to be in the case of a diffracting wedge, the values of the exterior angle  $n\pi$ , and the angles  $\phi$ ,  $\phi'$  and  $\beta_0$  have to be determined. The exterior angle is easily obtained from the angle between the two normals to the triangles. By projecting the incident field vector on a plane perpendicular to the edge of the wedge, one can determine the value of  $\phi (= \phi')$ . Here, a choice has to be made concerning which triangle will represent the reference plane from which  $\phi$  and  $\phi'$  will be measured. This choice is arbitrary, excepting if one of the triangles is normal to the incident field vector ( $\phi = \phi' = \pi/2$ , reflection boundary). Finally,  $\beta_0$  is immediately known and equals  $\pi/2$  (because we are in a monostatic case). The determination of those variables being accomplished, the coefficients  $D_s$  and  $D_h$  can be determined.

To integrate these results in the preceding reflection computations, one finally has to relate the edge fixed coordinate system (see figure 13) in which diffraction calculations were performed, to the absolute OXYZ system. This will be done via the intermediate coordinate system in  $(\vec{e}_\parallel, \vec{e}_\perp, \vec{n})$  which is bounded to the normal plane of incidence. In fact, the following relations are known:

$$\begin{aligned} (E_{ix}, E_{iy}) &\sim (E_\parallel, E_\perp) \sim \\ &\sim (E_{\beta'_0}, E_{\phi'}) \xrightarrow{D} (E_{d\beta_0}, E_{d\phi}) \sim (E_\parallel, E_\perp) \sim (E_{dx}, E_{dy}) \end{aligned}$$

with  $E_{dx}$  and  $E_{dy}$  the components of the diffracted field in OXYZ. The relations

$$\vec{\beta}'_0 = \vec{s}' \times \vec{\phi}' \quad \text{and} \quad \vec{\beta}_0 = \vec{s} \times \vec{\phi} \quad (8)$$

give

$$\vec{\beta}_0 = -\vec{\beta}'_0 \quad (\text{with } \vec{s} = -\vec{s}' \text{ and } \vec{\phi} = \vec{\phi}') \quad (9)$$

This enables us to find, among others, the following relations:

$$\begin{aligned} \begin{pmatrix} E_{\beta'_0} \\ E_{\phi'} \end{pmatrix} &= \begin{pmatrix} 0 & 1 \\ -1 & 0 \end{pmatrix} \cdot \begin{pmatrix} E_\parallel \\ E_\perp \end{pmatrix} \\ &= \frac{1}{\sqrt{n_x^2 + n_y^2}} \cdot \begin{pmatrix} 0 & 1 \\ -1 & 0 \end{pmatrix} \cdot \begin{pmatrix} n_x & n_y \\ -n_y & n_x \end{pmatrix} \cdot \begin{pmatrix} E_{ix} \\ E_{iy} \end{pmatrix} \end{aligned} \quad (10)$$

and

$$\begin{pmatrix} E_{d\beta_0} \\ E_{d\phi} \end{pmatrix} = \begin{pmatrix} -D_s & 0 \\ 0 & -D_h \end{pmatrix} \cdot \begin{pmatrix} E_{i\beta'_0} \\ E_{i\phi'} \end{pmatrix} \cdot \frac{e^{-jkr}}{\sqrt{r}} \quad (11)$$

Using (8), (9), (10), (11) and their derivatives one obtains:

$$\begin{aligned} \begin{pmatrix} E_{dx} \\ E_{dy} \end{pmatrix} &= \frac{1}{n_x^2 + n_y^2} \cdot \frac{e^{-jkr}}{\sqrt{r}} \cdot \\ &\cdot \begin{pmatrix} -D_h n_x^2 + D_s n_y^2 & -(D_h + D_s) n_x^2 n_y^2 \\ -(D_h + D_s) n_x^2 n_y^2 & D_s n_x^2 - D_h n_y^2 \end{pmatrix} \cdot \begin{pmatrix} E_{ix} \\ E_{iy} \end{pmatrix} \end{aligned} \quad (12)$$

which gives the expression of the diffracted field in function of the incident field, both expressed in the OXYZ system, and which enables an immediate deduction of the Radar Cross Section  $\sigma_{1d}$ , due to the two-dimensional diffraction field.

## 6.4 Results

The detection of the wedges, and the determination of the variables  $\phi$  and  $\beta_0$  were performed without any problem. However, the integration of the diffraction calculations in the reflection computations requires supplementary treatments to eliminate certain ambiguities in the recognition of the wedges. So no satisfactory curves were obtained at the moment.

## 7 Conclusions

If one considers an object with a general shape, Radar Cross Section determination not only involves the classical mathematical treatments, but also supplementary geometrical calculations. The Hidden Faces algorithm is relatively time consuming, and consequently has to be optimised.

In the reflection calculations, the application of the Hidden Faces program and the detection of the double reflection centres give results, which are in good agreement with those found in literature. The influence of the shape of the triangles is still to be analysed.

Concerning diffraction calculations, supplementary geometrical tests are to be developed, and work is done on the comparison between GTD and PTD.

Finally, the detection and treatment of cavities, and the development of a hybrid approach (to integrate the MoM in our calculations) is foreseen in the future.

## References

- [1] Stratton J.A., *Electromagnetic Theory*, McGraw-Hill, New York, 1941
- [2] Jones D.S., *The Theory of Electromagnetism*, Pergamon Press, London, 1964
- [3] Foley J.D. and Van Dam A., *Fundamentals of Interactive Computer Graphics*, Addison-Wesley Publishing Company, Reading, Massachusetts, 1983.
- [4] E. Schweicher, *Les Cibles Evasives en Télédétection Radar*, revue HF(Belgium) vol 13 no. 4 and 5, 1985.
- [5] Knott E.F., *Radar Cross Section*, Artec House, Dedham, MA, 1985
- [6] Ruck G.T., Barrick D.E. and Stuart W.D., *Radar Cross Section Handbook*, Plenum Press, New York, 1970
- [7] Knott E.F., *A Progression of High-Frequency RCS Prediction Techniques*, proc. of IEEE, vol 73 no 2, pp 252-264, 1985
- [8] Poggio A.J. and Miller E.K., *Integral Equation Solutions of Three-Dimensional Scattering Problems*, chapter 4 in *Computer Techniques for Electromagnetics*, Mittra R., ed., Pergamon Press, New York, 1973
- [9] Ufimtsev P.Ia., *Approximate Computation of the Diffraction of Plane Electromagnetic Waves at Certain Metal Bodies*, Soviet Physics/Technical Physics, a translation of the Zh. Techn. Fiz (USSR) vol 2 no 8, pp 1708-1718, 1957
- [10] Stein V., *Physical Optics Method: Prediction of Radar Signature*, AGARD lectures series no 152 on *Theoretical aspects of target classification*, 1987
- [11] Klement D., Preissner J. and Stein V., *Special Problems in Applying the Physical Optics Method for Backscatter Computations of Complicated Objects*, IEEE trans. Antennas and Propag., vol AP-36, no 2, pp 228-237, 1977
- [12] Sommerfeld A., *Lectures on Theoretical Physics*, in *Optics*, vol 4, Academic Press, New York, 1964
- [13] Kouyoumjian R.G. and Pathak P.H., *A Geometrical Theory of Diffraction for an Edge in a Perfectly Conducting Surface*, proceedings of the IEEE, vol 62 no 11, pp 1448-1461, 1974
- [14] Balanis C.A. and Griesser T., *RCS Predictions of Multiple Flat-Plate Targets Using GO-GTD(UTD) and PO-PTD Techniques: a Review*, in *Radar Cross Sections of Complex Objects*, Stone W.R., ed., IEEE Press, New York, 1990.
- [15] Ross R.A., *Radar Cross Section of Rectangular Flat Plates as a Function of Aspect Angle*, IEEE trans. Antennas and Propag., vol AP-14, no 3, 1966
- [16] Youssef N.H., *Radar Cross Section of Complex Objects*, Proc. IEEE vol 77, no. 5, pp 722-734, 1989

## DISCUSSION

G. Neininger, GE

Is the 90 - 100 dB m<sup>2</sup> RCS value really realistic?

Author's Reply

After discussion with Dr. Stein, we agreed that although the general shape of the curve is correct, real values are  $\pm 20$  dB too high. Investigations will be done to find the reason of this error. (The Y axes of Fig 9 & 12 have been adapted on the manuscript).

G. H. Hagn, US

1. Could you comment on your strategy for reducing the time to find hidden surfaces?
2. Have you considered the use of applied artificial intelligence tools for this type of problem?

Author's Reply

1. The aim is to include intermediate tests to avoid as much as possible to have to reach the resolution limit. For instance, the separating edge between two triangles, you still have information in the neighborhood of 2 triangles, so purchasing only ONE triangle is not ideal.
2. We did think of this approach but certainly not as a priority. We would first have to study the subject, to determine the correct approach of the problem of Hidden Faces using artificial intelligence, and this is not foreseen in the near future.

V. Stein, GE

Is your hidden surface algorithm capable of treating the perspective case?

Author's Reply

Perspective treatment for hidden faces. Because we consider the object as being at an infinite distance from the observer, we didn't treat the perspective approach to our Hidden Faces removal algorithm. This could be done however, by changing the quadrilateral volume containing the target into a pyramidal one. We then could apply our parallel method to the deformed target.

P. H. Pathak, US

1. You mentioned that you would like to make a comparison of your PTD-based results with the corresponding GTD results in the future. What do you hope to see from this comparison?
2. How do you propose to include the contribution to the scattering from the cavities present in your model?

Author's Reply

1. We started working with GTD, and parallel to the study of the method, we treated the problem of the determination of the angular parameters used to determine the diffraction coefficients. With time, we realized that PTD (which uses the same parameters) could in some cases be more useful to us. So we chose to purchase a parallel treatment of GTD and PTD, to validate our diffraction calculations, and get a deeper understanding of the physical interpretation of each method, and also because we cannot decide at this state of our knowledge which method is "the best" one.

2. I cannot answer this question, because we haven't really started yet with the treatment of cavities. That is why it is mentioned among our "future" domains of interest.

## Modèle de calcul de SER haute fréquence basé sur des techniques de CAO : SERMAT

D. Goupil & M. Boutillier/MATRA-DEFENSE  
37 av. L. Bréguet - 78146 Vélizy - FRANCE

### ABSTRACT

We have specified what has to be an industrial RCS calculation code, it must be able to exchange data with many CAD systems, it must be fast and have powerful graphic tools. Physical optic and equivalent currents classical technics have shown their efficiency on simple objects, since long time ago. But difficult geometric problems occur when objects with very complex shapes have to be computed. Only a specific geometric code can solve these problems. We have established that, once these problems have been solved :

- 1 - P.O and E.C give good results on complex objects with big sizes compared to wavelength.
- 2 - The implementation of these methods in a software (SERMAT) allows fast and precise enough RCS calculation to meet industrial requirements in the furtivity domain.

### I - INTRODUCTION

Les contraintes de furtivité sont de plus en plus importantes dans la conception des missiles.

La mise au point d'une forme furtive nécessite de comparer de nombreuses variantes, ce que les mesures ne permettent pas toujours.

Un code industriel doit :

- A. pouvoir traiter des géométries complexes  
Les formes à étudier deviennent de plus en plus complexes et les représentations analytiques sont insuffisantes
- B. être interfaçable avec divers systèmes de CAO  
Il est nécessaire pour le service furtivité de pouvoir échanger des formes avec les bureaux d'études, et tous les services intervenant dans l'élaboration des formes.
- C. être rapide  
La SER sous de très nombreux angles d'incidence de l'onde doit être calculée pour vérifier la conformité à une spécification  
Les calculs doivent être rapides pour mener une étude complète dans un délai raisonnable et pour un coût non prohibitif.
- D. disposer d'outils graphiques pour analyser les résultats.  
La masse importante des résultats à interpréter nécessite l'emploi d'outils graphiques appropriés pour bien percevoir le phénomène physique.
- E. être facile à mettre en oeuvre  
il doit être utilisable par des physiciens non-spécialistes en informatique et en CAO.

Pour répondre à ce besoin, MATRA-Défense a développé les logiciels

- INFOVISION : CAO orientée furtivité
- SERMAT : application au calcul de SER

## II - L'OUTIL CAO : INFOVISION

Nous n'avons pas utilisé un des systèmes de CAO existants car ils sont en général mal adaptés au calcul de SER, en effet:

- la richesse de leurs potentialités entraîne une structure très lourde qui permet rarement d'obtenir des temps de calcul rapides sur une application délicate comme le calcul de SER
- ils ne disposent pas de certains outils indispensables au calcul de SER

Le logiciel INFOVISION utilise les techniques géométriques de la CAO, mais il est orienté pour traiter les problèmes de furtivité (électromagnétique et infra-rouge).

Il comprend 3 bibliothèques fortran (a,b,c) et un interactif (d)

### a. Modeleur

permet de construire des formes, mais aussi d'en récupérer d'autres provenant de divers systèmes de CAO.

Les formes sont décrites par des surfaces polyédriques (les formes décrites à l'aide de surfaces biparamétriques sont préalablement facettisées).

### b. Calculs

calcul des informations géométriques nécessaires aux calculs de furtivité: contours apparents, frontières ombre-lumière, normales, aires, etc...

### c. Visualisation

sorties graphiques possibles (avec élimination des parties cachées)

- . dessin au trait
- . ombrage "réaliste"
- . remplissage de zones avec des couleurs représentant une grandeur physique.

### d. Interactif

utilisation de certaines fonctions des bibliothèques avec des facilités interactives (repérage graphique, zoom, habillage, etc...)

## Principales caractéristiques d'INFOVISION:

### - Portabilité

car il est écrit en fortran normalisé, seules quelques fonctions d'affichage sont dépendantes de la machine (et l'utilisation de standards graphiques comme PHIGS ou GKS les rend peu dépendantes)

### - Interface facile avec les autres systèmes de CAO

sur l'exemple de la figure 1, l'avant a été modélisé avec CATIA, le centre avec le modeleur volumique d'EUCLID, l'arrière avec le modeleur surfacique UNISURF. L'arrière a été modifié par INFOVISION.



- Propriétés non-géométriques dans la structure de données  
elles permettent, par exemple, de modéliser les matériaux
- Détection automatique des arêtes  
permet de créer dans la structure de données des arêtes telles  
que celles de la figure 2
- Rapidité  
pour la figure 1 (6254 facettes et 7604 points), 0.87s CPU sur  
IBM 9121/320 (2.8s sur SUN Sparcstation 2)

#### - Contours apparents

dans les systèmes de CAO, l'élimination des parties cachées n'est  
utilisée que pour visualiser les formes créées par le modelleur.  
Les algorithmes utilisés en CAO peuvent se répartir en 3 catégories

- . priorité  
affiche les facettes par ordre d'éloignement, de la plus éloignée  
de l'observateur à la plus proche. L'effet obtenu est uniquement  
visuel et aucune information ne peut être récupérée pour des calculs
- . résolution d'écran  
calcule les images pixel par pixel, ce qui est très long en CPU  
et peu précis pour le calcul de SER.
- . lignes vues  
on obtient les coordonnées des traits vus de chaque facette  
(figure 3.b pour l'exemple de la figure 3.a) mais aucune donnée  
sur ce qui se passe entre ces traits.

INFOVISION permet de calculer le contour apparent de chaque  
facette (figure 3.c)

La figure 4 montre des exemples de contours apparents sur un  
cas de calcul réel.

exemple: avant projet de missile stand-off

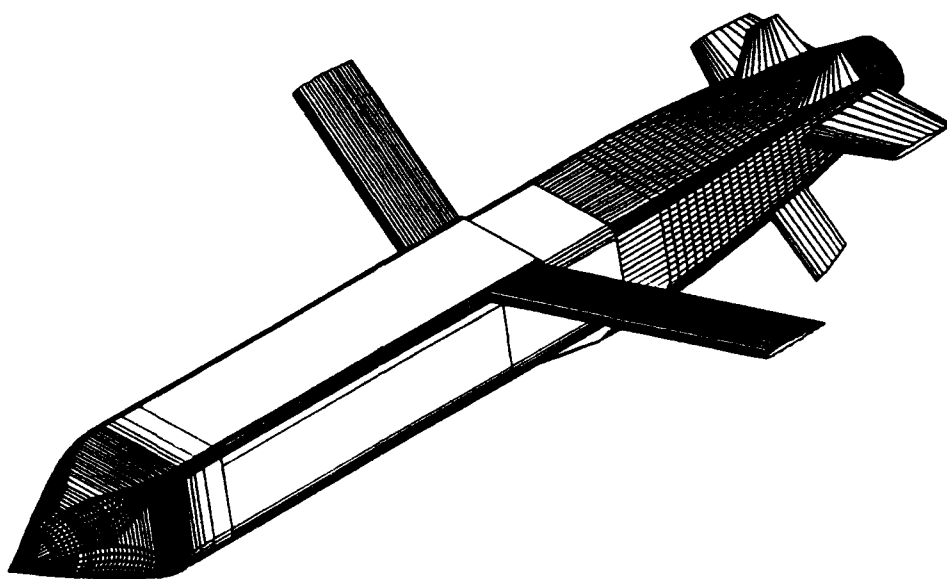
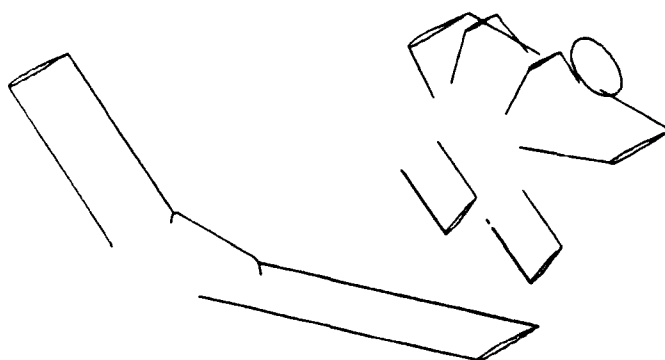


figure 1

figure 2

détection  
d'arêtes



**figure 3.a**

**la facette la plus grande  
est la facette cachée**

**les 9 autres facettes  
sont les facettes cachantes**

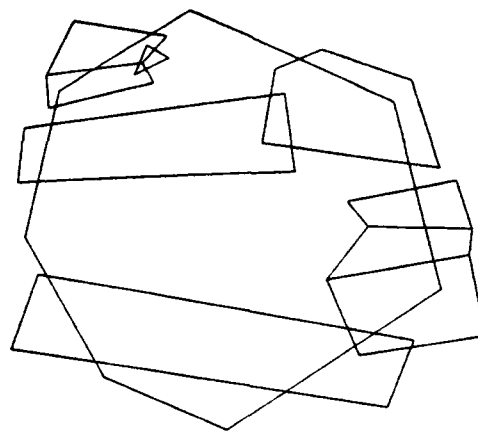


**figure 3.b**

**traits vus**

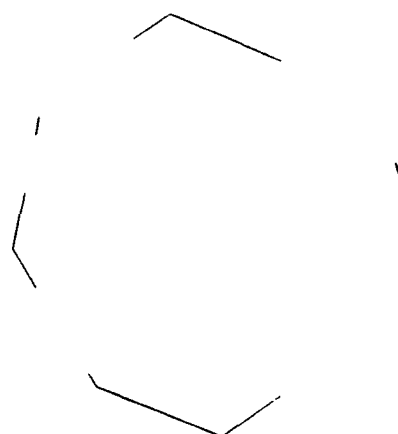
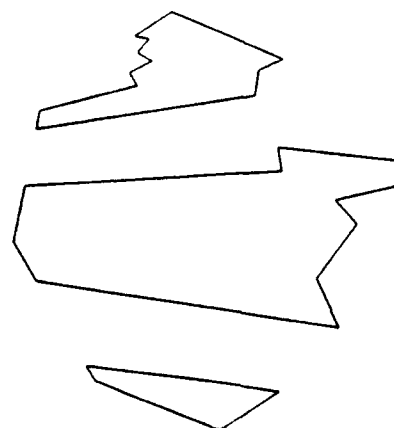


**figure 3.c**

**contours apparents**



exemple de contours apparents sur un  
autre avant projet de missile stand-off

les contours apparents de 3 facettes ont été hachurés horizontalement

figure 4

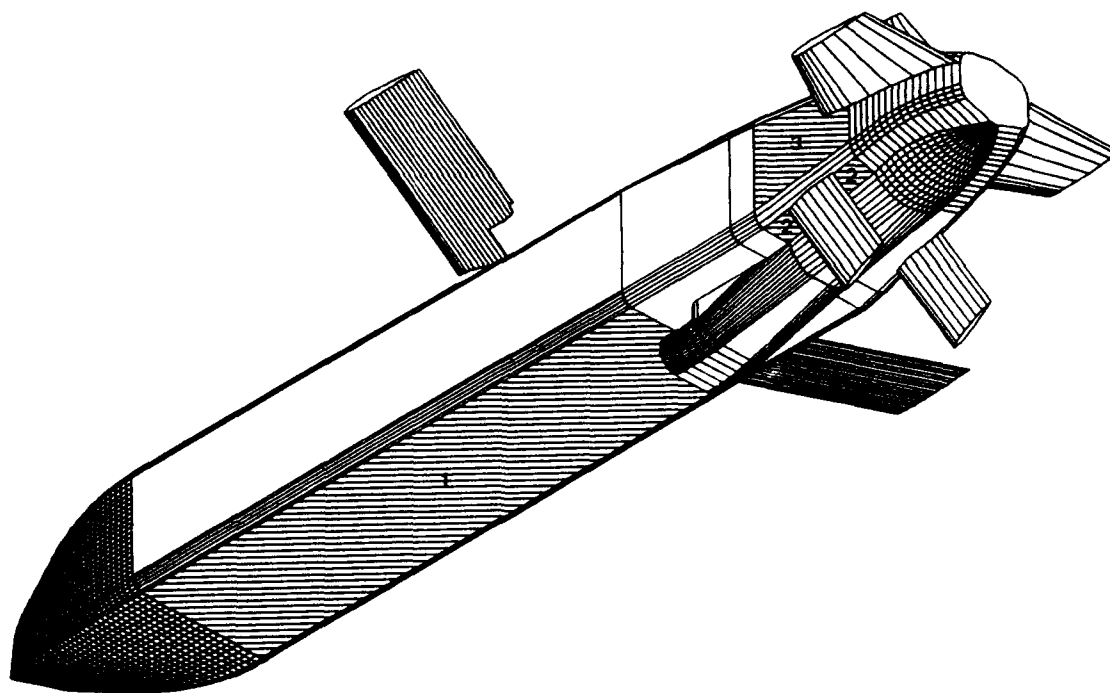
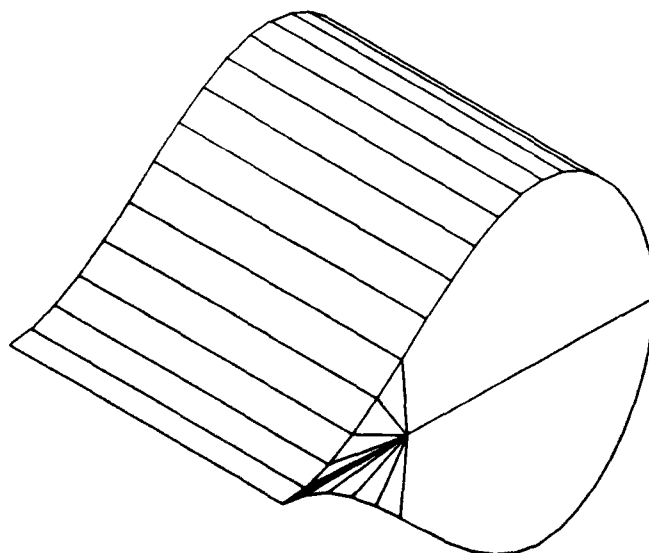


figure 5



### III - L'OUTIL SER

#### 1 - PRINCIPE

SERMAT s'appuie sur trois outils de base:

- INFOVISION précédemment décrit, pour la représentation des objets et tous les calculs de nature géométrique. Le nombre de facettes décrivant chaque partie de la cible dépend linéairement de la longueur d'onde de travail et des rayons de courbure locaux sur l'objet.
- l'OPTIQUE PHYSIQUE que l'on applique aux facettes.
- les COURANTS EQUIVALENTS que l'on applique aux arêtes détectées par INFOVISION.

#### 2 - CARACTERISTIQUES PRINCIPALES

A son point de développement actuel, SERMAT est validé et est utilisé de façon industrielle pour calculer des SER monostatiques sur des cibles métalliques de dimensions grandes devant la longueur d'onde.

SERMAT prend en compte:

- les réflexions simples.
- les réflexions multiples dans les cas simples de deux plaques planes rectangulaires jointives.
- les diffractions d'arêtes rectilignes ou curvilignes.

#### 3 - SORTIES GRAPHIQUES

Les grandeurs stockées par SERMAT sont, dans une même passe de calcul:

- les SER directes ( HH, VV ) et croisée, en amplitude et en phase.
- les modules des champs électromagnétiques, total et en projection sur les trois axes radar.

Ceci étant fait à chaque fréquence de calcul, on peut ainsi tracer les courbes habituelles:

$G = f(\text{angle})$  à une fréquence donnée

$G = f(\text{fréquence})$  à un angle donné

G pouvant être une SER, une phase ou un module.

Optionnellement, on peut également isoler les contributions par type de phénomène physique ( réflexions simples, réflexions multiples, diffractions ) et tracer les mêmes courbes que ci-dessus pour ces différentes contributions.

Une potentialité extrêmement intéressante du logiciel est de pouvoir calculer la SER sur une partie seulement de l'objet, tout en tenant compte des masquages induits par le reste de l'objet.

On peut ainsi descendre jusqu'au niveau ultime d'un contributeur élémentaire ( facette, arête ). Ce type de calcul permet la représentation, directement sur la cible, en 3 dimensions, de la SER de tous les contributeurs par une couleur fonction de leurs niveaux respectifs ( on représente en fait une densité de SER ), ce qui donne la localisation des points brillants sur la cible. Ceci constitue une aide précieuse à l'interprétation des résultats de calcul et de mesure.

#### 4 - VALIDATIONS

---

\* SERMAT a été validé par comparaison avec des résultats sur des formes canoniques, obtenus par des formulations analytiques exactes.

\* Il a également été validé sur des formes simples mais non canoniques, par comparaison avec des résultats obtenus par des méthodes dites "exactes", par exemple une méthode de moments sur un cylindre dont la section est celle d'une goutte d'eau ( figures 5, 6.a et 6.b ). Ces résultats ont été publiés dans la référence (1).

--> temps CPU: 5 s CPU sur IBM 9121/320, soit 0.028 s CPU par direction d'incidence.

\* Pour les besoins des programmes en développement à MATRA, on corrèle également les résultats du code sur des cibles de formes géométriques complexes qui font par ailleurs l'objet de mesures. Par exemple sur la cible de la figure 1, on retrouve correctement les niveaux mesurés ( figures 7.a et 7.b ).

--> temps CPU: 29 mn CPU sur IBM 9121/320, soit 1.3 s CPU par direction d'incidence.

Remarque : pour les temps calcul indiqués ci-dessus, on obtient les 10 grandeurs citées précédemment, à savoir 3 polarisations en amplitude-phase et 4 modules.

Remarque : le décalage angulaire et l'écart de niveau observés entre les calculs et les mesures sur le deuxième spéculaire sont dus au moyen de mesure disponible lors de l'étude de l'avant-projet ci-dessus, et sont parfaitement explicables quantitativement en appliquant une correction de champ proche sur la position et le niveau fournis par les mesures. Les mesures réalisées à l'heure actuelle sur des formes confidentielles montrent un très bon accord avec les calculs, moyennant cette correction.

On dispose également de représentations graphiques couleur permettant de représenter sur un seul dessin la SER d'une cible en fonction du site et du gisement. On peut ainsi comparer plusieurs formes de façon rapide et simple.

## 5 - CONCLUSION

---

Les techniques très classiques de l'OPTIQUE PHYSIQUE et des COURANTS EQUIVALENTS ont montré, depuis longtemps, leur efficacité sur des objets simples. Mais l'application à des objets de formes très complexes se heurte à des problèmes difficiles de traitement géométrique.

Nous avons montré que:

- l'utilisation d'un logiciel de géométrie spécifique permet de résoudre ces problèmes.
- grâce à ces techniques géométriques spécifiques, l'application de l'OPTIQUE PHYSIQUE et des COURANTS EQUIVALENTS donne de bons résultats sur des objets complexes et de dimensions grandes devant la longueur d'onde.
- la mise en oeuvre de l'ensemble de ces méthodes dans un logiciel ( SERMAT ) permet de réaliser de façon conviviale des calculs suffisamment précis et rapides pour répondre à des besoins industriels en matière de furtivité.

La conception du code SERMAT est modulaire, pour permettre aisément des adaptations et des évolutions en fonction des besoins.

- matériaux: en cours de validation. Les matériaux pourront être multicouches mais devront être homogènes et isotropes.
- remplacement des facettes planes par des facettes courbes: en cours de validation.
- réflexions multiples dans le cas général: des préétudes sont en cours.
- ondes de surface: des préétudes sont en cours.

nota: INFOVISION délivre toutes les informations géométriques nécessaires pour permettre ces évolutions.

Le code SERMAT est utilisé de façon intensive à MATRA. A titre d'exemple, le nombre d'angles d'incidence calculés en MARS 91 pour des besoins internes est d'environ 650.000, uniquement sur des formes comparables en complexité à celle de la figure 1. Si on compte également tous les autres calculs annexes sur des objets plus simples, on arrive à un nombre de l'ordre du million et demi d'angles d'incidence ).

## REFERENCES

---

- (1) PATHAK et LIANG: ' On a Uniform Asymptotic Solution Valid Across Smooth Caustics of Rays Reflected by Smoothly Indented Boundaries ': IEEE Transactions on Antennas and Propagation; Volume AP 38 N° 8; p 1192 à 1203, Août 90.

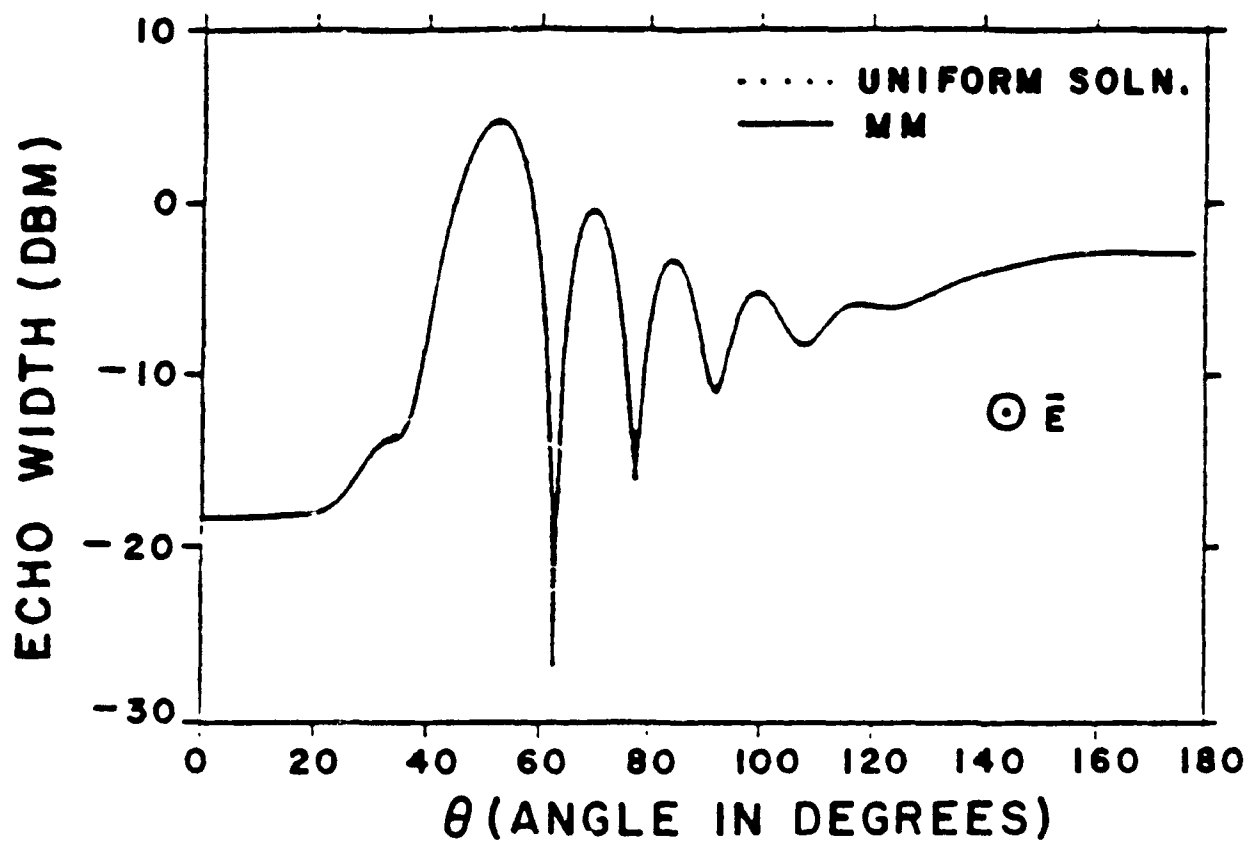


figure 6.a : REFERENCE ( 3 GHz, polarisation HH )

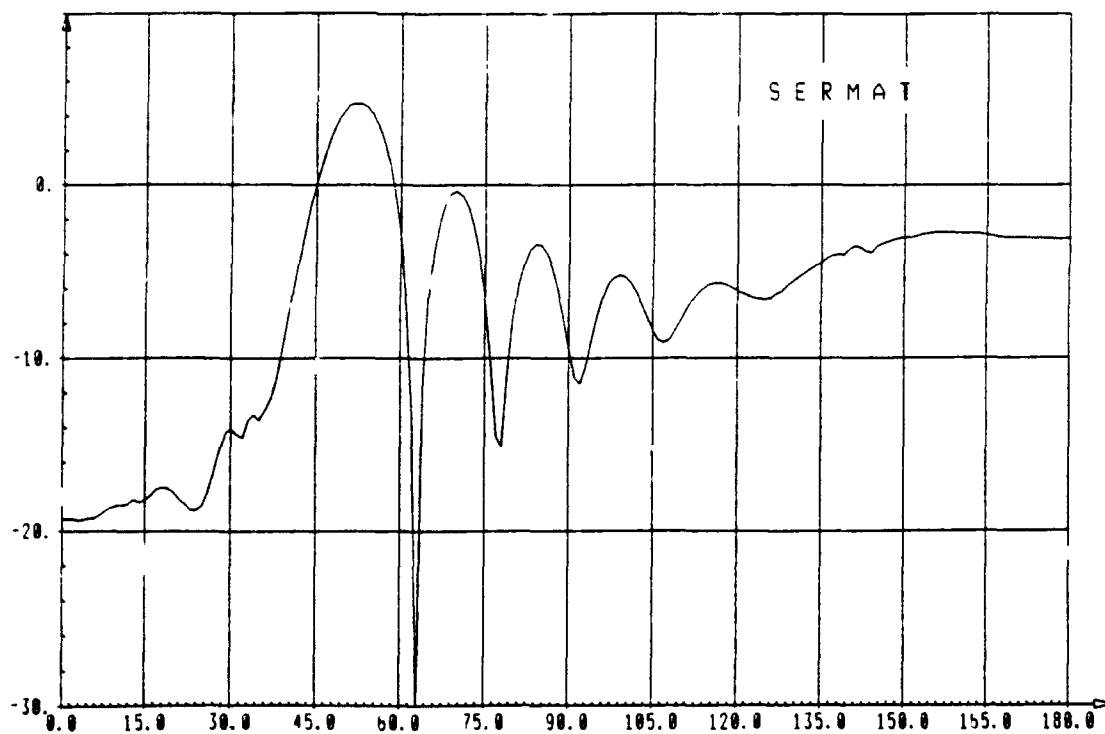


figure 6.b : SERMAT ( 3 GHz, polarisation HH )



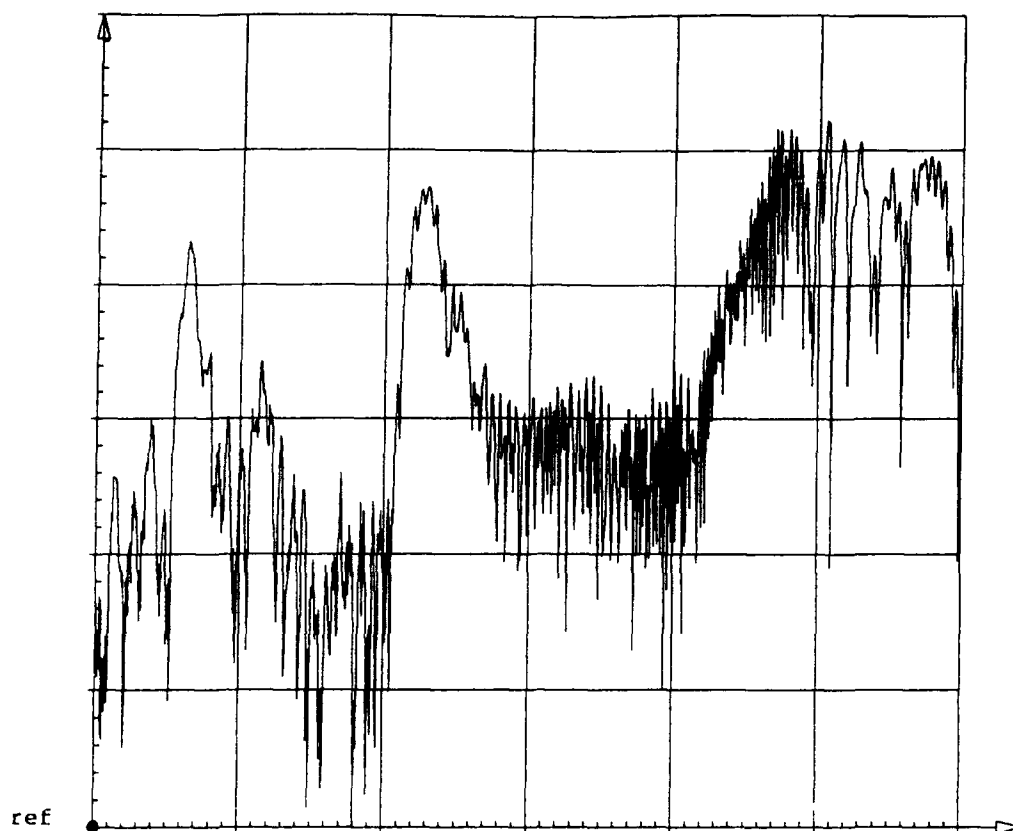


figure 7.a: MESURE ( 7.5 GHz, polarisation HH )

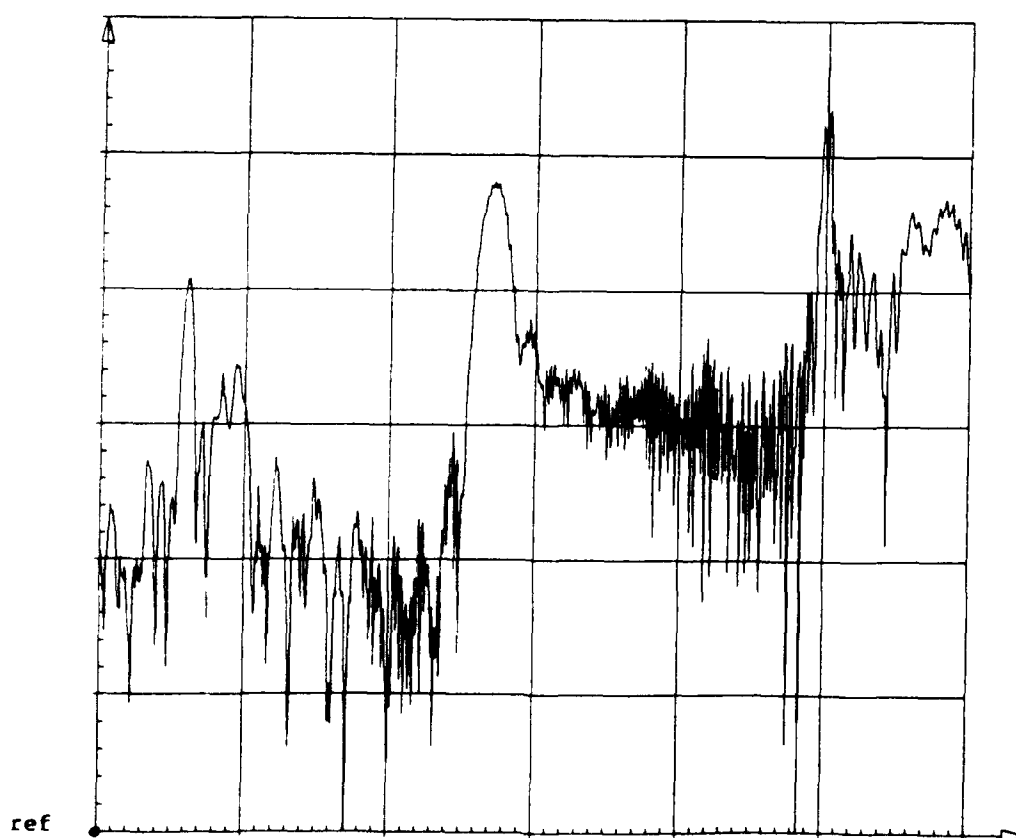


figure 7.b: SERMAT ( 7.5 GHz, polarisation HH )

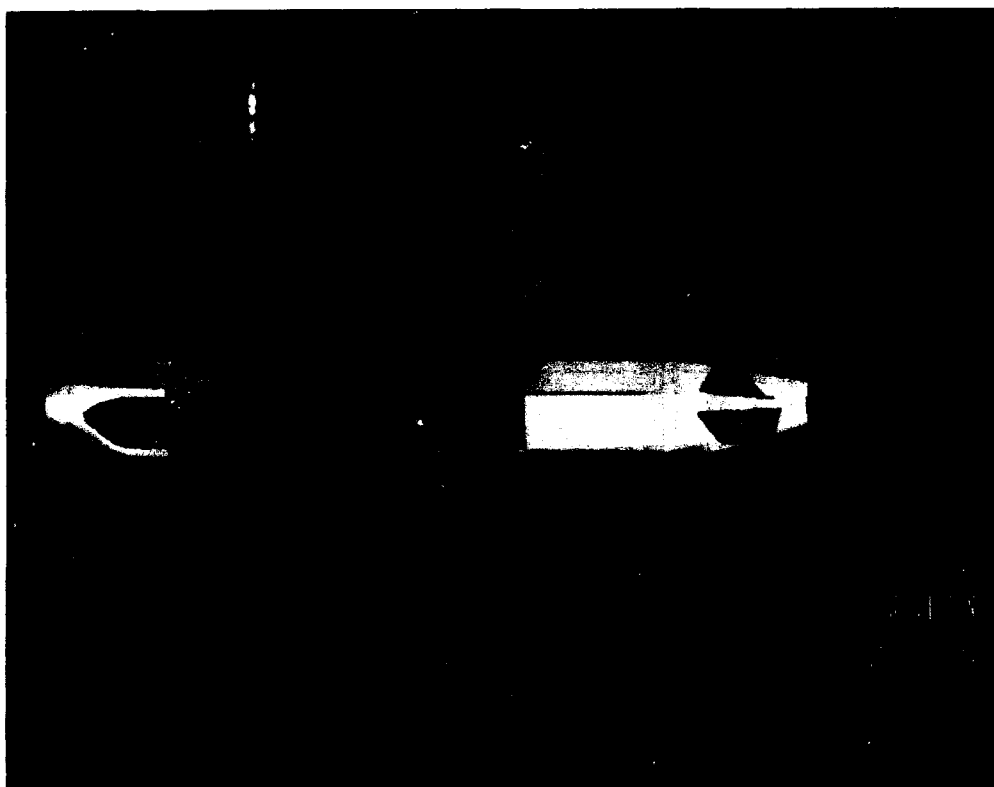


figure 8

# PARAMETRIC BICUBIC SPLINE AND C.A.D. TOOLS FOR COMPLEX TARGETS SHAPE MODELLING IN PHYSICAL OPTICS RADAR CROSS SECTION PREDICTION

A. DELOGU F. FURINI

ALenia  
AERITALIA E SELENIA  
SISTEMI DIFESA  
Strada Aeroporto  
10072 Caselle Torinese (Torino)  
ITALY

## Abstract

Increasing interest in RCS (Radar Cross Section) reduction is placing new demands on theoretical, computational and graphic techniques for calculating scattering properties of complex targets. In particular, computer codes capable of predicting the RCS of an entire aircraft at high frequency and of achieving RCS control with modest structural changes, are becoming of paramount importance in stealth design.

In this paper, a computer code, evaluating the RCS of arbitrarily shaped metallic objects CAD generated, and its validation with measurements carried out using ALenia RCS test facilities, are presented.

The code, based on the Physical Optics method is characterized by an efficient integration algorithm with error control, in order to contain the computer time within acceptable limits, and by an accurate parametric representation of the target surface in terms of bicubic splines.

## Keywords

RCS, High frequency techniques, Physical Optics, CAD models, RCS reduction.

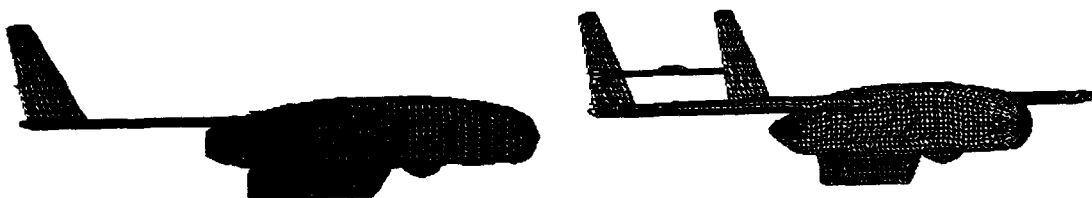


Fig. 1.1: Electromagnetic model for RCS evaluation in COBRA computer code.

## 1. Introduction

An existing need in the Radar Cross Section (RCS) community concerns computer codes capable of predicting the RCS for an entire aircraft at high frequency.

A first important problem in RCS computer programs is the representation on a two dimensional graphics screen of illuminated three dimensional scenes which may contain many solid objects and surfaces. In producing such images, the effects, which must be taken into account, include the obscuration of objects by other objects closer to the viewer, and the effects of different surface geometric properties on the scattered waves. Besides, a very good algorithm of surface description needs to be developed. Then, in order to compute the scattered field from metallic bodies that are large with respect to the wavelength, two approaches are widely used: ray techniques and Physical Optics. With the former, the search of reflection points can be extremely time consuming in the case of complicated surfaces specified with set of data points; moreover, the existence of caustic directions limits the applicability of the method. Physical Optics is not affected by the singularities of ray techniques but high efficiency integration algorithms are required to maintain the computer time within acceptable limits.

The computer code COBRA (Complex Object Backscattering Response Analysis) based on the Physical Optics method, characterized by an efficient integration scheme with error control and by an accurate parametric representation of the target surface in terms of bicubic splines, is presented.

## 2. Target geometrical description

In Radar Cross Section (RCS) prediction programs it is often required to extract numerical informations about the complex structure generated from a 3D CAD system, in order to create models adapt to electromagnetic processing. For this reason, the selection of a valid target geometrical description is extremely important.

In the past [1] flat plate modelling was used. The disadvantage of this method is that the flat plates are to be very small in terms of wavelength in order to obtain the correct value of the RCS of a smooth object and, this, requires a huge data base.

The actual efficiency of each numerical technique of target representation can be evaluated on the basis of the following considerations:

- Input data structure have to be compatible with data base coming from CAD systems already used in aeronautical and mechanical environment;
- The bodies have to be represented by simple, slim, non redundant, optimized and accurate descriptions: irregular and strange shapes shall be easily described;
- Full editing functions and quick visualization of the geometry and related modifications have to be integrated in the code;
- Data base shall immediately supply all informations, such as vector rays or surface normals, necessary for electromagnetic analysis.

Keeping into account these points, it was decided to use a "more economic" approach based on a parametric bicubic spline electromagnetic representation of the target surface, which is better suited to a smooth object.

#### a. CAD Data Acquisition

Bicubic splines guarantee  $C^2$  continuity which may be convenient for some part of the body, but not for the whole body. In fact, a complex target, such as an aircraft, can be generally considered to be a collection of smooth intersecting parts: fuselage, wings, cockpit, etc.

It is assumed that several sections of each object, orthogonal to a common axis are known. This information can be generated by means of a solid modeller, which generally provides the geometric model of the elements; in this work the solid modeller CATIA (Computer graphics Aided Three dimensional Interactive Applications) of Dassault Systemes copyright, has been used [2]. Geometric CAD elements can be defined through an exact definition respect a certain number of constraints; mathematically may have a canonical form, i.e. the elements are defined by their basic geometric characteristics, or a polynomial form, in which the elements are defined in a precise and unique manner.

There are two steps in the geometric design of an object:

1. At first, a mainframe design using points, lines and simple, calculated or interpolated curves, shall be developed;
2. then, the surface, conceived as an extension of the wireframe geometry in which the surfaces and faces are supported by wireframe object, shall be modelled.

The CAD generated surfaces can be:

- simple surfaces such as sphere, cylinders, cones and tori;
- interpolated surfaces;
- evolutive surfaces;
- net and patch;
- Bezier surfaces.

This CAD target geometrical description, is represented in fig. 2.1.

Once the geometric modelling of the object, of which we want to predict the RCS, is completed, it is necessary a careful sectioning, dependent on model characteristics, in order to obtain data ready to be processed from an electromagnetic point of view.

The curves, constituted by several arcs and obtained from the intersection of the surface model with parallel planes along a chosen axis, are stored in CATIA layers, that can be considered as sheets of tracing paper on which elements featuring common characteristics are grouped; an example of this sectioning technique is shown in fig 2.2.

An interface computer code reads the mathematical block associated at every curve in a layer and generates a data point file fully compatible with electromagnetic program. These steps are reported in fig. 2.3.

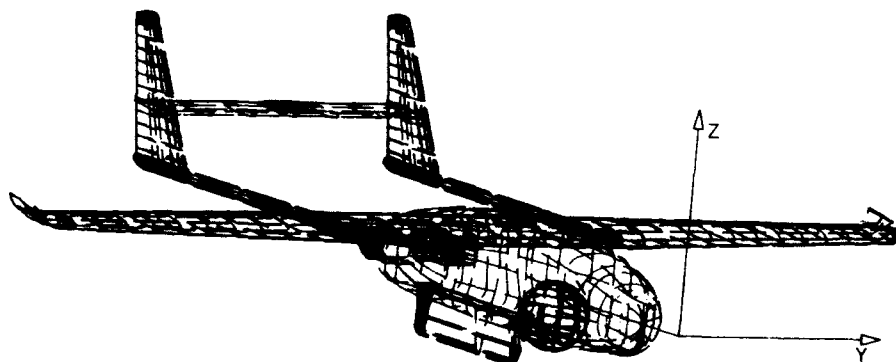


Fig. 2.1: CAD model geometrical construction.

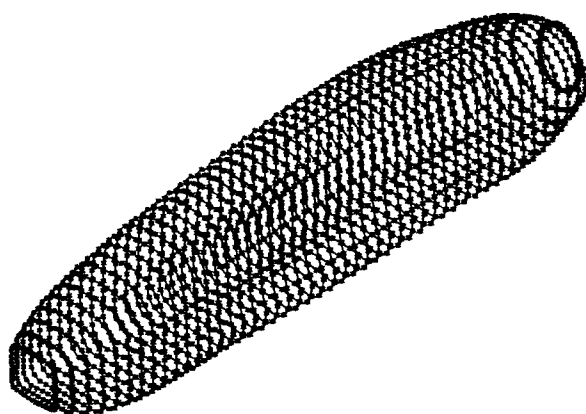


Fig. 2.2: CAD model geometrical sectioning.

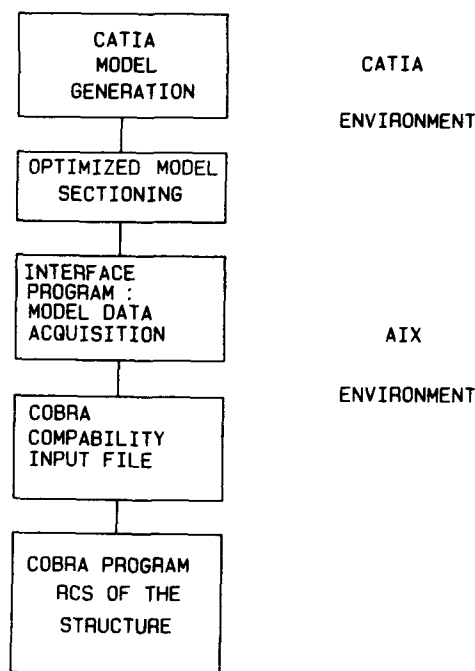


Fig. 2.3: Block structure for RCS evaluation of complex bodies.

#### b. Surface Parametrization

At this point, a surface with continuous curvature radius, passing by the assigned ordered points coming from the modeller, has been obtained by means of a bidimensional bicubic spline interpolation technique. Once the z-coordinate is known with respect to a local reference axis system, chosen in a convenient way for the test body, the section is assigned specifying x,y coordinates of a certain number of points called nodes. Beginning from cartesian coordinates in the local reference system  $S_L$  of the nodes constituting the sections, a parametric representation of the surface is given, introducing normalized incremental chordal coordinates, along each section (s) and across the sections (t):

$$x = x(s, t) \quad y = y(s, t) \quad z = z(s, t) \quad [2.1]$$

$$0 \leq s, t \leq 1$$

So, the generic surface is described through an ordered set of vector rays  $P(s_i, t_j)$ , where  $(s_i, t_j)$  defines the parametric coordinates of the node with connection numbers i,j. Each object surface is mapped one to one on the unit square of the s,t parametric plane: the points  $s_i, t_j$  form a cartesian regular lattice that subdivide the fundamental square  $T = [0,0;1,1]$  in a certain number of rectangles called "Patch Spline".

A bicubic spline interpolator, forcing  $C^2$  continuity of the functions with respect to s,t parameters, reconstructs the surface. The number and dimension of patch spline are correlated with the geometry of the target itself; in fact, while the position of the points on each curve, obtained from CAD sectioning, is dependant on the characteristics of the curve itself, the number of points increases in high curvature regions where are present some tips or wedges. An algorithm, distributing an assigned number of nodes (N) along a curve  $P(u)$  and condensing points near high curvature zones, has been implemented in these steps:

- At first, a metric monotonic growing function  $G(u)$  is defined:

$$G(u) = \int_0^u \left[ \left| \frac{dP(v)}{dv} \right| dv + k \left| \frac{d^2P(v)}{dv^2} \right| dv \right] \quad [2.2]$$

where k is a weight factor;

- then, the curvilinear abscissa normalized value  $u_i$  of every node is defined from [2.2];
- at last, curvilinear, curvature based, abscissas of all nodes  $u_i$  are defined :

$$\frac{\int_0^{u_i} \left[ \left| \frac{dP(v)}{dv} \right| dv + k \left| \frac{d^2P(v)}{dv^2} \right| dv \right]}{\int_0^1 \left[ \left| \frac{dP(v)}{dv} \right| dv + k \left| \frac{d^2P(v)}{dv^2} \right| dv \right]} = \frac{(i-1)}{(N-1)} \quad [2.3]$$

with

$$1 \leq i \leq N$$

It may be noted that the metric function  $G(u)$  depends from the curvature of the curve by means the second derivative terms in integral expression [2.2].

### c. Spline Interpolation

For  $(s, t) \in T$ , interpolation algorithm evaluates cartesian coordinates of the point  $P(s, t)$  and partial derivative

$$\frac{\partial P}{\partial s}, \frac{\partial P}{\partial t}, \frac{\partial^2 P}{\partial s^2}, \frac{\partial^2 P}{\partial t^2}, \frac{\partial^2 P}{\partial s \partial t}.$$

The coefficients of the interpolation are computed, at first, with a very heavy computer time waste; then in a second phase the desired values for every assigned pair  $(s, t)$  are obtained: this computation is not time consuming if the coefficients are known. Spline coefficients are calculated by imposing either the continuity of the function and of its derivative until the second order in all internal nodes and adapt boundary conditions on extremal nodes. In fig. 2.4 the three dimensional representation of two spheroids and their mapping in  $s, t$  parametric plane, are shown. Using appropriate boundary conditions in the spline interpolation, it is also possible to describe also geometric singularities, as tips on longitudinal axis and wedge on the coordinate curve  $s=0$ . Obviously, in this case, attention must be paid to define as first point of the cross sections the ones of the wedge; more complex singularities can be handled dividing the primitive surface in simple surfaces and making interpolation separately on these. Bicubic spline are defined as tensorial product of unidimensional cubic spline in the  $s$  and in the  $t$  variables.

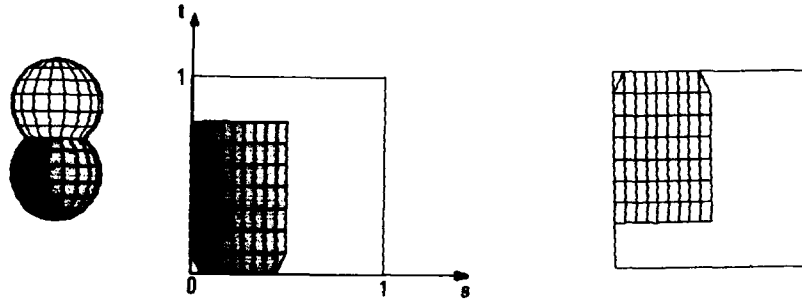


Fig. 2.4:  $s, t$  parametric mapping of two intersecting spheres.

A unidimensional cubic spline interpolation on  $s$  parametric coordinates in the points  $(s_i, F(s_i, t_j); i = 1, \dots, N_s)$  for every value of  $t_j$  ( $j = 1, \dots, N_t$ ) is performed and, from these  $N_t$  unidimensional splines, the values of  $\frac{\partial F}{\partial s}$  in all nodes  $s_i, t_j$  can be obtained.

Then an interpolation in  $t$  variable on the points  $(t_j, F(s_i, t_j); j = 1, \dots, N_t)$  for everyone of the values of  $s_i$  ( $i = 1, \dots, N_s$ ) is performed.

$\frac{\partial F}{\partial t}$  can be computed in all nodes from these  $N_s$  unidimensional splines. This process can be iterated, interpolating in  $s$  the function  $\frac{\partial F}{\partial t}$  i.e. on the points  $(s_i, \frac{\partial F(s_i, t_j)}{\partial t}; i = 1, \dots, N_s)$  for every of the values of  $t_j$  ( $j = 1, \dots, N_t$ ). In this manner the value of  $\frac{\partial^2 F}{\partial s \partial t}$  is evaluated in all nodes and all coefficients are known. The generic function  $F(s, t)$  could identify  $x, y$  or  $z$ , being independently quantities. For a generic point of the surfaces, either the vector ray  $P(s, t)$  and the fundamental vector product  $\frac{\partial P}{\partial s} \times \frac{\partial P}{\partial t}$  can be obtained; the absolute value of this vector, times  $ds dt$ , is the elementary surface area and its direction is the normal to surface itself.

### d. Simple Surfaces Composition

Once elementary surfaces are generated, the global description of the whole body, specifying the position and the orientation of different local reference systems ( $S_L$ ) in which the elemental surfaces are described, shall be obtained. By means of a rototranslation in laboratory system ( $S_0$ ), the position and orientation of simple surfaces are detected. While the reference system is fixed, all vectors of the space are transformed; this particular geometric transformation is called active transformation.

The translation of the local system ( $S_L$ ) is specified through the spherical coordinates  $R_{0L}, \theta_{0L}, \phi_{0L}$ , of the  $S_L$  origin with respect to  $S_0$ . Three angles are used:  $\theta, \phi, \psi$ ; while the angles  $\theta, \phi$  identify a rigid translation that connected the polar axis of the local reference system in the direction specified from those angles, angle  $\psi$  define a further rotation around polar axis  $S_L$ , in the anticlockwise verse. If  $\mathfrak{R}(\alpha, \vec{n})$  is the rotation operator that performs an angle  $\alpha$  rotation around the direction of  $\vec{n}$ , the previous transformation can be expressed as:

$$P_0 = \mathfrak{R}(\psi, \vec{r}) \mathfrak{R}(\theta, \vec{\phi}) P_{Li} \quad [2.4]$$

or

$$P_0 = \mathfrak{R}(\theta, \vec{\phi}) \mathfrak{R}(\psi, \vec{r}) P_{Li} \quad [2.5]$$

where  $P_{Li}$  is a generic point of the body *before* of the rotation and  $P_0$  is the same point *after* the rotation. It may be shown that these two ways of describing the full rotation are equivalent.[3]

The operator  $\mathfrak{R}(\alpha, \vec{n})$  shall be found. From mechanics, the instantaneous velocity  $\vec{v}$  of a generic point of the body, characterized from the vector  $\vec{r}$ , is given from the relation:  $\vec{v} = \vec{\omega} \times \vec{r}$  i.e.

$$\frac{d\vec{r}}{dt} = \vec{\omega} \times \vec{r} = \vec{\omega} \times I \vec{r} \quad [2.6]$$

where  $I$  is the identity dyadic. Solving with the position  $\vec{\omega} = \omega \vec{n}$  and  $\alpha = \omega(t - t_0)$ :

$$\bar{r}(\alpha) = \exp[(\hat{n}xI)\alpha] \bar{r}(t_0) \quad [2.7]$$

Developing the exponential in Taylor series:

$$\exp[(\hat{n}xI)\alpha] = \sum_{m=0}^{\infty} \frac{(\hat{n}xI)^m (\alpha^m)}{m!} \quad [2.8]$$

and being

$$\begin{aligned} (\hat{n}xI)^2 &= (\hat{n}xI) (\hat{n}xI) = \hat{n}\hat{n} - I = -I_{t,n} \\ (\hat{n}xI)^3 &= (\hat{n}xI) (-I_{t,n}) = -(\hat{n}xI) \\ (\hat{n}xI)^4 &= (\hat{n}xI)^2 (\hat{n}xI)^2 = (-I_{t,n}) (-I_{t,n}) = I_{t,n} \\ (\hat{n}xI)^5 &= (\hat{n}xI) \\ &\vdots \end{aligned}$$

where  $I_{t,n}$  is the trasversal identity dyadic with respect  $\hat{n}$ , then

$$\begin{aligned} \exp[(\hat{n}xI)\alpha] &= I + (\hat{n}xI) \sum_{n=0}^{\infty} \frac{(-1)^{2n+1} \alpha^{2n+1}}{(2n+1)!} + I_{t,n} \sum_{n=1}^{\infty} \frac{(-1)^n \alpha^{2n}}{(2n)!} = \\ &= I + (\hat{n}xI) \sin \alpha + I_{t,n} (\cos \alpha - 1) = \hat{n}\hat{n} + (\hat{n}xI) \sin \alpha + I_{t,n} \cos \alpha \quad [2.9] \end{aligned}$$

is obtained. Rotation operator can be expressed as:

$$\mathcal{R}(\psi, \bar{r}) = \exp[(\bar{r}xI)\psi] \quad [2.10]$$

$$\mathcal{R}(\psi, \hat{z}) = \exp[(\hat{z}xI)\psi] \quad [2.11]$$

$$\mathcal{R}(\theta, \hat{\phi}) = \exp[(\hat{\phi}xI)\theta] \quad [2.12]$$

These operator can be written in Cartesian fixed base  $S_0$ ; infact being

$$\begin{aligned} \hat{\phi} &= -\sin \phi \hat{x} + \cos \phi \hat{y} \\ \hat{n}\hat{n} = \hat{\phi}\hat{\phi} &\Leftrightarrow \begin{bmatrix} \sin^2 \phi & -\sin \phi \cos \phi & 0 \\ -\sin \phi \cos \phi & \cos^2 \phi & 0 \\ 0 & 0 & 0 \end{bmatrix} \quad [2.13] \end{aligned}$$

$$I_{t,n} = I - \hat{n}\hat{n} \Leftrightarrow \begin{bmatrix} \cos^2 \phi & \sin \phi \cos \phi & 0 \\ \sin \phi \cos \phi & \sin^2 \phi & 0 \\ 0 & 0 & 1 \end{bmatrix} \quad [2.14]$$

and then

$$\hat{n}xI \Leftrightarrow \begin{bmatrix} 0 & 0 & \cos \phi \\ 0 & 0 & \sin \phi \\ -\cos \phi & -\sin \phi & 0 \end{bmatrix} \quad [2.15]$$

In conclusion, applying [2.9] we have:

$$\mathcal{R}(\theta, \hat{\phi}) = \begin{bmatrix} \cos^2 \phi \cos \theta + \sin^2 \phi & \sin \phi \cos \phi (\cos \theta - 1) & \sin \theta \cos \phi \\ \sin \phi \cos \phi (\cos \theta - 1) & \sin^2 \phi \cos \theta + \cos^2 \phi & \sin \theta \sin \phi \\ -\sin \theta \cos \phi & -\sin \theta \sin \phi & \cos \theta \end{bmatrix} \quad [2.16]$$

Now  $\mathcal{R}(\psi, \hat{z})$  shall be calculated:

$$\hat{n}\hat{n} = \hat{z}\hat{z} \Leftrightarrow \begin{bmatrix} 0 & 0 & 0 \\ 0 & 0 & 0 \\ 0 & 0 & 1 \end{bmatrix} \quad [2.17]$$

$$I_{t,n} = I - \hat{n}\hat{n} \Leftrightarrow \begin{bmatrix} 1 & 0 & 0 \\ 0 & 1 & 0 \\ 0 & 0 & 0 \end{bmatrix} \quad [2.18]$$

and

$$(\hat{n}xI) = \hat{z} \times (\hat{z}\hat{z} + \hat{y}\hat{y} + \hat{x}\hat{x}) = \hat{y}\hat{z} - \hat{z}\hat{y} \quad [2.19]$$

$$\hat{n}xI \Leftrightarrow \begin{bmatrix} 0 & -1 & 0 \\ 1 & 0 & 0 \\ 0 & 0 & 0 \end{bmatrix} \quad [2.20]$$

at last:

$$R(\psi, \hat{z}) = \begin{bmatrix} \cos \psi & -\sin \psi & 0 \\ \sin \psi & \cos \psi & 0 \\ 0 & 0 & 1 \end{bmatrix} \quad [2.21]$$

where  $R(\psi, \hat{z})$  is the array in cartesian basis  $S_0$  corresponding to the operator  $\mathcal{R}(\psi, \hat{z})$ . Then from [2.5] we obtain the result:

$$P_0 = R(\theta, \hat{\phi}) R(\psi, \hat{z}) P_{L_1} = R P_{L_1} \quad [2.22]$$

where

$$R = \begin{bmatrix} \cos \phi \cos \theta \cos \delta + \sin \phi \sin \delta & \sin \delta \cos \phi \cos \theta - \sin \phi \cos \delta & \sin \theta \cos \phi \\ \cos \theta \cos \delta \sin \phi - \sin \delta \cos \phi & \sin \delta \sin \phi \cos \theta + \cos \phi \cos \delta & \sin \theta \sin \phi \\ -\sin \theta \cos \phi & -\sin \theta \sin \delta & \cos \theta \end{bmatrix} \quad [2.23]$$

with  $\delta = \phi - \psi$  [2.24]. This is the result.

It may be demonstrated that the same array can be obtained performing at first the rotation around  $\hat{\phi}$  and then around  $\hat{r}$ . At this point, the rototranslation connected to the surface  $j$  has been defined:

$$P_0 = R_j P_{Lj} + T_{Lj} \quad [2.25]$$

where  $R_j$  is defined from [2.23] and the translation vector  $T_{Lj}$  is :

$$T = \begin{bmatrix} R_{0j} \cos \phi_{0j} \sin \theta_{0j} \\ R_{0j} \sin \phi_{0j} \sin \theta_{0j} \\ R_{0j} \cos \theta_{0j} \end{bmatrix} \quad [2.26]$$

It is interesting to note that this transformation can be performed directly on the coefficients of spline interpolation, operating on vector from local to laboratory reference system by means of multiplication of rotation arrays:

$$P_0 = R_j P_{Lj} + T_{Lj} \quad [2.27a]$$

$$\frac{\partial P_0}{\partial s} = R_j \frac{\partial P_{Lj}}{\partial s} \quad [2.27b]$$

$$\frac{\partial P_0}{\partial t} = R_j \frac{\partial P_{Lj}}{\partial t} \quad [2.27c]$$

$$\frac{\partial^2 P_0}{\partial s \partial t} = R_j \frac{\partial^2 P_{Lj}}{\partial s \partial t} \quad [2.27d]$$

#### e. Surfaces Intersection

In order to calculate the Radar Cross Section it is not necessary to evaluate the curve obtained from the intersection of two surfaces, but rather the light zone of the surfaces. This calculation may be performed, subdividing spline patches in geometrical patches and approximating the surface in these elements with bilinear expression. In this manner, the problem can be reduced to the determination of the intersection between different sides of a geometrical patch with a bilinear surface.

A bilinear surface, defined on a rectangle on  $s, t$  plane which geometrical image vertex are the points  $P_1, P_2, P_3, P_4$  in the anticlockwise verse with respect to the output normal, can be represented as:

$$P(s, t) = P_1 + (P_4 - P_1)s + (P_2 - P_1)t + (P_1 - P_2 + P_3 - P_4)st \quad 0 \leq s, t \leq 1$$

The segment connecting two points PA and PB is described as:

$$P(u) = P_A + (P_B - P_A)u \quad 0 \leq u \leq 1$$

The following equation has to be solved:

$$P(s, t) = P(u) \quad 0 \leq s, t, u \leq 1$$

or

$$VC + VSs + VTt + VWst + VUu = 0 \quad [2.28]$$

This is a non linear system in three unknowns  $s, t, u$  that can be solved by introducing a new variable  $w = st$ . In a general case when all coefficients are different from zero, the vectors  $VS, VT, VW$  are not planar and the system is solved in  $s, t, w$  considering  $u$  as parameter. The  $u$  value may be found by imposing the relation  $w(u) = s(u)t(u)$ . In array formalism:

$$[VS \ VT \ VW] \begin{bmatrix} s \\ t \\ w \end{bmatrix} = -[VC] - [VU]u \quad [2.29]$$

i.e.

$$[A] \begin{bmatrix} s \\ t \\ w \end{bmatrix} = -[VC] - [VU]u \quad [2.30]$$

and

$$\begin{bmatrix} s \\ t \\ w \end{bmatrix} = -[A]^{-1}[VC] - [A]^{-1}[VU]u \quad [2.31]$$

This last expression may be written in the form:

$$\begin{bmatrix} s \\ t \\ w \end{bmatrix} = \begin{bmatrix} \alpha_1 \\ \alpha_2 \\ \alpha_3 \end{bmatrix} + \begin{bmatrix} \beta_1 \\ \beta_2 \\ \beta_3 \end{bmatrix} u \quad [2.32]$$

Now imposing  $w(u) = s(u)t(u)$ :

$$(\alpha_3 + \beta_3 u) = (\alpha_1 + \beta_1 u) \cdot (\alpha_2 + \beta_2 u)$$

we obtain:

$$(\beta_1 \beta_2) u^2 + (\alpha_1 \beta_2 + \alpha_2 \beta_1 - \beta_3)u + (\alpha_1 \alpha_2 - \alpha_3) = 0$$



Now it is immediate the evaluation of  $u$ ,  $s(u)$ ,  $t(u)$  and, from these, of the intersection point if  $0 \leq u, s, t \leq 1$ . Instead, if the vectors  $\underline{VS}$ ,  $\underline{VT}$ ,  $\underline{VW}$  are complanar, the array  $[A]$  is not invertible and a new way have to be followed. Starting from [2.28] and resolving with respect  $u, s, t$ , considering  $w$  as a parameter, being  $\underline{VW}$  linear combination of  $\underline{VS}$  and  $\underline{VT}$ , it derives:

$$[\underline{VS} \ \underline{VT} \ \underline{VU}] \begin{bmatrix} s \\ t \\ u \end{bmatrix} = -[\underline{VC}] - [\underline{VW}]w \quad [2.33]$$

i.e.

$$[A] \begin{bmatrix} s \\ t \\ u \end{bmatrix} = -[\underline{VC}] - [\underline{VW}]w \quad [2.34]$$

and

$$\begin{bmatrix} s \\ t \\ u \end{bmatrix} = -[A]^{-1}[\underline{VC}] - [A]^{-1}[\underline{VW}]w \quad [2.35]$$

and

$$\begin{bmatrix} s \\ t \\ u \end{bmatrix} = \begin{bmatrix} \gamma_1 \\ \gamma_2 \\ \gamma_3 \end{bmatrix} + \begin{bmatrix} \delta_1 \\ \delta_2 \\ \delta_3 \end{bmatrix} w \quad [2.36]$$

Now imposing  $w = s(w) t(w)$ :

$$w = (\gamma_1 + \delta_1 w) \cdot (\gamma_2 + \delta_2 w)$$

we obtain:

$$(\delta_1 \delta_2) w^2 + (\gamma_1 \delta_2 + \gamma_2 \delta_1 - 1)w + (\gamma_1 \gamma_2) = 0$$

Calculating  $w$ ,  $s(w)$ ,  $t(w)$ ,  $u(w)$  the coordinates of intersection points, if  $0 \leq u, s, t \leq 1$ , are evaluated

### 3. Physical Optics scattered field computation

The scattered electromagnetic field can be computed by integration of the induced current distribution; owing the large size in terms of wavelength of the targets we are interested in (an aircraft at X-band can be 1000 wavelength long), the induced current distribution can be determined by the Physical Optics approximation, which for metallic targets gives :

$$\underline{J}_s = \begin{cases} 2(\hat{n} \times \underline{\vec{H}}_i) & \text{in the lit region;} \\ 0 & \text{elsewhere.} \end{cases} \quad [3.1]$$

where  $\hat{n}$  is the surface outward unit normal and  $\underline{\vec{H}}_i$  is the incident magnetic field.

On the basis of equation [3.1], it can be shown that the backscattering RCS  $\sigma(\hat{r})$  is given by [3]:

$$\sigma(\hat{r}) = \frac{4\pi}{\lambda^2} \left| \hat{r} \int_{lit \ region} \hat{n} \exp(2jk_0 \hat{r} \cdot \underline{\vec{r}}_E) dS \right|^2 \quad [3.2]$$

where  $k_0 = \frac{2\pi}{\lambda}$  is the freespace wavenumber and  $\hat{r}$  is the observation direction. Fig.[3.1] shows the problem geometry.

It is convenient to carry out the surface integration directly in parameter space, and equation [3.2] becomes:

$$\sigma(\hat{r}) = \frac{4\pi}{\lambda^2} \left| \hat{r} \cdot \int_{\Xi} \frac{\partial \underline{\vec{r}}_E}{\partial s} \times \frac{\partial \underline{\vec{r}}_E}{\partial t} \exp(2jk_0 \hat{r} \cdot \underline{\vec{r}}_E(s, t)) ds dt \right|^2 \quad [3.3]$$

where  $\underline{\vec{r}}_E(s, t)$  is the parametric equation of each body. Being the scattered field parallel to the incident field, in this approximation no information is available on the behaviour of scattered body with respect to the depolarization of the field. In [3.3] a key point is the determination of the integration domain  $\Xi$ ; a surface element belong to it if:

- it is not internal to some of the intersecting objects;
- $\hat{n} \cdot \hat{r} \leq 0$ ; i.e. it faces the incoming wave;
- it is not shadowed by other parts of the same or of other objects.

The second is the easiest check because it is based on a local criterium; the other two can be performed by sorting the spline patches according to their distance from the observer and, then, carrying out a series of geometric tests. The actual computation of the integral is by no means a trivial matter since:

- the integral is two-dimensional and is to be carried out over a complicated domain;
- the exponential function in the integrand is very rapidly oscillating.

These problems are solved by an efficient numerical technique with error control, which is described in a next section.

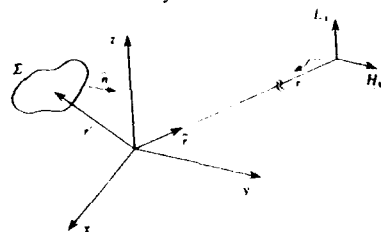


Fig. 3.1: Problem geometry

- a. **Phase Integrals** As before described, the object surface is represented through bicubic spline with vectorial coefficients:

$$\vec{r}_{\Sigma}(s, t) = \sum_{i=0}^3 \sum_{j=0}^3 \vec{r}_{ij} s^i t^j \quad [3.4]$$

and, also, the phase term has a bicubic spline behaviour:

$$\psi(s, t) = \sum_{i=0}^3 \sum_{j=0}^3 a_{ij} s^i t^j \quad [3.5]$$

where  $a_{ij} = 2\vec{r} \cdot \vec{r}_{ij}$  and

$$\frac{\partial \vec{r}_{\Sigma}}{\partial s} \times \frac{\partial \vec{r}_{\Sigma}}{\partial t} = \sum_i \sum_j \sum_m \sum_n [\vec{r}_{ij} \times \vec{r}_{mn}] i_j s^{i+m-1} t^{j+n-1} \quad [3.6]$$

Being:

$$M(s, t) = \frac{2\sqrt{\pi}}{\lambda} \left[ \vec{r} \cdot \frac{\partial \vec{r}_{\Sigma}}{\partial s} \times \frac{\partial \vec{r}_{\Sigma}}{\partial t} \right] \quad [3.7]$$

it is obtained the relevant RCS integral:

$$I = \int_{\Xi} M(s, t) \exp[jk_0 \psi(s, t)] ds dt \quad [3.8]$$

where  $M$  and  $\psi$  are slowly varying with respect to the exponential function and  $\Xi$  is the image in parametric space of the lit object region. A classical approach to the computation of phase integrals like equation [3.8] is the Ludwig method [4] which consists in approximating separately  $M$  and  $\psi$  over a conveniently small rectangular subdomain of size  $\Delta s, \Delta t$  by a linear function, performing analitically the resulting integral and summing the partial results. Gravelaeter et al. [5] suggested an improved criterium for the choice of the linear function and Pogorzelski [6] presented an algorithm for one dimensional integrals, where the phase is approximated by a complex polynomial. In order to improve the performances, the technique has been successively applied with a linear approximation to triangular regions [7]. In this method an error control integration technique has been implemented: in order to determine a more accurate value of the integral for complex bodies having complicated integration domains, due to intersections, blocking factors and obscuration, a predefined mean square error  $\epsilon$  in the approximations, inserted in integral calculation, is introduced. By means of the definition of a parameter space domain  $\Xi(s, t)$  and the knowledge of integrand function by points, an automatic subdivision, also non uniform, of the assigned region will be evaluated. The subdivision criterium is based on mean square error, in integral meaning, between the phase of the integrand function and his optimal linear approximations; this error shall be maintained under a predefined assigned value depending, besides of the wavelength of the radiation, also from the polynomial degree used to represent the slowly varying part.

- b. **Numerical integration technique**

In this method, the integration domain  $\Xi$  is subdivided into rectangular subregions with sides  $(\Delta s, \Delta t)$  to be determined, whose contributions can be written, without approximations:

$$\Delta I = \int_{s_0}^{s_0 + \Delta s} \int_{t_0}^{t_0 + \Delta t} G(s, t) \exp[jk_0 L(s, t)] ds dt \quad [3.9]$$

where

$$G(s, t) = M(s, t) \exp[jk_0(\psi(s, t) - L(s, t))] \quad [3.10]$$

and

$$L(s, t) = \alpha s + \beta t + \gamma \quad [3.11]$$

is a linear function chosen to minimize the difference  $\psi - L$ , in such a way that  $G(s, t)$  is still slowly varying. While with the Ludwig method all integration domains have the same physical dimensions with respect to the wavelength and the  $L$  function is determined minimizing the distance with the values assumed from  $\psi$  function in integration domain vertex, here  $L$  is chosen so that the root mean square error  $\epsilon$ , defined by

$$\epsilon^2(s_0, t_0, \Delta s, \Delta t) = \frac{1}{\Delta s \Delta t} \int_{s_0}^{s_0 + \Delta s} \int_{t_0}^{t_0 + \Delta t} |\psi(s, t) - L(s, t)|^2 ds dt \quad [3.12]$$

attains its minimum value for a given rectangle. It is introduced a matricial notation for calculating the coefficients  $\alpha, \beta, \gamma$ , supposing  $s_0 = t_0 = 0$ :

$$\epsilon^2 = \frac{1}{\Delta s \Delta t} \int_0^{\Delta s} \int_0^{\Delta t} (\vec{P} \cdot \vec{a} - \vec{L} \cdot \vec{C})^2 ds dt \quad [3.13]$$

where  $C$  and  $L$  are

$$\vec{C} \Leftrightarrow [\gamma \quad \alpha \quad \beta]$$

$$\vec{L} \Leftrightarrow [1 \quad s \quad t]$$

$\vec{a}$  is the coefficient bicubic spline vector, defined from [3.5]

$$\vec{a} \Leftrightarrow [a_{00} \quad a_{10} \quad \dots \quad a_{23} \quad a_{33}]$$

and

$$\vec{P} \Leftrightarrow [1 \ s \ t \ s^2 \ st \ t^2 \ \dots \ s^2 t^3 \ s^3 t^3]$$

In order to evaluate the integral, a variables changement shall be done:  $s = u\Delta s$ ,  $t = v\Delta t$  and the arrays

$$\underline{M} = \begin{bmatrix} 1 & 0 & 0 \\ 0 & \Delta s & 0 \\ 0 & 0 & \Delta t \end{bmatrix}$$

$$\underline{T} = \text{diag} [1, \Delta s, \Delta t, \Delta s^2, \Delta s \Delta t, \dots, \Delta s^3 \Delta t^3]$$

are introduced. Now the vectors  $\vec{P}$  and  $\vec{L}$  can be written as

$$\vec{P} = \vec{U} \cdot \underline{T}$$

$$\vec{L} = \vec{V} \cdot \underline{M}$$

where the vectors  $\vec{U}$ ,  $\vec{V}$  are defined as

$$\vec{V} \Leftrightarrow [1 \ u \ v]$$

$$\vec{U} \Leftrightarrow [1 \ u \ v \ u^2 \ uv \ v^2 \ \dots \ u^2 v^3 \ u^3 v^3]$$

So expression [3.12] may be written:

$$\epsilon^2 = \int_0^1 \int_0^1 (\vec{U} \cdot \underline{T} \cdot \vec{a} - \vec{V} \cdot \underline{M} \cdot \vec{C})^2 du dv \quad [3.14]$$

$\vec{C}$  is determined in such a way that  $\epsilon^2$  is minimized; nulling the gradient of [3.14] with respect to  $\vec{C}$ :

$$\nabla \epsilon^2 = -2 \int_0^1 \int_0^1 \vec{V} \cdot \underline{M} (\vec{U} \cdot \underline{T} \cdot \vec{a} - \vec{V} \cdot \underline{M} \cdot \vec{C}) du dv = 0 \quad [3.15]$$

and observing that

$$\vec{V} \cdot \underline{M} = \underline{M}^* \cdot \vec{V}$$

being  $\underline{M}$  diagonal it is obtained:

$$2 \int_0^1 \int_0^1 \underline{M} \cdot \vec{V} \vec{U} \cdot \underline{T} \cdot \vec{a} du dv = 2 \int_0^1 \int_0^1 \underline{M} \cdot \vec{V} \vec{V} \cdot \underline{M} \cdot \vec{C} du dv \quad [3.16]$$

Now defining the dyadics:

$$\underline{W} = \vec{V} \vec{V} = \begin{bmatrix} 1 & u & v \\ u & u^2 & uv \\ v & uv & v^2 \end{bmatrix}$$

and

$$\underline{Z} = \vec{V} \vec{U} = \begin{bmatrix} 1 & u & v & u^2 & uv & \dots & u^2 v^3 & u^3 v^3 \\ u & u^2 & uv & u^3 & u^2 v & \dots & u^3 v^3 & u^4 v^3 \\ v & uv & v^2 & u^2 v & u^2 v^2 & \dots & u^2 v^4 & u^3 v^4 \end{bmatrix}$$

the relation

$$2 \int_0^1 \int_0^1 \underline{M} \cdot \underline{Z} \cdot \underline{T} \cdot \vec{a} du dv = 2 \int_0^1 \int_0^1 \underline{M} \cdot \underline{W} \cdot \underline{M} \cdot \vec{C} du dv \quad [3.17]$$

and unknown coefficients:

$$\vec{C} = \underline{A} \cdot \vec{a}$$

where

$$\underline{A} = \left[ \int_0^1 \int_0^1 \underline{M} \cdot \underline{W} \cdot \underline{M} du dv \right]^{-1} \cdot \left[ \int_0^1 \int_0^1 \underline{M} \cdot \underline{Z} \cdot \underline{T} du dv \right] \quad [3.18]$$

are evaluated. The first integral in [3.18] is calculated with an integration on dyadic  $\underline{W}$ :

$$\underline{M} \cdot \int_0^1 \int_0^1 \underline{W} du dv \cdot \underline{M} = \underline{M} \cdot \underline{D} \cdot \underline{M} \quad [3.19]$$

where  $\underline{D}$  is:

$$\underline{D} = \int_0^1 \int_0^1 \underline{W} du dv = \begin{bmatrix} 1 & 1/2 & 1/2 \\ 1/2 & 1/3 & 1/4 \\ 1/2 & 1/4 & 1/3 \end{bmatrix} \quad [3.20]$$

With the same procedure, it is obtained for the second integral:

$$\underline{M} \cdot \int_0^1 \int_0^1 \underline{Z} du dv \cdot \underline{T} = \underline{M} \cdot \underline{E} \cdot \underline{T} \quad [3.21]$$

where  $\underline{E}$  is:

$$\underline{E} = \int_0^1 \int_0^1 \underline{Z} du dv = \begin{bmatrix} 1 & 1/2 & 1/2 & \dots & 1/8 & 1/12 & 1/16 \\ 1/2 & 1/3 & 1/4 & \dots & 1/10 & 1/16 & 1/20 \\ 1/2 & 1/4 & 1/3 & \dots & 1/12 & 1/15 & 1/20 \end{bmatrix} \quad [3.22]$$

Then:

$$\vec{C} = \underline{A} \cdot \vec{a} = [\underline{M} \cdot \underline{D} \cdot \underline{M}]^{-1} \cdot [\underline{M} \cdot \underline{E} \cdot \underline{T}] \cdot \vec{a} = \underline{M}^{-1} \cdot \underline{D}^{-1} \cdot \underline{E} \cdot \underline{T} \cdot \vec{a}$$

and if  $\underline{B} = \underline{D}^{-1} \cdot \underline{E}$  we obtain:  $\vec{C} = (\underline{M}^{-1} \cdot \underline{B} \cdot \underline{T}) \cdot \vec{a} \quad [3.23]$

### c. Evaluation of mean square error

Knowing the coefficients  $\alpha, \beta, \gamma$  of the linear function  $L$ , the error  $\epsilon$  has to be evaluated. Substituting the [3.23] in [3.14]:

$$\epsilon^2 = \int_0^1 \int_0^1 \left\{ \left[ (\bar{U}(u,v) \cdot T - \bar{V}(u,v) \cdot M \cdot M^{-1} \cdot B \cdot T) \cdot \bar{a} \right]^2 \right\} du dv \quad [3.24]$$

after some matrix calculations

$$\epsilon^2 = \bar{a} \cdot Q \cdot \bar{a}$$

with

$$Q = \int_0^1 \int_0^1 \left[ (B^* \cdot \bar{V}(u,v) - \bar{U}(u,v)) \cdot (\bar{U}(u,v) - \bar{V}(u,v) \cdot B) \right] du dv \quad [3.25]$$

is evaluated. Because  $Q$  array can be analytically evaluated, mean square error, expressed as a twelfth degree polynomial in  $\Delta s, \Delta t$ , can be written in the form [3],[11]:

$$\epsilon^2 = \frac{1}{180} a_{20}^2 \Delta s^4 + \frac{1}{144} a_{11}^2 \Delta s^2 \Delta t^2 + \frac{1}{180} a_{02}^2 \Delta t^4 + O(\Delta s, \Delta t) \quad [3.26]$$

### d. Largest integration determination area

Our goal now is to find the size of an integration subdomain for which the r.m.s. error  $\epsilon$  is not greater than a prescribed fraction of wavelength. The complete expression of eq. [3.26] is analytically untractable: therefore only the polynomial expression containing fourth degree terms is considered. By means of Lagrange multiplier technique,  $\Delta s \Delta t$  dimensions of maximum area, connected to a prefixed r.m.s. error  $\epsilon$ , are evaluated and trial values  $\Delta s \Delta t$  corrected by a very rapidly iterative procedure. Written the [3.26] as:

$$ax^4 + bx^2y^2 + cy^4 = d$$

with  $a = \frac{1}{180} a_{20}^2$ ,  $b = \frac{1}{144} a_{11}^2$ ,  $c = \frac{1}{180} a_{02}^2$ ,  $d = \epsilon^2$ ,  $x = \Delta s$ ,  $y = \Delta t$ , in order to maximize the  $xy$  rectangle area, a function, depending of a unknown parameter  $\lambda$ ,  $\phi(x,y)$ , have to be built :

$$xy + \lambda(ax^4 + bx^2y^2 + cy^4) = \phi(x,y)$$

Nulling partial derivative of  $\phi(x,y)$  with respect  $x$  and  $y$  and solving for  $\lambda$  :

$$\lambda = -\frac{y}{4ax^3 + 2bxy^2} = -\frac{x}{4cy^3 + 2bxy^2} \quad \text{i.e. } y^4 = \frac{a}{c} x^4 \text{ at last}$$

$$x^4 = \frac{d}{2a + b\sqrt{\frac{c}{a}}}$$

$$y^4 = \frac{d}{2c + b\sqrt{\frac{c}{a}}}$$

then

$$\Delta s = \left[ \frac{\epsilon^2}{\frac{a_{20}^2}{90} + \frac{a_{11}^2}{144} \left| \frac{a_{20}}{a_{02}} \right|} \right]^{1/4} \quad [3.27]$$

$$\Delta t = \left[ \frac{\epsilon^2}{\frac{a_{02}^2}{90} + \frac{a_{11}^2}{144} \left| \frac{a_{02}}{a_{20}} \right|} \right]^{1/4} \quad [3.28]$$

are obtained. An example of a contour of  $\epsilon$  in the  $\Delta s, \Delta t$  is shown in fig.[3.2]. The points of the contour represent integration subdomain characterized by the same r.m.s. error : M is the point defined from last two relations with the largest area .

If the integral were one dimensional, the choice of the largest subdomain, consistent with the error criterion, would lead to the most efficient evaluation of the integral. Since in this case the integration domain is two dimensional, this strategy has to be corrected in order to create a covering without holes or overlappings. In particular, an algorithm with the following steps has been developed:

- first one tries to cover the required domain with a maximum area rectangle;
- then, if one side of this rectangle overlaps other rectangles, or leaves out a "too small hole", its length is reduced, or increased, and the other dimension is determined according to [3.27], [3.28] so that the coverage efficiency loss is reduced to a minimum. In this way, the integration subregions can have different dimensions according to the local behaviour of the  $\psi$  function, while being all characterized by the same r.m.s. error. Indeed, the size of an integration subregion  $\Delta(s), \Delta(t)$  is not related to the physical size but to the curvature of the surface with equation  $\psi = \psi(s,t)$  and hence can be quite large where the  $\psi$  function has a quasi linear behaviour.

### e. Integral evaluation

Having decided the integration subdomain, the integration is actually carried out analytically by employing a Lagrange interpolation on the function  $G(s,t)$ :

$$G(x,y) \approx \sum_{i=1}^n g_i l_i(x,y)$$

where  $g_i$  is the value that the function  $G$  attains in the point  $i$  of the lattice and  $l_i(x,y)$  is a  $k$  degree polynomial such as

$$l_i(x_j, y_j) = \delta_{ij}$$

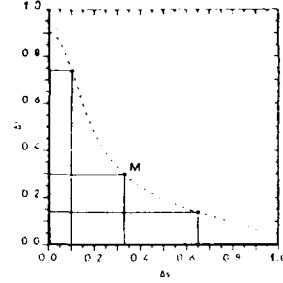


Fig. 3.2: Typical contour plot of mean square error  $\epsilon^2$ . Various integration subdomains characterized by the same error are shown, M has the largest area.  $\Delta s, \Delta t$  are measured in relative units.

where  $x_j, y_j$  are the coordinate of the  $j$  point in the lattice and  $x = s - (s_0 + \frac{\Delta s}{2})$   $y = t - (t_0 + \frac{\Delta t}{2})$  [3.29]

The [3.9] integral becomes:  $\Delta I = \exp[jk_0(\alpha a + \beta b + \gamma)] \int_{-a}^a \int_{-b}^b G(x, y) \exp[jk_0(\alpha x + \beta y)] dx dy$  [3.30]

with  $a = 4\lambda$ ,  $b = 4\lambda$ .

Concerning the degree of the interpolation, the choice of a low degree would require the specification of a very small r.m.s. error  $\epsilon$ , so as to have very small integration subdomains, because we have transferred to the function  $G(s, t)$  the error stemming from the replacement of  $\Psi$  with  $L$ . On the other hand, a high degree would allow quite large integration subdomains without loss of accuracy in the result. In practice, however, round off errors make unfeasible the use of polynomials with degree higher than four because the coefficients tend to be large and alternating in sign. For these reasons a 5x5 point interpolation is chosen. Introducing a vectorial notation for approximating polynomial:  $\tilde{P}(x) \cdot \underline{G} \cdot \tilde{P}(y)$  with

$$\tilde{P}(u) = (P_1(u) \ P_2(u) \ P_3(u) \ P_4(u) \ P_5(u)) [3.31]$$

with  $u = x, y$  and  $\underline{G}$  is the array of the values that the function  $G$  assumes in the nodes of the lattice, the equation [3.30] becomes:

$$\int_{-a}^a \int_{-b}^b G(x, y) \exp[jk_0(\alpha x + \beta y)] dx dy = \int_{-a}^a \tilde{P}(x) \exp(jk_0 \alpha x) dx \cdot \underline{G} \cdot \int_{-a}^a \tilde{P}(y) \exp(jk_0 \beta y) dy [3.32]$$

At this point, integrations are performed on the obtained polynomial expression. When an integration subdomain is clipped by the shadow boundary or by intersection line between two objects, the shape is approximated by a polygon and an integration procedure based on a triangle decomposition is used. The RCS value of an aircraft structure like that shown in fig. [3.3] has been computed for the wanted cut angles and frequency range.

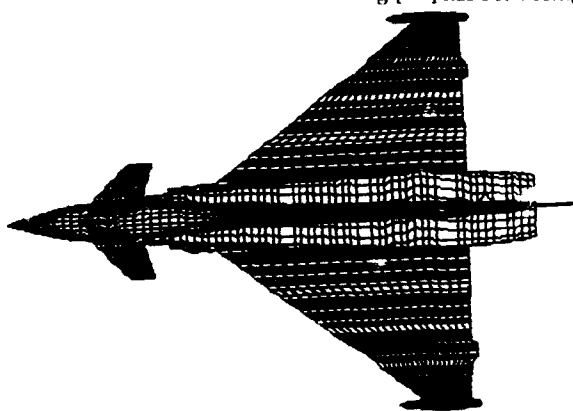


Fig. 3.3: Aircraft bicubic spline reconstruction by means of COBRA

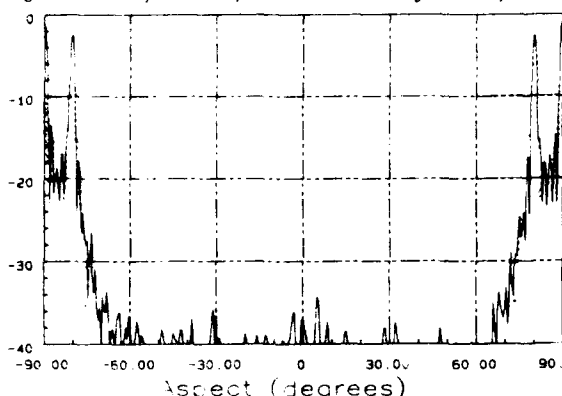


Fig. 4.2: Comparison between calculated (dotted line) and measured RCS (full line) for a cone, cylinder and semisphere.

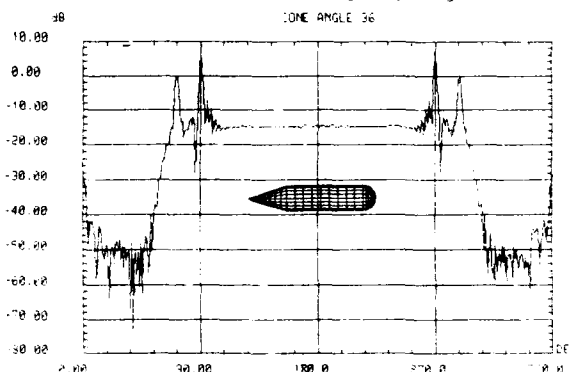


Fig. 4.1: RCS calculation of a simple shape constituted of a cone, a cylinder and a semisphere.

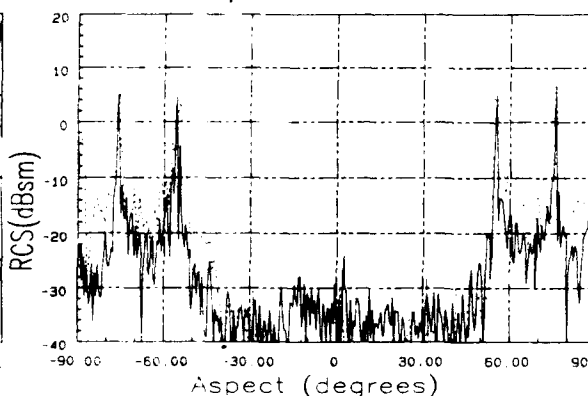


Fig. 4.3: Comparison between calculated (dotted line) and measured RCS (full line) for a stealth prototype.

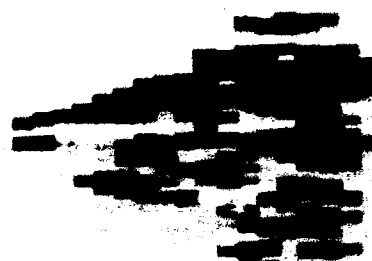
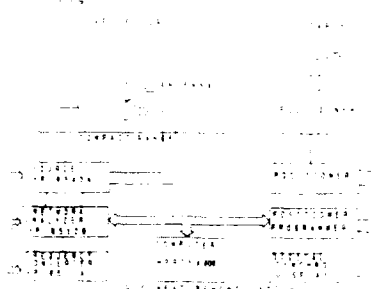


Fig. 4.4: Stealth prototype imaging from computed data.

#### 4. Numerical and experimental results

The results of computer code COBRA, have been tested with measurements carried out in ALENIA RCS facility for a class of simple conducting objects consisting of a cylinder capped by a cone and a semisphere. These test bodies well adapt to provide reference scattering signature in order to compare computer with experimental results, as shown in [10].

The RCS measurements were made with a HP8510 network analyzer in a 24 m. long, 14 m. wide and 9 m. high anechoic chamber, with a serrated edge reflector [11]. The test model, supported on a positioner, is illuminated by the signal coming from the generator through a transmitting antenna; the signal scattered back, sum of several contributions besides the signal from the target, such as coupling between transmitting and receiving antennas and unwanted reflections from the test range, is cleaned through software gating and calibration procedures. Fig. 4.1 shows the calculated RCS at 24 GHz versus aspect angles for such a body with cone aperture of 36 degree, sphere radius of 100 mm and total length of 1m. While at zero degree is visible the scattering of the tip of the cone, at 90 and 180 degrees the cylinder and semisphere's scattering is shown. In fig. 4.2, the comparison between calculated (dotted line) and measured (continue line) values for a body with cone aperture of 20 degrees is represented: the agreement is quite good until 40 dB under the peak [12]. The RCS has been calculated by means of COBRA program also for more complex objects like parts or full body of EFA metallic aircraft or of some RPV. These results cannot be reported in this paper because classified. The RCS of simplified stealth prototype (fig. 4.3) has been calculated and measured in anechoic room: the comparison of the obtained results shows a quite good agreement in spite of the presence in the measured model of several cracking and absorber material near the edges.

Fig. 4.4 represents, instead, a 2D imaging of this prototype coming from calculated data: the RCS centers, represented with different colours with respect RCS magnitudes, are shown versus range and cross range dimensions. This particular technique can improve the reduction techniques keeping into account the position of significant scatterers in the model.

#### 5. Conclusions

In this paper, the scattering phenomena from complex targets are studied by means of a computer code, COBRA, based on Physical Optics approach. From the geometrical model of the target, coming from a 3D CAD system, a suitable electromagnetic model is generated through a spline representation. Besides, significative properties of the target, like curvature or wedges, are keeping into account in the 1:1 mapping of the electromagnetic model to a s,t parametric plane. The numerical approach is based on Physical Optics integral equation which is solved using a modified Ludwig technique with error control. The approach is versatile and has no limitation on parameters, as target size and shape, and does not require extensive computer time waste. Because no informations can be supplied on the depolarization of the scattered wave and only metallic bodies scattering can be computed, further theoretical improvements are needed in these fields.

#### Acknowledgement

The authors would like to express their appreciation to the CIESPA(CNR) - Politecnico di Torino, particularly to Dr. R. Orta and Dr. R. Tascone for the joint venture with Alenia to the development of COBRA theory and code. The authors would also like to express their thank and appreciation to miss R. Allimondi for her excellent effort in graphical code support.

#### 6. References

1. Klement D., Preissner J. and Stein V.: "Special problems in applying the Physical Optics Method for backscattered computations of complicated objects", IEEE Trans. Antennas Propagation, 1988, AP-36, pp. 228-237.
2. Catia Reference manuals Version 3. Ibm-Dassault Systemes
3. Orta R., Savi P. and Tascone R.: "Complex object backscattering response analysis" Final report, October 1990.
4. Ludwig A.C.: "Computation of radiation patterns involving numerical double integration", IEEE Trans. Antennas Propagation, 1968, AP-16, pp. 767-769
5. Gravelaeter T. and Stamnes J.J.: "Diffraction by circular apertures. Method of linear phase and amplitude approximation", Appl. Opt., vol 21, pp. 3644-3645, 1982.
6. Pogorselski R.J. and Mallory D.C.: "Complex polynomial phase integration", IEEE Trans. Antennas Propagation, AP-33, pp. 800-805, 1985.
7. Pogorselski R.J.: "The Ludwig integration algorithm for triangular subregions", IEEE Proc., vol. 73, pp. 837-838, 1985
8. Orta R., Savi P. and Tascone R.: "Valutazione di integrali di fase a controllo di errore", Proceedings of VIII riunione di elettromagnetismo applicato Capri, Ottobre 1990.
9. Press W.H., Flannery B.P., Teukolski S.A., Vetterling W.T.: "Numerical recipes - The art of scientific computing", Cambridge University Press 1986.
10. Klement D., Preissner J. and Stein V.: "Computation of the scattering matrix of radar targets: concept of the method and first results" in Proc. AGARD-Symp. Target Signatures, London, CP 364, 1984, pp. 20.1-20.23. (NATO unclassified).
11. Audone B., Delogu A. and Furini F.: "A new perspective on Radar Cross Section Measurement system", 11th Proceedings of Estec Antenna Workshop on Antenna Measurements, June 1988, pp. 23-32.
12. Furini F., Orta R. and Tascone R.: "Prediction of Radar Cross Section of complex objects and experimental validation", Proceedings of International Conference on Electromagnetics in Aerospace Applications, September 1989, Torino, Italy.

## DISCUSSION

P. H. Pathak, US

Can you explain the reason for the noticeable discrepancy between your PO-based scattering calculations for the "prototype stealth" model and the corresponding measurements?

Author's Reply

This discrepancy is due to two factors: the first is the ripple in the measurement in an old Alenia anechoic room, where measurements were performed two years ago, all about 40 dB below the maximum. With the anechoic room presented at the end of the paper this problem is being overcome. The second reason is because the stealth prototype was modelled as a single body with the splines; for a correct value of the RCS prediction with the PO technique we have to use at least a subdivision of the model in three bodies in the modelling.

## MESURES DE SURFACES EQUIVALENTES RADAR EN VHF/UHF

Jacques SAGET  
DASSAULT ELECTRONIQUE  
55, Quai Marcel DASSAULT  
92214 SAINT CLOUD - FRANCE

### 1) INTRODUCTION : Radars VHF et UHF

Les scientifiques et techniciens chargés de développer les radars du futur semblent s'intéresser de plus en plus aux bandes de fréquence VHF et UHF (100 à 1000 MHz). Quelques systèmes existent depuis plusieurs décades, particulièrement côté soviétique, et sont utilisés pour la veille lointaine et l'alerte avancée contre les missiles ABM.

Pour les applications militaires tactiques et stratégiques, l'utilisation de ces bandes basses offrent certains avantages :

- les cibles, avions ou missiles, réputées furtives dans les bandes hyperfréquences (fréquences supérieures à 1 GHz) deviennent détectables en V/UHF. En effet, les dimensions proches des longueurs d'onde utilisées (0,3 à 3 mètres) et des phénomènes de résonances électromagnétiques ont tendance à augmenter la réflectivité des objets. D'autre part, l'efficacité des matériaux absorbants ou diélectriques, utilisés pour réduire la signature radar des aéronefs, est considérablement dégradée, toujours à cause des longueurs d'ondes très grandes devant l'épaisseur électrique des matériaux,
- les antennes utilisées par les radars V/UHF sont constituées de cellules actives réparties sur des surfaces au sol atteignant plusieurs hectares et assemblées en réseau à balayage électrique à grand gain. Les puissances utilisables à ces fréquences et dans des bandes étroites sont très importantes, pour chacun des éléments du réseau, ce qui permet d'obtenir des puissances rayonnées élevées dans un angle de couverture de l'espace très large. Cette structure de réseau actif à balayage électronique permet des reconfigurations très rapides des diagrammes d'antennes, procurant au radar une très grande efficacité de surveillance de l'espace avec une fiabilité de fonctionnement élevée pour une faible vulnérabilité du système. En effet, du fait de la répartition géographique des éléments actifs de l'antenne sur une très grande surface au sol, l'ensemble de l'antenne est difficilement destructible par des munitions ennemies. La mise hors service, par agression hostile ou panne technique de quelques cellules actives de l'antenne, ne produit qu'un fonctionnement dégradé du système qui reste efficace. De plus, les missiles anti-radar à guidage passif sont difficilement réalisables en raison des dimensions d'antennes, incompatibles d'un système de faible volume.
- la propagation dans les bandes VHF et UHF est peu sensible aux phénomènes atmosphériques telles que neige, pluie ou vapeur d'eau (nuages). D'autre part, le terme d'atténuation naturelle en  $\lambda^2$  de l'équation du radar est encore un élément favorable à l'utilisation des bandes métriques et décimétriques.

Ces radars VHF/UHF du futur semblent donc présenter de nombreux avantages, avec pour application principale les stations fixes.

Parallèlement au développement de ces futurs radars, de nouveaux problèmes se posent aux utilisateurs et concepteurs de véhicules militaires (missiles nucléaires ou avions de combat) : peu de données expérimentales fiables sont disponibles pour caractériser la signature radar des cibles en VHF/UHF.

Ces mesures de SER sont pourtant nécessaires pour déterminer la détectabilité d'un porteur face à un système équipé d'un radar décimétrique, et surtout pour entreprendre des travaux d'extension de la plage de discrétion radar des aéronefs et en optimiser l'emploi tactique. Les concepteurs de radar étant également demandeurs, pour d'autres raisons, de mesures de SER leur permettant d'utiliser des systèmes de reconnaissance de signatures.

Le manque de données précises de Surface Equivalente Radar (RCS) est dû essentiellement à la rareté des bases de mesures fonctionnant aux fréquences inférieures à 1 GHz.

Le faible nombre actuel de bases de mesure de SER en VHF/UHF s'explique par l'émergence du besoin mais surtout par la difficulté de réalisation et d'exploitation de ce genre d'installation.

### 2) PROBLEMES LIES AUX MESURES DE SER EN VHF/UHF

De nombreuses bases de mesure de SER existent et continuent de se développer dans le monde, de différentes dimensions et de types différents (compactes, espace libre, éclairage direct ...), pour des fréquences de fonctionnement généralement comprises entre 2 et 18 GHz, parfois 1 à 40 GHz ou même 1 à 100 GHz.

L'extension en fréquence d'une décade supplémentaire pour couvrir la gamme 0,1 à 1 GHz est très délicate et parfois incompatible d'un fonctionnement facilement reconfigurable en SHF (1 à 40 GHz).

Un inconvénient des bases de mesure intérieures, installées dans des chambres anéchoïdes de dimensions forcément limitées est la difficulté de réaliser des mesures sur des objets de grandes dimensions, tels que avions de combat à échelle réelle. Les méthodes de mesures sur maquettes à échelle réduite, très utilisées en ondes centimétriques ou millimétriques, sont difficilement applicables ici car les matériaux utilisés pour la confection de la maquette doivent présenter le même facteur d'échelle pour toutes les caractéristiques électromagnétiques (permittivité  $\epsilon$ , perméabilité magnétique  $\mu$ , résistivité  $\rho$ ) définissant les impédances de surface. Cette contrainte, de première importance pour la validité du modèle, conduit souvent à des matériaux inexistant.

Les difficultés de réalisation (ou de modification) d'une base de mesure de SER (RCS) fonctionnant entre 100 MHz et 1 GHz sont liées aux éléments suivants :

- système d'illumination,
- fouillis ambiant,
- instrumentation,
- traitement.



## 2.1) SYSTEME D'ILLUMINATION

Dans tous les systèmes de mesure de SER, cet élément régit la qualité et la validité des mesures. En effet, la notion de SER est liée à une illumination de la cible sous test par une onde plane, c'est-à-dire que la cible doit être éclairée par une onde électromagnétique ayant la même amplitude et la même phase en tous points d'un plan de la cible normal à la direction de propagation.

Ce critère de planéité de l'onde est lié au diagramme de rayonnement du système d'illumination pour l'amplitude et aux dimensions transverses de la cible et à la distance antenne/cible pour la phase, dans le cas d'une source d'illumination ponctuelle rayonnant une onde sphérique.

Les défauts d'éclairement se traduisent, sur les relevés de diagrammes de rétrodiffusion, par des zéros ou creux théoriques de SER mesurés à des positions angulaires déplacées et à des niveaux de creux beaucoup moins prononcés que la valeur réelle.

Une formule approchée donne un critère de qualité de planéité en phase du champ électrique rayonné par une source ponctuelle :

$$\delta_{\phi} = \frac{\pi}{8} = 22,5^{\circ} \quad \text{si} \quad x \geq \frac{2D^2}{\lambda}$$

avec  $x$  : distance de test antenne/cible,  
 $D$  : plus grande dimension de la cible,  
 $\lambda$  : longueur d'onde considérée.

Des mesures de bonne précision ( $\leq \pm 1,5$  dB d'erreur) demanderaient une planéité en phase  $\delta_{\phi}$  meilleure que 10 degrés, soit une distance de

mesure  $x = \frac{5D^2}{\lambda}$ , par exemple  $x = 15$  m pour une

cible de largeur  $D = 3$  m mesurée à 100 MHz et  $x = 150$  m à 1 GHz.

Les techniques de base compacte, très utilisées aux fréquences supérieures à 1 GHz, et qui permettent de recréer les conditions d'éclairement en champ lointain sur des distances de l'ordre de 10 à 20 m sont peu utilisables en VHF/UHF car les réflecteurs et leurs traitements de bords atteindraient des dimensions prohibitives en raison des longueurs d'ondes considérées.

Le critère de planéité du champ en amplitude conduit à utiliser des antennes à diagramme large afin de maintenir l'objet sous test dans la partie du lobe de rayonnement principal de l'antenne où la puissance rayonnée est constante. Une variation en amplitude de 1 dB le long de la surface de la cible sous test est la limite tolérable pour obtenir des mesures précises à  $\pm 1,5$  dB. Toutes les conditions de champ doivent être maintenues dans toute la bande de fréquence considérée, soit la décade 0,1 à 1 GHz.

Les considérations de largeur de faisceau dans une bande de fréquence étendue limite le choix de source d'illumination à l'utilisation d'antennes à structure périodique, de type spirale et surtout Log-périodique à dipôles (LPDA).

Un des problèmes posés par l'utilisation de cette antenne LPDA pour la mesure de SER est lié à sa structure périodique : le centre de phase de l'antenne se déplace de l'arrière vers l'avant de l'antenne lorsque la fréquence croît. Le déplacement du centre de phase en fonction de la fréquence, ou phénomène de dispersivité, se traduit pour les mesures de SER par une diminution de la distance apparente antenne-cible lorsque la fréquence augmente, d'une quantité plusieurs fois supérieure à la longueur physique de l'antenne.

Toutes ces considérations de qualité de champ et de variation de centre de phase de l'antenne doivent être prises en compte pour définir une base de mesure de SER en VHF/UHF et dans la plupart des cas le système réalisable est une somme de compromis entre les différents paramètres, la principale limitation étant généralement la distance de test. Des besoins de discrétion peuvent même imposer l'utilisation d'une base intérieure déjà existante mais non prévue pour un fonctionnement en VHF/UHF.

Deux cas de transformation de bases existantes ont été étudiés récemment par DASSAULT ELECTRONIQUE et l'une des études s'est conclue par la réalisation et l'exploitation du système de mesure, dont certains résultats sont présentés plus loin.

## 2.2) FOUILLIS AMBIANT

D'un point de vue économique, l'utilisation d'une base de mesure de SER prévue pour un fonctionnement à des fréquences supérieures à 1 GHz est intéressante pour les raisons suivantes :

- utilisation des locaux ou sites protégés (sécurité et intempéries),
- utilisation d'opérateurs déjà formés,
- utilisation de parties d'instrumentation existante et de matériels et logiciels informatiques disponibles,
- utilisation d'un positionneur de cible spécial pour mesures de SER, déjà existant et adapté aux cibles également testées en SHF ( $> 1$  GHz).

L'adaptation aux mesures VHF/UHF d'une base de mesure existante nécessite quelques aménagements, en particulier la mise en place du système d'éclairement, qui doivent autant que possible permettre la reconfiguration de la station de mesure dans l'une ou l'autre des bandes de fréquence en quelques heures.

La cohabitation entre les systèmes d'éclairement SHF et UHF est particulièrement difficile dans le cas d'un système SHF en base compacte où les réflecteurs sont des éléments pratiquement impossible à déplacer.

Mais l'inconvénient majeur des mesures de SER en VHF/UHF dans une base dimensionnée pour les fréquences supérieures à 1 ou 2 GHz est le niveau très élevé du fouillis en provenance des parois de la base de mesure. En effet, les matériaux absorbants de forme pyramidale ou en coins (wedges) ont une efficacité, ou réflectivité,

liée au rapport  $\frac{T}{\lambda}$ , épaisseur d'absorbant à la

longueur d'onde  $\lambda$  et à l'angle d'incidence de l'onde électromagnétique. En valeurs typiques, la réflectivité d'un absorbant pyramidal, en incidence normale, est de - 40 dB

pour  $\frac{T}{\lambda} = 2$  et tombe à - 15 dB pour  $\frac{T}{\lambda} = 0,15$

Ces valeurs sont applicables, par exemple, à une chambre anéchoïde recouverte de pyramides de 30 cm, dont la réflectivité est - 40 dB à 2 GHz et - 15 dB à 200 MHz. Les chambres dites "anéchoïques" deviennent très réfléchissantes dans la gamme de fréquence qui nous intéresse et créent un niveau de fouillis généralement non uniforme en distance puisque l'angle d'incidence entre antenne et parois de chambre varie. Les panneaux d'absorbant étant généralement collés sur des parois métalliques planes, une réflectivité réduite à 15 dB peut conduire à des niveaux apparents de SER de chambre, ou fouillis, supérieur à 10 mètres carrés en dessous de 200 MHz, pour une chambre fonctionnant parfaitement à 2 GHz, avec une SER de - 40 dBsm ou moins.

Vis à vis de la mesure de SER, le fouillis peut être défini comme la somme des signaux présents à l'entrée du récepteur ne provenant pas de la cible sous test. Il s'agit donc d'une combinaison vectorielle, quasi déterministe, de signaux d'origines très diverses : couplage émission/réception par le système d'antenne, TOS antennes, fuites RF d'instrumentation, rétrodiffusion par le positionneur de cible, la chambre anéchoïde ...

Comme indiqué par les chiffres donnés en exemple ci-dessus, le niveau de SER parasite dû au fouillis est très élevé alors que l'on peut être amené à évaluer des cibles particulièrement discrètes, de niveau inférieur à - 40 dBsm. On voit donc que le fouillis est le facteur limitant la précision de mesure de SER puisque, dans l'exemple ci-dessus, on a un rapport signal sur fouillis de - 50 dB. Le rapport signal sur bruit n'est, en général, pas limitatif car il est généralement possible d'augmenter la puissance d'émission, en particulier dans les bandes V/UHF où la technologie n'est pas très coûteuse.

En plus de l'augmentation de réflectivité des absorbants hyperfréquence en VHF/UHF, les antennes utilisées, à large bande passante, de type log-périodique, possèdent un faisceau très large (typiquement  $\pm 60^\circ$  à - 3 dB) conduisant à un éclairage à très fort niveau des parois de la chambre anéchoïde ou du sol dans une base extérieure.

La réduction du fouillis est donc le souci principal des ingénieurs demandant des mesures de SER précises dans les bandes VHF/UHF.

### 2.3) METHODES DE REDUCTION DU FOUILLIS DE MESURE

Une analyse temporelle du fouillis d'une base de mesure de SER fonctionnant en VHF/UHF, effectuée à l'aide d'instrumentation de mesure de réflectivité temporelle (Time Domain Reflectometry), permet de localiser les différentes sources de réflexion ou de diffraction. Le phénomène de dispersivité de l'antenne Log-périodique utilisée rend plus complexe l'identification physique des centres de diffraction puisque les distances apparaissent différentes suivant la fréquence d'observation. Cette dispersion rend, par ailleurs, pratiquement inutilisables les systèmes de réflectométrie temporelle utilisant la transformée de Fourier inverse fréquence-temps, qui font apparaître complètement étalés dans le temps des échos ponctuels.

- a) La première idée de réduction du fouillis est de limiter la somme des signaux présents à l'entrée du récepteur de mesure à la tranche distance contenant la cible sous test. Le moyen le plus simple est donc d'utiliser un système de mesure de SER équivalent au classique radar à impulsions mais avec une position de cible connue et fixe.

Dans le cas d'une base de mesure intérieure, donc de dimensions limitées, la sélection distance par découpe temporelle passe par l'utilisation d'impulsions et de porte distance de quelques dizaines de nanosecondes. Compte-tenu de l'utilisation d'une fréquence porteuse comprise entre 0,1 et 1 GHz, la génération de trains d'impulsions courtes et à fronts de transitions très courts (2 à 3 ns) pose des problèmes technologiques et de théorie du signal. D'une part, le spectre vidéo de la découpe et le spectre émis se chevauchent aux fréquences basses et d'autre part le spectre subit un repliement autour de la fréquence nulle, ce qui rend difficile la sélection des raies utiles par le récepteur de mesure. Les commutateurs RF rapides à diodes PIN ont généralement des fuites de commande vidéo qui superposent au signal RF découpé des pics transitoires dont l'amplitude crête à crête atteint parfois 8 à 10 volts, sur 50  $\Omega$ .

Le spectre de ces signaux parasites contient des composantes à énergie élevée jusqu'à 500 ou 600 MHz ( $\approx$  inverse du temps de montée de l'impulsion).

Dassault Electronique a développé une unité de découpe spéciale pour mesures de SER entre 100 MHz et 1 GHz, destinée à transformer un système d'analyseur de réseau vectoriel CW (HP 8510B) en radar à impulsions courtes ( $\leq 10$  ns). La découpe d'émission et la porte distance de réception sont effectuées par des commutateurs rapides MMIC à l'Arséniure de Gallium (Ga As) dont les fuites vidéo ne dépassent pas quelques dizaines de millivolts crête à crête. Associé à un choix judicieux des fréquences d'émission en fonction de la largeur des impulsions et de leur fréquence de récurrence, ce système permet d'effectuer des mesures de bonne qualité ( $\pm 1,5$  dB de 200 à 1000 MHz) à des niveaux proches de - 30 dBsm, dans une chambre anéchoïde hyperfréquence. Une technique particulière d'acquisition des mesures en fonction de la fréquence doit être utilisée afin de compenser le déplacement du centre de phase de l'antenne.

b) La méthode de réduction du fouillis par sélection temporelle ne permet pas d'annuler les échos parasites en provenance de réflecteurs situés à une distance électrique égale à celle de la cible sous test et la contribution de cette tranche distance peut être considérable. On trouve en particulier le signal diffracté par le positionneur ou support de cible. On utilise, pour réduire le fouillis dans le volume distance sélectionné, une méthode de soustraction vectorielle supposant une stabilité temporelle à moyen terme du fouillis et l'absence de couplage entre la cible et son environnement. Cette méthode nécessite 3 essais différents pour obtenir un résultat de mesure de SER calibré en mètres carrés :

- mesure de l'environnement seul (chambre vide) → CV,
- mesure d'un étalon de référence, dans le même environnement → E + CV',
- mesure de la cible et de l'environnement → C + CV''.

On calcule alors,

$$\sigma_{\text{en m}^2} = \frac{(C + CV'') - CV}{(E + CV') - CV} E_{\text{th}} \approx \frac{C}{E} \cdot E_{\text{th}}$$

avec  $E_{\text{th}}$  la SER théorique de l'étalon de référence, en mètres carrés.

Tous les termes sont complexes.

On voit donc que cette méthode permet, en théorie, l'élimination du fouillis et une bonne précision de mesure résultant de l'excellent rapport signal/fouillis obtenu.

Suivant les applications, cette méthode de soustraction vectorielle est plus ou moins nécessaire, applicable et efficace.

1) Dans le cas d'une cible de petites dimensions, généralement de SER faible (- 30 dBsm par exemple) mesurée dans une chambre anéchoïde pour hyperfréquence dont le niveau de fouillis brut moyen serait de l'ordre de + 10 dBsm, une mesure de précision acceptable ( $\pm 1,5$  dB), nécessite une efficacité de soustraction vectorielle supérieure à 50 dB pour obtenir un rapport signal/fouillis de 10 dB.

La soustraction vectorielle doit être telle que :

$$10 \log \frac{|CV'' - CV|}{CV} \leq - 50 \text{ dB.}$$

Ce chiffre exige une très haute stabilité de l'ensemble de la base de mesure entre les deux acquisitions CV et CV'' dont les variations d'amplitude et phase doivent être inférieures à 0,01 dB et 0,2°, ce qui exige :

- stabilité de l'instrumentation (gains, phase, fréquence ...),
- stabilité du fouillis : pas de mouvements de l'environnement (dilatations thermiques faibles).

Cette qualité de soustraction de - 50 dB est réalisable, dans la pratique, quand il est possible d'effectuer toutes les acquisitions de mesure de cible et d'environnement en un temps réduit (inférieur à 4 heures) et sans modification de l'environnement.

2) Dans le cas d'une cible de très grandes dimensions, comme un avion de chasse, par exemple, l'installation de la cible est longue et il n'est donc guère envisageable d'obtenir une soustraction vectorielle très importante, d'autant plus que la cible elle-même crée un très fort couplage avec l'environnement (avec le positionneur, masquage des parties derrière la cible ...). En revanche les niveaux de SER de la cible et de l'environnement sont très différents par rapport au cas précédent :

- environnement toujours voisin de + 10 dBsm,
- cible  $\geq 10$  dBsm.

Une soustraction de l'ordre de 10 dB serait alors suffisante pour éliminer l'influence de la tranche distance incluant la cible, le positionneur en particulier, à condition, bien sûr d'utiliser une instrumentation découpée qui réduira le fouillis extérieur au volume de test.

### III) EXPERIMENTATION

En appliquant les principes développés ci-dessus, des mesures expérimentales ont été menées afin de qualifier la méthode et l'installation.

Le système utilisé était le suivant :

- chambre anéchoïde de 11 m (haut) × 13 m (large),
- antenne log-périodique bipolarisation,
- instrumentation : analyseur de réseau vectoriel CW HP 8510B  
unité de découpe Dassault Electronique TD 1-10 (0,25 watts),
- calculateur : station de travail HP 9000-350,
- logiciel : Dassault Electronique Marmos pour acquisition, traitements et graphiques.

Le choix de la distance d'éclairage (antenne-cible) résulte d'un compromis, pour une cible de dimensions données, entre la qualité du champ électrique et la séparation des échos réels, résultant d'une illumination directe de la cible et d'échos fantômes dus à une illumination de la cible par des trajets multiples réfléchis par les parois de la chambre, peu absorbantes à ces fréquences.

Pour une distance de mesure de 7,5 m et une zone de mesure de 1,50 m de profondeur, la durée des impulsions utilisées est 15 ns, pour une porte de réception de 40 ns et une fréquence de récurrence de 2,2 MHz.

La mesure complète est effectuée en 3 essais, comme décrit en 2.3.b et la même procédure d'acquisition de la puissance reçue en fonction de la fréquence est utilisée pour chaque essai, avec correction du déplacement du centre de phase de l'antenne en cours d'acquisition.

On obtient alors les fichiers vectoriels C(f), CV(f) et E(f) et la réponse théorique  $E_{\text{th}}(f)$  de l'étalon de SER, une sphère de 20" de diamètre, est calculée.

La fréquence est balayée entre 100 et 1000 MHz, avec acquisition de 201 points de mesure. Ce balayage en fréquence permet d'acquérir une réponse fine dans toute la bande VHF/UHF mais également, par traitement FFT, d'obtenir une résolution temporelle supérieure à ce que permet la découpe temporelle : 17 cm contre 2,25 m en impulsions.

Les traitements effectués par le logiciel sur les fichiers bruts sont donc :

$$\text{calcul de } \sigma(f) = \frac{C(f) - CV(f)}{E(f) - CV(f)} \cdot E_{th}(f)$$

$$\text{Transformée de Fourier inverse : } F^{-1}[\sigma(f)] = \sigma(t)$$

Sélection distance, par logiciel, de la zone d'espace limitée aux dimensions de la cible, soit  $[t_1, t_2]$  dans le domaine temporel

$$\sigma(t) \times \text{rect}(t_1, t_2) = \sigma_g(t)$$

$$\text{Transformée de Fourier : } \sigma_g(f) = F[\sigma_g(t)]$$

Ce traitement logiciel permet d'obtenir une sélection distance éliminant la plupart des échos parasites dus aux illuminations de la cible par des trajets multiples.

Des essais de qualification de la base ont été effectués par mesure d'une sphère de diamètre moyen (6"), calibrée avec une sphère de 20" et par comparaison entre la mesure et le calcul théorique de la réponse de la sphère, dans la bande 100 à 1000 MHz.

La sphère parfaitement conductrice est pratiquement le seul objet dont la réponse théorique exacte est connue à toutes les fréquences ; c'est l'une des raisons pour lesquelles cette cible est largement utilisée pour la calibration des mesures de SER.

Les courbes montrent que la précision de mesure obtenue dans les conditions décrites ci-dessus atteint  $\pm 1$  dB, dans la bande 180-950 MHz, pour un niveau de SER aussi bas que -30 dBsm (à 200 MHz).

Le fouillis brut de l'installation, à 200 MHz, atteint +5 dBsm.

#### IV) CONCLUSION

Le développement des futurs radars VHF/UHF a créé des besoins en mesures de SER dans ces bandes et peu d'installations sont actuellement capables et disponibles pour effectuer des mesures de qualité sur des cibles furtives. Des mesures dans des bases existantes, prévues pour un fonctionnement au-dessus de 2 GHz, peuvent donner des résultats très satisfaisants, à condition d'utiliser une instrumentation, une méthode et des traitements appropriés afin de réduire le fouillis dont le niveau est très important, et constitue souvent la cible la plus "visible" contenue dans la base de mesure.

**FIGURE 1 MESURE ETALONNEE BRUTE D'UNE SPHERE METALLIQUE DE 6" ET REPONSE THEORIQUE**

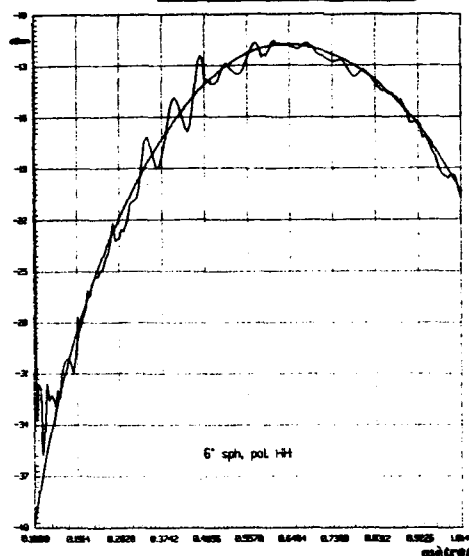


**FIGURE 2 REPONSE TEMPORELLE THEORIQUE ET MESUREE D'UNE SPHERE DE 6"**

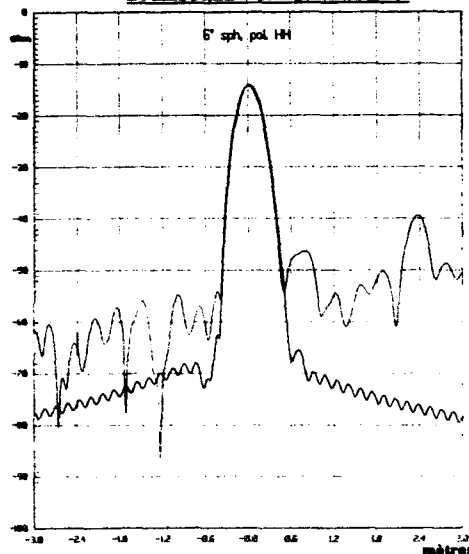
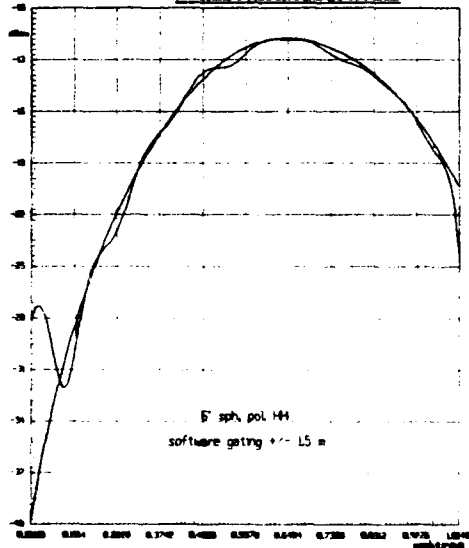


**FIGURE 3 REPONSE FREQUENTIELLE D'UNE SPHERE DE 6" APRES FILTRAGE SPATIAL**



## DISCUSSION

F. CHRISTOPHE (FR)

L'amélioration de sensibilité par soustraction de l'écho de chambre que vous présentez n'est elle pas limitée par les termes non additifs (le couplage entre la chambre et la cible) qui risquent d'être importants à ces fréquences pour lesquelles - comme vous l'avez indiqué - la chambre n'est pas très anéchoïque?

AUTHOR'S REPLY

La distance antenne-cible et les paramètres de découpe temporelle (largeur d'impulsion et de fenêtre de réception) sont choisis en fonction de la largeur de cible et des dimensions de la chambre anéchoïque afin de séparer le plus possible les échos principaux des échos parasites dans le domaine temporel. Le traitement temporel par FFT permet une sélection assez fine (résolution  $\approx 17$  cm) en complément de la sélection effectuée par la découpe impulsienne.

E. SCHWEICHER (BE)

J'ai beaucoup apprécié votre exposé très cartésien qui m'inspire deux questions:

1. Quel récepteur cohérent utilisez-vous?
2. Vous avez parlé de sphéricité et de planéité de l'onde d'illumination. Est-ce l'une ou l'autre et si vous utilisez une onde d'illumination sphérique faites-vous une correction pour en tirer les résultats valables pour une onde d'illumination plane?

AUTHOR'S REPLY

1. Le récepteur cohérent utilisé est un analyseur de réseau vectoriel HP8510B (20 MHz) précédé d'un convertisseur à mélange direct incorporé au matériel de découpe (D.E. TD 1-10).
2. L'onde utilisée lors des essais est sphérique et aucune correction n'est effectuée. La correction est délicate car le rayon de sphéricité varie avec la fréquence, du fait de l'utilisation de l'antenne log-périodique.

## Two-Dimensional Signal Processing for Airborne MTI

by

Richard Klemm

Joachim Ender

FGAN-FFM

Neuenahrer Str. 20

D 5307 Wachtberg 7

### 1. INTRODUCTION

This paper gives an overview over the field of airborne MTI-systems (AMTI). For introduction, the problems of airborne MTI is pointed out. Well-known techniques such as conventional MTI and DPCA (displaced phase center antenna) are briefly described. Then the authors give a prospective view of future AMTI-techniques, including an overview of their own work on novel algorithms (TASTE = Techniques for Airborne Slow Target Extraction). Although airborne radar is particularly addressed in this paper, the results may, with some modifications, be applied to other moving sensor configurations, such as active sonar, spaceborne radar, and Synthetic Aperture Radar (SAR). The paper is intended to be tutorial and gives an overview over the state of the art in AMTI techniques. Readers interested in more details are referred to the references given below.

The motion of the radar platform causes clutter returns to be Doppler coloured. The Doppler frequency of an echo due to an individual clutter patch is proportional to the azimuth of the scatterer relative to the radar and the platform velocity. Instead of a single spectral line at zero Doppler frequency (as in case of groundbased radar) clutter echoes received by a moving radar show a certain Doppler bandwidth determined by the platform velocity and the antenna beamwidth. Targets whose radial velocity is lower than the platform speed are buried in the clutter band. For any look direction other than perpendicular to the flight direction (squint angle) the Doppler spectrum is shifted by an amount proportional to the sine of the squint angle.

MTI systems of ground based radar discriminate between moving and stationary targets by use of their Doppler frequencies. Ground clutter is centered about Doppler zero while moving targets exhibit a Doppler frequency different from zero. The clutter portion may be removed by a notch filter operating on successive echo pulses. The remaining Doppler target can then be detected by threshold comparison.

If the radar is moving, then both clutter and target are Doppler shifted. The clutter echoes are more or less white within the bandlimits given by the beamwidth and the platform speed. In addition, the clutter background can be considered omnidirectional, i.e., spatially white. So, what is the clue to discriminate a Doppler target from a background that is white in time and space? The answer is simple: Echoes from stationary clutter show a one-to-one correspondence between azimuth and Doppler frequency while for a moving target Doppler frequency and azimuth are independent.

Let us consider Fig. 1 for illustration. It shows a two-dimensional clutter plot with the clutter power plotted versus azimuth and Doppler frequency (or velocity). Due to the one-to-one correspondence between azimuth and Doppler the clutter power is distributed along the diagonal of the  $v$ - $\phi$ -plane. The clutter spectrum is modulated by the antenna directivity pattern. Moving targets may appear anywhere in the plane. Fast targets fall into the antenna sidelobe region and can be detected by use of a temporal filter. For optimum clutter suppression, the filter characteristics should be the inverse clutter spectrum projected onto the time axis, as depicted below.

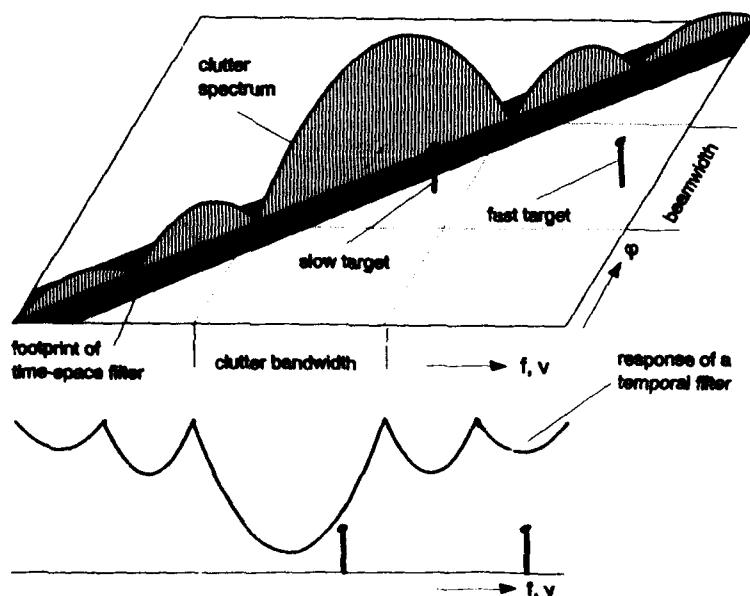


Fig. 1 Two-dimensional spectrum of airborne ground clutter

Slow targets, however, fall into the main beam clutter and will be suppressed by the broad notch of the inverse filter. Applying a narrow notch filter would result in imperfect clutter rejection.

The obvious solution of this problem is a time-space filter as indicated by the hatched strip (footprint of time-space filter) in Fig. 1. This footprint is to indicate a notch along the course of the space-time clutter spectrum. With such a filter the slow target inside the main lobe clutter can be detected. In the following we focus on such two-dimensional clutter filters.

## 2. TACCAR and DPCA

TACCAR (time-averaged-clutter coherent airborne radar, s. Ref. 1, pp. 15-61) is a phase locked loop to compensate for the mean Doppler frequency due to a squint angle. Phase advances between subsequent echo samples are used to control the coherent oscillator in such a way that the Doppler spectrum is centered about Doppler zero. Clutter locking as described in Ref. 2 is basically the same as TACCAR, however implemented in the base band.

DPCA techniques (displaced phase centre antenna) are well-known techniques for compensation of the motion induced effect on the clutter bandwidth. For illustration let us consider Fig. 2a. Two subsequent echo samples  $E_1$  and  $E_2$  due to an individual scatterer exhibit a phase advance which is proportional to the azimuth angle and the platform speed. The total of all phase shifts due to an omnidirectional background form a Doppler broadband clutter echo. There are two basic DPCA principles which are outlined briefly in the following.

In Refs. 1, pp. 16-8, and 4 the platform motion is compensated by switching two strongly overlapping subapertures between any two successive pulses. If the displacement of the two phase centres is matched to the platform velocity and the PRF then the array seems to be fixed for the duration of one pulse interval. The disadvantage of this technique is that only every second pulse can be used for target detection which means a loss of 3 dB. Technical problems might occur because the PRF has to be synchronized to the platform speed and the phase centre displacement which may require adaptive control of the PRF by use of an inertial navigation system. The main beam mean Doppler must be corrected by a TACCAR loop.

In Fig. 2c the motion induced phase shift is compensated for by an electronic DPCA-technique (Ref. 1, pp. 16-10). This is done by adding two correction patterns  $c_1$  and  $c_2$  in the way shown in Fig. 2c. The required correction signals are obtained from the output of a monopulse difference channel, multiplied by a constant factor to match to the actual platform speed. No loss has to be taken into account because any echo pulse can be used for forward and backward compensation. This technique depends very much on the shape of the difference pattern. Usual tapering techniques to obtain low sidelobes may distort the correction patterns so that degradation of the clutter cancellation occurs.

A similar approach for use with array antennas is given in Ref. 5. Two sets of beamformer coefficients applied to the TACCAR-corrected array are optimised in such a way that correction patterns as shown in Fig. 2c minimise the clutter output power.

## 3. TASTE

The TASTE algorithms (TASTE = technique for airborne slow target extraction) are related to DPCA in that several sensors are used for platform motion compensation. The philosophy, however, is different. In DPCA the platform motion is compensated for explicitly whereas TASTE algorithms use the received data and remove the influence of platform motion via adaptive 2D-clutter filtering (time-space generalisations of sidelobe cancellation techniques). It has been shown that TASTE compensate for the motion induced phase shifts as shown in Fig. 2d, s. Ref. 7. Compared with DPCA, TASTE has a number of attractive properties:

- No TACCAR loop for main beam mean Doppler correction is required
- No external estimates of the platform speed (e.g. via INS) are necessary
- The PRF has not to be synchronised with the platform speed as in case of Ref. 5
- Antenna concepts using either antenna arrays or reflector antenna/auxiliary sensor configurations are possible (Ref. 18)
- The number of sensors and echo pulses involved can be chosen arbitrarily (most DPCA-techniques involve only two pulses)
- Platform motion and perturbations of the flight path can

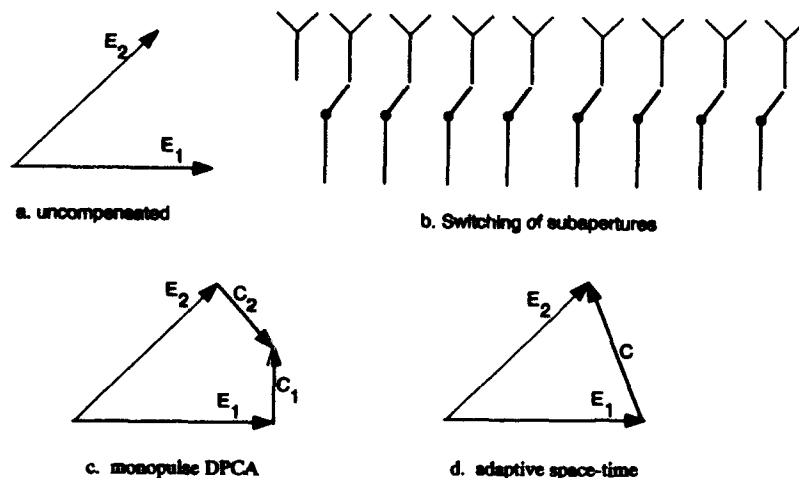


Fig. 2 Motion compensation techniques

- be compensated for
- Even with a linear array, small velocity components perpendicular to the flight path can be compensated for, s. Ref. 17
- By use of two- or three dimensional sensor arrays the AMTI can, in conjunction with adaptive processing, be motion compensated in all three spatial dimensions, s. Ref. 17

### 3.1 Small Array Case

The theoretical basis for adaptive array processors is the maximum likelihood test which, under the assumption of Gaussian clutter and deterministic target signal, leads to the well-known processing rule "pre-whiten and match". The principle of such a processor is shown in Fig. 3a. The whitening operation is included in the inverse clutter covariance matrix  $R^{-1}$ . The input samples may be either temporal (clutter filtering for stationary radar) or spatial (jammer cancellation) or both (clutter and jammer cancellation for moving radar). In the latter case  $R$  is a space-time matrix as indicated in Fig. 3c. The submatrices  $R(\tau)$  are spatial while the temporal correlation is between them.

The first investigations on space-time adaptive clutter filtering have been conducted by Brennan et al., s. Ref. 6. An eight element array and 2-pulse clutter cancellation has been considered. The convergence properties of three adaptive algorithms are discussed.

The problem associated with this type of processor is that it applies only to short arrays. Otherwise, the implementation

becomes expensive, and, in addition, the convergence of the adaptive loop may be poor. In Refs. 8 and 9 pre-transform processors are described, s. Fig. 3b. By use of a suitable pre-transform the number of samples can be reduced considerably. The idea of such pre-transform techniques is that the order of whitening and signal match is interchanged which leads to a space-time sidelobe canceller scheme. Auxiliary channels are used to estimate the covariance matrix after the pre-transform. Beamformers cascaded with Doppler filters matched to the beamformer mean clutter frequency or eigenvectors of the clutter covariance matrix have proven to be suitable auxiliary channels.

In Ref. 1, pp. 16-24, an adaptive implementation of such a processor is presented. Some performance values (improvement factor) are given for a 16-elements array. This processor can be considered a special case (2 temporal samples) of the space-time FIR filters described in Refs. 13 and 14. The principle of such a filter is indicated in Fig. 4. A space-time field of echo samples is obtained from a sensor array. The space-time FIR filter is a weighted sum over a segment of spatial and temporal samples. The filter moves in the time direction. The filter coefficients are optimised so that the output power is minimum.

Fig. 5 gives an indication of the performance of this kind of filter. The improvement factor (gain in signal-to-noise ratio) is plotted versus the radial target velocity.  $N$  and  $M$  are the numbers of sensors and temporal samples in the filter. The total number of filter coefficients is  $NM$ . 20 dB CNR were assumed. The platform velocity is  $0.8v_{\max}$  where  $v_{\max}$  is

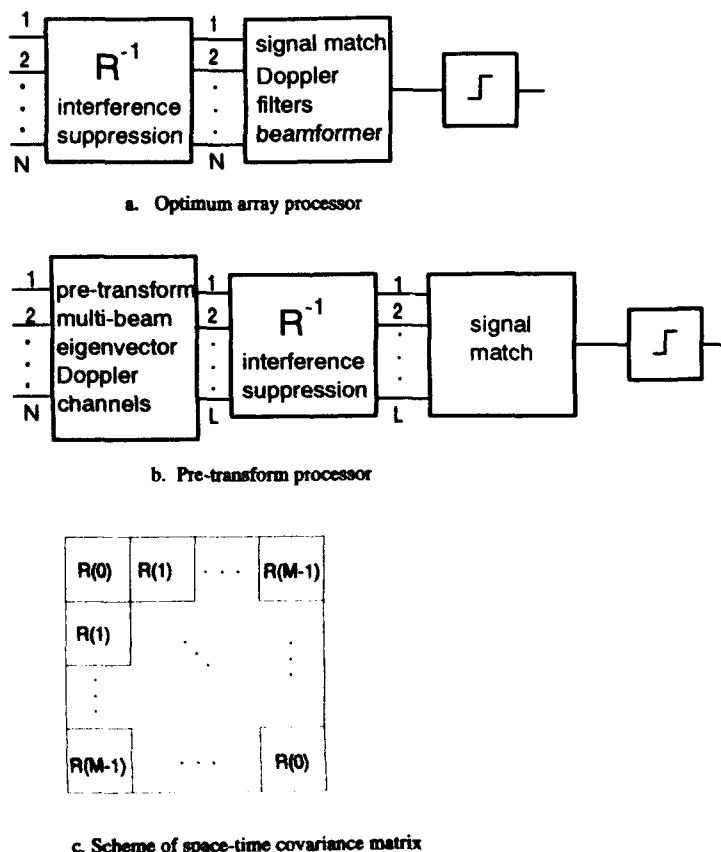


Fig. 3 Basic array processor schemes



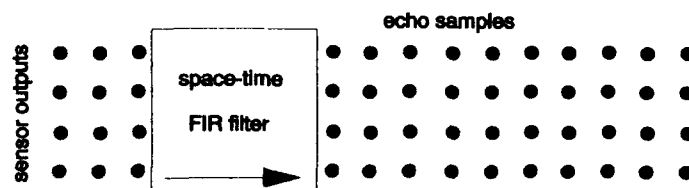


Fig. 4 Principle of a time-space FIR filter

the unambiguous velocity determined by the sampling rate. A sideways looking geometry was assumed. The target energy is integrated by a 33 point Doppler filter bank. The abscissa corresponds to the output of the Doppler filter bank.

$N=M=1$  means that no filter is applied. The curve shows the gain response of the Doppler filter bank. The clutter bandwidth between  $v/v_{\max} = -0.8 \dots 0.8$  can be recognised. Similar curves are obtained if either  $N$  or  $M$  are equal to 1 (spatial or temporal filter). As expected only a space-time filter ( $N=M=5$ ) gives satisfactory performance. At  $v=0$  the target frequency is equal to the clutter frequency in look direction which results in a clutter notch. The width of the clutter notch is a measure for the detectability of slow targets. The maximum gain far away from Doppler zero is about 42 dB which is the theoretical limit ( $20 \text{ dB CNR} \times 5 \text{ sensors} \times 33 \text{ Doppler filter length} = 16500 = 42.17 \text{ dB}$ ).

### 3.2 Large Arrays: Two-Dimensional Space-Time FIR Filters

The filter technique described in the previous section has the disadvantage that it is hardly applicable to large arrays. On the one hand it is a question of cost, complexity and, related to spaceborne systems, of weight. On the other hand, the convergence time of adaptive algorithms increases with the order of the filter which can lead to difficulties, especially in a moving configuration. Realistic array antennas will include several thousands of sensors, which is prohibitive for the implementation of an adaptive loop.

One possibility to overcome the convergence problems is to design a filter that operates in *space and time* as FIR filter, provided that the array is equispaced. The basic principle of such a filter is illustrated in Fig. 6. More details are given in Ref. 15. Again the filter coefficients are optimised so that the clutter output power becomes minimum. This filter has some attractive features:

- \* The filter size is independent of the array size.
- \* The order of the filter can be chosen small so that the convergence is supposed to be rapid
- \* Since the equispaced array has the same cross-covariance all over the aperture, the filter may adapt to the clutter while moving over the aperture.
- \* Thirdly, this kind of filter is a pure clutter rejection device without any beamformer included (as in case of the previous filters). A beamformer has to be applied to the output data separately. Therefore, adaptation of such a filter is independent of the look direction. It may adapt during scanning. Parallel beamforming is possible.

Fig. 7 shows the performance of the 2D FIR filter for different array apertures  $A$ . Of course, this technique requires that all elements of the array antenna have to be followed by full channels including amplifiers, demodulation and A/D-converters. This disadvantage applies also to the techniques discussed in the previous section.

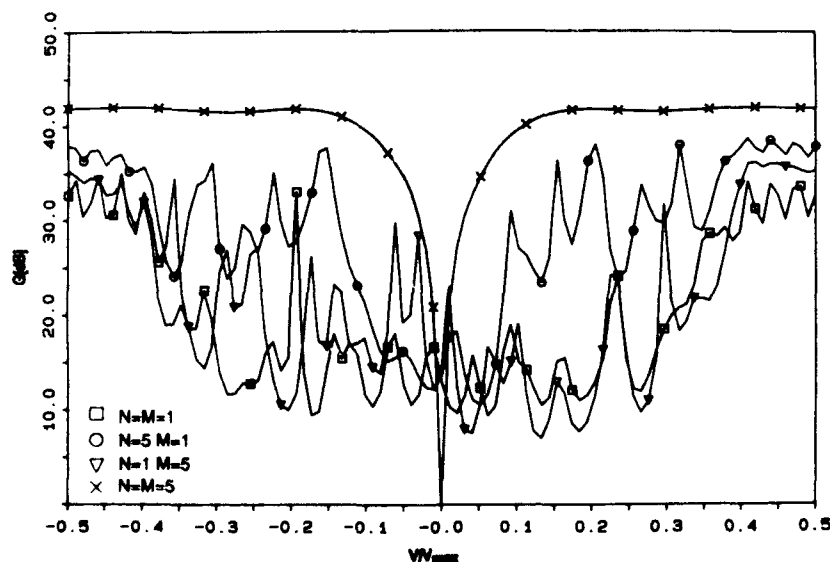


Fig. 5 Clutter suppression with small array

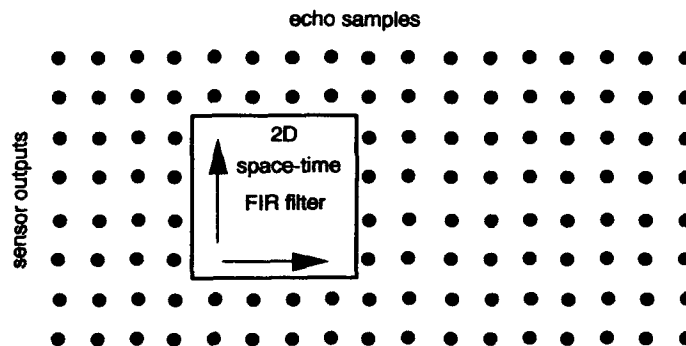


Fig. 6 Scheme of a two-dimensional space-time FIR filter

### 3.3 Large Antennas: Subgroup Processing

Recent results indicate that very simple antenna/filter structures may yield the desired AMTI performance, s. Ref. 18. Such processors are based on overlapping sensor subgroups like the two subapertures in Fig. 2b. An alternative solution is a configuration including auxiliary sensors and a main antenna which may also be a reflector type antenna. The order of this processor is again independent of the antenna size, and rapid convergence of an adaptive algorithm can be anticipated. Fig. 8 shows some gain curves for different apertures.

### 3.4 Drift Compensation with Planar Arrays

In all the above described applications of TASTE a linear array aligned in flight direction was used to compensate for the motion and, in case of adaptive realisations, for perturbations of the velocity in flight direction. In Ref. 17 the use of planar arrays for motion compensation in two dimensions is discussed. Fig. 9 shows the positions of such a planar array when moving at platform speed along the flight path and drifting sideways because of cross wind.

The processing scheme is basically the same as before. However, the spatial submatrices of the space-time covariance matrix are subdivided in turn into submatrices, s. Fig. 10a. The inner submatrices may describe the clutter statistics in

flight direction while the next level of submatrices relates to the direction perpendicular to the flight path. In Fig. 10b the space-time filter scheme is shown.

It has been shown in Ref. 17 that small drift velocities can be compensated for by a linear array in flight direction, as used for platform speed compensation. For drift velocities of the order of magnitude of the platform speed a planar array is necessary.

### 3.5 High Resolution Radar: Bandwidth Effects

Spatial decorrelation effects due to the system bandwidth are a well-known phenomenon that may have impact on spatial filtering such as beamforming and sidelobe cancellation. Any wave arriving at the array at an off-boresight angle is delayed while travelling across the antenna aperture. If the correlation length of the received wave is of the order of magnitude of the aperture size then the received signals across the array suffer from loss in cross correlation. Phase sensitive techniques such as adaptive nulling are degraded seriously.

This decorrelation effect is of particular importance for broad band radar such as synthetic aperture radar. Here the envisaged range resolution may be equal to the antenna size. This can also have impact on the performance of TASTE because these techniques operate partly in the spatial dimen-

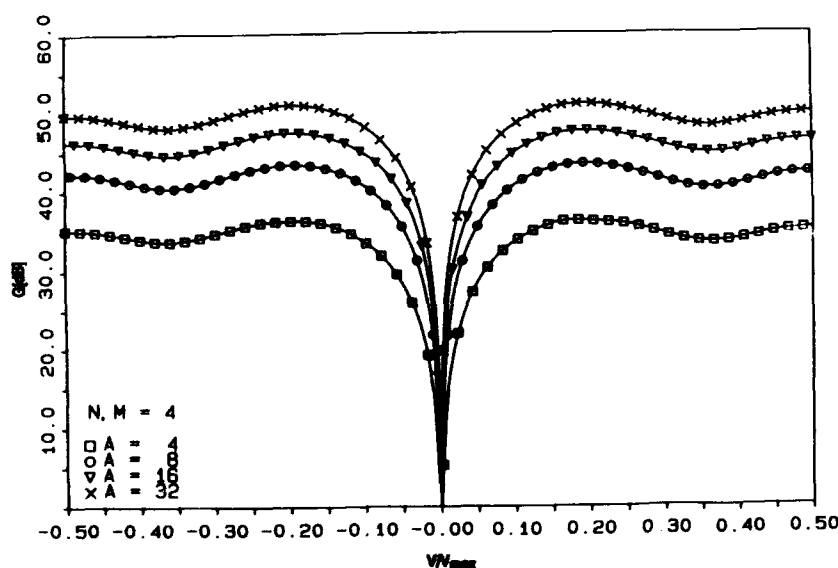


Fig. 7 2D-space-time clutter suppression filter

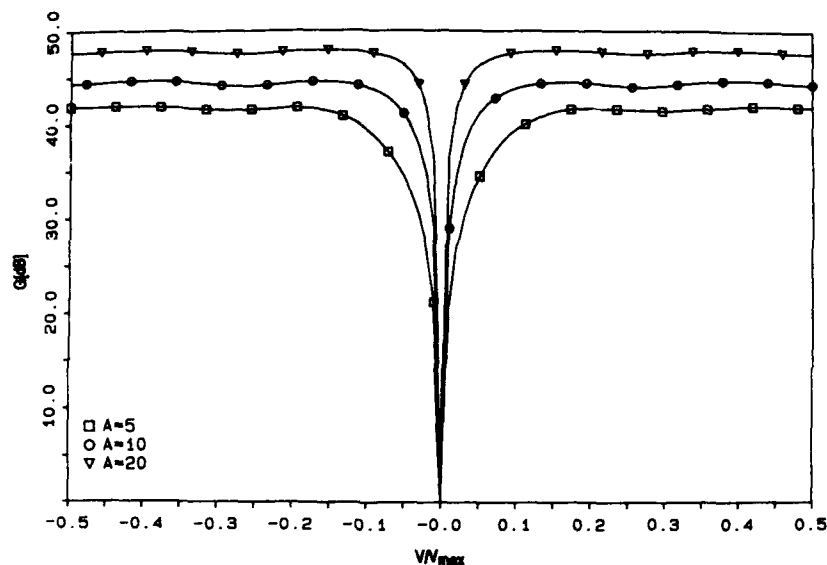


Fig. 8 Spatial subgroup processing

sion. In Ref. 13 it has been shown that no spatial decorrelation occurs if motion compensating techniques such as TASTE are applied.

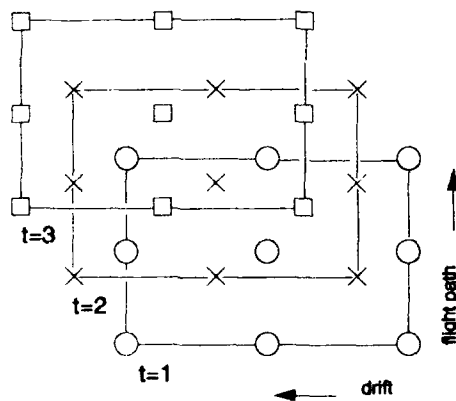


Fig. 9 Sensor positions of a sideways drifting array antenna

#### 4. SUMMARY AND CONCLUSIONS

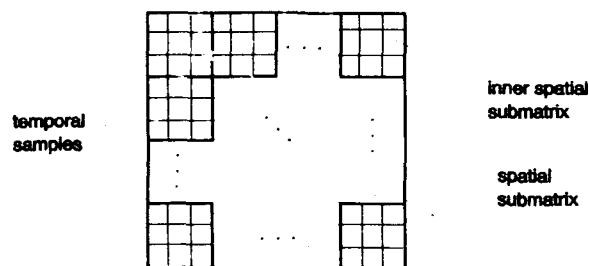
In this paper a summary of existing techniques for motion compensation for air- and spaceborne MTI radar was presented. The advantages of adaptive space-time filters (referred to as TASTE by the authors) were pointed out. The cost and computational workload can be reduced so that even for large arrays clutter returns can be rejected adaptively in real-time.

An experimental set-up (AER = Airborne Experimental Radar) to verify the theoretical results is under development. This system includes an X-band frontend with four active channels. First experiments will be conducted in the near future by use of a truck as moving platform. Autobahn bridges in the mountain area close to Bonn will be used to imitate an airborne geometry. Later on, airborne experiments will be conducted.

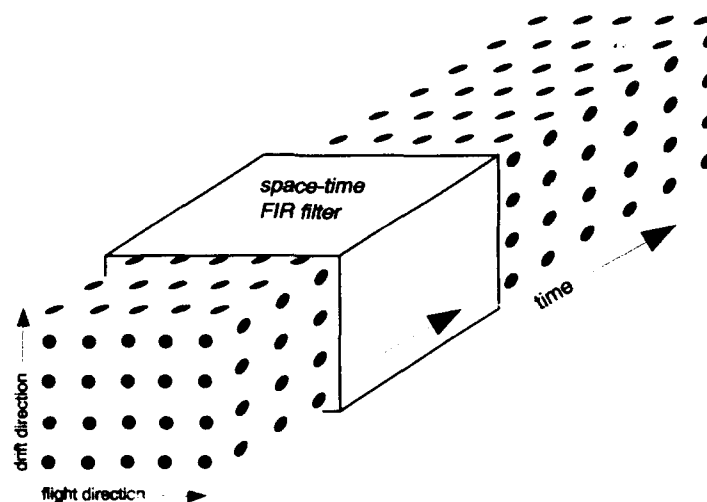
There are a few unsolved problems ahead that will need special attention. First of all, investigations on an appropriate antenna design for TASTE will be carried on. Such specifications have to be merged with the requirements of an operational antenna. Secondly, given a certain jamming scenario, how would an antenna capable of anti-jamming *and* TASTE look like? Recent results on anti-jamming will be taken into account (see, for example, Ref. 19). Other problems are in the field of implementing real-time hardware for TASTE in LSI technology.

#### REFERENCES

- [1] M. Skolnik, Radar Handbook, second edition. McGraw-Hill, 1990, chapter 16.
- [2] R. Voles: New approach to MTI clutter locking. Proc. IEE, Vol. 120, Nr. 11, November 1973, S. 1383-1390.
- [3] A.E. Zeger, L.R. Burgess: An adaptive AMTI Radar antenna array. NAECOM 1974 Record, S. 126-133
- [4] G. N. Tsandoulas: Unidimensionally scanned phased arrays. IEEE Trans. AP-28, No 1, 1980, pp. 86-99
- [5] G. A. Andrews: Radar antenna pattern design for motion compensation. IEEE Trans. AP-26, No 4, 1978, pp. 566-571
- [6] L. E. Brennan, J. D. Mallett, I. S. Reed: Adaptive arrays in airborne MTI. IEEE Trans. AP-24, 1976, pp. 607-615
- [7] R. Klemm: Some properties of space-time matrices. International Conference on Radar, 1984, Paris, pp.357-361.
- [8] R. Klemm: Adaptive airborne MTI: an auxiliary channel approach. IEE Proc., Vol 134, Pt. F, No 3, 1987, pp. 269-276.
- [9] R. Klemm: New airborne MTI techniques. Proc IEE Radar 87, London, pp.
- [10] Morphet, F. N., Payne, R. W.: Combined moving target detection and synthetic aperture radars. Proc Military Microwave 86, S. 211-215
- [11] Freeman, A.: Simple MTI using synthetic aperture radar. Proc IGARSS 84, S. 65-70
- [12] J. Ender, R. Klemm: Airborne MTI via digital filtering. IEE Proc., Vol 136, Pt. F, No 1, 1989, pp. 22-28



a. Scheme of space-time covariance matrix for planar array



b. Filtering scheme

Fig. 10 Space-time FIR filter for platform and drift motion compensation

- [13] R. Klemm, J. Ender: New aspects of airborne MTI. Proc. IEEE RADAR90, Arlington (USA), 1990.
- [14] R. Klemm, J. Ender: Two-dimensional filters for Radar and Sonar Applications. Proc. EUSIPCO 90, Barcelona, 1990
- [15] R. Klemm, J. Ender: Multi-dimensional digital filters for moving sensor arrays. IASTED90, 18.-21. June 90, Lugano, Switzerland
- [16] H. Wilden, J. Ender: The crow's nest antenna - experimental results. Proc. IEEE RADAR90, Arlington (USA), 1990.
- [17] R. Klemm: Adaptive airborne MTI with two-dimensional motion compensation. Submitted to Trans. IEE, Pt. F.
- [18] R. Klemm, J. Ender: Antenna design for airborne MTI. In preparation.
- [19] U. Nickel: Subarray configurations for interference suppression with phased array radar. Conf. Rec. of the International Conference on Radar, Paris, 1989, pp. 82-86

## DISCUSSION

A. E. Cetin, TU

What kind of adaptive algorithms do you use to update the filter coefficients?

Author's Reply

Sample Matrix Inverse

or

Updated Inverse Matrix

# THE APPLICATION OF LATTICE-STRUCTURE ADAPTIVE FILTERS TO CLUTTER-SUPPRESSION FOR SCANNING RADAR

by

C. Gibson

Environmental Research and Engineering Department  
Alberta Research Council  
PO Box 8330, Station F  
Edmonton, Alberta, T6H 5XZ  
Canada

## 1.0 Introduction

This paper describes the use of an adaptive filter to enhance the detection of moving targets in the presence of clutter. The scanning and pulsing rates of a typical surveillance radar produce, within each resolution cell, a time-series of samples at a given range, resulting from the consecutive pulses. In the case of coherent radar, this time-series corresponds to the Doppler spectrum of that resolution cell, containing radial velocity information on both targets and clutter within the cell. An adaptive filter can be used to enhance the target signal over the clutter signal by matching the clutter spectrum, thus whitening the filter output, so that only the target's spectral components stand out. It is possible for the filter to discriminate between the clutter spectrum and the target spectrum because clutter is generally a diffuse source, spread over many adjacent cells, while the target is generally a point source, occupying a single cell.

The adaptive digital-filtering structure examined for this research was the lattice-structure prediction-error filter. A number of adaptation algorithms were examined for this structure, with the best results being obtained with the harmonic-mean algorithm. Within this algorithm, two gradient methods were examined for adaptation in a non-stationary environment. To test these algorithms and methods, coherent radar data was gathered from a 10 cm air-traffic-control surveillance radar. This data included different targets (aircraft and bird flocks) in a variety of clutter conditions (ground, rain, ice pellet, snow, and anomalous propagation clutter). Quantitative results are presented, including improvement factors and sub-clutter visibility factors, that show significantly better performance for these adaptive filters, when compared with conventional moving-target-indicator filters.

## 2.0 Defining the Problem

The radar used for this analysis is a scanning, pulsed radar system with a vertical fan-beam antenna pattern, such as is normally found in air-traffic control environment. In typical radars of this type, because of the antenna pattern, between ten and twenty pulses may pass through the cell before the antenna has scanned past the cell. Any object in the cell may return an echo from each of these pulses, forming a time series of samples representative of the object. If these pulse echoes are detected coherently by the radar receiver, then the time series contains both amplitude and phase information; the amplitude being related to the size and reflectivity of the object (radar cross-section), and the phase being related to the change in range of the object (Doppler shift). This time series of samples, taken at a single range and analyzed either in blocks or continuously, forms the basis for many radar signal processing systems.

The need for some type of processing of the radar signal is dictated by the fact that targets (such as an aircraft) are not the only signals detected. Radar clutter is also detected from a variety of sources, the most common being reflections from the ground, or from objects at ground level. This clutter is especially strong near the radar site, but may occur at any range from high objects or hilly terrain. Another major source of clutter is weather disturbances. Rain, snow, and other storm conditions can result in the strong reflections from large areas of the sky, obscuring any targets in the area. A different sort of weather-related clutter results from atmospheric inversion; areas of denser air which reflect or refract the radar pulse. Echoes created this way are often moving and may resemble targets or cover significant areas. Another signal source analyzed in this study was the reflections from birds, especially in flocks, which were

treated as targets.

In conventional radar systems, targets can often be obscured by clutter, or lost due to the processing used to remove clutter. The traditional processing technique commonly in use is the moving-target indicator (MTI) filter which assumes that the target of interest is moving (radially to the radar) and that the clutter is not. It is essentially a high-pass filter applied to detect the Doppler signal in the time series of samples from a constant range. This is usually implemented using a fixed tapped-delay-line (TDL) canceller, comparing two or more successive pulses for any changes.

The assumption that the target is moving and the clutter is not results in two problems. First, strong targets may be lost due to a low radial velocity. (This includes slow-flying bird flocks, which are a definite threat to air safety near airports). Second, storms of even moderate intensity are often moving fast enough to break through the MTI filter and thus obscure much of the radar screen. The MTI filter often fails completely in the presence of clutter due to weather disturbances, and is inconsistent in the case of migrating flocks of birds. In practice, all that can generally be assumed about the targets is that they are concentrated spatially, while clutter tends to be diffuse spatially. To give the best performance in separating targets from clutter, the clutter-suppression filter response must be good estimate of the actual clutter spectrum. This, in turn, has led to the use of adaptive filters as a possible solution to all types of clutter.

### 3.0 Adaptive Filtering of Radar Clutter

The adaptive filter works by adapting its response so as to remove the clutter component from the filter output. The prediction-error filter (PEF) can perform such a function. One specific way in which the PEF may be used to detect a target in clutter takes advantage of the different area coverage of the targets and clutter. By using a large number of previous samples of the time series and their statistics, the value of the next sample in the time series is predicted. If the predicted value is then subtracted from the actual value, the clutter component is filtered out, while the target signal remains substantially unaltered.

Another way in which the target may be detected is quite similar to this, except that the filter is allowed to adapt quickly, so that it adapts to targets as well as clutter. Then, there is significant output from the filter only during a sudden change in the spectral characteristics of the input signal. This occurs during the

transition from no-target to target conditions, whether or not clutter is present. With the lattice filter, this latter mode of operation appears to be the more effective of the two.

In past attempts to use the PEF for this application, a tapped-delay-line structure has been used<sup>1</sup>. However, some of the characteristics of the tapped-delay-line make it a bad choice for this type processing. One of the most important of these is the convergence properties, which are very signal-dependent. Other negative characteristics include tendencies to instability, poor resolution, large levels of quantization noise with high filter orders, and the inability to alter the filter order during operation. Most of these characteristics are related to the fact that this structure is adapted by minimizing a single, global effort criterion.

The negative characteristics of the tapped-delay-line structure are overcome by using the serially-processed lattice-realization of the PEF. Unlike the tapped-delay-line structure, the operation criterion for the lattice filter minimizes the error output of each filter stage independently, escaping those negative characteristics peculiar to the tapped-delay-line structure. The advantages of the lattice structure include good convergence properties<sup>2</sup>, guaranteed stability, and insensitivity to quantization noise, regardless of filter order<sup>3</sup>. These factors suggest the lattice structure would be a good choice for application to radar, which is affirmed by experimental results.

The lattice filter operates as a clutter suppression filter by processing the radar data serially along each range ring (of one resolution cell in depth) inside the area of interest. Starting from an arbitrary point on the range ring, a sample is taken for each transmitted pulse. Thus, once the filter is started up, it goes on indefinitely.

The use of the lattice filter in this way requires the assumption that the clutter signal can be represented using an autoregressive model. This assumption appears to be justified<sup>4-7</sup>, however, it is complicated by the assumption in such models of a stationary signal, which is not the case for scanning radar. Also, the spectrum of a small clutter sample area may be quite untypical of the whole clutter population. This is not a significant problem, however, as the clutter spectrum can be represented as a fairly simple envelope function containing the actual complex, finely detailed structure of the spectrum. This fine detail is mainly related to the short-term variations and disturbances of the clutter, while the envelope is derived from longer term parameters. Thus, it is only necessary for

the filter to adapt to the optimum clutter spectrum envelope.

The performance values presented in this paper for lattice filter result from the analysis of radar signals recorded in a specific environment under varying conditions. As the environment has a bearing on the performance of the filter, it was decided that a comparative study was most valid. As the MTI filter is the component generally found in existing systems fulfilling the correspondent role to the lattice (as described in the previous paragraph), it became the basis for comparison used in this study. A more extensive presentation of these results is presented elsewhere<sup>13,14</sup>.

#### 4.0 The Lattice Filter

##### 4.1 Basic Structure

The form of the lattice-structure prediction-error filter, as it is applied here to autoregressive model signals, has been presented extensively in the literature<sup>9,10</sup>. Figure 1 presents a block diagram of this structure. The forward and backward prediction errors  $f_m(n)$  and  $b_m(n)$  for stage  $m$  of the lattice filter at time  $n$  are given, respectively, by

$$f_m(n) = f_{m-1}(n) + \rho_m(n) \cdot b_{m-1}^*(n-1) \quad (1)$$

$$b_m(n) = b_{m-1}(n-1) + \rho_m^*(n) \cdot f_{m-1}(n) \quad (2)$$

for  $n \geq 1$  and  $0 \leq m \leq M$ , where  $M$  is the filter order.

The  $\rho_m(n)$  is the reflection coefficient for stage  $m$  (also called a partial correlation coefficient) and  $\rho_m^*(n)$  in its complex conjugate. (Complex arithmetic is used throughout). The input data at time  $n$  is placed in both  $f_0(n)$  and  $b_0(n)$ .

A number of different algorithms have been proposed for the calculation of the reflection coefficient<sup>2,11</sup>.

Comparisons of these algorithms using simulated radar data have shown that Burg's harmonic-mean algorithm gives the best results in this application<sup>12</sup>. In addition, this algorithm has the strongest theoretical background<sup>11,13</sup>. The optimum values of the reflection coefficients are given by this algorithm as

$$\rho_m(n) = \frac{-2 E[f_{m-1}(n) \cdot b_{m-1}^*(n-1)]}{E[|f_{m-1}(n)|^2 + |b_{m-1}(n-1)|^2]} \quad (3)$$

where  $E$  is the expectation operator.

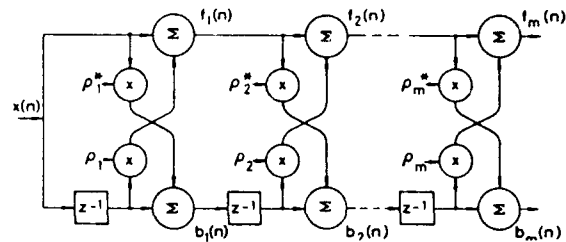


Figure 1: Lattice-structure prediction-error filter

In some applications, where the data is completely stationary, the reflection coefficients may be calculated by block processing, where the expectation of equation (3) are simply replaced by summations from  $m+1$  to  $N$ , where  $N$  is the size of the data block. In this manner the reflection coefficients are calculated only once for each filter state and static block of data. In other applications, however, such as that presented here, it is desirable to use serial processing, where a new value of the reflection coefficient is calculated with the arrival of each new data sample. This has the advantages of (a) achieving better tracking of nonstationary signals, and (b) filter outputs being available immediately (and continuously). There is the disadvantage of some reduction of accuracy for stationary signals, compared to the block processing. Rather than totally recomputing the reflection coefficients with each new data sample, they may now be computed recursively (updated with each new sample). Starting with an initial (arbitrary) value, the reflection coefficient is updated by correction terms, which are calculated to provide the greatest reduction of prediction errors per correction unit. Also, it is generally desirable to apply a weighting factor to the prediction error terms used in these calculations. This allows the filter to essentially "forget" the effects of samples beyond a certain distance or time (which may not represent current signal statistics), including any start-up effects. It should be noted that weighting the prediction errors is not in any way equivalent to weighting the input samples, which would result in a stationary signal of reduced resolution.

We will present two methods of recursive calculation of the reflection coefficients. Other methods exist, but these two exhibit the controlled convergence properties required for use as a radar clutter suppression filter.

##### 4.2 Serial Implementation Using the Standard Gradient Method

The first method is called the standard gradient method because it is the method that is generally arrived at by applying gradient techniques to the lattice

equation<sup>9,10</sup>. The standard gradient method consists of replacing the expectations of the various terms, used for the reflection coefficient calculation, with corresponding averages in which an exponential weighting has been added to the individual values. This weighting allows the characteristics of older data samples to be progressively forgotten, giving greater importance to current data. The reflection coefficients thus estimated are given by:

$$\hat{\rho}_{m+1}(n) = \frac{-2 \sum_{i=1}^n \mu^{(n-i)} [f_m(i) b_m^*(i-1)]}{\sum_{i=1}^n \mu^{(n-i)} [|f_m(i)|^2 + |b_m(i-1)|^2]} \quad (4)$$

where  $\mu$  is a weighting constant, normally in the range  $0 \leq \mu \leq 1$ . Small values of  $\mu$  result in quick adaptation to new signal characteristics, while values of  $\mu$  near one result in slower convergence and the reduction of noise by integration.

The reflection coefficient estimator of Eq. (4) differs from that used for block processing in two fundamental respects:

- (a) The inclusion of the weighting constant  $\mu$  makes the estimator of Eq. (4) having a fading memory. On the other hand, with  $\mu = 1$  (the block processing case), the estimator has a non-fading memory.
- (b) The lower limit in the summation in Eq. (4) is a fixed integer, namely, one. With increasing  $n$ , this situation therefore represents a growing memory. For block processing, on the other hand, the lower limit equals  $m+1$  for a filter order  $m$ ; accordingly, for fixed values of  $m$  and block length  $N$ , this second situation represents a fixed memory.

The exponential form of the weighting function is chosen because it can be applied as part of a simple recursive implementation. Thus, with each new sample, a new value for  $\hat{\rho}_{m+1}(n)$  is calculated from

$$\hat{\rho}_{m+1}(n) = \frac{v_{m+1}(n)}{y_{m+1}(n)} \quad (5)$$

where,

$$v_{m+1}(n) = \mu v_{m+1}(n-1) - 2 f_m(n) b_m^*(n-1) \quad (6)$$

and

$$y_{m+1}(n) = \mu y_{m+1}(n-1) + |f_m(n)|^2 + |b_m(n-1)|^2 \quad (7)$$

To apply the algorithm, we start with the initial conditions  $v_{m+1}(0) = y_{m+1}(0) = 0$  for all  $m$ .

### 4.3 Serial Implementation Using the Simple Gradient Method

The other method of recursively calculating the reflecting coefficients is called the simple gradient method, due to the use of an approximation which results in a simpler implementation than the more common standard gradient method<sup>10</sup>. This method starts by considering the new coefficient as being the sum of the old coefficient and a correction term, which is the difference between the new and old values of the coefficient. With a little manipulation, we find that the simple gradient algorithm may be written as<sup>10</sup>

$$\hat{\rho}_{m+1}(n) = [1 - \gamma_m(n)] \hat{\rho}_{m+1}(n-1) - \frac{2 \gamma_m(n) f_m(n) b_m^*(n-1)}{|f_m(n)|^2 + |b_m(n-1)|^2} \quad (8)$$

where

$$\gamma_m(n) = \frac{|f_m(n)|^2 + |b_m(n-1)|^2}{\sum_{i=1}^n [|f_m(i)|^2 + |b_m(i-1)|^2]} \quad (9)$$

We see that for the steady state (constant power) case,  $\gamma_m(n) = 1/n$  where  $n$  is the number of data samples processed. If, however,  $\gamma_m(n)$  is held constant in the calculation, then it may be replaced by using the weighting factor  $w$  as defined in the formula

$$w = 1 - \gamma = 1 - 1/n' \quad (10)$$

where  $n'$  is the theoretical data adaptive length of the filtering action. The resulting constant  $w$  has a value in the range  $0 \leq w \leq 1$ , with smaller values given quicker adaptation. Rewriting Eq. (8) with  $w$  gives

$$\hat{\rho}_{m+1}(n) = w \hat{\rho}_{m+1}(n-1) + \alpha_m(n) f_m(n) b_m^*(n-1) \quad (11)$$

where the adaptive step size  $\alpha_m(n)$  equals

$$\alpha_m(n) = \frac{-2(1-w)}{|f_m(n)|^2 + |b_m(n-1)|^2} \quad (12)$$

An implicit condition on the recursive relationship of Eq. (11) is that the power of the prediction error  $f_m(n)$  or  $b_m(n)$  is not a time-varying function. This condition results in a somewhat poorer response for nonstationary inputs, when compared with the standard gradient method. However, this shortcoming is partially offset by the desirable convergence properties, and the reduced storage and computation time requirements of the simple gradient method (which are less than the standard gradient method by 20% and 30% respectively).



## 5.0 Experimental Data

The purpose of this section is to describe that radar environment and given examples of the signals obtained from it under varying conditions. These signals include aircraft, bird flocks, ground clutter and weather clutter resulting from rain, snow, ice-pellets and atmospheric inversion systems. The presentation of these latter signals will show the inadequacy of traditional clutter processing.

The data used in this study was recorded from a Texas Instruments ASR-8 surveillance (air-traffic control) radar located at the Bagotville Canadian Forces Base in the province of Quebec, Canada. The radar used a klystron transmitter operating at 2768 MHz, with a pulse duration of 0.6  $\mu$ sec. and repetition rate of 1041 Hz (staggered). The baseband inphase and quadrature detected signals were recorded on a wideband video recorder for subsequent computer analysis (more details on this system are contained elsewhere<sup>13</sup>).

Included in the data were a number of examples of bird flocks (migrating snow geese), which produced signals very similar to those of slow moving aircraft. Some analysis was done on these signals in which the bird flocks became the targets used to assess the filtering performance, replacing the aircraft signals used otherwise. The use of bird flock data as a type of target signal may at first seem contradictory, as bird-flock returns are generally considered clutter. There is some justification for taking this course, however. A major argument for considering bird flocks as targets is the consideration of air safety, as birds pose a real collision threat to aircraft, especially when the aircraft are landing and taking off. It seems very desirable to treat bird-flock returns as targets to be avoided, rather than as clutter to be ignored and eliminated. The performance of the standard MTI filters presently used by most radars can best be described as hit-and-miss for this sort of data. Faster flocks are detected as targets, while returns from slower flocks are eliminated as clutter. The lattice-structure filters presented here, however, detect the flocks as targets with a high degree of consistency.

In order to remove weather returns from the MTI display, many radars use constant-false-alarm-rate (CFAR) processing. This processing tests each data point from MTI filter against a threshold of the average value from surrounding points. Detected returns covering a large area (such as weather clutter) are reduced to the level of system noise, while isolated returns (targets) are largely unaffected (in theory). The

CFAR display is not much of an improvement, however, as target returns occurring in regions of strong clutter are also eliminated from the display. Thus, the conventional MTI filter's inability to distinguish between moving clutter and targets becomes a real problem. This is the problem for which the adaptive lattice-structure filter is intended to be a solution.

Precipitation clutter seen during the study period at Bagotville included periods of rain, snow, and ice pellets (freezing rain), which were recorded and analyzed. In all these cases, significant portions of the radar PPI screen were obscured by the clutter, creating the problems discussed in the previous section.

A final type of clutter dealt with is inversion clutter, thought to be ground echoes refracted or reflected by layers of denser air near the ground. This type of clutter was generally recorded on clear, cold evenings with moderate winds, following a mild day. The MTI display would usually show two "blobs" of scattered fluctuating points, aligned with the wind. (In other displays of this type of clutter, the points have short tails, all aligned radially to the display center). The identification of atmospheric inversion as the source of clutter attributed to it here is not certain. This sort of clutter is often called "angel clutter", and some reports suggest that it is caused mainly by birds<sup>15</sup>. This seems unlikely for three reasons. They are: (a) No birds were seen in the area at the times when the clutter was present; (b) The clutter movement was aligned with the wind direction (and therefore presumably related); and, (c) The clutter always occurred during the same weather conditions. These were late afternoons or evenings with clear skies when the temperature was dropping rapidly. These are conditions which often lead to the formation of an inversion layer near to the ground<sup>16</sup>. This comes about when the ground cools faster than the air mass above it, resulting in a fairly stable layer of denser air. Movement of the layer or its boundaries could impart a Doppler shift to signals refracted or reflected by it, resulting in MTI detection. However, whether or not this is the true cause of this type of clutter is not very important to this study.

Computational requirements limited to the amount of the recorded data which could be fully analyzed. Selected range rings of data were analyzed, including several examples of every type of clutter present in the data. In all cases, the performances of the filters were very similar for all the samples of a particular clutter type, even though these samples were from different ranges and recorded at different times. In addition, all aircraft and bird flocks which could be

found in the data and properly identified were sampled.

The radar installation from which the data was collected make use of a staggered pulse-repetition frequency (PRF), with four sequenced periods. This can present a problem to the lattice-structure filter, which assumes a constant time period between samples. The solution used in this paper was the parallel operation of four separate lattice filters, each taking only every fourth sample in series. The outputs of the four lattice filters were then averaged together for simplicity, as were the input and MTI output signals for the same four sample pulses.

Because of the parallel filtering structure, and the non-stationary nature of the data, it could be expected that the optimum values of the adaptive constants used for the lattice-structure filters would be quite low. In fact, as will be shown in section 5, the best performance is achieved with  $w=0.0$  for the simple gradient  $\mu=0.1$  for the standard gradient method. At these values, the filters are able to partially adapt to the targets as well as the clutter, and target detection is based on the response to the transition region between clutter and target. In this region, the signal statistics belong to neither clutter nor target, but are changing between the two.

In the course of examining the recorded data, five aircraft targets which could be reliably identified were found. These five targets may seem to be a small data base from which to form any conclusions or derive any statistics. However, they are representative of the mid-size aircraft found at many airports, and more importantly cover the range of radial (Doppler) velocities, including zero, typical of such aircraft.

## 6.0 Performance Evaluation

### 6.1 Improvement Factors

The improvement factor of a radar clutter filter is defined as: "the signal-to-clutter ratio at the output of the system divided by the signal-to-clutter ratio at the input system, averaged uniformly over all target radial velocities of interest"<sup>17</sup>. This can be written as:

$$I = \frac{(T_{out}/C_{out})}{(T_{in}/C_{in})} \quad (13)$$

where  $T$  and  $C$  are the target and clutter powers. In applying this performance measure to the actual radar data collected for this paper the improvement factors ( $I$ ) were calculated from the ratios of the target gains

in the filter ( $T_{out}/T_{in}$ ) to the clutter gains in the same filter ( $C_{out}/C_{in}$ ).

Using the signals from the five aircraft peak amplitudes at the filter inputs and outputs were measured and the five resulting gains were averaged together to form a single target gain for each filtering set-up. Five targets may seem to be small number to form a "uniform" average, but these targets do represent a fair cross-section of the possible velocities (including zero). Besides, these were the only such signals readily available, and thus became the targets "of interest".

The clutter gains were measured by averaging the signal amplitudes over the entire range ring, and taking the ratio of the average output power. These gains were measured for more than one range-ring of each type of clutter, with these rings generally recorded at different range and times, to ensure uniformity of the results.

The improvement factors plotted in this chapter were calculated using the average of clutter gains from several such range-rings of each clutter type; however, improvement factors were also calculated using the gains of the individual rings. In general, the measured improvement factors for the single clutter rings and for the average for a clutter type were within 1/2 dB, except where noted. The exceptions involved only the MTI filters and apparently related to the overall velocity of the specific clutter record. As the above variance was much less than that between different clutter types, this was taken as evidence that the selected range-rings were representative of the clutter present.

The measured improvement factors, as a function of filter order, are plotted in Figures 2 to 6 for ground, rain, snow, ice-pellet, and inversion clutter, respectively. Each of these plots has three curves; one for the MTI filter, and one each for the simple gradient

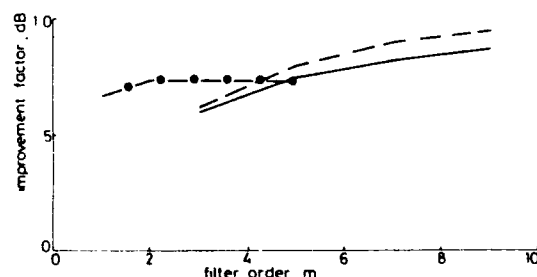


Figure 2: Improvement factors for ground clutter (Solid line is simple gradient filter, dashed line is standard gradient filter, and dot-dash line is MTI filter)

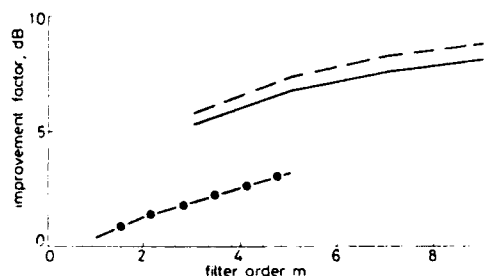


Figure 3: Improvement factors for rain clutter (Solid line is simple gradient filter, dashed line is standard gradient filter, and dot-dash line is MTI filter)

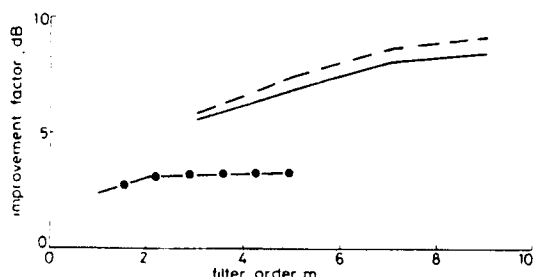


Figure 4: Improvement factors for snow clutter (Solid line is simple gradient filter, dashed line is standard gradient filter, and dot-dash line is MTI filter)

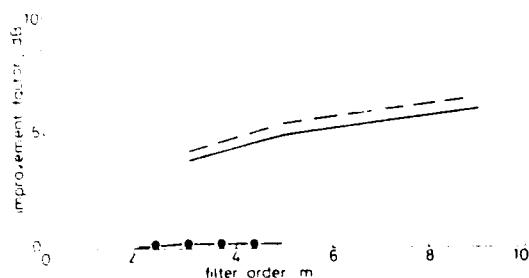


Figure 5: Improvement factors for ice-pellet clutter (Solid line is simple gradient filter, dashed line is standard gradient filter, and dot-dash line is MTI filter)

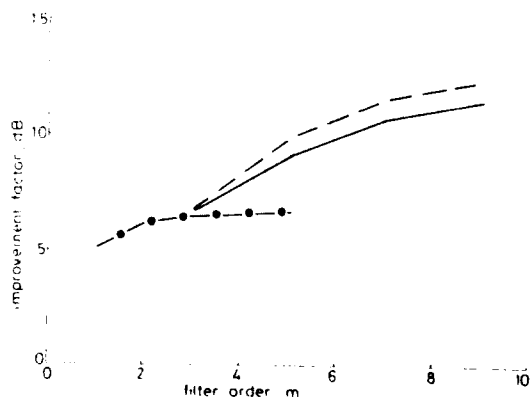


Figure 6: Improvement factors for inversion clutter (Solid line is simple gradient filter, dashed line is standard gradient filter, and dot-dash line is MTI filter)

and standard gradient implementations of the lattice filter. The lattice-structure filters had adaptive constant values of 0.2.

The set of curves for the lattice filters presents a very similar pattern in each of these five figures, with the only significant difference being in the overall level of the set of curves. Even this was fairly constant, with rain, snow, and ground clutter all resulting in approximately the same improvement factor levels (for each lattice filter). The improvement factors were about 3 dB lower for ice-pellet clutter. A common factor in all the lattice filter curves is the increase in improvement factor with increasing filter orders, suggesting that there is an upper limit to the improvement. As expected, the standard gradient method of adaptively implementing the lattice filter performed better than the simple gradient method.

Another factor of interest in the lattice filter response is the effect of the adaptive constant. Generally, lower values of adaptive constant resulted in better performance. Figure 7 plots improvement factors versus adaptive constants for both implementation methods (filter order = 9), and for three of the clutter types. (The other clutter types give very similar performance). The best values of adaptive constant for the standard gradient method occur in the range from 0 to 0.2, with an optimum value of  $\mu=0.1$ . For the simple gradient method, on the other hand, the optimum performance occurs only at  $w=0$ . (Note: at  $w=\mu=0$ , both methods simplify to a common set of equations).

The curves in Figures 2 to 6 for the MTI filter, unlike those for the lattice filters, show considerable variation with the type of clutter. The MTI filter performed best for ground clutter and worst for ice-pellet clutter. In addition, there was some variation in performance within specific clutter types, probably due to the velocity of the clutter. In particular, single range-rings for snow and inversion clutter both resulted in MTI performance about 2 dB below that shown in Figures 2 and 6 for an average of several rings. Some tests were also made using bird targets instead of the aircraft. This resulted in a further 3 dB reduction in MTI performance, with little effect on the lattice filters. The effect of MTI filter order also varied, depending on the type of clutter. For rain clutter, the improvement factor increased with filter order, up to  $m=5$ . For the other clutter types, however, there was little increase beyond  $m=2$ . (In fact, for some range-rings of clutter, there was a decrease in level with increasing filter order). This tends to validate the common choice of  $m=2$  for conventional radar MTI filters.

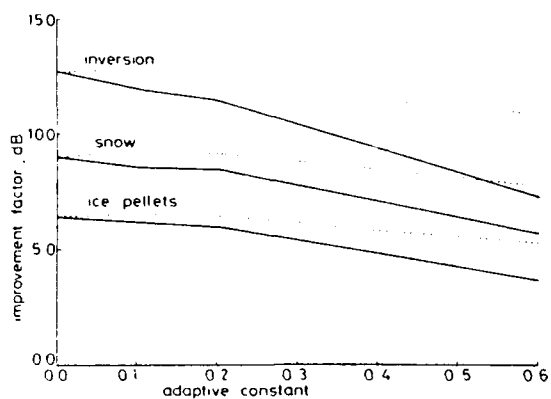


Figure 7: Improvement factors versus adaptive constant for  $m=9$  (Solid line is simple gradient filter, dashed line is standard gradient filter)

The relative performance of the lattice and MTI filters can be assessed from Figures 2 to 6. The most important observations are that the lattice filter always performed as well as, or better than, the MTI filter, and that the lattice filter performed consistently well. The improvement factors of the lattice and MTI filters were approximately the same for ground clutter, while for inversion clutter the lattice was 3 to 5 dB better, and for precipitation clutter the lattice was 4 to 6 dB better.

This does not tell the whole story, however. When the whole range-ring is analyzed as a unit, the performance is averaged over the whole spread of Doppler velocities present in the clutter. Also, some ground clutter is present in every range-ring. If only small sections of a range-ring are considered (as was done in section 4), the performance ranges from nearly identical (for well-behaved clutter moving tangentially), to improvement factors with as much as 20 dB difference, in favour of the lattice. Figure 8 shows a histogram of the improvement factors for 21 such sections, selected from all types of clutter (mainly at points of highest and lowest clutter velocities). Although not too significant in a statistical sense, this figure does show the wider spread of improvement factor values for the MTI filter compared to the lattice filter. Also, the MTI filter improvement factors are often negative (degrading performance), unlike the lattice filter improvement factors, which never go negative.

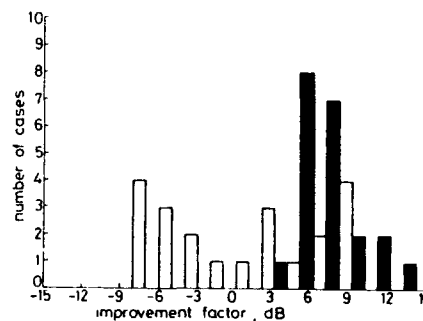


Figure 8: Histogram of sectional improvement factors for  $m=5$  (black is standard gradient filter, white is MTI filter)

## 6.2 Sub-Clutter Visibility

Sub-clutter visibility (SCV) is defined as "The ratio by which the target echo power may be weaker than the coincident clutter echo power and still be detected with specified detection and false-alarm probabilities. Target and clutter power are measured on a single pulse return and all target radial velocities are assumed equally likely"<sup>17</sup>. For this paper, we shall soften the definition slightly by assuming that the radial velocities of the five aircraft targets used are good enough approximation of "...equally likely".  $P_D$  and  $P_{FA}$  are here specified a 0.5 and 0.01, respectively; and SCV values are derived from the corresponding SCR values measured as part of an extensive receiver operating characteristic (ROC) analysis.

The sub-clutter visibility, as a function of filter order, is presented in Figures 9 to 13 for ground, rain, snow, ice-pellet, and inversion clutter, respectively. Higher SCV values indicate better performance. There are three curves in each figure, one for MTI filtering, one for lattice filtering using the simple gradient method ( $w=0.2$ ), and one for lattice filtering using the standard gradient method ( $\mu=0.2$ ). The SCV performance of the lattice filters as a function of adaptive constant peaked at  $w=0$  for all clutter types with the simple gradient method, while for the standard gradient method the peak values were found with  $\mu$  in the range from 0 to 0.1.

As before, these figures show the lattice filters outperforming or equalling the MTI filter. Looking at the SCV performance, given a filter order of five for example, the best lattice filter response equalled the MTI filter response for ground clutter, and exceeded it by 5 dB for ice-pellet clutter, 6 dB for rain clutter, 9 dB for snow clutter, and 11 dB for inversion clutter.

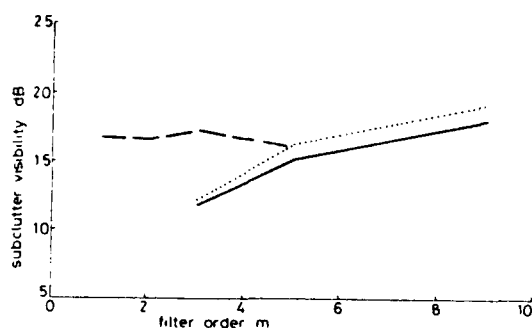


Figure 9: Subclutter visibility for ground clutter (Solid line is simple gradient filter, dotted line is standard gradient filter, and dashed line is MTI filter)

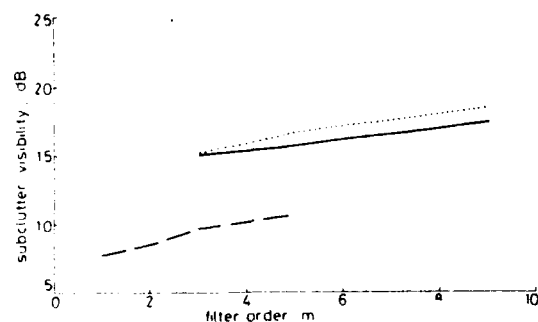


Figure 10: Subclutter visibility for rain clutter (Solid line is simple gradient filter, dotted line is standard gradient filter, and dashed line is MTI filter)

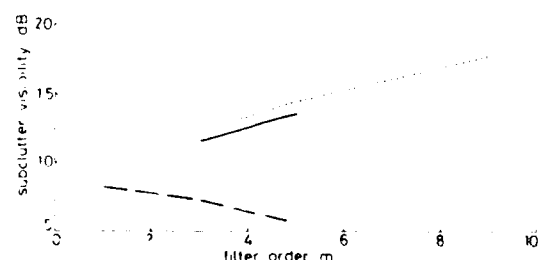


Figure 11: Subclutter visibility for snow clutter (Solid line is simple gradient filter, dotted line is standard gradient filter, and dashed line is MTI filter)

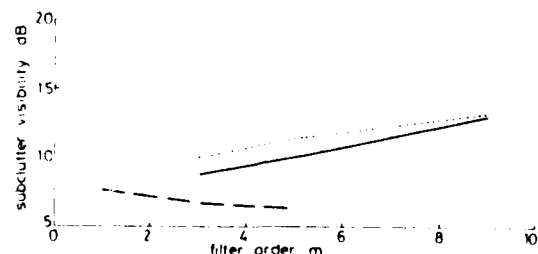


Figure 12: Subclutter visibility for ice-pellet clutter (Solid line is simple gradient filter, dotted line is standard gradient filter, and dashed line is MTI filter)

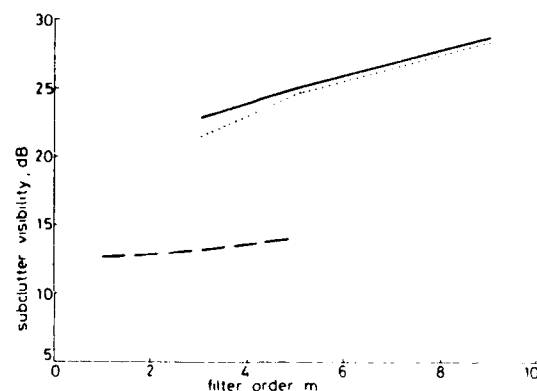


Figure 13: Subclutter visibility for inversion clutter (Solid line is simple gradient filter, dotted line is standard gradient filter, and dashed line is MTI filter)

The lattice filters showed a steady increase in performance with filter order, while the performance of the MTI filter was relatively independent of filter order. The standard gradient method was better than the simple gradient method in these examples. For inversion clutter, the lattice filters did especially well on the absolute scale.

## 7.0 Discussion

In conclusion, the results presented here should not be considered as an absolute measure of the performance of the lattice-structure filter or this application. Rather, this presentation should be considered as a "proof-of-concept" for this application of the structure. What has been shown here is that the lattice filter reliably reduces clutter signals (compared to target signals) and consistently out-performs the MTI filter, and that it does so using a simple structure and under adverse conditions. (It should be noted that the radar signals used in this study were limited to a SNR of 36 dB by the recording equipment used).

Both implementations of the lattice filter performed well, but the standard gradient method performed slightly better, as expected. However, in an operational system, the simple gradient method might be preferred, due to its lower memory and time requirements, which might allow a larger filter order within the system limitation than the standard gradient method. In fact, allowing  $w$  to go to zero (eliminating the coefficient memory), further increases the memory savings and speed of the algorithm, while still giving good results. Based on the results presented here, it can be said that the adaptive lattice filter represents a very promising structure for radar clutter processing.

## 8.0 Acknowledgement

This research was a project of the Communications Research Laboratory at McMaster University (Hamilton, Ontario, Canada), and was supported by the Natural Sciences and Engineering Research Council of Canada. The author would like to express his deep gratitude to Dr. Simon Haykin, under whose direction this project took place.

## 9.0 References

1. W. Burdick, "Detection of Narrowband Signals Using Time-Domain Adaptive Filters", *IEEE Trans. On Aerospace and Electronic Systems*, vol. AES-14, no. 4, pp. 578-591, July 1978.
2. L.J. Griffiths, "A Continuously-Adaptive Filter Implemented as a Lattice Structure", *Proc. IEEE Int. Conf. Acoust., Speech, and Signal Processing*, Hartford, CT, pp. 683-686, May 1977.
3. E. Satorius and J. Pack, "Application of Least Squares Lattice Algorithms to Adaptive Equalization", *IEEE Trans. on Communications*, vol. COM-29, no. 2, pp. 136-142, February, 1981.
4. E. Barlow, "Doppler Radar", *Proc. IRE*, vol. 37, pp. 340-355 (1949).
5. W. Fischbein, S. Graveline and O. Rittenback, "Clutter Attenuation Analysis", *Tech. Report ECOM 2808* (1967).
6. N. Currie, F. Dyer and R. Hayes, "Radar Land Clutter Measurements at Frequencies of 9.5, 16, 36 and 95 GHz", *Tech. Report #3, Project A-1485*, Georgia Inst. of Tech., Engineering Experiment Station (1975).
7. W. Flock, "Radar Signature Studies Applicable to Bird-Aircraft Collision Avoidance", *Final Report for period June 18, 1970 to Nov. 15, 1973*; Air Force Weapons Laboratory, Air Force System Command, Kirkland Air Force Base, NM.
8. C. Hawkes, "Adaptive Digital Filtering for Coherent MTI Radar", *Ph.D. Thesis, McMaster University* (1975).
9. J. Makhoul, "A class of All-Zero Lattice Digital Filters: Properties and Applications", *IEEE Trans. on ASSP*, vol. ASSP-26, no. 6, pp.681-691, December 1980.
10. C. Gibson and S. Haykin, "Learning Characteristics of Adaptive Lattice Filtering Algorithms", *IEEE trans. on ASSP*, vol. ASSP-28, no. 6, pp. 681-691, December 1980.
11. J. Makhoul, "Stable and Efficient Lattice Methods for Linear Prediction", *IEEE Trans. on ASSP*, vol. ASSP-25, pp. 423-428, 1977.
12. C. Gibson and S. Haykin, "A Comparison of Algorithms for the Calculation of Adaptive Lattice Filters", *Proc. 1980 IEEE Int. Conf. on ASSP*, vol. 80CH1559-4, pp. 987-983 (1980).
13. C. Gibson, "Adaptive Lattice Filtering for Radar Applications", *Ph.D. Thesis, McMaster University*, 1982.
14. C. Gibson and S. Haykin, "Radar Performance Studies of Adaptive Lattice Clutter-Suppression Filters", *IEE Proc.*, vol. 130, Pt. F, pp. 357-367 (1983).
15. L. Cartledge and R. O'Donnell, "Description and Performance Evaluation of the Moving Target Detector", *Project Report ATC-69*, Lincoln Laboratory, Mass. Inst. of Tech. (1977).
16. Environment Canada, "Weather Ways", *Supply and Services Canada* (1978).
17. IEE Standard Dictionary of Electrical and Electronics Terms, 2nd Ed., J. Wiley and Sons (1977).

## DISCUSSION

F. Le Chevalier, FR

Can you comment about the equivalent number of resolution cells used for the adaptation, in relation with point-like clutter or nonhomogeneous clutter?

Author's Reply

The equivalent number of resolution cells is quite small; on the order of ten. An exact number is not possible because the filter uses a fading memory approach.

# USE OF TARGET SPECTRUM FOR DETECTION ENHANCEMENT AND IDENTIFICATION

S. Pardini(\*), P.F. Pellegrini(\*\*), P. Piccini(\*)

(\*)Alenia - Aeritalia & Selenia S.p.A.

Via Tiburtina km. 12.400 - 00131 Rome (ITALY)

(\*\*)University of Florence

Via S. Marta, 3 - 50139 Florence (ITALY)

## ABSTRACT

The paper deals with modulation on the echo signal generated by rotating machinery of an air target.

An extensive measurement campaign has been carried out by means of an Air Traffic Control radar and some preliminary results are presented.

The problem of target spectra characterization and exploitation for detection enhancement and target identification, is considered in relation with the limitation imposed by the present radar features.

Some considerations regarding the application of this technique for Non Cooperative Target Recognition, in the radar of future generation, are developed.

conventional signal processing algorithm in order to improve detection, by resorting to adaptive filtering matched to target spectrum.

In order to acquire real data, a flexible registration tool, applied to an S-band ATC radar, has been assembled. At each scan it samples, with a high data rate, the in-phase and quadrature components of the base-band signal in a prefixed window of the radar sky and transfer it from the internal buffer in a memory for an off-line analysis.

The registration campaign, up to now limited to commercial aircraft, is still in progress, but some significant samples are presented with some concepts and results on benefits of using these spectra for detection enhancement and target identification. In addition intrinsic limitations due to the characteristics of the used radar are outlined and special radar mode to overcome them is envisaged.

## 1 INTRODUCTION

The problem of air target spectra characterization and how these spectra can be usefully exploited both for detection enhancement and target identification is challenging and still open. It is known that radar signal from aircraft is modulated by rotating propellers or turbine blades of jet engines, which cause side lines in the echo signal spectrum, where the center is the Doppler line of the rigid body of the aircraft. The energy associated to these side lines may be significant with respect to the total energy echoed by the aircraft. Therefore the spectrum of the echo may not be longer considered as a single Doppler line caused by radial velocity.

The fine structure of the spectrum carries also the imprinting of the engine characteristics which in turn identifies the aircraft. The knowledge of the spectrum shape of the echo signal, in principle, makes possible to revisit

## 2 ACQUISITION SYSTEM

The designed and assembled acquisition system, digitizing video radar signals, is a Personal Computer (PC) controlled structure, suitable for operations synchronized with various radar driving waveforms.

It can operate in an autonomous way by showing in real time on the PC display the synthetic PPI based on the plot data of the radar itself.

It works through an acquisition window whose dimensions are selected between wide limits and it can potentially perform up to 100 Msample/s per channel (4 channels simultaneously) and 12 bit/sample.

The system is mainly constituted by the following four parts:

- An auxiliary Personal Computer for airplane position and window presentation, and as interface with the operator for parameter selection.
- Digitizing apparatus (LeCroy 6810) which, synchronized by the Range Bin Clock (RBC) and sweep trigger signals performs the A/D conversion on the two I and Q video signals. The data storage is performed in its own transfer memory (12 bit/sample).
- Main PC computer controlling all the functions of the sampling equipment. Automatically the P.C. allows the sampling to take place only in the selected acquisition window. The output signals, from the transfer memory, are poured off in the main computer and written in files.
- Auxiliary circuits to count the Azimuth Counter Pulse (ACP) for synchronization of the acquisition window.

In addition to the video signal acquisition, the trigger-to-trigger time are acquired (resolution 1 usec).

### 2.1 HARDWARE DESCRIPTION

The hardware structure of the acquisition system has been oriented toward the use of parts as standard as possible. Modular structure were also used to fit different measurement situations.

With reference to the Fig. 1 the auxiliary PC acquires the radar plot information through its parallel port. The format is HDLC synchronized by a 9600 Hz signal. Such information is processed and shown on the display in a synthetic way. The operator, looking at the display, decides

which he has to acquire.

The A/D conversion system is a multichannel, modular apparatus driven by an interface. It include a transfer memory of about 0.5 Msample (extensible to 10 Msample).

Control operations performed by the PC on the acquisition apparatus are mainly concerned with the dimension of the transfer memory, number of channels, signals dynamic, number of segments (sweeps) to be acquired, external trigger synchronization, trigger delay, acquisition start, etc.

The range window is controlled either by the sweep trigger delay or by the signal segment size. In addition, for faster data transfer, the range interval can be further reduced by storing in files only portions of the signals.

The range and azimuth of the window center can be optionally entered by the operator taking into account the data obtained from the PPI presentation of the radar itself.

### 2.2 PERFORMANCE

The system works with a set of acquisition programs and a set of auxiliary quick look programs which allow a great reliability during the measurement campaign.

Many tests are possible on the apparatus itself. Furthermore preliminary acquisitions can be done to determine the operating characteristics of the radar (antenna rotation period, PRF, stagger, plot data format, etc.).

The used configuration employs acquisition windows of 64 sweeps and 128 range samples (5.76 degrees and 5.53 nmi) with 12 bit/sample. The I and Q signals are contemporaneously digitized at a frequency of 1.875 MHz.

The programs are implemented in Microsoft Quick Basic and in Assembler where faster operations are requested.

### 3 RADAR SYSTEM

All the measurements presented here have been carried out at Fiumicino Airport (Rome). The TMA radar site includes a primary S-band radar, in dual channel configuration, and a secondary monopulse IFF radar completely redundant.

The primary radar can operate either in single channel configuration, or in dual channel (diversity).

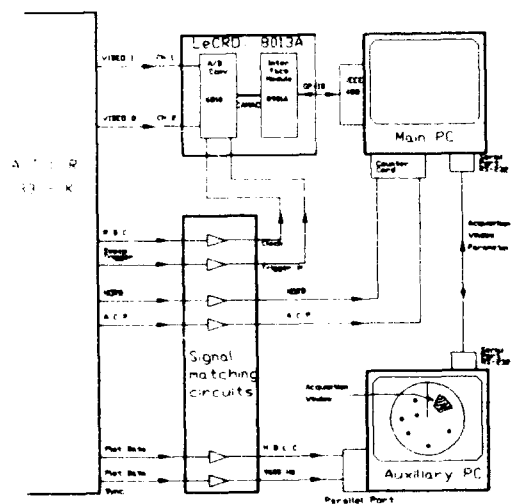


Fig. 1 Radar Data Acquisition System



### 3.1 PRIMARY RADAR

The primary radar is a fully coherent radar using a Klystron amplifier as power transmitter. The transmission frequency is fixed.

The relevant block diagram is shown in fig. 2.

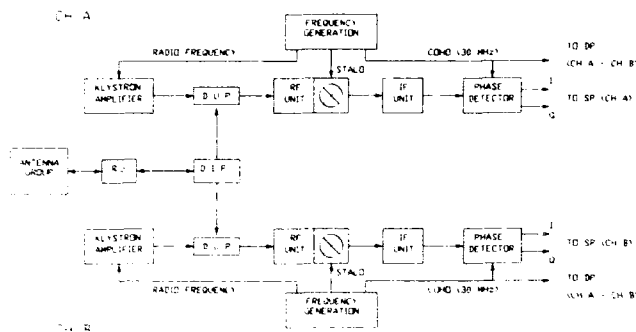


Fig. 2 ATCR 33-K RF-IF Block Diagram

The G33 antenna is a dual beam, supercosecant squared, reflector antenna rotating at 15 RPM.

In normal operation the radar transmits a burst of 8 pulses at the same PRF; the pulses are linearly processed in the receiver, down converted, phase detected (I and Q channels), sampled in 12 bits and coherently integrated in a Moving Target Detector (MTD) processor.

The linear dynamic of the radar is limited by the phase detector at 40 dB on the I and Q video channels.

A double stagger of the PRF is implemented to improve the MTD response.

The plot extraction, combining process (radar plots with the IFF plots) and tracking are performed by the radar Data Processor.

Out of the tracking algorithm all the information on the aircraft kinematics and type is available: range, azimuth, ground speed, height and identification code.

The plots and tracks are presented on the maintenance display and sent to the operative center where the control function is carried out.

In the following table, the main radar parameters are listed.

#### RADAR PARAMETERS

S-Band	2700 - 2900 MHz
Peak Power	1.2 KW
Rotation Speed	15 RPM
Unambiguous Range	80 N.M.
Beamwidth (-3dB)	1.5 deg.
Pulse length	1 microsec
PRF (Average)	1000 HZ
Stagger Ratio	+/- 7 %

### 3.2 SECONDARY RADAR

The IFF antenna, mounted on the top of the G33 primary antenna, is an Open Array type.

The aircraft identification code and height are provided by the IFF processor to the radar Data Processor. From the identification code it is possible to obtain the type and airline of the aircraft for subsequent classification.

### 3.3 RECORDING SETTING

The recording equipment samples the I and Q video channels, at the radar clock timing, in a suitable window centered at the plot coordinates.

In order to perform a coherent processing on the recorded samples, a different setting has been devised without stopping the normal data flow through the radar.

The STC variation in azimuth has been overridden and the main beam has been selected all over.

Any other intermediate frequency conditioning has been excluded.

The PRF stagger has been removed.

Due to the nature of the ATC radar, neither was possible to modify the rotation speed of the the antenna nor the PRF value. Therefore the Time On Target, measured at -3 dB of the antenna pattern, is 16 milliseconds and the relevant Doppler resolution is roughly 40 Hz. The ambiguous radial velocity, corresponding to 1000 Hz, is about 100 knots.

## 4 EXPERIMENTAL DATA

During the recording activity, a great deal of different aircraft data has been collected. They refer, for the most part, to commercial aircraft. Both jet and turbofan driven aircraft are equally represented. Few helicopters were also recorded.

For now, the attention has been focused on the jet aircraft, while the turboprop and helicopter will be subject of a future study. Therefore the present paper deals with the first results coming from the interpretation of the echo modulation produced by the jet engine (JEM).

Few words about the recording procedure are useful. Once the target has been designated, automatically the recording equipment, using the information coming from the tracking, centers the window on the plot estimated position and records the I and Q data belonging to the window, in a file on the Personal Computer hard disk.

The process of centering the window and recording is repeated at any scan until the operator stops it.

In each file a number of auxiliary information is recorded:

- \* Time and date
- \* Type of aircraft and airline
- \* Type of trajectory
- \* Range
- \* Azimuth
- \* Flight Level (FL)
- \* Ground speed
- \* Setting of the recording equipment

From the original file, a subsets of I and Q data, containing the target samples, are isolated for subsequent analysis.

The subsets of samples (16 range bin and 32 sweeps), are checked to be sure no saturation took place in the A/D converter amplifiers. As an example, the modulus of the time samples, in a tridimensional graphic, is presented in figure 3.

A discrete Fourier transform, namely Discrete Fourier Series algorithm (DFS), is applied to the 32 azimuth samples and presented in a tridimensional graphic to distinguish between the target features and the background (figure 4).

No weighting has been applied at the time samples due to the fact that the antenna pattern itself provides the amplitude smoothing keeping the target extension less than 32 azimuth samples.

From the DFS tridimensional graphic, the range bin in which the target is present, is isolated and shown in a bidimensional plot (figure 5).

On the horizontal axis the ambiguous Doppler frequency (0-1000 Hz) is presented.

On the vertical axis the modulus of the DFS, normalized to the noise standard deviation (Signal to Noise Ratio), is presented.

As matter of fact, for each target 3-5 files (or scans) are available.

Some considerations apply to the following figures in which recorded data are illustrated.

1. Civil aircraft recorded data only are presented. This is done mainly for two reasons:

- \* Civil aircraft are very common and a rich data base can be easily obtained.

- \* For the civil aircraft all the mechanical data, such as engine characteristics, are generally available.

2. Due to the limited Time On Target, the airframe line appears to be in the order of 40 Hz. This width corresponds roughly to the antenna pattern modulation effect on a sinusoidal wave, and represents the intrinsic radar Doppler resolution. From the analysis of a number of civil jet aircraft, flying a cruise path, it appears, as general rule, that the actual air target does not present a significant widening of the Doppler line. Sometimes the Doppler line results greater than expected for an other peak is folded in proximity of the main line, in such a way that the Doppler filtering is not capable to resolve.

In few cases, a spectrum spreading has been detected to exceed the usual width of the main line (figures 6 and 7).

3. In the most of cases, the time samples of the target present an amplitude variation which results in a multi-line spectrum, each line having the same width of the main line.

Just in few cases, the modulation peaks do not show up clearly since their amplitude is under the system noise, or the aspect angle is such to prevent the reflection of the rotating parts.

The 1000 Hz ambiguous Doppler range represents the most important limitation to the spectrum interpretation: for a complete understanding of the target spectrum the data obtained from the tracking are useful.

#### 4.1 POWER PLANT MODULATION

It is well known that rotating machinery produces modulation components around the airframe Doppler line. The amplitude, symmetry, number and the displacement of the modulation lines, are depending on the engine type, engine RPM, number of blades of the illuminated part of the engine.

It is pretty clear that the modulation effects are detected only when the aircraft aspect is such that a direct view of the engine blades is not obstructed by the aircraft structure.

The head-on and tail-on aspects are the most favorable condition to produce the modulation lines. Sometimes happens that, in one scan, the aircraft does not present the characteristic modulation of the previous scans. In other scan is the main

line that results deeply faded, while the modulation lines remain almost unchanged.

The engine modulation generates distinct components separated from the Doppler main line by integer multiples of some engine dependent fundamental frequency. The fundamental (F) is related to the mechanical data of the engine through a simple formula:

$$F = N \times W$$

where N is the number of blades of the engine fan (in head-on aspect), and the W is the engine rotation rate [1].

Due to the low PRF mode of the S-Band ATC radar, the aliasing phenomenon is always present. For the most common civil airplanes, the fundamental component of the rotating parts is also greater than the radar PRF. The result is that the recorded spectrum is an aliased version of the original, in which the relationship between the Doppler line and the sidebands is apparently lost.

The situation is even more complicated by the fact that a change, in the aircraft aspect, produces a variation on the relative amplitude of the spectrum components and also a different displacement, even though the aircraft is flying a straight path at constant speed.

Attempts have been made to derive, from the aliased spectrum, the unfolded one. To achieve the aforementioned goal, the auxiliary information on the aircraft motion and engine type, has been exploited. The Doppler line was usually the higher peak of the spectrum; when some uncertainty was present, the ground speed, correlated, over several scans, with the geometrical data obtained from the tracking, helped in the Doppler line identification process. Once the Doppler line had been identified, the modulation peak unambiguous frequency separation (Fsep) was obtained from the following formula:

$$F_{sep}(unamb.) = Df(amb.) + k * PRF$$

$k = +/- 1, +/- 2, ...$   
where Df is the frequency difference in the ambiguous spectrum. The Fsep was then compared with the possible condition of the engine rotation rate, according to the engine data and company prescriptions. For the most part of cases, only one RPM, among all the values obtained from the above mentioned formula, fitted, with its harmonics, the ambiguous spectrum. The attribution of the peaks of the ambiguous spectrum, to the fundamental and its lower and higher harmonics, was the key to generate the synthetic unfolded spectrum.

In many cases, the presence of more than one engine, rotating at slightly different speed, and observed under different aspect angles, produces peaks of not equal amplitude and separated in frequency for a small amount. Though the separation in frequency increases with the order of the harmonic, the low Doppler resolution of the radar, due to the very low time on

target, is not sufficient, in many cases, to discriminate between those peaks. Therefore the spectrum, usually, presents peaks whose width and shape are not uniform and depend on the combination of the original single engine lines.

## 4.2 EXAMPLES OF SPECTRA

Figures 9 through 11 show the spectra of a DC9-30 aircraft in the different positions depicted in figure 8. Beside the aliased spectrum (a), obtained from the time samples, the resolved one, in a synthetic way, is presented (b).

It is interesting to make some remarks:

- The unfolded spectra present a great degree of similarity for the frequency location of the lines. The engine rotation rate, obtainable from those, is in accordance with the typical cruise data available from Alitalia company.
- Figures 11 are relevant to the aircraft illuminated by the rear and, yet, present the typical modulation peaks seen in the head-on aspect. Moreover, the fundamental frequency, obtainable from the ambiguous spectrum, results to be the same as the preceding spectra, regardless the difference in the number of blades between the first stage (fan) and the last stage of the turbine, visible respectively in head-on and tail-on aspect.

Figures 12 through 15 refer to a different DC9-30. Yet the unfolded spectra match with the ones obtained for the previous DC9-30. The spectrum of figure 13.a presents modulation peaks whose amplitude results under the system noise.

Figures 16 through 19 refer to a MD80 aircraft. Also in this case the resolved spectra match with the typical data given by the company. The last spectrum does not present modulation peaks such to permit the resolution process.

The figures 20 through 22 refer to a B747 aircraft. The resolved spectra allow to perform an estimation of the engine RPM that are in accordance with the typical cruise steady condition.

## 4.3 DOPPLER SPECTRUM EXPLOITATION

In the present ATC radar and long range surveillance radar, the exploitation of the composite spectrum results quite difficult. The main reasons are the low Pulse Repetition Frequency (from 400 Hz through 1000 Hz) which produces the wandering of the spectrum components in the ambiguous Doppler range, and the low

time on target (roughly tens of milliseconds) which reduces the Doppler discrimination capability of the radar.

What has been proven can be done with the actual recorded data is briefly indicated below.

#### 4.3.1 IDENTIFICATION

It has been seen that comparison among ambiguous spectra taken at different moments, even of the same aircraft, is impossible due to the dependence of the folding on the variable radial speed. The only way to obtain a significant spectrum is to resolve the Doppler ambiguity through the above outlined empirical algorithm, which uses additional information on the mechanical aircraft data and those from the tracking function.

Instead comparison of unfolded spectra pertaining to the same aircraft shows an high degree of consistency regardless the aspect angle of measurements.

Each aircraft type at its cruise speed presents a fundamental frequency which does not vary much from an individual aircraft to another. On the basis of the fundamental frequency recognition it is possible to enter the identification process reducing the set of the possible aircraft attribution and in some cases to obtain directly a positive identification.

The relationship between the line amplitude and order could help as well in the identification process but, at present, a statistic on such a topic is not available yet, and no attempt has been made to correlate those spectral features with the aircraft type.

#### 4.3.2 DETECTION

Two different processing have been devised to obtain a detection enhancement:

1. Adaptive filtering matched to target spectrum
2. Non linear optimum filtering

The first requires a knowledge of the target type and flight condition that can be achieved only when detection has taken place and tracking function is stable.

Hence a true improvement could be obtained when the SNR is at such a level that enhancement is no more required.

The second scheme is based on a quadratic processing which has been proven to be optimum. This algorithm gives a performance better than more common linear scheme when target shows a degree of correlation between one (Swirling 1 case) and zero (Swirling 2 case).

The application to the collected data of such an algorithm, does not produces a significant enhancement due to the high correlation (narrow spectrum) found in the majority of cases.

Therefore the potential does not justify the great increase in complexity required by the implementation of the new techniques.

Instead, the presence of many lines in the Doppler spectrum results in a natural improvement in the velocity response of the radar: due to the sidebands, the typical notches of the response are partially filled producing a more uniform coverage in the velocity domain.

#### 4.3.3 ASSOCIATION

In surveillance radar the extraction of target radial velocity from the Doppler information is sometimes implemented [2]. Sidebands of the spectrum usually hinder the extraction process. A large error in the radial velocity estimation occurs when one of the modulation components is mistaken for the Doppler line generated by the body reflection.

A very accurate algorithm, using the information coming from the tracking, has to be devised. Anyhow, a low reliability of the velocity estimation has to be accepted. Even more, the purpose of the velocity extraction should be limited to resolve the conflict situation and to help the correct track correlation.

### 5 CONCLUSIONS

From the above considerations it results that the most suitable application of the Doppler spectrum, pertains to the Non Cooperative Target Recognition (NCTR) techniques.

For a complete spectrum characterization, it is necessary to identify the peak number and location along with the their amplitude distribution. It is likely that several looks have to be used and correlated with the aspect angle and manoeuvring condition of the aircraft.

It is also clear that a proper implementation requires a more sophisticated radar with flexible waveform capabilities and a greater time on target. More specifically, in a small sector around the target of interest, and for the number of scans strictly necessary to perform the spectrum characterization, the normal radar operation will be suspended and a suitable radar mode will be selected. A greater time on target will permit to achieve the required Doppler resolution and, the high PRF, though it impedes the ranging function of the radar, will permit to obtain an unambiguous spectrum as requested for the identification process.

## REFERENCES

- [1] Hayes, R. and Gardner, R.E., "Doppler spectra of S-band and X-band signals", Supplement to IEEE Transactions on Aerospace and Electronic Systems, Vol. AES-3, no. 6, pp. 356-365, November 1967.
- [2] Nelson, N., "Aircraft tracking problems from range rate Turbine Modulation", NAECON 77 Record, pp. 679-682.

## ACKNOWLEDGEMENTS

The authors sincerely thank Dr. S. Cuomo, Dr. P. Dragoni, Dr. G. Puliatti of the University of Florence, for their contribution to the development of the acquisition system and data collection. Special thanks are due to Mr. M. Lepri of Alitalia and his staff for all the information concerning the aircraft engines.

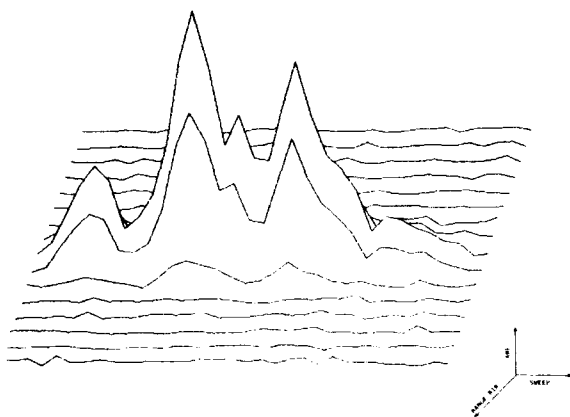


Fig. 3 B747/AZA1 Time Samples

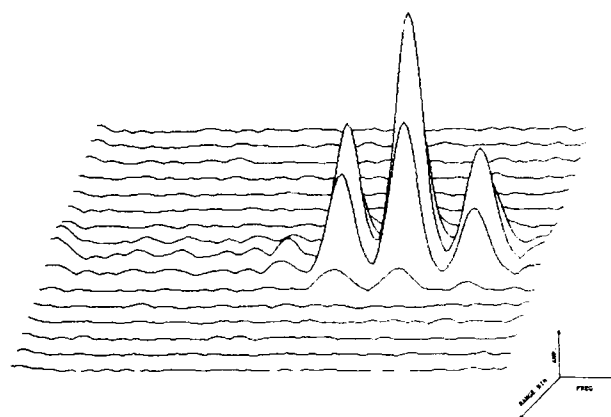


Fig. 4 B747/AZA1 DFS

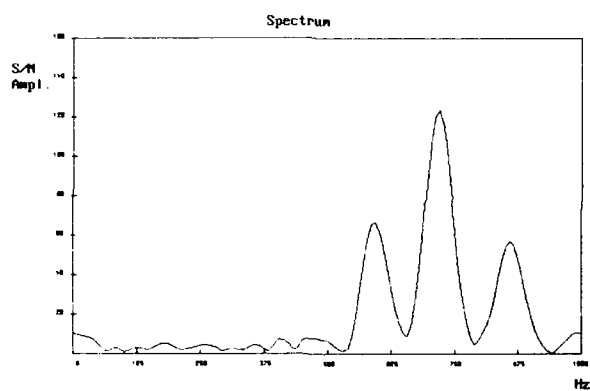


Fig. 5 B747/AZA1 DFS (Range Bin #8)

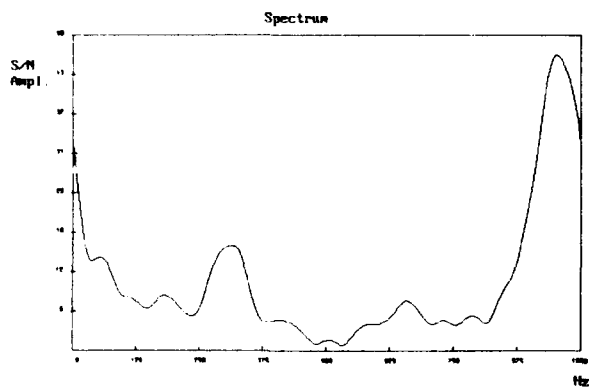


Fig. 6 MD80/AZA10 (Landing)

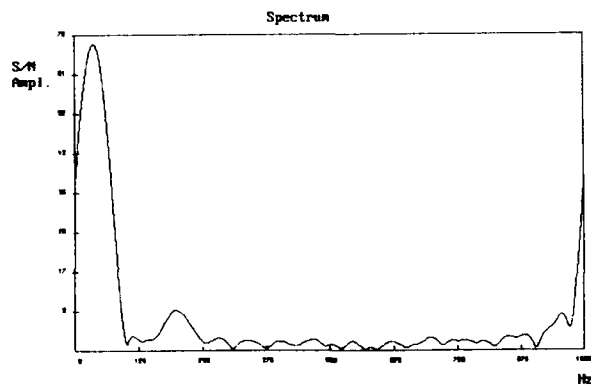
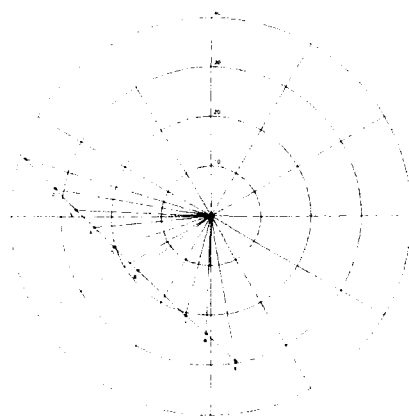


Fig. 7 MD80/AZA2 (Take-Off)



DC9-30/AZA12  
FLIGHT LEVEL 290  
GROUND SPEED 470 KN

Fig. 8 PPI Presentation

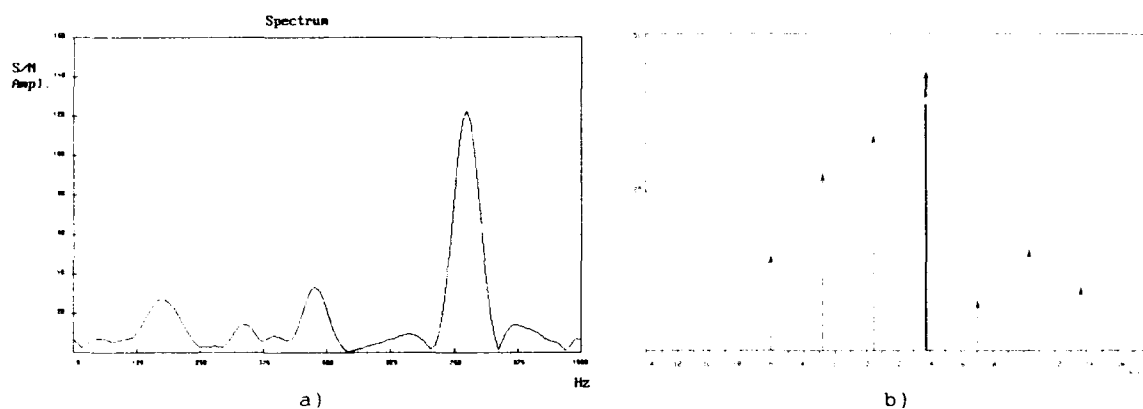


Fig. 9 SCAN #2

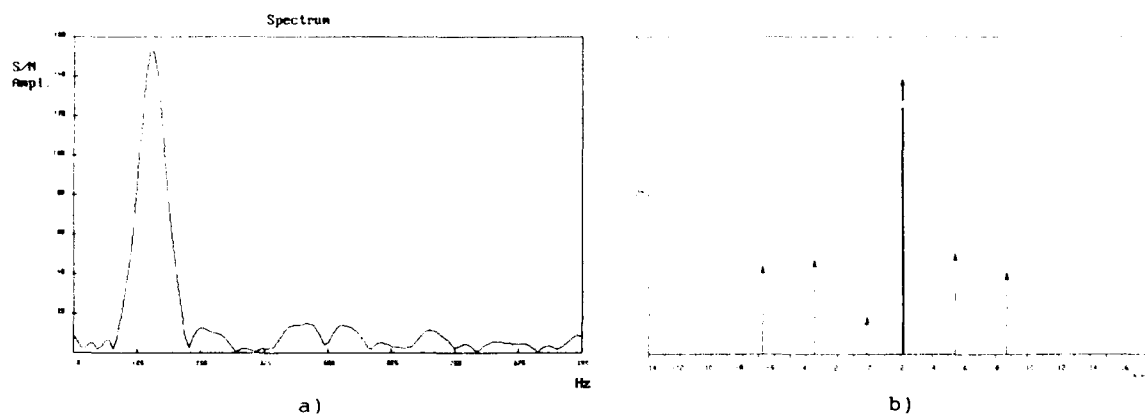


Fig. 10 SCAN #5

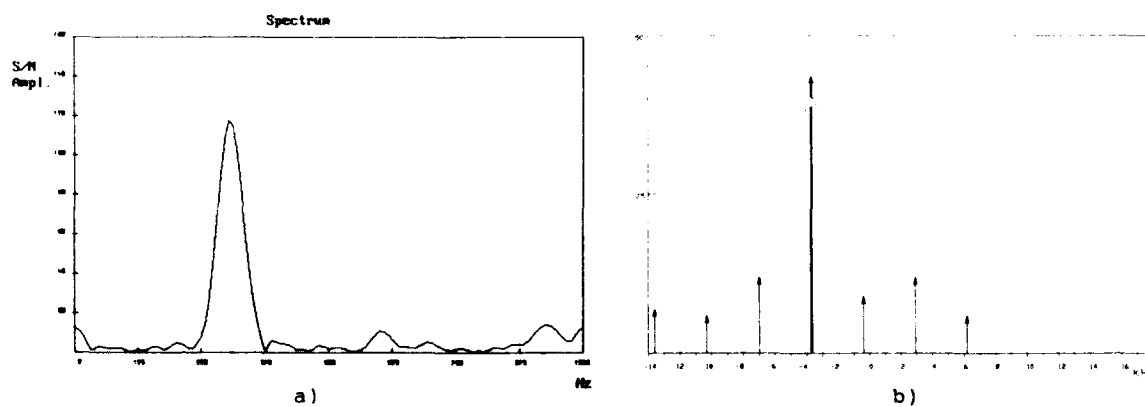
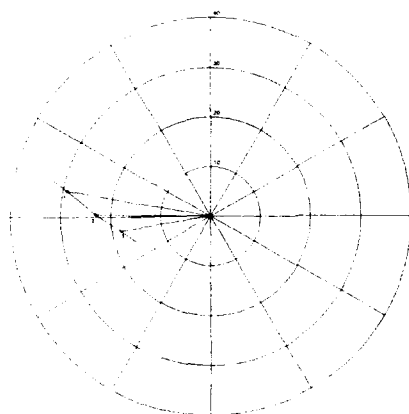


Fig. 11 SCAN #9



DC9-30/AZA6  
FLIGHT LEVEL 270  
GROUND SPEED 390 KN

Fig. 12 PPI Presentation

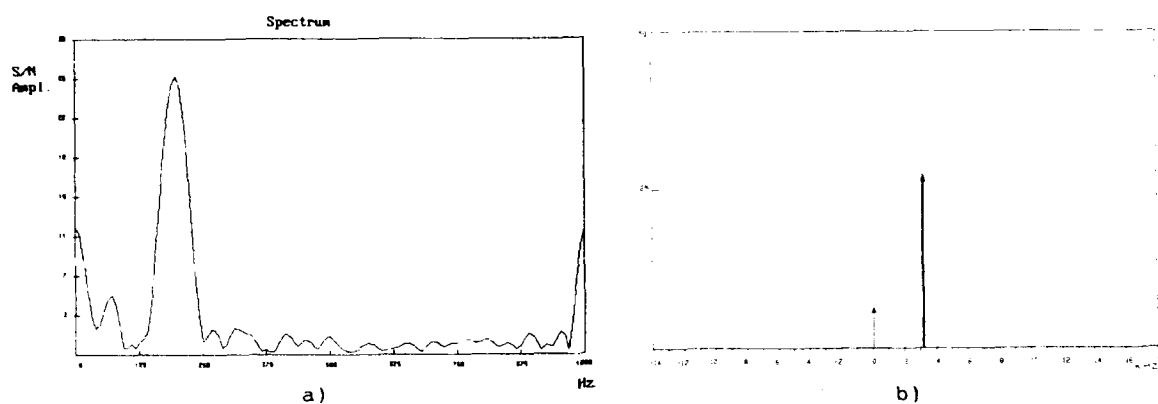


Fig. 13 SCAN #1

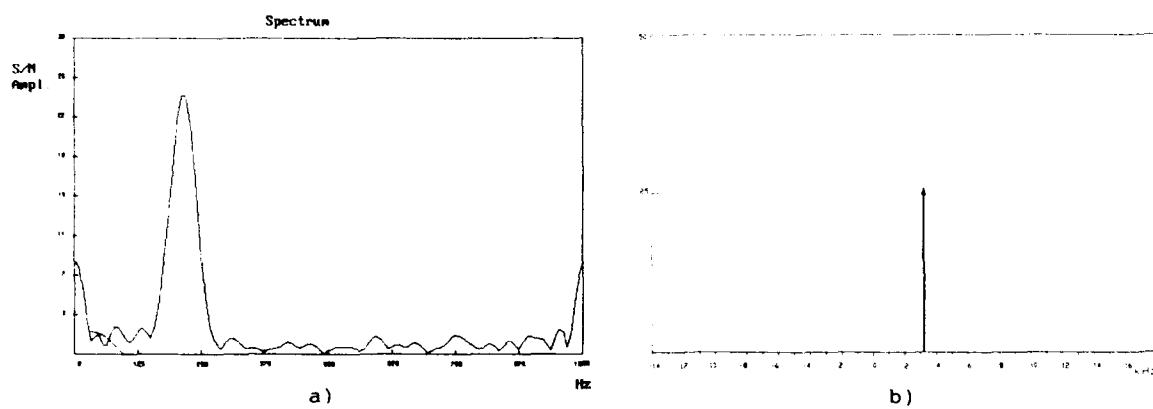


Fig. 14 SCAN #2

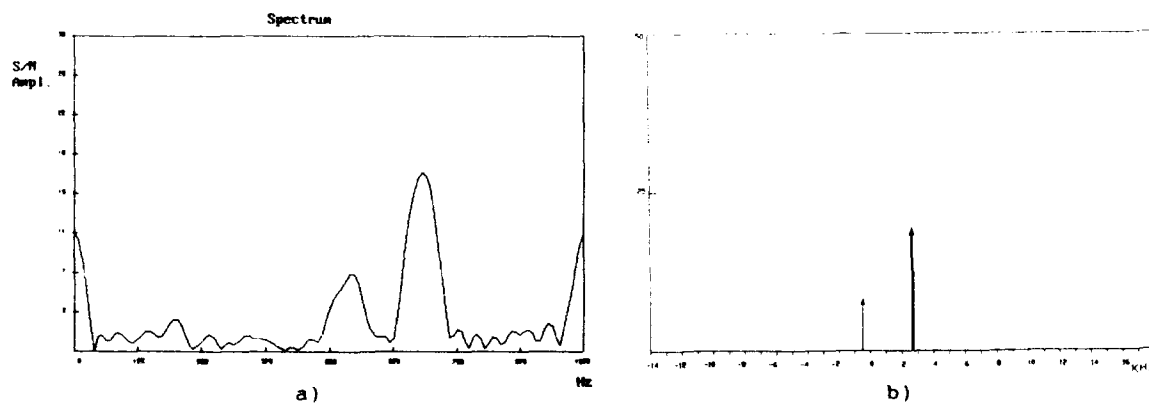
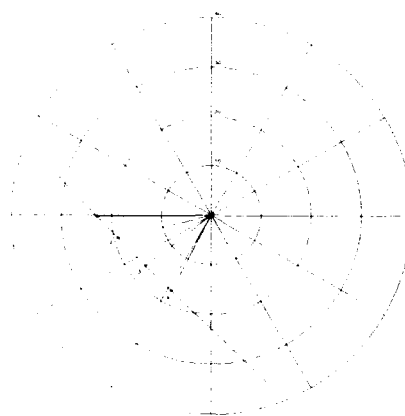


Fig. 15 SCAN #3





MD80 - AZA15  
FLIGHT LEVEL 290  
GROUND SPEED 490 KN

Fig. 16 PPI Presentation

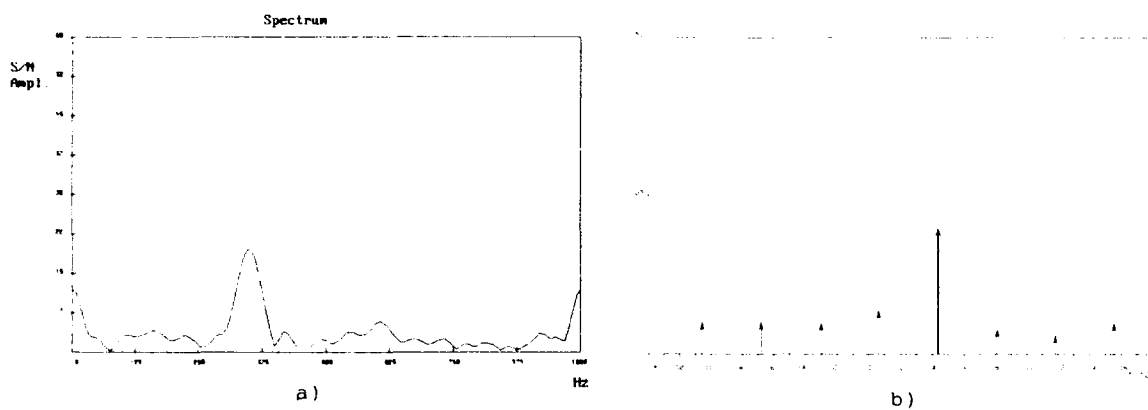


Fig. 17 SCAN #1

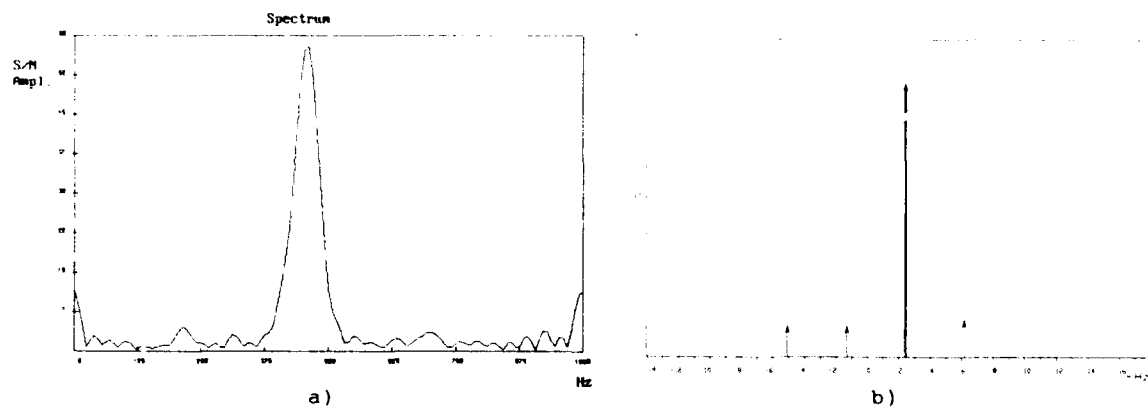


Fig. 18 SCAN #2

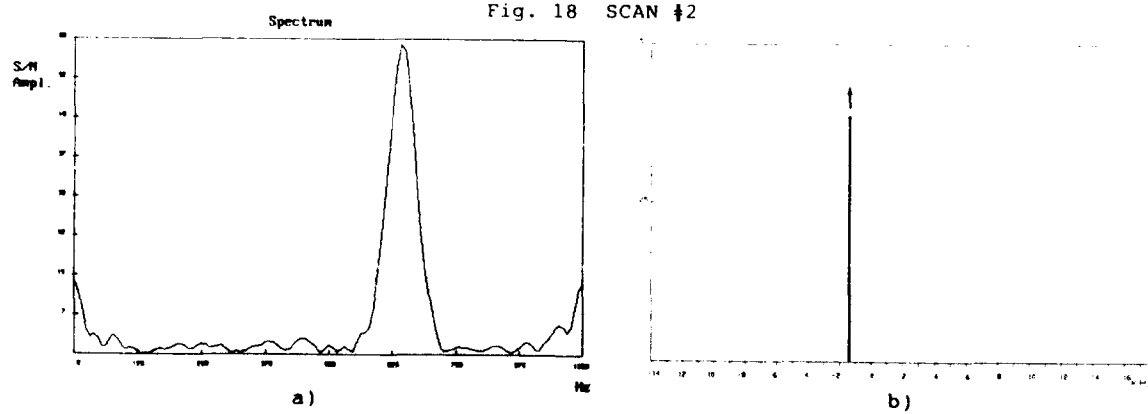
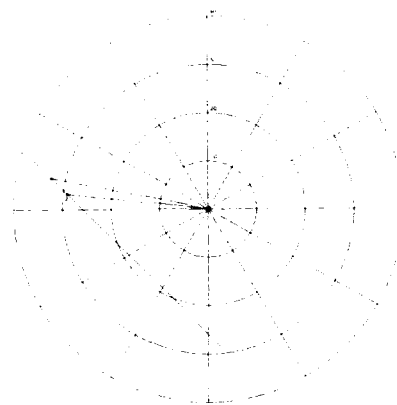
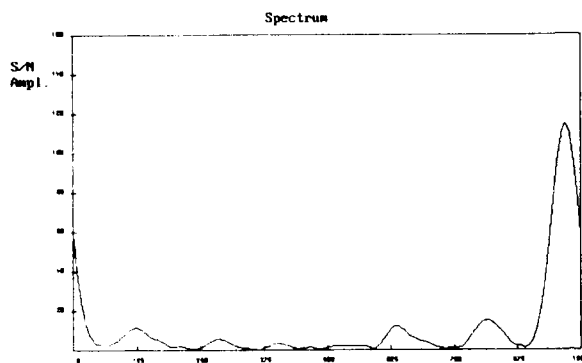


Fig. 19 SCAN #4

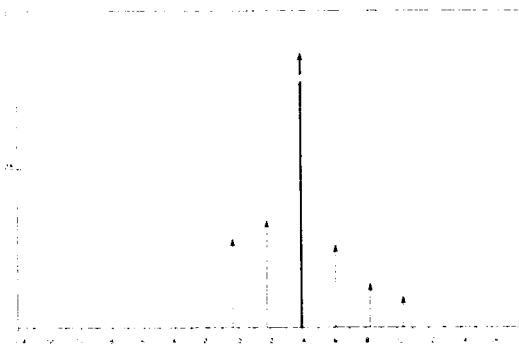


B7474/AZA1  
FLIGHT LEVEL 331  
GROUND SPEED 486 KN

Fig. 20 PPI Presentation

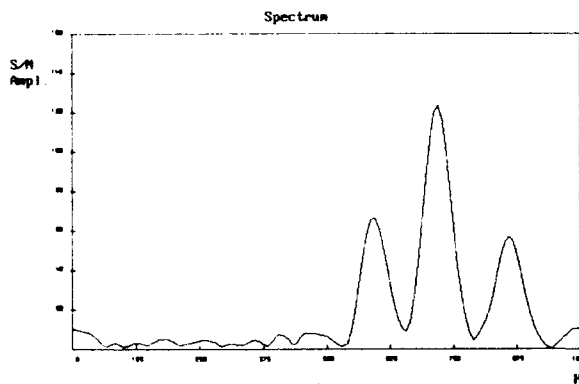


a)

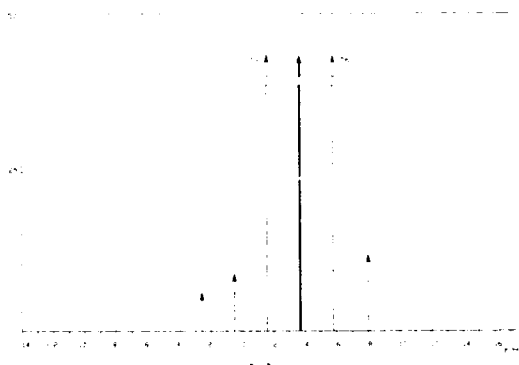


b)

Fig. 21 SCAN #1



a)



b)

Fig. 22 SCAN #2

## DISCUSSION

E. Schweicher, BE

Even without using higher PRFs, is it not possible to eliminate the spectrum ambiguity by utilizing different PRFs?

Author's Reply

The ATC radar used for the recording activity has a quite low time on target: 16 msec measured at 3 dB points of the antenna pattern. Some aircraft data have been recorded with a double stagger of PRF (batch of 8 pulses). Two different algorithms have been applied.

1. Elaboration of each batch separately: the very low Doppler resolution (125 Hz) is not sufficient to achieve significant results.

2. All the pulses used for spectrum computation, taking into account the different arrival times: the unfocused peaks mask the JEM lines preventing the desired resolution.

## CLASSIFICATION D'IMAGES SAR EN VUE DE DETECTION DE CIBLES

A. BEAUPERE, G. FOULON  
ONERA29, Avenue de la Division Leclerc  
92320 CHATILLON  
FRANCERésumé

Le traitement automatique de l'aide à la photo-interprétation d'images radar a pour but de fournir les outils pertinents nécessaires à l'interprétation d'un très grand volume de données en un temps réduit. Parmi ces outils figurent, en tout premier lieu, des outils de segmentation et de classification d'images qui permettent, d'une part, le zonage en grandes entités d'occupation du sol et d'autre part, la détection de rupture de texture.

Nous proposons ici une méthode utilisant la modélisation du clutter de sol par la rugosité de la surface et la rétrodiffusion de l'onde radar.

Les villes et autres constructions humaines sont lisses pour des radars en bande centimétrique, le sol cultivé (prairies, parcellaire) et les zones aquatiques sont totalement rugueux, les arbres présentent une partie lisse (tronc) et une partie rugueuse (feuillage).

La signature utilisée est la loi de distribution du module de l'amplitude complexe (niveaux de gris de l'image) qui dépend directement du déphasage de l'onde radar rétrodiffusée et donc de la rugosité du sol.

Parallèlement et de manière à traiter le problème inverse, nous avons mis au point une méthode de simulation de texture SAR à partir d'un modèle tridimensionnel de rugosités du sol. Cet algorithme de simulation nous permet également de prévoir l'évolution de la qualité de la texture-image pour les radars futurs à très haute résolution.

Notations :

$a(x,y)$  =amplitude complexe de l'image  
 $a_r(x,y)$  =partie réelle  
 $a_i(x,y)$  =partie imaginaire  
 $s_1$  =variance de  $a_r(x,y)$   
 $s_2$  =variance de  $a_i(x,y)$   
 $\alpha$  =moyenne de  $a_r(x,y)$   
 $r(x,y)$  =module de l'amplitude complexe  
 $\phi(x,y)$  =phase de l'amplitude complexe  
 $k(x_1, y_1)$  =k=réflecteur élémentaire du sol  
 $a(k)$  =onde complexe rétrodiffusée  
 $|a(k)|$  =module de l'onde  $a(k)$

$\phi(k)$  =phase de l'onde  $a(k)$   
 $h(x)$  =histogramme des niveaux de gris de l'image.

Introduction

Il est accordé actuellement une grande importance au traitement automatique de l'aide à la photo-interprétation, le but étant de fournir les outils pertinents nécessaires au photo-interprète pour traiter un très grand volume de données en un temps réduit. Parmi ces outils figurent, en tout premier lieu, des outils de segmentation et de classification en grandes entités d'occupation du sol. Alors qu'il existe une pléthore de tels outils pour des images visibles, ceux-ci sont plus rares pour les images SAR dont la texture peut être plus ou moins entachée de speckle, et dont les propriétés radiométriques et géométriques sont très particulières.

Certaines méthodes ayant recours à la réduction du speckle par filtrage moyen peuvent présenter de bons résultats mais restent limitées.

En fait, il peut être montré que la distribution statistique au premier ordre des niveaux de gris de l'image permet, dans une certaine mesure, la discrimination de classes différentes présentant une SER moyenne égale.

Dans ce cadre, Ulaby et al. (1986) fait intervenir les variations de SER liées à la texture de la scène (dièdres, zones d'ombre, surfaces réfléchissantes, etc). Il utilise, pour classer des images multi-look en grandes entités d'occupation du sol, la statistique d'ordre 2 ou le ratio écart type / moyenne. Il nous semble cependant intéressant d'étudier l'apport de l'histogramme  $h(x)$  complet d'images mono-look c'est-à-dire sans altération de la résolution, dont le calcul est rapide et qui contient une information intrinsèque au speckle. Cette question a été étudiée par Zito (1988) qui considère l'histogramme  $h(x)$  des niveaux de gris comme une somme de lois de Rayleigh dont les modes suivent une distribution donnée. Mais, pour ce faire, il apparaît indispensable de travailler sur la fenêtre de calcul la plus grande possible, afin de préciser cette distribution, ce qui est incompatible avec la contrainte de temps de calcul, et l'hypothèse même de stationnarité sur la totalité de la fenêtre.

Tenant compte de ce qui précède, nous présentons dans ce qui vient une méthode de discrimination en grandes classes

d'occupation du sol (eau, forêts, prairie parcellaire, zones urbaines) d'images SAR, qui découle de l'interprétation du biais existant entre l'histogramme de l'image et la loi de Rayleigh de même moyenne, en utilisant, pour ce faire, une décomposition en série de polynômes orthogonaux.

En première partie, nous présentons le type de signature traitée, et nous l'interprétons au moyen de coefficients issus de la décomposition polynomiale. Durant la seconde partie, l'algorithme de segmentation et classification utilisé est décrit. Enfin, la troisième partie contient un élément de réponse au problème inverse consistant à simuler une texture SAR et à comparer les histogrammes des textures ainsi obtenus avec les histogrammes calculés sur l'image radar.

Les résultats sont validés à l'aide d'images Varan S couvrant les régions de Neuf Brisach-Freiburg et Oberpfaffenhofen.

### Présentation théorique

L'amplitude complexe en un pixel de l'image est la somme d'ondes élémentaires en interférence de phase :

$$a(x, y) = r e^{i\phi} \sum_{x_1, y_1} |a(k(x_1, y_1))| \exp(i\phi(k(x_1, y_1)))$$

$\phi(k(x_1, y_1))$  est une quantité aléatoire sur l'intervalle  $[0, 2\pi]$  distribuée selon une certaine densité, elle-même fonction, en particulier, du relief du sol. Cette densité est par exemple constante lorsque le sol est totalement rugueux devant la longueur d'onde.

### Lois théoriques physiques proposées par Beckmann et Spizzichino

Dans le cas où les réflecteurs élémentaires du sol vérifient les hypothèses du Théorème Central Limite, la distribution de la partie réelle (resp. imaginaire) de l'image complexe est une gaussienne.

Les quantités  $a_r(x, y)$  et  $a_i(x, y)$  étant supposées indépendantes, l'on montre (Beckmann et Spizzichino, 1987) que  $p(|a(x, y)|=r)$  dépend en particulier du ratio  $s_1/s_2$ ,  $s_1$  et  $s_2$  correspondant aux variances des parties réelles et imaginaires:

$$p(|a(x, y)|=r) = \frac{r}{2\pi\sqrt{s_1 s_2}} \int_0^{2\pi} \exp\left[-\frac{(r\cos(\phi)-\alpha)^2}{2s_1} - \frac{(r\sin(\phi))^2}{2s_2}\right] d\phi$$

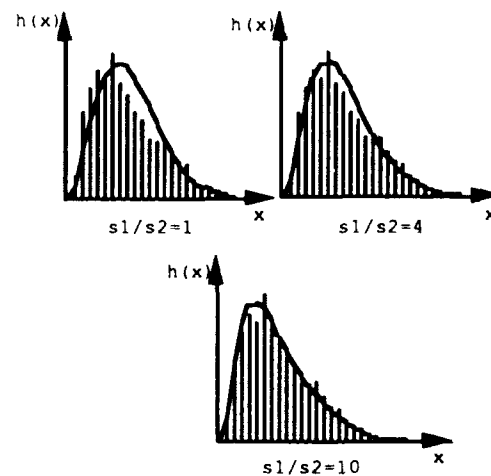
Soit, en appliquant la théorie des fonctions de Bessel :

$$p(|a(x, y)|=r) = \frac{r}{\sqrt{s_1 s_2}} \exp\left[-\frac{\alpha^2}{2s_1} - \frac{(s_1 + s_2)r^2}{4s_1 s_2}\right] \sum_{m=0}^{\infty} (-1)^m \epsilon_m I_m\left(\frac{(s_2 - s_1)r^2}{4s_1 s_2}\right) I_{2m}\left(\frac{\alpha r}{s_1}\right)$$

avec  $I_m$  = fonction de Bessel modifiée.

Lorsque la phase de l'onde rétrodiffusée est aléatoire et distribuée uniformément sur  $[0, 2\pi]$  (sol totalement rugueux),  $s_2 = s_1$  et  $\alpha = 0$ , et l'on retrouve bien l'expression de la loi de Rayleigh.

Dans tous les autres cas, les lois  $p(r)$  diffèrent de la loi de Rayleigh, et peuvent approximer de manière satisfaisante (cf fig. 1) les histogrammes  $h(x)$  calculés sur l'image correspondants aux différentes classes d'occupation du sol. On constate notamment que les histogrammes prélevés sur les zones urbaines, dont les queues de distribution sont plus importantes, sont bien représentés par une loi  $p(r)$  de fort ratio  $s_1/s_2$ , égal à 10.



Appariement entre  $h(x)$  et les lois  $p(r)$   
 $h(x)$  : région urbaine  
 — :  $p(r)$

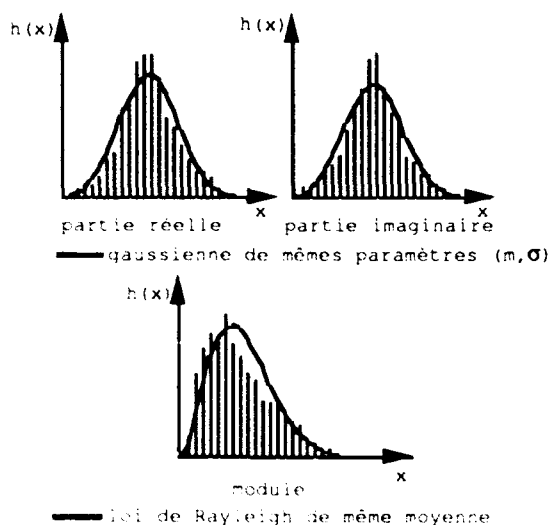
Fig. 1

### Utilisation d'une série de polynômes orthogonaux

Les données d'images complexes, difficiles à obtenir car coûteuses en capacité d'enregistrement, ont permis d'approfondir les propriétés énoncées ci-

dessus et de mettre en évidence la caractéristique suivante :

Les histogrammes des parties réelles (resp. imaginaires) calculés sur l'image complexe (fig. 2) présentent un biais par rapport à une gaussienne de mêmes paramètres.



comparaison entre  $h(x)$  et la loi de Rayleigh, illustrant le biais de l'amplitude complexe.

Fig. 2

La théorie proposée par Beckmann et Ryzanski, reposant sur une distribution gaussienne des parties réelles et imaginaires (théorème central limite) semble alors insuffisante d'autant que le biais de l'histogramme du module par rapport à la loi de Rayleigh de même moyenne est du même ordre que le biais de l'histogramme de la partie réelle (resp. imaginaire) par rapport à la gaussienne de même variance et de même moyenne.

L'interprétation la plus plausible est que les réflecteurs ne sont pas indépendants et ne suivent pas la même loi (variation locale de SFR, Ulaby, 1986).

Par ailleurs, Zito (1988) montre qu'une somme de lois de Rayleigh dont les modes suivent une loi gaussienne (variation de SFR) présente un léger biais par rapport à la loi de Rayleigh.

Nous proposons de quantifier ce biais existant entre l'histogramme de l'image et la loi de Rayleigh correspondante à l'aide d'une décomposition en série polynômiale orthogonale de Laguerre (expansion de Gram-Charlier adaptée à Rayleigh), de façon à minimiser l'information au sens mathématique. Cette évaluation par l'intermédiaire d'une série, semblable au premier ordre à des évaluations telles que skewness (biais) et peakedness (dynamique), est néanmoins plus fine.

Posons :

$$h(x) = \frac{x}{\sigma^2} \exp\left(-\frac{x^2}{2\sigma^2}\right) \left[ \sum_{k=0}^N \alpha_k L_k^{1/2} \left(\frac{x^2}{\sigma^2}\right) \right]$$

où  $L_k^{1/2}$  correspond au polynôme de Laguerre généralisé d'ordre  $\frac{1}{2}$ .

Formules de récurrence :

$$L_0^{1/2}(u) = 1 \quad L_1^{1/2}(u) = \frac{3}{2} - u$$

$$\{n+1\} L_{n+1}^{1/2}(u) = \left[2n + \frac{3}{2} - u\right] L_n^{1/2}(u) - \left[n + \frac{1}{2}\right] L_{n-1}^{1/2}(u)$$

La relation d'orthogonalité des polynômes s'écrit :

$$\int_0^\infty \sqrt{x} \exp(-x) L_n^{1/2}(x) L_m^{1/2}(x) dx = \delta_{mn} \frac{\Gamma(n + \frac{3}{2})}{n!}$$

avec  $\delta_{mn} = 1$  lorsque  $m=n$ ; 0 sinon.

Le choix des polynômes de Laguerre permet alors de calculer simplement les coefficients  $\alpha_k$  :

$$\alpha_k = \frac{n!}{\Gamma(n + \frac{3}{2})} \int_0^\infty h(x) \left[ \frac{x}{\sigma^2} \exp\left(-\frac{x^2}{2\sigma^2}\right) L_k^{1/2} \left(\frac{x^2}{\sigma^2}\right) \right] dx$$

Ces coefficients  $\alpha_k$  seront les paramètres d'entrée de l'algorithme de segmentation et de classification décrit ci-après.

### Segmentation et classification d'images radar

La classification des images radars selon le type d'occupation du sol (villes-bâtiments, zones aquatiques, clutter) permet l'élimination des zones réputées inintéressantes pour le photo-interprète (par exemple : absence présumée de cibles).

Les images à traiter étant des images de textures, une classification de chaque pixel séparément des autres donne un résultat trop bruité et il est donc indispensable d'opérer une segmentation préalable de l'image en régions homogènes avant de les classer.

Cet algorithme de segmentation-classification ne s'applique pas directement à l'image radar mais à des "informations" qui sont le résultat d'un filtrage particulier de l'image faisant apparaître des réponses caractéristiques de chacune des différentes entités que l'on cherche à extraire. Ces informations sont décrites ci-dessous.

### Calcul des informations caractéristiques de la scène

Pour le calcul de chaque information, on utilise un pavé de taille  $32 \times 32$  entourant le pixel. Sur chaque pavé, 2 informations sont calculées. Il s'agit respectivement de :

1) Niveau de gris moyen = SER (= INFO1)

2) Premiers coefficients  $\alpha_0$  et  $\alpha_1$  de la série polynomiale de Laguerre extraits de l'histogramme calculé sur le pavé. Le coefficient  $\alpha_0$  (resp.  $\alpha_1$ ) est d'autant plus élevé et proche de 1 (resp. faible et proche de 0) que l'histogramme est semblable à loi de Rayleigh.

Au delà du 3ème ordre, les coefficients  $\alpha_k$  convergent rapidement vers 0.

En pratique, il existe une redondance d'information entre les coefficients  $\alpha_0$  et  $\alpha_1$  et il est suffisant d'utiliser le coefficient  $\alpha_1$  (= INFO2). Cependant, l'utilisation du coefficient  $\alpha_0$  peut être utile pour des discriminations fines concernant notamment certaines zones aquatiques. L'apport ultérieur des coefficients supérieurs est inutile pour l'obtention d'une classification plus complète.

### Segmentation d'images radar

Les détecteurs de contours classiques (gradient, laplacien...) liés à la notion de contraste ne sont pas suffisants (contours ouverts), et peu adaptés aux images SAR.

En revanche, la méthode de segmentation basée sur l'analyse de textures par corrélation des histogrammes locaux (voire des histogrammes de co-occurrences) et développée depuis plusieurs années à l'ONERA (Secchi, 1990) permet l'extraction de segments homogènes au sens d'un degré statistique donné, par un processus de croissance automatique.

Elle s'applique simplement aux informations issues du filtrage de l'image SAR décrites ci-dessus et fournit le préalable nécessaire à la classification d'images.

Cette méthode de segmentation hiérarchique a pour objet la détermination de segments présentant localement approximativement la même distribution et ceci peut être mesuré en calculant un coefficient de corrélation (rapport du produit scalaire et des normes euclidiennes)

entre histogrammes locaux des niveaux de gris de l'image.

De plus, la norme euclidienne des histogrammes locaux présente la propriété importante de mettre en évidence le degré d'homogénéité local servant à l'initialisation des segments à extraire.

L'algorithme est appliqué, dans un souci de fusion d'informations, selon le mode multi-information consistant en un "ET LOGIQUE" des segmentations des 2 informations décrites précédemment.

### Classification d'images radar

L'objectif de cet algorithme est d'extraire d'une image SAR les grandes entités suivantes:

- villes-bâtiments.
- clutter :
  - \* zones aquatiques
  - \* forêts
  - \* prairie-parcellaire

Pour ce faire, on utilise les informations INFO1 et INFO2 obtenues par filtrage de l'image radar d'origine.

- Les zones de villes-bâtiments, à cause de la présence des dièdres et surfaces réfléchissantes lisses devant la longueur d'onde (réflexion spéculaire), "saturent" l'image et les niveaux de gris correspondants se situent dans le haut de la dynamique (INFO1).

Par ailleurs, l'alternance de faces réfléchissantes et de zones d'ombre entraîne un fort biais par rapport à Rayleigh et la valeur du coefficient  $\alpha_1$  correspondante est élevée, supérieure à 0.08 (INFO2).

- Les zones aquatiques correspondent à une SER très faible : niveau de gris dans le bas de la dynamique (INFO1).

Notons cependant que les zones d'ombre des forêts correspondent, elles aussi, au bas de la dynamique et peuvent être parfois confondues avec les zones aquatiques. Il serait intéressant, dans ce cadre, d'utiliser le coefficient  $\alpha_0$  qui permet la mise en évidence de certaines zones aquatiques telles que les lacs.

- Les zones de clutter sont homogènes et correspondent à un coefficient  $\alpha_1$  faible, proche de 0 et la loi suivie par le module de l'amplitude complexe est, dans ce dernier cas, la loi de Rayleigh. Parmi ces dernières, on constate que les zones de forêts présentent un caractère Rayleigh, bien qu'important, moins marqué que les zones de prairie et de parcellaire agricole, et, en tout cas, suffisant pour les discriminer, une explication plausible étant une décorrélation

plus grande au niveau des réflecteurs dans le cas des zones de prairie que dans le cas des zones forestières.

La valeur de  $\alpha_1$  est donc, en moyenne, plus faible sur les zones de prairie que sur les zones de forêt.

En vertu des remarques précédentes, on peut donner un algorithme simple de classification appliqué aux images Varan S après apprentissage en se limitant aux grandes entités sus-mentionnées :

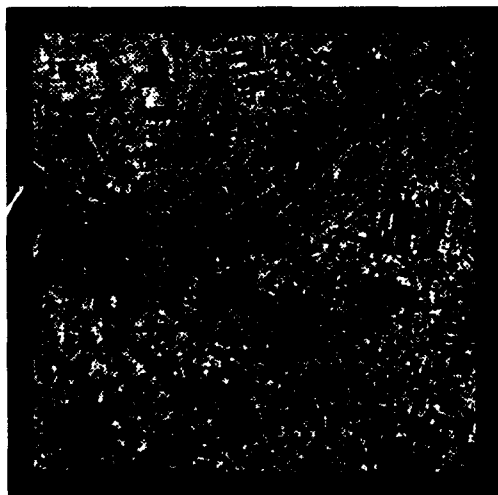
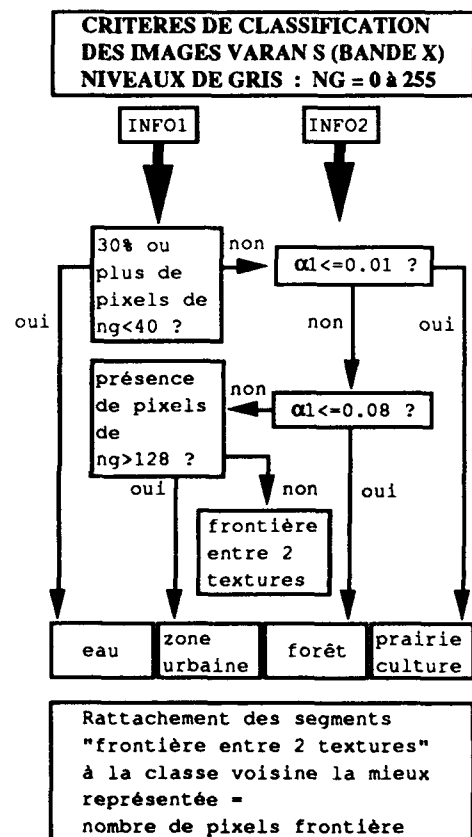
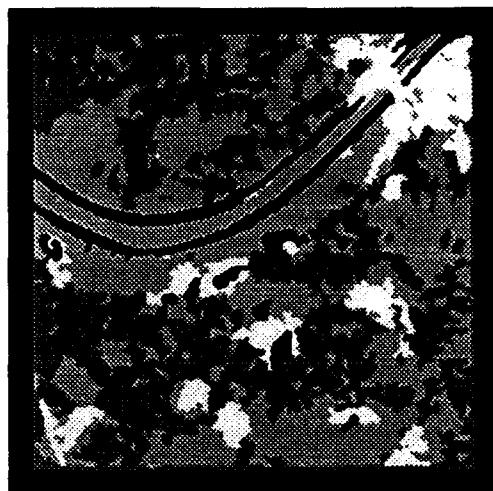


Image après filtrage moyen (SER)



Résultats de classification en 4 classes :  
blanc = villes, gris clair = forêts, gris foncé = prairies-cultures, noir = eau.

Application de l'algorithme de segmentation-classification aux images Varan S. Exemple de l'image couvrant la région de Neuf-Brisach. Cette image a été obtenue lors d'une campagne programmée par le JRC (Joint Research Center)-ISPRa avec le radar Varan S du CNES (Centre National d'Etudes Spatiales)-France, prétraitée par le CNES.

Fig. 3

### Problème inverse

Afin de valider le choix de la signature servant à l'algorithme de segmentation-classification, nous fournissons dans cette section des éléments d'interprétation du phénomène physique à l'aide d'une synthèse de texture SAR, basée sur une analogie avec l'optique cohérente (Goodman, 1972) permettant de mettre en évidence d'une part l'influence de la variation de la SER et d'autre part l'influence de la rugosité intra-pixel.

En ce qui concerne l'influence de la variation de la SER, l'algorithme comprend 2 étapes successives :

1) Tirage de la SER selon soit une gaussienne, modèle préconisé par Zito (1988), soit 2 diracs (niveaux de gris) distincts, avec un déphasage aléatoire de l'onde rétrodiffusée uniformément réparti sur  $[0, 2\pi]$ .

2) Fixation du nombre  $N_r$  de réflecteurs par pixel et filtrage passe-bas de l'onde rétrodiffusée.

Afin de valider les résultats obtenus par la simulation, ceux-ci sont comparés avec les images réelles fournies par le radar Varan S (bande X, résolution au sol = 2.5m x 2.5m).

La comparaison s'appuie sur le calcul de l'histogramme des niveaux de gris de la texture-image synthétisée et la détermination des coefficients  $\alpha_k$  correspondants.

On choisit un nombre de réflecteurs suffisamment important sans être trop calculatoire, à savoir,  $N = 8 \times 8$  réflecteurs par case de résolution.

Les valeurs des coefficients  $\alpha_k$  correspondants sont consignées dans la table 1 ci-dessous :

ecart type	$\alpha_0$	$\alpha_1$	$\alpha_2$	$\alpha_3$
30.	0.97	0.039	0.054	0.013
20.	0.98	0.024	0.038	0.012
10.	0.98	0.008	0.024	0.013
5.	0.98	0.003	0.020	0.012

Coefficients  $\alpha_k$  - SER gaussienne ( $m, \sigma$ )

Table 1

La moyenne des gaussiennes est choisie égale à la moyenne globale d'une image Varan S soit un niveau de gris de 50. Il est ainsi permis, au vu des résultats ci-dessus, de quantifier l'influence de l'écart type sur le biais existant entre l'histogramme et la loi de Rayleigh (biais croissant avec l'écart type).

Le coefficient  $\alpha_1$  ainsi calculé correspond aux valeurs calculées sur l'image pour des zones de forêt et de prairie-cultures. Un modèle de SER gaussien peut donc expliquer la distinction entre zones de forêt (écart type élevé) et zones de prairies et cultures (écart type plus faible).

Cependant, dans le cas des zones urbaines, il semble que l'alternance entre les zones d'ombre et les faces réfléchissantes soit plus marquée et l'on propose un modèle d'histogrammes somme de 2 lois de Rayleigh, les SER étant distribuées selon 2 diracs (de niveaux de gris respectifs  $ng1$  et  $ng2$ ). Sur une telle texture, les coefficients  $\alpha_k$  calculés sont présentés dans la table 2 ci-dessous :

ng 1	ng 2	$\alpha_0$	$\alpha_1$	$\alpha_2$	$\alpha_3$
30	30	0.99	0.001	0.019	0.013
30	50	0.98	0.012	0.029	0.010
30	80	0.97	0.034	0.053	0.015
30	110	0.96	0.043	0.066	0.019
30	150	0.95	0.047	0.077	0.025

Coefficients  $\alpha_k$  - 2 niveaux de SER :  $ng1, ng2$

Table 2

Par ailleurs, il a été également étudié l'influence de la rugosité intra-pixel, en tenant compte du déphasage de l'onde rétrodiffusée par les différents réflecteurs élémentaires intra-pixels, aspect

complémentaire de celui de la SER. Les résultats obtenus sont illustrés par la fig. 4 et l'algorithme correspondant, par rapport à celui décrit précédemment, possède les particularités suivantes :

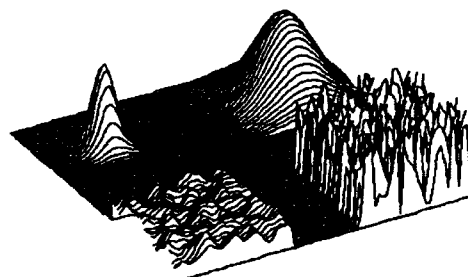
- Tirage de SER constante.
- Prise en compte de la rugosité du sol modélisée par une distance de corrélation  $d_{corr}$  et un écart type des hauteurs  $\sigma_r$ .
- Tirage de la phase de l'onde rétrodiffusée par les réflecteurs élémentaires en fonction de la rugosité du sol et non aléatoirement dans l'intervalle  $[0, 2\pi]$ .

Fonction d'autocorrélation initiale

$$C(u, v) = \sigma_r^2 \exp \left[ \frac{(-u^2 - v^2)}{d_{corr}^2} \right]$$

Transformée de Fourier de la fonction

d'autocorrélation



Profil de sol tridimensionnel

Profil de phase ramené dans  $[0, 2\pi]$ 

Fig. 4

Le biais existant entre les histogrammes des textures ainsi synthétisées et la loi de Rayleigh est de même nature que celui obtenu par variation de la SER, et les coefficients  $\alpha_k$  correspondants sont donnés dans la table 3 ci-dessous :

$\sigma_r$	$d_{corr}$	$\alpha_0$	$\alpha_1$	$\alpha_2$	$\alpha_3$
1.5	1.0	0.99	0.004	0.018	0.007
1.5	5.0	0.98	0.029	0.034	0.005
1.5	8.0	0.95	0.081	0.087	0.019
1.0	1.0	0.99	0.004	0.008	0.004
1.0	5.0	0.98	0.044	0.042	0.003
1.0	8.0	0.96	0.075	0.079	0.014
0.5	1.0	0.99	0.011	0.021	0.005
0.5	5.0	0.99	0.023	0.028	0.002
0.5	8.0	0.96	0.012	0.052	0.027

Coefficients  $\alpha_k$  - sol rugueux ( $\sigma_r, d_{corr}$ )

Table 3

Les résultats figurant ci-dessus corroborent ceux obtenus, à partir des images, sur les zones de cultures, forêts et villes et fournissent ainsi un élément



supplémentaire d'interprétation de l'histogramme d'images radar. On constate bien que, pour des rugosités de même hauteur, l'histogramme s'écarte d'autant plus de Rayleigh que la corrélation est importante. Par ailleurs, il apparaît que cet écart est plus sensible à une variation de la corrélation plutôt qu'à celle de  $\sigma_r$ . Enfin, l'on constate que les 2 algorithmes de synthèse de texture présentées ci-dessus fournissent des résultats à la fois similaires et complémentaires.

### Conclusion

L'algorithme de simulation est simple (transformations de Fourier bidimensionnelles) et fournit plusieurs interprétations des résultats de classification, par ailleurs satisfaisants :

Toutes les zones urbaines (villes, villages, hameaux, bâtiments) ont été extraites du clutter et ceci indépendamment de la polarisation ou de l'inclinaison. Les zones aquatiques : fleuves, canaux, lacs ont été mises en évidence dans l'ensemble des images. Les régions boisées : forêts de conifères ou de feuillus sont séparées des zones de prairie-parcellaire.

Les résultats obtenus permettent la séparation en classes de zones non distinctes visuellement (villes et clutter) et le zonage de l'image (sous résolue) en grandes classes d'occupation du sol, avec la possibilité dans un second temps de détailler certaines parties (pleine résolution).

Ces résultats, lors d'investigations ultérieures, seront évalués sur des images de radars spatiaux (bande X, C, L).

L'algorithme de segmentation-classification est rapide et souple d'exécution :

- traitement automatique;
- traitement supervisé = le photo-interprète "pointe" la région qu'il désire extraire à l'aide du curseur.

Par ailleurs, le calcul préalable des informations INFO1 (filtrage moyen de l'image), et INFO2 (biais par rapport à la loi de Rayleigh) peut être effectué en temps différé, les informations n'étant calculées qu'une seule fois pour chaque image.

### Références

1- A. BEAUDOIN, T. Le TOAN, Q.H.J. GWYN, "Observation on the Effect of Geometric Properties of Agricultural Soils on Radar Backscatter, from C-SAR Images", Proc. of IGARSS'88 Symposium, Edinburgh, ESA SP-284, vol. 3, pp 1595-1598, 13-16 Sept. 1988.

2- A. BEAUPERE, Segmentation et Classification d'Images de Radar à Vision

Latérale et Simulation de Texture de Radar Spatial à très Haute Résolution, ONERA - RT n° 7/3692 SY - 1990.

3- P. BECKMANN, A. SPIZZICHINO  
The Scattering of Electromagnetic Waves from Rough Surfaces, Artech House 1987.

4- F. BRETAUDEAU, C. ENAULT, P. SECCHI,  
"Segmentation d'Images Texturées : Application à des Images de Télédétection", Congrès AFCET-INRIA - Antibes 1987.

5- F. BRETAUDEAU, "Une Méthode d'Analyse des Images de Texture pour la Détection des Frontières, la Segmentation et la Poursuite", 54<sup>ème</sup> Symposium on the Avionics Panel - Athènes 1987.

6- J. DARRICAU, Physique et Théorie du Radar, Sodipe - 2<sup>ème</sup> édition 1981.

7- J.W. GOODMAN, Statistical Properties of Laser Speckle Patterns, Speckle and Related Phenomena, Dainty, Springer-Verlag - 1975.

8- J.W. GOODMAN, Introduction à l'Optique de Fourier et à l'Holographie, Masson - 1972.

9- M. KUNT, Traitement Numérique des Signaux Dunod, 1981.

10- H. LAUR, Analyse d'Images Radar en Télédétection : Discriminateurs Radiométriques et Texturaux, Thèse de 3<sup>ème</sup> cycle - Toulouse 1989.

11- D. MASSONNET, "Preprocessing of the Varan Synthetic Aperture Airborne Radar", Proc. of IGARSS'88 Symposium, Edinburgh, ESA SP-284, pp 715-720, 13-16 Sept. 1988.

12- F.T. ULABY, "Textural Information in SAR Images", IEEE Trans. Geosci. Remote Sensing, vol. GE-24, no. 2, pp 235-245, 1986.

13- P. SECCHI, Segmentation d'Images et Fermeture de Contours par Corrélation d'Histogrammes Locaux : Application aux Images de Télédétection SPOT, Thèse de 3<sup>ème</sup> cycle - Paris 1990.

14- A.J. SIEBER, "Radar Observation Over Freiburg", IEEE Trans. Geosci. Remote Sensing, vol. GE-24, no. 4, July 1986.

15- K. TOMIYASU, "Computer Simulation of Speckle in a Synthetic Aperture Radar Image Pixel", IEEE Trans. Geosci. Remote Sensing, vol. GE-21, no. 3, July 1983.

16- D.R. WEHNER, High Resolution Radar, Artech House - 1987.

17- R.R. ZITO, "The Shape of SAR Histograms", Computers Vision, Graphics, Image Proc., vol. 43, pp 281-293, 1988.

## DISCUSSION

E. Schweicher, BE

Avez-vous songé à caractériser la texture à l'aide des différents paramètres de Haralick ou à l'aide de la distance de Bathakarya?

Author's Reply

Les travaux d'Haralick s'appuient sur la matrice de co-occurrence qui constitue une statistique d'ordre 2, or nous avons proposé pour cette étude de n'utiliser que la statistique d'ordre 1 afin de montrer son intérêt pour la classification d'images SAR. Cependant, nous avons comparé nos résultats avec la fonction d'autocorrélation, montrant ainsi la forte ressemblance entre les deux méthodes.

**COMPARAISON DES PERFORMANCES EN DETECTION ET RECONNAISSANCE  
D'UN RADAR IMAGEUR BIPOLARISATION HH-VV ET D'UN  
POLARIMETRE TOTAL HH-HV-VH-VV**

par

J.M. NASR

AEROSPATIALE DS - Groupe Télédétection  
Etablissement de Cannes, 100 Boulevard du midi, BP 99  
06322 CANNES LA BOCCA cedex  
FRANCE

## RESUME

Dans l'optique de mettre sur orbite un satellite d'observation portant un radar à synthèse d'ouverture à vocation militaire, il est important de s'intéresser à la mesure simultanée de plusieurs polarisations pour augmenter les performances du système. Cependant, l'incidence de ces techniques sur le débit de données n'est pas négligeable aux résolutions que l'on souhaite atteindre. Il faut donc analyser l'intérêt de ces nouvelles méthodes multipolarisations en termes de gain de performances en détection et reconnaissance de cibles et effectuer un compromis avec des techniques classiques (très haute résolution). Le propos de cet article est de quantifier les performances en détection et reconnaissance d'une configuration de points brillants à l'aide d'un radar imageur multipolarisation connu. On confirme ainsi que la bipolarisation HH - VV suffit dans bien des cas et qu'il n'est donc pas nécessaire de mesurer les canaux croisés HV et VH qui sont très coûteux en terme de technologie.

## 1. INTRODUCTION

L'observation de la terre en technologie hyperfréquence s'est particulièrement développée avec l'avènement des radars à synthèse d'ouverture qui allient une haute résolution géométrique à une information extrêmement riche puisque le système est actif, insensible à la couverture nuageuse et complémentaire de l'optique. Une nouvelle étape a été franchie lorsque l'on a introduit le principe de la diversité de polarisations. En effet, l'émission de deux polarisations orthogonales (notées H et V par conventions) et la réception des canaux directs et croisés pour chaque polarisation émise, permet de fabriquer 4 images au lieu d'une seule, notées HH, HV, VH et VV (voir fig.1). Chaque pixel est donc représenté par 4 complexes formant une matrice dite "matrice de rétrodiffusion". Or, il a été montré (ref. 6) que toute polarisation elliptique peut se décomposer de manière unique sur la base (H, V). Ainsi, il est possible de calculer l'image dans n'importe quelle polarisation en multipliant simplement le champ électrique émis quelconque par la matrice de rétrodiffusion mesurée.

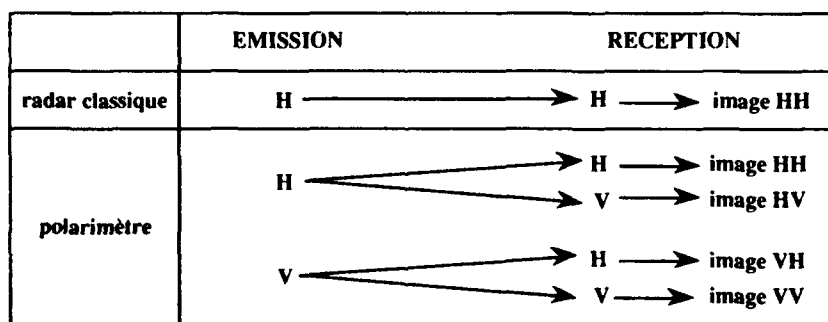


Figure 1: principe général du polarimètre.

On mesure donc l'impact de cette technique: en effet, si à partir de quatre images il est possible de générer toutes les polarisations, on a accès à la description électromagnétique totale de la cible et on peut alors se placer dans les meilleures conditions (couple (polarisation d'émission, polarisation de réception)) pour observer une cible donnée.

L'idée d'implanter cette technologie dans des satellites de surveillance et d'observation est donc tout-à-fait séduisante. Par contre, l'incidence sur les spécifications techniques n'est pas négligeable. En effet, pour réaliser un polarimètre, il est nécessaire d'implanter deux antennes au lieu d'une seule. Celles-ci devront être suffisamment isolées entre elles pour qu'il n'y ait pas pollution d'une polarisation par l'autre. De plus, la cadence des données à enregistrer et à transmettre est multipliée par 4 à résolution et PRF constantes. Il est alors possible d'atteindre des débits de 800 millions de bits par secondes ce qui est incompatible avec les technologies disponibles d'ici la fin du siècle. Ainsi, il est légitime de s'interroger sur l'apport de la polarimétrie en termes d'aide à la détection et à la reconnaissance de cibles, travaux couramment effectués par les photo-interprètes et officiers de renseignement.

Cet article présente une méthode de **quantification** de l'intérêt de la pluralité des canaux cohérents d'un radar multipolarisation. Le développement est organisé en deux parties:

- Aide à la détection
- Aide à la reconnaissance.

Les études présentées ici ont été menées sur des images multipolarisation cohérentes effectuées par le radar aéroporté NASA JPL. Ce radar est implanté à bord d'un DC8. Il opère sur trois fréquences (bandes L, C et P). Seule la bande C, plus proche de nos préoccupations a été utilisée. La description exacte des paramètres de ce radar est donnée en référence 6. Deux images ont été exploitées:

- en détection: une image sur la zone de San Francisco et plus particulièrement sur la zone du Golden Gate Park
- en reconnaissance: une image sur la zone du lac de Goldstone où des mires de calibration (dièdres et trièdres) avaient été placées.

## 2. AIDE A LA DETECTION

La détection d'une cible sur une image radar se fait par seuillage, soit visuellement sur un écran, soit automatiquement. En imagerie hyperfréquence tout le problème est en fait ramené à une réduction du speckle, "bruit" multiplicatif du à la nature cohérente de l'onde, toujours présent sur les images radar. Cette réduction peut se faire "à priori", c'est-à-dire sans connaissance préalable du contenu des images ou "à posteriori", c'est-à-dire en exploitant le contenu des images. Les deux méthodes sont ici exposées.

### 2.1 Aide à la détection à priori (DAP)

Le moyen utilisé pour quantifier la qualité radiométrique de l'image est le tracé de la probabilité de classer un point dans sa zone d'appartenance en fonction de la probabilité de faire une erreur de classement. Cette technique s'apparente tout à fait aux courbes  $P_d = f(P_{fa})$  utilisés couramment en traitement de signal radar.

Ces probabilités sont calculées à partir des histogrammes locaux des images. En effet: soit  $p(I)$  la probabilité d'occurrence d'un niveau  $I$  dans une image radar sur une zone homogène. Celle-ci s'exprime par:

$$p(I) = \frac{I^{n-1}}{(n-1)!} \beta^{-n} \exp\left(-\frac{I}{\beta}\right) \quad (1)$$

où  $n$  est le nombre de vues additionnées de manière incohérente (nombre de looks ou de polarisations)

où  $\beta$  est la valeur moyenne des radiométries sur la zone:  $\beta = \langle I \rangle$

Ainsi, soient deux zones différentes voisines dans l'image pour lesquelles on veut quantifier le contraste: appelons cible ( $c$ ) l'une des zones et environnement ( $e$ ) l'autre zone. La probabilité de classer un point de la zone ( $c$ ) de niveau  $\alpha$  dans la zone ( $c$ ) est donnée par  $P_d(\alpha)$  et la probabilité de classer un point de la zone ( $e$ ) de niveau  $\alpha$  dans la zone ( $c$ ) est donné par  $P_{fa}(\alpha)$  avec:

$$P_d(\alpha) = \int_{\alpha}^{+\infty} P_c(t) dt \quad \text{et} \quad P_{fa}(\alpha) = \int_{\alpha}^{+\infty} P_e(t) dt \quad (2)$$

remplaçons  $P_c$  et  $P_e$  par leur expression (1), on trouve:

$$P_d(\alpha) = \exp\left(-\frac{\alpha}{\langle I \rangle_c}\right) \sum_{i=0}^{n-1} \frac{\left(\frac{\alpha}{\langle I \rangle_c}\right)^i}{i!} \quad \text{et} \quad P_{fa}(\alpha) = \exp\left(-\frac{\alpha}{\langle I \rangle_e}\right) \sum_{i=0}^{n-1} \frac{\left(\frac{\alpha}{\langle I \rangle_e}\right)^i}{i!} \quad (3)$$

La théorie montre donc que plus on additionne de canaux indépendants, plus la qualité de l'image sera élevée. C'est bien la technique utilisée (multilook) pour réduire le speckle. Cette technique peut être réutilisée ici en additionnant de manière incohérente les différentes polarisations obtenues. On obtient l'image SPAN ( $HH+HV+VH+VV$ ). Pour quantifier l'importance des différents canaux, nous allons mesurer les courbes de probabilité sur les trois systèmes suivants simulés à partir du SAR JPL.

- Monopolarisation HH
- SPAN bipolarisation HH+VV
- SPAN multipolarisation HH+HV+VH+VV

Les zones utilisées pour cette mesure ont été prises à l'intérieur du parc du Golden Gate (voir figure 2) où l'on identifie deux types de radiométries: des zones sombres correspondant au stade, aux lacs et aux chemins (non rugueuses) et des zones claires (arbres).



Figure 2: Zone du Golden Gate Park: en rouge: zone de type "environnement", en vert: zones de type "cible"

La figure 3 montre les résultats:

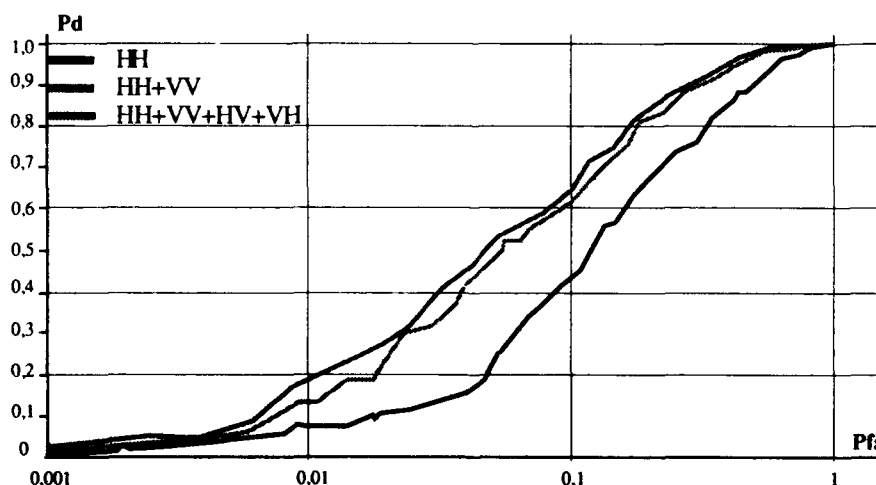


Figure 3: Courbes de quantification sur les zones du Golden Gate Park: DAP

Deux remarques peuvent être immédiatement effectuées concernant ces résultats:

- 1- On constate une nette amélioration entre HH et HH+VV (gain de 0.15 en probabilité) ce qui est conforme à la théorie.
- 2- On constate une très faible amélioration entre HH+VV et HH+HV+VH+VV, ce qui tend à montrer que les canaux croisés n'ont qu'une faible importance dans le processus de détection. Cela peut être expliqué par le fait que la radiométrie de ces derniers est

plus faible que celle des canaux directs et qu'ainsi leur contribution à l'amélioration de contraste est 5 fois plus faible que celle qui est constatée sur les canaux directs (voir figure 3).

## 2.2 Aide à la détection maximale à posteriori (DMAP)

On se place maintenant dans le cas où le comportement polarimétrique des cibles est connu. La zone de travail reste la même (parc du Golden Gate) zones (e) et (c). Par la mesure des matrices de rétrodiffusion associées à ces zones, il est possible de générer une image dans une polarisation "optimisant" la zone (c) par rapport à la zone (e). Les techniques utilisées ici ont été développées abondamment par le JPL (ref. 1 et 3). Le processus a été mené en bipolarisation: on obtient une image dite OPT2 (optimale pour 2 canaux), et en multipolarisation 4 canaux: on obtient une image dite OPT4. Les courbes de quantification ont alors été tracées, on obtient les résultats suivants:

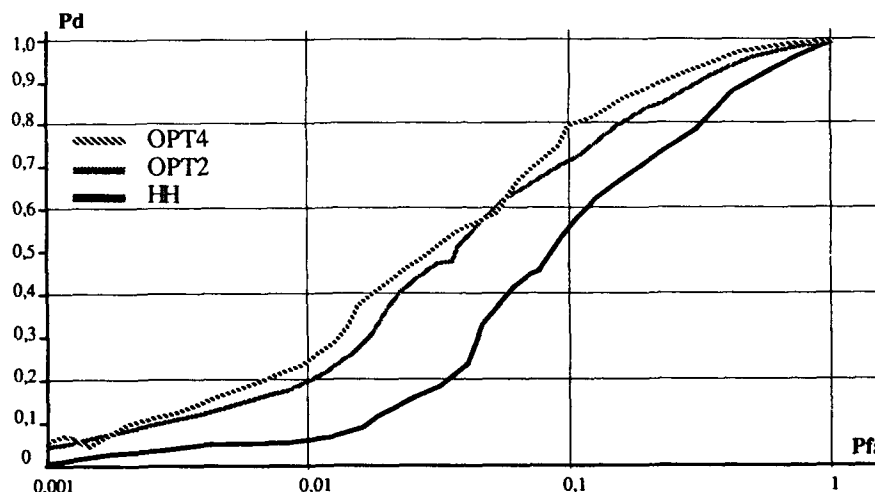


Figure 4: Courbes de quantification sur les zones du Golden Gate Park: DMAP

2 remarques doivent être faites:

- 1- On constate une amélioration des résultats par rapport à la DAP. Cela est dû à l'optimisation effectuée sur les matrices de rétrodiffusion. On remarque de plus que OPT2 est meilleur que HH+HV+VH+VV.
- 2- On ne constate pas d'améliorations notables entre OPT2 et OPT4. Cela confirme les premiers résultats obtenus en DAP et nous permet de conclure pour ce cas à la très nette prépondérance des canaux directs par rapport aux canaux croisés.

## 2.3 Discussion et conclusions sur la détection

Les résultats obtenus peuvent être généralisés aux systèmes radars dont la cellule de résolution est grande devant la longueur d'onde: le rapport devant être au moins supérieur à 20. En effet, tant que le speckle reste statistique, les théories développées et appliquées ci-dessus restent valables. Ainsi, on montre ici que les canaux croisés n'ont qu'une faible incidence sur les performances en détection et qu'un système bipolarisation HH - VV cohérent est suffisant et même meilleur radiométriquement qu'un système haute résolution monopolarisation. Cependant, pour être complets, ces travaux doivent être étendus à la reconnaissance. C'est ce qui est proposé dans la seconde partie de cet article.

## 3. AIDE A LA RECONNAISSANCE

Le propos de cette partie est de quantifier l'apport de la multipolarisation en tant qu'outil d'aide à la reconnaissance de cibles de l'is une image radar. Ne disposant pas pour l'instant de cibles militaires mesurées en multipolarisation, nous nous sommes reportés sur des configurations de points brillants identifiés sur une image radar multipolarisation du lac de Goldstone (USA) où avaient été disposées des mires de calibration diédriques et triédriques. Nous nous sommes placés dans la position du photo-interprète qui cherche à retrouver dans une image une configuration connue par ailleurs. La démarche classiquement utilisée est alors la suivante: on effectue une comparaison entre une référence connue de cette cible et l'image de travail. En optique, cette comparaison est souvent matérialisée par une corrélation entre la référence et l'image. Cette corrélation donne alors une figure qui est seuillée pour conclure à la présence ou à l'absence de la cible dans l'image. La figure suivante illustre cette démarche classique:

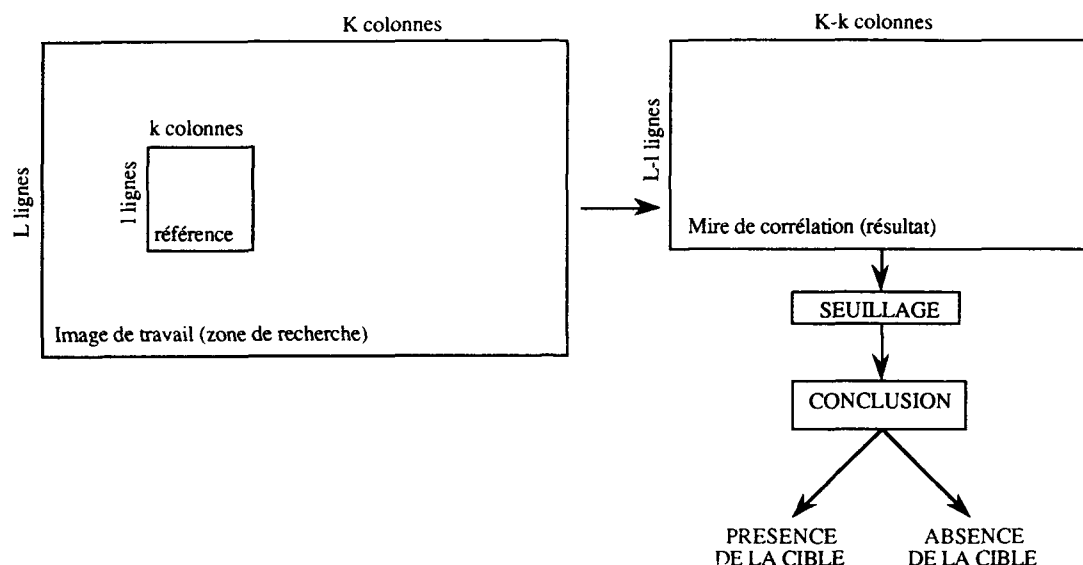


Figure 5: Diagramme de corrélation d'images

Dans le cas où l'on traite des images monopolarisation, on est en présence de fonctions échantillonnées de  $R^2$  dans  $R$  (images classiques). La formule de corrélation est alors simple et nous la nommerons "corrélation scalaire" (CS). On obtient:

$$C(m,n) = \left( \frac{\sum_p \sum_q F(m-p, n-q) \cdot T(p,q)}{\sqrt{\sum_p \sum_q F(m-p, n-q)^2 \cdot \sum_p \sum_q T(p,q)^2}} \right)^2$$

où,

$F(m,n)$  est l'image de travail dans laquelle on cherche la cible,  $m \in [0, K]$  et  $n \in [0, L]$

$T(p,q)$  est la mire de référence (image de la cible mesurée),  $p \in [0, k]$  et  $q \in [0, l]$

$C(m,n)$  est l'image résultat de la corrélation ou mire de corrélation,  $m \in [0, K-k]$ ,  $n \in [0, L-l]$ ,  $p \in [0, k]$  et  $q \in [0, l]$  voir figure 5.

Si une image pixel peut être assimilée à l'échantillonnage d'une application de  $R^2$  dans  $R$  qui a tout couple de coordonnées discrètes  $(k,l)$  fait correspondre un niveau radiométrique  $n$ , l'image polarimétrique est d'une toute autre nature. Elle est en particulier multispectrale, c'est-à-dire qu'à tout couple de coordonnées  $(k,l)$ , on fait correspondre un **vecteur complexe** dont la dimension est variable en fonction du nombre de polarisations dont on dispose. Une manière de considérer le problème est la suivante: on décompose les champs électriques sur la base  $(H,V)$  classique. On considérera ici que nous sommes en monostatique parfait, c'est-à-dire que  $HV=VH$ .

Soit  $F(m,n)$  le vecteur image de base et  $T(j,k)$  le vecteur mire à corréler. Pour chaque indice,  $F$  et  $T$  contiennent donc les éléments de la matrice de rétrodiffusion définissant le pixel polarimétrique. On aura donc:

$$F(m,n) = \begin{pmatrix} HH \\ VV \\ HV \end{pmatrix} \quad (5)$$

$HH$ ,  $HV$  et  $VV$  sont les termes complexes de la matrice de rétrodiffusion

Dans le cas d'un radar bipolarisation, les canaux croisés peuvent être annulés et l'expression de  $F$  devient:

$$F(m,n) = \begin{pmatrix} HH \\ VV \end{pmatrix} \quad (6)$$

Nous nous trouvons donc confronté à des applications de  $R^2$  dans  $C^3$  ou  $C^2$ . La formule classique de corrélation se transforme alors de la manière suivante:

$$C(m,n) = \left( \frac{\left| \sum_p \sum_q \langle F(m-p,n-q) \cdot T^*(p,q) \rangle \right|}{\sqrt{\sum_p \sum_q |F(m-p,n-q)|^2 \cdot \sum_p \sum_q |T(p,q)|^2}} \right)^2$$

On remarquera au numérateur la transformation sesquilinéaire qui corrèle le conjugué de la mire ( $T^*$ ) avec le signal complexe  $F$ . Le module du résultat est ensuite divisé par les paramètres de normalisation. Le résultat  $C(m,n)$  est encore un scalaire compris entre 0 et 1 qui mesure le taux d'homothétie entre l'image et la mire de référence. On appellera cette opération "corrélation cohérente complexe" (CCC).

#### APPLICATION:

L'image du GoldStone est constituée d'une série de dièdres et de trièdres disposés sur un lac asséché plat. Pour pouvoir tester l'efficacité de la polarimétrie, la mire utilisée doit être constituée de réflecteurs ayant un comportement polarimétrique différent. C'est pourquoi nous avons choisi d'utiliser une mire constituée d'un trièdre et de deux dièdres orientés de manières différentes. On trouvera ci-dessous l'image de Goldstone et un graphique montrant la cible choisie parmi les dispositifs de calibration.



Figure 6: Image de Goldstone

Les réflecteurs sont disposés perpendiculairement à la ligne de vol du radar et inclinés de 45 degrés par rapport au sol (l'angle de visée utilisé étant de 45 degrés). Le réflecteur numéro 1 est un trièdre simple orienté à 45°. Le réflecteur numéro 3 est un dièdre orienté à 0 degré par rapport à la ligne de vol. Il n'est donc vu que pendant la moitié de la traversée dans le lobe d'antenne et répond uniquement en HH et en VV.

Le réflecteur numéro 2 est un dièdre orienté à 45 degrés par rapport à la ligne de vol. La rétrodiffusion est importante dans les canaux croisés et faible pour les canaux directs. Cependant, lors de l'expérimentation du GoldStone, ce réflecteur n'a pas été correctement positionné et n'est donc pas très visible (Ref 3). Ces réflecteurs se repèrent facilement sur l'image du GoldStone où les réflecteurs sont alignés de manière ordonnée. La Figure 7 permet de les situer et de les décrire.



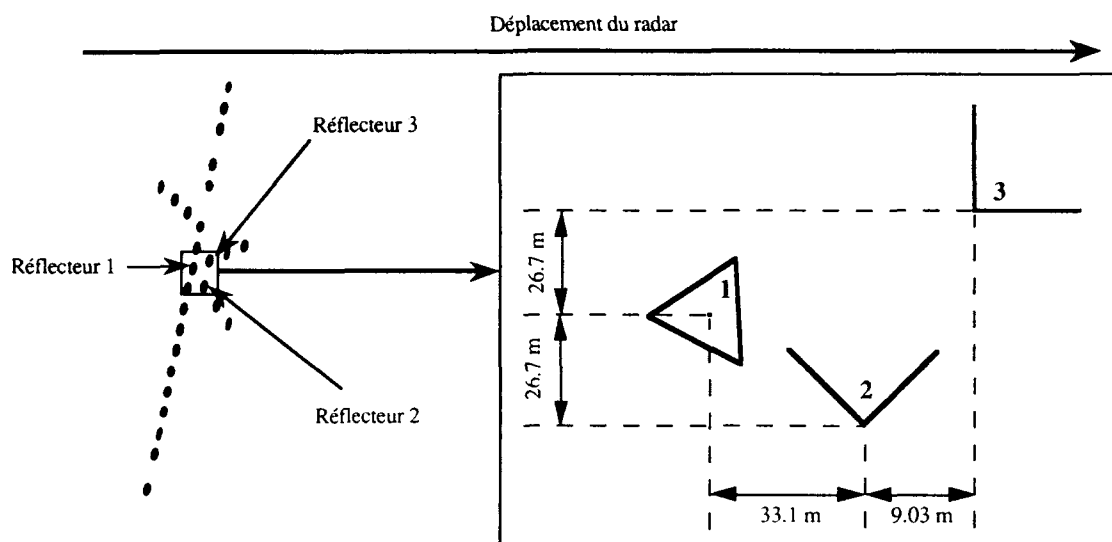


Figure 7: Les réflecteurs du GoldStone, la localisation de la cible choisie et la description des points brillants.

#### RESULTATS:

La figure 8 présente les résultats obtenus pour toute une série d'expériences de corrélation. La mire de référence a été simulée à partir d'un simulateur d'images radar de cibles géométriques simples (ref. 4). Elle a été simulée en HH, HV, VH et VV. On dispose ainsi de tous les paramètres nécessaires.

La première série d'expériences a été réalisée en CS. On a donc corrélié la mire HH+HV+VV avec les images suivantes:

- Image HH
- Image HH+VV
- Image HH+HV+VH+VV
- Image OPT2
- Image OPT4

La seconde série a été réalisée en CCC. On a donc corrélié le vecteur mire simulé avec les vecteurs images suivants:

- Vecteur image composé des canaux directs (D) --> bipolarisation HH - VV
- Vecteur image composé des canaux croisés (C) --> bipolarisation HV- VH
- Vecteur image complet (DC) --> polarimètre

Type	Expérience	Valeur du pic de corrélation	$\frac{\text{pic}}{\text{environnement}}$	Correct
CS	Image HH	0,46	6 dB	NON
	Image HH+VV	0,47	12 dB	NON
	Image HH+HV+VH+VV	0,49	14 dB	NON
	Image OPT2	0,4	18 dB	OUI
	Image OPT4	0,37	20 dB	OUI
CCC	Vecteur canaux directs	0,041	40 dB	OUI
	Vecteur canaux croisés	0,070	26 dB	NON
	Vecteur complet	0,042	38 dB	OUI

Figure 8: Résultats de corrélation.

#### DISCUSSION:

Sur la corrélation scalaire: on remarque que la taille normalisée du pic de corrélation augmente de HH à HH+HV+VH+VV, ce qui est normal puisque le speckle a diminué. Il en est de même pour le rapport pic de corrélation sur environnement. Par contre, le pic de corrélation n'est pas bien placé. Cela est dû au fait que l'information phase n'est pas utilisée. Par contre, les images OPT2 et OPT4 donnent une corrélation correcte bien que le pic soit moins élevé. L'information phase est ici utilisée indirectement puisqu'elle sert à générer l'image optimale. On remarquera au passage que les gains sont plus élevés quand on passe de la monopolarisation à la bipolarisation que de la bipolarisation au polarimètre. Cela confirme les résultats obtenus en détection quant aux incidences comparées des canaux directs et croisés.

Sur la corrélation cohérente complexe: La valeur normalisée du pic de corrélation est dix fois moins importante que dans le cas scalaire. Cela est dû au fait que l'on corréle aussi des phases qui ne sont pas de même nature que les modules. Par contre, le rapport pic sur environnement atteint 40 dB. Le résultat est donc bien meilleur, au sens du taux de fausse alarme. La corrélation sur les canaux croisés ne donne pas un résultat correct car l'approximation utilisée pour simuler la mire de référence dans les canaux croisés n'est pas fiable. Cependant, ce mauvais résultat ne perturbe pas la corrélation complète, ce qui confirme une fois de plus la faible importance des canaux croisés.

#### 4. CONCLUSIONS

Ces résultats permettent d'apporter les conclusions suivantes: la bipolarisation HH - VV est au sens de la détection et de la reconnaissance de cibles un outil très utile pour le photo-interprète quand celui-ci se sert de l'image comme support du signal. En effet, la réduction de 4 à 2 voies ne fait baisser que très légèrement les performances. Plus précisément, les méthodes développées n'offrent qu'une faible sensibilité aux canaux croisés qui sont radiométriquement 20 dB inférieurs aux canaux directs.

Ces conclusions sont cependant tirées de tests effectués à partir de cibles simulées par approximations. En particulier les trièdres et dièdres du GoldStone ont été assimilés à des cibles géométriques simples ce qui ne correspond pas à la réalité. Il sera donc nécessaire par la suite de **confirmer ces conclusions** en utilisant des **mesures de cibles réelles**. On peut penser que les résultats seront **meilleurs** puisque les mesures nous rapprocheront encore plus de la réalité. Ceci est d'autant plus vrai en ce qui concerne les canaux croisés pour lesquels on aura une mesure fiable.

#### 5. REFERENCES

- (1) Nasr.JM, Fernin.P, **Imagerie Radar et Polarimétrie : Analyse des compromis de base**, Etude DEn No 89 70 177, Doc STS/M 45159, 1 Mars 1990
- (2) Pratt.WK, **Digital Image Processing**, University of Southern California, Mars 1977.
- (3) Freeman.A, **Polarimetric SAR calibration experiment using active radar calibrators**, IEEE Transactions on Geoscience and Remote Sensing, Vol 28, No 2, Mars 1990.
- (4) Nasr.JM, **Etude et réalisation d'un simulateur d'images de cibles géométriques simples vues par un radar à synthèse d'ouverture embarqué sur satellite**, Thèse, Université Paris 7, 1989.
- (5) Olivier.P, **Principes de l'imagerie haute résolution au moyen d'un radar à ouverture synthétique embarqué sur satellite**, CRPE, Note technique CRPE/179
- (6) Ulaby.F, Elachi.C, **Radar Polarimetry for Geoscience Applications**, The Artech House, Avril 1990.

#### DISCUSSION

**R. KLEMM (GE)**

**Is multi-polarization frequency dependent? Would it bring advantages for detection and imaging of hard targets at X-band?**

**AUTHOR'S REPLY**

**Yes.**

# CONTRIBUTION DE LA POLARIMETRIE DANS LA DISCRIMINATION, LA CLASSIFICATION ET L'IDENTIFICATION DE CIBLES RADAR.

E. POTTIER - J. SAILLARD  
Laboratoire S2HF, I.R.E.S.T.E  
La Chantrerie - CP3003  
44087 NANTES Cédex 03, FRANCE.

*Actuellement, l'analyse fine de la structure d'une cible radar, en vue de sa caractérisation et de sa reconnaissance, est un centre d'intérêt de la recherche scientifique.*

*Le but de cet article concerne l'amélioration du pouvoir de discrimination et de classification des zones brillantes d'une cible par l'introduction du concept de la polarimétrie dans le domaine de l'imagerie électromagnétique haute résolution.*

## 1 - INTRODUCTION.

L'imagerie Radar est utilisée pour effectuer l'analyse fine de la signature de cibles. Le problème inverse de la diffraction électromagnétique est en voie d'être résolu en retrouvant à partir de la connaissance du champ complexe rétrodiffusé, les coordonnées géométriques et les propriétés physiques des contributeurs élémentaires. Par calculs, se construit une image Electromagnétique Haute Résolution de la cible dans le plan d'observation.

L'apport du concept de la polarimétrie dans l'analyse fine de la signature d'une cible nous a permis de développer une méthode originale permettant d'obtenir une image électromagnétique haute résolution qui soit optimale dans la discrimination des zones brillantes, en réalisant une adaptation des états de polarisation de l'onde émise à la sensibilité maximale de la cible afin que celle-ci rétrodiffuse le maximum d'énergie.

En parallèle à l'étude sur l'amélioration du pouvoir de discrimination, sont venus se greffer les problèmes classiques de la "reconnaissance", qui consistent à déterminer quelles sont les caractéristiques physiques et géométriques de la cible qui sont à l'origine des zones brillantes localisées à partir des images électromagnétiques haute résolution.

A partir de la "théorie phénoménologique des cibles radar", énoncée par J.R. HUYNEN, nous avons développé une méthode originale de classification, qui nous a conduit à la conception d'un système "intelligent" de caractérisation de la structure d'une cible, basée sur l'utilisation des modèles de réseaux neuronaux.

## 2 - HOLOGRAPHIE RADAR.

L'holographie radar [1],[2] est un procédé conduisant à la réalisation d'une image électromagnétique haute résolution d'une cible radar complexe, à partir de la connaissance des valeurs du champ électromagnétique rétrodiffusé par celle-ci relevé en fonction de deux paramètres de mesure: la fréquence d'émission ( $f$ ) ainsi que la position angulaire ( $\theta$ ) du radar par rapport au centre de phase de la cible.

Le coefficient de rétrodiffusion représente le rapport du champ de l'onde réfléchie

par la cible et de l'onde incidente au niveau de la source. Ce coefficient complexe traduit un affaiblissement et un déphasage.

De plus, le coefficient de rétrodiffusion est fonction du couple de polarisation utilisé à l'émission et à la réception.

L'image électromagnétique haute résolution est obtenue par sommation cohérente sectorielle des réponses impulsionnelles représentant les fonctions temporelles de l'écho renvoyé par la cible. L'image radar, ainsi obtenue, représente la projection des points brillants dans le plan d'observation, ce qui permet de localiser spatialement les positions des centres de diffraction.

La figure n°1 donne la représentation géométrique d'une image radar. ( $O', x_r, y_r, z_r$ ) est le trièdre de référence radar, définissant la base de polarisation. ( $O, X, Y, Z$ ) est le trièdre de référence cible, dénommé également "repère avionneur". Le point  $O$  représente le centre de phase de la cible. Après construction, nous obtenons l'image radar de la cible, où le centre de phase est situé au centre de l'image, et où l'onde incidente provient du haut de l'image

### 2.1 - Formulation mathématique.

Considérons qu'une cible radar puisse se décomposer en une somme finie de  $N$  contributeurs indépendants et possédant la propriété d'isotropie fréquentielle.

Le coefficient de rétrodiffusion s'exprime alors par:

$$S(\vec{k}) = \sum_{i=1}^N a_i e^{-2j\vec{k}\vec{x}_i} \quad (1)$$

où  $a_i$  désigne l'amplitude complexe du  $i$ ème contributeur, et  $\vec{x}_i$  le vecteur définissant sa position spatiale dans le repère cible.

L'expression (1) peut également se mettre sous la forme:

$$S(\vec{k}) = \iiint \left[ \sum_{i=1}^N a_i \delta(\vec{x} - \vec{x}_i) \right] e^{-2j\vec{k}\vec{x}} d\vec{x} \quad (2)$$

où  $\delta(\vec{x})$  désigne la distribution de Dirac tridimensionnelle. Posons:

$$I(\vec{x}) = \sum_{i=1}^N a_i \delta(\vec{x} - \vec{x}_i) \quad (3)$$

où  $I(\vec{x})$  représente l'image tridimensionnelle de la cible radar. Dans ce cas, la relation (2) peut être considérée comme la transformée de Fourier tridimensionnelle de l'image, ce qui donne:

$$I(\vec{x}) = \iiint S(\vec{k}) e^{2j\vec{k}\vec{x}} d\vec{k} \quad (4)$$

Habituellement, l'analyse est restreinte au cas bidimensionnel en imposant  $k_z = 0$ . Ceci permet d'obtenir une représentation des contributeurs projetés sur le plan  $z=0$ . Ainsi, à partir de la connaissance du coefficient de

rétrodiffusion global mesuré en fonction du couple  $(f, \theta)$ , l'image électromagnétique haute résolution de la cible complexe est déterminée par :

$$I(\vec{\lambda}) = 4 \left[ \frac{\pi}{c} \right]^2 \int_{\Gamma} \int_{\Theta} fS(f, \theta) e^{2j\pi f^2 (x \cos \theta + y \sin \theta)} df d\theta \quad (5)$$

où le couple  $(x, y)$  représente les coordonnées du vecteur  $\vec{\lambda}$  dans le plan de la cible.

### 3 - CIBLE COMPLEXE MESUREE.

Afin de vérifier les travaux effectués dans le domaine de la Polarimétrie, et de valider, par la mesure, les résultats obtenus par simulation, une campagne de mesure a été effectuée sur une cible complexe dans la chambre anéchoïque du CELAR, durant le mois de Mars 1989, [3].

La cible complexe est constituée de quatre cibles simples, canoniques et indépendantes, à savoir :

- un dipôle métallique horizontal d'une longueur de 65 cm et d'un diamètre de 1 mm.
- une plaque métallique carrée de surface  $S = 2 \text{ cm}^2$ .
- une sphère de diamètre 7 cm.
- un dipôle métallique, de mêmes caractéristiques que le précédent, mais orienté d'un angle  $\theta = 45^\circ$  autour de la ligne de visée du radar. Ce dipôle n'appartient pas au plan de la cible mais lui est perpendiculaire.

La localisation de ces éléments sur le support de mesure est représentée sur la figure n°2.

En fonction de la bande d'analyse [8-12.4 GHz], les dimensions des cibles canoniques ont été déterminées afin de vérifier le postulat suivant, à savoir :

"Toute cible complexe peut se décomposer en une somme finie de cibles simples, canoniques, indépendantes et isotropes".

Ainsi, en travaillant en zone optique, c'est-à-dire en limite supérieure de la zone de résonance, la cible complexe peut être modélisée par un ensemble de sources ponctuelles indépendantes appelées encore contributeurs élémentaires, ou tout simplement points brillants.

#### 3.1 - Images Electromagnétiques obtenues.

Afin d'obtenir, toute l'information relative à la cible complexe, il est nécessaire de concevoir et d'utiliser un système radar vectoriel possédant deux antennes émission réception, dont l'état de polarisation de chacune d'entre elle est lié à une base canonique de l'espace des états de polarisation, soit par exemple Horizontal - Vertical.

A l'émission, le champ électrique  $\vec{E}$  de l'onde électromagnétique aura en alternance, la polarisation horizontale puis verticale. La cible rétrodiffuse pour ces deux états de polarisation une onde électromagnétique, dont le champ électrique possède un état de polarisation qui est d'une manière générale purement elliptique. A la réception, ce champ rétrodiffusé se décompose sur la base canonique des états de polarisation en deux composantes (horizontale et verticale) représentant les amplitudes des oscillations linéaires le long des axes  $\vec{x}$  et  $\vec{y}$  du trièdre de propagation.

Un tel système radar vectoriel est alors capable de fournir toute l'information relative à la cible sous la forme d'une matrice de rétrodiffusion et non plus d'un simple coefficient de rétrodiffusion.

En effectuant une mesure de la cible au moyen d'un tel système vectoriel dont le couple de base des états de polarisation est le couple  $(H, V)$ , quatre Images Electromagnétiques Haute Résolution correspondant à chacun des termes de la matrice de rétrodiffusion peuvent alors être construites. L'antenne radar se situant en haut des images, il est alors aisé de déterminer la correspondance de ces zones brillantes par comparaison avec la localisation des cibles élémentaires sur le support de mesure. Ces images sont représentées figure n°3.

L'examen de ces représentations graphiques montre que les images "cross-polarisées", c'est-à-dire celles obtenues à la réception, avec une polarisation orthogonale à celle de l'émission  $(HV, VH)$ , ne font apparaître qu'une seule zone brillante correspondant au dipôle orienté à  $45^\circ$  par rapport à la ligne de visée du radar. Due à son orientation, cette cible rétrodiffuse toute son énergie d'une manière équirépartie dans chaque canal  $(HH, HV, VH$  ou  $VV)$ . Il est important de noter lors de l'examen de l'image électromagnétique  $VV$ , l'absence significative de toute zone brillante liée à la présence du dipôle horizontal. En examinant plus attentivement l'image électromagnétique obtenue lors d'une émission et d'une réception horizontale, une quatrième zone brillante apparaît en haut de l'image. Cette zone correspond au dipôle horizontal.

L'examen global de ces quatre Images Electromagnétiques Haute Résolution montre que toute l'information relative à la cible est bien contenue dans la Matrice de rétrodiffusion, et qu'il est nécessaire de la connaître afin d'étudier au mieux toute cible complexe. De plus, étant à la base même de la théorie Polarimétrique des ondes, il est absolument indispensable de pouvoir mesurer et d'obtenir la matrice de rétrodiffusion d'une cible par un système radar vectoriel avant d'introduire tout concept, quel qu'il soit, de la Polarimétrie dans le domaine de l'imagerie radar.

### 4 - INTRODUCTION DU CONCEPT DE LA POLARIMÉTRIE DANS LE DOMAINE DE L'IMAGERIE ELECTROMAGNETIQUE HAUTE RESOLUTION.

La discrimination des zones brillantes d'une cible complexe à partir des images électromagnétiques haute résolution peut-être améliorée lorsque celles-ci sont construites à partir de la connaissance des matrices de rétrodiffusion délivrées par un système radar vectoriel.

Cette discrimination pourra être optimisée en introduisant lors de la construction des images électromagnétiques haute résolution, la théorie de la polarimétrie des ondes électromagnétiques basées sur l'étude des propriétés algébriques des matrices de rétrodiffusion.

La première approche consiste à reconstruire les matrices de rétrodiffusion à partir des réponses fréquentielles, afin d'être en accord avec la définition première d'une matrice de rétrodiffusion qui est en fait, caractéristique d'une cible pour une fréquence, une position et un couple de polarisation donnés. Cependant, les matrices de rétrodiffusion construites à partir des réponses fréquentielles ne peuvent fournir qu'une information globale sur la cible complexe, c'est-à-dire en considérant comme une entité l'ensemble des cibles simples (contributeurs élémentaires) formant la cible complexe étudiée.

A partir des réponses fréquentielles, il est aisé de déterminer les réponses impulsionnelles correspondantes en appliquant une simple transformée de Fourier. Ainsi nous est fournie

une information supplémentaire permettant la localisation des contributeurs et la détermination de leur position spatiale projetée sur l'axe radar-cible. L'examen des réponses impulsionnelles, montre que toute l'information relative à la cible complexe y est contenue, notamment l'information de position qui est non-négligeable lors de la discrimination des points brillants. Pour cette raison, il semble alors assez naturel de reconstruire les matrices de rétrodiffusion à partir des réponses impulsionnelles obtenues.

Dénomons par "Opérateur IEHR", le procédé permettant de construire les Images Electromagnétiques Haute Résolution. Cet opérateur s'exprime sous la forme suivante:

$$I(\vec{X}) = \left( \frac{2\pi}{c} \right)^2 \int_f \int_\theta f S(f, \theta) e^{j2\pi f \tau} df d\theta \quad (6)$$

L'expression  $S(f, \theta)$  est la réponse fréquentielle de la cible pour une position  $\theta$  et une fréquence  $f$  données. L'examen de l'expression de l'opérateur IEHR, montre que celui-ci fait intervenir la Transformée de Fourier Inverse de la fonction  $(f.S(f, \theta))$ , calculée en fonction de  $\tau$ . L'opérateur IEHR ne réalise en fait qu'une sommation cohérente des dérivées des réponses impulsionnelles.

Il a été montré explicitement dans [4] qu'il était parfaitement possible de reconstruire directement les matrices de rétrodiffusion à partir des images électromagnétiques haute résolution ainsi obtenues. La démarche retenue consiste à reconstruire la matrice de rétrodiffusion à partir des valeurs complexes (amplitude, phase) contenues dans les pixels des images électromagnétiques haute résolution, correspondant au contributeur étudié, permettant aussi d'obtenir une "matrice de rétrodiffusion spatiale".

## 5 - APPORT DU CONCEPT DE LA POLARIMETRIE DANS L'IMAGERIE HAUTE RESOLUTION.

### 5.1 - Introduction.

Maintenant qu'il est possible de reconstruire les matrices de rétrodiffusion spatiales à partir de la connaissance des quatre Images Electromagnétiques Haute Résolution, nous pouvons assimiler les quatre images à une "Matrice Image" et lui appliquer les techniques propres à la Polarimétrie.

L'objectif fixé est d'obtenir à partir de la connaissance des quatre Images Electromagnétiques Haute Résolution, une image unique qui puisse contenir à elle seule, toute l'information relative à la cible, et qui soit donc performante au niveau de la discrimination des zones brillantes.

Cela revient en fait à déterminer la base des états de polarisation "optimale" qu'il faut appliquer aux antennes d'Emission et de Réception pour obtenir le maximum de puissance rétrodiffusée par la cible dans un des deux canaux de copolarisation (XX ou YY).

Comme il est impossible, sans connaissance a priori de l'état de polarisation optimale, d'agir physiquement au niveau des antennes, nous allons pouvoir, uniquement par traitement, reconstruire une image qui soit performante du point de vue de la discrimination et qui reste cependant cohérente du point de vue de la réalité physique.

Cette méthode va nous permettre de réaliser une adaptation à la sensibilité maximale de la cible, vue dans son ensemble, du point de vue de sa "polarisation", en vue de la maximisation de sa puissance rétrodiffusée.

### 5.2 - Détermination de l'Image "SPAN".

A partir de la connaissance des quatre Images Electromagnétiques Haute Résolution, nous construisons l'image Span représentant la puissance transportée dans la matrice de rétrodiffusion spatiale avec :

$$\text{Span } [S] = |S_{11}|^2 + |S_{12}|^2 + |S_{21}|^2 + |S_{22}|^2 \quad (7)$$

La propriété importante du Span est son invariance quelle que soit la base des états de polarisation Emission / Réception utilisée [5]. L'image SPAN est présentée figure n°4.

Cette image Span contient toute l'information de puissance liée à la cible et maximise, par là même, la dynamique de l'image.

Cette image non cohérente, fournit un support d'information permettant la localisation des maxima locaux.

### 5.3 - Détermination de l'Image "FULL-POLAR"

La première idée lors de la construction d'une image performante pour la discrimination des surfaces brillantes, a été de maximiser chaque zone de l'espace cible, en déterminant l'état de polarisation caractéristique correspondant.

Ainsi pour chaque zone de l'image, la matrice de rétrodiffusion spatiale est reconstruite à partir des énergies contenues dans les quatre pixels correspondants.

La base des vecteurs pseudo-propres ( $X_1$ ,  $X_2$ ) est alors déterminée, permettant ainsi de diagonaliser la matrice de rétrodiffusion spatiale.

La puissance maximale reçue dans la base des vecteurs pseudo-propres est égale à la magnitude de la cible ( $m$ ), qui correspond au module de la valeur propre maximale de la matrice de rétrodiffusion spatiale diagonalisée.

L'image "full-polar" présente ainsi, en chacun de ses points, la S.E.R maximale de la cible, à condition que ceux-ci soient éclairés par l'état de polarisation caractéristique qui leur est associé. Cette image est représentée à la figure n°5.

Il est évident que cette image, bien que très riche en information, ne présente qu'un maigre intérêt physique, puisqu'il n'existe aucune cohérence de point en point en ce qui concerne les bases de polarisation caractéristique utilisées.

En effet, chaque point est lié à une base caractéristique unique, dans laquelle la puissance rétrodiffusée par la cible, en ce point de l'espace, est maximale. Ceci se vérifie par l'examen de l'image "co-polar X-X", qui permet de retrouver le dipôle horizontal obtenu par un couple de polarisation Emission/Réception horizontale ainsi que le dipôle orienté à 45° qui, lui, a été obtenu par un couple de polarisation Emission/Réception linéaire de 45°.

### 5.4 - Etude et maximisation d'une zone particulière de l'Image Radar.

Une autre application de l'utilisation du principe des états de polarisation caractéristique consiste à étudier une zone particulière de l'image en cherchant à déterminer la polarisation caractéristique permettant d'obtenir une réponse maximale du point brillant étudié.

Prenons comme exemple la zone brillante correspondant au dipôle orienté à 45°. A partir des quatre Images Electromagnétiques Haute Résolution la matrice de rétrodiffusion spatiale est reconstruite, et s'exprime par :

$$[S] = \begin{bmatrix} -1,116 + j1,932 & -1,140 + j1,898 \\ -1,065 + j1,925 & -1,147 + j2,011 \end{bmatrix} \quad (8)$$

La résolution du problème aux valeurs propres conduit à la détermination de l'état de polarisation caractéristique XPOLL Null, donné par le vecteur  $X_1$  suivant :

$$X_1 = \frac{1}{\sqrt{2,041}} \begin{bmatrix} 1 \\ 1,02 + j0,021 \end{bmatrix} \quad (9)$$

Le vecteur de Jones  $X_1$  correspond en fait, à une polarisation elliptique, qui est très proche d'une polarisation linéaire canonique de +45° donnée par le vecteur de Jones :

$$X = \frac{1}{\sqrt{2}} \begin{bmatrix} 1 \\ 1 \end{bmatrix} \quad (10)$$

A partir de la connaissance du vecteur de Jones  $X_1$ , la matrice de passage unitaire [U], formée des deux vecteurs XPOLL Nulls est égale à :

$$[U] = \frac{1}{\sqrt{2,041}} \begin{bmatrix} 1 & 1,02 \\ 1,02 + j0,021 & -0,99 - j0,02 \end{bmatrix} \quad (11)$$

Les Images Electromagnétiques Haute Résolution correspondant à ces états de polarisations remarquables appliquées aux antennes Emission/Réception sont obtenues en effectuant le changement de base dans l'espace des polarisations en appliquant la relation :

$$[S'] = [U]^T [S] [U] \quad (12)$$

Les images ainsi reconstruites sont représentées figure n°6.

L'examen de ces quatre nouvelles Images Electromagnétiques Haute Résolution montre que la zone brillante correspondant au dipôle orienté à 45° se retrouve maintenant uniquement dans l'IEHR correspondant au canal AA (A représentant l'état de polarisation XPOLL Null  $X_1$  et B représentant l'état polarisation XPOLL Null  $X_2$ ) où toute l'énergie rétrodiffusée s'y trouve regroupée.

Il n'existe plus de zones brillantes dans les Images Electromagnétiques Haute Résolution cross-polarisées (AB; BA) ce qui prouve que la matrice de diffraction spatiale a bien été diagonalisée.

De plus, il n'existe pas de zone brillante dans le canal BB correspondant à une émission réception orthogonale à l'orientation du dipôle, d'où l'absence de rétrodiffusion.

Les zones brillantes correspondant à la plaque et à la sphère ne subissent aucun changement d'orientation à leur insensibilité polarimétrique aux changements d'états de polarisations linéaires.

De plus, dû au changement de la base des états de polarisation Emission Réception, passage de (H;V) à (+45°;-45°), le dipôle horizontal est maintenant vu comme étant orienté de 45° par rapport à l'axe de visée du radar. Cette "pseudo" orientation se traduit par la présence de quatre zones brillantes correspondant au dipôle horizontal dans chaque Image Electromagnétique Haute Résolution.

## 5.5 - Détermination de l'Image Optimale d'une cible.

Dans les paragraphes précédents il a été montré qu'il était possible de déterminer la polarisation remarquable liée à une zone brillante particulière permettant ainsi d'optimiser la puissance rétrodiffusée dans un canal co polarisé.

Nous allons maintenant montrer qu'il est possible d'effectuer le même traitement afin de déterminer un état de polarisation qui soit optimal pour la cible vue dans son ensemble, afin de maximiser sa puissance rétrodiffusée dans un des deux canaux co-polarisés.

Pour cela, nous avons développé un algorithme [4] dont le synopsis est représenté figure n°7.

A partir de la connaissance des quatre Images Electromagnétiques Haute Résolution, l'image Span représentant la puissance transportée par la matrice de rétrodiffusion spatiale est construite.

A partir de l'image Span, qui contient toute l'information de puissance liée à la cible, il est alors possible de localiser par un simple procédé de balayage ligne-colonne, les positions de ces maxima locaux appartenant à l'espace cible.

Après application d'un critère d'élimination, qui consiste en un simple seuillage à ne garder que les maxima significatifs, l'état de polarisation optimal est alors en mesure d'être déterminé à partir des états de polarisation caractéristique lié à chacun de ces maxima.

Afin de lever toute ambiguïté sur l'amplitude et la phase propre de chaque vecteur de polarisation caractéristique, l'état de polarisation est représenté par son rapport de polarisation circulaire [4].

A partir de la connaissance de tous les rapports de polarisation déterminés pour chaque maximum, le rapport de polarisation optimale pour l'ensemble de l'image est obtenu à partir d'un procédé de calcul basé sur la méthode du barycentre.

Une fois le rapport de polarisation optimale déterminé, il est alors aisé de reconstruire le vecteur de Jones associé, et de former ainsi la matrice unitaire de changement de base grâce à la relation (12).

La détermination des nouvelles Images Electromagnétiques Haute Résolution dans la base optimale s'effectue par un simple changement de base dans l'espace des états de polarisation permettant d'obtenir des images d'une cible radar qui soient performantes pour la discrimination des contributeurs élémentaires la composant.

Il est important de noter que la notion de "performance" est définie ici, d'une manière heuristique, par la quantité et la qualité de l'information contenue dans l'image.

### 5.5.1 - Détermination géométrique de l'état de polarisation optimale.

L'espace de travail que nous utilisons est la sphère de Poincaré, qui permet de faire correspondre d'une manière directe chacun de ses points avec un état de polarisation unique et physiquement réalisable.

La méthode utilisée, est basée sur l'étude de l'angle saillant  $2\gamma$ , qui possède la propriété intéressante d'être liée directement à la puissance totale de l'onde rétrodiffusée par la cible.

A partir de la connaissance de la matrice de rétrodiffusion spatiale liée à chaque maxi-

mun local, la base des vecteurs pseudo-propres diagonalisant la matrice [S] est alors déterminée en à partir de la résolution d'un problème aux valeurs propres. Le vecteur de Jones  $\underline{X}_1$  de la base orthonormale des vecteurs pseudo-propres ( $\underline{X}_1, \underline{X}_2$ ) détermine l'état de polarisation qui permet d'obtenir une puissance rétrodiffusée maximale dans le canal de co-polarisation  $\underline{X}_1 - \underline{X}_1$ . Cette puissance est égale à la magnitude de la cible ( $m^2$ ) et correspond au module de la plus grande valeur propre de la matrice [S].

Le vecteur de Jones  $\underline{X}(a, \alpha, \phi, \tau)$ , lié à l'état de polarisation de l'antenne de réception, est représenté sur la sphère de Poincaré par un point P. Considérons une onde incidente sur cette antenne de réception, représentée par le vecteur de Jones  $\underline{E}(b, \beta, \phi', \tau')$ , obtenu à partir de:

$$\underline{E} = [T] \underline{X} \quad (13)$$

où [T] est la matrice de rétrodiffusion spatiale caractéristique d'une partie quelconque de la cible. Cette onde est représentée sur la sphère de Poincaré par un point P'.

Définissons l'angle saillant  $2\gamma$  sous lequel est vu, du centre de la sphère, l'arc de cercle d'extrémités P et P'. La puissance totale de l'onde incidente reçue dans la base ( $\underline{X}_1, \underline{X}_2$ ) s'exprime par:

$$P_{\text{TOT}} = a^2 b^2 \cos^2(\gamma) \quad (14)$$

La puissance reçue dans le canal de co polarisation  $\underline{X} - \underline{X}$  s'exprime par la relation:

$$P_{XX} = \frac{1}{2} [\underline{g}(\underline{X})]^T [M] [\underline{g}(\underline{X})] = |T_{11}|^2 \quad (15)$$

où [M] est la matrice de Mueller liée à la matrice de rétrodiffusion [T].

La matrice de rétrodiffusion spatiale a l'inconvénient d'être dépendante de la phase absolue, ce qui peut être source d'erreurs fondamentales dans toute manipulation mathématique lors de l'oubli de la notion de cohérence.

La matrice de Mueller a l'avantage d'être réelle et indépendante de la phase absolue, puisqu'elle est liée à la notion de puissance et non à la notion de champ. Pour cela, toute manipulation mathématique peut être effectuée d'une manière tout à fait incohérente.

Considérons une cible composée de N contributeurs indépendants, isotropes en fréquence et suffisamment éloignés les uns des autres afin d'éviter tout phénomène de couplage et d'interaction électromagnétique. Dans ce cas la puissance totale rétrodiffusée dans le canal de co-polarisation  $\underline{X} - \underline{X}$ , par l'ensemble de la cible peut s'écrire:

$$P_{XX} = \frac{1}{2} [\underline{g}(\underline{X})]^T \left[ \sum_{i=1}^N [M_i] \right] [\underline{g}(\underline{X})] = \sum_{i=1}^N |T_{11}|^2 \quad (16)$$

L'objectif de la méthode est donc de déterminer l'état de polarisation, représenté par le vecteur de Jones  $\underline{X}$ , qui maximise la puissance  $P_{XX}$  rétrodiffusée dans le canal de co-polarisation  $\underline{X} - \underline{X}$ .

### 5.5.2 - Procédure de détermination.

Après avoir déterminé pour chaque maximum local le vecteur pseudo-propre  $\underline{X}_1$  qui lui est associé, un classement de ces maxima par ordre croissant est effectué en fonction de la valeur du SPAN correspondante. Ce classement détermine l'ordre d'application de la méthode.

Cette procédure est initialisée en affectant au vecteur de  $\underline{X}_{\text{opt}}$  le vecteur de polarisation  $\underline{X}_1$  lié au maximum local possédant la valeur du SPAN la plus élevée.

Dans ce cas la base des états de polarisation optimale ( $\underline{X}_{\text{opt}}, \underline{X}_{\text{opt}\perp}$ ) est confondue avec

la base des vecteurs pseudo-propres ( $\underline{X}_1, \underline{X}_2$ ) et la puissance reçue dans le canal de co-polarisation  $\underline{X}_{\text{opt}} - \underline{X}_{\text{opt}}$  est égale à la magnitude  $m_{(1)}^2$  lié à ce contributeur.

Considérons maintenant le deuxième maximum local, représenté par son vecteur de Stokes  $\underline{g}(\underline{X}_1)$  sur la sphère de Poincaré. En prenant le vecteur de Stokes  $\underline{g}(\underline{X}_{\text{opt}})$  comme vecteur de référence, il est alors possible de définir entre ces deux vecteurs, un angle saillant  $2\gamma$ . La longueur de l'arc séparant ces deux vecteurs est égale à  $2\gamma R$ , mais comme la sphère est prise de rayon unité, cette distance se réduit à la valeur  $2\gamma$ .

Le fait de rendre l'angle  $2\gamma$  nul a comme effet de faire coïncider de nouveau les deux vecteurs de Stokes  $\underline{g}(\underline{X}_{\text{opt}})$  et  $\underline{g}(\underline{X}_1)$ , c'est-à-dire de privilégier physiquement la puissance rétrodiffusée par ce deuxième contributeur.

Or le vecteur de polarisation  $\underline{X}_{\text{opt}}$  est déjà lié au contributeur précédent par la puissance  $m_{(1)}^2$  associée.

L'état de polarisation globale  $\underline{X}_{\text{opt}}$  lié à ces deux contributeurs est déterminé à partir d'un nouvel angle saillant  $2\gamma'$  satisfaisant la relation:

$$2\gamma' = \frac{m_{(2)}^2}{m_{(1)}^2 + m_{(2)}^2} 2\gamma \quad (17)$$

Le nouvel angle saillant  $2\gamma'$  est ainsi déterminé, et il est alors possible de retrouver le nouveau vecteur de polarisation  $\underline{X}_{\text{opt}}$  par construction géométrique.

Nous sommes maintenant en présence d'une nouvelle base de polarisation optimale ( $\underline{X}_{\text{opt}}, \underline{X}_{\text{opt}\perp}$ ) liée à ces deux contributeurs. Il reste

cependant à déterminer la puissance reçue dans ce nouveau canal de co-polarisation  $\underline{X}_{\text{opt}} - \underline{X}_{\text{opt}}$ .

Pour cela, il est aisé de déterminer l'état de polarisation des ondes rétrodiffusées par ces deux contributeurs lorsque ceux-ci sont éclairés par le vecteur de polarisation  $\underline{X}_{\text{opt}}$ ,

en utilisant la relation:

$$\underline{E} = [S] \underline{X}_{\text{opt}} \quad (18)$$

ou:

$$[\underline{g}(\underline{E})] = [M] [\underline{g}(\underline{X}_{\text{opt}})] \quad (19)$$

La puissance reçue dans le canal de co polarisation  $\underline{X}_{\text{opt}} - \underline{X}_{\text{opt}}$  est alors donnée par:

$$P_{\underline{X}_{\text{opt}} - \underline{X}_{\text{opt}}} = \frac{1}{2} [\underline{g}(\underline{X})]^T \left[ \sum_{i=1}^N [\underline{g}(\underline{E}_i)] \right] \quad (20)$$

Cette puissance est alors affectée au vecteur de polarisation  $\underline{X}_{\text{opt}}$  et prend valeur de "poids" lors de la détermination du nouvel angle saillant  $2\gamma'$  à l'étape suivante.

Considérons la procédure réitérée à l'ordre  $i$ . Le vecteur de polarisation optimale  $\underline{X}_{\text{opt}}$  a donc été déterminé à partir des  $(i-1)$  étapes précédentes, et le poids qui lui est affecté est égal à  $m_{\text{opt}}^2 = P_{\underline{X}_{\text{opt}} - \underline{X}_{\text{opt}}}$ .

Il est alors possible de définir entre les vecteurs de Stokes  $\underline{g}(\underline{X}_{\text{opt}})$  et  $\underline{g}(\underline{X}_i)$ , lié au maximum local  $n^{\circ}i$ , l'angle saillant  $2\gamma$ .

L'angle  $2\gamma'$  définissant le nouveau vecteur de polarisation optimale  $\underline{X}_{\text{opt}}$  lié cette fois

aux 1 contributeurs, est déterminé suivant:

$$2\gamma' = \frac{m_{(1)}^2}{m_{(1)}^2 + m_{opt}^2} 2\gamma \quad (21)$$

Une fois, le nouveau vecteur de polarisation  $\underline{X}_{opt}$  déterminé par construction géométrique à partir de la connaissance de l'angle  $2\gamma'$ , la puissance rétrodiffusée dans ce nouveau canal de co-polarisation  $\underline{X}_{opt} - \underline{X}_{opt}$  est égale à:

$$P_{\underline{X}_{opt} - \underline{X}_{opt}} = \frac{1}{2} [\underline{g}(\underline{X})]^T \left[ \sum_{j=1}^N [\underline{g}(\underline{E}_j)] \right] \quad (22)$$

La procédure est répétée pour tous les maxima locaux de l'image. Une fois terminée, les états de polarisation  $\underline{X}_{opt}$  et  $\underline{X}_{opt\perp}$  vont

permettre de définir une matrice unitaire de changement de base  $[U]_{opt}$ .

La détermination des nouvelles Images Electromagnétiques Haute Résolution dans la base de polarisation optimale, s'effectue par simple changement de base selon (12) dans l'espace des polarisations permettant d'obtenir les images de la cible radar où la puissance rétrodiffusée se trouve maximisée dans le canal de co-polarisation  $\underline{X}_{opt} - \underline{X}_{opt}$ .

Le synopsis de cette procédure est représenté figure n°8, en considérant la présence de N maxima locaux.

### 5.5.3 - Résultats.

Les Images Electromagnétiques Haute Résolution ainsi reconstruites sont présentées figure n°9.

L'examen de ces Images Electromagnétiques Haute Résolution, montre une fois de plus, que toute l'information relative à la cible complexe est contenue dans un seul canal co-polarisé correspondant au couple de polarisation émission-réception  $\underline{X}_{opt} - \underline{X}_{opt}$ .

La méthode utilisée n'a pas permis de diagonaliser la matrice image puisque l'état de polarisation déterminé correspond à l'état de polarisation optimale globale pour la cible vue dans son ensemble.

Cependant, cette méthode a permis de minimiser l'énergie reçue dans les canaux cross-polarisés, et maximiser celle contenue dans le canal co-polarisé correspondant au couple de polarisation  $\underline{X}_{opt} - \underline{X}_{opt}$  (-14,05dB au lieu de -15,14dB).

Le couple des états de polarisation optimale, représenté ici par les lettres X et Y, correspond à un couple de polarisations orthogonales purement elliptique.

Ce couple est représenté par le vecteur de Stokes  $\underline{g}(\underline{X}_{opt})$ :

$$\begin{cases} (g_0)_{opt} = 1 \\ (g_1)_{opt} = 0,457801 \\ (g_2)_{opt} = 0,887362 \\ (g_3)_{opt} = 0,058470 \end{cases} \quad (23)$$

qui est lié aux paramètres géométriques de l'ellipse de polarisation suivants:

$$\phi_{opt} = 31,36^\circ \text{ et } \tau_{opt} = 1,618^\circ$$

définissant un couple d'états de polarisation quasiment linéaire ( $31,36^\circ$ ) et possédant une assez faible ellipticité.

### 5.6 - Conclusion.

Au cours de ce chapitre, nous avons exposé une méthode permettant d'obtenir à partir de la connaissance des quatre Images Electromagnétiques Haute Résolution, une Image unique qui puisse contenir à elle seule, toute l'information relative à la cible, et qui soit donc "performante" au niveau de la discrimination des zones brillantes.

L'objectif était en fait de déterminer la base des états de polarisation "optimale" qu'il fallait appliquer aux antennes d'Emission et de Réception pour obtenir le maximum de puissance rétrodiffusée par la cible dans un des deux canaux de co-polarisation (XX ou YY).

Les résultats obtenus ont montré que le couple des états de polarisation optimale, représenté d'une manière générale par les lettres X et Y, correspond à un couple de polarisations orthogonales purement elliptique.

Ainsi, sans aucune connaissance de la cible, ou plutôt de la localisation de ses zones brillantes dans l'espace cible, il aurait été impossible d'agir physiquement a priori, sur les états de polarisation des antennes d'Emission et de Réception pour obtenir une telle image de la cible. Image qui peut être considérée, maintenant, comme performante pour la discrimination des contributeurs élémentaires de la cible radar.

## 6 - APPORT DU CONCEPT DE LA POLARIMETRIE DANS LA CLASSIFICATION DE CIBLES.

### 6.1 - Introduction.

En parallèle avec l'étude sur l'image électromagnétique haute résolution développée au chapitre précédent, sont venus se greffer les problèmes classiques de la reconnaissance des cibles, en vue de classer puis d'identifier les zones brillantes.

L'objectif consiste à déterminer qu'elles sont les caractéristiques physiques et géométriques de la cible qui induisent les points brillants localisés sur l'image électromagnétique haute résolution. Pour cela, est isolée à partir des quatre images radar, la zone contenant le point brillant à étudier. A partir des matrices de rétrodiffusion spatiales, il est possible de caractériser les formes géométriques de la cible canonique qui ont contribué à la formation du point brillant, grâce aux méthodes classiques de reconnaissance polarimétriques, basées notamment sur l'étude de la fourchette de polarisation qui conduit à la définition d'une classification des cibles dites simples, ou à partir des signatures polarimétriques définies par ZEBKER et VAN ZYL. Ces signatures polarimétriques représentent la variation de la puissance rétrodiffusée dans les canaux de co polarisation et de cross polarisation, en fonction des différentes combinaisons prises par les états de polarisation à l'émission et à la réception. Un jeu de signatures polarimétriques lié à des modèles de cibles canoniques permet l'identification du phénomène de rétrodiffusion observé par l'analyse de la typologie des courbes obtenues.

Toute l'information qu'il est possible d'extraire d'une cible est obtenue à partir de la matrice de rétrodiffusion. L'information contenue dans cette matrice décrit le processus complexe de l'interaction entre la structure de la cible et l'onde émise. La "théorie phénomé-



nologique des cibles radar" énoncée par J.R HUYNEN permet d'en dégager la structure et les propriétés caractéristiques de la cible. Dans ce chapitre, nous présentons le "diagramme structurel d'une cible", ainsi que les neuf "paramètres de Huynen" qui en découlent. A partir des réponses impulsionnelles de la cible, vue en spéculaire, nous montrons la corrélation existante entre les valeurs prises par ces paramètres et les caractéristiques physiques et géométriques des contributeurs de la cible.

A partir de la théorie phénoménologique, nous présentons une méthode "intelligente" de caractérisation de la structure d'une cible, basée sur l'utilisation des modèles de réseaux neuronaux.

## 7 - DESCRIPTION PHENOMENOLOGIQUE D'UNE CIBLE RADAR.

### 7.1 - Les paramètres de HUYNEN.

La matrice de rétrodiffusion [S] établit une relation linéaire entre les vecteurs de polarisation associés aux ondes incidente et rétrodiffusée telle que :

$$\underline{E}_s = [S] \underline{E}_i \quad (24)$$

Cette matrice représente le champ électromagnétique rétrodiffusé décrivant en amplitude et en phase une entité qui peut être dénommée "cible". Il convient en ce point de lever une ambiguïté qui est souvent source de confusion dans l'interprétation de la matrice de rétrodiffusion.

En effet, il ne faut pas oublier que cette matrice, une fois mesurée, fournit une représentation de ce que perçoit le radar, et que l'information qu'elle contient est altérée par la variation des paramètres d'observation mis en jeu (fréquence, état de polarisation, forme d'onde) ainsi que par la localisation de la cible dans son environnement et par sa position vis à vis du radar. La confusion généralement faite est de considérer la matrice de rétrodiffusion comme la réponse d'une "cible pure" à une excitation électromagnétique. Mais c'est oublier que la matrice [S] est dépendante de la phase absolue, ce qui signifie qu'elle résulte d'un processus complexe de sommation cohérente de tous les phénomènes électromagnétiques créés par la source d'émission dans l'environnement radar-cible.

Le but de la théorie phénoménologique est de caractériser la cible comme un "objet" de la façon la plus précise qu'il soit, autrement dit de discriminer et d'extraire cet "objet" de son environnement, en le considérant alors comme "débarassé" de toutes les altérations occasionnées par l'observation. L'objectif final de cette caractérisation est de déterminer à travers l'analyse du signal rétrodiffusé, une représentation de la cible qui soit non bruitée.

Pour cela, il est nécessaire d'utiliser une représentation en terme de puissance pour la description du phénomène de rétrodiffusion. L'avantage de cette représentation est l'élimination de la phase absolue de la cible, c'est-à-dire qu'elle fait appel à une notion de sommation non cohérente des phénomènes électromagnétiques. Il est alors possible d'interpréter plus aisément la contribution de chaque points brillants, considérés maintenant comme indépendants.

C'est le cas, par exemple, d'une cible placée dans deux environnements totalement différents. La cible reste toujours la même, alors que les matrices de rétrodiffusion mesurées sont tout à fait différentes à cause de

cette notion de sommation cohérente. En utilisant la représentation en puissance, il est alors plus aisé de discriminer la cible de ces deux environnements grâce à cette notion d'addition non cohérente, où la cible et les deux environnements sont alors considérés comme trois entités totalement indépendantes.

Ce principe de discrimination est à la base même du théorème de décomposition de J.R HUYNEN [5].

La matrice de réflexion de Stokes, ou Matrice de Mueller [M], établit une relation linéaire entre les vecteurs de Stokes associés aux ondes incidente et rétrodiffusée [4], avec:

$$[M] = [A]^* \left( [S] \otimes [S]^* \right) [A]^{-1} \quad (25)$$

$$\text{où: } [A] = \begin{bmatrix} 1 & 0 & 0 & 1 \\ 1 & 0 & 0 & -1 \\ 0 & 1 & 1 & 0 \\ 0 & j & -j & 0 \end{bmatrix} \quad (26)$$

J.R. HUYNEN a redéfini cette matrice de MUELLER, [5], avec:

$$[M_0] = \begin{bmatrix} A_0+B_0 & C & H & F \\ C & A_0+B & E & G \\ H & E & A_0-B & D \\ F & G & D & -A_0+B_0 \end{bmatrix} \quad (27)$$

où les coefficients  $A_0$ ,  $B_0$ , B, C, D, E, F, G,

et H sont connus sous le nom des "paramètres de HUYNEN", qui sont de la plus grande importance dans la théorie phénoménologique des cibles, car indépendants de tout modèle, donc applicables à tout type de cible. Sachant qu'il existe une corrélation très forte entre les valeurs prises par ces paramètres et les caractéristiques physiques et géométriques de la cible, il convient de rappeler brièvement leur signification:

- AO : générateur de symétrie de la cible.
- BO-B : générateur de la non-symétrie de la cible.
- BO+B : mesure de l'irrégularité de la cible.
- C : facteur de forme.
- D : indicateur de la forme locale.
- E : phénomène de la torsion de la cible.
- F : phénomène d'hélicité de la cible.
- G : couplage entre les parties symétriques et non-symétriques de la cible.
- H : orientation de la cible.

L'étude des paramètres de Huynen liés à une zone brillante permet une bonne approche dans la reconnaissance des caractéristiques physiques et géométriques de la cible élémentaire étudiée [4] puisqu'il existe une corrélation très forte entre les valeurs prises par les paramètres de Huynen et les caractéristiques physiques et géométriques de la cible.

### 7.2 - Identification de la structure d'une cible radar par la méthode des réseaux neuronaux.

A partir de la théorie phénoménologique de la cible, il est alors possible de concevoir une méthode "intelligente" de caractérisation de la structure d'une cible, permettant ainsi à un système radar de classer puis d'identifier l'objet. La méthode proposée repose sur l'utilisation des réseaux neuronaux, dont l'objectif consiste en une modélisation primaire de l'architecture du cerveau humain, dont le but est d'employer ses capacités d'apprentissage et de décision.

Par analogie avec le problème de la reconnaissance visuelle des formes, l'architecture

des réseaux de neurones mis en place pour la caractérisation de la structure de la cible, est calquée sur l'organisation du système visuel humain. Dans une telle architecture, chaque couche reçoit l'information de la couche précédente et transmet le résultat de sa décision vers la couche suivante. Les deux couches extrêmes correspondent à la couche qui reçoit ses entrées du milieu extérieur d'une part, et la couche qui fournit le résultat final d'autre part. Les couches intermédiaires sont appelées les couches cachées. La structure d'un réseau de neurones mono-couche est représentée figure n°10.

### 7.3- Définition du réseau de neurones.

La principale définition d'un réseau de neurones consiste à déterminer le nombre de neurones d'entrées, celui des couches cachées, et le nombre de sorties.

L'étude précédemment menée, a montré qu'il était tout à fait possible de caractériser la structure d'une cible à partir de la connaissance de la matrice de Mueller. L'information contenue dans cette matrice de puissance va donc imposer le nombre de neurones d'entrées à 16, correspondant aux seize coefficients contenus dans la matrice de Mueller.

Le nombre de sorties est par définition sans limite. Celui-ci est fixé à 6, correspondant au nombre de cibles canoniques définissant a priori la population des cibles test choisies arbitrairement.

Ayant choisi une structure de réseau mono couche (par analogie entre reconnaissance de cibles et perception visuelle), le nombre de neurones appartenant à la couche cachée est, de toute évidence assez délicat à déterminer. Si ce nombre est trop important, le réseau a tendance à dupliquer les éléments de la couche cachée. Si ce nombre est trop petit, le réseau requiert dans ce cas, un grand nombre d'itérations lors de l'apprentissage, et la précision finale n'est pas optimale. En étudiant pour chaque axone de sortie la sensibilité de l'erreur globale (E) à l'élimination de celui-ci, suivant:

$$S_{(k,j)} = E_{\left| WS_{(k,j)} = 0 \right|} - E_{\left| WS_{(k,j)} = WS_{(k,j)}^{(Finale)} \right|} \quad (28)$$

il est alors possible de déterminer le nombre optimal de neurones cachés pour que ceux-ci aient finalement une sensibilité voisine. Dans notre modèle, le nombre de neurones de la couche cachée est fixé à 10.

L'opération la plus délicate, lors de la définition du réseau de neurones, consiste à déterminer les exemples les plus appropriés pour l'apprentissage.

Pour cela, nous avons voulu faire figurer six types de cibles canoniques, liées chacune à une caractéristique particulière de la structure générale d'une cible. Les six cibles choisies sont la plaque, le dièdre, le dipôle horizontal, le dipôle vertical, ainsi que les deux hélices gauche et droite. Ces cibles sont représentatives des cibles linéaires, symétriques, isotropes ainsi que non-symétriques, illustrant soit un phénomène de rétrodiffusion directe soit un phénomène de rétrodiffusion multiple.

Les matrices de Mueller liées à ces cibles pures sont les suivantes:

$$[M_{\text{PLAQUE}}] = \begin{bmatrix} 1 & 0 & 0 & 0 \\ 0 & 1 & 0 & 0 \\ 0 & 0 & 1 & 0 \\ 0 & 0 & 0 & -1 \end{bmatrix} \quad [M_{\text{DIÈDRE}}] = \begin{bmatrix} 1 & 0 & 0 & 0 \\ 0 & 1 & 0 & 0 \\ 0 & 0 & -1 & 0 \\ 0 & 0 & 0 & 1 \end{bmatrix}$$

$$[M_{\text{DIP H}}] = \frac{1}{2} \begin{bmatrix} 1 & 1 & 0 & 0 \\ 1 & 1 & 0 & 0 \\ 0 & 0 & 0 & 0 \\ 0 & 0 & 0 & 0 \end{bmatrix} \quad [M_{\text{DIP V}}] = \frac{1}{2} \begin{bmatrix} 1 & -1 & 0 & 0 \\ -1 & 1 & 0 & 0 \\ 0 & 0 & 0 & 0 \\ 0 & 0 & 0 & 0 \end{bmatrix}$$

$$[M_{\text{HEL G}}] = \frac{1}{2} \begin{bmatrix} 1 & 0 & 0 & 1 \\ 0 & 0 & 0 & 0 \\ 0 & 0 & 0 & 0 \\ 1 & 0 & 0 & 1 \end{bmatrix} \quad [M_{\text{HEL D}}] = \frac{1}{2} \begin{bmatrix} 1 & 0 & 0 & -1 \\ 0 & 0 & 0 & 0 \\ 0 & 0 & 0 & 0 \\ -1 & 0 & 0 & 1 \end{bmatrix}$$

La phase d'apprentissage est la phase la plus importante car décisive des performances du réseau. Elle consiste à présenter séquentiellement aux neurones d'entrée les cibles canoniques à mémoriser. Pour chacune d'entre elles, la réponse observée est comparée à la réponse théorique attendue. Un algorithme d'apprentissage est mis en place qui vient modifier les coefficients synaptiques de façon à obtenir une réponse satisfaisante [4]. L'algorithme d'apprentissage utilisé, est l'algorithme de rétro propagation du gradient.

### 7.4 - Exemple d'application.

A partir de la connaissance des quatre images électromagnétiques haute résolution, il est possible de reconstruire la matrice de rétrodiffusion spatiale correspondant au contributeur que nous cherchons à caractériser.

La matrice de rétrodiffusion spatiale reconstruite, correspondant au dipôle orienté à 45°, est donnée par:

$$[S_{\text{DIP 45}}] = \begin{bmatrix} -1,1267 + j1,3248 & -1,1535 + j1,8903 \\ -1,0763 + j1,9175 & -1,3595 + j2,2022 \end{bmatrix}$$

A partir de cette matrice, il est possible de déterminer les "paramètres d'Euler" correspondants [4]. Ces paramètres prennent les valeurs suivantes:

$m^2$	Span	$\psi (^{\circ})$	$\tau (^{\circ})$	$\nu (^{\circ})$	$\gamma (^{\circ})$
19,4078	19,4825	50,45	1,688	75,66	12,77

Les paramètres de Huynen bruts correspondants, sont donnés par:

A0	B0	B	C	D
4,65545	5,11011	-4,6981	-1,8366	0,6802

E	F	G	H
-1,92709	0,57216	0,63114	9,5354

Si nous appliquons ces valeurs à l'entrée du processus de caractérisation nous obtenons les résultats suivants:

Sphère	Dièdre	Dip H	Dip V	HéliceG	HéliceD
1,334X	23,200X	77,675X	0,001X	71,231X	0,2812X

Nous pouvons constater que le système ne peut pas caractériser le dipôle orienté à 45°, puisqu'il présente des résultats faisant apparaître la présence d'un dipôle horizontal, d'une hélice gauche, ainsi que d'une cible du type dièdre. L'application directe des paramètres de Huynen bruts ne permet pas d'obtenir des résultats satisfaisants.

Au regard, des valeurs prises par les paramètres d'Euler, il se dégage une orientation de la cible autour de la ligne de visée du radar non nulle ( $\psi=50.4513^{\circ}$ ), ce qui est

confirmé par la forte valeur du paramètre H (H=9.53545).

Dans ce cas, il s'avère indispensable d'effectuer une opération de désorientation, afin d'éliminer l'angle d'orientation de la cible. Les paramètres de Huynen ainsi obtenus, sont alors égaux à:

A0	B0	B	C	D
4,65545	5,11011	5,07779	9,71074	-0,748

E	F	G	H
0,044409	0,57216	0,54860	0,0000

Les résultats obtenus après l'application du processus de caractérisation sont les suivants:

Sphère	Dièdre	Dip H	Dip V	HéliceG	HéliceD
100,0%	100,0%	100,0%	100,0%	100,0%	100,0%

Nous constatons que le modèle de réseaux neuronaux mis en place a été saturé, cet état peut s'expliquer par les valeurs assez élevées prises par les paramètres de Huynen par rapport à celles utilisées lors de l'apprentissage.

Afin d'atténuer les valeurs d'entrée, nous appliquons sur les paramètres de Huynen "désorientés" l'opération de normalisation en divisant chaque paramètre par la valeur du SPAN correspondant au dipôle orienté à 45°.

Les paramètres de Huynen "désorientés" et "normalisés" sont égaux à:

A0	B0	B	C	D
0,23920	0,26256	0,26090	0,49894	-0,038

E	F	G	H
0,00226	0,02839	0,02818	0,0000

Les résultats obtenus après l'application du processus de caractérisation sont les suivants:

Sphère	Dièdre	Dip H	Dip V	HéliceG	HéliceD
3,878%	2,393%	95,18%	0,000%	21,758%	0,4890%

La cible a donc été caractérisée comme un dipôle horizontal à 95%. Il ne faut pas oublier que l'angle d'orientation de la cible a été intégré aux états de polarisation émission réception, aussi, dans cette nouvelle base le radar perçoit maintenant le dipôle comme étant aligné ici, avec le vecteur de polarisation parallèle unitaire, d'où l'identification à un dipôle horizontal. L'angle d'orientation étant  $\psi=50.4^\circ$ .

Au vue des résultats obtenus au cours des différentes étapes de la caractérisation du dipôle orienté à 45°, il s'avère indispensable d'effectuer les opérations de désorientation et de normalisation sur les paramètres de Huynen bruts, afin de s'assurer d'une identification potentielle de la cible.

### 7.5 - Conclusion.

Dans ce chapitre, nous avons présenté une méthode originale de reconnaissance basée sur l'utilisation de modèles de réseaux neuronaux.

Il semble qu'un tel processus de caractérisation, utilisant les capacités d'apprentissage et de décision "équivalentes" à celles du cerveau humain, devienne rapidement un axe de recherche très prometteur.

Une étude plus approfondie de certains modules caractéristiques devrait permettre d'aboutir à la conception d'un processus de caractérisation "intelligent" des plus performants. Nous nous sommes limités jusqu'à présent à n'effectuer qu'une simple étude de faisabilité.

### 8 - CONCLUSION.

Dans cet article nous avons introduit le concept de la POLARIMETRIE dans le domaine de l'imagerie électromagnétique haute résolution afin d'améliorer le pouvoir de discrimination des contributeurs élémentaires d'une cible radar. Nous avons montré qu'il est possible de définir une matrice de rétrodiffusion spatiale, appartenant à l'espace cible, obtenue à partir de la valeur des énergies contenues dans les pixels des quatre images électromagnétiques.

L'apport du concept de la polarimétrie dans l'imagerie électromagnétique haute résolution se traduit par la détermination d'une image unique d'une cible, qui soit performante dans la discrimination de ses zones brillantes, et qui contienne toute l'information la concernant.

En parallèle avec l'étude sur l'image électromagnétique haute résolution sont venus se greffer les problèmes classiques de la reconnaissance des cibles, en vue de classifier puis d'identifier les zones brillantes. A partir de la théorie phénoménologique, nous avons défini une méthode "intelligente" de caractérisation de la structure d'une cible, basée sur l'utilisation des modèles de réseaux neuronaux.

L'évolution technologique considérable, ainsi que l'avance théorique des études sur la polarimétrie, sont à l'origine de cette expansion actuelle des recherches sur les applications potentielles de ce concept dans le domaine du radar.

### 9 - REMERCIEMENTS.

Les auteurs souhaitent exprimer leurs remerciements au CELAR (Centre Electronique de l'Armement, Division ASRE, BRUZ, FRANCE) sans qui, cette étude n'aurait pu être menée à bien.

### 10 - REFERENCES.

- [1] C. POUIT  
"Holographie radar".  
Revue de l'armement.  
N°59, pp 17-41, Février 1980.
- [2] C. POUIT, F. LE CHEVALIER  
"Imagerie par radar et synthèse tomographique".  
Revue du CETHEDC - Ondes et signal.  
N° 76, pp 119-132, 1983.
- [3] E. POTTIER, J. SAILLARD  
"Contribution de la Polarimétrie dans la discrimination de cibles radar. Application à l'imagerie électromagnétique haute résolution".  
Rapport final (1989), Convention n°009/41/88, OS n°01/SA AM  
IRESTE, Laboratoire S2HF.  
CELAR, Division ASRE/SRH/TE.

## [4] E. POTTIER

"Contribution de la Polarimétrie dans la discrimination de cibles radar. Application à l'imagerie électromagnétique haute résolution".  
Thèse de l'UNIVERSITE DE RENNES I.  
13 Décembre 1990.

## [5] J.R. HUYNEN

"Phenomenological theory of radar targets".  
Ph.D Dissertation.  
DRUKKERIJ BRONDER-OFFSET N.V.  
ROTTERDAM, 1970.

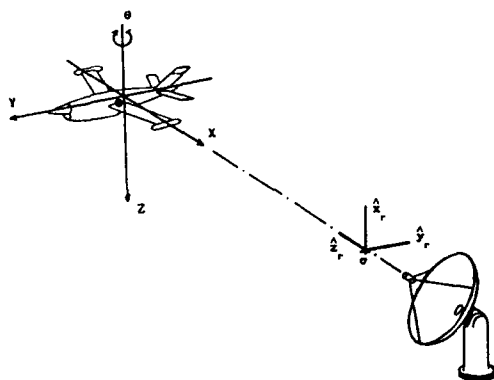


FIGURE N° 1

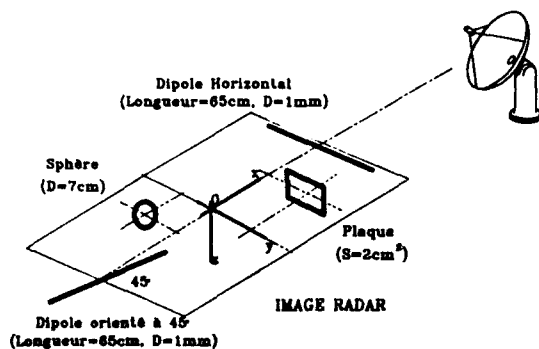


FIGURE N° 2

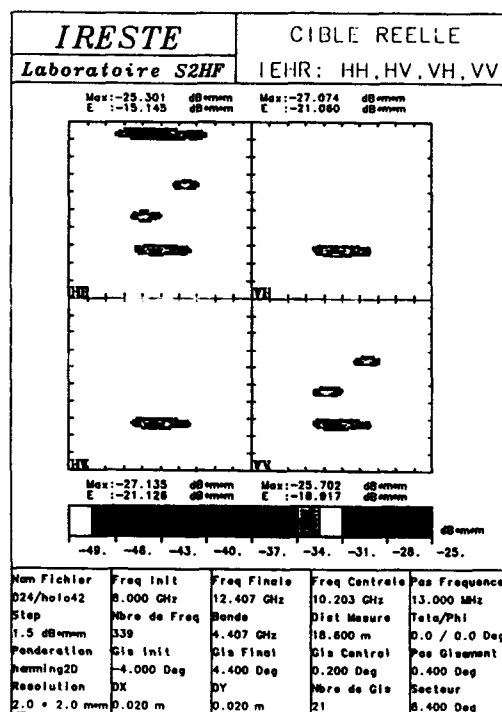


FIGURE N° 3

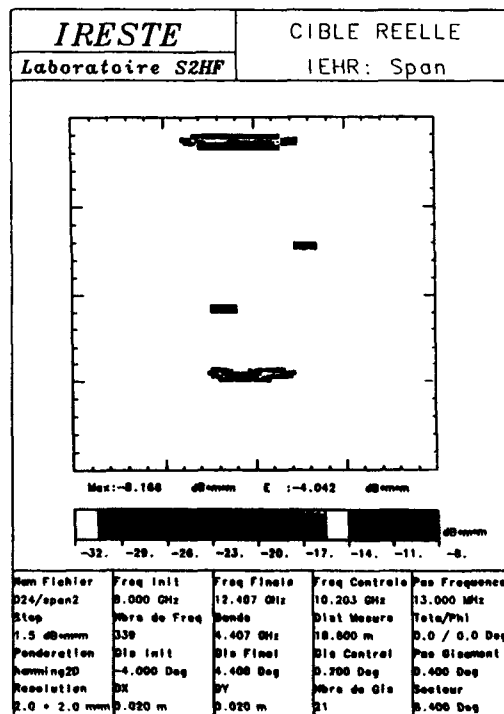


FIGURE N° 4

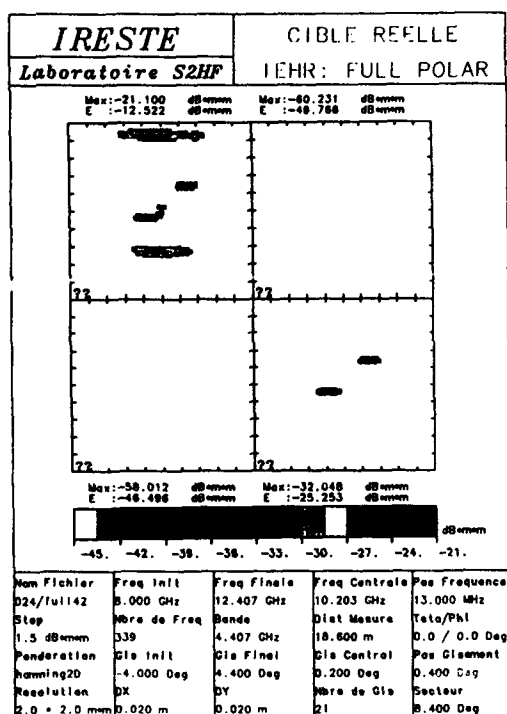


FIGURE N° 5

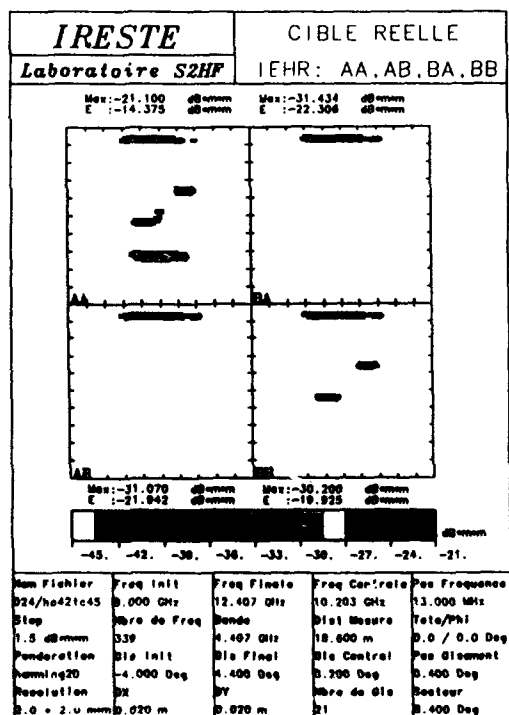


FIGURE N° 6

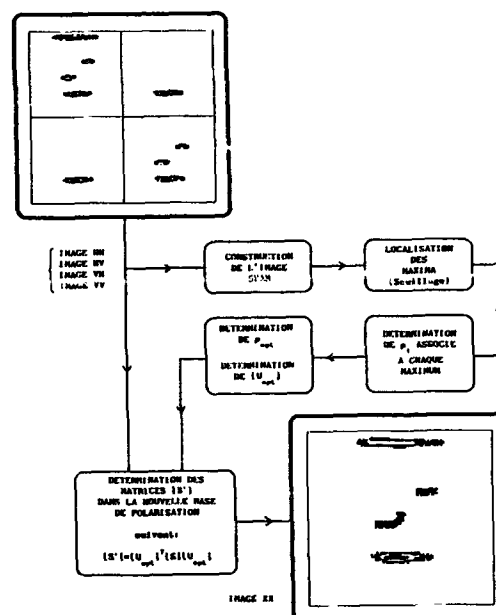


FIGURE N° 8

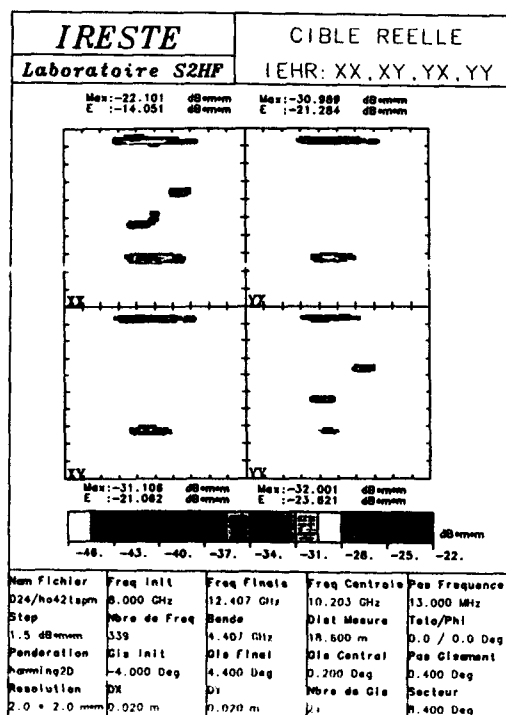


FIGURE N° 9

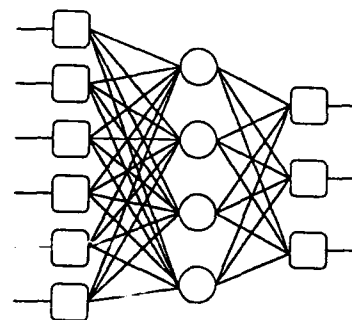


FIGURE N° 10

## DISCUSSION

R. Klemm, GE

Did you consider the effect of noise on classification?

## Author's Reply

Our measurements have been made in the Anechoic chamber of CELAR (Centre Electronique de l'Azimut, France) where we can consider there is no chamber noise. In this case our classification method gives good results. However, there is a polarimetric theory based on the "famous target decomposition theorems" (Huyren, Cloude, Holm, Barnes...) which allows to separate the target from its environment (clutter, noise, etc...). I have applied these decomposition theorems, but the classification results were not improved because we have not noise and the waves are completely polarized.

## UTILISATION DE LA POLARISATION POUR L' ANALYSE FINE DES CIBLES RADAR

C. TITIN-SCHNAIDER

ONERA  
29 avenue de la Division Leclerc  
92320 Chatillon - FRANCE

### RESUME

La prise en compte de la polarisation en imagerie holographique permet de restituer les matrices de rétrodiffusion associées à chaque pixel. La polarimétrie a été appliquée au niveau de ces matrices de rétrodiffusion élémentaires : les paramètres de la fourchette de polarisation ont été calculés.

Les résultats des tests effectués à partir de données expérimentales montrent que la polarimétrie appliquée au niveau des pixels de l'image radar haute-résolution d'une cible peut permettre d'identifier la nature de ces points brillants.

### 1. INTRODUCTION

Depuis une dizaine d'années des études sont menées à l'ONERA dans le but d'améliorer la discrétion des cibles radar. Dans cet objectif, l'ONERA s'est équipé de plusieurs bases de mesures électromagnétiques. Pour analyser ces mesures, une méthode d'imagerie bidimensionnelle baptisée "holographie radar" [1] a été mise au point. Elle permet d'obtenir la carte des positions et des niveaux de Surface Equivalente Radar (SER) des éléments les plus brillants de la cible étudiée. La nécessité d'une meilleure compréhension des phénomènes électromagnétiques réclame une analyse plus fine de ces images.

L'efficacité de la polarimétrie pour discriminer et identifier les cibles radar est bien connue [2]. Nos travaux s'inscrivent dans une évolution récente de la polarimétrie visant à réaliser une analyse fine des cibles. Dès 1985, une analyse polarimétrique de la réponse impulsionnelle d'une cible a été tentée [3]. Plus récemment, l'utilisation de la polarimétrie au niveau des pixels d'une image radar a été proposée [4], [5].

Le travail présenté examine, à partir de mesures effectuées en laboratoire, la possibilité d'utiliser la polarimétrie au niveau des pixels d'une image radar haute-résolution, dans le but de déterminer la nature des interactions électromagnétiques élémentaires.

L'holographie radar est rappelée et discutée. La polarisation est ensuite introduite en holographie radar. Divers jeux de paramètres permettant une identification en théorie de la polarisation sont examinés. Les paramètres choisis sont calculés à partir de données expérimentales obtenues sur des cibles complexes. Les résultats sont présentés.

### II. LES IMAGES HOLOGRAPHIQUES

L'hologramme  $S(\vec{k})$  d'une cible contient tous les signaux rétrodiffusés par cette cible pour toutes les valeurs possibles du vecteur d'onde :

$$\vec{k} = \frac{2\pi f}{c} \frac{\vec{r}}{r}$$

c'est à dire pour toutes les fréquences émises et tous les aspects possibles de la cible par rapport au radar.

La représentation holographique 3D [1] :

$$\mathcal{I}(\vec{x}) = \frac{1}{\pi^3} \int S(\vec{k}) e^{-j2\vec{k} \cdot \vec{x}} d\vec{k} \quad (1)$$

permet d'obtenir une image radar de la cible au moyen d'une transformée de Fourier 3D.

Les moyens de mesure mis en place à l'ONERA ne permettent pas d'obtenir l'hologramme complet d'une cible : l'hologramme est relevé en fonction de l'angle de gisement de la cible (elle tourne autour d'un axe vertical) et pour  $k_z = 0$  car le rayon radar est horizontal. La transformée de Fourier 2D de la partie mesurée de l'hologramme :

$$I(x, y) = \mathcal{F}(S(k_x, k_y)) = \int \mathcal{I}(x, y, z) dz \quad (2)$$

correspond à la projection complexe sur le plan  $z=0$  de  $\mathcal{I}(x, y, z)$ . La fonction  $I(x, y)$  est couramment appelée "image holographique".

Le modèle des points brillants facilite l'interprétation de la représentation holographique. Selon ce modèle, la cible est représentée par un nombre fini de centres rétrodiffusants indépendants et ponctuels.

Le signal rétrodiffusé par N points brillants est :

$$S(\vec{k}) = \sum_{i=1}^N s_i(\vec{k}) e^{j2\vec{k} \cdot \vec{x}_i} \quad (3)$$

sachant que le  $i^{\text{ème}}$  point brillant situé en  $\vec{x}_i$  renvoie un signal d'amplitude  $s_i(\vec{k})$ .

La transformée de Fourier étant une opération linéaire, l'image résultante est la somme complexe des images associées à chaque point brillant :

$$I(\vec{x}) = \sum_{i=1}^N I_i(\vec{x}) \quad (4)$$

avec :

$$\begin{aligned} I_i(\vec{x}) &= \frac{1}{\pi^2} \int s_i(\vec{k}) e^{-j2\vec{k} \cdot \vec{x}} d\vec{k} \\ &= \mathcal{F}(s_i(\vec{k})) \end{aligned} \quad (5)$$

Les points brillants sont généralement supposés "blancs" et isotropes : le signal renvoyé par chaque point brillant est indépendant de la fréquence d'analyse et de l'orientation de la cible.

Par conséquent, (5) devient :

$$I_i(\vec{x}) = s_i \delta(\vec{x} - \vec{x}_i) \quad (6)$$

où  $\delta(\vec{x})$  représente la distribution de Dirac.

L'image holographique s'écrit donc sous la forme :

$$I(\vec{x}) = \sum_{i=1}^N s_i \delta(\vec{x} - \vec{x}_i) \quad (7)$$

Dans le cadre du modèle des points brillants indépendants blancs et isotropes, la représentation "holographique" permet de restituer les amplitudes et les positions des points brillants.

Dans la pratique, l'hologramme est relevé sur un domaine réduit. L'intégrale (5) n'est plus véritablement une transformée de Fourier car elle est calculée sur le support borné  $(\{k_1, k_2\}, \{\theta_1, \theta_2\})$ . Elle peut être mise sous la forme :

$$I_i(\vec{x}) = \mathcal{F}(g(\vec{k}) s_i(\vec{k})) \quad (8)$$

avec :

$$g(\vec{k}) = \begin{cases} 1 & \text{pour } k \in \{k_1, k_2\} \text{ et } \theta \in \{\theta_1, \theta_2\} \\ 0 & \text{partout ailleurs} \end{cases}$$

Compte tenu des propriétés de la transformée de Fourier :

$$I_i(\vec{x}) = \mathcal{F}(s_i(\vec{k})) \otimes \mathcal{F}(g(\vec{k})) \quad (9)$$

l'image du point brillant est égale au produit de convolution de la transformée de Fourier de sa réponse  $s_i(\vec{k})$ , par la transformée de Fourier du support d'intégration  $g(\vec{k})$ .

Du fait de la limitation du domaine d'intégration, les points brillants n'ont plus une représentation ponctuelle. La tache correspondant à un point brillant est décrite par la fonction :

$$G(\vec{x}) = \mathcal{F}(g(\vec{k}))$$

Cette fonction s'écrit en coordonnées polaires :

$$G(\vec{x}) = \frac{1}{\pi^2} \int_{k_1}^{k_2} \int_{\theta_1}^{\theta_2} e^{-j2kr \cos(\theta-\psi)} k dk d\theta \quad (10)$$

si :  $\vec{k} = (k \cos \theta, k \sin \theta)$  et  $\vec{x} = (r \cos \psi, r \sin \psi)$

Le comportement de cette fonction peut être estimé en remplaçant le domaine d'intégration par un rectangle équivalent. On obtient :

$$G(\vec{x}) = \Delta k \bar{k} \Delta \theta e^{-j2\vec{k} \cdot \vec{x}} \frac{\sin(\Delta k x)}{\Delta k x} \frac{\sin(\bar{k} \Delta \theta y)}{(\bar{k} \Delta \theta y)} \quad (11)$$

avec :

$$\bar{k} = (k_2 + k_1)/2, \Delta k = k_2 - k_1, \Delta \theta = \theta_2 - \theta_1, \theta = 0$$

Si les points brillants sont blancs et isotropes, on a :

$$I(\vec{x}) = \sum_{i=1}^N s_i G(\vec{x}_i - \vec{x}) \quad (12)$$

L'image résultante peut être considérée comme la somme complexe des images correspondant à chaque point brillant. Des interférences sont susceptibles de se produire si les points brillants sont proches. La zone d'influence d'un point brillant dépend fortement de son niveau : un point brillant fort masque les points brillants plus faibles de son voisinage.

En holographie radar classique, on cherche à séparer les taches correspondant aux points brillants et à leur associer une SER. La SER d'un point brillant peut être faussée par les contributions des points voisins.

### III. LES IMAGES POLARIMÉTRIQUES

Le choix de la polarisation de l'antenne d'émission et de la polarisation de l'antenne de réception peut faire apparaître ou disparaître certains points brillants sur une image radar. La théorie de la polarisation considère que toute l'information concernant la cible est contenue dans sa matrice de rétrodiffusion. Des antennes susceptibles d'émettre et de recevoir deux polarisations orthogonales et dont les canaux d'émission et de réception sont étalonnés de façon cohérente permettent de mesurer la matrice de rétrodiffusion d'une cible. Des antennes polarisées rectilignement fonctionnant en polarisation horizontale (H) ou en polarisation verticale (V) sont généralement considérées. L'installation permet de relever la matrice de rétrodiffusion d'une cible pour toutes les fréquences de la bande émise et tous les aspects de la cible en rotation.

Les développements du paragraphe précédent se généralisent facilement.

Conformément au modèle des points brillants (3), la matrice de rétrodiffusion mesurée :

$$[S]_{(\vec{k})} = \sum_{i=1}^N [s_i]_{(\vec{k})} e^{j2\vec{k} \cdot \vec{x}_i} \quad (13)$$

s'exprime en fonction des matrices élémentaires de rétrodiffusion  $[s_i]_{(\vec{k})}$  de chaque point brillant.

L'ensemble des matrices de rétrodiffusion de la cible mesurées en fonction de la fréquence et de l'incidence permet de constituer son hologramme matriciel.

La représentation holographique (1) appliquée sur l'hologramme matriciel  $[S]_{(\vec{k})}$  permet de construire

l'image matricielle de la cible  $[I]_{(\vec{x})}$  :

$$[I]_{(\vec{x})} = \frac{1}{\pi^3} \int [S]_{(\vec{k})} e^{-j2\vec{k} \cdot \vec{x}} d\vec{k} \quad (14)$$

Si les points brillants sont supposés blancs et isotropes, les matrices élémentaires  $[s_i]$  sont constantes. De façon analogue à (7), on a :

$$[I]_{(\vec{x})} = \sum_{i=1}^N [s_i] \delta(\vec{x} - \vec{x}_i) \quad (15)$$

Le modèle des points brillants indépendants blancs et isotropes facilite l'interprétation de ces images : selon ce modèle, cette extension de l'imagerie holographique permet de restituer les positions et les matrices de rétrodiffusion de chaque point brillant.

Dans la pratique l'intégration (14) est effectuée sur un support limité. La distribution de Dirac est remplacée par la fonction de pondération  $G(\vec{x} - \vec{x}_i)$  :

$$[I]_{(\vec{x})} = \sum_{i=1}^N [s_i] G(\vec{x}_i - \vec{x}) \quad (16)$$

La même matrice de rétrodiffusion élémentaire est par conséquent associée à tous les pixels de la tache d'un même point brillant. Au niveau de chaque pixel, les matrices de rétrodiffusion élémentaires  $[s_i]$  pondérées par la fonction de pondération  $G$  s'additionnent (16). Le niveau des lobes secondaires de la fonction  $G$  peut avoir une incidence sur la qualité de la restitution des



matrices de rétrodiffusion élémentaires. Diverses méthodes d'apodisation dont les qualités et les limitations sont abondamment discutées dans la littérature peuvent être envisagées, si nécessaire. Les matrices de rétrodiffusion des points brillants forts et éloignés sont restituées. Pour étudier plus précisément un point brillant on a toujours la possibilité d'utiliser des absorbants pour masquer les contributions gênantes.

L'utilisation de la polarimétrie en imagerie holographique permet de générer les matrices de rétrodiffusion élémentaires associées à chaque pixel. L'application de la théorie de la polarisation au niveau des pixels correspondant aux taches des points brillants est donc envisageable.

#### IV. LA THEORIE DE LA POLARISATION

##### IV.1. Les cinq paramètres indépendants :

La théorie de la polarisation a fait l'objet de multiples publications depuis de nombreuses années. Elle a été formulée de façon cohérente par Huynen [2].

Les mesures en chambre anéchoïques sont déterministes. Les ondes considérées sont par conséquent complètement polarisées. Les états de polarisation possibles sont représentés par des points situés sur la surface de la Sphère de Poincaré.

Dans ces conditions de mesure, la validité du Principe de Réciprocité est généralement admise. Les matrices de rétrodiffusion considérées sont donc supposées symétriques et dépendent de cinq paramètres indépendants.

Plusieurs jeux de paramètres ont été proposés :

##### IV.2. Les polarisations caractéristiques :

Les polarisations caractéristiques d'une cible correspondent aux polarisations de l'onde incidente pour lesquelles la cible rétrodiffuse un maximum (MAX) ou un minimum (MIN) d'énergie sur la même polarisation (COPOL) ou sur la polarisation orthogonale (XPOL).

Pour une matrice de rétrodiffusion symétrique, les points représentatifs sur la Sphère de Poincaré des polarisations caractéristiques (figure 1) sont répartis sur le même grand cercle.

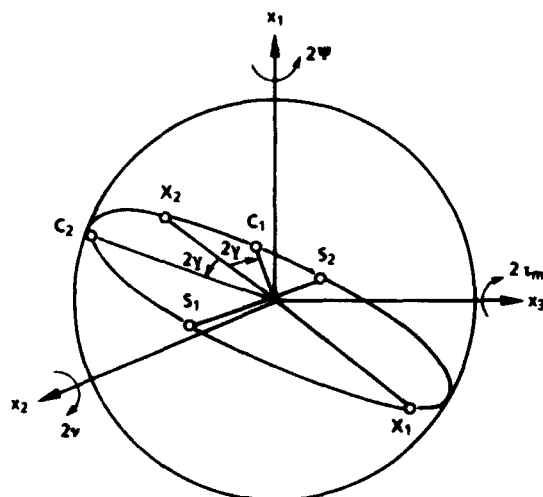


Figure 1 : Représentation de la fourchette de polarisation sur la sphère de Poincaré.

Les points  $X_1$  et  $X_2$  représentent les zéros croisés ou XPOL NULS ( $X_1$  correspond aussi au maximum copolaire ou COPOL MAX). Les points  $C_1$  et  $C_2$  correspondent aux zéros copolaires ou COPOL NULS. Les points  $S_1$  et  $S_2$  figurent les maxima croisés ou COPOL MAX. En reliant ces points au centre de la Sphère de Poincaré, on obtient un motif en forme de fourchette qui est généralement appelé "fourchette de polarisation". La fourchette de polarisation est complètement déterminée par la connaissance de deux polarisations caractéristiques particulières :

- le zéro de polarisation croisée correspondant au point  $X_1$
- le zéro copolaire correspondant au point  $C_1$

Les coordonnées sphériques des points  $X_1$  et  $C_1$  fournissent un jeu de cinq paramètres caractéristiques :

$\theta_{X_1}$ ,  $\tau_{X_1}$ ,  $\theta_{C_1}$ ,  $\tau_{C_1}$  et le rayon  $\mu$  de la sphère.

Le domaine de validité de ces paramètres est :

$$\begin{cases} 0 < \mu < \infty \\ -\pi/2 < \theta_{X_1} < \pi/2 \\ -\pi/4 < \tau_{X_1} < \pi/4 \\ -\pi/2 < \theta_{C_1} < \pi/2 \\ -\pi/4 < \tau_{C_1} < \pi/4 \end{cases} \quad (17)$$

##### IV.3. les paramètres de la fourchette de polarisation :

Huynen a montré que la matrice de rétrodiffusion  $S$  peut être mise sous la forme :

$$\mu e^{-i\psi} \sigma_3 e^{-i\tau_m} \sigma_2 e^{i\psi} \sigma_1 s_d e^{i\psi} \sigma_1 e^{-i\tau_m} \sigma_2 e^{-i\psi} \sigma_3 \quad (18)$$

$$\text{avec : } s_d = \begin{pmatrix} 1 & 0 \\ 0 & \tan^2 \gamma \end{pmatrix} \quad (19)$$

en fonction des matrices de Pauli :

$$\sigma_0 = \begin{pmatrix} 1 & 0 \\ 0 & 1 \end{pmatrix}, \sigma_1 = \begin{pmatrix} 1 & 0 \\ 0 & -1 \end{pmatrix}, \sigma_2 = \begin{pmatrix} 0 & 1 \\ 1 & 0 \end{pmatrix} \quad (20)$$

$$\text{et } \sigma_3 = \begin{pmatrix} 0 & -i \\ i & 0 \end{pmatrix}$$

Les cinq paramètres  $\mu$ ,  $\psi$ ,  $\tau_m$ ,  $\gamma$  et  $v$  mis en évidence par (18) et (19) permettent aussi de définir la fourchette de polarisation :

- l'angle  $2\gamma$  représente la demi-ouverture de la fourchette,
- les trois angles d'Euler  $2\psi$ ,  $2\tau_m$ ,  $2v$  permettent de positionner la fourchette dans l'espace,
- le paramètre  $\mu$  correspond au rayon de la sphère.

Ces paramètres sont reliés à certaines propriétés des cibles :

- l'angle  $\psi$  : donne l'orientation de la cible relativement à la polarisation dite horizontale, dans le plan perpendiculaire au rayon radar,

- l'angle  $\gamma$  : mesure la capacité de la cible à polariser le signal rétrodiffusé sur une polarisation particulière indépendante de la polarisation du signal incident (si  $\gamma = 0$ , la cible est polarisante ; si  $\gamma = \pi/4$ , la cible n'est pas polarisante),

- l'angle  $v$  : mesure la parité du nombre de réflexions (si  $v = 0$ , le nombre de réflexions est pair ; si  $v = \pi/4$ , il est impair),

- l'angle  $\tau_m$  : indique si la cible possède un plan ou un axe de symétrie contenant l'axe de visée du radar ( si  $\tau_m = 0$  la cible est symétrique ; si  $\tau_m = \pi/4$ , la cible n'est pas symétrique ),

- le paramètre  $\mu$  : donne l'amplitude maximale de l'onde rétrodiffusée par la cible .

Les domaines de validité de ces paramètres sont :

$$\begin{cases} -\pi/2 < \psi < \pi/2 \\ -\pi/4 < \tau_m < \pi/4 \\ -\pi/4 < \nu < \pi/4 \\ 0 < \gamma < \pi/4 \\ 0 < \mu < \infty \end{cases} \quad (21)$$

#### IV.4. Les paramètres de la matrice de Mueller:

La matrice de Mueller permet de représenter la cible en termes quadratiques . Huynen [2] a proposé de l'écrire sous la forme :

$$M_\psi = \begin{pmatrix} A_0+B_0 & F & C_\psi & H_\psi \\ F & -A_0+B_0 & G_\psi & D_\psi \\ C_\psi & G_\psi & A_0+B & E_\psi \\ H_\psi & D_\psi & E_\psi & -A_0-B_\psi \end{pmatrix} \quad (22)$$

Les termes de cette matrice s'expriment en fonction des cinq paramètres de la fourchette de polarisation , au moyen des relations :

$$\begin{aligned} H_\psi &= C \sin 2\psi + H \cos 2\psi \\ C_\psi &= C \cos 2\psi - H \sin 2\psi \\ G_\psi &= G \cos 2\psi - D \sin 2\psi \\ D_\psi &= G \sin 2\psi + D \cos 2\psi \\ E_\psi &= E \cos 4\psi + B \sin 4\psi \\ B_\psi &= -E \sin 4\psi + B \cos 4\psi \end{aligned} \quad (23)$$

et

$$\begin{aligned} A_0 &= Q f \cos^2 2\tau_m \\ B_0 &= Q (1 + \cos^2 2\gamma - f \cos^2 2\tau_m) \\ B &= Q (1 + \cos^2 2\gamma - f (1 + \sin^2 2\tau_m)) \\ C &= 2Q \cos 2\gamma \cos 2\tau_m \\ D &= Q \sin^2 2\gamma \sin 4\nu \cos 2\tau_m \\ E &= -Q \sin^2 2\gamma \sin 4\nu \sin 2\tau_m \\ F &= 2Q \cos 2\gamma \sin 2\tau_m \\ G &= Q f \sin 4\tau_m \\ H &= 0 \end{aligned} \quad (24)$$

avec :

$$Q = \frac{\mu^2}{8 \cos^4 \gamma} \quad (25)$$

$$f = 1 - \sin^2 2\gamma \sin^2 2\nu$$

La matrice de Mueller dépend de neuf paramètres  $A_0, B_0, B, F, C, H, G, D, E$ . Ces paramètres ne sont pas indépendants car ils sont liés par quatre relations . Huynen a montré que ces paramètres permettent de décrire certaines propriétés de la cible . Une analyse des valeurs prises par ces paramètres [3] a été tentée au niveau des réponses impulsionnelles .

Les valeurs de ces neuf paramètres ne sont pas définies sur des supports bornés . Une classification basée sur ce jeu de paramètres doit

faire appel à un algorithme . L'analyse de ces paramètres semble est mal adapté à une étape de validation . On verra (VI) que la matrice de Mueller (22) à (25) permet d'estimer simplement la précision avec laquelle les angles de la fourchette de polarisation peuvent être restitués .

#### IV.5. Paramètres choisis :

Pour étudier la possibilité d'utiliser la polarimétrie au niveau des matrices de rétrodiffusion élémentaires associées aux pixels des images holographiques , nous avons choisi de calculer les deux jeux de paramètres :

$$1 - \theta_{x_1}, \tau_{x_1}, \theta_{C_1}, \tau_{C_1}, \mu$$

ces paramètres sont déduits des polarisations caractéristiques XPOL NULS et COPOL NULS calculés à partir des matrices de rétrodiffusion élémentaires .

$$2 - \psi, \tau_m, \gamma, \nu, \mu$$

ces paramètres sont calculés à partir des matrices de Mueller élémentaires ; ils sont extraits des relations (23) à (25) .

Les paramètres significatifs en polarimétrie sont des angles définis sur des domaines limités , ce qui facilite une interprétation directe des résultats . Ces deux jeux décrivent la fourchette de polarisation de façon équivalente . Ils sont calculés par des méthodes différentes ce qui permet de contrôler la cohérence des résultats .

#### V - RESULTATS DES TESTS :

A partir de données expérimentales , les images holographiques de diverses cibles ont été calculées pour les quatre couples de polarisation émises et reçues HH , HV , VH et VV . Une analyse polarimétrique pixel par pixel de ces images n'est possible que si les matrices de rétrodiffusion élémentaires associées à chaque pixel sont reconstituées avec une précision suffisante . Pour chaque pixel appartenant aux taches figurant les points brillants , les jeux de paramètres significatifs  $(\theta_{x_1}, \tau_{x_1}, \theta_{C_1}, \tau_{C_1})$  et  $(\psi, \tau_m, \gamma, \nu)$  ont été calculés

Les coefficients de rétrodiffusion HH , HV , VH et VV des cibles ont été relevés sur la bande de fréquence 8.2 GHz à 12.4 GHz avec un pas de 100 MHz et pour une plage d'incidence de 25 degrés avec un pas de 0.9 degrés .

Diverses cibles ont été considérées .

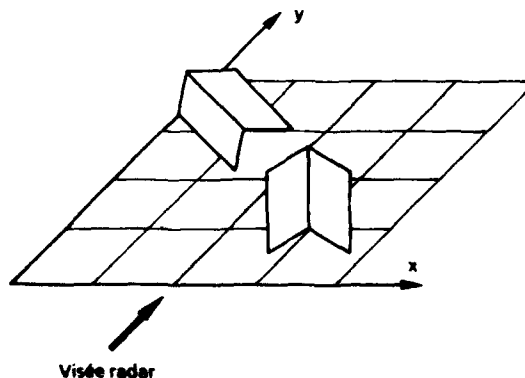


Figure 2 : Disposition des deux dièdres.

A titre d'illustration, les résultats concernant une cible composée de deux dièdres dont les orientations sont différentes (figure 2) sont présentés : un dièdre est vertical et l'autre dièdre est incliné de 45 degrés. Les images holographiques HH, HV, VH et VV de cette cible sont représentées sur la figure 3 : le dièdre vertical apparaît sur les images copolaires, par contre le dièdre incliné ne brille que pour les images en polarisation croisées.

Les paramètres caractéristiques ( $\theta_{x_1}$ ,  $\tau_{x_1}$ ,  $\theta_{C_1}$ ,  $\tau_{C_1}$ )

et ( $\psi$ ,  $\tau_m$ ,  $\gamma$ ,  $\nu$ ) ont été calculés pour tous les pixels correspondant à une énergie rétrodiffusée  $|S_{hh}|^2 + |S_{hv}|^2 + |S_{vh}|^2 + |S_{vv}|^2$  suffisante.

Les histogrammes construits à partir des valeurs des paramètres caractéristiques pour chaque point brillant sont présentés sur les figures 4 et 5.

On constate :

- un bon accord avec les valeurs théoriques,
- les valeurs de ces paramètres évoluent peu sur la tache d'un point brillant (III),
- les résultats concernant les paramètres déduits des polarisations caractéristiques sont parfaitement cohérents avec ceux qui sont relatifs aux paramètres de la fourchette de polarisation.

Cette méthode a aussi été appliquée à des cibles réelles. Pour un petit missile, la répartition de  $|p|$  a été représentée en niveaux de gris (figure 6) : le nez se comporte comme une sphère ( $|p|$  est indéterminé), on retrouve les ailes horizontales ( $|p|$  voisin de 0 degrés), la dérive verticale ( $|p|$  voisin de 90 degrés) et les dérives latérales légèrement relevées ( $|p|$  voisin de 20 degrés) ....

## VI ANALYSE DES RESULTATS :

Les écarts sur la restitution des angles de la fourchette de polarisation peuvent être facilement estimés en fonction des termes de la matrice de Mueller ((22) à (25)). Les termes de la matrice de Mueller sont des quantités réelles qui sont reliés aux termes complexes de la matrice de rétrodiffusion par des expressions quadratiques.

- l'angle  $\psi$  est déduit de :

$$\operatorname{tg} \psi = \frac{H_v}{C_v} \quad (26)$$

l'écart sur  $\psi$  est alors :

$$\Delta \psi = \frac{\sin 4\psi}{4} \left( \frac{\Delta H_v}{|H_v|} + \frac{\Delta C_v}{|C_v|} \right) < \frac{1}{4} \left( \frac{\Delta H_v}{|H_v|} + \frac{\Delta C_v}{|C_v|} \right) \quad (27)$$

- l'angle  $\tau_m$  est déduit de :

$$\operatorname{tg} \tau_m = -\frac{E}{D} = \frac{F}{C} \quad (28)$$

l'écart sur  $\tau_m$  est alors :

$$\Delta \tau_m = \frac{\sin 4\tau_m}{4} \left( \frac{\Delta E}{|E|} + \frac{\Delta D}{|D|} \right) < \frac{1}{4} \left( \frac{\Delta E}{|E|} + \frac{\Delta D}{|D|} \right) \quad (29)$$

- l'angle  $\gamma$  est déduit de :

$$p = \frac{A_0 + B_0}{\sqrt{C^2 + F^2}} = \frac{1 + \cos^2 2\gamma}{2 \cos 2\gamma} \quad (30)$$

l'écart sur  $\gamma$  est alors :

$$\Delta \gamma = \frac{\Delta p}{2 |\sin 2\gamma|} \left( 1 + \frac{p}{\sqrt{p^2 - 1}} \right) \quad (31)$$

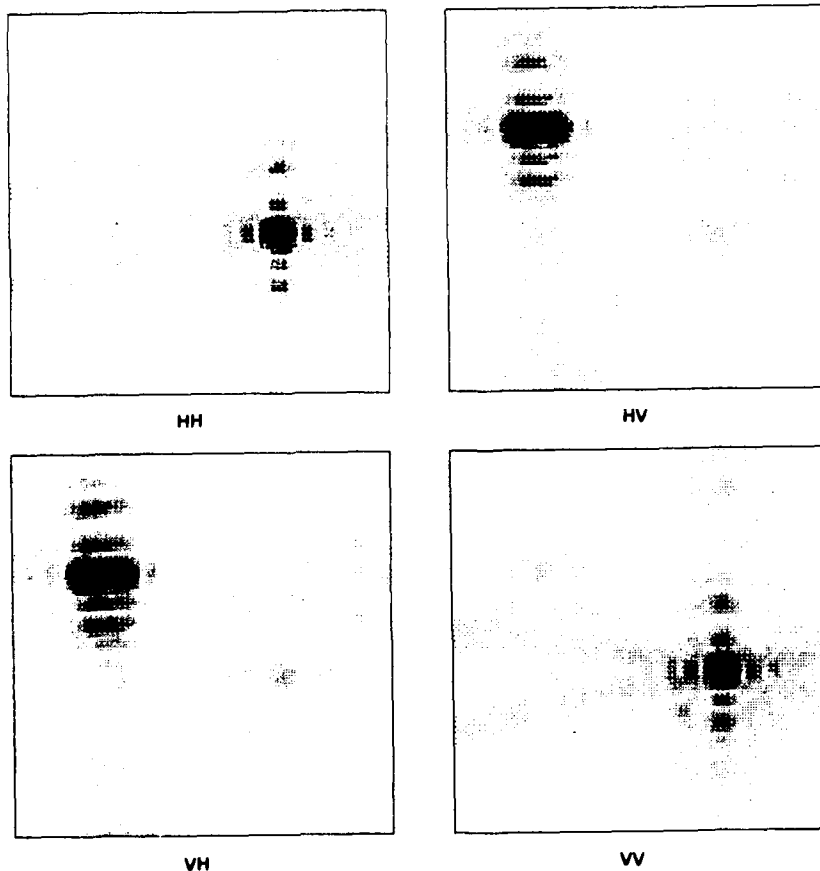


Figure 3 : quatre images holographiques des deux dièdres.

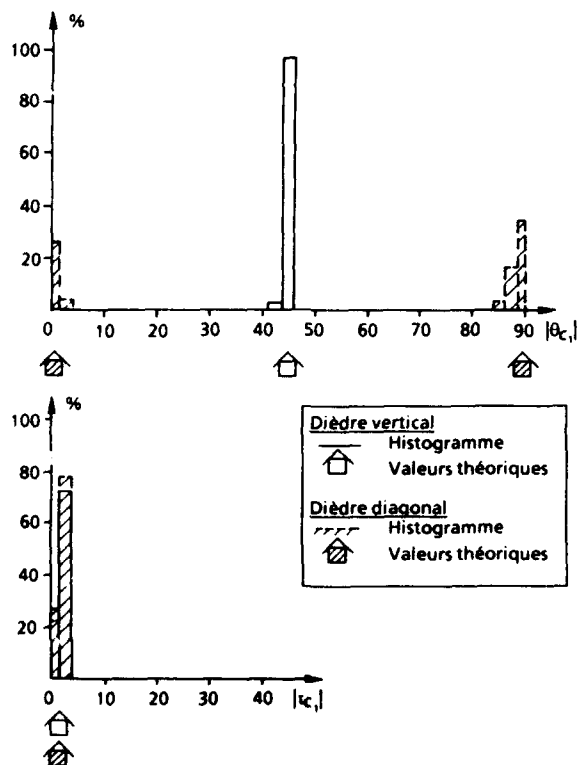
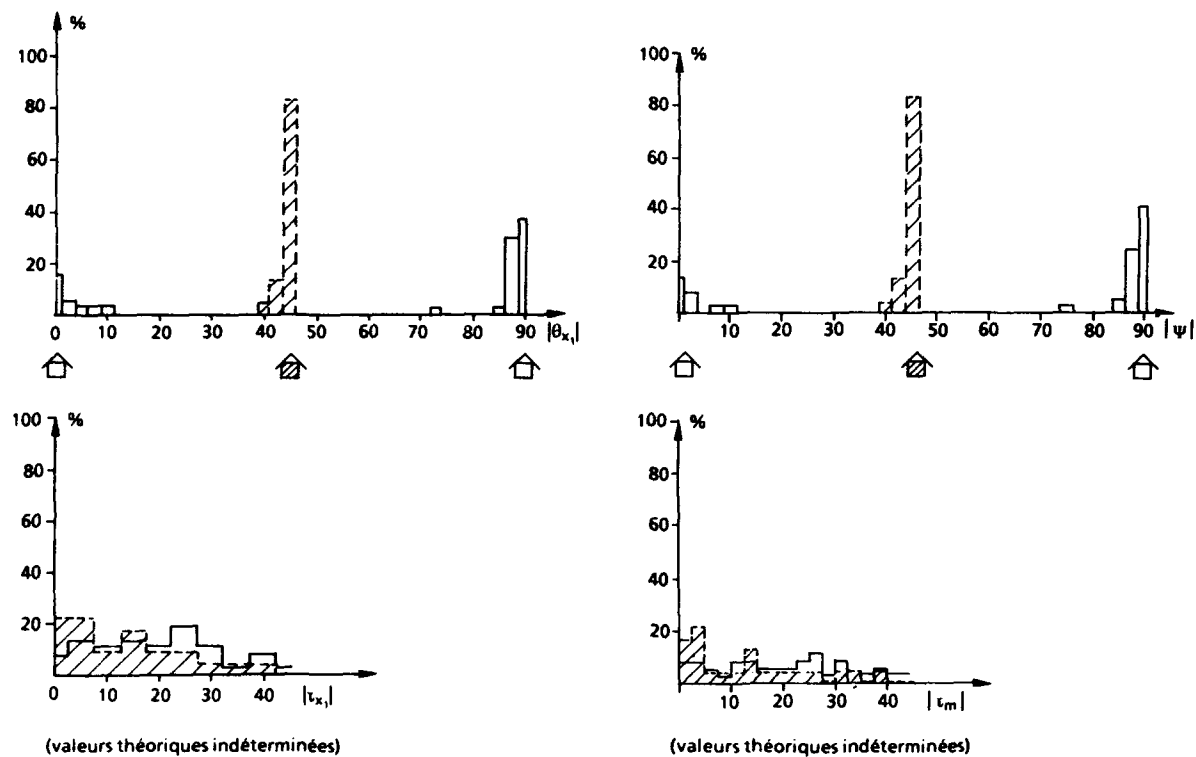


Figure 4 : Histogrammes des paramètres de polarisations caractéristiques  $\theta_{xr}$ ,  $\epsilon_{xr}$ ,  $\theta_{cr}$ , et  $\epsilon_{cr}$ , calculés sur les taches des points brillants correspondant aux deux dièdres.

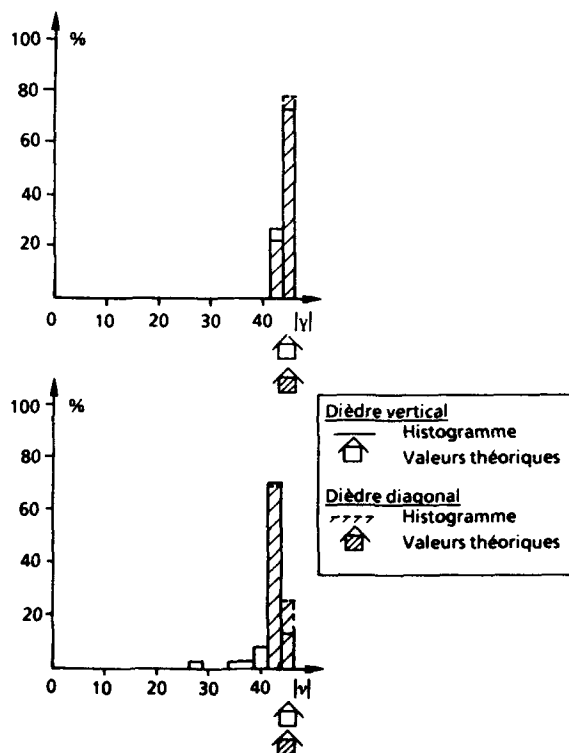


Figure 5 : Histogrammes des paramètres de la fourchette de polarisation  $\psi$ ,  $\epsilon_m$ ,  $\gamma$  et  $\nu$ , calculés sur les taches des points brillants correspondant aux deux dièdres.

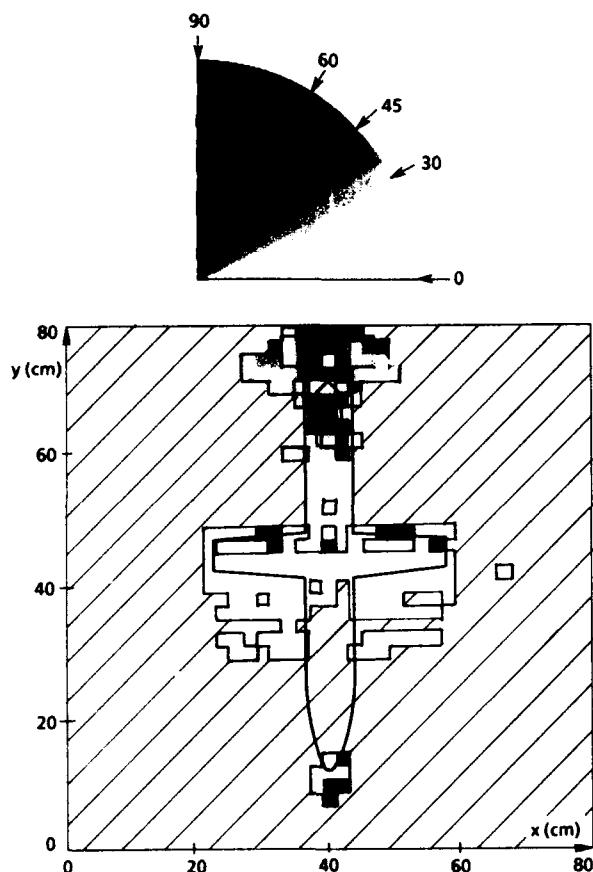


Figure 6 : Répartition de  $|\psi|$  en niveau de gris sur un petit missile.  $0 < |\psi| < 90$  degrés.

Si  $\gamma$  est petit ; alors  $p$  est voisin de 1 et  $\Delta\gamma$  croît très rapidement

Si  $\gamma$  tend vers  $\pi/4$ , alors  $p$  tend vers  $\infty$  et  $\Delta\gamma$  tend vers  $\Delta p$  qui vaut :

$$\frac{1}{\sqrt{C^2 + F^2}} (\Delta A_0 + \Delta B_0 + \frac{A_0 + B_0}{C^2 + F^2} (C \Delta C + F \Delta F)) \quad (32)$$

Pour un dièdre,  $\gamma$  est voisin de  $\pi/4$ , il est restitué avec une excellente précision.

Un fil fin horizontal peut être modélisé par un cylindre de très faible diamètre dont la matrice de rétrodiffusion satisfait les conditions :

$$S_{hh} > S_{vv} \gg S_{hv} \text{ et } S_{vh}$$

$$\text{Alors : } p = \frac{1+x^2}{1-x^2} \quad \text{si} \quad x^2 = \frac{S_{vv}S_{vv}^*}{S_{hh}S_{hh}^*} \quad (33)$$

On obtient :  $\gamma < 10$  degrés, si :  $|S_{vv}| < 0.03 |S_{hh}|$ .

A 10 GHz, le diamètre de ce fil doit être inférieur à 0.8 mm d'après [9, p123].

Cet exemple montre que l'interprétation des valeurs des paramètres caractéristiques n'est pas forcément immédiate. Elle nécessite une bonne connaissance des interactions électromagnétiques élémentaires et de leur modélisation.

Compte tenu de ces réserves, la pleine exploitation des paramètres de la fourchette de polarisation pour identifier la nature des points brillants d'une cible radar, peut être envisagée dans les conditions de mesures d'une chambre anéchoïque dotée d'une procédure d'étalonnage polarimétrique performante.

## VII. CONCLUSION:

L'introduction de la polarisation en holographie radar fournit des images haute-résolution associant à chaque pixel une matrice  $2 \times 2$  complexe. Le modèle des points brillants montre que ces matrices sont assimilables aux matrices de rétrodiffusion associées aux interactions électromagnétiques qui siègent au niveau des pixels. La polarimétrie a été appliquée au niveau de ces matrices de rétrodiffusion élémentaires : deux jeux de paramètres caractérisant la fourchette de polarisation ont été calculés pour tous les pixels correspondant à une énergie réémise suffisante.

Les résultats obtenus à partir de mesures expérimentales concernant diverses cibles, confirment que polarimétrie appliquée au niveau des pixels d'une image radar haute-résolution, peut permettre de déterminer la nature des points brillants.

## VIII. REFERENCES :

- [1] PÔUIT C.  
" Caractérisation des échos radar sur les avions ". La Recherche Aérospatiale, Mars-Avril 1980, n°2.
- [2] HUYNEN J.R.  
" Phenomenological theory of radar targets " Electromagnetic Scattering, Chapter 11, Academic Press, NY P.L.E. Yslenghi, 1978.
- [3] MANSON A.C., BOERNER W.M.  
" Interpretation of high-resolution polarimetric radar target down-range signatures using Kennaugh's and Huynen's target characteristic operator theories " Inverse Methods in Electromagnetic Imaging D. Reidel Publishing Company, 1985.
- [4] POTTIER E., SAILLARD J.  
" Contribution de la polarimétrie dans la Discrimination de Cibles Radar. Application à l'Imagerie Electromagnétique Haute - Résolution " Journées Internationales de la Polarimétrie Radar, Nantes, Mars 1990.
- [5] TITIN-SCHNAIDER C.  
" Polarimétrie appliquée à l'imagerie radar " La Recherche Aérospatiale, Avril 1991.
- [6] RUCK T., BARRICK D.E., STUART W.D., KRICHBAUM C.K.  
" Radar Cross Section Handbook ", Vol 1, Plenum Press. New York - London - 1970.

## Polarimetric Covariance Matrix Analysis of Random Radar Targets

E. Lüneburg, V. Ziegler, A. Schroth, K. Tragl  
German Aerospace Research Establishment (DLR)  
Institute for Radio Frequency Technology  
D-8031 Wessling/Obb.  
Germany

### Abstract

Two equivalent approaches for the description of mean polarimetric backscattering features of random radar targets exist, the so-called Mueller matrix and the covariance matrix approach.

The covariance matrix contains measurable radar observables and is directly related to the statistics of the elements of the scattering matrix which determines the instantaneous backscattering features of a target.

In this paper, a covariance matrix analysis for reciprocal random targets is performed by unitary similarity transformations preserving important polarimetric invariances.

The derivatives of covariance matrix elements with respect to the transmitter polarization reveal interesting functional relations between characteristic polarization states and covariance matrix elements. Analytical and numerical algorithms to determine optimal polarizations for cross- and copolar power are presented. The connection of the covariance matrix approach with the Mueller matrix formulation is shown in detail.

Polarimetric covariance matrix analysis is illustrated by polarimetric radar measurements of terrain, rain and man-made clutter and documented with according graphical evaluation.

### Polarimetric Covariance Matrix

Polarimetric backscatter target characteristics in the coherent case can be fully represented by the complex 2x2 Sinclair scattering matrix  $S$ . In the case of incoherent or partially coherent backscattering phenomena, however, a complete characterization of target backscattering characteristics is given by the 4x4 real Mueller matrix  $M$ , see [1] [2] [3].

Alternatively, a very promising approach to partially coherent radar polarimetry is the polarimetric covariance matrix concept [4] [5] [6]. The polarimetric covariance matrix directly contains measurable radar observables such as scattered power in orthogonally polarized radar channels and cross correlations between the two channels.

For backscattering from reciprocal targets the scattering matrix  $S$  will be symmetric  $S = S^T$ , if a common orthogonal polarization basis is used (backscatter alignment convention). It is convenient to introduce a target feature vector in the arbitrary orthonormal  $\{A, B\}$  basis of the form [5]

$$\Omega(AB) = [S_{AA} \quad \sqrt{2} S_{AB} \quad S_{BB}]^T \quad (1)$$

The polarimetric covariance matrix corresponding to this feature vector is defined as

$$\Sigma(AB) = \langle \Omega(AB) \Omega(AB)^+ \rangle = \begin{bmatrix} \langle |S_{AA}|^2 \rangle & \sqrt{2} \langle S_{AA} S_{AB}^* \rangle & \langle S_{AA} S_{BB}^* \rangle \\ \sqrt{2} \langle S_{AB} S_{AA}^* \rangle & 2 \langle |S_{AB}|^2 \rangle & \sqrt{2} \langle S_{AB} S_{BB}^* \rangle \\ \langle S_{BB} S_{AA}^* \rangle & \sqrt{2} \langle S_{BB} S_{AB}^* \rangle & \langle |S_{BB}|^2 \rangle \end{bmatrix} \quad (2)$$

In eq. (2)  $^+$  denotes the Hermitian adjoint and angular brackets indicate temporal (spatial) ensemble averaging assuming stationarity (homogeneity) of the random scattering medium.

$\Sigma(AB)$  is a semi-definite Hermitian matrix that contains all second order moments of the target scattering coefficients. For a deterministic target, spatial or temporal ensemble averaging as indicated by angular brackets  $\langle \cdot \rangle$  becomes obsolete.  $\Sigma(AB)$  has rank 1 in this particular case.

The transition from a particular reference basis, e.g. the  $\{H, V\}$  basis, to a general  $\{A, B\}$  basis is provided by the unitary  $^T$  congruence [8] [9].

$$S(AB) = U^T S(HV) U \quad (3)$$

where  $U$  is an element of  $SU_2$  (unitary unimodular group of dimension 2). Here use is made of the restricted form [5] [6] [7] [9] [13]

$$U = U(\rho) = \frac{1}{\sqrt{1 + \rho \rho^*}} \begin{bmatrix} 1 & -\rho^* \\ \rho & 1 \end{bmatrix} = (\hat{e}_A, \hat{e}_B) \quad (4)$$

The columns of  $U$  are the new orthonormal polarization vectors  $\hat{e}_A$  and  $\hat{e}_B$  expressed in the old  $\{H, V\}$  basis.  $\rho$  is the so-called complex polarization ratio which completely determines the geometric parameters  $\varphi$  (orientation angle) and  $\tau$  (ellipticity) of the polarization ellipse according to

$$\rho = \frac{\cos(2\tau) \sin(2\varphi) + j \sin(2\tau)}{1 + \cos(2\tau) \cos(2\varphi)} \quad (5)$$

and conversely

$$\varphi = \frac{1}{2} \arctan \left[ \frac{2\operatorname{Re}\{\rho\}}{1 - \rho\rho^*} \right] + \pi \pmod{\pi} \quad (6)$$

$$\tau = \frac{1}{2} \arcsin \left[ \frac{2\operatorname{Im}\{\rho\}}{1 + \rho\rho^*} \right] \quad (7)$$

For  $\rho = 0$  ( $\varphi = 0$ ,  $\tau = 0$ ) follows  $U(0) = I = [\hat{e}_H, \hat{e}_V]$ .

The feature vector now transforms in accordance with

$$\Omega(AB) = T(\rho)\Omega(HV) \quad (8)$$

with the unitary unimodular 3x3 matrix

$$T(\rho) = \frac{1}{(1 + \rho\rho^*)} \begin{bmatrix} 1 & \sqrt{2}\rho & \rho^2 \\ -\sqrt{2}\rho^* & (1 - \rho\rho^*) & \sqrt{2}\rho \\ \rho^{*2} & -\sqrt{2}\rho^* & 1 \end{bmatrix} \quad (9)$$

and

$$T(\rho) T^\dagger(\rho) = I \quad (10)$$

$$\det T(\rho) = 1 \quad (11)$$

It should be noted that the norm of  $\Omega$  is a target invariant with respect to the transformation of eq. (8)

$$\|\Omega\|^2 = \operatorname{span} S = \operatorname{trace} S^\dagger S = \text{invariant} \quad (12)$$

In order to guarantee the unitarity of  $T(\rho)$  and the transformation invariance of  $\|\Omega\|$  a factor  $\sqrt{2}$  was introduced in the definition of the second component of  $\Omega$ . Note  $T(0) = I$ . Since  $\rho$  is the only variable we denote  $\Sigma(AB) \equiv \Sigma(\rho)$  and  $\Sigma(HV) \equiv \Sigma(0) \equiv \Sigma_0$ ; correspondingly for  $\Omega$ .

The general polarimetric covariance matrix now reads

$$\begin{aligned} \Sigma &\equiv \Sigma(\rho) = \langle \Omega(\rho) \Omega^\dagger(\rho) \rangle \\ &= T(\rho) \langle \Omega_0 \Omega_0^\dagger \rangle T^\dagger(\rho) \\ &= T(\rho) \Sigma_0 T^\dagger(\rho) \end{aligned} \quad (13)$$

and is obtained from  $\Sigma_0$  by means of an unitary similarity transformation.

Writing the covariance matrix  $\Sigma$  in the form

$$\Sigma(\rho) = \begin{bmatrix} P_{co}^A(\rho) & \sqrt{2} R_x^A(\rho) & R_{co}(\rho) \\ \sqrt{2} R_x^A(\rho)^* & 2 P_x(\rho) & \sqrt{2} R_x^B(\rho)^* \\ R_{co}(\rho)^* & \sqrt{2} R_x^B(\rho) & P_{co}^B(\rho) \end{bmatrix} \quad (14)$$

its main diagonal directly contains mean backscattered copolar powers  $P_{co}^A(\rho)$ ,  $P_{co}^B(\rho)$  and mean crosspolar power  $P_x(\rho)$  as a function of the complex polarization ratio  $\rho$ .  $R_x^A(\rho)$  and  $R_x^B(\rho)$  will denote the correlation of backscattered orthogonal wave components if polarization A or B is transmitted. Finally,  $R_{co}(\rho)$  signifies the correlation of the copolar scattering coefficients  $S_{AA}$  and  $S_{BB}$ .

Once the covariance matrix has been measured in one basis, e.g.  $\Sigma_0$  in the  $\{H, V\}$  basis, it can easily be determined analytically for any other basis. Explicit expressions for the elements of  $\Sigma(\rho)$  in the form of polynomials in  $\rho$  and  $\rho^*$  have been given in reference [5].

Plotting the mean power return and signal correlations as functions of the complex polarization ratio  $\rho$  or of the geometrical polarization parameters  $\tau$  and  $\varphi$  (cf. eqs. (6) and (7)) yields the familiar polarimetric signatures. Some typical examples for different random targets are shown below.

Similar signatures can be obtained for

- degree of coherence

$$\mu_{AB}(\rho) = \frac{|R_x^A(\rho)|}{\sqrt{P_{co}^A(\rho) P_x(\rho)}} \quad (15)$$

- degree of polarization

$$P_{AB}(\rho) = \frac{([P_{co}^A(\rho) - P_x(\rho)]^2 + 4|R_x^A(\rho)|^2)^{\frac{1}{2}}}{P_{co}^A(\rho) + P_x(\rho)} \quad (16)$$

as function of  $\rho$  [1][5]. Note that

$$0 \leq \mu_{AB}(\rho) \leq P_{AB}(\rho) \leq 1 \quad (17)$$

Since for deterministic targets  $\mu_{AB} = P_{AB} \equiv 1$ , values of  $\mu_{AB}$ ,  $P_{AB}$  less than one emphasize the depolarizing properties of random (fluctuating) targets.

The polarization state described by  $-1/\rho^*$  is orthogonal to a polarization state characterized by the complex polarization ratio  $\rho$ . It can be shown that

$$\begin{aligned} \Sigma(-\frac{1}{\rho^*}) &= \begin{bmatrix} P_{co}^B(\rho) & -\frac{\rho}{\rho^*} \sqrt{2} R_x^B(\rho) & \frac{\rho^2}{\rho^{*2}} R_{co}(\rho)^* \\ -\frac{\rho^*}{\rho} \sqrt{2} R_x^B(\rho)^* & 2 P_x(\rho) & -\frac{\rho}{\rho^*} \sqrt{2} R_x^A(\rho)^* \\ \frac{\rho^{*2}}{\rho^2} R_{co}(\rho)^* & -\frac{\rho^*}{\rho} \sqrt{2} R_x^A(\rho) & P_{co}^A(\rho) \end{bmatrix} \\ &\stackrel{(18)}{=} \begin{bmatrix} P_{co}^B(\rho) & -\frac{\rho}{\rho^*} \sqrt{2} R_x^B(\rho) & \frac{\rho^2}{\rho^{*2}} R_{co}(\rho)^* \\ -\frac{\rho^*}{\rho} \sqrt{2} R_x^B(\rho)^* & 2 P_x(\rho) & -\frac{\rho}{\rho^*} \sqrt{2} R_x^A(\rho)^* \\ \frac{\rho^{*2}}{\rho^2} R_{co}(\rho)^* & -\frac{\rho^*}{\rho} \sqrt{2} R_x^A(\rho) & P_{co}^A(\rho) \end{bmatrix} \end{aligned}$$

This leads to the following interchannel relations

$$P_{co}^A(-\frac{1}{\rho^*}) = P_{co}^B(\rho) \quad (19)$$

$$|R_x^A(-\frac{1}{\rho^*})| = |R_x^B(\rho)| \quad (20)$$

and symmetry relations

$$P_x(-\frac{1}{\rho^*}) = P_x(\rho) \quad (21)$$

$$|R_{co}(-\frac{1}{\rho})| = |R_{co}(\rho)|. \quad (22)$$

The polarimetric covariance matrix  $\Sigma$  of a reciprocal target contains in general nine independent parameters, namely three real power values and three complex cross-correlations. Since  $\Sigma$  is Hermitian and positive semi-definite the eigenvalues of  $\Sigma$  are real and non-negative:  $0 \leq \lambda_1 \leq \lambda_2 \leq \lambda_3$ . Whenever necessary the eigenvalues of a general matrix  $M$  will be denoted by  $\lambda_i(M)$  ( $i=1,2,\dots$ ).

The field of values of a general matrix  $A \in \mathbb{C}^{n \times n}$  is defined as the set  $F(A)$  of complex numbers [18]

$$F(A) = \{(Ax, x) | x^+ x = 1\} \quad (23)$$

For a Hermitian matrix like the covariance matrix  $\Sigma$  it can be shown that

$$F(\Sigma) = F(\Sigma_0) = [\lambda_1, \lambda_3] \quad (24)$$

where  $[\lambda_1, \lambda_3]$  denotes the segment from  $\lambda_1$  to  $\lambda_3$  on the real axis.

Setting  $x = e_1 = [1, 0, 0]^T$  and similarly  $x = e_2$  and  $x = e_3$  the following bounds become immediately evident from eq. (14):

$$0 \leq \lambda_1 \leq P_{co}^A(\rho), 2P_x(\rho), P_{co}^B(\rho) \leq \lambda_3 \leq \|\Omega_0\|^2 \quad (25)$$

In general, minimal and maximal eigenvalues  $\lambda_1, \lambda_3$  of  $\Sigma$  cannot be realized by  $P_{co}^A(\rho), 2P_x(\rho), P_{co}^B(\rho)$ , however, since the transformation matrix  $T(\rho)$  of eq. (9) represents a restricted subset of all  $3 \times 3$  unitary unimodular matrices. In other words: notwithstanding the fact that it is always possible to diagonalize the Hermitian matrix  $\Sigma$  by means of an unitary similarity transformation, it may not be possible to do so with the restricted subset given by eq. (9). Hence

$$0 \leq \lambda_1 \leq \min_{\rho} P_{co}^A(\rho) \leq P_{co}^A \leq \max_{\rho} P_{co}^A(\rho) \leq \lambda_3 \leq \|\Omega_0\|^2 \quad (26)$$

and similarly for  $P_{co}^B$  and  $P_x$ .

The target invariant eigenvalues of the covariance matrix  $\lambda_i$  ( $i=1,2,3$ ) comprise interesting information on random target polarimetric backscattering features.

- The smallest eigenvalue  $\lambda_1$  indicates the degree of randomness of the target. For a deterministic target  $\Sigma_0 = \Omega_0 \Omega_0^+$  and invoking the spectral theorem of matrix algebra [18] one obtains immediately  $\lambda_1 = \lambda_2 = 0$  and  $\lambda_3 = \|\Omega_0\|^2$ . In this case, so-called null-polarizations exist, as detailed for instance by Agrawal et al. [13], producing vanishing power returns for the copolar or crosspolar radar channel. Random targets, on the other hand, have a non-vanishing minimum eigenvalue  $\lambda_1$  ( $\text{rank}(\Sigma) = 3$ ) and, therefore, only minimisation rather than complete suppression of mean backscattered power can be achieved by appropriate choice of the transmitter polarization. Note the substantial differences for rain (nearly deterministic) and chaff (truly random) as shown in Figure 3 and Figure 5.

- The eigenvalue difference

$$\Delta\lambda = \lambda_{\max} - \lambda_{\min} = \lambda_3 - \lambda_1 \quad (27)$$

of extremal eigenvalues  $\lambda_3, \lambda_1$  of the covariance matrix determines the range in which the mean power return  $P_{co}^A(\rho)$  and  $2P_x(\rho)$  can be varied by polarimetric means. The actual difference may be even smaller as outlined in connection with eq. (26). A similar indicator called coefficient of variation (ratio of minimum to maximum received power) has been introduced by van Zyl [3].

- From (13) follows that

$$\begin{aligned} \text{trace } \Sigma &= \text{trace } \Sigma_0 = \text{trace } \langle \Omega \Omega^+ \rangle = \langle \text{trace } \Omega \Omega^+ \rangle \\ &= \langle \|\Omega\|^2 \rangle = \langle \text{span } S \rangle \\ &= \langle |S_{HH}|^2 \rangle + 2\langle |S_{HV}|^2 \rangle + \langle |S_{VV}|^2 \rangle \\ &= \lambda_1(\Sigma) + \lambda_2(\Sigma) + \lambda_3(\Sigma) \end{aligned} \quad (28)$$

is a polarization invariant quantity giving the total backscattered power in the four polarization configurations of a particular orthogonal basis.

### Characteristic Polarizations Functional Relations

Characteristic polarizations comprise the location of polarization states for local and global maxima and minima (optimal polarizations) and for saddle points in the polarization state space of power and correlation signatures.

Following a procedure developed by Tragl et al. [12], cf. also [5], these extrema can be found by taking the derivative of the covariance matrix  $\Sigma$  with respect to  $\rho$  and equating it to zero.

From eq. (13) follows

$$\frac{\partial \Sigma(\rho)}{\partial \rho} = \frac{\partial T(\rho)}{\partial \rho} \Sigma_0 T(\rho)^+ + T(\rho) \Sigma_0 \frac{\partial T(\rho)^+}{\partial \rho} \quad (29)$$

Differentiation of eq. (10) yields

$$\frac{\partial T(\rho)}{\partial \rho} T(\rho)^+ + T(\rho) \frac{\partial T(\rho)^+}{\partial \rho} = 0 \quad (30)$$

and, hence, expressing  $\Sigma_0$  in eq. (29) by  $\Sigma(\rho)$

$$\frac{\partial \Sigma(\rho)}{\partial \rho} = T_D(\rho) \Sigma(\rho) - \Sigma(\rho) T_D(\rho) \quad (31)$$

with

$$\begin{aligned} T_D(\rho) &:= \frac{\partial T(\rho)}{\partial \rho} T(\rho)^+ \\ &= \frac{1}{1 + \rho \rho^*} \begin{bmatrix} -\rho & 0 & 0 \\ -\sqrt{2} & 0 & 0 \\ 0 & -\sqrt{2} & \rho \end{bmatrix} \end{aligned} \quad (32)$$

Explicitly, the derivatives of copolar and crosspolar powers can be expressed as follows



$$\frac{\partial P_{co}^A(\rho)}{\partial \rho^*} = \frac{2}{(1 + \rho \rho^*)} R_x^A(\rho) = 0 \quad (33)$$

$$\frac{\partial P_x(\rho)}{\partial \rho^*} = \frac{1}{(1 + \rho \rho^*)} (R_x^B(\rho)^* - R_x^A(\rho)) = 0 \quad (34)$$

$$\frac{\partial P_{co}^B(\rho)}{\partial \rho^*} = -\frac{2}{(1 + \rho \rho^*)} R_x^B(\rho)^* = 0 \quad (35)$$

From eqs. (15) and (33) it can be seen that copolar power optimal characteristic polarizations correspond to a vanishing degree of coherence  $\mu_{AB}$ . In other words, if a copolar power characteristic polarization state is transmitted then the backscattered orthogonal wave components are mutually incoherent. In this case the degree of polarization assumes the simple form [1]

$$P_{AB} = \frac{|P_{co}^A - P_x|}{P_{co}^A + P_x} \quad (36)$$

Derivatives of the various correlation functions can be determined similarly. For instance, the derivative of the absolute value of the copolar correlation function can be expressed as

$$\frac{\partial |R_{co}(\rho)|}{\partial \rho^*} = \frac{R_{co}(\rho)}{|R_{co}(\rho)|} \left( \frac{\partial P_x(\rho)}{\partial \rho^*} \right)^* = 0 \quad (37)$$

This quantity is of particular interest in radar meteorology as described by Jameson [16] and Balakrishnan and Zrnic [17] (canting effects of hydrometeors, hail size inferences). From eq. (37) follows that optimal polarizations of the copolar correlation  $R_{co}(\rho)$  coincide with those of the crosspolar power functions  $P_x(\rho)$ .

The extremal conditions which determine characteristic transmitter polarizations for specific covariance matrix elements (radar observables) can be solved by standard numerical techniques either directly in the complex plane or by reducing the problem to the numerical solution of two coupled nonlinear equations by separating real and imaginary parts, see Tragl [5]. For the cross- and co-polar power optimization problem, however, more elegant solution methods will be presented in the following.

### Crosspolar Power

Denoting the column vectors of the transformation matrix  $T^1(\rho)$ , cf. eq. (9), as

$$T^1(\rho) = [\hat{z}_1(\rho), \hat{z}_2(\rho), \hat{z}_3(\rho)] \quad (38)$$

with the normalized 2-parametric complex vector

$$\hat{z}_2(\rho) = [-\sqrt{2}\rho, 1 - |\rho|^2, \sqrt{2}\rho^*]^T / (1 + |\rho|^2) \quad (39)$$

the crosspolar power term  $P_x(\rho)$  can be expressed from eqs. (13) and (14) as

$$P_x(\rho) = \frac{1}{2} \hat{z}_2(\rho)^+ \Sigma_0 \hat{z}_2(\rho) \quad (40)$$

Rather than optimizing this Hermitian quadratic form with a complex vector  $\hat{z}_2$  that is constrained due to the special form of eq. (39) it is possible to introduce an unconstrained real vector  $\hat{v}(\rho)$  of the form

$$\hat{v}(\rho) = [1 - \rho \rho^*, 2 \operatorname{Re} \rho, 2 \operatorname{Im} \rho]^T / (1 + |\rho|^2) \quad (41)$$

by the  $\rho$ -independent linear transformation

$$\hat{v}(\rho) = Q \hat{z}_2(\rho) \quad (42)$$

with the unitary matrix

$$Q = \frac{1}{\sqrt{2}} \begin{bmatrix} 0 & \sqrt{2} & 0 \\ -1 & 0 & 1 \\ j & 0 & j \end{bmatrix}, \quad Q Q^+ = I \quad (43)$$

Hence,  $P_x(\rho)$  can be written as

$$P_x(\rho) = \frac{1}{2} \hat{v}^T(\rho) A_0 \hat{v}(\rho) \quad (44)$$

with the Hermitian matrix

$$A_0 = Q \Sigma_0 Q^+ \quad (45)$$

and the constraint

$$\hat{v}^T \hat{v} = 1 \quad (46)$$

Splitting up  $A_0$  into its symmetric and skew-symmetric parts and taking into account that only the symmetric part contributes to the quadratic form yields

$$P_x(\rho) = \frac{1}{2} \hat{v}^T(\rho) \operatorname{Re} A_0 \hat{v}(\rho) = \frac{1}{2} F(\operatorname{Re} A_0) \quad (47)$$

where

$$\operatorname{Re} A_0 = \frac{1}{2} (A_0 + A_0^*) = \frac{1}{2} (A_0 + A_0^T) \quad (48)$$

The extremal values of the quadratic form eq. (45) can be found by calculating the eigenvalues  $\lambda_i(\operatorname{Re} A_0)$ ,  $i = 1, 2, 3$ , of  $\operatorname{Re} A_0$ . The optimal polarization ratios  $\rho$  can then be determined from the corresponding normalized real eigenvectors via eq. (41). According to eq. (41), eigenvectors with opposite signs lead to orthogonal polarization states characterized by  $\rho$  and  $-1/\rho^*$ , i.e. pairs of orthogonal polarizations attain the same crosspolar power value as indicated already in eq. (21), cf. [12]. Note that  $\operatorname{trace} \operatorname{Re} A_0 = \operatorname{trace} A_0 = \operatorname{trace} \Sigma_0$ . Explicit expressions for the elements of the symmetric matrix  $\operatorname{Re} A_0$  read

$$\begin{aligned}
[\text{Re}A_0]_{11} &= 2\langle |S_{HV}|^2 \rangle \\
[\text{Re}A_0]_{12} &= \text{Re}\{\langle S_{HV} S_{VV}^* - \langle S_{HH} S_{HV}^* \rangle\} \\
[\text{Re}A_0]_{13} &= \text{Im}\{\langle S_{HV} S_{VV}^* - \langle S_{HH} S_{HV}^* \rangle\} \\
[\text{Re}A_0]_{22} &= 1/2 (\langle |S_{HH}|^2 \rangle + \langle |S_{VV}|^2 \rangle \\
&\quad - 2 \text{Re}\{\langle S_{HH} S_{VV}^* \rangle\}) \\
[\text{Re}A_0]_{23} &= -\text{Im}\{\langle S_{HH} S_{VV}^* \rangle\} \\
[\text{Re}A_0]_{33} &= 1/2 (\langle |S_{HH}|^2 \rangle + \langle |S_{VV}|^2 \rangle \\
&\quad + 2 \text{Re}\{\langle S_{HH} S_{VV}^* \rangle\}) .
\end{aligned} \quad (49)$$

Invoking a general result of Weyl [21] on the eigenvalues of a sum of Hermitian matrices one finds

$$\lambda_1(A_0) \leq \lambda_1(\text{Re}A_0) \leq \lambda_2(A_0) \leq \lambda_3(\text{Re}A_0) \leq \lambda_3(A_0) \quad (50)$$

For a deterministic target (coherent case)  $\lambda_1(\text{Re}A_0) = 0$  due to  $\text{rank}(\text{Re}A_0) = 2$  and, hence,  $\min_{\rho} P_x(\rho) = 0$ . This corresponds to Takagi's factorization of the symmetric scattering matrix  $S$  [21].

Writing

$$\frac{1}{2} \text{Re}A_0 = M_{11} I - Q_0 \quad (51)$$

where

$$M_{11} = 1/4 \text{trace Re}A_0 = 1/4 \text{trace } \Sigma_0 \quad (52)$$

$$Q_0 = 1/4 (\text{trace } \Sigma_0 I - 2 \text{Re}A_0) \quad (53)$$

the crosspolar power expression  $P_x(\rho)$  assumes the form

$$\begin{aligned}
P_x(\rho) &= M_{11} - \hat{v}^T(\rho) Q_0 \hat{v}(\rho) \\
&= \mathbf{g}_1^T(\rho) \mathbf{M} \mathbf{g}_1(\rho)
\end{aligned} \quad (54)$$

$\mathbf{g}$  is the Stokes vector for the transmitting antenna polarization

$$\mathbf{g}(\rho) = [1 \quad \hat{v}^T(\rho)]^T \quad (55)$$

and  $\mathbf{g}_1$  is the Stokes vector for the receiving antenna polarization

$$\mathbf{g}_1(\rho) = [1 \quad -\hat{v}^T(\rho)]^T \quad (56)$$

$\mathbf{g}_1(\rho)$  is orthogonal (antipodal) to  $\mathbf{g}(\rho)$ , i.e.  $\mathbf{g}_1 \cdot \mathbf{g} = 0$ .

In eq. (54)  $\mathbf{M}$  denotes the symmetric Stokes reflection (Mueller) matrix

$$\mathbf{M} = [\mathbf{M}_{\psi}]_{h,i}^{1,4} = \begin{bmatrix} M_{11} & 1/2 b_0^T \\ 1/2 b_0 & Q_0 \end{bmatrix} \quad (57)$$

which can be represented as, cf. e.g. [9]

$$\mathbf{M} = (\mathbf{A}^{-1})^T \langle \mathbf{S} \otimes \mathbf{S}^* \rangle \mathbf{A}^{-1} \quad (58)$$

with

$$\mathbf{A} = \begin{bmatrix} 1 & 0 & 0 & 1 \\ 1 & 0 & 0 & -1 \\ 0 & 1 & 1 & 0 \\ 0 & j & -j & 0 \end{bmatrix} \quad (59)$$

Here  $\otimes$  indicates the Kronecker (tensor) product. Note that

$$\begin{aligned}
M_{11} &= \text{trace} Q_0 = M_{22} + M_{33} + M_{44} \\
&= 1/4 \text{trace } \Sigma_0
\end{aligned} \quad (60)$$

and hence

$$\text{trace} \mathbf{M} = M_{11} + \text{trace} Q_0 = 1/2 \text{trace } \Sigma_0 \quad (61)$$

Thus, a connection between the covariance matrix approach and the Mueller matrix formulation for the crosspolar power expressions has been derived.

In eq. (54)  $P_x(\rho)$  does not depend upon the term  $b_0/2$ . This corresponds to the fact, that  $P_x(\rho)$  is dependent only on the elements of the matrix  $\text{Re}A_0$ . Furthermore, since in eq. (47)  $\hat{v}(\rho)$  can be replaced by  $-\hat{v}(\rho)$ , the Stokes vectors  $\mathbf{g}(\rho)$  and  $\mathbf{g}_1(\rho)$  can be interchanged in eq. (54).

#### Copolar Power

The copolar power term  $P_{\infty}^A(\rho)$  assumes the form

$$P_{\infty}^A(\rho) = \hat{z}_1(\rho)^+ \Sigma_0 \hat{z}_1(\rho) \quad (62)$$

with

$$\hat{z}_1(\rho) = [1, \sqrt{2} \rho^*, \rho^{*2}]^T / (1 + |\rho|^2) \quad (63)$$

Applying the same transformation matrix  $\mathbf{Q}$  of eq. (43) to  $\hat{z}_1(\rho)$  now yields

$$\mathbf{Q} \hat{z}_1(\rho) = \frac{1}{\sqrt{2}} [\hat{x}(\rho) + j\hat{y}(\rho)] \quad (64)$$

with the real orthogonal normalized vectors

$$\begin{aligned}
\hat{x}(\rho) &= [2 \text{Re} \rho, \text{Re}^2 \rho - \text{Im}^2 \rho - 1, 2 \text{Re} \rho \text{Im} \rho]^T \\
&\quad / (1 + |\rho|^2)
\end{aligned} \quad (65)$$

$$\begin{aligned}
\hat{y}(\rho) &= [-2 \text{Im} \rho, -2 \text{Re} \rho \text{Im} \rho, \text{Re}^2 \rho - \text{Im}^2 \rho + 1]^T \\
&\quad / (1 + |\rho|^2)
\end{aligned} \quad (66)$$

$P_{\infty}^A(\rho)$  can now be expressed in the following form

$$P_{co}^A(\rho) = \frac{1}{2} \hat{x}^T(\rho) \text{Re} A_0 \hat{x}(\rho) + \frac{1}{2} \hat{y}^T(\rho) \text{Re} A_0 \hat{y}(\rho) + \hat{y}^T(\rho) \text{Im} A_0 \hat{x}(\rho) \quad (67)$$

The matrix  $\text{Im} A_0 = -j(\Lambda_0 - \Lambda_0^T)/2$  is real and antisymmetric and has the general form

$$\text{Im} A_0 = \begin{bmatrix} 0 & b_{03} & -b_{02} \\ -b_{03} & 0 & b_{01} \\ b_{02} & -b_{01} & 0 \end{bmatrix} \quad (68)$$

with

$$b_{01} = \frac{1}{2} (\langle |S_{HH}|^2 \rangle - \langle |S_{VV}|^2 \rangle) \quad (69)$$

$$b_{02} = \text{Re}\{\langle S_{HV} S_{VV}^* \rangle + \langle S_{HH} S_{HV}^* \rangle\} \quad (70)$$

$$b_{03} = \text{Im}\{\langle S_{HV} S_{VV}^* \rangle + \langle S_{HH} S_{HV}^* \rangle\} \quad (71)$$

It is easily seen that with  $b_0 = [b_{01}, b_{02}, b_{03}]^T$

$$\text{Im} A_0 \hat{x}(\rho) = \hat{x}(\rho) \times b_0 \quad (72)$$

where  $\times$  denotes the usual vector product. Thus

$$\begin{aligned} \hat{y}^T \text{Im} A_0 \hat{x} &= \hat{y} \cdot (\hat{x} \times b_0) = (\hat{y} \times \hat{x}) \cdot b_0 \\ &= \hat{v} \cdot b_0 = \hat{v}^T b_0 = b_0^T \hat{v} \end{aligned} \quad (73)$$

since

$$\hat{v}(\rho) = \hat{y}(\rho) \times \hat{x}(\rho) \quad (74)$$

The matrix

$$O = \{\hat{x}(\rho), \hat{y}(\rho), \hat{v}(\rho)\} \quad (75)$$

is obviously orthogonal  $OO^T = I$ .

Hence the trace of the expression

$$O^T \text{Re} A_0 O = \begin{bmatrix} \hat{x}^T \text{Re} A_0 \hat{x} & & \\ & \hat{y}^T \text{Re} A_0 \hat{y} & \\ & & \hat{v}^T \text{Re} A_0 \hat{v} \end{bmatrix} \quad (76)$$

yields

$$\begin{aligned} \text{trace}(O^T \text{Re} A_0 O) &= \text{trace}(\text{Re} A_0 O O^T) \\ &= \text{trace} \text{Re} A_0 \\ &= \hat{x}^T \text{Re} A_0 \hat{x} + \hat{y}^T \text{Re} A_0 \hat{y} + \hat{v}^T \text{Re} A_0 \hat{v} \end{aligned} \quad (77)$$

or

$$\hat{x}^T \text{Re} A_0 \hat{x} + \hat{y}^T \text{Re} A_0 \hat{y} = \text{trace} \text{Re} A_0 - \hat{v}^T \text{Re} A_0 \hat{v} \quad (78)$$

and thus

$$P_{co}^A(\rho) = \hat{v}^T(\rho) B_0 \hat{v}(\rho) + b_0^T \hat{v}(\rho) \quad (79)$$

where

$$B_0 = 1/2 (\text{trace}(\text{Re} A_0) I - \text{Re} A_0) \quad (80)$$

For the special case  $b_0 = 0$  eq. (79) is reduced to a real quadratic form similar to eq. (47). Moreover, copolar and crosspolar characteristic polarizations are identical in this particular case.

Note that

$$\text{trace} B_0 = \text{trace} \text{Re} A_0 = \text{trace} A_0 = \text{trace} E_0 \quad (81)$$

With eqs. (52) and (53) follows from eq. (80)

$$B_0 = M_{11} I + Q_0 \quad (82)$$

and the copolar power expression  $P_{co}^A(\rho)$  can be written in the form

$$\begin{aligned} P_{co}^A(\rho) &= M_{11} + \hat{v}^T(\rho) Q_0 \hat{v}(\rho) \\ &\quad + 1/2 b_0^T \hat{v}(\rho) + 1/2 \hat{v}^T(\rho) b_0 \\ &= g^T(\rho) M g(\rho) \end{aligned} \quad (83)$$

$g$  is the Stokes vector for the transmitting and receiving antenna polarization, cf. eq. (56)

$$g(\rho) = [1 \quad \hat{v}^T(\rho)]^T \quad (84)$$

and  $M$  denotes the symmetric Stokes reflection (Mueller) matrix defined by eq. (57).

The last lines establish the agreement of the covariance matrix method with the Mueller matrix approach to the copolar optimization problem as performed for instance by van Zyl et al. [19] and Yamagouchi et al. [10].

Applying the method of Lagrange multipliers, cf. e.g. Leitmann [20], the vectors  $\hat{v}$  which extremise the quadratic form eq. (79) for  $P_{co}^A(\rho)$  are solutions of the set of coupled non-linear equations in  $\hat{v}$  and  $\mu$ :

$$B_0 \hat{v} - \mu \hat{v} = -1/2 b_0 \quad (85)$$

$$\hat{v}^T \hat{v} = 1 \quad (86)$$

Using eq. (82) the first of these equations may be replaced by

$$Q_0 \hat{v} - \nu \hat{v} = -1/2 b_0 \quad (87)$$

where, cf. [19], the Lagrange multipliers  $\nu$  and  $\mu$  are related by

$$\nu = \mu - M_{11} \quad (88)$$

Assuming  $B_0$  to be simple with eigenvalues  $\mu_i = 2M_{11} - \lambda_i(\text{Re} A_0)$  ( $i=1,2,3$ ) with  $\mu_1 \leq \mu_2 \leq \mu_3$  and corresponding normalized orthogonal eigenvectors  $\hat{x}_i$  one can expand  $\hat{v}$  and  $b_0/2$  into

$$\hat{\mathbf{v}} = \sum_{i=1}^3 \alpha_i \hat{\mathbf{x}}_i \quad (89)$$

$$\frac{1}{2} \mathbf{b}_0 = \sum_{i=1}^3 \beta_i \hat{\mathbf{x}}_i \quad (90)$$

and obtains for  $\mu \neq \mu_i$

$$\alpha_i = \frac{\beta_i}{\mu - \mu_i} \quad (i = 1, 2, 3) \quad (91)$$

Hence, from eqs. (89) and (91) follows

$$\hat{\mathbf{v}}^T \hat{\mathbf{v}} = \sum_{i=1}^3 \frac{\beta_i^2}{(\mu - \mu_i)^2} \quad (92)$$

The normalization condition (86) yields

$$\sum_{i=1}^3 \frac{\beta_i^2}{(\mu - \mu_i)^2} = 1 \quad (93)$$

Multiplying eq. (93) by  $(\mu - \mu_1)^2(\mu - \mu_2)^2(\mu - \mu_3)^2$  leads to a polynomial  $p(\mu)$  in  $\mu$  of sixth order with coefficients depending on the eigenvalues  $\mu_i$  and the expansion coefficients  $\beta_i$  ( $i = 1, 2, 3$ ), cf. [19] for details. The roots of this polynomial are denoted by  $\mu^{(k)}$  ( $k = 1, 2, \dots, 6$ ) where  $\mu^{(1)} \leq \mu^{(2)} \leq \dots \leq \mu^{(6)}$ .

For a deterministic target (coherent case) ensemble averaging  $\langle \cdot \rangle$  becomes obsolete and it follows with eqs. (2), (43), (45) and (48)

$$\begin{aligned} \text{Re} \Lambda_0 &= \text{Re}\{Q \Omega_0\} \text{Re}\{Q \Omega_0\}^T \\ &\quad + \text{Im}\{Q \Omega_0\} \text{Im}\{Q \Omega_0\}^T \end{aligned} \quad (94)$$

The spectral theorem for matrices [18] immediately yields  $\text{rank}(\text{Re} \Lambda_0) = 2$ , i.e. one of the eigenvalues of  $\text{Re} \Lambda_0$  is zero. Since direct calculation shows that

$$\text{Im}\{Q \Omega_0\} \times \text{Re}\{Q \Omega_0\} = \mathbf{b}_0 \quad (95)$$

where  $\mathbf{b}_0$  is given by eqs. (69)-(71) (without averaging brackets  $\langle \cdot \rangle$ ), it follows that  $\mathbf{b}_0$  is eigenvector of  $\text{Re} \Lambda_0$  corresponding to the eigenvalue  $\lambda_1(\text{Re} \Lambda_0) = 0$

$$\text{Re} \Lambda_0 \mathbf{b}_0 = 0 \quad (\text{coherent case}). \quad (96)$$

Applying eq. (96) to the crosspolar case, cf. eq. (47) and text following eq. (50), it becomes evident that in the coherent case there exist two orthogonal polarization states, corresponding to  $\pm \mathbf{b}_0/\|\mathbf{b}_0\|$ , for which the crosspolar power  $P_{\times}(\rho)$  vanishes. These same polarization states lead to optimal copolar polarizations as follows.

Using eq. (96) one finds from eq. (80)

$$\mathbf{B}_0 \mathbf{b}_0 = \mu_1 \mathbf{b}_0 = 2M_{11} \mathbf{b}_0. \quad (97)$$

Identifying  $\hat{\mathbf{x}}_1 = \mathbf{b}_0/\|\mathbf{b}_0\|$  in eq. (90) yields  $\beta_1 = \|\mathbf{b}_0\|/2$ ,  $\beta_2 = \beta_3 = 0$  and, hence,

$$\alpha_1 = \frac{\|\mathbf{b}_0\|}{2} \frac{1}{\mu - 2M_{11}}, \quad \alpha_2 = \alpha_3 = 0 \quad (98)$$

and

$$\hat{\mathbf{v}}^T \hat{\mathbf{v}} = \alpha_1^2 = \frac{\|\mathbf{b}_0\|^2}{4} \frac{1}{(\mu - 2M_{11})^2}. \quad (99)$$

The normalization condition  $\hat{\mathbf{v}}^T \hat{\mathbf{v}} = 1$ , cf. eq. (92), yields

$$\mu^{(1,2)} = 2M_{11} \mp \frac{\|\mathbf{b}_0\|}{2} \quad (100)$$

and

$$\alpha_1^{(1)} \equiv \alpha_1(\mu^{(1)}) = -1 = -\alpha_1^{(2)} \equiv -\alpha_1(\mu^{(2)}) \quad (101)$$

$$\hat{\mathbf{v}}^{(1)} = -\hat{\mathbf{x}}_1 = -\frac{\mathbf{b}_0}{\|\mathbf{b}_0\|} = -\hat{\mathbf{v}}^{(2)} \quad (102)$$

This yields

$$P_{\text{co}}^A(\rho^{(1)}) = \frac{1}{2} \text{trace} \Sigma_0 - \|\mathbf{b}_0\| \quad (103)$$

$$P_{\text{co}}^A(\rho^{(2)}) = \frac{1}{2} \text{trace} \Sigma_0 + \|\mathbf{b}_0\|. \quad (104)$$

Thus, there exist two optimal polarization states in the coherent case, namely  $\pm \mathbf{b}_0/\|\mathbf{b}_0\|$  which take antipodal positions in the Poincaré sphere representation. The coherent case can be studied directly using the Sinclair matrix  $S$ , of course. Formally the coherent case is included in the incoherent case for  $\beta_2 = \beta_3 = 0$ .

### Numerical Examples and Graphical Evaluation

The polarimetric covariance matrix concept with its polarization invariant parameters can be used as a tool for polarimetric analysis. This will be illustrated for both SAR-data (spatial ensemble averaging) and weather radar data (temporal ensemble averaging), assuming homogeneity respectively stationarity of the random scattering media. Two different types of target areas as part of a synthetic aperture radar (SAR) image of the Oberpfaffenhofen test site will be considered. The data has been analysed at DLR Oberpfaffenhofen; Held et al. [14] give a description of the NASA-JPL airborne SAR-system.

In the following table target invariant parameters of the covariance matrices of a representative area of buildings and an area of grass are given.

It should be remembered that a deterministic target has eigenvalues  $\lambda_1 = \lambda_2 = 0$ .

Area	$\lambda_1$	$\lambda_2$	$\lambda_3$	$\Delta\lambda$	trace( $\Sigma$ )
Grass	0.06	0.14	0.79	0.73	3.7 dB
Buildings	0.01	0.27	0.72	0.71	23.5 dB

Table 1. Invariant parameters of two different target areas within an L-Band SAR-image of the Oberpfaffenhofen test site; the eigenvalues  $\lambda$  of the target covariance matrices have been normalised by the trace of the matrices.

The grass area clearly resembles a deterministic target. At L-Band, the observed grass area can be described as a rough surface with insignificant random variations since two eigenvalues are close to zero. In fact, corresponding power signatures, cf. Figure 1, are similar to the power spectrum one would expect for a flat plate.

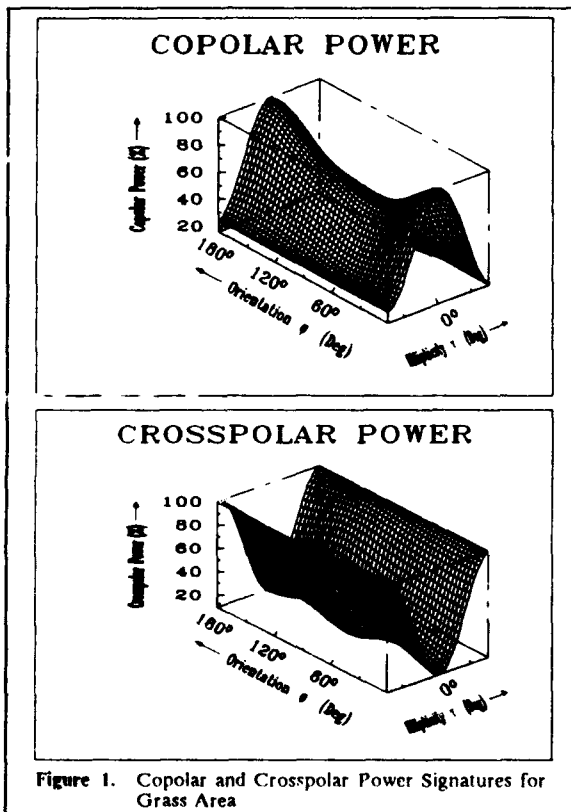


Figure 1. Copolar and Crosspolar Power Signatures for Grass Area

The covariance matrix of the test area of buildings has only one almost vanishing eigenvalue. Analysing the power spectra, cf. Figure 2 it becomes clear that one could approximately model the covariance matrix of this area of buildings by the sum of a corner reflector type and a noise covariance matrix (cf. target decomposition theorem [4] [15]).

This way, the two considered targets both resemble a deterministic target as far as their smallest eigenvalue  $\lambda_{\min} = \lambda_1$  is concerned.

The range in which the mean power return can be varied by polarimetric means is determined by the eigenvalue difference  $\Delta\lambda$ , see (27). Interestingly enough, for the two considered target areas this value is about the same. The total backscattered power in the four orthogonal polarizations, however, is roughly 20 dB higher for the test area of buildings.

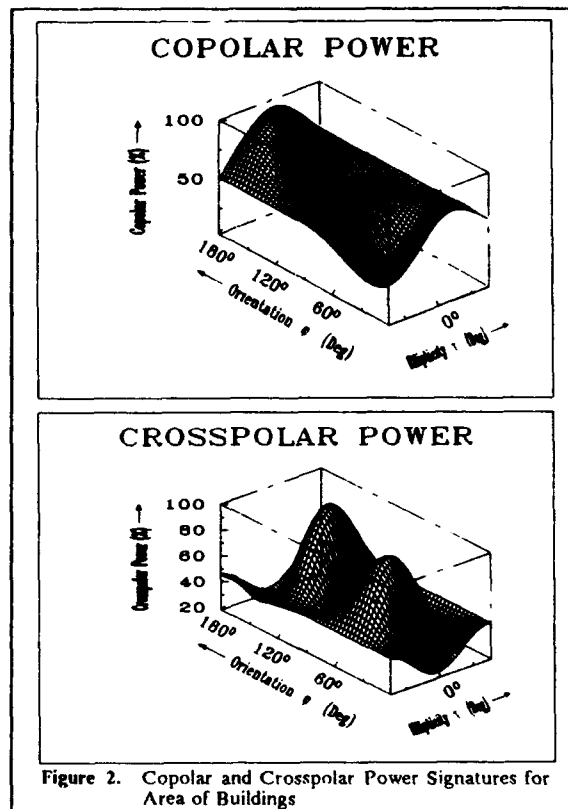


Figure 2. Copolar and Crosspolar Power Signatures for Area of Buildings

Polarization invariant covariance matrix parameters as derived above for two test areas can serve for classification purposes as special target features.

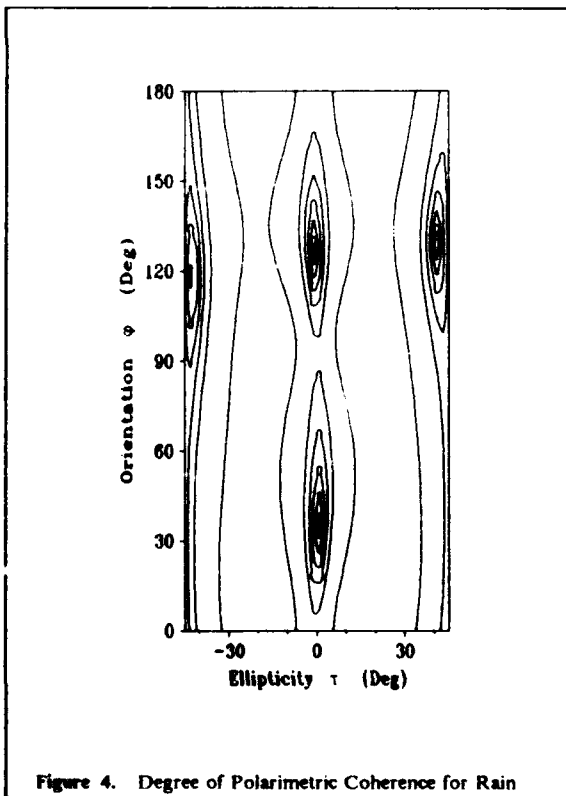
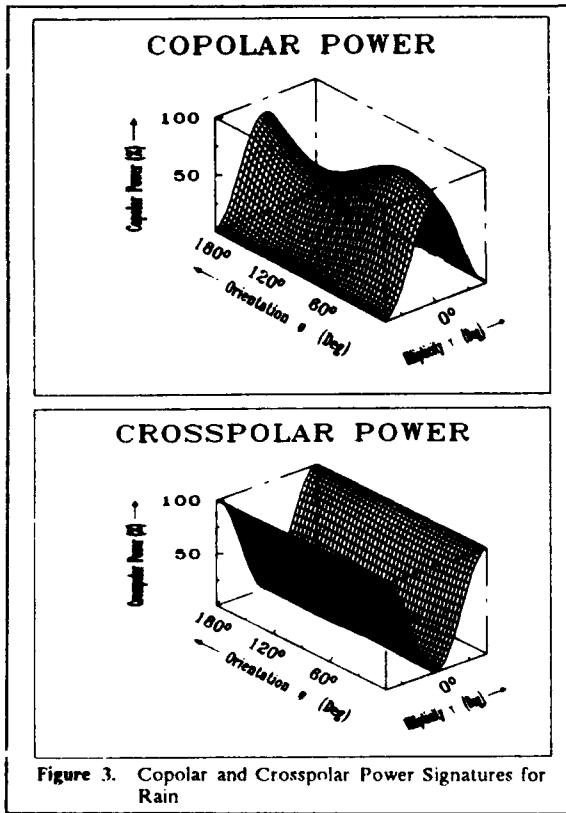
For meteorological reciprocal random targets covariance matrix parameters and representations of covariance matrix elements (radar observables) are very meaningful and directly connected to microphysical parameters, cf. [5] [6].

Copolar and crosspolar power signatures are shown for rain and chaff measurements (as performed with the DLR weather radar [11]) in Figure 3 and Figure 5.

The copolar power signature as function of transmitter polarization  $\rho$  for rain is typical for an ensemble of almost sphere-like single scatterers: Minima are to be found close to circular polarizations, whereas for linear polarizations high values of mean copolar backscattered power can be found. Correspondingly, one expects for the mean crosspolar backscattered power due to the geometric form of the single scatterers maximal values for circular polarizations; minima can be found along the axis of linear polarizations.

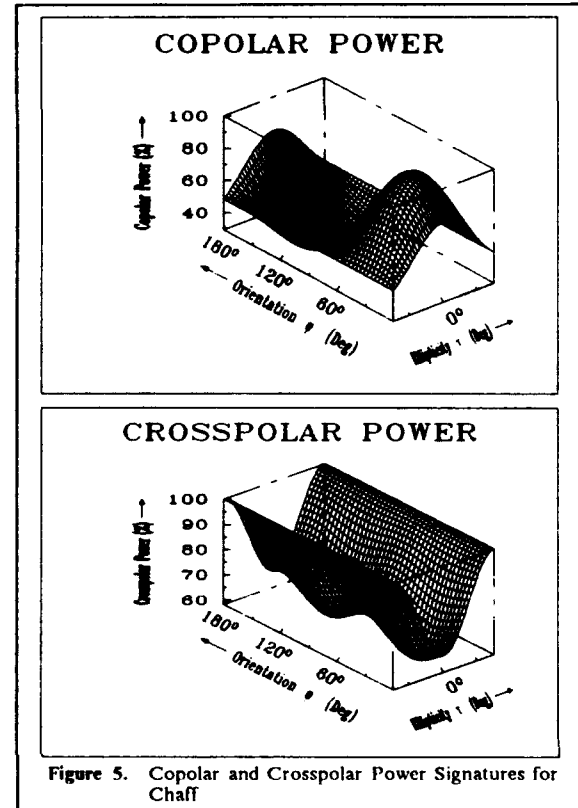
The polarimetric degree of coherence as defined in eq. (15) serves as an indicator of the randomness of a target for a specific transmitter polarization: The observed rain cell can be compared to a deterministic target, since except for optimal polarizations the backscattered waves are almost completely coherent as depicted in Figure 4.

The location of extremal values of the copolar power signature of a chaff (metallized  $\lambda/2$ -synthetic fibres) measurement, see Figure 5, directly reflects mean dipole cant-



ing angles (extremal values for co- and crosspolar power for  $\phi = 31^\circ$  respectively  $\phi = 121^\circ$ ).

The overall structure of the crosspolar signature plot of chaff data is typical for clutter-like targets, even though the locations of local extrema again reflect mean dipole canting angles [5].



Mean dipole canting angles and their location can be seen also in a contour diagram Figure 6 of the correlation difference  $R_x^{B*} - R_x^A$ . Crosspolar extrema correspond to correlation difference nulls, cf. eq. (34). In a signature plot of the mean degree of polarization Figure 7 it can be seen that the ratio of polarized wave components power to total power is extremal at polarization ratios  $\rho$  corresponding to mean dipole canting angles.

In previous sections of this paper analytical and numerical algorithms to determine optimal polarizations in the co- and crosspolar case have been presented.

The covariance matrix of the observed area of grass (see power signatures Figure 1) is

$$\Sigma_0 = \begin{bmatrix} 2.0120 & .0931 e^{j150.1^\circ} & 1.1966 e^{j7.3^\circ} \\ .0931 e^{-j150.1^\circ} & .2774 & .1483 e^{-j108.9^\circ} \\ 1.1966 e^{-j7.3^\circ} & .1483 e^{j108.9^\circ} & 1.4790 \end{bmatrix} \quad (105)$$

Evaluation of  $P_x(\rho) = 1/2 \hat{v}^T(\rho) \text{Re} A_0 \hat{v}(\rho)$  (cf. eq. (44)) determines extremal values for the crosspolar power calculating the eigenvalues of  $\text{Re} A_0$ . With

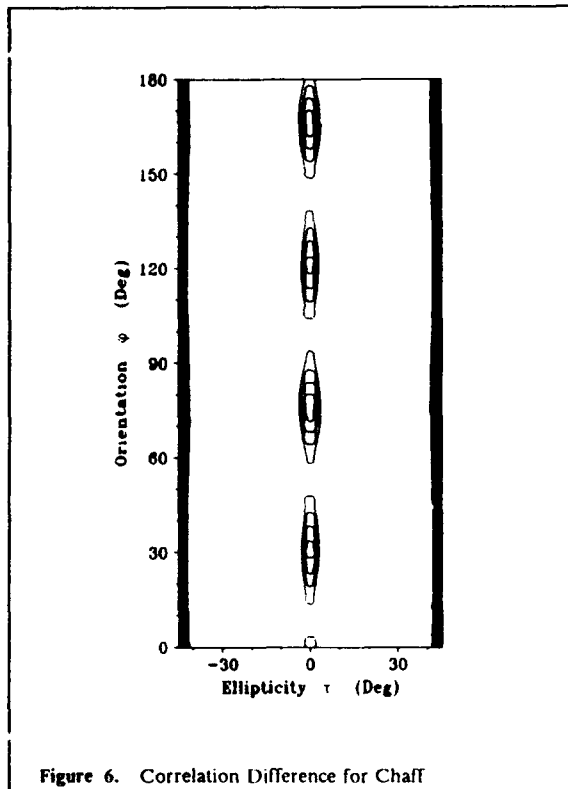


Figure 6. Correlation Difference for Chaff

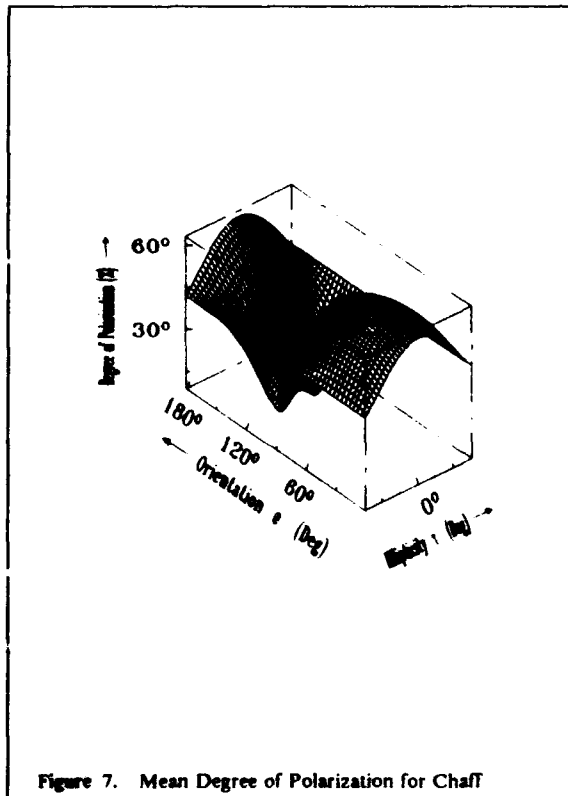


Figure 7. Mean Degree of Polarization for Chaff

$$\lambda_1(\text{Re}A_0) = .2700, \lambda_2(\text{Re}A_0) = .5497, \lambda_3(\text{Re}A_0) = 2.9487$$

follow optimal polarization ratios

$$\rho_1 = .0362 e^{j140.2^\circ}, \rho_2 = .9488 e^{j3.8^\circ}, \rho_3 = 1.0511 e^{j93.7^\circ}$$

and, since polarization ratios  $-1/\rho^*$  result in extremal crosspolar power values also, six crosspolar power optimal polarizations with corresponding values  $P_x$ , see Table 2.

$\tau$	$\varphi$	$P_x$
$1.3^\circ$	$178.4^\circ$	.1350
$-1.3^\circ$	$88.4^\circ$	.1350
$1.9^\circ$	$43.5^\circ$	.2748
$-1.9^\circ$	$133.5^\circ$	.2748
$42.7^\circ$	$116.0^\circ$	1.4744
$-42.7^\circ$	$26.0^\circ$	1.4744

Table 2. Crosspolar Power Optimal Polarizations for Grass Area

For the copolar case, eq. (92) yields for the magnitude of the polarization variability vector  $v$

$$|v| = \left( \sum_{i=1}^3 \frac{\beta_i^2}{(\mu - \mu_i)^2} \right)^{\frac{1}{2}} \quad (108)$$

where

$$\beta_i = \frac{1}{2} \mathbf{b}_0^T \hat{\mathbf{x}}_i \quad (i = 1, 2, 3) \quad (109)$$

Making use of the normalization condition  $|v| = 1$ , (108) can be transformed into a polynomial  $p(\mu)$  in  $\mu$  of sixth order.

The number of solutions  $\mu$  for  $|v(\mu)| = 1$  respectively  $p(\mu) = 0$  directly determine the number of characteristic polarizations for a specific target.

The roots of the polynomial  $p(\mu)$  can be found by using Newton's method of successive approximations, cf. [22] [19]. However, convergence may not be achieved or the proper root may not be found.

Instead, a golden section search algorithm [22] can be implemented to determine the existing roots of  $p(\mu)$  in a fully operational manner.

The search is to be conducted in an interval  $[\mu_a, \mu_b]$  and  $[\mu_3, \mu_6]$  ( $\mu_1, \mu_3$  corresponding to the smallest respectively largest eigenvalue of  $\mathbf{B}_0$ ) to determine the smallest and largest root of  $p(\mu)$  whose existence is guaranteed even for deterministic targets (see below). Interval limiters  $\mu_a, \mu_b$  are found by a golden section interval expansion starting from  $\mu_1$  respectively  $\mu_3$  until  $p(\mu)$  changes sign.

For a non-deterministic target another two roots may be found in the interval  $[\mu_1, \mu_2]$  and similarly in the interval  $[\mu_2, \mu_3]$ . The intervals  $[\mu_1, \mu_2]$  and  $[\mu_2, \mu_3]$  are subdivided into  $[\mu_1, \mu_A^D]$  and  $[\mu_A^D, \mu_2]$  respectively  $[\mu_2, \mu_B^D]$  and  $[\mu_B^D, \mu_3]$  where  $\mu_A^D, \mu_B^D = \mu |_{p'(\mu)=0}$ .

The magnitude of the polarization variability vector  $|v(\mu)|$  is well suited for graphical evaluation illustrating the root finding problem.

Analyzing L-band data for an area of grass,  $|v(\mu)|$  reveals a total of only four power optimal characteristic polarization states, see Figure 8. Between  $\mu_2$  and  $\mu_3$  the values of  $|v(\mu)|$  are always larger than one.

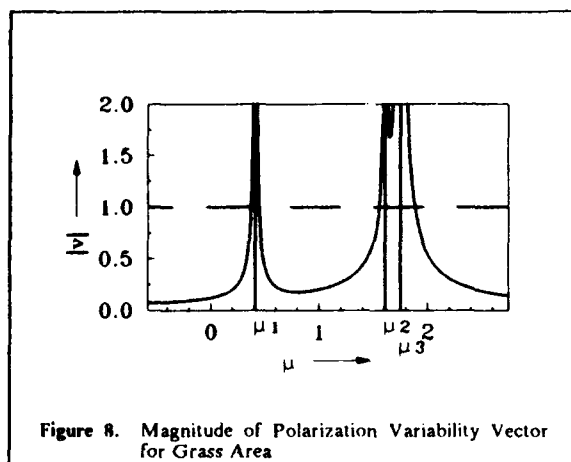


Figure 8. Magnitude of Polarization Variability Vector for Grass Area

The eigenvalues of  $B_0$  are

$$\mu_1 = .4098, \mu_2 = 1.6094, \mu_3 = 1.7492$$

and with

$$b_0^T = (.2665 \quad -.0910 \quad -.0664)$$

follow the coefficients  $\beta_i$

$$\beta_1 = -.0368, \beta_2 = -.0405, \beta_3 = .1339$$

and the sixth order polynomial  $p(\mu)$

$$p(\mu) = \mu^6 - 7.5368\mu^5 + 22.5628\mu^4 - 33.8092\mu^3 + 26.1342\mu^2 - 9.5929\mu + 1.3116$$

The above polynomial yields for  $p(\mu) = 0$  four real roots

$$\mu^{(1)} = .3728, \mu^{(2)} = .4469, \mu^{(3)} = 1.5391, \mu^{(4)} = 1.8882$$

and, thus, with eqs. (89) and (91) follow polarization variability vectors  $\hat{v}$  that can be directly converted into complex polarization ratios  $\rho$  via eq. (41). The following Table 3 contains the four copolar power optimal polarizations with corresponding values  $P_\infty$ .

$\tau$	$\varphi$	$P_\infty$
40.8°	95.0°	.3218
-41.7°	57.9°	.4683
-1.0°	57.1°	1.4429
.3°	174.3°	2.0239

Table 3. Copolar Power Optimal Polarizations for Grass Area

As has been pointed out, the coherent case is included in the presentation derived for the general case of incoherent or partially coherent backscatter.

As an example for a deterministic target, the scattering matrix  $S$  for a horizontally oriented dipole is

$$S = \begin{bmatrix} 1 & 0 \\ 0 & 0 \end{bmatrix}$$

Figure 9 shows  $|v|$  as a function of  $\mu$ .

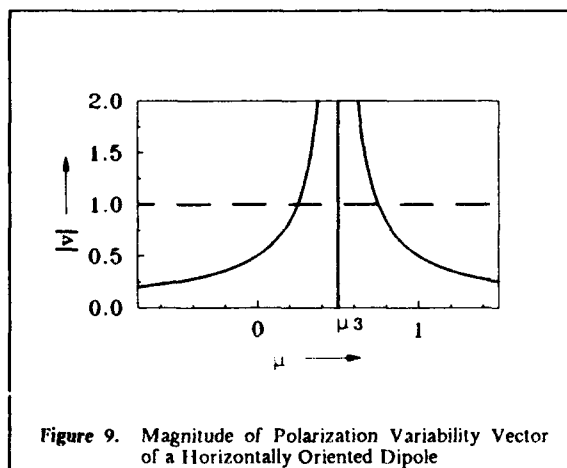


Figure 9. Magnitude of Polarization Variability Vector of a Horizontally Oriented Dipole

The fact, that there are only two values  $\mu$  for which  $|v|$  attains the value  $|v| = 1$ , corresponds to a  $p(\mu)$ -polynomial of second order: For a deterministic target two expansion coefficients vanish, i.e.  $\beta_2 = \beta_3 = 0$ .

### Conclusion

A polarimetric covariance matrix concept has been presented, in this paper, which describes the polarimetric backscattering features of reciprocal random radar targets. The polarisation dependence of second-order radar observables can be obtained by unitary similarity transformations of the covariance matrix. Invariant target parameters, such as the minimum and maximum eigenvalue or the eigenvalue difference of the covariance matrix are introduced providing quite interesting information upon the randomness of a target and the polarimetric features of the radar observables. A method to determine the polarimetric variation and optimal polarisations of any arbitrary second-order observable has been presented and illustrated. Furthermore, a new analytical formulation of the problem of optimal polarisations for the mean copolar and crosspolar power return is derived. This way, the operational computation of optimal polarisations within large data sets, e.g. in the case of SAR-images, becomes feasible. The interrelationship of the presented covariance matrix concept with the Mueller matrix formulation appears to be of particular interest.



## Bibliography

- [1] Born, M., and Wolf, E., 1964, "Principles of Optics", Pergamon Press, Oxford, U.K.
- [2] Huynen, J.R., 1970, "Phenomenological Theory of Radar Targets", Ph.D. Dissertation, Technical University Delft, The Netherlands
- [3] van Zyl, J.J., 1986, "On the Importance of Polarization in Radar Scattering Problems", Ph.D. Dissertation, California Institute of Technology, Pasadena, U.S.A.
- [4] Cloude, S.R., 1986, "Polarimetry: The Characterisation of Polarisation Effects in Electromagnetic Scattering", Ph.D. Dissertation, University of Birmingham, U.K.
- [5] Tragl, K., 1990, "Polarimetric Radar Backscattering from Reciprocal Random Targets", IEEE Trans. Geosci. Remote Sensing, GE-28 (5), pp. 856-864.
- [6] Schroth, A., Tragl, K., Lueneburg, E., and Chandra, M., 1991, "Polarimetric Signal Processing of Random Target Observations", European Transactions on Telecommunications, submitted for publication
- [7] Schroth, A., Chandra, M., Meischner, P., 1988, "A C-Band Polarimetric Radar for Propagation and Cloud Physics Research", T.J. Atmos. Oceanic Technol., vol. 5, no. 6, pp. 803-822
- [8] Boerner, W.-M., Al-Arini, M.B., Chan, C.-Y., and Mastoris, P.M., 1981, "Polarization Dependence in Electromagnetic Inverse Problems", IEEE Trans. Antennas Propag., AP-29 (2), pp. 262-271.
- [9] Boerner, W.-M., Wei-Ling Yan, An-Quing Xi, 1990 "Basic Equations of Radar Polarimetry and its Solutions: the Characteristic Radar Polarization States for the Coherent and Partially Polarized Cases", SPIE Vol. 1317, Polarimetry: Radar, Infrared, Visible, Ultraviolet and X-Ray, pp. 16-79
- [10] Yamaguchi, Y., Sasagawa, K., Sengoku, M., Abe, T., Boerner, W.-M., 1990, "On the Characteristic Polarization States of Coherently Reflected Waves in Radar Polarimetry", Tech. Rep. of Antennas & Propagation IEICE Japan, AP 90-35, pp. 23-30
- [11] Tragl, K., Schroth, A., and Lueneburg, E., 1989, "Optimal Polarizations for Statistically Distributed Scatterers: Theory and Measurements with the DFVLR Weather Radar", ICAP-89, Warwick, U.K. - IEE Publ. 301, pp. 88-95.
- [12] Tragl, K., Lueneburg, E., Schroth, A., Ziegler, V., 1991, "A Polarimetric Covariance Matrix Concept for Random Radar Targets", ICAP-91, York, U.K.
- [13] Agrawal, A.P., and Boerner, W.-M., 1989, "Redevelopment of Kennaugh's Target Characteristic Polarization State Theory Using the Polarization Transformation Ratio Formalism for the Coherent Case", IEEE Trans. Geosci. Remote Sensing, GE-27 (1), pp. 2-14.
- [14] Held, D.N., Brown, W.E., Freeman, A., Klein, J.D., Zebker, H., Sato, T., Miller, T., Nguyen, Q., and Lou, Y., 1988, "The NASA/JPL Multifrequency, Multipolarization Airborne SAR System", Proceedings of IGARSS '88 Symposium, vol. 1, pp. 345-350., ESA SP-284, (IEEE 88CI12497-6).
- [15] Cloude, S.R., 1987, "The Importance of Polarisation Information in Optical Remote Sensing", SPIE, vol. 810, Optical Systems for Space Applications, pp. 21-27.
- [16] Jameson, A.R., 1987, "Relations among Linear and Circular Polarization Parameters Measured in Canted Hydrometers", J. Atmos. Ocean. Tech., vol. 4 (6), pp. 634-645.
- [17] Balakrishnan, N., and Zrnic, D.S., 1989, "Suggested Use of Crosscorrelation between Orthogonally Polarized Echoes to Infer Hail Size", 24th Conf. Radar Meteorology, Tallahassee, U.S.A. - Proc., pp. 292-296.
- [18] Lancaster, P., and Tismenetsky, M., 1985, "The Theory of Matrices", 2. Edt., Academic Press, Orlando, U.S.A.
- [19] van Zyl, J.J., Papas, C.H., and Elachi, C., 1987, "On the Optimum Polarizations of Incoherently Reflected Waves", IEEE Trans. Antennas Propag., AP-35 (7), pp. 818-825.
- [20] Leitmann, G., 1962, "Optimization Techniques", Academic Press, London, U.K.
- [21] Horn, R.A., Johnson, C.A., 1985, "Matrix Analysis", University Press, Cambridge, U.K.
- [22] Wilde, D.J., Beightler, C.S., 1967, "Foundations of Optimization", Prentice Hall, N.J., U.S.A.

## DISCUSSION

W. Flood, US

Were the rain data presented from a frontal system or a convective storm? In other words was the reflectivity of the rain volume homogeneous?

Author's Reply

The author replied that he thought the reflectivity of the rain volume was reasonably homogeneous.

# MILLIMETER WAVE POLARIMETRIC SCATTEROMETER SYSTEMS: MEASUREMENT AND CALIBRATION TECHNIQUES

Y. Kuga, K. Sarabandi, A. Nashashibi, F. T. Ulaby and R. Austin

University of Michigan

The Radiation Laboratory

Department of Electrical Engineering and Computer Science

3228 EECS Building

Ann Arbor, Michigan 48109-2122

## SUMMARY

The target and system phase-stability during the time to measure the scattering matrix is a major problem for millimeter wave polarimetric radars. This is particularly true for network analyzer-based systems. To circumvent this phase-stability problem, we have developed new fully polarimetric radars at 35 and 94 GHz. The system is based on a relatively inexpensive network analyzer and is capable of operating in either the coherent or the incoherent polarimetric measurement mode. In the coherent mode, the scattering matrix can be measured within 2 ms. In the incoherent mode, the average Mueller matrix is measured directly by transmitting four different polarizations and measuring the Stokes vector of the backscattered signal. To compare the performance of the true measurement modes, the average Mueller matrix and the statistics of the phase difference of the two co-polarized signals were measured for a rhododendron tree and for a metallic tree. The average Mueller matrices obtained from the coherent and incoherent polarimetric measurement modes were similar. The target motion during the data acquisition period did not change the average Mueller matrix in the incoherent measurement mode. The probability density function of the phase difference of the two co-polarized signals computed from the average Mueller matrix is essentially the same as the one measured with the coherent polarimetric measurement mode.

## 1 INTRODUCTION

Increasing interest has been expressed in recent years for understanding the statistical properties of data obtained with fully polarimetric radars for remote sensing applications [Ulaby and Elachi, 1990]. At centimeter wavelengths, polarimetric data has been found to be useful for land-use classification [Van Zyl et al., 1987] and for measuring the biophysical properties of forest canopies [McDonald et al., 1990]. For the MMW region, however, it is still not clear what type of information can be extracted from polarimetric radar, over and above the magnitude information provided by conventional radar systems. Unlike the microwave region, the complexity and the cost of building a fully polarimetric radar at millimeter-wave frequencies is still very expensive, and progress has been rather slow, which is due, in part, to the limited availability of experimental data.

At microwave frequencies the traditional approach used for measuring the polarimetric radar response of a given target is based on the direct measurement of the target's scattering matrix,  $S$ . For distributed targets, such as terrain surfaces, multiple measurements of  $S$  are made, corresponding to statistically independent samples, each measurement is used to compute its corresponding Mueller matrix  $L$ , and then an ensemble average is performed to obtain an estimate of the average Mueller matrix,  $\langle L \rangle$ . Whereas the scattering matrix measurement technique is appropriate at microwave frequencies, it is difficult to implement at millimeter wavelengths because it requires that both the system and target phases remain stable during the time it takes to measure  $S$ . This is particularly true for network analyzer-based polarimetric radars [Ulaby et al., 1990].

To circumvent this phase-stability problem, we have developed new fully polarimetric radars at 35 and 94 GHz. The system is based on relatively inexpensive network analyzer and is capable of operating in either the coherent or the incoherent polarimetric measurement mode. In the coherent mode, the scattering matrix can be measured within 2 ms. In the incoherent mode the average Mueller matrix is measured directly by transmitting four different polarizations and recording the horizontally polarized and vertically polarized components of the backscattered field. This paper includes a detailed analysis of the two measurement modes, and provides comparisons of data measured using the two modes for a rhododendron tree and an artificially made metallic tree.

## 2 NWA BASED POLARIMETRIC RADARS

The fully polarimetric radar configuration based on the vector network analyzer (NWA) is easy to construct and is widely used for remote sensing investigations [Ulaby et al., 1990]. These systems usually are operated in the swept frequency mode over a given bandwidth. The minimum sweep time, which depends on the number of frequency points and the type of NWA, is typically between 100 to 400 ms. The decorrelation time of the MMW wave scattered from trees, on the other hand, can be shorter than 10 ms [Narayanan et al., 1988]. Hence, when using the fully coherent measurement configuration, it is necessary that all four components of the scattering matrix be measured within a few milliseconds in order to obtain accurate data. If the  $V$ - and  $H$ -polarized signals are transmitted sequentially in the swept frequency mode, it will take at least 0.5 to 1 second to get a complete scattering matrix, including the data transfer time between the NWA and the computer. Obviously, the NWA-based MMW radar used in the swept frequency mode is not suited for coherent polarimetric measurements.

There are two ways to overcome the shortcoming of the traditional swept-frequency NWA based polarimetric radar. The first approach is the incoherent polarimetric measurement technique. With this technique the swept frequency mode can still be used for the NWA operation but the radar transmitter must be modified to transmit four independent polarizations. The data processing and calibration are substantially more complicated than those associated with the coherent polarimetric technique. The second approach is the coherent polarimetric measurement technique using Coupled/Chop mode and point by point external triggering of the NWA. We have developed both coherent and incoherent polarimetric radars based on these techniques at 35 and 94 GHz. The radar front end and data acquisition system are the same for both systems. The only difference is the operating mode of the NWA and the data processing. It is, therefore, possible to obtain polarimetric data of the same targets coherently and incoherently. The block diagram of the MMW radar system and the 35 GHz front end are shown in Figs. 1 and 2. The block diagram of the 94 GHz is essentially the same as that of the 35 GHz system. In the following section the details of the coherent and incoherent systems will be discussed.

### 2.1 Coherent Polarimetric Radar

The coherent polarimetric radar has many advantages over the incoherent polarimetric radar. For example, with the coherent polarimetric radar the statistical data including the phase difference between the two copolarized channels, can be easily obtained. Another advantage is the significantly simpler signal processing and calibration processes compared to those of the incoherent polarimetric radar. As discussed in the previous section, the NWA-based radar operated in the swept frequency mode is not suited for coherent polarimetric measurements. In this section, we will describe a new technique which utilizes a relatively inexpensive NWA (HP8753C) that allows the acquisition of coherent polarimetric data at a much faster rate. With this system it is possible to measure the scattering matrix within 2 ms at 35 and 94 GHz.

The Hewlett-Packard network analyzer, HP8753C, has two independent receiving channels which can be used in the Coupled/Chop mode. It also has a point by point external triggering capability in the swept frequency mode. These functions are ideally suited for the coherent polarimetric radar. For example, the simultaneous acquisition of  $V$  and  $H$  channels can be done by operating  $A$  and  $B$  inputs in the Coupled/Chop mode. The point by point external triggering can be used for transmitting  $V$  and  $H$  sequentially and synchronizing a polarization control circuit to create different polarizations. At present, HP8753C does not support the external point by point triggering in the CW mode but a near CW mode can be created

in the swept frequency mode by choosing the output frequency bandwidth to be 1 Hz. The minimum time to get a complete scattering matrix is approximately 2 ms in the present system. The polarization of the transmitted MMW signal is controlled by a Faraday rotator whose switching time is less than 5  $\mu$ s. Using the maximum number of points provided by the HP8753C, it is possible to obtain 800 scattering matrices within 3.2 s without transferring data into a computer.

The separation of signal from unwanted noise, such as antenna coupling, is accomplished by the hardware gating circuit in the IF path as shown in Fig. 2. The transmitted pulse length is 20 ns and the pulse-repetition-rate is 5 MHz. Although it is not necessary to scan the RF frequency band in the coherent polarimetric mode, additional independent samples can be realized by averaging the backscattering coefficient over the RF bandwidth [Ulaby et al., 1988]. A bandwidth of 1 GHz at 35 GHz, for example, offers 5 to 10 independent samples per spatial observation for the tree measurements.

The calibration of the coherent system is straightforward. Because the system has more than 23 dB of isolation between the V and H channels, a simple calibration technique that requires a sphere and a depolarizing target is used [Sarabandi et al., 1990].

## 2.2 Incoherent Polarimetric Radar

In the incoherent polarimetric radar technique, the Mueller matrix of the target is measured directly by transmitting four independent polarizations and receiving the Stokes vector of the scattered signal. Because the correlation between the V- and H- polarized signals is inherently included in the received Stokes vector, the measurement time between the different incident polarizations can be much longer than the decorrelation time of the target. The incoherent polarimetric technique also permits the use of MMW sources that do not have good phase-stability in the transmitter section [Mead, 1990]. A desired polarization can be created by placing two quarter-wave plates in front of the transmitting antenna and by adjusting the orientation angle of each wave plate relative to the incident polarization.

The received Stokes vector for a given incident polarization is usually obtained by two different approaches, incoherent and coherent-on-receive techniques. The incoherent receive technique, which often is employed in optics measures the intensity of six different receive polarizations, but the phase measurement is not required. The Stokes vector is obtained by taking appropriate ratios of the receive intensities, as shown in Appendix A.

The receiver of the coherent-on-receive technique is similar to that of the coherent polarimetric radar. The coherent-on-receive method requires the measurement of the magnitudes of the V- and H- polarized receive signals and the phase difference between them, but it does not have to measure the phase angle relative to the transmitted signal, as is the case with the coherent polarimetric radar. The Stokes vector can be computed from the magnitudes of the V and H components of the received signal and the phase difference between them as shown in Appendix A. Because it is relatively easy to measure the phase difference between the V and H channels, our system is based on the coherent-on-receive technique.

Calibration of incoherent polarimetric radar systems involves two steps [Mead, 1990]. In the first step, the receiver distortion matrix is obtained by placing a wire grid polarizer in front of the receiving antenna at three different positions. In the second step, the exact polarization properties of the transmitter are determined by measuring the backscatter from a point target with known scattering matrix using the calibrated receiver.

## 3 EXPERIMENTAL DATA

To demonstrate that the coherent and incoherent polarimetric measurement techniques do indeed provide identical information for distributed targets, experiments were conducted using a rhododendron tree and a metallic structure resembling a short tree. Photographs of these targets are shown in Fig. 3. The metallic structure is used for creating a target return with strong correlation between the  $S_{vv}$  and  $S_{hh}$  components. To create many independent samples and also to show that the incoherent polarimetric technique can provide accurate results even if the data acquisition time is much longer than the target decorrelation time, the trees were rotated at slow (0.67 rpm) and fast (1.33 rpm) speeds during the data-collection process.

Table 1 shows the average Mueller matrices of the rhododendron and metallic trees obtained by the coherent and incoherent polarimetric radar techniques. The Mueller matrices are normalized with respect to the  $L_{11}$  component to show the relative magnitude of the matrix elements. The average Mueller matrix of the coherent polarimetric radar technique was computed from the 8000 scattering matrices obtained over the 34-35 GHz band. Because of the slow data-acquisition speed in the incoherent polarimetric radar, the average Mueller matrix is obtained from only 500 samples, including those due to frequency averaging over the 1-GHz RF bandwidth.

The sum of the Mueller matrix elements  $L_{33}$  and  $L_{44}$ , which is a function of the correlation between  $S_{vv}$  and  $S_{hh}$ , is higher for the metallic tree than for the rhododendron tree. Although the polarimetric signature computed from the average Mueller matrix is useful for showing the characteristics of the target, it is not easy to directly relate the target characteristics to the values of the Mueller matrix elements.

Figure 4 shows the probability density function of the phase difference between the two co-polarized channels ( $\phi_c$  = phase of  $S_{vv}$  - phase of  $S_{hh}$ ) obtained with the coherent polarimetric radar. As expected,  $p(\phi_c)$  of the metallic tree is much narrower than that of the rhododendron tree, showing strong correlation between  $S_{vv}$  and  $S_{hh}$ .

Unlike the coherent polarimetric radar, the information obtained with the incoherent polarimetric radar is limited to the average Mueller matrix and it is not possible to measure the probability density function  $p(\phi_c)$  directly. Due to a recent theoretical derivation, however, the phase statistics of  $\phi_c$  can be estimated from the average Mueller matrix [Sarabandi, 1991]. The probability density function  $p(\phi_c)$  is given by

$$p(\phi_c) = \frac{\lambda_{11}\lambda_{33} - \lambda_{13}^2}{2\pi B^2} \frac{\lambda_{14}^2}{\left\{1 + \frac{D}{B} \left[ \frac{\pi}{2} + \tan^{-1} \left( \frac{D}{B} \right) \right] \right\}}$$

where

$$\begin{aligned} \lambda_{11} &= \frac{L_{11}}{2}, & \lambda_{33} &= \frac{L_{22}}{2}, \\ \lambda_{13} &= \frac{L_{33} + L_{44}}{4}, & \lambda_{14} &= \frac{L_{34} - L_{43}}{4}, \\ D &= \lambda_{13} \cos \phi_c + \lambda_{14} \sin \phi_c, \\ B &= [\lambda_{11}\lambda_{33} - D^2]^{\frac{1}{2}}. \end{aligned}$$

The function  $p(\phi_c)$  is completely specified in terms of the elements of the average Mueller matrix  $\mathcal{L}_m$ .

The average Mueller matrix given in Table 1 and the probability density function of the phase difference shown in Fig. 4 are obtained from the same target by two different polarimetric measurement techniques. If the probability density function given by Eq. 1 is correct,  $p(\phi_c)$  estimated from the average Mueller matrix must be similar to the one shown in Fig. 4. Figure 5 shows the probability density function computed from the average Mueller matrix obtained by the incoherent polarimetric radar. The agreement between Figs. 4 and 5 is excellent for both trees.

## 4 CONCLUSION

The work described in this paper has demonstrated that the average Mueller matrices obtained using the coherent and incoherent polarimetric measurement techniques are essentially identical. The advantage of the coherent polarimetric radar over the incoherent polarimetric radar is its ability to measure the statistical distributions of the magnitudes and relative phases of the scattering matrix elements. The incoherent polarimetric radar, however, is particularly useful if the target decorrelation time is much faster than the data acquisition time.

## REFERENCES

- [1] Ulaby, F.T., and C. Elachi, *Radar Polarimetry for Geoscience Applications*, Artech House Inc., Massachusetts, 1990.
- [2] Van Zyl, J.J., H.A. Zebker, and C. Elachi, "Imaging Radar Polarization signatures: Theory and Observation," *Radio Science*, 1987, Vol. 22, pp. 529-543.
- [3] Sarabandi, K., F.T. Ulaby, and M.A. Tasmoudji, "Calibration of Polarimetric Radar Systems with Good Polarization Isolation," *IEEE Trans. on Geosci. Remote Sensing*, 1990, GE-28.

- [4] Ulaby, F.T., T.F. Haddock, and R.T. Austin, "Fluctuation Statistics of Millimeter-Wave Scattering from Distributed Target," *IEEE Trans. on Geosci. and Remote Sensing*, 1988, Vol. 26, pp. 268-281.
- [5] McDonald, K.D., M.C. Dobson, and F.T. Ulaby, "Using MIMICS to Model L-Band Multiangle and Multitemporal Backscatter from a Walnut Orchard," *IEEE Trans. on Geosci. and Remote Sensing*, 1990, Vol. 28, pp. 477-491.
- [6] Mead, J.B., "Polarimetric Measurements of Foliage and Terrain at 225 GHz," (Ph.D. Thesis, Univ. of Mass., 1989).
- [7] Ulaby, F.T., M.W. Whitt, and K. Sarabandi, "AVNA-based Polarimetric Scatterometers," *IEEE Antennas Propagation Magazine*, 1990.
- [8] Sarabandi, K., "Derivation of Phase Statistics of Distributed Targets from the Averaged Mueller Matrix," Technical Report 026511-T, 1991, Radiation Laboratory, University of Michigan, Ann Arbor, MI.
- [9] Narayanan, R.M., C.C. Borel, R.E. McIntosh, "Radar Backscattering Characteristics of Trees at 215 GHz," *IEEE Trans. on Geosci. and Remote Sensing*, 1988, Vol. 26, pp. 217-218.

## APPENDIX A

### COHERENT-ON-RECEIVE TECHNIQUE

Complete polarimetric characterization of the scattering properties of a distributed target can be obtained by measuring either the scattering matrix  $S$  or the Mueller matrix  $\mathcal{L}_m$ . Measurement of the scattering matrix requires accurate phase measurements. Also 4 elements of  $S$  must be obtained within the decorrelation time of the target which is in the order of milliseconds at MMW frequencies. The scattered electric field  $E^r$ , in terms of the scattering matrix  $S$  and the incident electric field  $E^i$ , is given by

$$E^r = \frac{e^{ikr}}{r} S E^i \quad (A.1)$$

$$E^r = \begin{bmatrix} E_v \\ E_h \end{bmatrix} \quad E^i = \begin{bmatrix} E_v \\ E_h \end{bmatrix} \quad S = \begin{bmatrix} S_{vv} & S_{vh} \\ S_{hv} & S_{hh} \end{bmatrix} \quad (A.2)$$

To obtain  $S$ , we need to send  $[E_v, 0]^t$  and  $[0, E_h]^t$ , and measure  $E_v$  and  $E_h$  simultaneously.

The polarized wave can also be expressed in terms of the Stoke's vector  $F_m$  which is defined as

$$F_m = \begin{bmatrix} I_1 \\ I_2 \\ U \\ V \end{bmatrix} = \begin{bmatrix} |E_v|^2 \\ |E_h|^2 \\ 2\text{Re}[E_v E_h^*] \\ 2\text{Im}[E_v E_h^*] \end{bmatrix} \quad (A.3)$$

then (A.1) in terms of Stokes vector becomes

$$F_m^r = \frac{1}{r^2} \mathcal{L}_m F_m^i \quad (A.4)$$

$$\mathcal{L}_m = \begin{bmatrix} |S_{vv}|^2 & |S_{vh}|^2 & \dots & \dots \\ |S_{hv}|^2 & |S_{hh}|^2 & \dots & \dots \\ 2\text{Re}(S_{vv} S_{hh}^*) & 2\text{Re}(S_{vh} S_{hh}^*) & \dots & \dots \\ 2\text{Im}(S_{vv} S_{hh}^*) & 2\text{Im}(S_{vh} S_{hh}^*) & \dots & \dots \\ \text{Re}(S_{vh}^* S_{vv}) & -\text{Im}(S_{vh}^* S_{vv}) & \dots & \dots \\ \text{Re}(S_{hh}^* S_{vh}) & -\text{Im}(S_{hh}^* S_{vh}) & \dots & \dots \\ \dots & \dots & \dots & \dots \\ \text{Re}(S_{vv} S_{hh}^* + S_{vh} S_{hv}^*) & -\text{Im}(S_{vv} S_{hh}^* - S_{vh} S_{hv}^*) & \dots & \dots \\ \text{Im}(S_{vv} S_{hh}^* + S_{vh} S_{hv}^*) & \text{Re}(S_{vv} S_{hh}^* - S_{vh} S_{hv}^*) & \dots & \dots \end{bmatrix} \quad (A.5)$$

where  $\mathcal{L}_m$  is called the Mueller matrix.

The totally incoherent method does not require phase measurements. With this method, the 4 elements of Stokes vector are obtained by receiving 6 polarizations ( $V, H, 45, 135, LHC, RHC$ ). For example, the third element of Stokes vector  $U$  is given as a ratio of intensities at 45 linear to 135 linear. For a given incident polarization, therefore, we can obtain a column of the Mueller matrix. To get the complete Mueller matrix, we need to repeat this process for 4 independent incident polarizations. Altogether, at least 24 magnitude only measurements are required to obtain the complete Mueller matrix. Although the phase measurement is not required with the incoherent method, it is necessary to receive all 6 polarizations. The elements of the Stokes vector, in terms of 6 polarizations and a set of 4 independent incident polarizations, given by:

$$I_1 = \frac{W_v}{W_h + W_v} \quad (A.6)$$

$$I_2 = \frac{W_h}{W_h + W_v} \quad (A.7)$$

$$U = \frac{W_{45} - W_{135}}{W_{45} + W_{135}} \quad (A.8)$$

$$V = \frac{W_{LHC} - W_{RHC}}{W_{LHC} + W_{RHC}} \quad (A.9)$$

$$I_v = \begin{bmatrix} 1 \\ 0 \\ 0 \\ 0 \end{bmatrix}, I_h = \begin{bmatrix} 0 \\ 1 \\ 0 \\ 0 \end{bmatrix}, I_{45} = \begin{bmatrix} 1/2 \\ 1/2 \\ 1 \\ 0 \end{bmatrix}, I_{LHC} = \begin{bmatrix} 1/2 \\ 1/2 \\ 0 \\ 1 \end{bmatrix} \quad (A.10)$$

where  $W$  is the received intensity of polarization.

If a receiver is able to measure the phase between the  $V$  and  $H$  channels, it is possible to do the incoherent method without measuring 6 polarizations. This method is called the coherent-on-receive (COR) technique. The elements of the Stokes vector can be expressed as

$$I_1 = |E_v|^2 \quad (A.11)$$

$$I_2 = |E_h|^2 \quad (A.12)$$

$$U = 2 |E_v| |E_h| \cos \delta \quad (A.13)$$

$$V = 2 |E_v| |E_h| \sin \delta \quad (A.14)$$

where  $\delta$  is the phase difference between  $V$  and  $H$  channels.

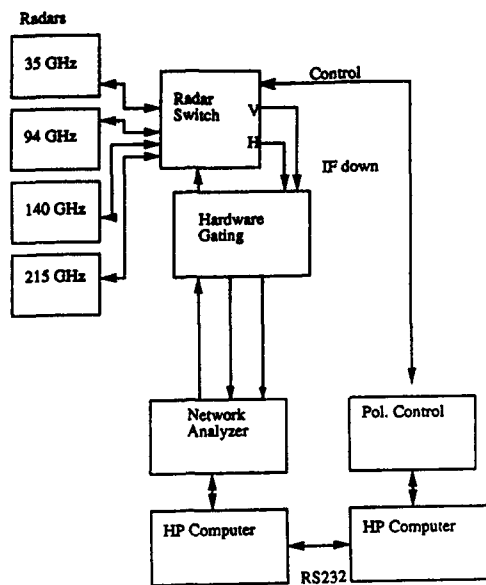


Figure 1 Block Diagram of the MMW Polarimetric Radar.

### 35 GHz Radar (Fully Polarimetric)

#### Transmitter

IF bandwidth up to 2 GHz  
 Power +23 dBm  
 Antenna 6" Lens (beamwidth 4.2 degrees)  
 Polarization Any polarization

#### Receiver

Dual Channel V and H  
 Mixers Fundamental mixing  
 Antenna 6" Lens (beamwidth 4.2 degrees)

#### Polarimetric data

Incoherent (coherent-on-receive)  
 Mueller matrix

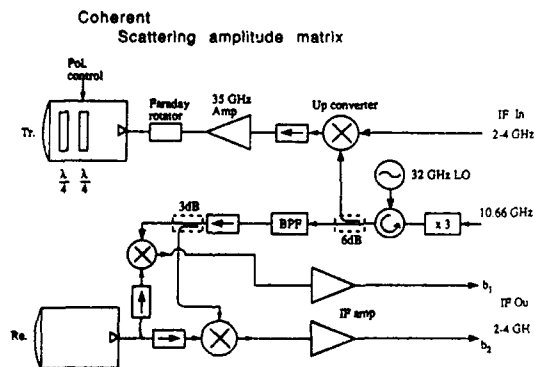


Figure 2 Block Diagram of the 35 GHz Radar Frontend.

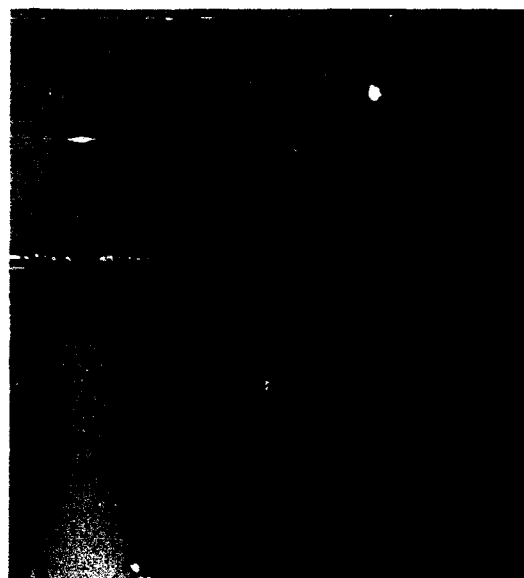


Figure 3 Photographs of the Metallic Tree and Rhododendron Tree.

### Rhododendron Tree (Target in motion)

Incoherent Polarimetric Measurement Mode (500 samples)  
 Fast Motion

1	0.16	-0.006	0.007
0.186	0.828	-0.017	0.017
0.04	0.059	0.735	0.056
-0.059	-0.023	-0.019	0.472

Slow Motion

1	0.231	-0.052	0.012
0.126	1.035	-0.021	0.049
-0.038	0.082	0.697	0.003
-0.013	-0.015	-0.064	0.619

Coherent Polarimetric Measurement Mode (8000 samples)

1	0.159	-0.002	-0.006
0.179	0.823	-0.003	-0.018
0.0	-0.01	0.683	-0.023
-0.033	-0.001	0.003	0.596

### Metallic Tree (Target in motion)

Incoherent Polarimetric Measurement Mode (500 samples)  
 Fast Motion

1	0.089	0.02	0.03
0.094	0.74	0.02	0.001
0.026	0.011	0.888	0.105
-0.028	-0.007	-0.126	0.619

Coherent Polarimetric Measurement Mode (8000 samples)

1	0.06	0.0	0.0
0.06	1.16	0.009	0.004
0.011	0.002	0.973	-0.053
0.008	0.002	0.049	0.89

Table 1. Average Mueller matrices of rhododendron and metallic trees measured with coherent and incoherent polarimetric measurement modes.

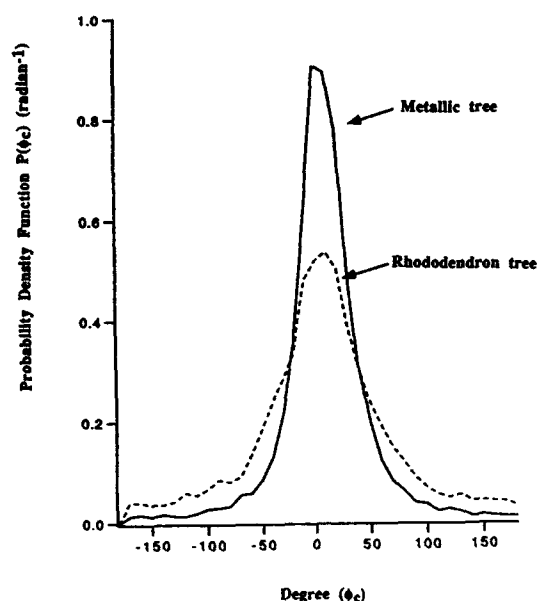


Figure 4 Probability Density Function Measured by the Coherent Polarimetric System.

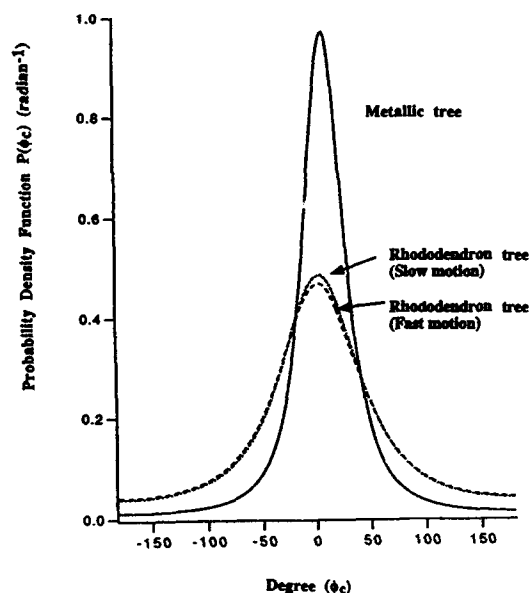


Figure 5 Probability Density Function Computed from the Average Mueller Matrix.

## DISCUSSION

G. Neininger, Germany

What is the realized cross polarization isolation?

Author's Reply

I am not sure but I believe that it is listed in the preprint article.

E. Schweicher, BE

You mentioned (in your second talk) a solid state design. Does that mean a solid-state transmitter and in that case what kind of transistors are used at 36 GHz and 94 GHz?

Author's Reply

The presenter did not know.

G. Brown, US

The histograms of the phase differences between the co- and cross polarization returns for data (from real and metallic trees) were relatively narrow in spread. What range bin was used to generate these data and how do you explain the rather small phase difference variance?

Author's Reply

I do not know the range bin used in the phase distribution plots since I did not work on those data. However, I do know that a very large number of samples were used in the preparation of the phase statistics, so I imagine that the bin was rather small.

# Polarimetric Techniques and Measurements at 95 and 225 GHz

James Mead, Robert McIntosh, Phillip Langlois, Paul Chang

University of Massachusetts  
Microwave Remote Sensing Laboratory  
Amherst, MA 01003, U.S.A.

## Summary

The University of Massachusetts has developed two high-power portable polarimetric radars operating at 95 and 225 GHz. The 95 GHz coherent polarimeter is configured to measure the complex scattering matrix of a target by transmitting a pair of orthogonally polarized pulses in rapid succession. We have also developed a noncoherent 225 GHz polarimetric radar which directly characterizes the target Mueller matrix by transmitting a sequence of four or six polarization states. In addition to reviewing the radar design and calibration, this paper summarizes measurements of natural and man-made objects made to date. These measurements include several varieties of trees, terrain, and snowcover. A model which approximates the Mueller matrix with a single parameter is introduced for a restricted class of clutter and is found to accurately predict the polarimetric behavior of vegetation and terrain at low incidence angles. We also present a two parameter approximation of the Mueller matrix that accurately models scattering from snowcover at large incidence angles.

## Introduction

The ability of a radar to classify an object beyond simply measuring its radar cross-section and velocity can be enhanced through knowledge of how the target modifies the polarization state of the incident electromagnetic wave. Simple geometric structures such as plane reflectors and spheres have well known scattering properties that modify the incident polarization in a predictable manner.

Distributed targets, such as foliage and terrain, will transform the incident polarization in a random fashion and are usually characterized in terms of the target Mueller matrix,  $\mathcal{L}$  (or Stokes scattering operator,  $M$ ), which describes the time or ensemble averaged scattering behavior of a target. The Mueller matrix is often measured indirectly, by first measuring the instantaneous complex scattering matrix,  $S$ , from which the Mueller matrix may be found [1]. The 95 GHz radar operates in this way. The 225 GHz radar, while not capable of measuring the complex scattering matrix,  $S$ , uses a noncoherent technique to directly measure the Mueller matrix. Both measurement techniques are described below.

## Coherent 95 GHz Polarimeter

The 95 GHz polarimeter consists of a single box, dual antenna radar, a Polarimetric Radar Control and Data Acquisition system (PRACDA), and a data logging/display computer. A block diagram of the 95 GHz polarimetric radar, designed and fabricated by the University of Massachusetts Microwave Remote Sensing Laboratory, is shown in Figure 1. The system consists of a multiplied reference oscillator at 93.6 GHz, which acts as both receiver local oscillator and driver for the transmitter amplifier chain. The transmitter amplifier consists of a solid-state injection locked amplifier, followed by an Extended Interaction klystron Amplifier (EIA), manufactured by Varian, Canada. Alternate transmission of vertically and horizontally polarized 95 GHz pulses is achieved with a waveguide ferrite switch. An orthomode transducer

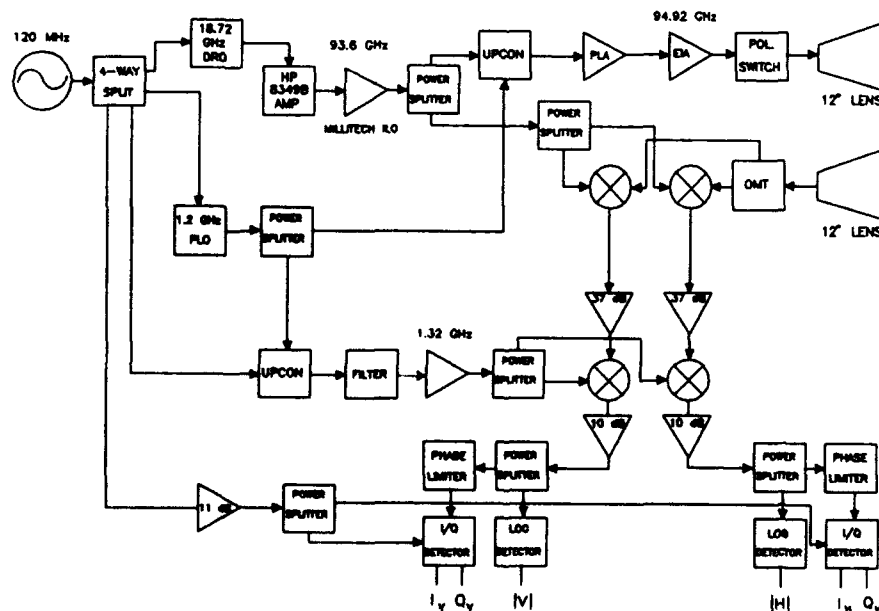


Figure 1 95 GHz polarimetric radar block diagram.

is used to separate the horizontally and vertically polarized components of the scattered signal, which is downconverted to 1.32 GHz using single-balanced mixers employing Schottky-barrier beam lead diodes. The signal is then amplified and downconverted again to 120 MHz where the signal is divided for separate amplitude and phase detection. A log amplifier/detector is employed in the amplitude channels, providing a dynamic range of 80 dB. The phase detector is preceded by a constant phase limiter, which maintains nearly constant phase over a dynamic range of 70 dB.

#### Coherent Measurement Technique

Measurement of the complex scattering matrix,  $S$ , is achieved by alternately transmitting horizontally and vertically polarized waves in rapid succession, i.e., fast enough to freeze motion in the target. Elements of the first column of the scattering matrix  $S_{hh}$  and  $S_{vh}$  are measured during the first pulse period (horizontal transmit) while  $S_{hv}$  and  $S_{vv}$  are measured during the second (vertical transmit). For a typical measurement, several hundred scattering matrices are measured, each representing a particular realization of the target. Since the complex scattering matrix can only characterize fully polarized targets (i.e., a single realization of a fading target or a hard target from a particular aspect angle) it is necessary to convert the individual scattering matrices to Mueller matrices, which may be averaged. While the Mueller matrix is not a complete description of the target (it contains neither Doppler information, nor higher order moments) it is useful in describing the average polarization transformation behavior of a target.

#### Noncoherent Polarimetric Methodology

The polarization state of a TEM wave traveling in the  $+z$  direction can be described in terms of the ellipse traced out by the electric field vector at the point  $z = z_0$ , as shown in Figure 2. The ellipse parameters,  $\phi$  and  $\tau$ , completely specify the polarization state of the wave and are expressed in terms of electric field quantities by [2]:

$$\tau = \frac{1}{2} \sin^{-1} \left( \frac{2|V||H|\sin\delta}{|V|^2 + |H|^2} \right) \quad (1)$$

$$\phi = \frac{1}{2} \tan^{-1} \left( \frac{2|V||H|\cos\delta}{|H|^2 - |V|^2} \right) \quad (2)$$

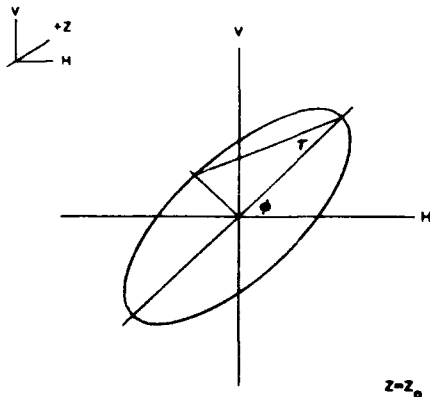


Figure 2 Ellipse parameters  $\phi$  (orientation) and  $\tau$  (ellipticity).

where  $|V|$  and  $|H|$  represent the magnitude of the electric field in the vertical and horizontal planes, and  $\delta$  is the phase difference between the vertical and horizontal field components. Waves having a right-hand polarization sense are represented by  $\tau > 0$ . Wave polarization can also be described by the Stokes vector [2]:

$$\mathbf{g} = \begin{bmatrix} g_0 \\ g_1 \\ g_2 \\ g_3 \end{bmatrix} = \begin{bmatrix} \langle |H|^2 + |V|^2 \rangle \\ \langle |H|^2 - |V|^2 \rangle \\ \langle 2|V||H|\cos\delta \rangle \\ \langle 2|V||H|\sin\delta \rangle \end{bmatrix} \quad (3)$$

where the  $\langle \cdot \rangle$  brackets indicate temporal or spatial averaging. The relationship between the Stokes vectors of the incident and scattered fields is characterized by the Mueller matrix,  $\mathcal{L}$  [4,5]. The Stokes vector,  $\mathbf{r}$ , of the scattered field, corresponding to the incident Stokes vector,  $\mathbf{g}$ , is given by

$$\mathbf{r} = \mathcal{L}\mathbf{g} \quad (4)$$

For the measurements reported in this paper, a technique is used to determine the Mueller matrix of various natural targets by sequentially transmitting six different polarization states [3]. The Mueller matrix is obtained from the six transmitted Stokes vectors,  $\mathbf{g}_i$ , ( $i = 1$  to 6), and the corresponding scattered Stokes vectors,  $\mathbf{r}_i$ , according to:

$$\mathcal{L} = [(\mathbf{G}\mathbf{G}^T)^{-1}\mathbf{G}\mathbf{R}^T]^T \quad (5)$$

where  $\mathbf{G}$  and  $\mathbf{R}$  are given by

$$\mathbf{G} = \begin{bmatrix} g_{0V} & g_{0H} & g_{0P} & g_{0M} & g_{0R} & g_{0L} \\ g_{1V} & g_{1H} & g_{1P} & g_{1M} & g_{1R} & g_{1L} \\ g_{2V} & g_{2H} & g_{2P} & g_{2M} & g_{2R} & g_{2L} \\ g_{3V} & g_{3H} & g_{3P} & g_{3M} & g_{3R} & g_{3L} \end{bmatrix}$$

and

$$\mathbf{R} = \begin{bmatrix} r_{0V} & r_{0H} & r_{0P} & r_{0M} & r_{0R} & r_{0L} \\ r_{1V} & r_{1H} & r_{1P} & r_{1M} & r_{1R} & r_{1L} \\ r_{2V} & r_{2H} & r_{2P} & r_{2M} & r_{2R} & r_{2L} \\ r_{3V} & r_{3H} & r_{3P} & r_{3M} & r_{3R} & r_{3L} \end{bmatrix}$$

The first column of  $\mathbf{G}$  and  $\mathbf{R}$  corresponds to the incident and scattered Stokes vector, respectively, when the transmitted field is vertically polarized ( $\phi = 90^\circ$ ;  $\tau = 0^\circ$ ). The remaining columns correspond to incident and scattered Stokes vectors when transmitting horizontal ( $\phi = 0^\circ$ ;  $\tau = 0^\circ$ ); positive  $45^\circ$  linear ( $\phi = 45^\circ$ ;  $\tau = 0^\circ$ ); minus  $45^\circ$  linear ( $\phi = -45^\circ$ ;  $\tau = 0^\circ$ ); right-hand circular ( $\phi$  arbitrary;  $\tau = 45^\circ$ ); and left-hand circular ( $\phi$  arbitrary;  $\tau = -45^\circ$ ) polarized waves, respectively.

Once the Mueller matrix is known, it is often useful to compute the response of a target using an arbitrary combination of transmit and receive antennas. The power received,  $p_{rec}$ , by an antenna whose polarization state is specified by the Stokes vector  $\mathbf{g}_{rx}$ , depends on the Stokes scattering operator,  $\mathbf{M}$ , and the Stokes vector of the transmit antenna,  $\mathbf{g}_{tr}$ , according to [1,4,5]:

$$p_{rec} = k\mathbf{g}_{rx}^T\mathbf{M}\mathbf{g}_{tr} \quad (6)$$

where  $k$  accounts for propagation effects between the radar and the target, and  $\mathbf{g}^T$  is the transpose of  $\mathbf{g}$ . The Stokes scattering operator is related to the Mueller matrix by



$$\mathbf{M} = \begin{bmatrix} 1 & 0 & 0 & 0 \\ 0 & 1 & 0 & 0 \\ 0 & 0 & 1 & 0 \\ 0 & 0 & 0 & -1 \end{bmatrix} \mathcal{L}. \quad (7)$$

The Stokes scattering operator for reciprocal media is symmetric [5]. However, the Stokes scattering operator found using (5) and (7) will not be exactly symmetric due to residual calibration errors in the radar and natural statistical variability. Specifically, for the data presented below, the received Stokes vectors were measured sequentially, so the scattered fields result from different sets of target realizations. Secondly, Stokes vectors are computed by incoherently summing a finite number of instantaneous realizations. Therefore, measured  $r_i$  values will converge to the true value of  $r_i$  as  $N^{-0.5}$ , where  $N$  is the number of independent samples. Furthermore, (5) will provide a good estimate of  $\mathcal{L}$  only if the scattered Stokes vectors are stationary (in the mean) during the measurement process.

### 225 GHz Polarimeter

The 225 GHz polarimeter shown in Figure 3 consists of a multiple polarization transmitter, a dual polarization receiver, the Polarimetric RADar Control and Data Acquisition (PRACDA) subsystem and a data logging computer [6]. Scalar feed lens antennas were selected for both the transmitter and receiver to minimize side-lobe levels and to provide low cross-polarization across the main beam. During polarimetric measurements, the transmitter's multiple-polarization lens antenna is sequentially switched between the six polarization states given in (5). The magnitude of the vertical and horizontal components of the scattered wave along with the phase difference between these components is measured using a dual-polarization receiver for each transmit state. This provides sufficient information to determine the received Stokes vector,  $r$ , using (3).

### Calibration

Calibration of the 95 and 225 GHz polarimeters follows a procedure described previously by Wood [7]. Wood's technique employs four in-scene reflectors, three of which scatter waves having known polarization and the fourth being an odd-bounce reflector. We use an alternate technique [6], that is equivalent to Wood's procedure, whereby a polarizing grid is placed in front of the receiver, allowing the three polarized targets to be replaced by a single odd-bounce reflector. The calibration procedure removes the effects of cross-coupling between vertical and horizontal receiver channels, and also accounts for gain and phase imbalance between the two channels. Once the receiver has been calibrated, it may be used to calibrate the transmit polarization states using the same odd-bounce reflector.

### Properties of the Mueller Matrix for Natural Surfaces

For backscattering from reciprocal media the Mueller matrix may be represented by up to nine independent parameters [4]. Measured data from natural surfaces at microwave [8] and millimeter-wave frequencies [9] show that there is no appreciable correlation between the copolarized and cross-polarized return, i.e.,  $\langle S_{ii}S_{jj}^* \rangle = 0$ , where  $S_{ij}$  is an element of the complex scattering matrix, [5]. For such targets, the Mueller matrix takes the form [8]

$$\mathcal{L} = \begin{bmatrix} A + B_0 & B & 0 & 0 \\ B & A - B_0 & 0 & 0 \\ 0 & 0 & C + B_0 & D \\ 0 & 0 & -D & C - B_0 \end{bmatrix} \quad (8)$$

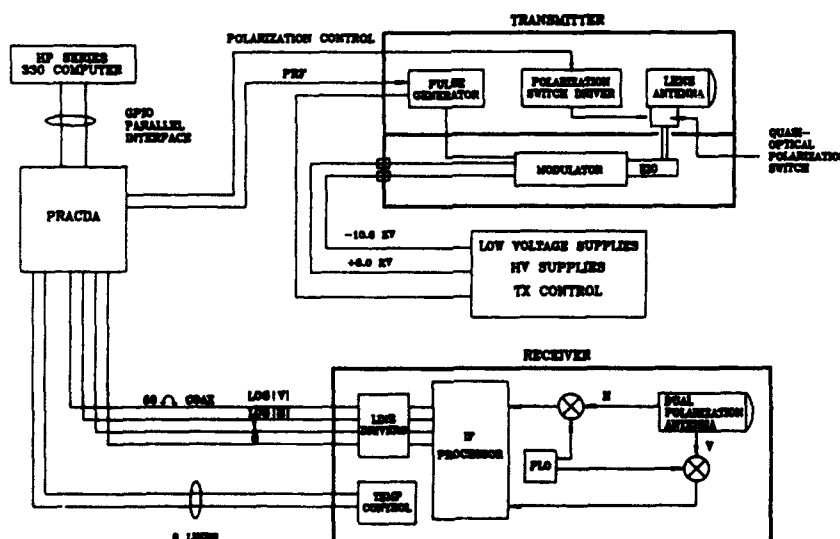


Figure 3 225 GHz polarimeter system diagram.

where

$$A = \frac{1}{2}(|S_{hh}|^2 + |S_{vv}|^2) \quad (9)$$

$$B = \frac{1}{2}(|S_{hh}|^2 - |S_{vv}|^2) \quad (10)$$

$$B_0 = |S_{hv}|^2 \quad (11)$$

$$C = \langle \text{Re}(S_{hh}^* S_{vv}) \rangle \quad (12)$$

$$D = \langle \text{Im}(S_{hh}^* S_{vv}) \rangle \quad (13)$$

In (12) and (13),  $\text{Re}(\ )$  signifies the real part of the operand and  $\text{Im}(\ )$  signifies the imaginary part of the operand. Thus, the Mueller matrix may be characterized by five independent parameters. Radars that measure only co- and cross-polarized power may be used to determine  $A$ ,  $B$ , and  $B_0$  but not  $C$  and  $D$ . Van Zyl [8] classifies targets in terms of the dominant scattering mechanism as odd bounce, even bounce, or diffuse scatterers. For targets where  $\langle |S_{hh}| \rangle, \langle |S_{vv}| \rangle > \langle |S_{hv}| \rangle$ , the following classifications may be made:

- $C > B_0$ : primarily odd bounce
- $-C > B_0$ : primarily even bounce
- $|C| < B_0$ : diffuse scatterer.

#### Presentation and Analysis of Measurements

The data presented below was collected during an extensive measurement program carried out in Amherst, Massachusetts during 1989-91. Backscattering was measured from a variety of targets, including foliage, terrain, and snowcover. Most of the data presented below was measured at 225 GHz, as the 95 GHz radar became operational in December, 1990. However, we show that the models developed from the 225 GHz data appear to be applicable to recent data collected with the 95 GHz system.

Copolarized signatures of two distributed natural targets are shown in Figure 4. These signatures are computed from the measured Mueller matrix using (5) and assuming  $g_{rx} = g_{tr}$ . The signature of a highly polarized scatterer (Weeping Willow tree) is shown in Figure 4a and of a highly unpolarized scatterer (dry sand) is shown in Figure 4b. The pedestal at  $\tau = \pm 45^\circ$  indicates that the scattered field contains significant unpolarized energy. The depolarization of the scattered fields is more easily seen in

Figures 5a and 5b, where histograms of the scattered field ellipse parameters  $\phi$  and  $\tau$  are shown for vertical polarization incident upon the target. Note that the distribution of  $\phi$  and  $\tau$  is clustered near  $\phi = 90^\circ$  and  $\tau = 0^\circ$  (vertical polarization) for the Weeping Willow tree, indicating little depolarization of the scattered wave. In contrast, the distribution for dry sand is widely dispersed over the  $\phi - \tau$  plane, indicating substantial depolarization.

Table 1 presents polarimetric data for the Willow tree, dry and wet sand, and other natural targets measured at 225 GHz. For comparison purposes, we have listed the targets in Table 1 in order of increasing depolarization ratio. The depolarization ratio,  $\chi$ , is defined as [10]

$$\chi = \frac{\sigma_{vh}^\circ + \sigma_{hv}^\circ}{\sigma_{hh}^\circ + \sigma_{vv}^\circ},$$

where the normalized radar cross-section,  $\sigma_{ij}^\circ = \langle |S_{ij}|^2 \rangle$ ,  $i$  refers to the receiver polarization,  $j$  the transmitter polarization.

Normalized radar cross-sections  $\sigma_{vv}^\circ$  and  $\sigma_{hh}^\circ$  are given in the second and third columns. The fourth and fifth columns list measured values of degree of polarization for horizontal and vertical transmit polarizations. The degree of polarization,  $P$ , of the scattered wave is defined in terms of the Stokes parameters of the scattered waves according to [2]:

$$P = \frac{\sqrt{r_1^2 + r_2^2 + r_3^2}}{r_0} \quad (14)$$

In the sixth column we have listed the average degree of polarization of the four linear polarizations used in making the Mueller matrix measurement (vertical, horizontal,  $+45^\circ$ , and  $-45^\circ$ ). Similarly, in column seven we have tabulated the average degree of polarization of the scattered wave for left and right hand circular transmit polarization.

All measurements presented in Table 1 were based on 1000 data points per polarization state using the measurement technique described above. The number of independent samples, as computed from the  $e^{-1}$  point of the power autocovariance function, was greater than 400 in all cases. All measurements were made with an illuminated footprint diameter on the order of 1-5 m. Additional information on these measurements can be found in [3].

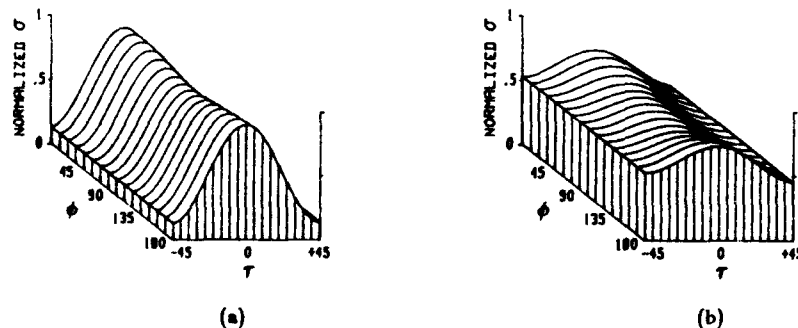


Figure 4 Copolarized signatures for Weeping Willow (left) and Dry Sand (right).

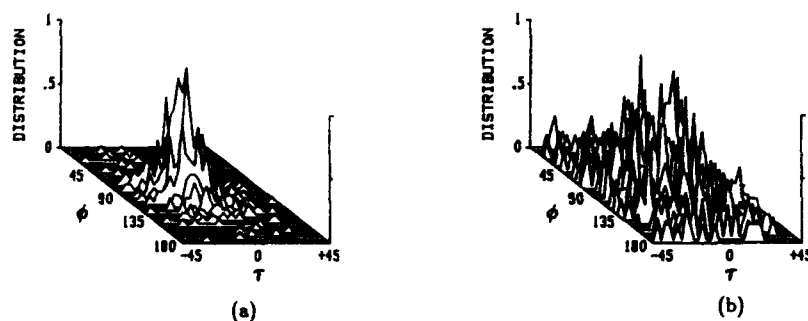


Figure 5 Scattered wave ellipse parameter histogram for Weeping Willow (left) and Dry Sand (right) for vertical transmit polarization.

Table 1. Summary of various polarimetric quantities for a variety of natural distributed targets listed in order of increasing depolarization ratio.

COLUMN:	1	2	3	4	5	6	7
TARGET	DEPOLARIZATION RATIO (dB)	$\sigma_{hh}^0$ (dBm <sup>2</sup> )	$\sigma_{vv}^0$ (dBm <sup>2</sup> )	HORIZONTAL	VERTICAL	( LINEAR )	( CIRCULAR )
Weeping Willow	-12.8	-4.1	-4.3	.91	.88	.89	.80
Arbor Vitae	-12.1	-9.2	-9.1	.87	.87	.87	.74
Red Maple	-11.0	-2.4	-2.3	.88	.87	.86	.78
American Elm	-10.4	-5.4	-5.6	.86	.82	.84	.71
Norway Maple	-9.4	-4.5	-4.8	.81	.80	.81	.66
Silver Maple	-9.3	-2.8	-3.0	.81	.75	.78	.58
Short Grass (30° - 50° Incidence)	-8.9	-6.6	-6.5	.67	.81	.75	.54
White Pine	-8.3	-5.9	-6.3	.78	.74	.77	.57
Snowcover (40° Incidence)	-7.8	-3.1	-3.1	.67	.69	.67	.46
Wet Sand (26° Incidence)	-7.3	-8.5	-7.2	.65	.79	.66	.40
Snowcover (80° Incidence)	-6.5	-21.0	-16.3	.39	.75	.61	.43
Snowcover (65° Incidence)	-4.7	-5.9	-4.4	.45	.55	.51	.13
Dry Sand (26° Incidence)	-4.4	-0.2	0.3	.43	.44	.42	.10

### Degree of Polarization for Transmission of Linear Polarizations

The degree of polarization shown in Table 1 for the average of the four linear transmit polarizations is seen to decrease with increasing  $\chi$ . This trend can be explained as follows. Substitution of the Mueller matrix for natural surfaces (8) and the Stokes vector of a horizontally polarized transmit field into (4) results in an expression for the scattered field Stokes vector,  $r_h$ . Using (14), the degree of polarization,  $P_h$ , of the scattered wave is given as

$$P_h = \frac{|A - B_0 + B|}{A + B_0 + B}. \quad (15)$$

For a vertically polarized transmit field, the scattered wave degree of polarization,  $P_v$ , is found to be:

$$P_v = \frac{|A - B_0 - B|}{A + B_0 - B}. \quad (16)$$

Measurements of all of those targets listed in Table 1 show that the degree of polarization for  $\pm 45^\circ$  linear transmit polarizations is nearly equal to the average of (15) and (16). Solving (15) and (16) for the average of horizontal and vertical degree of polarization gives:

$$P_{\text{linear}} = \frac{A^2 - B_0^2 - B^2}{(A + B_0)^2 - B^2}. \quad (17)$$

Where "linear" denotes the average of the four linear polarizations, vertical, horizontal,  $+45^\circ$  and  $-45^\circ$ . Dividing the numerator and denominator of (17) by  $A^2$  and noting from (9) and (11) that  $\chi = B_0/A$  leads to:

$$P_{\text{linear}} = \frac{(1 - \chi)(1 + \chi) - (\frac{B}{A})^2}{(1 + \chi)^2 - (\frac{B}{A})^2}. \quad (18)$$

The ratio  $B/A$  is obtained from (9) and (10):

$$\gamma = \frac{B}{A} = \frac{\langle |S_{hh}|^2 \rangle - \langle |S_{vv}|^2 \rangle}{\langle |S_{hh}|^2 \rangle + \langle |S_{vv}|^2 \rangle} = \frac{\sigma_{hh}^o - \sigma_{vv}^o}{\sigma_{hh}^o + \sigma_{vv}^o}.$$

Our measurements show that the ratio of  $\sigma_{hh}^o$  to  $\sigma_{vv}^o$  is within  $\pm 1.5$  dB for vegetation and for terrain at incidence angles below  $50^\circ$  (measured off nadir). Thus, the sum of  $\sigma_{hh}^o$  and  $\sigma_{vv}^o$  is much greater than their difference for all of the targets in Table 1. Consequently,  $(B/A)^2$  can be neglected and (18) simplifies to:

$$P_{\text{linear}} = \frac{1 - \chi}{1 + \chi}. \quad (19)$$

Equation (19) is plotted in Figure 6 along with measured values of the average linear degree of polarization from Table 1.

The quantity  $C$  in (8) strongly affects the degree of polarization of both  $\pm 45^\circ$  linear and circular polarizations.  $C/A$  can also be expressed in terms of  $\chi$  using the following argument. The degree of polarization for transmission of  $\pm 45^\circ$  linear polarizations,  $P_{\pm 45^\circ}$ , is given by:

$$P_{\pm 45^\circ} = \frac{\sqrt{B^2 + (C + B_0)^2 + D^2}}{A + B_0}. \quad (20)$$

Our data indicate that for those targets for which (19) is valid, the distribution of  $\arg(S_{hh}) - \arg(S_{vv})$  has a mean value near zero, thus, (13) implies that  $D$  will be small.

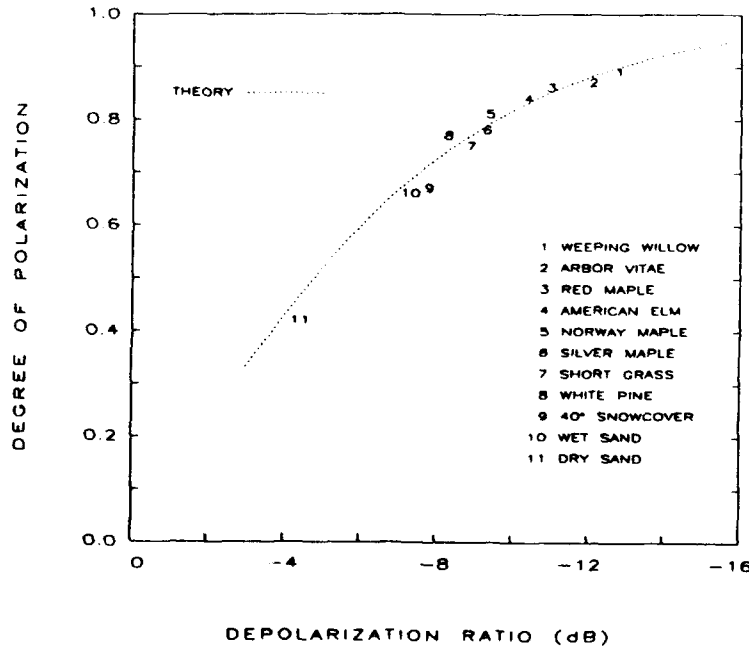


Figure 6 Scattered wave degree of polarization for the average of four linear polarizations ( $V, H, \pm 45^\circ$ ) for various natural targets. Equation (19) shown for comparison.

For  $B^2$  and  $D^2 \ll (C + B_0)^2$ , equating (20) to (19) yields:

$$C = A - 2B_0 \quad \text{or} \quad \frac{C}{A} = 1 - 2\chi. \quad (21)$$

All natural targets measured to date have resulted in positive values of  $C$ , indicating either odd-bounce or diffuse scattering [8]. If we require  $C$  to be positive, then (19) and (21) are valid for  $\chi < 0.5$ .

#### Degree of Polarization for Transmission of Circular Polarizations

The degree of polarization for left and right hand circular transmit polarization,  $P_{cp}$ , is given by:

$$P_{cp} = \frac{\sqrt{B^2 + D^2 + (B_0 - C)^2}}{A + B_0}. \quad (22)$$

Applying (21) with the additional condition that  $B^2$  and  $D^2 \ll (B_0 - C)^2$ , leads to:

$$P_{cp} = \frac{|1 - 3\chi|}{1 + \chi}. \quad (23)$$

The circular degree of polarization listed in Table 1, representing the average of left and right hand circular transmit polarization, is plotted with (23) in Figure 7. The scattered wave polarization sense is opposite from that of the incident wave for values of  $\chi < 1/3$  (-4.33 dB), and is likewise for  $\chi > 1/3$ . For  $\chi$  values near  $1/3$  the condition that  $B^2$  and  $D^2 \ll (B_0 - C)^2$  will no longer hold, indicating that  $P_{cp}$  will be slightly greater than zero for  $\chi = 1/3$ .

#### Single Parameter Approximation of the Normalized Mueller Matrix

While the degree of polarization of much of our 225 GHz data may be described by a single parameter,  $\chi$ , we emphasize that this data represents a limited, but important, class of natural targets. From the above discussion, the normalized Mueller matrix for these targets can be expressed as:

$$\mathcal{L}_\chi = \frac{1}{1 + \chi} \begin{bmatrix} 1 + \chi & 0 & 0 & 0 \\ 0 & 1 - \chi & 0 & 0 \\ 0 & 0 & 1 - \chi & 0 \\ 0 & 0 & 0 & 1 - 3\chi \end{bmatrix} \quad (24)$$

valid for  $\chi < 0.5$ .

The simplified Mueller matrix in (24) appears to be a good approximation for 225 GHz foliage measurements as well as terrain measurements at low incidence angles. In Figure 8a we present measured copolarized and degree of polarization signatures at 225 GHz for the White Pine from Table 1. Figure 8b presents similar signatures computed using  $\mathcal{L}_\chi$ . A similar comparison for White Pine measurements at 95 GHz is shown in Figures 8c and 8d.

#### Scattering from Snowcover at Large Incidence Angles

Although most of the targets given in Table 1 are modeled accurately using (24), it is clear that the snowcover data at  $65^\circ$  and  $80^\circ$  departs from this description. One approach to modelling the Mueller matrix for these surfaces is to carry through a similar derivation without setting  $B = 0$ . However, the measured Mueller matrix shows that  $P_{\pm 45^\circ}$  does not equal the average of  $P_v$  and

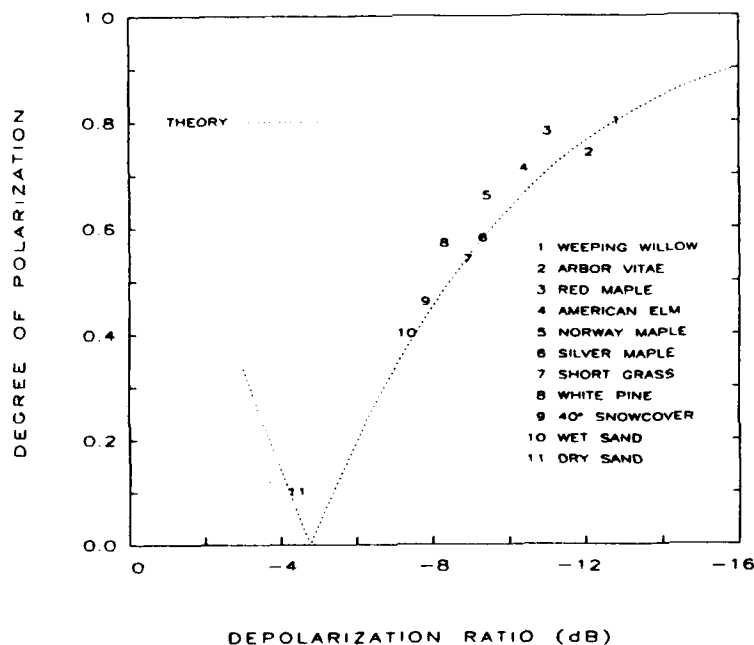


Figure 7 Scattered wave degree of polarization for the average of left and right hand circular polarization for various natural targets. Equation (23) shown for comparison.

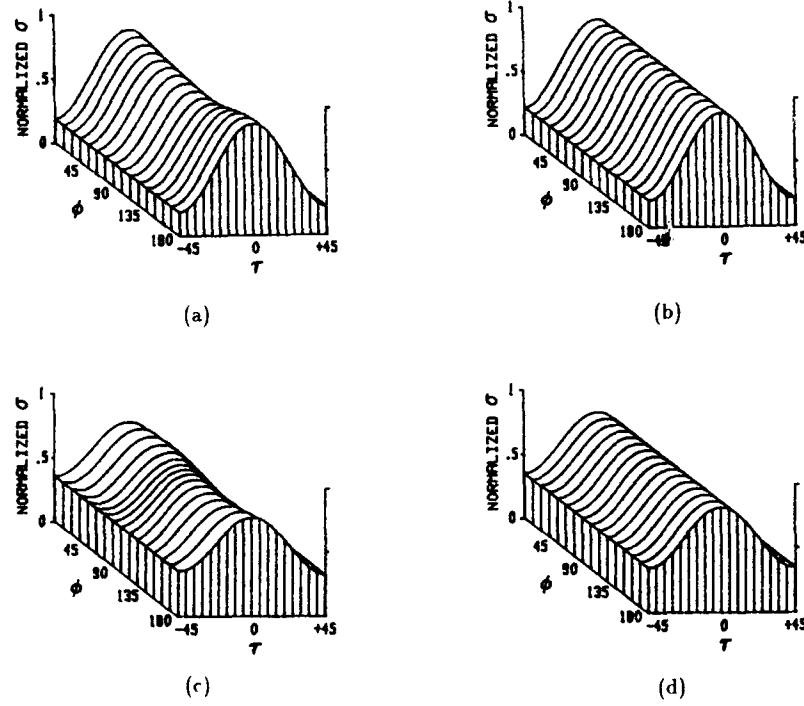


Figure 8 Copolarized signatures for White Pine: (a) measured signature at 225 GHz; (b) 225 GHz signature computed from  $\mathcal{L}_\chi$ ; (c) measured signature at 95 GHz; (d) 95 GHz signature computed from  $\mathcal{L}_\chi$ .

$P_h$  when  $B$  is large. Instead,  $P_{\pm 45^\circ}$  is biased towards  $P_v$  if  $\sigma_{vv}^\circ > \sigma_{hh}^\circ$ . This bias suggests computing  $P_{\pm 45^\circ}$  using a power weighted average of  $P_v$  and  $P_h$ , i.e.,

$$P_{\pm 45^\circ} = \frac{P_v \sigma_{vv}^\circ + P_h \sigma_{hh}^\circ}{\sigma_{vv}^\circ + \sigma_{hh}^\circ} \quad (25)$$

Although this expression gives excellent agreement with measured data, it leads to a fairly complicated expression for the Mueller matrix, in terms of two parameters,  $\chi$  and  $\gamma$ . Another drawback to this approach is that there is no obvious theoretical basis for (25). Therefore, we sought a physical-based model to achieve similar agreement with the measured data.

One straightforward scattering model for snowcover is shown in Figure 9, where we consider two separate effects: transmission through the air-snow interface and volume scattering within the snow layer. In general, the transmission coefficient for the vertically polarized field,  $t_{v12}$ , will be different than the transmission coefficient for the horizontally polarized field,  $t_{h12}$ . The normalized transmissivity matrix for the air-snow interface, relating the incident and transmitted Stokes vectors is given by [4]

$$\mathbf{T}_{as} = \frac{1}{|t_{h12}|^2 + |t_{v12}|^2} \begin{bmatrix} |t_{h12}|^2 + |t_{v12}|^2 & |t_{h12}|^2 - |t_{v12}|^2 & 0 & 0 \\ |t_{h12}|^2 - |t_{v12}|^2 & |t_{h12}|^2 + |t_{v12}|^2 & 0 & 0 \\ 0 & 0 & 0 & 0 \\ 0 & 0 & 0 & 0 \\ \text{Re}(t_{v12}t_{h12}^*) & -\text{Im}(t_{v12}t_{h12}^*) & 0 & 0 \\ \text{Im}(t_{v12}t_{h12}^*) & \text{Re}(t_{v12}t_{h12}^*) & 0 & 0 \end{bmatrix} \quad (26)$$

For this model we assume that  $t_{v12}$  and  $t_{h12}$  are in phase, thus  $\mathbf{T}_{as3,4}$  and  $\mathbf{T}_{as4,3}$  will equal zero.

Volume scattering is thought to be the dominant scattering mechanism in snowcover [10]. The random nature of the snow suggests that scattering within the volume should be independent of orientation angle,  $\phi$ . This implies that (24) is a reasonable choice to model scattering within the volume. Combining the effects of the surface and volume, the total normalized Mueller matrix for the snowcover is given by:

$$\mathcal{L}_{\text{total}} = \mathbf{T}_{as} \mathcal{L}_\chi \mathbf{T}_{as}$$

where  $\mathbf{T}_{as}$  is of the form of  $\mathbf{T}_{as}$  with  $t_{x21}$  substituted for  $t_{x12}$ , and  $\tilde{\chi}$  refers to the depolarization ratio within the volume. Dividing  $\mathbf{T}_{as}$  by  $t_{h12}$  and  $\mathbf{T}_{as}$  by  $t_{h21}$  and noting that for linear, isotropic media,  $t_{v12}/t_{h12} = t_{v21}/t_{h21}$ , the total Mueller matrix may be written as

$$\mathcal{L}_{\text{total}} = \frac{1}{(1 + \alpha^2)^2} \mathbf{T}_\alpha \mathcal{L}_\chi \mathbf{T}_\alpha \quad (27)$$

where  $\mathbf{T}_\alpha$  is given by

$$\mathbf{T}_\alpha = \begin{bmatrix} 1 + \alpha^2 & 1 - \alpha^2 & 0 & 0 \\ 1 - \alpha^2 & 1 + \alpha^2 & 0 & 0 \\ 0 & 0 & 2\alpha & 0 \\ 0 & 0 & 0 & 2\alpha \end{bmatrix}$$

and  $\alpha = t_{v12}/t_{h12}$ . Simplifying (27) yields an expression in terms of  $t_{v12}$ ,  $t_{h12}$ , and  $\tilde{\chi}$ . By equating (27) to (8), the following relationships are found:

$$t_{h12}^4 = \frac{A+B}{2} \quad t_{v12}^4 = \frac{A-B}{2} \quad \tilde{\chi} = \frac{B_0}{\sqrt{A^2 - B^2}}$$

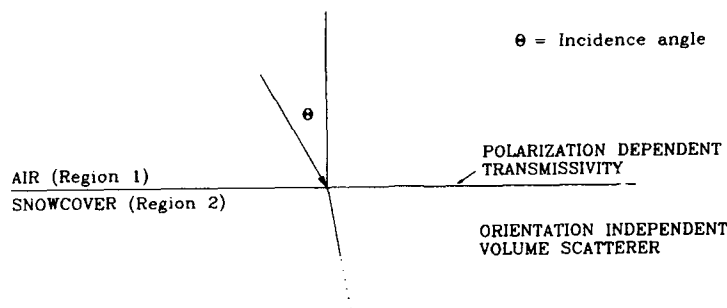


Figure 9 Snowcover model including the effects of surface transmissivity and orientation independent volume scattering.

Using the relationships given above, the total normalized Mueller matrix for the snowcover is

$$\mathcal{L}_{\text{total}} = \frac{1}{1+\chi} \begin{bmatrix} 1+\chi & \gamma & 0 & 0 \\ \gamma & 1-\chi & 0 & 0 \\ 0 & 0 & \sqrt{1-\gamma^2}-\chi & 0 \\ 0 & 0 & 0 & \sqrt{1-\gamma^2}+3\chi \end{bmatrix} \quad (28)$$

Note that (28) does not require any knowledge of the transmission coefficients used in deriving this model. Rather, the effect of unequal transmission of the vertical and horizontal fields is accounted for by  $\gamma$ , which may be derived from  $\sigma_{vv}^0$  and  $\sigma_{hh}^0$ .

In Figures 10a through 10d we compare copolarized and degree of polarization signatures for snowcover measured at  $80^\circ$  incidence, showing excellent agreement between the experimental and modeled response at 225 GHz. Preliminary measurements at 95 GHz show similar agreement between the measured Mueller matrix and (28).

#### Conclusions

The normalized Mueller matrices of those tree species listed in Table 1 have been shown to be closely predicted as a function of a single parameter,  $\chi$ . In addition, backscatter from (short) grass-covered terrain for incidence angles between  $30^\circ$  and  $50^\circ$ , snowcover at  $40^\circ$  incidence, and wet and dry sand surfaces at  $26^\circ$  incidence are also modeled accurately by  $\chi$ . All of these targets satisfy the three conditions leading to (24): (1)  $\sigma_{hh}^0$  and  $\sigma_{vv}^0$  are nearly equal, (2) the scattered wave degree of polarization when transmitting  $\pm 45^\circ$  linear polarization is nearly equal to the average of vertical and horizontal transmit polarization, and (3) the mean value of the distribution of  $\arg(S_{hh}) - \arg(S_{vv})$  is close to zero.

For snowcover at incidence angles greater than  $50^\circ$ , we have shown that the normalized Mueller matrix can be modeled using two parameters,  $\chi$  and  $\gamma$ , both of which depend solely on co- and cross polarized radar cross-sections. It seems likely that clutter requiring the more general form of  $\mathcal{L}$  (both B and D non-negligible) will be encountered at these short wavelengths. However, the significant variety of targets presented above indicates that there exists a class of scatterers suitable to a more simplified description.

#### REFERENCES

- [1] Van Zyl, J. J., H. A. Zebker, C. Elachi, "Imaging Radar Polarization Signatures: Theory and Observation," *Radio Science*, Vol. 22, No. 4, April, 1987, pp. 529-544.
- [2] Born, M. and E. Wolf, *Principles of Optics*, 3rd. edition, Pergamon Press, New York, pp. 30-31 and 554-555, 1965.
- [3] Mead, J.B. and R.E. McIntosh, "Polarimetric Backscatter Measurements of Deciduous and Coniferous Trees at 225 GHz," *IEEE Trans. on Geoscience and Remote Sensing*, vol. 29, No. 1., January, 1991, pp. 21-28.
- [4] Huynen, J.R., *Phenomenological Theory of Radar Targets*, Ph.D. Dissertation, Drukkerij Bronder-Offset N.V., Rotterdam, 1970.
- [5] Ulaby, F.T. and C. Elachi, *Radar Polarimetry for Geoscience Applications*, Artech House, Norwood, MA, 1990, pp. 17-25, 145.
- [6] Mead, J.B. and R.E. McIntosh, "A 225 GHz Polarimetric Radar," *IEEE Trans. on Microwave Theory and Techniques*, vol. 38, September, 1990, pp. 1252-1258.
- [7] Wood, M.A., "A Theoretical Study of Calibration Procedures for Coherent and Non-Coherent Polarimetric Radars," Royal Signals and Radar Establishment, Malverne, England, Report No. 86011.
- [8] Van Zyl, J. J., "Unsupervised Classification of Scattering Behavior Using Radar Polarimetry Data," *IEEE Trans. on Geoscience and Remote Sensing*, Vol. 27, No. 1, January, 1989, pp. 36-45.

- [9] Wnitt, M.W. and F.T. Ulaby, "Millimeter-Wave Polarimetric Measurements of Artificial and Natural Targets," *IEEE Trans. on Geoscience and Remote Sensing*, Vol. 26, No. 5, September, 1988, pp. 562-573.
- [10] Narayanan, R.M., and R.E. McIntosh, "Millimeter-Wave Backscatter Characteristics of Multilayered Snow Surfaces," *IEEE Trans. on Antennas and Propagation*, vol. 38, No. 5, May, 1990, pp. 693-703.

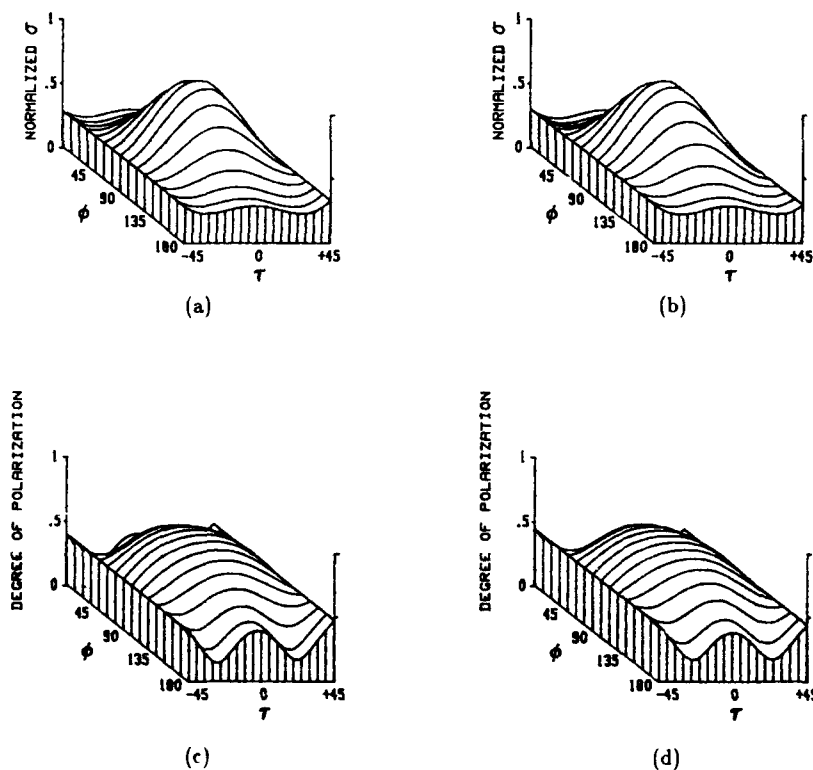


Figure 10 Copolarized and degree of polarization signatures for snowcover at  $80^\circ$  incidence: (a) measured copolarized signature at 225 GHz; (b) 225 GHz copolarized signature computed from  $\mathcal{L}_{\text{total}}$ ; (c) measured degree of polarization signature at 225 GHz; (d) 225 GHz degree of polarization signature computed from  $\mathcal{L}_{\text{total}}$ .

## DISCUSSION

E. Schweicher, BE

For your 95 GHz system you mentioned a  $NF = 10$  dB for the receiver. Does this receiver start with a LNA and in that case what kind of LNA? Same question for the 225 GHz system.

Author's Reply

Both receivers have mixer inputs -- do not use an LNA (low noise amplifier).



## POLARIMETRIC MONOPULSE RADAR SCATTERING MEASUREMENTS OF TARGETS AT 95 GHz

by

R. J. Wellman, J. Nemerich, H. Dropkin  
D. R. Hutchins, J. L. Silvious, and D. A. Wikner  
Harry Diamond Laboratories  
US Army Laboratory Command  
Adelphi, MD 20783-1197, USA

### Summary

This paper describes a 95-GHz polarimetric monopulse instrumentation radar and selected scattering measurement results for an armored vehicle. The radar is all-solid-state, coherent, frequency steppable over a 640-MHz bandwidth, and completely polarimetric for linearly or circularly polarized radiation. Details of the methods used to perform the amplitude and phase calibrations and the effectiveness of polarization distortion matrix corrections are included in the paper. Measurements made with the radar of various vehicles on a turntable have allowed quasi-three-dimensional polarimetric ISAR images of the targets to be generated. Sample images for an infantry combat vehicle are presented together with high-resolution range profiles of the target for all monopulse channels.

### 1. Introduction

Sensor systems operating at about 95 GHz are being investigated for use in smart munitions designed to defeat armored vehicles.<sup>1</sup> Specific radar scattering properties of these targets frequently are required for evaluating the performance of a sensor system. In this paper a 95-GHz polarimetric monopulse instrumentation radar is described that is capable of acquiring the required target signature data.

Measurements have been made for several vehicles with the radar located on the US Army Missile Command (MICOM) 100-m tower at Redstone Arsenal, AL, and the target mounted on a tiltable turntable. Data were collected for various radar depression angles and target azimuth angles to allow computation of radar cross section (RCS) polar plots, high-resolution range (HRR) profiles for the two-angle monopulse sum and difference channels, and inverse synthetic aperture (ISAR) images for the monopulse channels.

Section 2 of this report describes the basic characteristics of the radar and Section 3 contains a discussion of the procedures used for calibration of the radar. Some sample target signatures obtained for an infantry combat vehicle are given in Section 4 to demonstrate the radar's capabilities. Conclusions reached regarding the radar system, the calibration procedures, and the scattering measurements are contained in Section 5.

### 2. Description of the Radar System

The radar described in this paper was designed for obtaining 95-GHz target signature data of ground-based targets with the radar located on a tower and with computer-controlled operation from a remote ground station. Fig. 1 shows the radar head and pedestal. A video camera that is boresighted with the radar and a metallic cover for the system are not shown in the photograph to allow a view of the radar hardware. The radar head is covered during operation, if needed, to allow it to be air-conditioned for temperature control. Data recording and control of the tower-mounted radar are performed at a ground station located in an 11-m-long semi-trailer. Data from the target platform also are recorded at that location.

The basic characteristics of the radar are summarized in Table 1. The radar is a completely polarimetric two-coordinate amplitude-comparison monopulse system. It is a coherent, pulsed radar that operates in a frequency-stepped mode between 95.00 and 95.64 GHz. The frequency-step size can be selected to be 1, 2, 5, 10, or 20 MHz, and the radar pulse repetition frequency (PRF) is also selectable to be 1, 2, 5, or 10 kHz. The system was operated with 64 10-MHz steps and a transmit PRF of 10 kHz for the measurements reported here. The peak power of the all-solid-state transmitter is 45 W, the pulse width is 100 ns, and there is one adjustable range gate.

Either circularly or linearly polarized radiation can be transmitted by the radar according to which mode of operation is selected. For example, one pulse with either right-hand circular polarization (RHCP) or left-hand circular polarization (LHCP) may be transmitted and both senses of polarization can be received. The polarization of succeeding pulses may be right- or left-circular depending on the transmit format selected. A similar mode of operation is possible with horizontal (H) and vertical (V) polarization.

The radar has a lens antenna that can be easily removed and replaced with another having a different diameter. For a specific measurement scenario a lens with a diameter between 3.8 and 15.2 cm may be selected from six available lenses. The one-way 3-dB beamwidths of these lenses range between about 1.5 and 5.2 deg.

A simplified schematic diagram of the radar circuit is shown in Fig. 2. It is seen in the

figure that the transmitter output is routed via the switchable circulator into either the H-channel or the V-channel monopulse comparator and then to the lens via a multi-mode feed horn. A wire-grid diplexer is placed between the feed horns and the lens for proper routing of the radiation. The quarter-wave-plate (QWP) between the diplexer and the lens may be aligned to maintain the original incident linear polarization, or it may be rotated to convert the radiation of one channel to RHCP and the other to LHCP. If the QWP is oriented for the linear polarization mode, the vertical and horizontal components of reflected radiation are diplexed into the V- and H- channel comparators, respectively, and the resulting sum, elevation difference, and azimuth difference signal may be detected for each polarization. If the QWP is oriented for the circular polarization mode, the sum and difference signals for the RHCP and LHCP components of the reflected radiation are similarly detected.

The oscillator source for the six sum and difference channel mixers is frequency stepped synchronously with the transmitter source and maintains a constant offset of 3 GHz.

The radar Data Acquisition System (DAS) has six I/Q detectors for the monopulse sum and difference signals. The relative phase of the two sum channels and their log amplitudes also are processed in the DAS. For each transmitted pulse the signals received in each of the 16 channels are sampled, multiplexed, and digitized by two 12-bit A/D's. The multiplexed data are transmitted from the radar via a fiber-optic data link to the remote computer control/recording system. The latter is a PC that includes an 80386 20-MHz processor, 4 Mbytes of memory, and two 300-Mbyte disc drives. Data are archived on 150-Mbyte, streaming 112.5-Kbyte/s cassette tapes. Although the custom interface to the radar DAS has a 240-Kbyte/s capability, the limit on the recording rate reduces the maximum data rate to 120 Kbytes/s.

The radar is mounted on a pedestal that can be computer controlled locally or from a remote station to scan the radar or to orient it to a fixed position. The pedestal is an elevation-over-azimuth type with 0.01-deg pointing accuracy. It has scanning rates that can be selected to be between 0.1 and 10 deg/s.

As indicated above, a video camera is mounted on the radar head, and it can be boresighted with the radar to video record the target whose signature is being measured.

### 3. Radar Calibration Procedures

The radar calibration procedure is very complicated due to the number and types of data channels. The procedure can be broken up into three distinct sections: the amplitude calibration for the log receiver in the sum-channels, the sum-channel relative polarimetric phase calibration, and coherent sum and difference channels calibration. Some preliminary calibrations were done in the laboratory before the

radar was taken to the field measurement site at Redstone Arsenal, and a series of pre-measurement checks and calibrations were done at the field test site. Only the basic features of these checks and calibrations are given here since many are well-known procedures.<sup>2</sup> These include taking proper account of gain imbalances in I/Q detectors and nonlinear responses in detectors and amplifiers.

The radar calibrations at the field measurement site were performed using the reflectors listed in the calibration target array of Table 2. The range of each reflector to the radar and its RCS were chosen so that the signal levels from reflectors 1, 2, and 4 were approximately equal and in the linear range of the receivers (about 6 dB below A/D saturation). The log receivers were calibrated using reflectors 2 and 4. Reflector 3 was used for calibrating the relative polarimetric phase channel and for determining a sign in the polarization distortion matrix (PDM) calibration described below.

The dynamic range of the system was more than adequate to insure that the maximum signal levels from the target were below the saturation level of the detectors and the amplifiers were well above the noise level of the system. The dynamic range was about 66 dB for the linear channels and about 72 dB for the log channels. Stability checks were made periodically, and corrections were made for the minimal drifts that were observed.

Transfer curves for the log receiver in each sum channel were generated in the laboratory using a 3-GHz source to simulate the IF signal from the sum channel mixer and with a precision attenuator to vary the signal level. The amplitude calibrations at the field site were performed by boresighting the radar on the appropriate corner reflector and varying the precision attenuator to simulate the expected range of signal levels for the target. These measurements were used to verify the transfer curves measured in the lab. Absolute calibration of the amplitude for each polarization channel was determined using the signal level corresponding to the known RCS of the reflector, the transfer curve for that channel, and the ratio of the radar range to that reflector and the range to the target to be measured.

The relative polarimetric phase channel initially was calibrated in the laboratory and a reference look-up table was generated. This table related the phase angle of the signal into the I/Q detector to that at its output. A gridded trihedral was used at the field site as the reference reflector, and the phase difference between the coherent sum channels was measured. These values then were used to determine their relationship to the phase angle values in the reference table for each of the coherent sum channels. A correction table was generated from this measurement as a function of frequency so that the actual polarimetric phases could be computed directly from the measured values for each frequency. The polarimetric phase calibration was checked using the

gridded trihedral by comparing the phase differences between RHCP and LHCP signals for both senses of transmitted polarizations. These values agree to within  $\pm 3$  deg overall.

The effects of imperfect cross-polarization isolation in the radar can be mitigated by use of the PDM calibration technique.<sup>3</sup> This calibration method is intended to remove the radar system parameters from the data so that the target polarization scattering matrix can be determined without degradation due to the system. It can be used for both linear and circular polarization by making measurements of the four reflectors listed in Table 2. For this report, the PDM calibration technique was carried out for circular polarization. The calibration method for the coherent receivers is shown in block form in Fig. 3.

For calibration purposes, 200 ramps of data are taken for each of the four reflectors, where a ramp consists of 64 frequency-stepped pulses transmitted with RHCP and 64 pulses transmitted with LHCP. The sum channel I/Q corrections were generated by characterizing each I/Q detector at four signal levels for every 22.5 deg change in input phase from 0 to 360 deg. This I/Q correction reduced the amplitude variation due to I/Q errors to 40 dB below the average signal level and the maximum phase correction was 3 deg. The PDM calibration is applied to the coherent sum channels only. The PDM correction parameters are calculated for each frequency and for each polarization, and then they are applied to the data to obtain the calibrated amplitudes and phases.

The difference (or delta) channels are calibrated by taking the ratio of the delta channel and sum channel signal levels and then adjusting the delta channel phase to compensate for phase variations in the sum channel due to the PDM correction and phase variations between sum and difference channels versus frequency.

The PDM calibration technique described above improved the cross-polarization isolation of the system to about 35 dB. Table 3 shows a comparison of the frequency-averaged RCS amplitudes for two reference reflectors after performing the other calibrations and applying the PDM calibration to the linear sum channels. The RCS's in dBsm were used to compute the averages. The RCS amplitudes representing the various transmitted/received polarization combinations are  $\sigma_{RR}$ ,  $\sigma_{RL}$ ,  $\sigma_{LR}$ , and  $\sigma_{LL}$ , where the first subscript is the polarization of the transmitted radiation and the second is the polarization of the received radiation. The data for the log channels indicates the cross-polarization isolation levels without compensation. The improvement in the cross-polarization isolation using the PDM calibration technique is between 5 and 10 dB, but this was limited by the influence of scatterers in the antenna sidelobes. The agreement between the log channel and the PDM-corrected linear channel amplitudes for these reflectors is good. The small root-mean-

square deviations (RMS's) for the copolarized returns indicate the degree of amplitude stability of the system.

Ideally there should have been no cross-polarized reflection from the dihedral for circular polarization. The small values of  $\sigma_{RL}$  and  $\sigma_{LR}$  shown in Table 3 are believed to result from a combination of incomplete cross-polarization cancellation by the PDM calibration, slight imperfections in the calibration targets, spurious returns from the reflector poles, and sidelobe clutter. The total for all of these possible effects is seen to be at least 35 dB below the copolarized reflection for all polarizations after the PDM calibration.

The results of the phase measurements on the various reflectors after the PDM and other calibrations are indicated in Table 4. The table gives the corrected phases and their RMS's at 95.3 GHz. As shown, the measured phases have an RMS deviation of about  $\pm 3$  deg. Another measure of the phase performance of the calibrated system is shown in Table 5. This table gives the average difference in phase between adjacent frequency steps and the phase difference for one particular mid-band frequency pair. The RMS deviations also are listed. Any measurement phase errors will influence the quality of HRR profiles and ISAR images, but as indicated the phase errors are small. In fact, the capability of the system is such that an HRR profile of a single reflector using a single ramp of data and a 64-point FFT approaches the processing sidelobe levels.

A method was devised for removing the effects of small motions of the radar platform while measurements of a target were being performed. The motion compensation is done by tracking the phase of a fixed corner reflector set up away from the target and with its return peaked in one difference channel. An FFT of a single ramp of data is performed and the phase of the peak signal from the reference reflector is determined. Each ramp of target data is then adjusted for the phase variation in the reference reflector from ramp to ramp.

Antenna radiation patterns were obtained at the test site using the various reflectors. The approximate two-way sum channel beamwidth for the 5-cm lens used for the target measurements reported here was 3 deg. Sidelobe levels were difficult to determine due to the trees in the area, but in pretest measurements one-way antenna pattern sidelobes averaged well below 20 dB from the peak. Laboratory measurements of the cross-polarization isolation of the antennas showed that on average the isolation was more than 25 dB, one way. The responses of the monopulse difference channels were calibrated by scanning the radar across the appropriate reflector. The relative phase of the difference channel with respect to that of the sum channel was calibrated by scanning to one side of the reflector and establishing a look-up table for setting the relative phase to be 0 deg at each of the system frequencies. Laboratory

measurements of the monopulse null depths showed that they averaged at least 25 dB below the sum peak. The radar monopulse boresight angle was determined for each polarization channel using the appropriate reflector. The boresights were found to vary slightly, with most of the variations being in the azimuth delta channels. The overall boresight angle difference for the RR and RL channels, for example, was about 0.3 deg, with most of the difference being in azimuth. The optical boresight on the video camera was set to coincide with the LR radar boresight for field measurements.

#### 4. Target Signature Measurements

Target signatures were measured at the US Army MICOM Target and Seeker Measurement Facility which includes a stable tower and a self-propelled mobile turntable. The tower has a 9x5 m laboratory at a height of 91 m and a 3x2 m laboratory elevator that can be stopped at various heights. The measurements reported here were made with the radar in the tower elevator about 61 m above ground level. The radar was positioned in front of an opened elevator window to allow an unobstructed view of the target.

The target was mounted on the mobile turntable that was positioned about 115 m from the base of the tower. The turntable platform can tilt up to 45 deg and rotate continuously from 0 to 360 deg about an axis normal to the platform. The rotation rate is variable from 0.5 to 2.5 deg/s. Quasi-continuous data on the turntable tilt and azimuth angles were transmitted to the radar ground station for recording.

Efforts were made to shield the turntable as much as possible to prevent spurious reflections. Standard US Army Diamond/Hexagon Camouflage netting (for frequencies up to about 100 GHz) and radar-absorbing material were used. Some measurements were made to determine the magnitude of any spurious reflections from the turntable or ground that affect the target signatures. The total returns from the screening nets and from sidelobes were typically -5 dBsm or less. Reflections from the turntable generally were -10 to -15 dBsm. The turntable was located as far as possible from trees in the area, and no significant problem was encountered during the course of the measurements due to radar scattering from trees.

A meteorological station was not available at the site, but a station was located at the Redstone Arsenal base. Weather data were obtained on a daily basis throughout the period during which measurements were made.

The measurements of the target signatures were made at various radar depression angles. For each radar depression angle the radar was boresighted on the center of rotation of the target. The turntable then was rotated at its slowest rate (0.5 deg/s) while data were collected with the radar fitted with the 5-cm lens. The radar was operated in the pulse-to-pulse polarization switching mode with 64 frequency

steps of 10 MHz each. Each data buffer includes the signal returns for 128 transmitted pulses where the transmit polarization was switched every pulse and the frequency was stepped every other pulse. The basic data were taken at a 10-KHz PRF but only every other data buffer was recorded due to recording system limitations. The target rotates 0.006 deg during one data buffer. The target data are accumulated for 370 deg of rotation of the turntable so that there is some overlap in the data. The turntable position is recorded along with the data and is inserted into the co-boresighted video camera data stream. A typical 12-min data file contains 85 Mbytes of data before calibration. After calibration the data can be processed further and used for various purposes.

Measurements were made on various armored vehicles, including the Soviet BMP infantry combat vehicle shown in Fig. 4. Polar plots of the polarimetric RCS's for the BMP and with the radar at a 45-deg depression angle are presented in Fig. 5. The data were sampled every 0.5 deg and averaged over 64 frequencies to generate the plot. The RCS's in dBsm were used to compute the averages. It is apparent that the RL and LR polar plots are almost identical, as they should be theoretically. The RR and LL pair are very similar, but there are some small differences. Table 6 shows some comparison RCS statistics for the BMP vehicle at 30-, 45- and 60-deg radar depression angles. The RCS data for target azimuth angles between 0 and 360 deg were averaged for each frequency. All data points were used to obtain the average; that is, the average sample interval was 0.013 deg. The resulting single-frequency averages then were averaged across the frequency band. Included with the bandwidth averages for comparison is the azimuth-angle-averaged RCS at one particular frequency (95.3 GHz).

It is seen in Table 6 that the RMS deviation for the single frequency average is much larger than that for the bandwidth average of the mean for each of the frequencies. An explanation of this result may be the following. The target can be viewed as a complex array of scatterers that appears to be different to the radar after the target has rotated through a small angle. When viewed at a single frequency the various independent sets of scatterers interfere differently, and there is a relatively large standard deviation from the mean RCS value. As the frequency is changed each member of the independent set of scatterers also interferes differently, but there is a degree of correlation when the whole (0 to 360 deg) set of scatterers is viewed at the different frequencies. Apparently the 64 10-MHz frequency steps are sufficient for the data to exhibit this correlation, and the result is the smaller RMS deviation in the average of the mean for each of the frequencies.

The calibrated monopulse sum and difference channel data can be used to generate HRR profiles that display both the RCS amplitude and the elevation- and azimuth-angle errors for each range subcell. These HRR profiles for the BMP at a 90-deg azimuth angle (left

broadside) and a radar depression angle of 45 deg are shown in Fig. 6. The profiles were generated by doing a 64-point FFT on the calibrated sum and difference channel data. The difference channel angle errors were generated using the calibrated ratios in the look-up tables derived from the monopulse response patterns. The plots are for an average of 64 ramps of data and the range resolution is 0.23 m. HRR profiles shown in Fig. 6 are for the RR and LR polarizations. The LL and RL profiles are similar to the RR and LR plots, respectively, and are not presented here.

Fig. 6 shows that the RCS profiles for the RR and LR polarizations have a similar extent in range, but otherwise they are quite different. The plots for the azimuth and elevation-angle differences show the angular location for the effective single scatterer in each range subcell, and these values also are different for the copolarized and cross-polarized radar returns. This type of data may be quite useful for classification, identification, and tracking of a target in a MMW polarimetric monopulse seeker application.

The measurements also allowed the generation of ISAR images of the target, and typical ISAR images of the BMP for RR and LR polarization are shown in Fig. 7. The target azimuth angle was 90 deg (left broadside) and the radar depression angle was 45 deg. The left side of the target is to the left in the images, and the front of the target is at the top. The ISAR images were created by computing a two-dimensional FFT of 64 sets of frequency-stepped data for the sum- and elevation-angle channels. The total rotation of the target during the data-taking time for the ISAR images was 0.812 deg. The downrange resolution for the images was 0.23 m and the cross-range resolution was 0.15 m. The sum channel ISAR image shows the RCS amplitude associated with each of the radar resolution cells of  $0.23 \times 0.15$  m, and the elevation-angle-difference ISAR image shows the angular location above and below the plane of the sum channel ISAR of the effective single scatterer associated with each resolution cell. It is evident that the monopulse elevation angle data provides the third-coordinate information needed for construction of a point-scatterer model of the target without recourse to a geometric model of the target.

The images shown in Fig. 7 use the same set of data that were used to generate the HRR profiles of Fig. 6. It can be seen that these HRR profiles and ISAR images are quite consistent with one another.

## 5. Conclusions

A detailed description has been given of the characteristics of a 95-GHz fully polarimetric monopulse instrumentation radar and the procedures used for calibration of the radar. In particular, it was shown that the use of the PDM calibration technique improved the radar's cross-polarization isolation to 35 dB and the

phase accuracy to  $\pm 4$  deg across a 630-MHz frequency band.

Polarimetric monopulse radar target signature data for a Soviet BMP infantry combat vehicle were presented to show the capabilities of the radar. The fully polarimetric RCS polar plots for the BMP showed that the LR and RL RCS's are virtually the same (as they should be) and those for RR and LL are very similar.

The RCS amplitude and the azimuth- and elevation-angle-difference HRR profiles of the target also were presented for RR and LR polarizations. It was indicated that distinctive features and differences in these profiles may be useful for classification, identification, and tracking of a target in a MMW seeker application.

Standard ISAR imaging techniques were used to generate two-dimensional polarimetric images of the BMP target. These images were presented along with the corresponding polarimetric ISAR images of the elevation angle differences. It was pointed out that the elevation-angle information in the monopulse channels provides a third dimension to the images which can be very useful for the generation of point-scatterer models of a target.

In conclusion, the instrumentation radar described in this report has been shown to be capable of providing target signature data of various types that may prove useful for the evaluation of target detection, classification, and identification algorithms and for the generation of target models.

## Acknowledgements

The work reported on here would not have been possible without the encouragement and managerial support of Peter B. Johnson and Z. G. Sztankay. Their efforts are gratefully acknowledged. Thanks also are extended to H. Haralamos and a number of US Army MICOM staff members for their contributions to obtaining the results presented here.

## References

1. N. C. Currie and C. E. Brown (Editors), "Principles and Applications of Millimeter-Wave Radar," Artech House, Norwood, MA, 1987.
2. N. C. Currie (Editor), "Radar Reflectivity Measurement: Techniques and Applications," Artech House, Norwood, MA, 1989.
3. R. M. Barnes, MIT Lincoln Laboratory, "Polarimetric Calibration Using In-Scene Reflectors," 1986, MIT Lincoln Laboratory Project Report TT-85 on Contract F19628-85-C-0002.

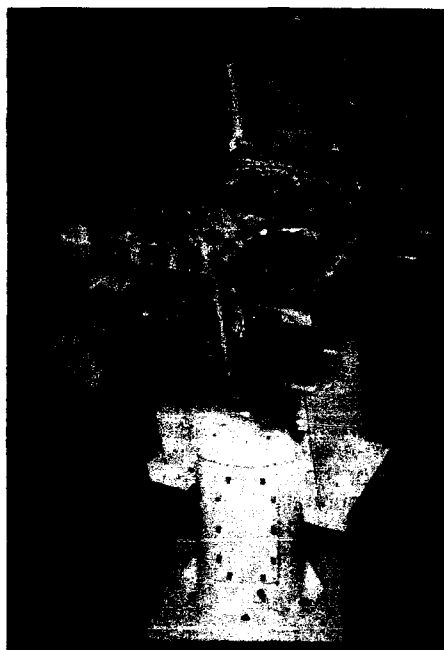


Figure 1. 95-GHz polarimetric monopulse radar.

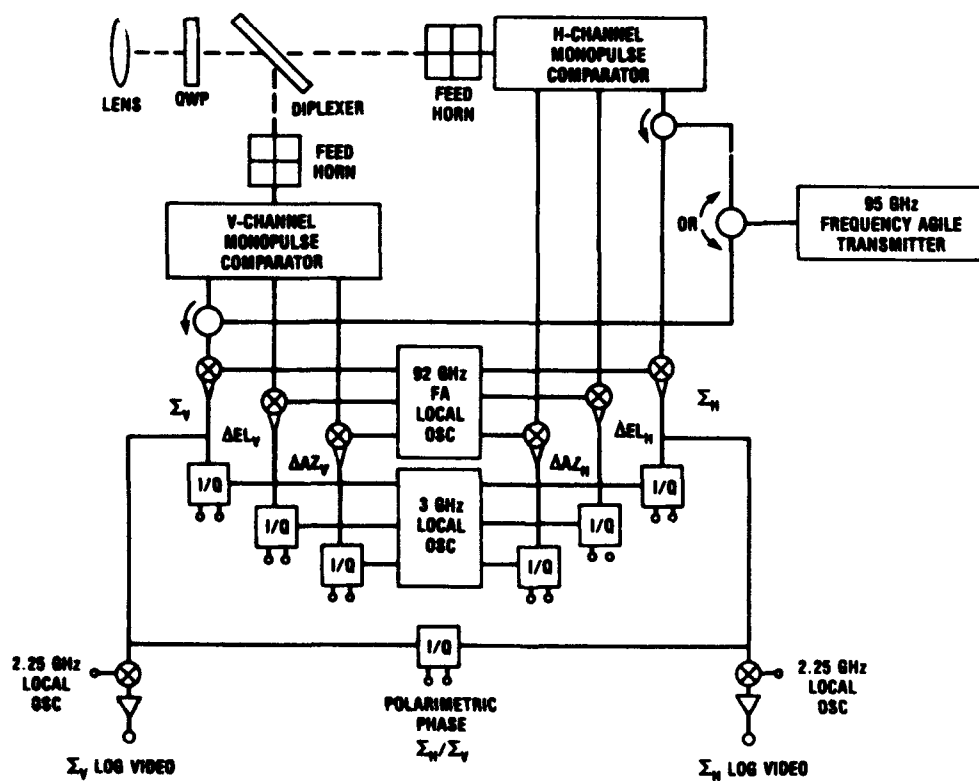


Figure 2. A simplified schematic of the 95-GHz polarimetric monopulse radar.

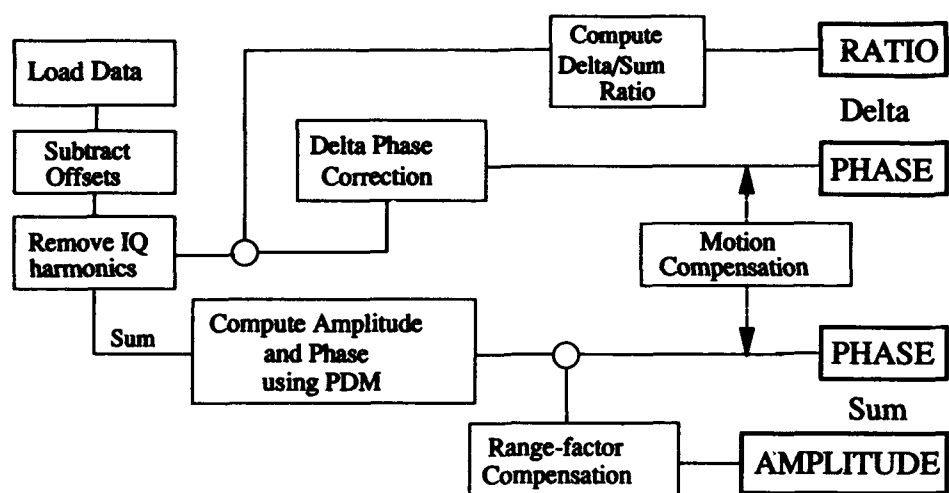


Figure 3. Block diagram of the coherent receiver calibration procedure.

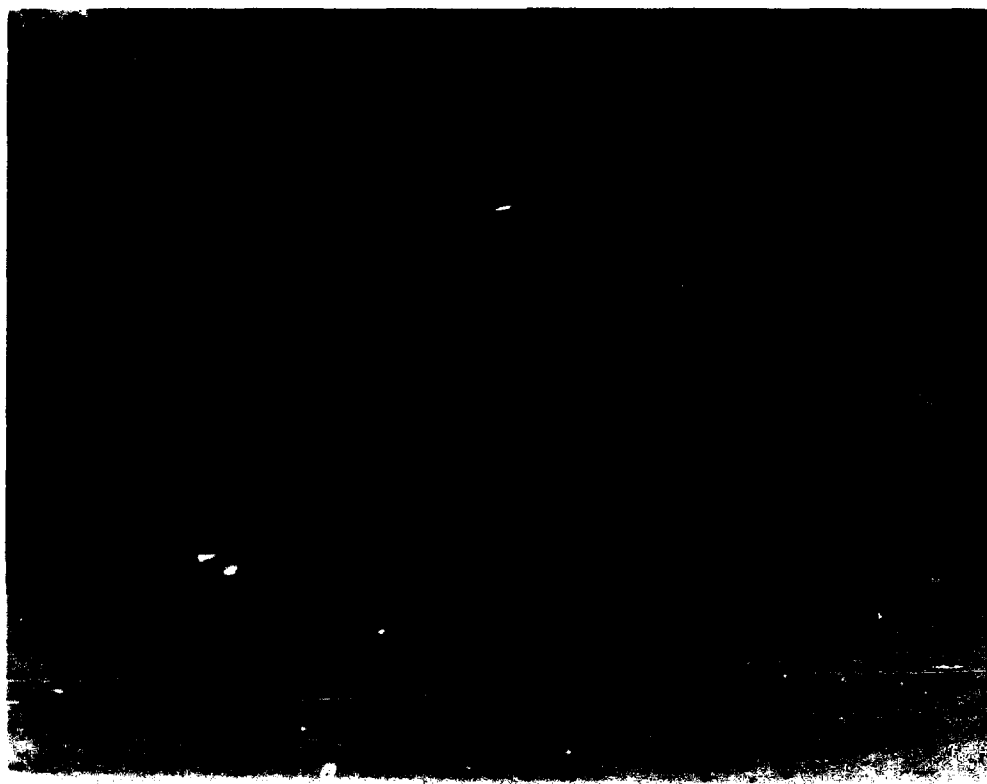


Figure 4. Soviet BMP infantry combat vehicle.

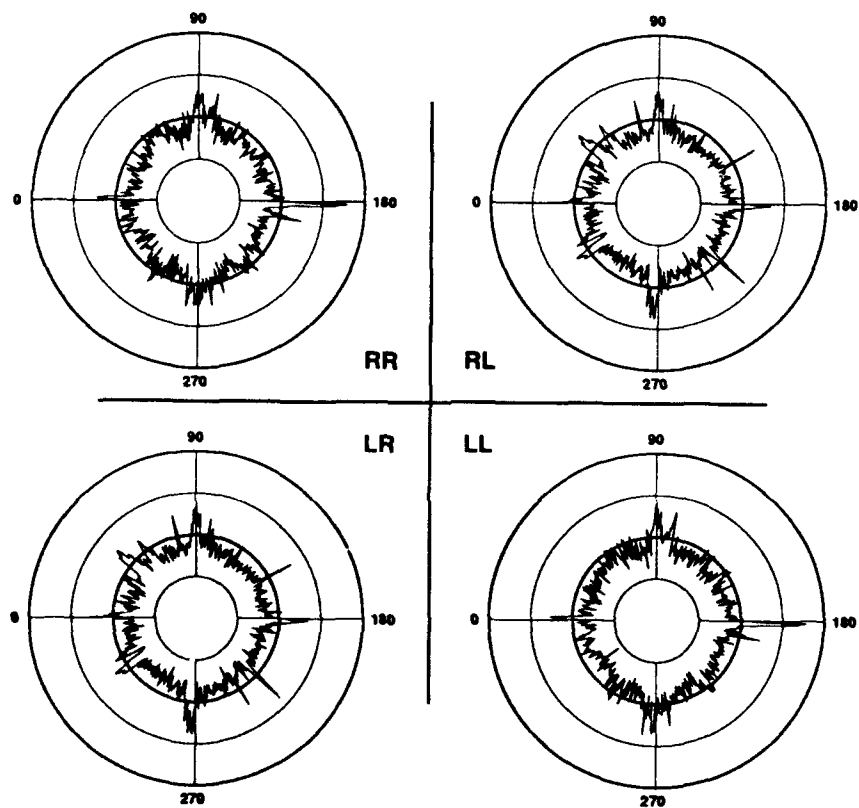


Figure 5. Polar plots of frequency-averaged RCS's for a Soviet BMP. The RCS range on the plots is 0 to 30 dBsm, and the radar depression angle was 45 deg.



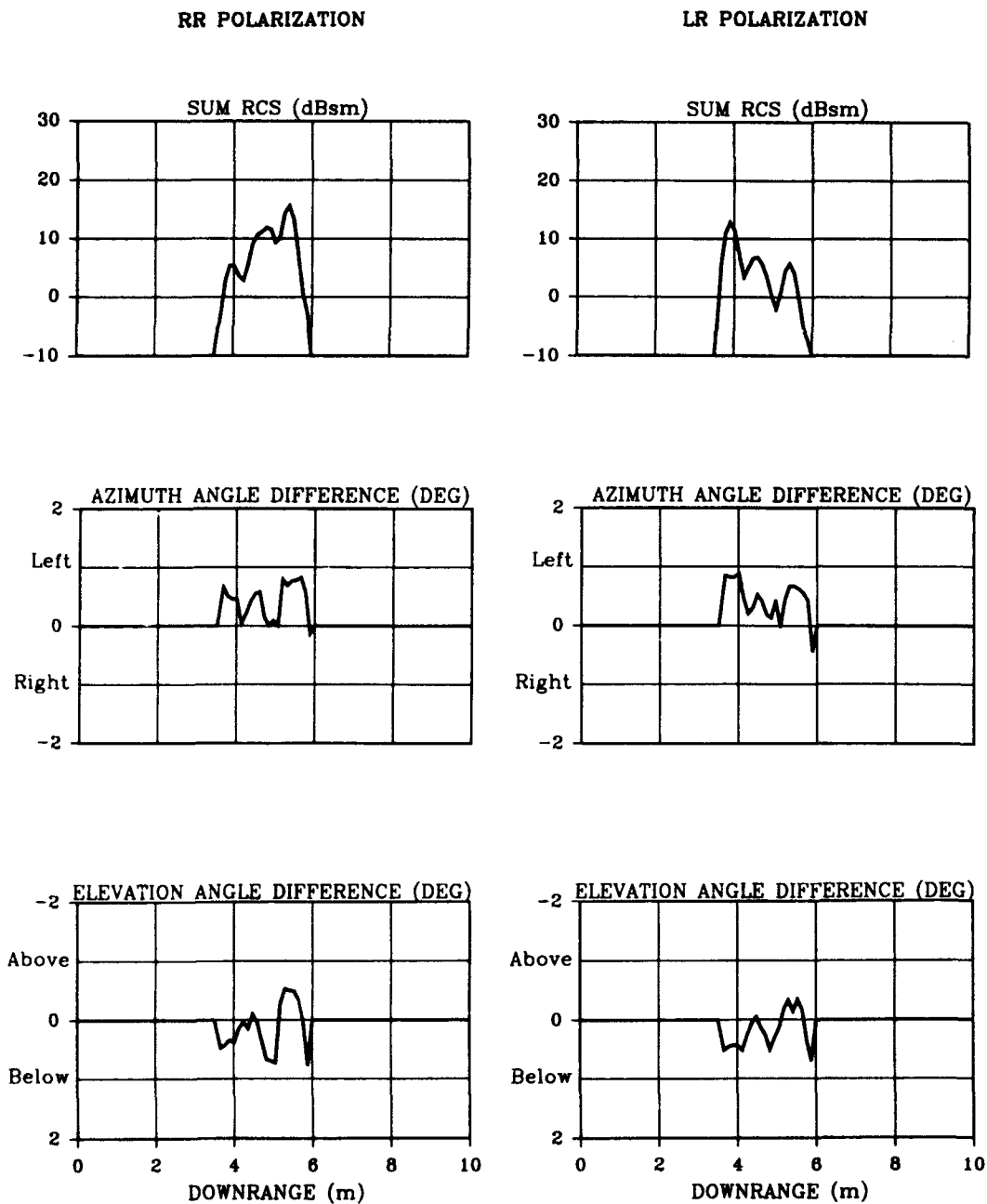


Figure 6. Monopulse sum and difference channel high-resolution range profiles for a Soviet BMP. The radar depression angle was 45 deg., and the target azimuth angle was 90 deg. (left broadside).

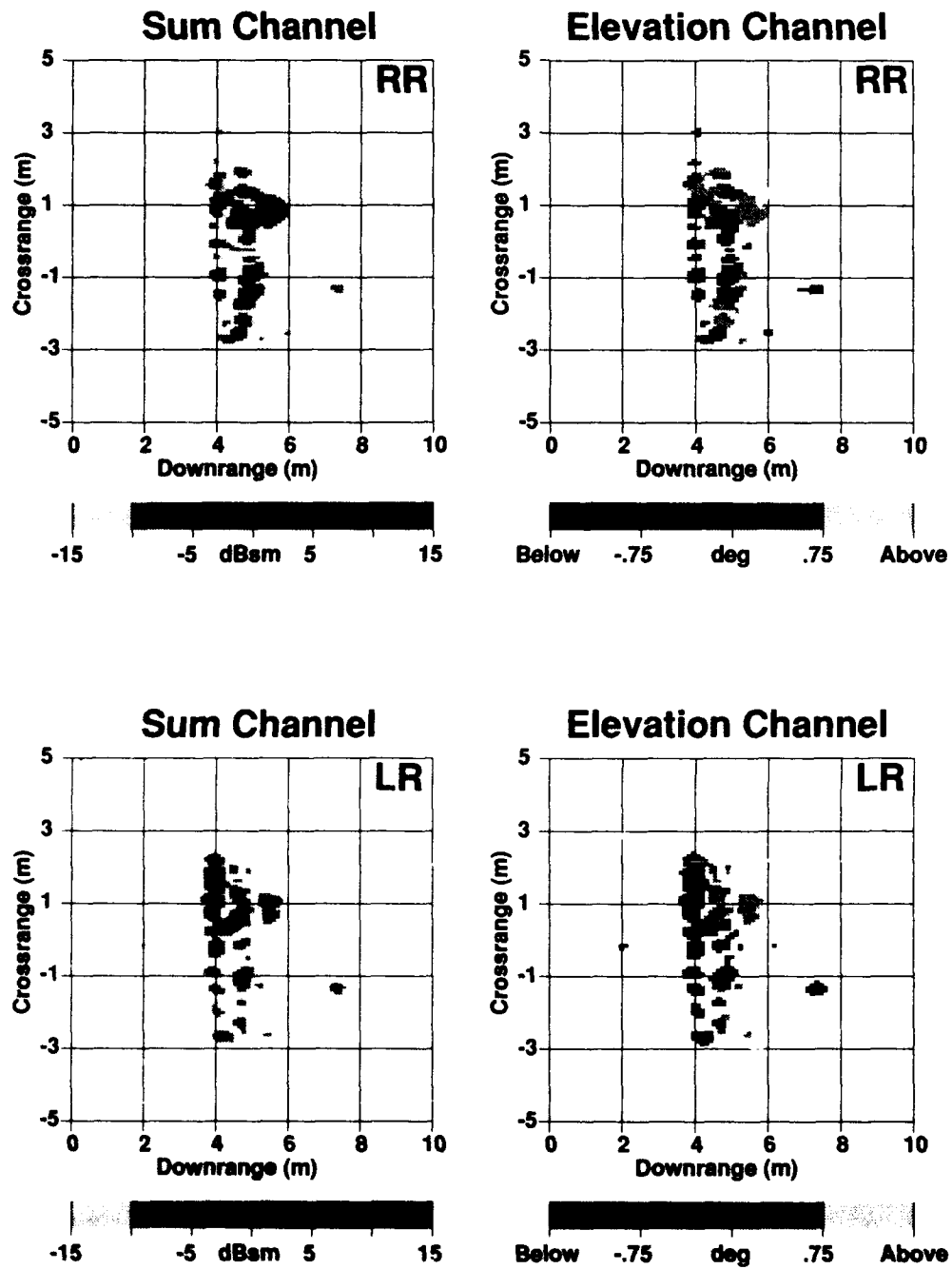


Figure 7. Monopulse sum and elevation-angle-difference channel ISAR images for a Soviet BMP. The radar depression angle was 45 deg, and the target azimuth angle was 90 deg (left broadside).

TABLE 1. BASIC FEATURES OF THE RADAR SYSTEM

- 
- Frequency: 95.0 GHz
  - Two-coordinate amplitude-comparison monopulse
  - Polarization agile: RHCP/LHCP or V/H (selectable)
  - Coherent and wide bandwidth
  - Frequency steppable: 64 10-MHz steps
  - Peak power: 45 W
  - Pulse width: 100 ns
  - Pulse repetition frequency: 10 kHz
  - Antenna beamwidth (one way): 1.5 to 5.2 deg (selectable)
  - Receiver IF bandwidth: 30 MHz
  - Receiver noise figure: 8 dB
  - Dynamic range (amplitude):  $\geq 66$  dB
  - Data recording: 16 channels for each pulse
- 

TABLE 2. REFLECTORS IN TARGET ARRAY USED FOR CALIBRATIONS

---

Reflector No.	Reflector Type	RCS(dBsm)	Range to Radar (m)
1	Dihedral (45 °)	20	99
2	Dihedral	23	119
3	Gridded trihedral	14	139
4	Trihedral	30	158

---

TABLE 3. FREQUENCY-AVERAGED RCS (dBsm) FOR CALIBRATION REFLECTORS

---

Reflector Type	Receiver	$\sigma_{RR}$	$\sigma_{RL}$	$\sigma_{LR}$	$\sigma_{LL}$
Dihedral	Linear	$23.0 \pm 0.1$	$-15 \pm 2$	$-15 \pm 2$	$23.1 \pm 0.1$
	Log	$23.0 \pm 0.1$	$-7 \pm 3$	$-7 \pm 4$	$23.1 \pm 0.1$
Trihedral	Linear	$-5 \pm 4$	$30.0 \pm 0.3$	$30.0 \pm 0.3$	$-4 \pm 4$
	Log	$-4 \pm 6$	$30.0 \pm 0.1$	$29.9 \pm 0.1$	$0 \pm 4$

---

$$T_{aa} = \frac{1}{|t_{h12}|^2 + |t_{v12}|^2} \begin{bmatrix} |t_{h12}|^2 + |t_{v12}|^2 & |t_{h12}|^2 - |t_{v12}|^2 & 0 & 0 \\ |t_{h12}|^2 - |t_{v12}|^2 & |t_{h12}|^2 + |t_{v12}|^2 & 0 & 0 \\ 0 & 0 & Re(t_{v12}t_{h12}^*) & -Im(t_{v12}t_{h12}^*) \\ 0 & 0 & Im(t_{v12}t_{h12}^*) & Re(t_{v12}t_{h12}^*) \end{bmatrix} \quad (26)$$

$$T_a = \begin{bmatrix} 1 + \alpha^2 & 1 - \alpha^2 & 0 & 0 \\ 1 - \alpha^2 & 1 + \alpha^2 & 0 & 0 \\ 0 & 0 & 2\alpha & 0 \\ 0 & 0 & 0 & 2\alpha \end{bmatrix}$$

and  $\alpha = t_{v12}/t_{h12}$ . Simplifying (27) yields an expression in terms of  $t_{v12}$ ,  $t_{h12}$ , and  $\tilde{\chi}$ . By equating (27) to (8), the following relationships are found:

$$t_{h12}^4 = \frac{A+B}{2} \quad t_{v12}^4 = \frac{A-B}{2} \quad \tilde{\chi} = \frac{B_0}{\sqrt{A^2 - B^2}}$$

30-12

TABLE 4. SINGLE-FREQUENCY PHASE (deg) FOR CALIBRATION REFLECTORS

Reflector Type	$\phi_{RR}$	$\phi_{RL}$	$\phi_{LR}$	$\phi_{LL}$
Trihedral		$290 \pm 3$	$290 \pm 3$	
Dihedral	$350 \pm 3$			$347 \pm 3$
Gridded trihedral	$115 \pm 4$	$112 \pm 4$	$113 \pm 4$	$107 \pm 4$

TABLE 5. AVERAGE PHASE DIFFERENCE (deg) PER FREQUENCY STEP FOR CALIBRATION REFLECTORS

Reflector Type	$\Delta\phi_{RR}$	$\Delta\phi_{RL}$	$\Delta\phi_{LR}$	$\Delta\phi_{LL}$
Dihedral (all pairs)	$12 \pm 1$			$12 \pm 1$
Dihedral (one pair)	$14 \pm 4$			$14 \pm 3$
Trihedral (all pairs)		$223 \pm 2$	$223 \pm 2$	
Trihedral (one pair)		$223 \pm 4$	$223 \pm 4$	
Gridded trihedral (all pairs)	$130 \pm 2$	$130 \pm 3$	$130 \pm 3$	$130 \pm 2$
Gridded trihedral (one pair)	$129 \pm 5$	$130 \pm 6$	$130 \pm 5$	$132 \pm 6$

TABLE 6. AVERAGE RCS (dBsm) FOR A SOVIET BMP OVER 0 TO 360 DEG AZIMUTH ANGLES AND FOR VARIOUS RADAR DEPRESSION ANGLES

Type Average	Dep. Angle	$\sigma_{RR}$	$\sigma_{RL}$	$\sigma_{LR}$	$\sigma_{LL}$
Bandwidth	30	$8.0 \pm 0.2$	$7.2 \pm 0.8$	$7.2 \pm 0.8$	$8.1 \pm 0.2$
	45	$7.9 \pm 0.2$	$7.4 \pm 0.8$	$7.5 \pm 0.8$	$7.9 \pm 0.1$
	60	$7.8 \pm 0.1$	$7.6 \pm 0.6$	$7.7 \pm 0.6$	$7.8 \pm 0.2$
Single Freq.	45	$8.0 \pm 5.9$	$6.9 \pm 5.9$	$7.0 \pm 6.0$	$8.1 \pm 5.9$

## DISCUSSION

G. Neininger, GE

Illuminating a target like a tank at approximately 200 meters there will exist probably more than one scatterer within the detection area. Does this not confuse the monopulse comparator?

Author's Reply

If one does a high range resolution image, with range resolution of 23 meters, the monopulse channels can give angle information versus range, thereby separating some of the scatterers. If there are two scatterers at one range the monopulse channel will give the composite scattering center. However, by doing the ISAR processing, this ambiguity can be resolved.

E. Schweicher, BE

You mentioned a 45 W peak power. What kind of solid-state transmitter did you use at 95 GHz?

Author's Reply

The transmitter uses injection locked impact oscillators. The final stage has a 40-diode power combiner to get the 45 watts and the 640 MHz bandwidth.

U. Lammers, US

What kinds of phase excursions did you get due to tower sway, and at what rate did you have to compensate for them?

Author's Reply

For moderate wind conditions less than 10 mph, phase variations due to tower motion were about  $\pm 15-20^\circ$ . This consisted of a slow variation  $< 1$  Hz and a 5 Hz resonance. I have not looked at this in detail, but we have compensated for this when calibrating the data. The compensation is done ramp by ramp where a ramp of 64 pulses at each polarization stepping frequency 10 MHz per pulse sequences 12.8 ms. The total sample rate is 40 Hz.

## REDUCTION OF TARGET SCATTERING BY TROPOSPHERIC MODIFICATION

K.H. Craig  
Radio Communications Research Unit  
Rutherford Appleton Laboratory  
Chilton, Didcot, OX11 0QX  
United Kingdom

### Summary

This paper examines the possibility of reducing the effective radar cross-section of an aircraft by actively modifying the refractive index of the air surrounding it. The mechanism proposed is heating of the atmosphere by a laser mounted on the aircraft. The equations for the refractive index changes caused by absorption of laser radiation are derived, and refractive index profiles are calculated. A shielding factor specifying the reduction in target cross-section is introduced. The shielding factor is evaluated for typical laser beam geometries by using these profiles in a parabolic equation based electromagnetic propagation model. A parametric study is presented in order to optimise the laser wavelength and beam geometry. It is concluded that laser powers in the megawatt range can yield shielding factors greater than 10 dB. A  $10.6\text{ }\mu\text{m}$   $\text{CO}_2$  laser appears to be optimum in terms of efficiency of cross-section reduction, and is also the laser type for which the highest CW powers are achievable.

### 1 Introduction

It is well known that radars can be affected by anomalous propagation caused by meteorological effects. In certain cases, a target may remain undetected well within the normal detection range of the radar. This is illustrated in Figure 1, showing the coverage diagram of an S-band radar at a height of 9000 m. The coverage "hole" is due to a radio duct caused by a sloping elevated layer typical of those occurring in the troposphere during conditions of anticyclonic subsidence. A target that is capable of exploiting this coverage hole would effectively have a reduced cross-section for detection by this radar.

The difficulty, of course, is that the correct meteorological conditions occur only sporadically and the position of the layers tends to vary with time; furthermore it is generally difficult to forecast the position of the coverage hole with sufficient accuracy for its exploitation. In this paper we investigate the possibility of artificially creating a localised coverage hole by heating the atmosphere using a laser. If an aircraft were able to deploy such a device, it could hide in its own locally generated radio duct, effectively reducing its radar cross-section.

There are three aspects to the problem. Firstly, a laser beam geometry must be devised that can generate a layer with a suitable refractive index anomaly;

a strategy is proposed, and the equations describing the resultant refractive index profiles are derived. Secondly, the effect of the layer on signal loss must be calculated. Since the layers will be two- or three-dimensional, a radar propagation model capable of dealing with complex refractive index profiles is required; the recent parabolic equation propagation model is used. Parametric studies show the optimum beam geometry for cross-section reduction. The third aspect is that of laser technology. It will be shown that high laser powers and large beam cross-sections are required; the feasibility of developing such systems will be considered.

### 2 Laser induced refractive effects

Consider an aircraft-mounted laser radiating a beam at a small angle to the horizontal, as shown in Figure 2. If a suitable laser frequency is chosen, the laser energy will be converted to heat by molecular absorption in the atmosphere; this in turn will cause a decrease in the refractive index of the heated air. As the aircraft flies along, the laser beam will sweep out a refractive layer above the aircraft. A typical vertical refractive index profile is shown in Figure 2; the shape is easily explained. In region (a) below the beam, no heating has yet occurred. In region (b) within the beam, the greater the height, the longer the duration of heating by the advancing beam and therefore the greater the refractive index anomaly. In region (c) above the beam the air will have experienced the full heating effect of the beam; the decrease in refractive anomaly with height is due to the decreasing strength of the beam with distance as energy is extracted from it.

This refractive index profile is similar to those occurring naturally at the interface of two different air masses, which are known to cause anomalous effects on the radar coverage of targets lying within the layers. The main difference here is that the anomaly will completely disappear a few tens or hundreds of metres above the aircraft where the heating effect of the laser becomes negligible. In the meteorological case, a refractive index change may be maintained over much greater heights on the scale of the extent of the upper air mass. It will be important to optimise such parameters as the beam inclination angle, beam diameter, and laser absorption coefficient to maximise the impact of the anomaly on radar coverage.

It will be shown that the effect of cross-section reduction can be enhanced significantly if the "target"

is located some way behind the laser beam, so that the coverage hole has had more distance over which to "open up" (cf. Figure 1); it is therefore worth considering an extension to the scenario of Figure 2 where a "hole-burning" low cross-section laser-carrying aircraft flies ahead of the main targets to lay down a refractive layer for them to fly through.

## 2.1 The effect of heating on refractive index

In order to investigate the effect of heating on a radar signal, we must first calculate the changes in the refractive index structure produced by the heating. Because of the closeness of the refractive index  $n$  of the air to unity, it is usual to work with the refractivity  $N$ , defined by:

$$N = (n - 1) \times 10^6 \quad (1)$$

$N$  depends on the pressure  $P$  (mb), the absolute temperature  $T$  (K) and the partial pressure of water vapour  $e$  (mb):

$$N = 77.6 \frac{P}{T} + 3.73 \times 10^5 \frac{e}{T^2} \quad (2)$$

It is worth recalling that this is derived from the Debye formula for the polarizability of polar and non-polar molecules, with the constants being determined empirically [1]. The first (dry) term is due principally to the non-polar nitrogen and oxygen molecules, while the second (wet) term comes from the polar water vapour molecules.

Assuming that the air behaves as an ideal gas, the equation of state is

$$pV = \mu RT \quad (3)$$

where  $p$  is the pressure (Pa),  $V$  is the volume occupied by  $\mu$  moles of the gas,  $T$  is the absolute temperature, and  $R$  is the universal gas constant. Eqn (2) can therefore be written:

$$N = 0.776R \frac{\rho_a}{M_a} + 3730 \frac{R}{T} \frac{\rho_w}{M_w} \quad (4)$$

where  $\rho_{a,w}$  and  $M_{a,w}$  are the density and molecular weight of air and water vapour, respectively. Using values of  $M_a = 0.0288$  kg and  $M_w = 0.018$  kg gives

$$N = 224\rho_a + 1.72 \times 10^6 \frac{\rho_w}{T} \quad (5)$$

Now consider the effect of laser heating. As will be shown, the passage of a laser beam of suitable wavelength (an infrared CO<sub>2</sub> laser being optimum) through the atmosphere deposits energy via molecular absorption. The absorbed energy is rapidly converted to kinetic energy which induces a near-instantaneous rise in pressure and temperature. This creates a pressure wave that propagates away from the source of the heating at the speed of sound. On a timescale large compared to the acoustic timescale (the time taken for sound to propagate across the heated volume) the pressure will return to its ambient value. The temperature will however remain higher than ambient, and

as a consequence of eqn (3), the density will drop. Eqn (5) shows that this will give rise to a region of lower refractivity. On a longer timescale, the instabilities caused by the thermal gradients will give rise to turbulent mixing with the surrounding air; this will eventually disperse the refractivity anomaly created by the heating.

To quantify the fractional refractivity change induced by heating, consider a timescale longer than the acoustic timescale, but less than the timescale for the evolution of turbulence. Assuming that the dry contribution to the refractivity dominates (as will be true in cases of interest), the logarithmic derivative of eqns (5) and (2) gives (assuming isobaric expansion)

$$\frac{dN}{N} = \frac{d\rho_a}{\rho_a} = -\frac{dV}{V} = -\frac{dT}{T} \quad (6)$$

Let  $q_v$  be the heat energy absorbed per unit volume. Then

$$q_v = c_p \frac{\mu}{V} dT \quad (7)$$

where  $c_p$  is the molar specific heat at constant pressure. Combining eqns (6) and (7),

$$\frac{dN}{N} = -\frac{V}{\mu T} \frac{1}{c_p} q_v \quad (8)$$

If  $\gamma$  is the ratio of the molar specific heats  $c_p$  and  $c_v$  at constant pressure and volume, respectively, then

$$c_p = \frac{\gamma}{\gamma - 1} R \quad (9)$$

and eqns (3), (8) and (9) finally give

$$\frac{dN}{N} = -\frac{\gamma - 1}{\gamma p} q_v \quad (10)$$

This equation relates the change in refractive index to the heat energy absorbed per unit volume. We now consider the absorption process itself.

## 2.2 Absorption of laser radiation by the atmosphere

Consider a laser beam propagating in the  $\zeta$  direction with initial intensity  $I_0$  (Wm<sup>-2</sup>). The intensity  $I(\zeta)$  at a distance  $\zeta$  from the laser is given by:

$$I(\zeta) = I_0 \exp(-\alpha\zeta) \quad (11)$$

$\alpha$  is the attenuation coefficient. The ratio  $I/I_0$  is called the transmittance,  $\tau$ . The amount of power lost from the beam per unit volume is obtained by differentiating this, giving

$$-\frac{dI}{d\zeta} = \alpha I \quad (12)$$

If the heating is applied for a period of time,  $t_0$ , the heat energy absorbed per unit volume is therefore

$$q_v = \alpha I t_0 \quad (13)$$

More generally, if the beam intensity varies with time,

$$q_v = \alpha \int I(t) dt \quad (14)$$

The attenuation is the result of absorption and scattering by molecules and by aerosols. Molecular absorption is caused by the excitation of molecular resonances; since these involve quantum transitions, molecular absorption varies strongly as a function of wavelength,  $\lambda$ , and must be determined from high resolution spectroscopy. On the other hand, because air molecules are much smaller than the laser wavelengths of interest, molecular scattering shows the smooth dependence of scattering cross-section on wavelength ( $\propto \lambda^{-4}$ ) typical of Rayleigh scattering; molecular scattering will be less important at longer wavelengths. The absorption and scattering contribution of the aerosol component depends on the constituents of the aerosol (finely dispersed particles of ice, dust and organic material) and their concentration (denser sols giving lower visibility): as the particle sizes are comparable with the wavelength, Mie scatter calculations are required, using an effective (complex) refractive index for the aerosol; the cross-sections are reasonably slowly varying functions of the laser wavelength.

Both absorption and scattering remove energy from the beam as it propagates, but only absorption contributes to the heating of the atmosphere. Clearly then, to maximise the heating we must maximise the ratio of absorption to scattering. Table 1 is based on tables of attenuation coefficients given in [2]. The figures are for the 0-1 km height range in a midlatitude summer atmosphere. The "clear" and "hazy" columns represent aerosol densities corresponding to visibilities of 23 and 5 km, respectively.

Laser type	$\lambda$ ( $\mu\text{m}$ )	Clear		Hazy	
		$\tau_a$	$\tau$	$\tau_a$	$\tau$
N <sub>2</sub>	0.337	99.98	79	99.98	46
HeNe	0.633	99.79	91	99.08	66
Nd glass	1.06	98.7	94	94.3	77
Er glass	1.536	98.4	96	93.3	83
HeNe	3.393	17	16	16	15
CO <sub>2</sub>	10.591	72	72	71	71
H <sub>2</sub> O	27.9	0	0	0	0

Table 1: Total ( $\tau$ ) and absorption ( $\tau_a$ ) transmittance over a 1 km path, expressed as a percentage.

At the shortest wavelengths, the total transmittance is much lower than that due to absorption, showing that scattering is dominant; there are also large differences between clear and hazy conditions and this is undesirable. At the longest wavelength (27.9  $\mu\text{m}$ ) absorption by H<sub>2</sub>O molecules is very rapid, and whilst this would produce very strong heating in the vicinity of the laser, it would not prove possible to lay down a heated layer several kilometres in front of the laser. This holds for most longer wavelengths in the far infrared. We conclude therefore that the most promising wavelengths for tropospheric modification are in

the near infrared. Here nearly all the energy extracted from the beam is turned into heat via molecular absorption, while the transmittance is still sufficient to produce heating effects over path lengths of a few kilometres. In particular we will consider the HeNe wavelength of 3.393  $\mu\text{m}$ , with an attenuation coefficient of  $\alpha = 0.0018 \text{ m}^{-1}$ , and the CO<sub>2</sub> wavelength of 10.591  $\mu\text{m}$ , with  $\alpha = 0.00033 \text{ m}^{-1}$ ; the latter is of particular interest as CO<sub>2</sub> lasers can generate significant amounts of power.

### 2.3 Effect of a moving laser

Eqn (14) gives the amount of heating produced by laser absorption applied for a finite time. Consider now the proposed laser geometry of Figure 2. The heating of a volume of air is caused by the passage of the moving laser beam across the volume (assumed to be at rest). Eqn (14) can be generalised as

$$q_v(x, z) = \frac{\alpha}{v_o} \int I(x', z) dx' \quad (15)$$

where  $v_o$  is the (horizontal) velocity of the aircraft, and the limits of the integral are determined by the extent of the beam that has passed over the point  $(x, z)$  at which the heating  $q_v$  is being evaluated.

The heating mechanism discussed here is similar to the problem of thermal blooming of a laser beam propagating in an atmosphere in the presence of a wind. A more rigorous derivation of eqn (15) shows [3] that this expression holds for wind velocities that are less than the speed of sound. When the wind speed exceeds that of sound, the acoustic timescale becomes important, and the quasi-static derivation given above no longer holds. In our geometry this means that the derivation is only valid for the case of subsonic flight. The problem of laser induced heating at supersonic velocities poses a difficult fluid dynamical problem, and for simplicity we will assume subsonic conditions.

Before evaluating the integral, we combine eqns (10) and (15):

$$\frac{dN}{N} = -S(I_o, v_o) K(x, z, \alpha, d, \theta) \quad (16)$$

with

$$S(I_o, v_o) = \frac{\gamma - 1}{\gamma} \frac{I_o}{p v_o} \quad (17)$$

and

$$K(x, z, \alpha, d, \theta) = \frac{\alpha}{I_o} \int I(x', z) dx' \quad (18)$$

We show below that the limits of the integral (and hence  $K$ ) depend on the vertical thickness  $d$  of the beam, and on the angle of the beam to the horizontal,  $\theta$ .

This factorisation is useful for two reasons. Firstly, the  $K$  term contains all the beam-geometry dependent terms; these determine the shape of the refractive index anomaly induced by the heating. The  $S$  term is geometry independent, being primarily a function of



the beam intensity and the velocity of the aircraft;  $S$  will be referred to as the "beam strength".

Secondly, the factorisation allows us to make an order of magnitude estimate of the effects that can be achieved. The maximum value of  $K$  is 1 (from eqns (11) and (12)) and we will show below that we can come close to this limit by a suitable choice of beam geometry; thus an estimate for  $dN/N$  is obtained by evaluating  $S$ .  $\gamma$  is a constant (ratio of specific heats) = 1.4, and we can put  $p = 10^5$  Pa (atmospheric pressure at the surface). The choice of the aircraft velocity,  $v_0$ , will normally be fixed by operational considerations, although smaller velocities would lead to larger effects (subject to layer decay constraints: see below); bearing in mind the subsonic restriction, we put  $v_0 = 100 \text{ ms}^{-1}$ .

The choice of  $I_0$  is set by laser technology. Average powers of 100 kW were reported for  $\text{CO}_2$  lasers in the early 1980s [4] and efficiencies are of the order of 10%. Since jet engine powers of  $10^7$ – $10^8$  W are available, it is not inconceivable that airborne lasers with powers in the range  $10^6$ – $10^7$  W may be achieved. We will assume that a CW laser is used to supply continuous heating, although a pulsed system could be used if the pulses were rapid enough to form a quasi-continuous layer. The beam intensity depends on the beam cross-section over which the power is spread. To maximise the radar cross-section reduction, we need to submerge the aircraft within the refractive layer generated. The beam must be a few metres wide and a few metres deep; assume a beam cross-section of  $10 \text{ m}^2$ . (We do not discuss here the technological problem of obtaining such a large beam aperture; in practice, the beam would presumably be defocussed to provide a suitable divergence angle. We assume in this analysis that the beam is optically tailored to produce a near constant cross-section of this order of magnitude). These assumptions lead to beam intensities in the range  $10^5$ – $10^6 \text{ Wm}^{-2}$ .

Substituting in eqn (16), gives a value of  $dN/N$  in the range 0.003–0.03, or values of  $dN$  in the range 1–10 N-units. This level of refractivity change can give rise to significant anomalous propagation effects, and we conclude that it is worth pursuing the analysis further.

## 2.4 Refractive index profiles

In order to quantify the effect of laser heating on target cross-section, we must investigate the effect of the refractive index anomalies on the propagation of radio waves. This requires the refractive index structure represented by the function  $K$  (eqn (18)).

Assume, as above, that we can generate a laser beam with a cross-section of a few square metres. To simplify matters further, assume that the beam has a rectangular cross-section, of width  $w$  and depth  $d$  (loosely called the beam "diameter"), and that the intensity is constant in a plane perpendicular to the beam axis. (The generalisation to circular cross-section and gaussian

beam intensity would complicate the analysis, without significantly affecting the results). The geometry is shown in Figure 3; the beam is inclined at an angle  $\theta$  to the aircraft trajectory (assumed horizontal). The radar, aircraft and laser beam are assumed to be coplanar (the optimum geometry for cross-section reduction), and together with the assumption of constant beam intensity, this allows a reduction of the problem to two-dimensions. Let  $(x, z)$  be coordinates parallel and perpendicular to the aircraft trajectory, and let  $(\zeta, \xi)$  be coordinates parallel and perpendicular to the laser axis; both coordinate systems are assumed to move with the aircraft/laser system. Then

$$\begin{aligned}\zeta &= x \cos \theta + z \sin \theta \\ \xi &= -x \sin \theta + z \cos \theta\end{aligned}\quad (19)$$

The beam intensity is given by

$$I(x, z) = \begin{cases} I_0 \exp(-\alpha \zeta) & \text{if } \zeta \geq 0 \text{ and } 0 \leq \xi \leq d \\ 0 & \text{otherwise} \end{cases}\quad (20)$$

Now consider a small volume of air,  $O$ , at  $(x, z)$ . Depending on its location relative to the moving laser beam,  $O$  can be in one of four distinct regions, labelled  $A$ – $D$  in Figure 3. The upper limit of the  $K$  integral is  $x_Q$  ( $\xi = 0$ ), while the lower limit is  $\max(x, x_P)$ , with  $P$  lying either on the line  $\zeta = 0$  or the line  $\xi = d$ . Carrying out the  $K$  integration using eqns (19) and (20), gives

$$K(x, z, \alpha, d, \theta) = \sec \theta [e^{-\Gamma} - e^{-\alpha z \csc \theta}] \quad (21)$$

with

$$\begin{aligned}\Gamma &= \alpha(z \csc \theta - d \cot \theta) & O \in A \\ &0 & O \in B \\ &\alpha(x \cos \theta + z \sin \theta) & O \in C \\ &\alpha z \csc \theta & O \in D\end{aligned}\quad (22)$$

Figure 4 shows a  $K$  profile as a function of the height  $z$  above the laser origin for  $x = 1 \text{ km}$ ,  $\alpha = 0.00033 \text{ m}^{-1}$ ,  $d = 5 \text{ m}$  and  $\theta = 0.1^\circ$ . The profile is seen to have the shape predicted in Figure 2. For the assumed uniform beam illumination and stable layers, it is actually possible to overlay the  $K$  profiles for different values of  $d$  and  $x$ , as is done in Figures 5–7. The lower arc of the profile is obtained by following the required range ( $x$ ) curve; this arc is independent of  $d$  since the heating is independent of the radial distance from the beam axis for uniform beam illumination. The upper arc is obtained by following the required beam diameter ( $d$ ) curve; above the beam, the heating is independent of range if we assume that the layer remains stable indefinitely after the laser beam has swept past (but see below). The point of intersection of these two curves is at the point of maximum  $K$ ; for small beam elevation angles, the lower arc will cover a height range equal to the beam diameter.

Figures 5 and 6 are for a beam elevation angle of  $0.1^\circ$  and correspond to  $\alpha = 0.00033 \text{ m}^{-1}$  ( $\text{CO}_2$  laser) and

$\alpha = 0.0018 \text{ m}^{-1}$  (HeNe laser) respectively. The higher absorption case (Figure 6) yields the maximum value of  $K$  (i.e. 1) at the aircraft ( $x = 0$ ) for beam diameters greater than 5 m, but  $K$  falls off rapidly with range in front of the aircraft. Thus there will be a strong refractive anomaly close to the aircraft, but this will not extend far in front of it. Figure 5 shows lower values of  $K$ , but the effect persists at longer ranges in front of the aircraft. Figure 7 shows the  $K$  profile for a beam elevation of  $0.5^\circ$  and  $\alpha = 0.00033 \text{ m}^{-1}$  (note the change in height scale). The maximum  $K$  value is lower than in Figure 5 (the horizontal cross-section through the laser beam, and hence the heating time, is less for higher elevations); however, the effect of heating falls off much more slowly with height than at lower elevation angles.

So far the effect of the refractive index gradient on the laser beam itself has been ignored. Since the refractive index created across the beam is approximately linear with height, and we have assumed that the illumination across the beam is constant, the beam will be deflected downwards without significant focussing or defocussing. (This contrasts with the case of a gaussian intensity distribution where the nonlinear refractive index profile across the beam causes beam defocussing or "blooming" [3]). The vertical deflection of the beam,  $\Delta h$ , in traversing a path length,  $r$ , is easily shown to be

$$\Delta h = \frac{r^2}{2 \times 10^6} \frac{dN}{dh} \quad (23)$$

where  $dN/dh$  is the refractivity gradient across the beam. Assuming a  $10 \text{ N}$  change across a  $10 \text{ m}$  diameter beam, the beam deflection amounts to  $0.5 \text{ m}$  in  $1 \text{ km}$ . This small beam deflection can be accounted for approximately by adjusting the beam elevation angle. A rigorous solution would not only need to take account of the effect of this beam deflection on the shape of the layers formed, but would also need to consider the corrections to the  $K$  integral in eqn (21). This is a coupled fluid dynamics and electromagnetic propagation problem which would require a numerical solution; here we retain the approximate analytical solution.

The effect of these  $K$  profiles on target shielding will be considered in Section 3 below. First, we must consider the limits of validity of our quasi-static analysis caused by layer instabilities.

## 2.5 Layer instability

For the  $K$  profiles to be as derived above, we must ensure that (a) the profile has had time to form and (b) it has not decayed to its ambient value due to mixing with the surrounding air mass.

The profile is only fully formed after the heating has been applied for a time that is much greater than  $\tau_a$ , the acoustic timescale. Now

$$\tau_a \sim \frac{l}{v_a} \quad (24)$$

where  $l$  is the characteristic length of the heated region and  $v_a$  is the speed of sound. Since in practice (i) the beam is nearly horizontal, and (ii)  $\alpha \ll 1$  so that horizontal temperature gradients are small, the acoustic shock wave will travel in a vertical direction across the beam diameter. Thus we put  $l \sim d$ . As the beam is moving horizontally at velocity  $v_o$ , in the acoustic timescale it moves a distance  $dv_o/v_a < d$  as  $v_o < v_a$ . This is a small proportion of the horizontal cross-section through the beam,  $d \csc \theta$ , as  $\theta$  is small. We conclude that the early time behaviour will only have an effect on  $K$  very close to the leading edge of the moving beam; the  $K$  profile is therefore only affected at the very lowest heights for which  $K \neq 0$ , and this will have minimal effect on the refractive properties of the layer.

A further mechanism which could potentially affect the early time behaviour of heating by a  $10.6 \mu\text{m}$   $\text{CO}_2$  laser is kinetic cooling of the atmosphere [5]. At this wavelength, energy is absorbed by both water vapour and carbon dioxide. While the energy absorbed by the water vapour is essentially transformed into heat instantaneously (within  $1 \mu\text{s}$ ), the energy absorbed by the carbon dioxide induces a series of molecular transitions involving  $\text{CO}_2$  and  $\text{N}_2$  that extracts kinetic energy from the air, causing an initial lowering of temperature. The cooling is slight (a few tens of mK), but the timescale for the release of the vibrational energy (and therefore the delay in the onset of heating) can be as much as a few tenths of a second. For the velocities and beam geometries being considered, the affected region will be a small fraction of the horizontal cross-section through the beam, and again there will be minimal effect on the refractive properties of the layer.

The main mechanism causing the layer to decay is thermal instability generated by the heating. Buoyancy forces on the heated air will cause it to rise, eventually establishing equilibrium with the surrounding air by a process of turbulent mixing. The timescale,  $\tau_t$ , for the development of the initial vortex motion [6] is

$$\tau_t = \left[ \frac{T}{\Delta T g} \right]^{1/2} \quad (25)$$

where  $T$  is the absolute temperature,  $\Delta T$  is the temperature difference across the heated region,  $l$  is the characteristic size of the heated region, and  $g$  is the acceleration due to gravity. As before, we put  $l \sim d$ , and since from eqn (6)  $|\Delta T/T| = |\Delta N/N|$ , we can write

$$\tau_t = \left[ \frac{N}{\Delta N g} \right]^{1/2} \quad (26)$$

$\tau_t$  is greater for larger beams and smaller heating/refractive index effects. For beam diameters in the range  $1\text{--}10 \text{ m}$  and refractivity anomalies in the range  $1\text{--}10 \text{ N}$ ,  $\tau_t$  is in the range  $1\text{--}20 \text{ secs}$ . This limits the range over which the layer persists ( $v_o \tau_t$ ) to a few kilometres. Since at the very least, the horizontal beam

cross-section must be less than this distance, the onset of turbulence limits the minimum beam inclination angle  $\theta_i$  that can be used:

$$\sin \theta_i = \frac{d}{v_o \tau_i} \quad (27)$$

$\theta_i$  is typically a few tenths of a degree.

The onset of turbulence will cause the overlaid  $K$  profiles in Figures 5-7 to separate at some height above that of maximum  $K$ . We assume in the following that  $\theta$  is sufficiently greater than  $\theta_i$  to prevent the decay of the profiles above the  $K$  maximum from significantly affecting the refractive properties of the layer. A more thorough study of the time evolution of the layer is highly desirable.

Another mechanism contributing to the decay of the layer *behind* the aircraft is the passage of the aircraft itself through the layer. The turbulence is likely to destroy the coherence of the layers within a short distance of the aircraft. Note however that it does not follow that the refractive effects are negligible behind the aircraft; this is discussed further below.

### 3 Results

The final step in the investigation is to show the effect of the heating produced refractive index anomalies on an incoming radar signal. This requires an electromagnetic propagation model that can deal with the two-dimensional refractive index profiles. The recently developed parabolic equation model [7,8] is especially suited to this type of problem. It can handle essentially arbitrary two-dimensional refractive index distributions specified analytically or numerically, and has an efficient solution based on fast Fourier transform methods. The basic output of the model is the one-way path loss between a radar system and field points defined on a range-height grid. In the current problem, the radar signal passes twice through the anomalous refractive index structures on its way to and from the target aircraft. Thus the effective reduction in target cross-section is given by twice the path loss between radar and target relative to the path loss in a standard atmosphere. We call this the "shielding factor",  $SF$ .

Figure 8 shows the radar coverage diagram in the vicinity of a laser beam at a height of 500 m and a range of 370 km, close to the horizon of the radar shown in Figure 1. (The aircraft/laser is flying from right to left towards the radar at 0 km range). The laser beam parameters used were: beam strength  $S = 0.05$ ;  $\theta = 0.1^\circ$ ;  $d = 5$  m;  $\alpha = 0.00033 \text{ m}^{-1}$ . A significant hole has been caused by the laser heating. Also shown are vertical cross-sections at the aircraft's range, and at 5 and 10 km behind the aircraft. The shielding factor is 5 dB at the aircraft's range, but this increases to over 30 dB 10 km behind the aircraft. Actually for this strength of beam, layer instability will limit the layer to 1-2 km behind the aircraft whereas Figure 8 has assumed a stable layer. It is important to note however that a coverage hole behind the aircraft does not depend on the layer persisting at these

ranges. Once refractive bending has taken place, the energy will continue to diverge from the aircraft altitude even if the refractive index returns to normal behind the aircraft. The shielding factor will be less in this case, but will still be greater than the shielding factor at the aircraft's range. Numerical results are given below.

The height of the maximum shielding factor in Figure 8 is slightly above the base of the beam: this height varies with the beam and radar geometry, and the aircraft height relative to the beam would have to be chosen carefully; the width of the shielding factor curve close to the maximum appears to be sufficient to enclose the aircraft completely.

Figure 9 shows the situation for a laser beam at the shorter range of 300 km from the radar. The beam parameters are the same as before except that we choose  $\theta = 0.5^\circ$ , since at this shorter range the radar is seen at a higher elevation angle from the target aircraft. The main feature to note is that the shielding factor is much smaller than in the previous case, especially at the 5 and 10 km ranges; there is little extra protection to be gained from flying the aircraft behind the laser.

In order to examine the sensitivity of the shielding factor to the beam geometry, the parameters  $\theta$ ,  $\alpha$ ,  $d$  and  $S$  were varied, keeping the other parameters constant. (The only exception is the variation with  $d$ , where we have kept the product  $Sd$  fixed at 0.25: since  $S \propto I_o$  (the beam intensity),  $Sd \propto P$  (the beam power); we assume that the power, rather than the intensity, is limited by technology). Figure 10 shows this parametric study for the aircraft's range, and at 5 and 10 km behind the aircraft, for the parameters corresponding to Figure 8. The conclusions are:

1. The shielding factor increases as the elevation angle decreases (larger horizontal beam cross-sections and therefore longer heating times).
2. The variation with absorption coefficient shows a maximum between  $\alpha = 0.0001$  and  $0.001$ . Indeed, at the range of the aircraft, the compromise between a short range, strong layer and a long range, weak layer appears to be optimum at a value of  $\alpha$  close to that of the  $10.6 \mu\text{m}$   $\text{CO}_2$  laser ( $0.00033$ ); this is fortuitous as these lasers can generate the highest powers.
3. The variation with beam diameter is fairly weak although at the shorter ranges, the shielding factor increases slightly with decreasing beam size.
4. As expected, the shielding factor increases with beam strength, although it "saturates" at the longer ranges for very high beam strengths. Realistic values of  $S$  will be less than  $0.05$ , and in this region the shielding factor is almost proportional to  $S$ ; for example, at the aircraft range,  $SF$  (dB)  $\approx 90S$ .

Figure 11 gives the reduction in shielding factor to be expected due to the decay of the layer behind

the aircraft. The layer has been assumed to decay exponentially with range, and the shielding factor is shown as a function of "layer decay length", defined as the distance at which the layer decays by a factor of  $1/e$ . The layer parameters are those used in Figures 8 and 10. As expected, the shielding factor at the aircraft's range is independent of the layer decay, while the shielding factor 5 and 10 km behind the aircraft reduces for more rapidly decaying layers. Clearly a shielding factor of 30 dB at 10 km range is overoptimistic given a layer decay length of 1-2 km; however, the shielding factor is still about 10 dB. If it is desired to operate with a hole-burning aircraft protecting the main targets further back, it will be necessary to ensure that the aircraft/laser system disturbs the layer as little as possible.

Figure 12 shows the variation of the shielding factor with  $\theta$  and  $\alpha$ , for the parameters corresponding to Figure 9. A new feature is the distinct peak at an elevation angle between  $0.4^\circ$  and  $0.5^\circ$ . This corresponds to the elevation of the radar from the target aircraft: the benefit of a lower elevation angle in increasing the horizontal beam cross-section is outweighed by the loss of shielding caused by depointing the beam from the radar direction. Again it appears that an absorption coefficient of  $0.00033 \text{ m}^{-1}$  is about optimum.

#### 4 Discussion

Proposals for reducing the effective radar cross-section of an aircraft by active modification of the medium surrounding it have been made. Heating of the atmosphere by a laser mounted on the aircraft was seen to be a feasible mechanism. Shielding factors of greater than 10 dB could be obtained using a  $10.6 \mu\text{m}$   $\text{CO}_2$  laser in the megawatt range.

There are many questions that should be investigated further:

- The technical feasibility of generating sufficient laser power on an aircraft, and producing a beam with adequate aperture (several metres) must be assessed. In particular, the analysis should be extended to deal with defocussed and multi-beam systems.
- The problem of layer instabilities and decay should be addressed, particularly if the higher shielding factors obtainable behind the laser are to be quantified more accurately.
- Beam bending and defocussing due to the self-generated refractive index gradients and gaussian beam profile should be incorporated; numerical thermal blooming computer codes could be adapted for this purpose.
- The break up of the layers via turbulent mixing will itself cause enhanced backscatter of the radar energy (cf. clear-air radar echoes); the level of this backscatter should be estimated since if it is large,

it could produce a radar signature that would nullify some of the benefits of reduced radar cross-section.

- The extension of the analysis to supersonic flight is clearly important for military aircraft.
- The analysis has assumed clear-air absorption.  $10.6 \mu\text{m}$  radiation is strongly absorbed by liquid water and this mechanism has been exploited for cloud hole-boring [9]. The refractive effects of evaporation in rain and clouds should be investigated.

#### References

- [1] Bean B.R. and Dutton E.J., "Radio meteorology", NBS Monograph 92, 1966, 1-9.
- [2] McClatchey R.A., Fenn R.W., Selby J.E.A., Volz F.F. and Garing J.S., "Optical properties of the atmosphere", Air Force Cambridge Research Laboratories report *AFCRL-72-0497*, 1972.
- [3] Walsh J.L. and Ulrich P.B., "Thermal blooming in the atmosphere", in "Laser beam propagation in the atmosphere", Topics in Applied Physics, Vol 25, Springer-Verlag, 1978, 223-320.
- [4] CRC Handbook of Laser Science and Technology, CRC Press Inc., 1982.
- [5] Weichel W., "Laser beam propagation in the atmosphere", Tutorial Texts in Optical Engineering, Vol TT3, SPIE Optical Engineering Press, 1989, 78-81.
- [6] Carpenter R.L., Droegemeier K.K., Woodward P.R. and Hane C.E., "Application of the piecewise parabolic method (PPM) to meteorological modeling", *Monthly Weather Review* 118, 1990, 586-612.
- [7] Craig K.H., "Propagation modelling in the troposphere: parabolic equation method", *Elec. Lett.* 24, 1988, 1136-1139.
- [8] Craig K.H. and Levy M.F., "Parabolic equation modelling of the effects of multipath and ducting on radar systems", *IEE Proc. F* 138, 1991, 153-162.
- [9] Quigley G.W., Webster R.B. and York G.W., "Cloud hole-boring with long pulse  $\text{CO}_2$  lasers", *SPIE Proc.* 1221, 1990, 370-380.

#### Acknowledgement

This work has been carried out with the support of the USAF through the European Office of Aerospace Research and Development. The author would like to thank Owen Côté for suggesting the problem and for valuable discussions.

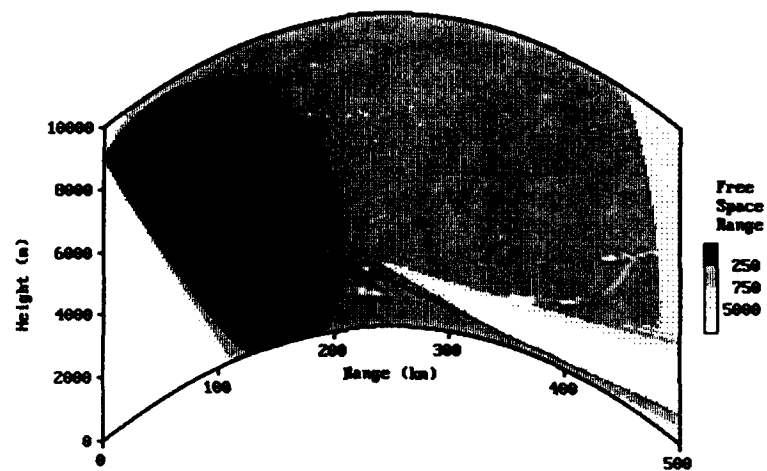


Figure 1: Coverage diagram of an S-band radar in terms of free space range (i.e. the contours show the limits of detectability of a radar with the given range capability in free space). The hole is caused by a sloping elevated layer.

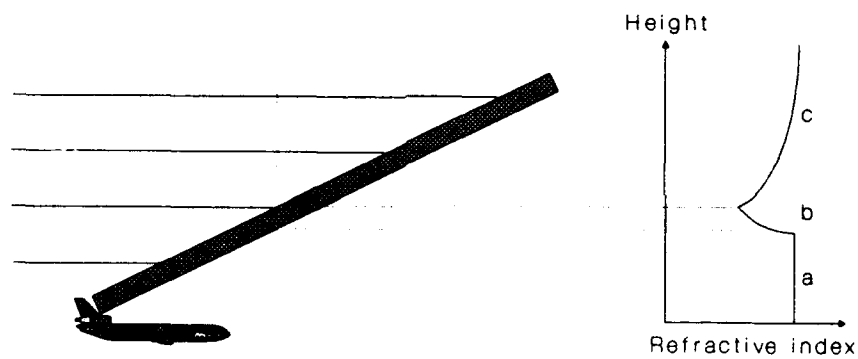


Figure 2: Anomalous refractive index layer produced by an aircraft-mounted laser.

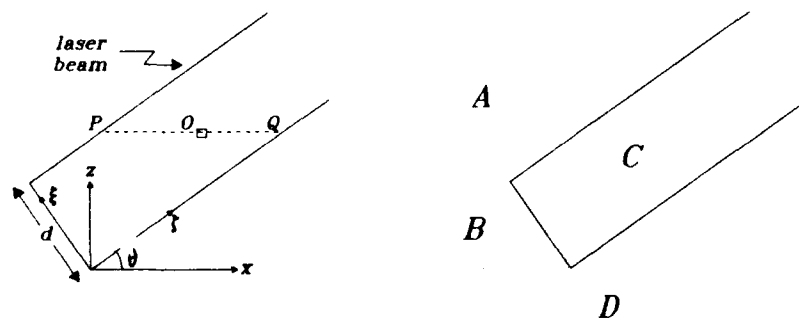


Figure 3: Laser beam geometry.

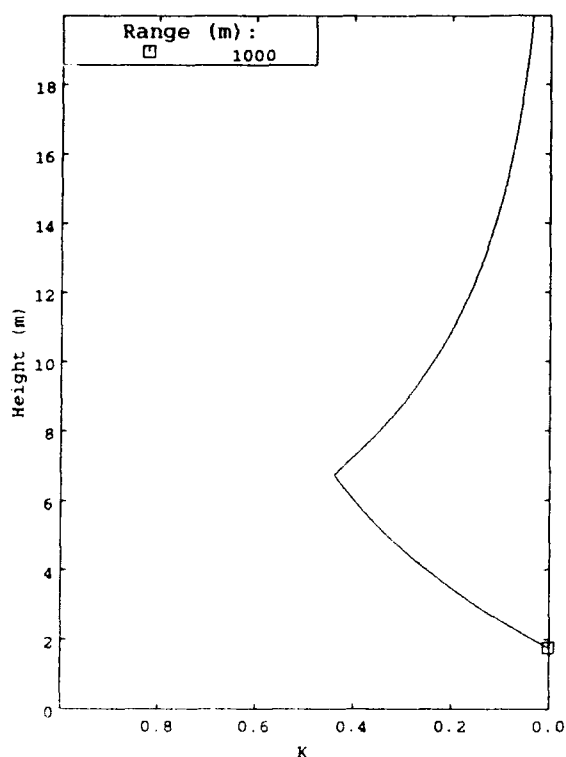


Figure 4: Laser generated  $K$  profile: beam parameters are  $x = 1 \text{ km}$ ,  $\alpha = 0.00033 \text{ m}^{-1}$ ,  $d = 5 \text{ m}$  and  $\theta = 0.1^\circ$ .

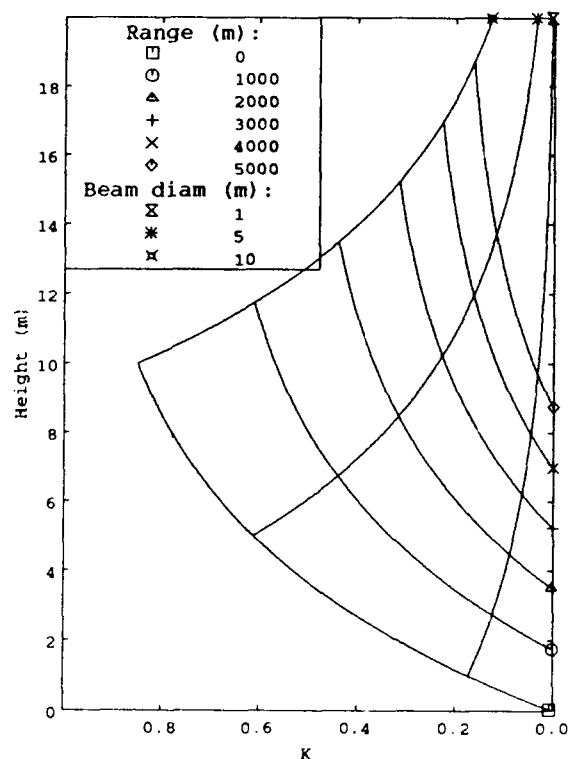


Figure 5:  $K$  profiles for  $\alpha = 0.00033 \text{ m}^{-1}$ ,  $\theta = 0.1^\circ$ .

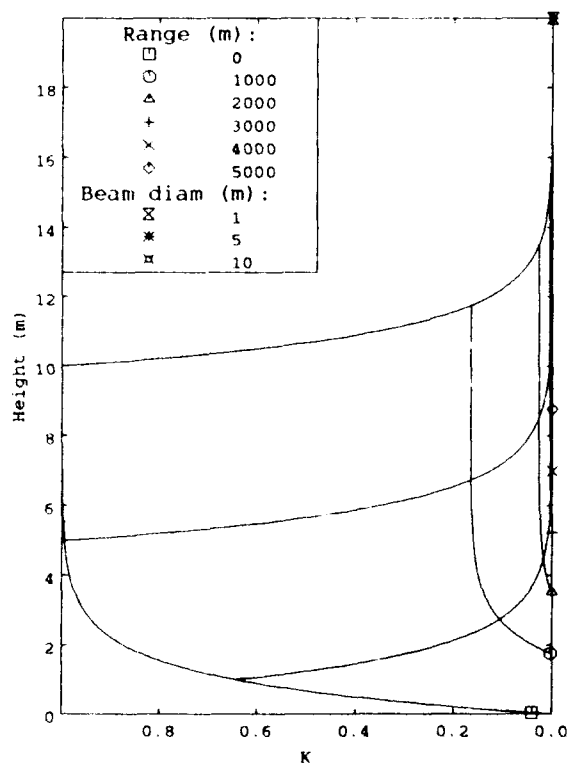


Figure 6:  $K$  profiles for  $\alpha = 0.0018 \text{ m}^{-1}$ ,  $\theta = 0.1^\circ$ .

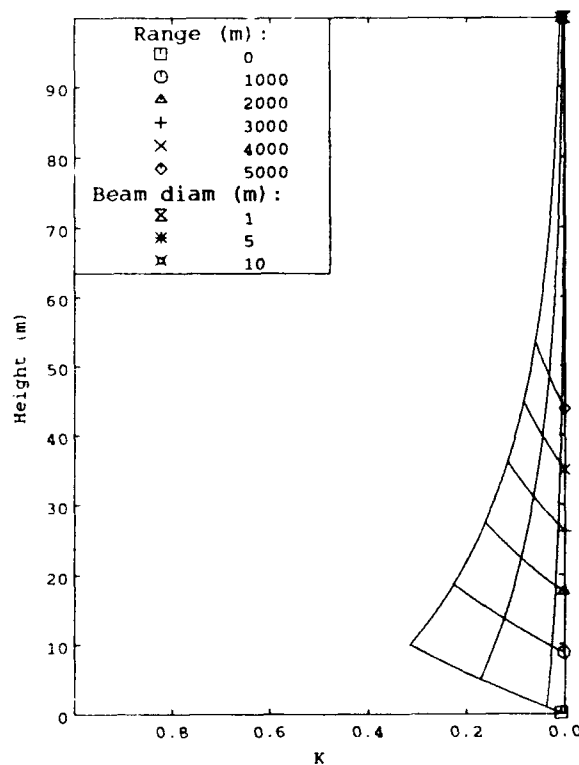


Figure 7:  $K$  profiles for  $\alpha = 0.00033 \text{ m}^{-1}$ ,  $\theta = 0.5^\circ$ . (Note different height scale).

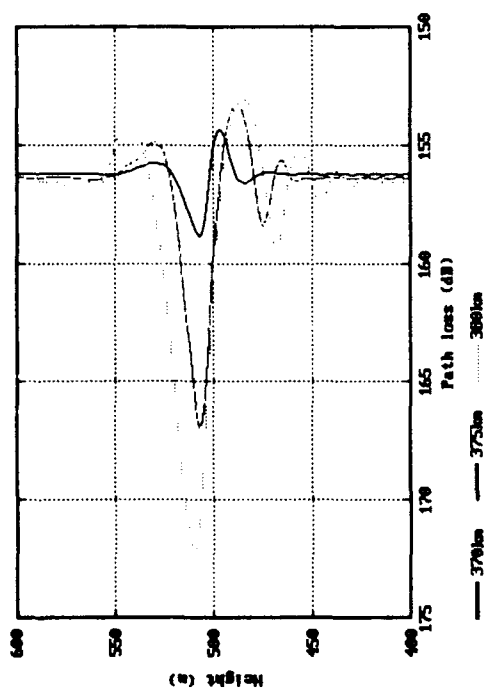
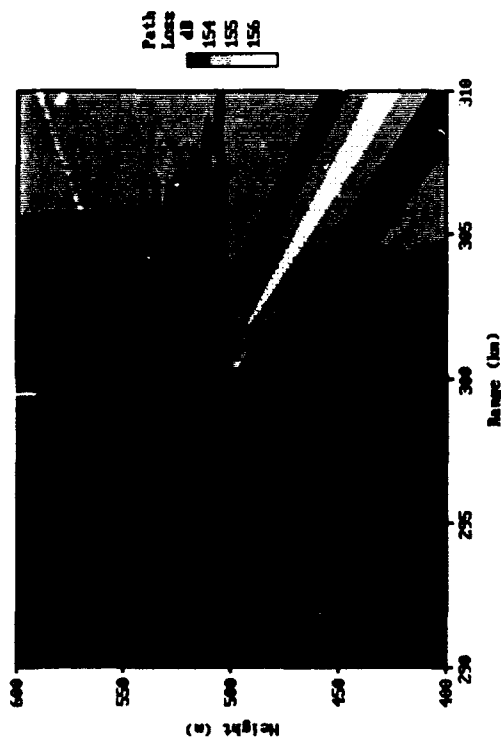


Figure 8: Radar coverage diagram (in terms of one-way path loss). The laser is located at 370 km range and 500 m height. Beam parameters are:  $S = 0.05$ ;  $\theta = 0.1^\circ$ ;  $d = 5$  m;  $\alpha = 0.00033 \text{ m}^{-1}$ . The lower graph shows path loss along vertical cross-sections.

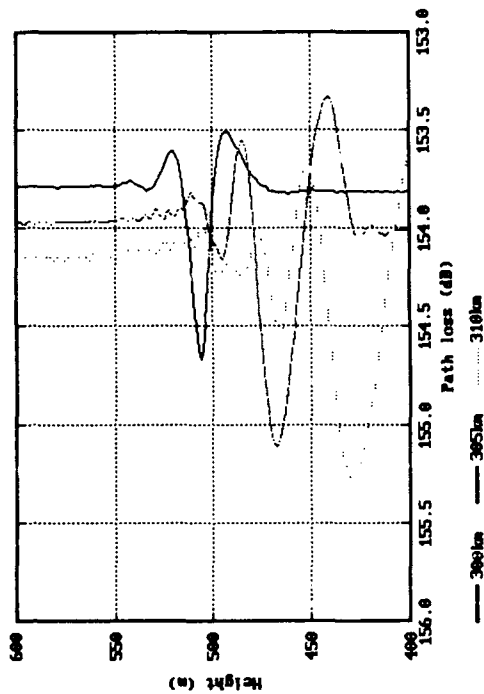
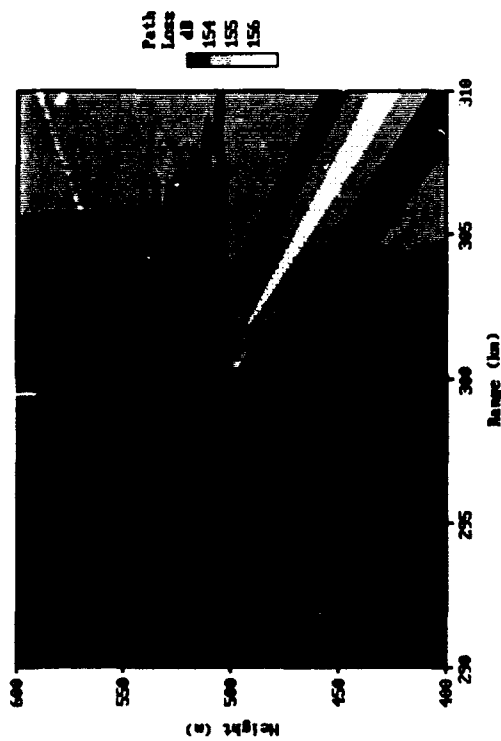


Figure 9: Radar coverage diagram (in terms of one-way path loss). The laser is located at 300 km range and 500 m height. Beam parameters are:  $S = 0.05$ ;  $\theta = 0.5^\circ$ ;  $d = 5$  m;  $\alpha = 0.00033 \text{ m}^{-1}$ . The lower graph shows path loss along vertical cross-sections.

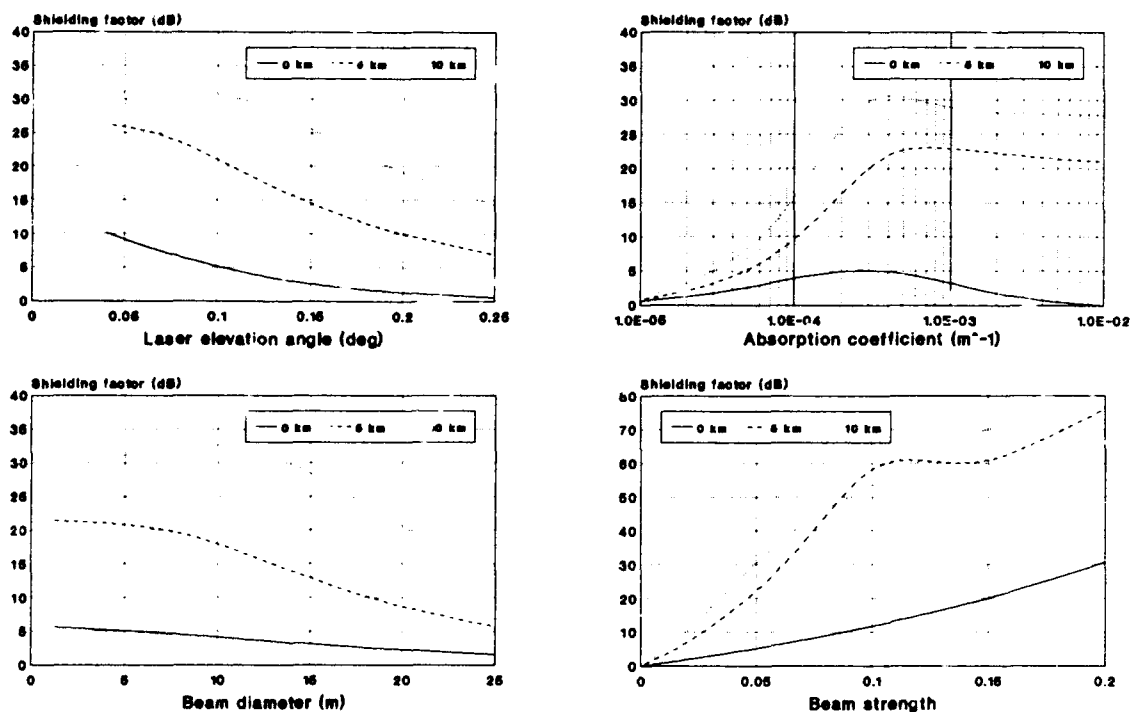


Figure 10: Parametric study of the shielding factor for the laser geometry of Figure 8.

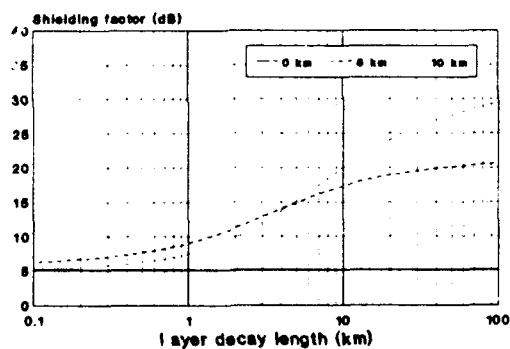


Figure 11: Reduction in shielding factor caused by layer decay.

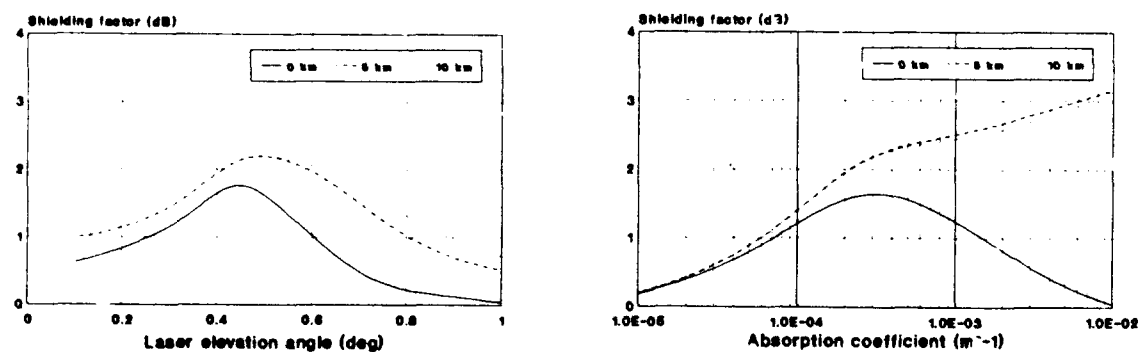


Figure 12: Parametric study of the shielding factor for the laser geometry of Figure 9.



## DISCUSSION

## E. Schweicher, BE

Your talk was very interesting but raises some questions.

1. You did not take into account the laser beam divergence. Why?
2. Why did you not mention the DF laser radiating at  $3.8\mu$  (not far away from the He-Ne laser at  $3.3\mu$ ) and featuring a much better efficiency (about 5% compare to less than 1% for the He-Ne laser) as well as much higher powers (the US DF ALPHA laser, which is a laser weapon, radiates 5 MW CW)
3. Your radar hole could be blown away if you have a cross wind because the laser beam always tends to bend towards the wind.

## Author's Reply

1. I discuss this point briefly in the paper. A constant beam cross-section was assumed in order to obtain a simple analytical solution to the K-integral. I agree that a collimated beam cross-section of a few square meters is unlikely and expect that a "practical" system would involve a diverging beam. I leave the problem of designing the optics to the laser experts, but the refractive effects of different beam geometries should be investigated.

2. When I wrote the paper my only source of high spectral resolution molecular absorption data was Reference 2 which predates the DF system you mention. I was unaware of the 5 MW power capability which is certainly impressive. Unfortunately the DF wavelength is only weakly absorbed by the atmosphere (hence its use for weapons) and so the heating efficiency will be low; the shorter wavelength HF laser experiences strong water vapor absorption and is perhaps more useful in this application. The  $\text{CO}_2$  laser is probably still the best choice due to its ideal absorption characteristics.

3. I accept your point. I would hope that the effect is small enough to be ignored to first order. This is another of the nonlinear effects that could be tackled by using a laser thermal blooming computer code.

## F. Christophe, FR

Since the major shielding seems to occur behind the aircraft, did you consider the interaction between its wake and the heated layer?

## Author's Reply

In the paper I mention that the passage of the aircraft through the layer is likely to destroy the coherence of the layer behind the aircraft. The problem of maximizing layer stability clearly needs to be examined further. Of course the shielding factor behind the aircraft is always at least as great as the value at the aircraft range, independently of the layer breakup (Figure 11).

# STOCHASTIC MODEL OF TERRAIN EFFECTS UPON THE PERFORMANCE OF LAND-BASED RADARS

S P TONKIN  
Smith Associates Limited  
Guildford Surrey GU2 5YP  
UK

M A WOOD  
Royal Signals and Radar Establishment  
Great Malvern Worcestershire WR14 3PS  
UK

## Summary

A stochastic model of land clutter visibility and of terrain screening of targets, with particular application to low-flying targets under surveillance by a microwave land-based radar system, is described.

The model is non-site-specific, but detailed. It allows radar performance measures such as the mean length of track to be obtained analytically, without averaging large numbers of site-specific simulations or requiring high fidelity terrain data. The trajectories of terrain-following targets are described in terms of ensembles of Markov processes. The main dependencies of the model are on:

- terrain relief;
- radar height;
- target altitude;
- distance of closest approach between the target and the radar.

The model can be used to generate simulated clutter maps and target screening diagrams, and indeed this is done to compare the model results with experimental data. However, the main aim is to predict the effects of target screening and land clutter directly from the model, rather than through large numbers of simulations. The equations which can be used to derive such predictions are given, and applied to a simple case: the time at which an incoming target first enters a cluttered cell. This approach to such calculations is extremely computationally efficient.

## Introduction

In performance assessments of ground based air defence radar systems, the quantity of interest is usually a general measure such as the mean track length. Ultimate limits upon such performance measures are provided by certain characteristics of the terrain: in particular, terrain screening and land clutter. An important feature of these terrain effects is their patchiness: for example, low-flying targets may move in and out of clutter several times while flying towards the radar site. The path of a low-flying air vehicle relative to such terrain features

can critically affect the radar performance; this is illustrated in Figure 1.



Figure 1  
*Illustration of the effect of the path of a low-flying air vehicle on its detectability*

Two classes of model have been used to predict such effects. Detailed site-specific models<sup>1</sup> can predict radar performance for a particular radar site and air vehicle trajectory; such models rely on high fidelity terrain and land cover data. However, while the performance for a well-specified site and trajectory can be found, it is not clear how many sites and how many trajectories for each site would have to be analysed to give a statistically significant answer; furthermore, this approach is computationally expensive. In contrast, simplistic spherical-earth clutter and screening models do not address the wide variability of clutter and screening effects with different target paths.

The purpose of this paper is to outline a stochastic model of terrain screening and land clutter, which provides a middle way between the detailed site-specific and simple spherical-earth models. The stochastic model, which has been tested against measured clutter data and digital terrain elevation data (DTED), describes the large-scale spatial correlations of target screening and of clutter for three generic classes of terrain (level, low-relief and high-relief).

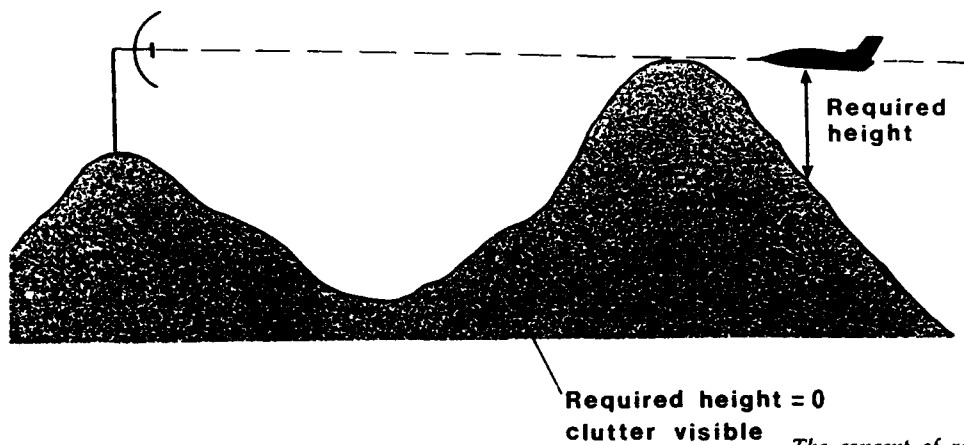


Figure 2  
The concept of required height

### Terrain-following Targets and Ground Clutter

The screening of terrain following targets can be described in terms of a single quantity, the height,  $h_r$ , above the terrain that the target must reach to be visible. The concept of required height is illustrated in Figure 2; the occurrence of (line of sight) ground clutter corresponds to regions where this required height is zero. The required height can be defined at every point within the region of interest, giving:

$$h_r = h_r(R, \theta) \quad (1)$$

where  $R$  and  $\theta$  are polar coordinates relative to the radar site as origin.

The proposed stochastic model characterises the required height  $h_r(R, \theta)$  as a random field, with a different ensemble of such fields corresponding to each of the terrain classes of interest. The terrain classes considered are:

- (i) **Level sites:** these are generally well modelled in terms of a spherical earth. At X-band, the clutter visibility, defined as the fraction of cells at a given range which are cluttered, gradually falls away with range, the main drop in clutter visibility occurring near the spherical earth horizon.
- (ii) **Low-relief sites** (eg gently rolling farm-land): in these regions, the clutter persists beyond the spherical earth horizon, and there is patchiness, or correlation, in the clutter visibility. An X-band clutter map for such a site, Spruce Home, is given in Figure 3 (upper map). The maximum range in this figure (and all other clutter maps shown here) is 24 km; the "spherical earth" clutter horizon for the given radar height (18 m) is only 16 km.
- (iii) **High-relief sites** (ie mountainous areas): here, the clutter persists at very long ranges, and there may be anisotropy and periodicity in the clutter visibility due to regular mountain

ridges. The illustrative clutter map shown in Figure 3 (lower map) was measured at Scranton.

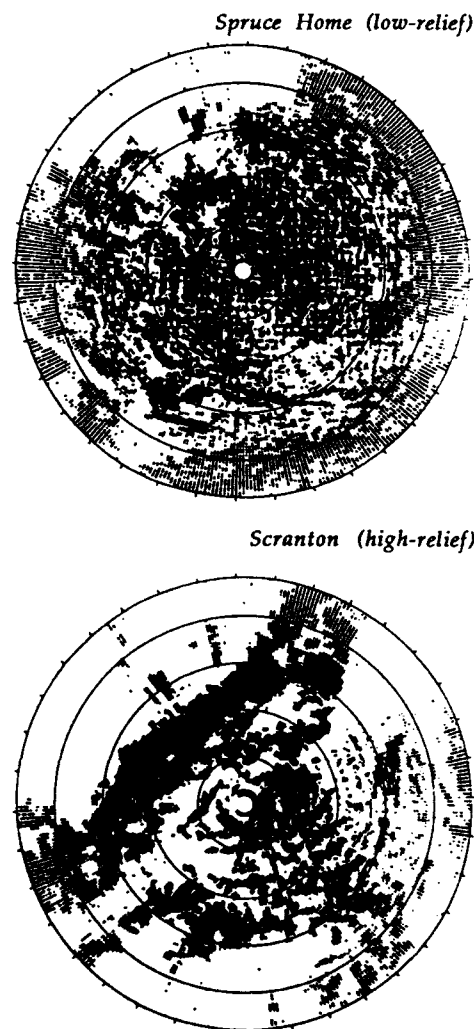


Figure 3  
Clutter maps for a low-relief site, Spruce Home, and a high-relief site, Scranton.

A reasonable statistical description of the terrain shadowing is obtained in terms of an underlying random field,  $g(R, \theta)$ , such that:

$$\begin{aligned} h_r(R, \theta) &= g(R, \theta)^2 & g(R, \theta) > 0 ; \\ h_r(R, \theta) &= 0 & g(R, \theta) \leq 0 . \end{aligned} \quad (2)$$

The root required height,  $\sqrt{h_r(R, \theta)}$ , follows a truncated Gaussian distribution characterised by a mean,  $\mu(R)$ , and a standard deviation,  $\sigma(R)$ , with the following functional forms:

$$\begin{aligned} \mu(R) &= A + BR + Ch^* ; \\ \sigma(R) &= \sigma . \end{aligned} \quad (3)$$

The parameters  $A, B, C$  and  $\sigma$  are constant for a given terrain type, and  $h^*$  is the height of the radar above the mean terrain height. Figure 4 illustrates this truncated Gaussian distribution for  $\sqrt{h_r(R, \theta)}$ ; histograms of the root required height at different ranges, constructed from a single (low-relief) shadowing diagram, are shown, together with the best fit (maximum likelihood) Gaussian. The spike at zero required height, corresponding to cluttered regions, has been removed.

The two point correlation function of the normal field  $g$  can be expressed:

$$\rho(r_0, r_1) = \exp \left\{ - \int_{r_0}^{r_1} \alpha(R, \psi, \zeta) dr \right\} . \quad (4)$$

The function  $\alpha(R, \psi, \zeta)$  is terrain type dependent. The angle  $\psi$  describes the direction of the target's path relative to the radial direction (ie  $\psi=0$  implies a radial path and  $\psi=90^\circ$  implies a tangential path), and the angle  $\zeta$  describes the path's direction relative to a fixed direction (this latter dependence only arises in high-relief sites, in which a preferred direction is defined by the mountain ridges).

The model parameters,  $A, B, C, \sigma$  and the function  $\alpha$  have been evaluated from DTED corresponding to each of the classes of site. The values given here are tentative, since a sufficiently large data set to give firm values has yet to be analysed.

- (i) **Level sites:** as the scattering arises from vertical discretises<sup>1</sup>, simulated screening diagrams can be constructed by applying an uncorrelated clutter distribution to a screening diagram for a spherical earth, modelled deterministically. Formally, this gives the following parameterisation (where  $a_E$  is the earth radius):

$$\mu(R) = \frac{R - \sqrt{2a_E h^*}}{\sqrt{2a_E}} ;$$

$$\sigma(R) = 0 ;$$

$$\rho(r_1, r_2) = 0 . \quad (4)$$

- (ii) **Low-relief sites:** Table 1 gives values for the parameters  $A, B, C$  and  $\sigma$  (note that since  $g$  is the square root of a height, the units of  $\mu$  and  $\sigma$  are  $\sqrt{\text{metres}}$ ). The site height  $h^*$  for the particular case considered, Spruce Home, is 37 m. In addition, the two-point correlation function (defined in terms of  $\alpha$ ) can be written:

$$\begin{aligned} \alpha(R, \psi, \zeta) &= P_0 \exp \left( - \frac{R^2}{R_0^2} \right) + P_1 + \\ &+ Q_\psi \sin \psi + Q_\zeta \sin \zeta . \end{aligned} \quad (5)$$

The parameters  $P_0, P_1, R_0, Q_\psi$  and  $Q_\zeta$  are given in Table 2. For low-relief sites, the parameter  $Q_\zeta$  (describing the dependence of the correlations upon the direction of the path relative to a preferred direction) vanishes, implying that, on average, the screening diagrams are isotropic.

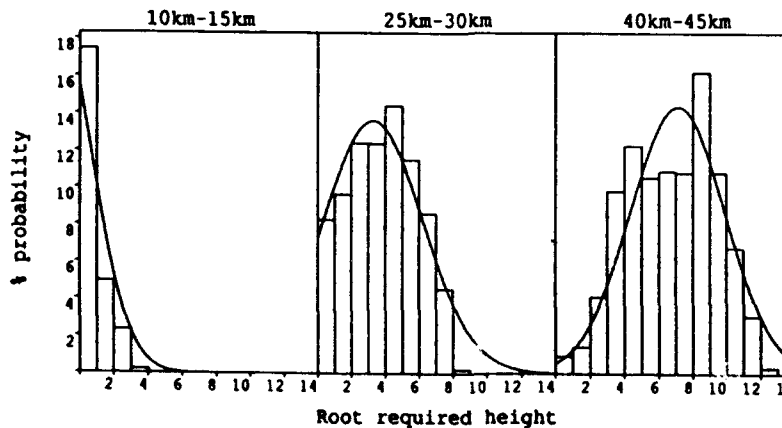


Figure 4  
Histograms of the square root of the required height for three different ranges; zero-height values removed

	$A/\sqrt{m}$	$B/m^{-1/2}$	$C/m^{-1/2}$	$\sigma/\sqrt{m}$
Low-relief	-3.6	$0.3 \times 10^{-3}$	-0.05	3.2
High-relief	+14.7	$0.6 \times 10^{-3}$	-0.07	6.3

Table 1  
Parameters describing the single-point statistics of  $g$

	$P_0/\text{km}^{-1}$	$P_1/\text{km}^{-1}$	$R_0/\text{km}$	$Q_\psi/\text{km}^{-1}$	$Q_\zeta/\text{km}^{-1}$
Low-relief	0.25	0.005	40.	0.02	0.0
High-relief	0.20	0.005	20.	0.005	$0.02+0.14i$

Table 2  
Parameters describing the correlations of  $g$

- (iii) **High-relief sites:** clutter visibility and target screening are much more variable for high-relief than for low-relief and level sites. The parameters describing the required height field are given in Tables 1 and 2; Scranton has a site height of 203 m. The most salient feature of this parameter set is the parameter  $Q_\zeta$ , which is not only non-zero but also complex. Exponentiation of this complex  $\alpha$  (as in Eqn 4) gives a periodic correlation; this is needed to describe the periodicity of the ridges illustrated in Figure 3.

Given this complete parameter set, screening diagrams can be simulated for each class of site. Figures 5 and 6 give such simulated screening diagrams, together with a screening diagram generated from DTED, for the low-relief and high-relief terrain types. In these diagrams, the black areas indicate cluttered regions (required height zero), and the grey scales indicate required heights ranging from below 50 metres (white areas) to above 200 metres (dark grey areas). The simulations have captured the essential features of the screening diagrams for the different classes.

#### Performance Prediction

The purpose of this work is not to produce simulated screening diagrams to be used in place of measured ones; rather, quantities useful for performance prediction can be extracted directly from it. Two quantities which can be derived from the model are:

- clutter visibility, that is, the fraction of cells at a given range that are cluttered;

- the probability that a target is visible and in an uncluttered cell.

For example, the clutter visibility  $V(R)$  is:

$$V(R) = \frac{1}{2} \operatorname{erfc} \left( \frac{A + B R + C h^*}{\sigma \sqrt{2}} \right). \quad (6)$$

At long ranges,  $V(R)$  is proportional to  $\exp(-B^2 R^2 / 2\sigma^2)$ .

For more detailed predictions, the evolution of the probability distribution function  $P(g)$  is used. By describing the way in which  $P(g)$  changes along a straight line path defined relative to the radar site, the whole ensemble of equivalent paths can be described at once - at no time is it necessary to consider a number of specific paths and simulate particular values for the required heights along those paths. Thus, it is possible to use a single, probabilistic calculation to describe target detection along all radial paths, or all paths with (say) 10 km as the distance of closest approach.

Let  $P(g;s)$  be the probability distribution of the root required height  $g$  at a position on a straight-line path parameterised by  $s$ . The two-point correlation function of  $g(s)$  is, from Eqn 4:

$$\rho(s_0, s_1) = \exp \left\{ - \int_{s_0}^{s_1} \alpha(s') ds' \right\}. \quad (7)$$

This exponential form, together with the assumed normal distribution for  $g(s)$ , means that  $g(s)$  is described by a normal Markov process<sup>2</sup>.

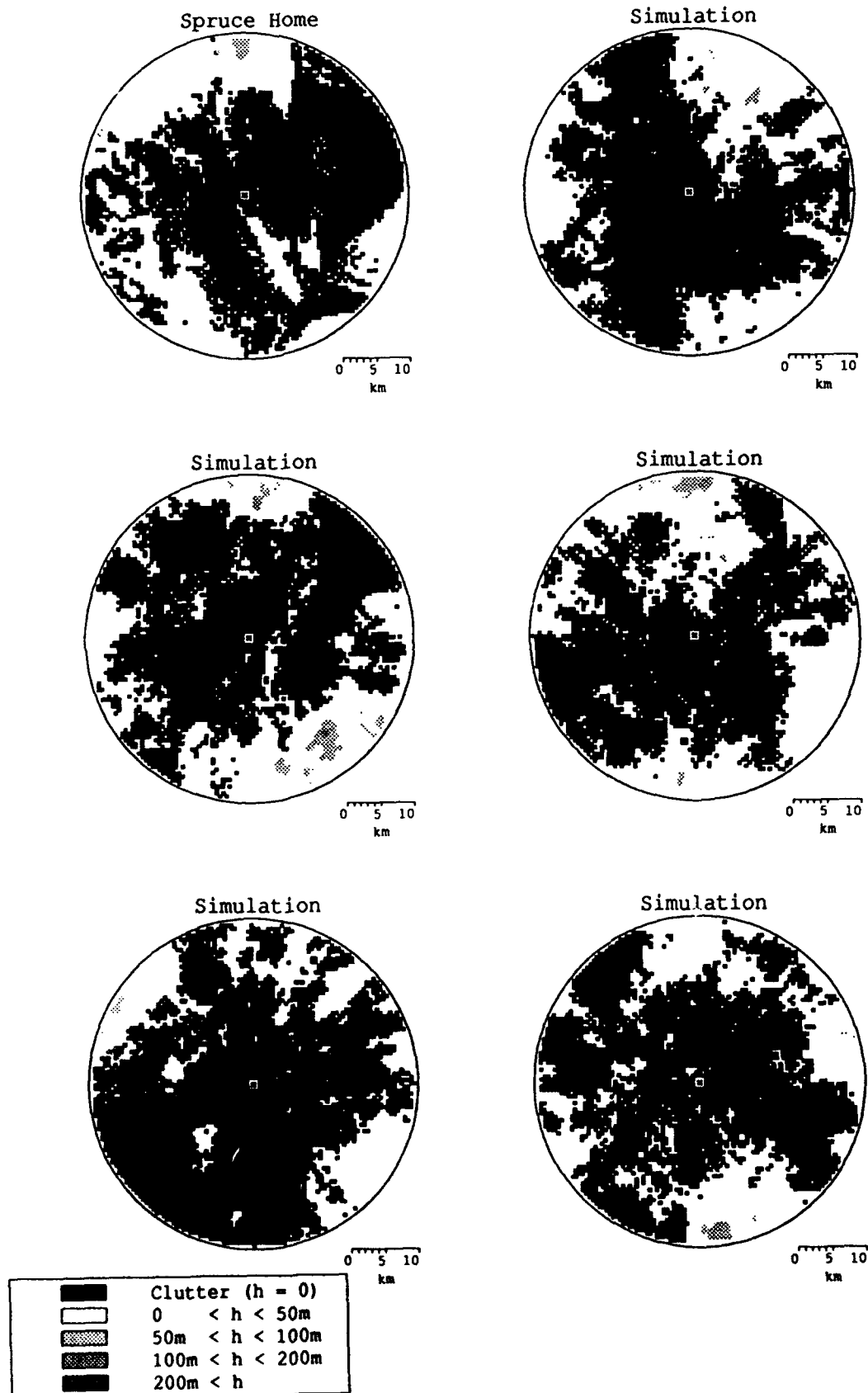


Figure 5  
Comparison of a low-relief screening diagram produced using the DTED for Spruce Home (top left-hand corner) with simulations produced using the non-site-specific model

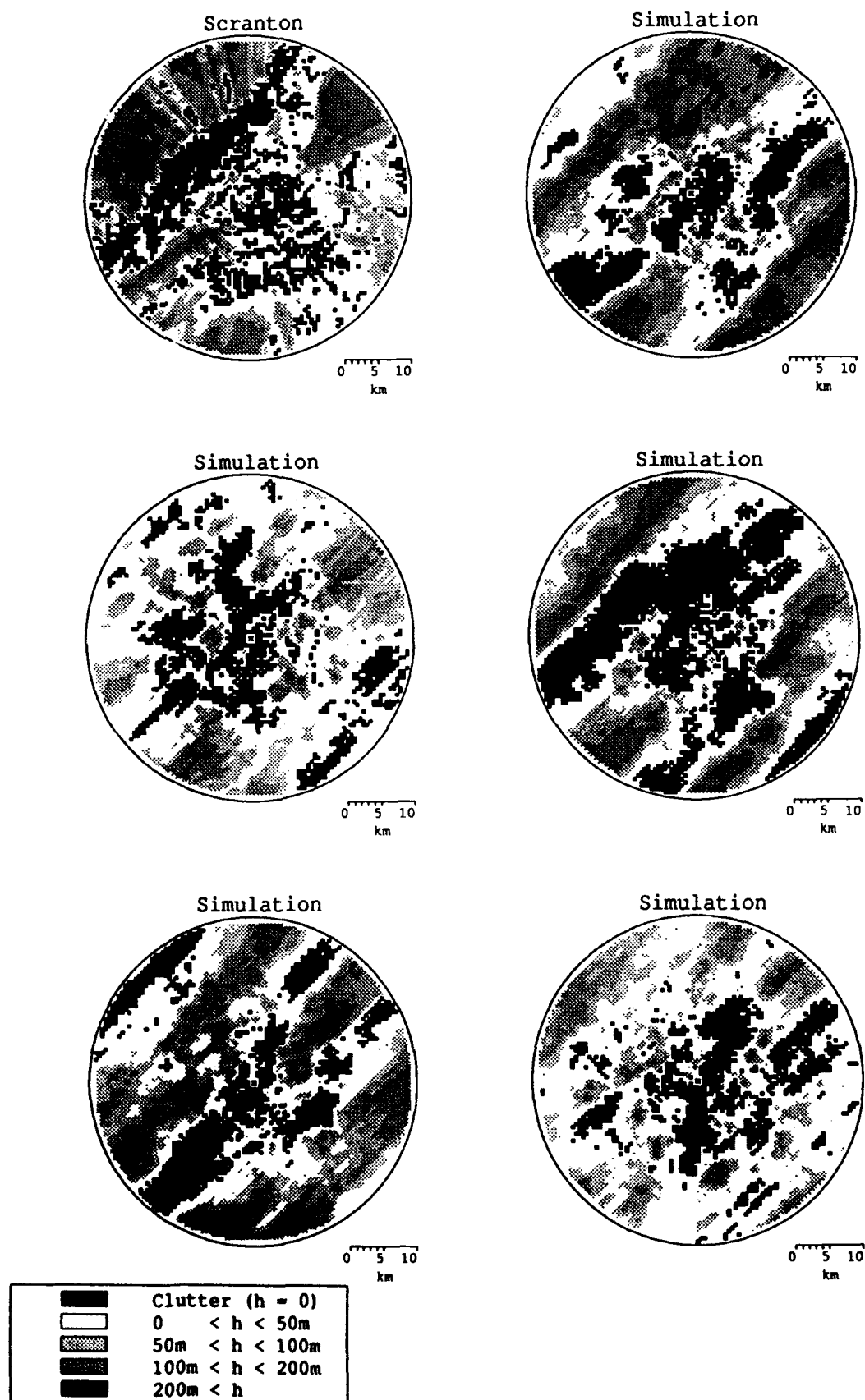


Figure 6  
Comparison of a high-relief screening diagram produced using the DTED for Scranton (top left-hand corner) with simulations produced using the non-site-specific model

This in turn means that the probability distribution function for  $g(s)$ ,  $P(g;s)$ , obeys the (forward) Kolmogorov equation<sup>2</sup>:

$$\begin{aligned} \frac{\partial P(g;s)}{\partial s} &= \alpha(s) \frac{\partial^2 P(g;s)}{\partial g^2} + \\ &+ \left( \alpha(s)[g - \mu(s)] - \frac{d\mu(s)}{ds} \right) \frac{\partial P(g;s)}{\partial g} + \\ &+ \alpha(s) P(g;s) \\ &\equiv K_g[P(g;s)] \end{aligned} \quad (8)$$

In this equation,  $\alpha(s)$  is the rate of decorrelation at a position  $s$  along the path,  $\mu(s)$  is the mean value of  $g$  at position  $s$ , and  $\sigma$  is the (range-independent) standard deviation of  $g$ . The quantities  $\alpha$ ,  $\mu$ , and  $\sigma$  depend on the range to the radar site, the radar height and the terrain type; the different possible paths are described through the dependence of the range  $R$  upon the distance  $s$ . For example, for radial paths beginning at range  $R^0$ , that range is  $(R^0 - s)$ . For non-radial paths, the range depends on the distance of closest approach, as well as upon  $R^0$  and  $s$ . The operator  $K_g[P(g;s)]$  is defined by the right-hand-side of Eqn 8.

Because the Kolmogorov equation is a parabolic partial differential equation, it is easy to solve numerically for a range of boundary conditions<sup>3</sup>.

As an example of the use of this equation, consider the problem of the range at which a terrain-following target flying along an incoming radial path, starting at a range  $R^0$ , first becomes unshadowed. Suppose that the target flies at a height  $h_t$  above the terrain. This means that the target will first become unmasked when the required height for a line of sight first drops below  $h_t$ ; that is, when the root required height  $g(r)$  first drops below  $\sqrt{h_t}$ . The probability that the target has become unshadowed at or before range  $R$  is equal to the probability that  $g(r')$  drops below  $\sqrt{h_t}$  between  $R' = R^0$  and  $R' = R$ .

To calculate this probability, the Kolmogorov equation is integrated from  $R' = R^0$  to  $R' = R$ . The initial state for  $P(g;s)$  is the distribution function for the root required height  $g$  at the initial position  $R^0$ ,  $P(g(R^0))$  or  $P(g;s=0)$ . This is a normal distribution with mean  $\mu(R^0)$  and standard deviation  $\sigma$ . By integrating Eqn 8 from this initial state, the distribution of  $g(R)$  at any range  $R$  (ie any position  $s$  along the path) can be found. If the boundary condition

$$P(g \leq \sqrt{h_t}; s) = 0 \quad (9)$$

is applied, that is equivalent to removing from the distribution function all paths for which the root required height  $g$  has dropped below the square root

of the target height  $\sqrt{h_t}$ ; the resulting distribution function  $P(g;s)$  then refers to that subset of paths in which the root required height  $g$  has never passed  $\sqrt{h_t}$ . Therefore, the probability at any position  $s$  that  $g$  has never passed  $\sqrt{h_t}$  (and consequently the target has never become unshadowed) is:

$$\begin{aligned} P(\text{the target has not yet become visible}) \\ = \int_{\sqrt{h_t}}^{\infty} dg P(g;s) \end{aligned} \quad (10)$$

Figure 7 illustrates this approach. A number of different curves are shown, indicating the distribution function  $P(g)$  at different positions  $s$  along the path. The lowest curve illustrates the initial state:  $g$  is normally distributed, with a rather high mean value  $\mu(s=s_0)$ . As the target progresses along the path, the distribution function moves over to the left, until it reaches the boundary at  $\sqrt{h_t}$ . The boundary condition of Eqn 9 is applied, so that the part of the distribution function which refers to paths which have passed the point  $g = \sqrt{h_t}$  has vanished. The probability that a target path has not passed this point is equal to the area under the curve.

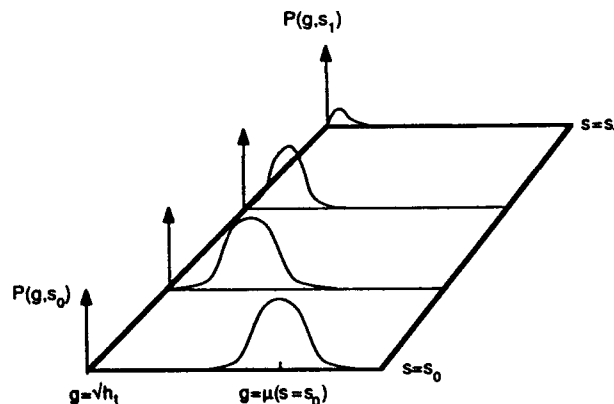


Figure 7  
Illustration of the evolution of the probability distribution function  $P(g;s)$

Figure 8 illustrates the results which can be obtained. The curve shows the probability, calculated from the Kolmogorov equation, that an incoming radial target approaching a low-relief site has yet to enter a cluttered cell; that corresponds to setting the target height  $h_t$  to zero. The figure also shows the result obtained for the particular site, Spruce Home, by explicitly examining each of 360 radial paths. The curve was very much quicker to obtain computationally (~ 2 seconds cpu time), and it clearly gives similar results to the site-specific case.



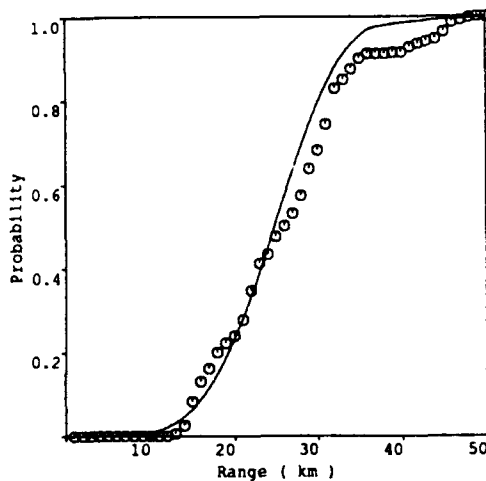


Figure 8  
The probability that an incoming radial target has yet to encounter a cluttered cell

A very similar calculation can be used to find the probability that a target at a given range has been detected. Detection probabilities per unit length of path can be defined for:

- regions where the target is unmasked but in clutter, ie  $g < 0$ ;
- regions where the target is masked and clear of clutter, ie  $0 \leq g < \sqrt{h_t}$ ;
- regions where the target is masked by the terrain, ie  $\sqrt{h_t} \leq g$  (the detection probability per unit range will be zero in this case).

In place of the simple boundary condition of Eqn 9, an additional term is added to the Kolmogorov equation (Eqn 8):

$$K_g [P(g; s)] \rightarrow K_g [P(g; s)] - p_{det}(g, s, h_t) P(g; s) \quad (11)$$

where  $p_{det}$  is the probability per unit length of path that the target is detected (the arguments of  $p_{det}$  take into account the three regions just listed). This additional term ensures that the probability that the target is still undetected at a given position on the path drops at the appropriate rate. The simple boundary condition of Eqn 9 corresponded to the following limiting choice of  $p_{det}$ :

$$p_{det}(g, s, h_t) = \begin{cases} 0, & g > \sqrt{h_t}; \\ \infty, & g \leq \sqrt{h_t}. \end{cases} \quad (12)$$

It is just as straightforward to evaluate (for example) the range at which there is a 50% chance that a target has been detected as it is to find the range at which there is a 50% chance that it has been unmasked.

### Conclusions

The non-site-specific, stochastic model of land clutter visibility and of terrain screening of targets described in this paper appears to fit the data well. The model accounts for the correlations in target screening and clutter visibility, as well as their mean levels. It makes it possible to answer quite detailed questions (eg concerning the length of track which is likely to be available to a land-based radar system) relating to general classes of sites, with a high degree of computational efficiency.

### Acknowledgements

This work has been carried out with the support of the Procurement Executive, Ministry of Defence.

The radar ground clutter measurement data referred to in this paper were collected by Lincoln Laboratory, a centre for research operated by Massachusetts Institute of Technology. This work was sponsored in the United States by the US Defense Advanced Research Projects Agency and the US Department of the Air Force under Air Force Contract F19628-85-C-0002 (ARPA Order 3724). Many of the measurements were conducted in Canada under a Memorandum of Understanding between the US Department of Defense and the Canadian Department of National Defence.

### References

- 1 BILLINGSLEY J B, 'Radar Ground Clutter Measurements and Models, Part 1', this conference.
- 2 PAPOULIS A, 'Probability, Random Variables and Stochastic Processes', McGraw-Hill, 1965.
- 3 'NAG Fortran Library, Introductory Guide - Mark 13', 1988.

## DISCUSSION

E. Luneburg, GE

The approaching aircraft follows the natural terrain. Is this accounted for in your modelling?

Author's Reply

The aircraft follows the terrain in the sense that it remains at a constant height above the local terrain (e.g., it goes up when it encounters a hill). The model does not account for the possibility that the aircraft might choose to fly around a hill rather than over it; however, modelling such detailed aspects of the aircraft's trajectory is probably better done in a site-specific framework.

# OVERVIEW OF WEATHER CLUTTER RESEARCH AT THE ALBERTA RESEARCH COUNCIL

by

C. Gibson and B. Kochtubajda  
Environmental Research and Engineering Department  
Alberta Research Council  
PO Box 8330, Station F  
Edmonton, Alberta, T6H 5XZ  
Canada

## 1. Introduction

The Alberta Research Council operates a unique variable polarization-diversity 10 cm radar at its facility in Penhold, Alberta (located adjacent to CFB Penhold, at 52.2°N, 113.8°W, and elevation 904 m). This radar is part of a meteorological radar complex owned and operated by the Alberta Research Council. This facility, which also includes 5 cm and 3 cm radars, is primarily used for meteorological and radio propagation research.

Weather radars have been used at this facility since 1957 to study severe storms in central Alberta. These studies were designed to gather information on the mechanisms of hailstorm and hailstone formation and growth, and to assess the effectiveness of weather modification techniques. With the addition of computer interfaces in 1974, a systematic archive of radar data was initiated. This archive now includes close to 200 Gb (giga-bytes) of data, representing approximately 12,000 hours of multi-parameter radar data. In addition, approximately 18 Gb of data was recorded between 1983 and 1985 aboard an instrumented aircraft flying through significant storm conditions. Also, quantitative precipitation reports (rain, hail) were obtained from approximately 500 ground stations within the radar coverage, for each year from 1974 to 1985.

In recent years, a number of interesting research projects have been conducted, based on the polarization capabilities of the 10 cm radar, with the objectives of quantifying and classifying meteorological radar phenomena (weather clutter). This paper will describe the unusual polarization features of this radar, and provide an overview of recent and on-going weather clutter research projects. These projects include the discrimination of clutter type (rain or hail) based on polarization parameters, the measurement of rainfall

by differential propagation phase, and the statistical examination of bright-band phenomena (the transition zone between snow and rain). Mention will also be made of hydrometeorological applications (primarily involving a C-band radar which is also part of the facility).

## 2. The Alberta Research Council Radar Facility

### *a) Polarization Diversity S-band Radar*

The S-band radar system was primarily designed to perform research on rain and hail precipitation, and many of its design features reflect this research orientation. The transmitter uses a coaxial magnetron with a frequency of 2.88 GHz, a pulse duration of 1.05  $\mu$ S, a PRF of 478 Hz, and a peak power of 450 kW. The antenna assembly consists of a 6.7 meter diameter parabolic reflector, fed by a feedhorn and turnstile, to which are connected two rectangular waveguides. This is shown in figure 1. The antenna has a gain of 43.2 dB and a 3 dB beamwidth of 1.15 degrees in both azimuth and elevation. The antenna is capable of transmitting elliptically polarized radiation at any chosen axial ratio or orientation, and receiving both that polarization and the orthogonal polarization simultaneously.

The polarization diversity capabilities of the radar are derived from the turnstile, which couples the two waveguides to a circular dual-mode feedhorn. The turnstile converts the linearly polarized signal from either rectangular waveguide to circular polarization. The lower waveguide signal is transformed to left-hand circular polarization and the upper waveguide signal is similarly transformed to right-hand circular polarization. When there are signals in both waveguides, the two signals combine into an elliptically po-

larized wave. If the two signals are equal, the polarization becomes linear. The turnstile is bidirectional; thus, elliptical waves received by the antenna are resolved back into the two circularly polarized components which are transformed to linear and fed to the two waveguides, which are connected to two receivers.

A phase shifter alters the phase of the lower waveguide signal relative to the upper waveguide, thus introducing a phase shift between the two signals as they reach the turnstile. If the two signals are equal amplitude with no phase shift, a vertically polarized wave is transmitted. If the two signals are equal amplitude with a 180 degree phase shift, a horizontally polarized wave is transmitted. Antenna polarization is controlled by a power divider which determines the relative power fed to each waveguide. The normal operating mode is to adjust for a total mismatch, which transmits left-hand circular polarization and receives left-hand circular to one receiver and right-hand circular to the other.

The antenna normally performs a volume scan, rotating clockwise at approximately 8.2 r.p.m. and spiralling upwards at one degree per rotation to an upper elevation limit of either 8 or 20 degrees. Prior to being digitized, the signals are integrated to a range resolution of 1.05 km per range gate. Data is recorded in 147 range gates, from 3 km to 157 km. The azimuthal resolution of the recorded data is one degree, which is the result of summing the ten adjacent pulses occurring in degree of rotation. Table 1 summarizes the main features of the S-band radar system. A remote, variable-polarization transmitter, situated on top of a 27.4 m tower located 400 m from the radar, is used for calibration.

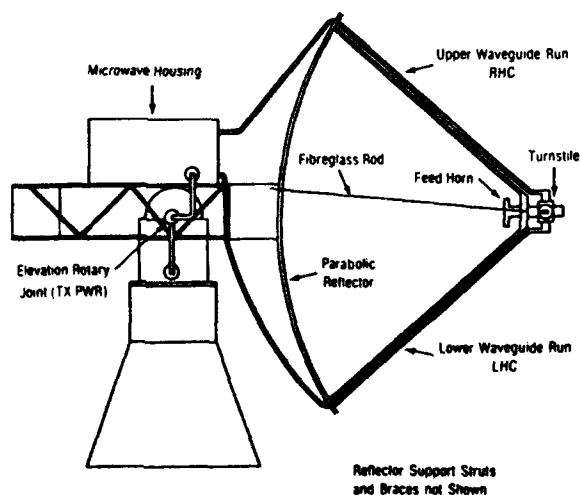


Figure 1: S-band radar antenna assembly.

## b) Software System

A comprehensive radar software package, developed and maintained by ARC, is responsible for all radar control, data logging, processing, and display. This software can synchronously control any of the three radars making up the complex, while recording the raw radar data. Due to the research orientation of the past radar operations, processing and display generally takes place off-site, using logged data. The processing software consists of a variety of specialized functions, to which new functions can be added easily and quickly. The display software consists of a generalized set of routines and drivers which can produce displays on a wide variety of graphics terminals, workstations, and hardcopy devices.

Two reflectivity channels (normal and orthogonal polarization) and two channels of differential polarization phase are recorded simultaneously from the S-band radar, as well as the signals from the other

Table 1: Normal Operating Characteristics of the ARC S-band Polarization Diversity Radar System

Frequency	2.88 GHz
Polarization	LHC
Beamwidth	1.15 degrees
Diameter (antenna reflector)	6.67 m
Gain	43.2 dB
Peak power	450 Kw
Pulse width	1.05 $\mu$ s
PRF	478 Hz
Range gate size	1.05 km
Number of gates	147
Time averaging	21 ms per bin
Measurements	(i) RHC (co-polar) power (ii) LHC (cross-polar) power (iii) correlation of LHC and RHC signals (iv) phase between LHC and RHC signals

radars in the complex. In keeping with the research philosophy of corrupting the data as little as possible, the only preprocessing done before recording is that necessary to optimize the A/D conversion process. Each ray (the echo signal for one azimuth-integrated pulse) is compressed by removing bins which fall below a threshold, and a header containing the current time, azimuth, and elevation is added. The compressed data from a number of rays is then collected into a data block, recorded on tape, and possibly also directed for concurrent processing and display. The data is stored sequentially in the same range - azimuth - elevation format as when it was acquired, with a resolution of one km in range and one degree in azimuth and elevation. This archival policy allows maximum flexibility in later reconstruction of radar products.

Base products are generated from the signals recorded from the four received channels. These include the reflectivity, the differential reflectivity (in dBZ), the circular depolarization ratio, the apparent mean orientation angle, and the degree of common hydrometer alignment. The differential polarization phase data can be used to correct the other values for the effects of precipitation attenuation along the pathlength (using the equations of Bebbington et al.<sup>1</sup>). Rainfall rates may be generated from dBZ values using the Marshall-Palmer equation and may be integrated over selected areas and time-periods to produce average basin rainfall intensities. Special functions exist for processing storms, including functions to define the area of a storm, calculate its centroid (either with or without dBZ weighting), and identify contiguous echo areas to allow tracking of multiple storms over time. Further processing is generally applied to define a spatial format (selecting a plane within the radar volume) which is then displayed pictorially.

### c) Radar Parameters

Four channels of data are simultaneously recorded from the S-band radar. These are the co-polar signal power ( $W_1$ ), the cross-polar signal power ( $W_2$ ), and the magnitude and phase of the complex correlation of the two ( $W$ ). With the addition of the radar constant ( $C$ ), the slant range ( $r$ ) and the atmospheric refraction constant ( $K$ ), it is possible to calculate the equivalent reflectivity factor ( $Z_e$ ), the differential reflectivity factor ( $Z_{DR}$ ), the circular depolarization ratio (CDR), the apparent mean orientation angle (ALD), and the degree of common hydrometer alignment (ORTT). Equations for these values are given as follows:

$$Z_e = 10 \log_{10} \left( \frac{W_2 r^2}{C |K|^2} \right)$$

$$Z_{DR} = 10 \log_{10} \left( \frac{W_1 + W_2 - 2 \operatorname{Re}(W)}{W_1 + W_2 + 2 \operatorname{Re}(W)} \right)$$

$$\text{CDR} = 10 \log_{10} (W_1/W_2)$$

$$\text{ALD} = \frac{1}{2} [\arg(W) - \pi]$$

$$\text{ORTT} = \frac{|W|}{(W_1 W_2)^{1/2}}$$

It should be noted that the  $Z_{DR}$  measured with circular polarization is an estimate of a parameter normally measured with linear polarization. The estimate is accurate so long as the mean canting angle of the scattering particles is small. (Normally, this is applied to raindrops, which generally satisfy this criteria by having a mean canting angle which is approximately vertical. Other types of scattering particles often have randomly distributed canting angles, which also satisfies this criteria). Other values, such as estimated rainfall, can be derived from the above, as described in the following sections.

## 3. Recent Applications

Research conducted with this radar has been concerned primarily with the effects of weather clutter on circularly polarized signals. Precipitation in the radar path distorts the polarization from circular to elliptical; severe precipitation can completely reverse the polarization. Using the two orthogonal-polarization receivers, these distortions can be accurately measured. The following projects illustrate some of the potential applications for these measurements that are being explored.

### 3.1 Hail/rain discrimination

An application which is of considerable interest is to classify weather clutter, based on polarization parameters of the radar signals. An in-depth study was carried out to identify and separate rain from hail, using ARC S-band radar data<sup>2</sup>. In addition to the radar data, ground reports were obtained from several hundred volunteers distributed throughout the area covered by the radar. These reports were used to corroborate the radar findings.

It is to be expected that the polarization parameters would be different for raindrops and hailstones, because of the differences in shape, orientation, and falling behavior. Large raindrops are generally oblate spheroids, with canting angles (minor axis of the spheroid) nearly vertical. They tend to be fairly uniform, particularly in orientation. Hailstones, on the other hand, are generally irregular in shape and tumble as they fall, resulting in random orientations. Accordingly, it is expected that for hail and rain with equivalent reflectivity  $Z_e$ , the hail would have lower values of ORTT and  $Z_{DR}$ , while the CDR would be lower or possibly higher, depending on the shape and behavior of the hailstones.

After examining various combinations of these parameters, it was found that the ratio of  $Z_{DR}$  to  $Z_e$  provided the best basis for this discrimination. Figure 2 provides a scatter graph of results, using this approach, for a number of storm conditions. The three open symbols used in this figure represent case studies where only rain was present at the ground, while the four closed symbols represent cases where hail was observed. Figures 3 and 4 present PPI displays of  $Z_e$  and  $Z_e/Z_{DR}$ , respectively. Figure 4 corresponds very closely to the reports of hail and rain from the ground stations. It can be seen that the areas of hail are not always in the areas of highest reflectivity. (The reflectivity data was corrected for propagation errors using the differential propagation phase, using the method of Bebbington, et al.<sup>1</sup>).

### 3.2 Rainfall Measurement by Differential Propagation Phase

A project<sup>3</sup> concerning the measurement of rainfall by polarization diversity radar was conducted jointly by the Alberta research Council and the University of Essex in the summer of 1989. The objective of the experiment was to test the theory that differential propagation phase shift can give a better estimate of rainfall with high rainrates (about 30 mm/hr and greater) than reflectivity measurements.

As an electromagnetic wave propagates through precipitation, it is progressively attenuated and shifted in phase. Because of this process, quantitative measurements of reflectivity and polarization for objects of interest will be attenuated and phase-shifted by precipitation in the path. (In this experiment, the objects of interest were areas of rainfall which were separated from the radar by other areas of rainfall). With raindrops, and other highly oriented clutter, the attenuation and phase shift are different, depending

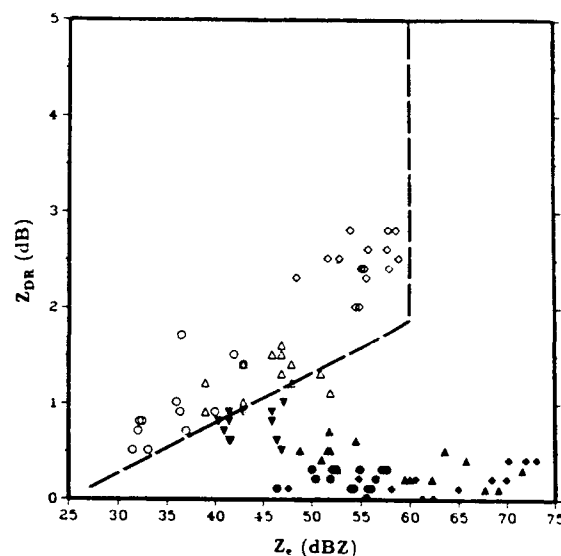


Figure 2: Scatter plot of corrected  $Z_{DR}$  vs  $Z_e$  for three rainstorms and four rain/hail mixture storms.

- 28 July 1983 (3 mm/hr rain)
- △ 8 July 1983 (56 mm/hr rain)
- ◇ 24 July 1983 (77 mm/hr rain)
- ▼ 31 July 1982 (45 mm/hr rain and pea-size hail)
- 12 July 1983 (38 mm/hr rain and grape-size hail)
- ▲ 15 August 1983 (83 mm/hr rain and grape-size hail)
- ◆ 25 June 1984 (52 mm/hr rain and walnut-size hail)

on whether horizontal or vertical polarization is used. These differences are quantified as differential attenuation and differential propagation phase. As circular polarization can be decomposed into vertical and horizontal polarization components with a relative phase shift of 90 degrees, these differential quantities can be measured using circular polarization. At S-band frequencies, only the differential propagation phase is significant.

There is strong evidence<sup>4</sup> that for heavy rainfall, the differential phase shift is a much better estimator of rainfall rate than the reflectivity is. With the ARC S-band radar, the differential phase shift  $\varphi_{DP}$  is measured directly. From this a differential phase shift constant  $K_{DP}$  is derived for each bin, and the rainfall rate is calculated from that value, using the formula

$$K_{DP}^n = (\varphi_I^n - \varphi_{DP}^{n-1})/L$$

$$= R^{1.15}/3.172 \lambda$$

where  $n$  is the range gate number,  $L$  is the gate length,  $\varphi_{DP}$  is the differential phase,  $R$  is the rainfall rate, and  $\lambda$  is the wavelength.

The project comprised a field experiment that was conducted in central Alberta during the period 20 July

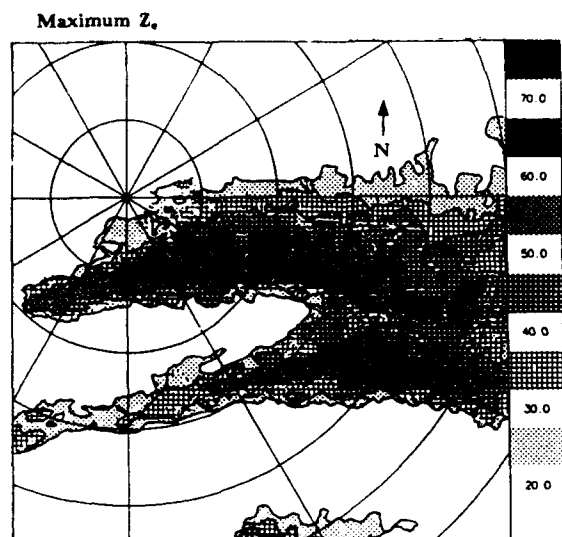


Figure 3: Reflectivity map for August 15, 1983 storm. (Range rings are at 20 km intervals).

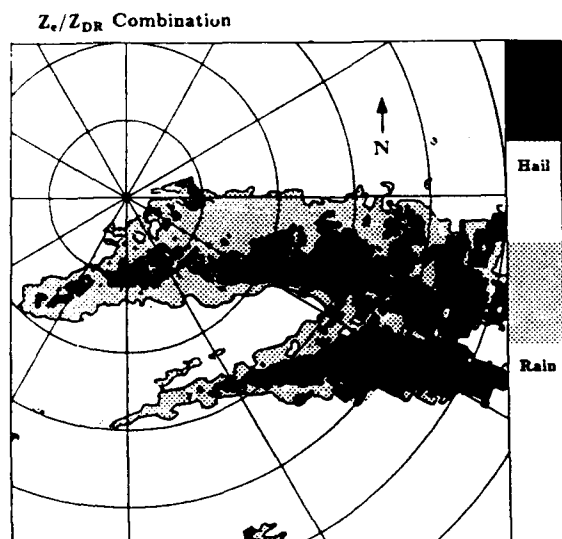


Figure 4: Hail occurrence map, based on  $Z_e/Z_{DR}$ , for August 15, 1983 storm. (Range rings are at 20 km intervals).

to 2 August 1989. The field experiment involved observing storms within about a 70-km radius from Penhold with the S-band radar and measuring rainfall at the ground through a network of fixed, volunteer observers and a mobile-chase operation.

Data collected on three days during the experiment, totalling 31 time-resolved samples, have been analyzed. These data, comparing the predicted rainfall amounts from the  $K_{DP}$  and Z-R methods with ground measurements, are plotted in figure 5. The solid line represents complete agreement between the radar

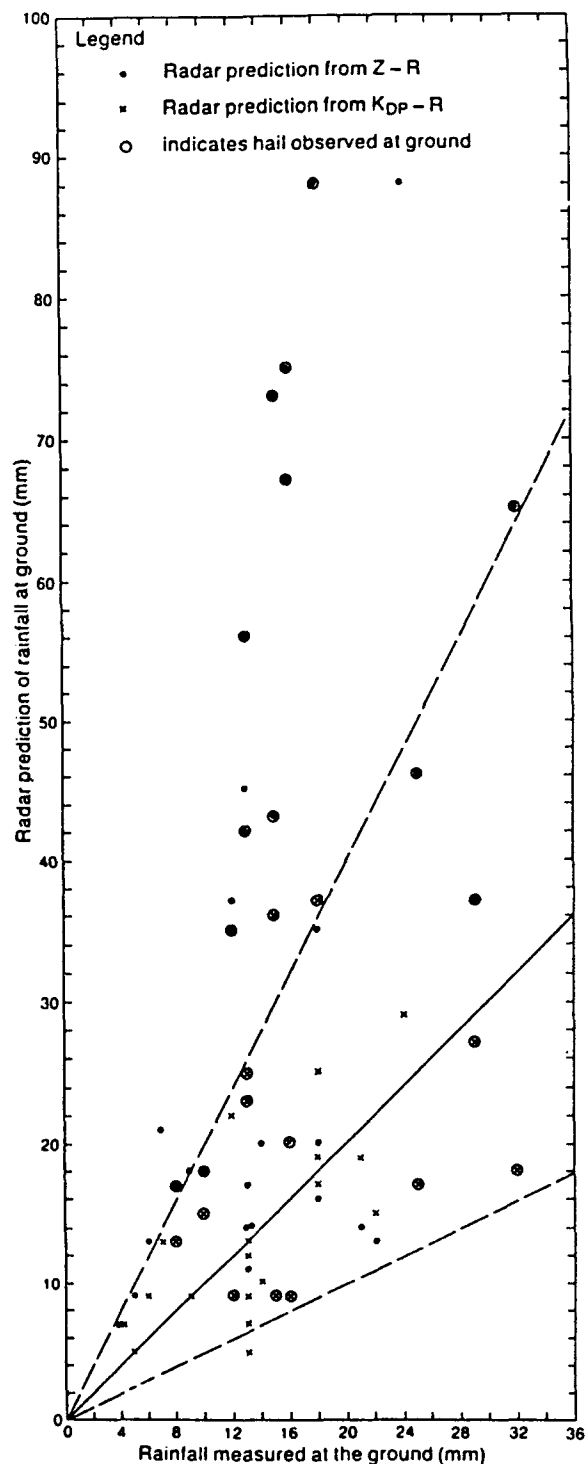


Figure 5: Comparison of rainfall amounts measured at the ground with those predicted by radar, using  $K_{DP}$  (x) and Marshall-Palmer Z-R relationships (•). (The solid line is a one-to-one ratio; the dotted lines indicate a factor of two difference).

predictions and ground measurements. The dotted lines represent a factor of 2 difference between the predictions and measurements. Events that were known to have hail present are identified. All but 3 of the 31  $K_{DP}$  predictions lie within the factor-of-2 limits.

The average ratio of total rainfall predicted, based on the differential propagation phase, to the total rainfall measured at the ground is 1.16 for the 31 samples. This suggests that on average, the total rainfall amount predicted from  $K_{DP}$  is only 16% higher than that measured at the ground. Predictions using a Z-R relationship, on the other hand, result in a large overestimate of the ground rainfall. Using the Marshall-Palmer Z-R relationship, the average ratio of total rainfall predicted to the total rainfall measured at the ground is 2.43 for this data.

### 3.3 Statistics of the Radar Bright Band

Statistical information on the attenuation of satellite communication signals by precipitation is useful in the planning of satellite systems. With the long-term plans to use the 18, 20 and 30 GHz bands for satellite communications and the existence of shared frequencies in these bands with terrestrial links, there is a need to develop interference prediction models. One interference mechanism for which no current prediction techniques exist and which may pose a particular problem in Canada is scattering from the melting level. This is a layer where snow from higher levels is warmed above freezing, and becomes rain which falls to the ground. This layer results in a "bright band" on radar reflectivity plots, due to the fact that melting snow has a much higher effective radar cross-section than either snow or rain of the same water content.

Plans to develop an interference prediction technique for melting snow scatter in Canada prompted the Communications Research Centre to sponsor a study to obtain measurements of melting level reflectivity statistics, using the Alberta Research Council S-band radar. A feasibility study was conducted<sup>5</sup> during which melting level statistics were compiled from archived radar data, for five days of stratiform rain from 1983 and 1985. Examples of statistics for these five days are given in figures 6-10. These figures present vertical reflectivity profiles, which are defined as the cumulative statistics of radar reflectivity exceeded for 10% of the time. Each point on each of these figures represents a cumulative statistic from between 50,000 and 300,000 bins of reflectivity data. Typically, the bright band showed a reflectivity enhancement of about 6 dB and a thickness of 500 meters.

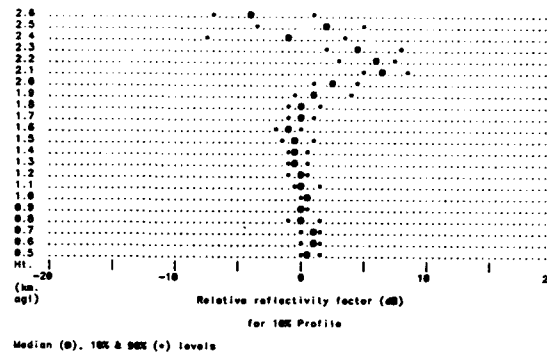


Figure 6: Reflectivity profile statistics from June 30, 1983.

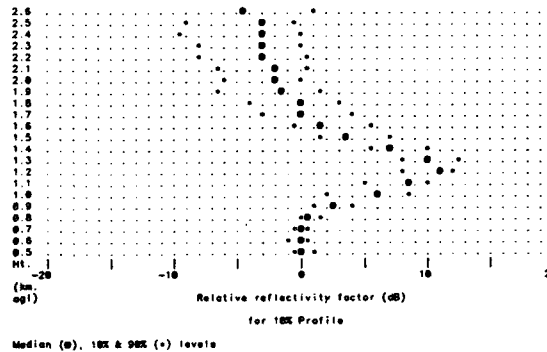


Figure 7: Reflectivity profile statistics from July 14, 1983.

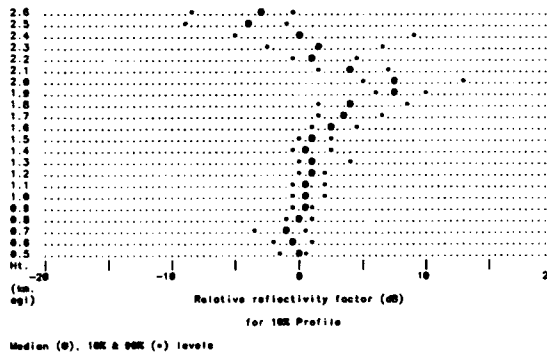


Figure 8: Reflectivity profile statistics from July 28, 1985.

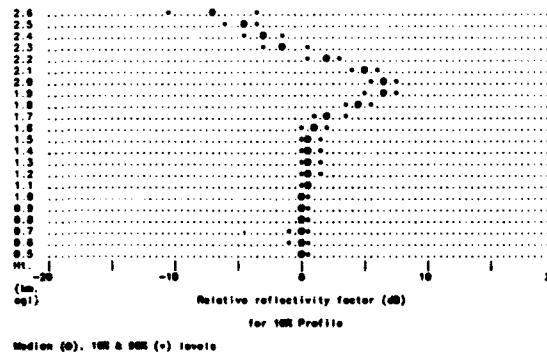


Figure 9: Reflectivity profile statistics from August 14, 1985.



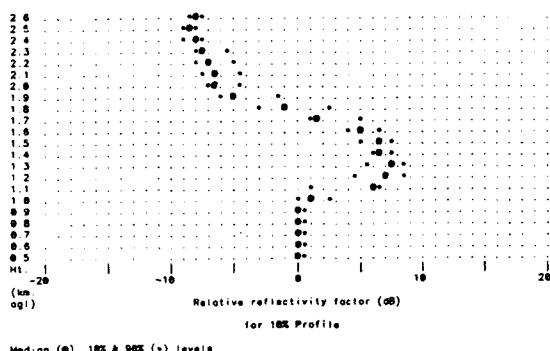


Figure 10: Reflectivity profile statistics from August 21, 1985.

### 3.4 Hydrometeorological Applications

Another application of radar data, related to weather clutter, is hydrometeorology. This generally involves the cumulative quantitative measurement of precipitation over a specified area and a given length of time. The area may be a farmer's field or a river basin, and the length of time may be hours or days. This information is useful in a variety of applications, such as agriculture, flood control, and water management. Research in this field at the Alberta Research Council to date has used the C-band radar, which provides only reflectivity information from which the rainfall is calculated.

In a study of needs for quantitative prediction of convective precipitation<sup>6</sup>, jointly sponsored by the Hydrometeorological Research Division of the Canadian Climate Centre and the Atmospheric Environment Service (Central Region), water resource planners identified a strong requirement for timely information regarding convective storm paths and precipitation amounts. Over the last two summers, the Alberta Research Council has pursued the establishment and operation of an unmanned operational radar designed for storm monitoring and precipitation measurement. Two projects were developed and completed, in 1989, which illustrated the potential hydrometeorological applications of radar rainfall measures using the C-band weather radar.

The results from the Alberta Hail and Crop Insurance Corporation (AHCIC) project<sup>7,8</sup> demonstrated that combining radar and gauge measurements produces rainfall estimates superior to those produced by either alone. The hydrologic modelling of small Alberta rural basins study was carried out to examine the feasibility of integrating radar measurements of rainfall

with a distributed hydrologic model to provide real-time runoff forecasting for small rural catchments. The analysis<sup>9</sup> suggests that it is possible to interface the radar data to any number of hydrologic models. Agencies responsible for the forecasting and/or mitigating the impacts of floods caused by convective storms over small rural catchments would benefit from the development of this application.

### 4.0 Current and Future Radar Operations

The immediate program for the ARC radar facility involves operations over the summer season, from May 1, 1991 to September 30, 1991, which covers the period when most of the more interesting precipitation events are expected to occur. During this period, the C-band radar will be run continuously, to provide uninterrupted hydrometeorological data, weather forecasting support, and to monitor for significant precipitation events. When significant precipitation events are detected, the S-band radar will be used to acquire polarization and reflectivity data. One form of significant precipitation includes severe convective storms, which will be used to continue the studies on rain-hail discrimination and differential phase (as described in sections 3.1 and 3.2), in association with researchers from the University of Essex (UK). Another form of significant precipitation includes widespread stratiform rain, which will be used to continue statistical studies of the bright band (as described in section 3.3) in association with the Communications Research Centre (Ottawa). Other projects in this program will involve researchers from various other academic and government organizations.

Future considerations for the radar facility include a number of promising possibilities. Among these are a proposal to add coherent reception and Doppler capabilities to the S-band radar, increased diversification away from strictly meteorological applications, and the possibility of moving one or more of the radars to a second site.

## 5.0 References

1. Bebbington, D.H.O., R. McGuinness, and A.R. Holt, 1987: Correction of Propagation Effects in S-band Circular Polarization-Diversity Radars. *IEE Proc.*, part H, 134, 431-437.
2. Al-Jumily, K.J., R.B. Charlton, and R.G. Humphries, 1991: Identification of Rain and Hail with Circular Polarization Radar. *J. Appl. Meteorology* (in press).
3. English, M., B. Kochtubajda, F. Barlow, A. Holt, and R. McGuinness, 1991: Radar Measurement of Rainfall by Differential Propagation Phase: a Pilot Experiment. *Atmosphere-Ocean*, 29, 357-380.
4. Holt, A.R., and R. McGuinness, 1990: Rainrate Measurements Using a Circular Polarization-Diversity Radar. *Weather Radar Networking*, C.G. Collier and M. Chapus (eds), Kluwer Academic, Dordrecht, Netherlands, 304-313.
5. Gibson, C.J., B. Kochtubajda, and F. Bergwall, 1991: Feasibility Study for the Extraction of Melting Layer Statistics from Archived Alberta Research Council S-band Weather Radar Observations. Report submitted to Communications Research Centre, Ottawa, 119pp.
6. Kochtubajda, B., and F.E. Robitaille, 1989: A review of the status and needs for the quantitative prediction of convective precipitation. Final report prepared for the Hydrometeorological Research Division, Canadian Climate Centre, Saskatoon, Saskatchewan. 74pp.
7. Kochtubajda, B., 1989: A real-time demonstration to provide radar-derived rainfall measurements for a Forage Insurance Program. Final report prepared for Alberta Hail and Crop Insurance Corporation, Lacombe, Alberta. 45pp.
8. Kochtubajda, B., 1991: Application of radar-derived rainfall measurements in a forage insurance program. 25th International Radar Meteorology Conference. Paris, France, 4pp.
9. Kochtubajda, B., D. Andres, and G. Van Der Vinne, 1990: Towards real-time runoff forecasting in small rural Alberta basins. Eighth AMS Conference on Hydrometeorology. Kananaskis Park, Alta., 160-164.

## DISCUSSION

E. Luneburg, GE

Do you intend to measure the Mueller matrix by power measurements only?

Author's Reply

At the moment, the answer is no. We are limited by the measurements we can make now.

## Round Table Discussion

### SESSION I, PART A: CLUTTER MODELS AND MEASUREMENTS

K. C. Yeh, US: Ladies and Gentlemen. As you read the program, you will find that this symposium is divided into two parts and each part is concluded with a round table discussion. The first part is the unclassified part and the second is classified. The members of the round table discussion are composed of session chairmen plus one. For the first part there are 5 sessions but session 1 has part A and part B so there are 6 chairs. Mr. Christophe suggested that at the beginning of this meeting that each chair should address two points in the round table discussion. The first point has to do with the summary of papers presented followed by discussion about future directions. We will start our round table discussion in the order of the meeting. So let me ask Mr. Christophe who chaired session 1, part A, clutter models and measurements. He will talk about his session first.

F. Christophe, FR: Les trois premières présentations dans cette session ont décrit les caractéristiques d'une importante base de données d'échos de sol, mesurés aux Etats-Unis et au Canada, à des fréquences depuis la VHF jusqu'à la bande X.

L'utilisation de ces données pour la mise au point de modèles de fouillis et la prévision des performances des nouveaux systèmes radar également été présentée dans ces communications.

La démarche ainsi illustrée, d'estimer les performances de systèmes non encore développés et, éventuellement, de mettre au point leur traitement à partir des modèles validés sur le terrain, apparaît d'un bon rapport coût/efficacité. Cependant, les radars du futur seront -- et certains le sont déjà -- bistatiques ou polarimétriques ou à haute résolution spatiale ou temporelle et combineront sans doute plusieurs de ces caractères. Sera-t-il alors raisonnable d'adopter la même démarche ou bien le très grand nombre des paramètres nécessaires pour décrire les données conduira-t-il plutôt à des expérimentations représentatives de chacun des systèmes envisagés et servant à valider des modèles relativement généraux?

C'est plutôt dans cette dernière optique qu'on peut situer les deux communications suivantes: l'une (Papa et al.) établit un modèle de diffusion bistatique du sol recouvert de végétation en combinant la diffusion de surface et celle de volume et est validé par comparaison avec des mesures. L'autre (Rao et al.) analyse expérimentalement la variation du signal réfléchi vers l'avant selon la polarisation de l'antenne de réception et montre l'existence de minima marqués, assez proches de ce que les modèles indiquent.

On peut penser que la prise en compte optimale du fouillis de sol par les radar du futur fera appel à de telles méthodes de caractérisation.

K. C. Yeh, US: After each presentation we will have a question period or comments from the floor. However we will follow the procedure of the regular presentation. If you have a question or comment would you also fill out a question form so it can be recorded and published in the final proceedings. Any questions now for either Mr. Christophe or some of the authors? When you take the mike please give your name and country.

Le Chevalier, FR: A la suite de ce que vient de dire Mr Christophe, je voudrais insister sur un point qui suscitera sans doute d'autres commentaires, la modélisation des cibles et du clutter. Sur la modélisation des cibles, il me semble que son intérêt principal n'est pas tellement pour la détection mais plutôt pour la reconnaissance ou pour la discrimination; si l'on utilise un radar pour faire un avant projet ou pour définir ses performances en détection de façon relativement précise, les modèles de Swerling ont finalement des qualités satisfaisantes, par contre lorsque l'on essaye de prévoir les performances en reconnaissance d'un radar, et désormais tous ont besoin d'une fonction reconnaissance, on a besoin d'une signature radar et le problème de la base de données se pose effectivement, non seulement pour mettre au point le radar mais aussi pour effectuer l'apprentissage nécessaire. J'ai l'impression que les modélisations électromagnétiques de cibles sont essentiellement intéressantes pour cette fonction discrimination, ceci impose des qualités qu'ils n'ont pas actuellement. C'est à dire que l'on demande au modèle de signature de représenter finement tous les effets de rugosité sur la cible, tous les petits détails qui sont utilisés par la procédure de reconnaissance. J'ai l'impression que le modèle doit encore faire un saut qualitatif, en particulier dans les hautes fréquences, en millimétrique ou en bande X pour les rendre utilisables comme base de données d'apprentissage pour les procédures de reconnaissance. Peut-être est-ce l'objectif à se fixer pour la définition des modèles électromagnétiques hautes fréquences actuels.

K. C. Yeh, US: Anyone wishing to respond? If not, I'd like to ask for more comments or questions from the floor. I have a question. I find that in experimental work the experimenters use a set of parameters to describe their experimental data, usually of a statistical nature, while the theoreticians use a different set of parameters to model the terrain. It seems to me there is a gap between the two approaches, using the experimental data to describe data and using a physical model for the terrain. Is that notion correct or not? Do we have people who are authors of the first session here? Any comments to make?

G. C. Sarno, UK: Yes, I agree. There is a gap between the experimental empirical models of the ground clutter being discussed and relating them to the physical environment. That is a step that should be taken. To close the gap it would need a very large data base to safely compare the abstract parameters of your models with those of the terrain features.

### SESSION I, PART B

M. Vant, CA: This session was a continuation of the discussion of clutter. Our session was slightly abbreviated due to the late arrival of two of the speakers and consisted of only 3 papers. These papers fell into two broad categories: ionospheric propagation and sea clutter.

The first paper by Knepp dealt with the phenomena of backscatter enhancement at UHF. The ionosphere was shown to enhance propagation over the case without scintillation by up to 3 dB over limited time periods of 1 - 2 sec. This area is not in my field of expertise, so I am curious as to whether this is an infrequent occurrence or happens very reliably and for longer periods of time. I remember our concern back in 1978 over possible disturbance by the ionosphere of the coherency of the signals from the SEASAT Synthetic Aperture Radar system. This system operated at L-Band (1 - 2 GHz) and at that time it seemed as though, in the Arctic, the signal could be disturbed at least some of the time. Could anyone comment on this discrepancy between the two effects?

The second two papers dealt with sea clutter. The first by Dr. Levy consisted of a simulation of sea backscatter under conditions of low grazing angle and the presence of evaporation ducts. She presented some very interesting results. These results were based on a two-stage model of the sea surface and used a parabolic equation approximation for the scattering. The main thing lacking was experimental results to confirm the simulation. The second sea clutter paper by Corsini, presented some experimental results for sea scattering on the Mediterranean Sea. He compared his results to both K-distributions and Weibull clutter distributions and found a better match with Weibull. This stimulated some discussion on the on-going K-distribution vs Weibull debate. Dr. Corsini also investigated some special techniques for finding a better match to the tails of the distribution.

Despite the fact that sea clutter measurements have been going on for a long time, there is still a lack of a good model and adequate set of experimental results at low grazing angles. I know from my own experience when trying to evaluate the performance of search radars that there is very little available. This is especially true when it comes to the problem of assessing techniques for removing the effects of sea spikes by their scan-to-scan integration or frequency hopping. I wonder whether the model of Dr. Levy treats the problem of sea spikes adequately in her two-stage model? Do the spikes arise from the Bragg scattering from the capillary waves or do they come from foam and droplets which she does not include in the model? In summary, I think it is safe to say that despite all the work that has been done, there is still quite a bit to do in this area.

K. C. Yeh, US: Thank you Dr. Vant. Any questions or comments or remarks from anyone?

S. P. Tonkin, UK: It seems that there is a difficulty in predicting a priori the backscatter from the sea surface, as we do not know the physical structure of the sea surface at small scales (e.g., the Bragg scatterers). Does anyone know how that physical structure might be measured?

K. C. Yeh, US: Anyone have any bright ideas on measuring sea state?

J. Mead, US: There is a researcher in our group who is using optical techniques to measure sea state. Basically there are two cameras looking down at the ocean surface and using these cameras he hopes to be able to actually measure the profile of the ocean surface at various instants in time. He can make a motion picture of the height profile of the ocean surface and the resolution is of course very good. It is stereo photography.

K. C. Yeh: Thank you Jim. Any more questions or comments?

G. Hagn, US: Is Dr. Levy here? I talked with her after her paper about the effect of the critical angle near grazing and how if you have near normal incidence the specular reflection as angle changes towards grazing sort of a plateau dropping off in diffuse scatter and then a critical angle when shadowing starts to cut in and you don't get anything back. If she could comment about that critical angle part if it would play back into her model.

M. F. Levy, UK: All I can say is that what we're talking about is what is happening for angles which are below the critical angle. I think the backscatter below the critical angle is caused by the capillary waves. What I don't know is the transitional drop between the diffuse scatter and the small roughness backscatter. I cannot explain further until I study the physical reasons for this critical angle effect.

M. Vant, CA: Does anyone know at this point what really causes the sea spikes? Is it included in the two stage model of the capillary wave surface or is it from droplets of the breaking foam which you don't include in your model?

M. F. Levy, UK: I don't know for sure what is causing them. It is in the numerical simulations. When you use Pearson-Moscovitz's sea spectrum you can see bunches of waves in the X-band to cause spikes. Of course that is only numerical, which has to be confirmed by measurements to see if it is realistic.

C. J. Baker, UK: I'd like to make 2 comments. The first one is about sea spikes. It is not clear what the mechanisms are that give rise to sea spikes but they still appear to be a modulated noise process that is observed in the data but still described by statistical models that have been put forward to describe this behavior. I'd also like to pick up Dr. Vant's point about his concern over the coherency of the SeaSat data due to phase perturbations by the ionosphere. As we move to more modern radar systems which have higher resolution requirements operating from space platforms the coherency requirements are even more severe. I'm wondering if Prof. Yeh can say anything about whether it would be possible to predict when the coherency of such a system may break down from the point of experiments he described in his presentation or whether its for the author to say something.

K. C. Yeh, US: The paper was by Knepp. It is one of the few instances where the presence of the ionosphere irregularities actually helps with the radar measurements. This is generally grouped under the heading of backscatter enhancement that has been observed both for scattering on the discrete scatterers, the random surface scatterer, and the volume scattering case. For that kind of work I think Drs. Flood and Brown are intimately familiar with its progress. It seems that for the ionosphere case there is experimental evidence which show, based on the data of the Altair radar, a 3-dB increase in the radar cross section. If you do a highly mathematical calculation of the two-position, two-frequency, two-time mutual coherent function that Knepp calculated, the theory would also predict in the limit of monostatic radar case there is a 3-dB gain. Also he used statistics to show that in the presence of scintillation the signal would follow a Nakagami distribution then for the round trip signal because of reciprocity you also expect a 3-dB gain. But then the question still can be raised what is the physical reason for the 3-dB gain. The only explanation that can be given is that there is a focusing effect because of the presence of irregularities. The concern of coherence of course has to do with temporal correlation. It depends on how the radar will respond to that. In this case he was averaging the data over a few seconds. The coherence time depends on two factors: the scale of the irregularities in the ionosphere and the drift speed in the horizontal direction. In the equatorial region the ionosphere can drift with a speed as high as 100-200 meters per second in the evening sector of the diurnal day. So that is the kind of coherence time you can expect.

Le Chevalier, FR: J'avoue que ce gain de 3-dB me laisse un peu perplexe est-ce que cela signifie que lorsque l'émetteur est un peu trop faible, il suffit de mettre une surface de mauvaise transmission devant l'antenne pour récupérer les 3-dB qui manquent? Je ne comprends pas bien comment une dégradation dans la propagation peut améliorer le bilan de liaison du système.

K. C. Yeh, US: In the case of Dennis Knepp it is compared with the case when there is no scintillation. So there's a 3-dB gain there. He measures the RCS in per square meter under the condition when there is no scintillation as well as when it is present, and he finds that there is a 3-dB gain. The radar cross section has been increased by a factor of 2.

M. Vant, CA: Is that because the ionosphere is acting like a lense and is changing the gain in the receiving aperture to focus more energy?

K. C. Yeh, US: That is the physical reason given by Dennis Knepp.

W. A. Flood, US: I really can't answer that question because I don't understand all that Dennis has said. But I think we can address something about the coherence to the satellite because a number of people, RSRE particularly, and also within the US and DOD, the DNA models of propagation through striated regions all give rise to coherence effects. I think those things can be addressed pretty well. We have beaucoup data for that. The 3-dB backscatter enhancement is recorded for surfaces and for dense discrete scatterers. It almost always comes about because in the direct backscatter direction if the differences in refractive index from the dense scatterers from the background medium is strong enough, then in essence double scattering can occur. If we go from point A which is the transmitter to an irregularity B to an irregularity C, if you will, and back out again you can go from C to B then A and the way it tends to work out for discrete random media there is always something less than up to a 3-dB enhancement, but it does require strong contrast between the scatterers and the background medium. It is not clear exactly what Dennis is seeing when he sees strong scintillation as against the background. I don't know what he is measuring in the absence of scintillation, what is he measuring in the terms of cross section? What is there?

K. C. Yeh, US: The cross section from the satellite. The COSMO calibration satellite which is of known diameter.

G. Brown, US: What are the physics behind enhanced backscattering as discussed by Knepp's paper? Knepp appears to be dealing with what is termed single scattering backscattering enhancement, i.e., where multiple scattering is not important. This is related to the fact that a ray traveling into a medium can always come back along the backscatter path because of the unity correlation between the entrance and exit paths at backscatter only. For multiple scatter, the cause of the enhancement is related to the fact that any multiple scatter path can also be traversed in the reverse direction. Thus, there are two ways a given path causing backscatter can be traversed. There is only one way that this can happen during bistatic scattering.

I guess I've held my tongue long enough on the backscatter from the ocean, so let me comment on that too. How good is the two-scale model for rough surface scattering near grazing incidence? Not very good. The approximations upon which the model is based fail near grazing incidence. Measurements show that there are many instances where  $\sigma_{VV}^0/\sigma_{HH}^0$  is of order unity which is totally contrary to the two-scale model. The two-scale model also fails to predict the presence of "sea spikes".

## SESSION II, TARGET SCATTERING

L. C. Oldfield, UK: The session on target scattering was dominated by papers covering radar cross section predictions and I think the reason for that is that computers now developing are such that realistic targets can be analyzed, particularly with the availability of computer-aided design packages, RCS characteristics can be put in right at the design stage along with the aerodynamic ones. Methods for RCS prediction generally depend on the electrical size of the target. We didn't hear very much in the session about electrically small ones; they are normally handled by the moment type method and those predicted models have a proven record. They do allow for all types of scattering phenomena but as you may be aware the computer capability is rapidly exhausted through that approach. The target dimensions are typically of a few hundred lambda such as for an aircraft at microwave frequencies. The physical optics techniques are appropriate and they were the subject of four out of six or seven papers in the session. Ideally these topics should be applicable to electrically very large targets such as ships, but in practice, again because of computer capability, some shortcuts have to be taken. The paper by Wendiggensen sought a less computer-intensive method for large targets. His collection of primitive shapes and structures such as plates, wedges, cylinders and cones show that it is possible to construct a very good geometrical model of a ship and also to deduce the RCS by summation of scattering from the various elements. The noblest aspect of this work was the way in which rules were formulated governing potential shadowing between the primitives. In any case, the shadowing should never occur so you can find it out right at the beginning of the problem and save a lot of computing time. The technique appears to give very good results within the limitations of the models you can build.

It seems to me it is necessary to modify the method if microstructure of a real ship is going to be treated.

The paper by Stein showed that for flat facets the physical optics method coupled with PTD using the method of equivalent currents give good results for flat plates. He demonstrated for a cylindrical type body and the dependence of the result on the size of the facets. He showed that the departure of the faceted surface from the true surface shouldn't be more than about  $\lambda$  by 18 at any point. He also demonstrated multiple reflections of the shadowing capabilities and concluded with some validation results on a periscope.

The paper by De Leeneer describing the use of triangular flat plates to discretize the target uses the physical optics GTD techniques to calculate the scattering. In that case the geometry package was able to identify special parts such as defracting edges and hidden surfaces. Double reflections can be treated when they've been identified by examining the gradients of the facet normals. Validation was carried out using the same targets as that used by Dr. Stein.

The paper by Goupill and Boutillier emphasized the need for RCS prediction software to interface with CAD systems used by aerodynamicists. He pointed out that the CAD systems normally available are not usable directly for radar cross section calculations and some kind of interface program has to be used which takes the geometry and puts it into a form that can produce the facets for the calculations. The calculations used physical objects and PTD accounts for most of the effects of shadowing. I believe about 6000 facets had to be used to make a model of the standoff missiles and the correlation was demonstrated between the measurements and predictions. I think the useful facility of this code is the ability to select parts of the target in order to find out where the main scattering areas are, and it is also good to see the image plots and to see how the bright spots from that varies as the frequency varies. The paper by Furini uses the CAD system, the geometrical definition, and the interface program to produce a set of bicubic patches so that a complex target could be constructed without discontinuities. This RCS algorithm is able to handle shadowing and validation results were obtained for an RPV and also used on the EFA metallic aircraft.

None of the papers that I've talked about so far have been able to handle scattering within electrically large cavities. So we come to the paper by Pathak with two methods for treating the problem we outlined. The first one uses a dense bundle of ray tubes coincident upon the aperture and the method then traces via geometric optics the evolution of the rays as they are reflected from the cavity inner walls and the termination. This is called the shooting and bouncing ray method, SBR. The second approach, called the generalized ray expansion method, divides the aperture into patches where each patch acts as a radiator weighted according to the incidence direction. This seems to bring the potential benefit of not requiring ray tracing to be repeated for every instant direction although it requires more work at the start. So these methods have been validated and compared favorably with each other.

The conclusion for the papers on prediction seems to be that all algorithms produced validated results for fairly simple metallic targets. I think the next step for these methods will be to be able to analyze more complex targets perhaps to incorporate bistatic scattering, near field scattering, and cavity scattering to be able to cope with non-conductive materials and to be able to look at edge traveling waves, perhaps even creeping waves. Physical optics and PTB deal with localized scattering perhaps it is time to explore other theoretical techniques. All these prediction methods depend upon experimental validation. It is important that measurement methods continue to develop to meet the increasing challenge of low signatures.

In the final paper by Saget the need for measurements of frequencies between 100 MHz and 1000 MHz was emphasized. The problem of background clutter at these frequencies is significant. He used hardware gating and back-to-back ground subtraction and came up with a very impressive performance.

I think I've woven my comments into the summary of the papers and will stop there for more discussion.

K. C. Yeh, US: Thank you Dr. Oldfield. Any comments or questions or remarks?

I. DeLeeneer, BE: I would like to comment on a question I had when I finished my talk. It was about 90 dB in one of the curves. At that moment I was trapped so I could not really answer clearly. After rethinking I realized that I was about 20 dB too high. When I included hidden faces I only compared the shape of the curve and didn't look really at the numbers because I was not expecting such a problem. I suppose I did some stupid scaling error and am very glad I've had it pointed out.

E. Luneburg, GE: For perfectly conducting bodies the foundation of PO (Kirchhoff integral) should be remembered: removal of the discontinuity between the illuminated and the shadowed region of the geometrical optics along the shadow boundary. The connection with Young's principle (integration along the rim of the shadow boundary) should be kept in mind. Reference: Rubinowicz: Kirchhoff's integral in the theory of diffraction, Warsaw 1920-1930 (in German). PO has at the moment no rigorous mathematical foundation. It is a summation method in general not well understood.

K. C. Yeh, US: Thank you for the comment. You mention about the techniques so maybe I can call on Prof. Pathak to describe to us some of the progress that has been made in RCS community in the US. He is involved with the RCS group in comparing different numerical techniques, codes, etc.

P. Pathak, US: The viewgraph reinforces what Dr. Oldfield mentioned and also what Dr. Luneburg commented on. Of course I do not mean for these comments to be very critical, but you have to remember the ray method more than the physical optics method or the PTD method. Of course every method has its place and I will enter the discussion after we go over some of these comments. First of all I'd like to mention in most cases the physical optics approximation provides a dominant scattering effect. It looks like the interest is also going in the direction of predicting low cross section. In that case we have to be concerned with some other things, for instance the internal factor and PO modeling that is used quite often. It yields some sort of facet noise. This could be a problem especially for low cross section objects because the noise is about on the same level as the low cross section. The third comment is that the physical theory of diffraction can be used to improve the physical optics approximation for predicting the low level scattering but we have to remember that the PTD has only been developed for edge bodies. In other words, the scattering body has to have an edge on it, furthermore the edge has to be directly illuminated. For the edge shadow then you get spurious contribution so that leads to an error. Now of course the physical optics and the PTD scattering from flat surfaces is not accurate in the grazing angles of incidence neither are the ray methods because that is where the edge effects become significant and has not been studied so it is a subject for further study. The physical optics also gives spurious contribution arising from the truncation of the geometrical optics terms and this is exactly the shadow boundary that Dr. Luneburg was pointing out. If the current goes to zero smoothly, it is not such a serious problem. If the current goes to zero abruptly, it creates a spurious contribution for one of the polarizations. This spurious contribution is like a spurious diffraction effect which really isn't there in the problem. One thing that could be done is that the spurious contribution could be subtracted out in the asymptotic method and indeed this has been published recently in a paper by Gupta and Burnside in the IEEE Transaction AP. So that could be used to improve the PO solution.

The GTD on the other hand or the UTD which is the uniform version of the GTD can handle both edges and curved surfaces so it has an advantage there. The physical optics and PTB cannot handle multiple edge interaction and again this becomes significant when you're looking at low cross section. On the other hand the GTD and UTD can handle such things. If you want to stick with PTD or PO, one thing that could be done is you could do the multiple interactions using GTD and add them separately to the PO contribution.

The next thing I'd like to comment on is that the PO PTD is required to integrate over the scattering object. Now the GTD and UTD does not. However I want to point out you may have to trace rays or you may have to search for the ray paths in the GTD or the UTD type of analysis and that also could take time in certain cases. In one case you have to look for ray paths and in the other case you have to integrate over a large body. So, from my own personal point of view, it seems like one of the most efficient analysis for scattering may be possible with a combination where you do the GTD and UTD for predicting the scattering effect in all directions except maybe in those directions where the ray method has a problem such as the caustic region. In that case you could augment the GTD and UTD in those special regions by the equivalent current method of the PTD because only then would you need the integration in most small range effects where this might occur.

For the future certainly the GTD, UTD, PTD and all these PDs need to be extended to handle the grazing incidence to take care of the edgewise phenomena. Also one needs to study the scattering by tips and by material coated bodies. This is going to be more and more important when you start looking at low cross section objects. Furthermore again as Chairman Oldfield pointed out, and I think Dr. Luneburg said the same thing, we need more experimental verification



and independent solutions like solutions to regular boundary value problems and for scattering by complex bodies to validate these high frequency methods.

As far as the progress in the US is concerned I really can't make very specific comments but I can say a lot of space companies in the US have been using the physical optics and the PTD type of approach for doing the scattering. Some of them are using the planar faceted models. On the other hand others are going into the cubic spline or the curve patched models like one of the papers from Italy discussed it. Not much has been done to really speed up the integration in the physical optics approximation; however, recently there has been some indication that by using the curved patches it is possible to reduce your integrals by an approximate means, which leads to a very accurate approximation by the way, to speed up the integration so you get somewhat close from solutions, maybe at least in one direction. Furthermore, you can also make those patches relatively light so you don't have very tiny increments in dividing up your original object. Some of these things I think would be very useful when one looks at the PTD or PO now.

Another effort that is going on is to try to see if the people from various aerospace companies will donate their codes. There is reluctance in giving out their codes to people, but the Department of Defense is trying to get them to put their codes on the table and have them run different test cases so one could compare how fast, accurate, and easy to implement, etc. In general not everyone is up on trying to understand uniform ray methods, in dealing with pathological problems in shadow boundaries and caustics so this may be one of the reasons why it is not as popular. On the other hand the PTD is conceptually much easier to implement. You do the integration and with the advent of more and more parallel process computers, maybe efficiency is not such a big question. I still favor the use of ray method for most of the aspect angle except for those regions where caustics and other ray singularities occur.

K. C. Yeh, US: Thank you Prof. Pathak. Gary you have a question?

G. Brown, US: Prof. Pathak I'd like to ask a question -- as sure as the sun comes up tomorrow people are going to start wanting to push these models lower and lower in frequency. Do we have a good handle on where they really start to break down and if we do, do we know how to improve them?

P. Pathak, US: First of all if you look at the geometrical diffraction type of solution then you know they are constructed in terms of diffraction coefficient which again are deduced for canonical problems. To do that you start with a canonical problem that has an exact solution and hope that the integral representation can be evaluated asymptotically from which the diffraction coefficient can be extracted. So right then we have a way to compare where the diffraction solution will fail, compared to the exact representation, so the use of the diffraction coefficient deduced we certainly need a test and figure out where it tends to break down. This sorta gives us an indication of what you might do in a complex object because the nice thing about the ray solution is that you can always break up the total scattering contribution from the complex object in terms of those coming from flash points like the points of defraction, points of reflection, etc. There again the solution can be related to the canonical solution where the accuracy has been tested so you might have some idea where it could break down. But in general you have to compare that, maybe with a boundary value problem that may be solved rigorously, and make a further test with measurements that are continually going on. In case some of the parts of the object are electrically small, while the others are large, a nice procedure would be a hybred procedure where you solve the currents on the part that is electrically small, using subsection basis functions in a moment method formulation, and elsewhere maybe you could use the entire domain traveling wave type basis function deduced from the geometrical theory of diffraction so that is an approach worth looking at.

K. C. Yeh, US: I understand there are people outside waiting to sweep the room for the classified session tomorrow so I'll take one more question.

J. Belrose, CA: A comment on comments I've heard. Dr. Oldfield spoke about wire grid modeling and I heard a comment about how to go to lower and lower frequencies. Well the way to go to lower and lower frequencies is wire grid modeling and radar cross sections have been computed by Canadians for a ship at HF. You can compute the radar cross section even up to VHF and certainly you can compute the radar cross section for airplanes. The problem is that you rapidly get out of computer time if you want to go to higher and higher frequencies so the two methods overlap and there are programs which I know nothing about. We use NEC, the numerical electro-magnetic code at our laboratory but there is GMAX which is a combination between the

geometric theory of diffraction and plates and moment method using wire grid models so there are these copies of models out. In our experience in modeling ships you maybe need 600 to 3000 elements to properly describe a ship and the computing time goes up as a square of the number of elements used. So if you are using VAX 750 or VAX 3800 you rapidly get up to the point where you're using thousands of current elements requiring anywhere from 5 to 50 hours of computer time, so you in fact have to use a Cray to do these kinds of calculations as you go to higher and higher frequencies, but it can be done. It is just a question of computing speed. There are in fact on the market now computers using NEC numerical electromagnetic code. There is a company in the US selling a network of PCs called Transputers and you can operate anything from a few up to 64 of them. The computing time goes down as the number of computers in parallel goes up so the future is bright for computing the radar cross section of large objects at lower and lower frequencies using a technique which has not been described at this meeting.

### SESSION III: SIGNAL PROCESSING AND S.A.R.

K. C. Yeh, US: Now we go to session 3 which was chaired by Dr. Klemm. What I'm going to do now is ask the 3 remaining chairs to make their presentations and we'll take the questions at the end.

R. Klemm, GE: Ladies and gentlemen I will give you just a very brief presentation of the signal processing session. It is quite logical after the session on clutter and the session on target scattering we have to have a session on signal processing, a session which makes use of such models and theories. We had in this session 7 papers, one of them is concerned with what you call a target, namely the paper by Pardini and Piccini who used Fourier transform methods to analyze the Doppler spectrum of the target returns and especially in order to use the wide Doppler frequency band to analyze the number of propeller blades for classification of the aircraft. There are a lot of investigations on these so-called jet engine modulations and things are going on in NATO and also in various countries.

The other 6 papers are all concerned with what we refer to as clutter although by clutter we do not mean something that we throw away while the SAR people don't throw it away at all they just want to image. We have 2 papers of people who want to throw away the clutter, among them myself, and the paper by Gibson who talks about adaptive and nonadaptive MTI filters and compares them with the various kinds of clutter such as ground inversion and ice pellets. The paper by Mr. Ender and myself is concerned with the problem of detecting low and slowly moving targets by means of a fast radar such as a satellite-borne radar. These techniques seem to be very promising so far only in theory and they have to be tested experimentally. Then in the remaining 4 papers, one paper is related to the polarimetric radar and is concerned with a bipolar HH and VV radar. As far as I remember from the talk there is no significant degradation so that some expense can be saved in the radar design. Then we have 3 papers on SAR, one of them by Beaupere and Foulon is concerned with image processing, detection of various kinds of roughness and identification of the broader between areas of roughness. The paper given by Dr. Baker is concerned with the dependency of grazing angle of SAR imagery which I find most interesting in particular because it seems to me that there is quite a small variation of a few degrees near the grazing angle that has considerable influence on the quality of the image. For very low grazing angles such as 1 degree, the image quality in general can be improved. On the other hand there is the problem of low grazing angle shadowing or masking by terrain and so there has to be a compromise.

The paper by Damini and Haslam deals with the impact of the target motion on spotlight target by SAR imaging. I think it is quite difficult to draw a general conclusion out of such a heterogeneous session. I came up with some questions which I have but before I ask them I'll ask the floor to raise their questions.

### SESSION IV: POLARIMETRICS

K. C. Yeh, US: We go on to session 4 which was chaired by Dr. Flood.

W. A. Flood, US: The papers in the session I chaired were of two kinds:

a) Papers of the first kind were concerned with the recognition of canonical shapes from polarimetric measurements. As such they minimized or ignored the effects of clutter, noise, and of less than perfect polarimetric systems. These papers seemed to be driven by standoff SAR polarimetry where the frequencies were in the microwave region.

b) The second class of papers was concerned with polarimetric measurements of clutter and these papers were primarily at millimeter wave frequencies. I found the results of Dr. Mead to be extremely interesting and potentially very important. He showed that for certain classes of clutter types, conventional measurements of the backscattered power for HH, VV, and HV would suffice to approximate the clutter Mueller matrix with a simple, diagonal matrix. While Dr. Mead's analysis was tested on a limited number of clutter types at millimeter wavelengths, they may hold for clutter at longer wavelengths provided the clutter characteristics are similar. It would be very worthwhile to make further checks of these hypotheses at both microwave as well as millimeter wavelengths.

## SESSION V: APPLICATIONS

K. C. Yeh, US: Thank you Dr. Flood. Now we go to session 5, Applications, which was chaired by Mr. Fuerxer.

Fuerxer, FR: Il m'est assez difficile d'analyser cette session, d'une part parce qu'elle était relativement inhomogène et d'autre part parce que de nombreuses applications seront présentées dans les sessions classifiées. J'ai essayé de trouver un point commun et la leçon à tirer de ces exposés. Le point commun est que les exposés ont porté sur des modélisations; il faut modéliser la propagation à partir d'un radar sol et le comportement des nuages de pluie pour en tirer des informations. Il faut également modéliser les erreurs de pointage d'un radar à site bas et déterminer, comme dans le cas de l'exposé sur la propagation millimétrique, les différences de comportement des gammes de fréquence. Il est nécessaire de modéliser les phénomènes avec une finesse de description plus élevée que celle utilisée dans le système. Je crois que cela montre l'intérêt des travaux présentés. Dans quelques années, faire un radar simple, n'utilisant pas la polarisation, devra être justifié, parce que la connaissance des phénomènes existera, il faudra expliquer que pour faire simple et bon marché on n'a pas pris en compte telle et telle connaissance déjà acquise. Il est essentiel que nous ayons sur les techniques que nous utilisons pour la caractéristique des cibles et du fouillis des connaissances supérieures à celles qui sont nécessaires au système lui-même pour être capable de le concevoir, de l'évaluer et d'en prédire les performances. C'est ce que je retiendrai de ces exposés qui montrent bien que dans la diversité des applications il existe toujours un besoin de connaissances de base qui s'est manifesté au long des sessions précédentes.

K. C. Yeh: Thank you very much. Are there questions or comments or remarks for the last 3 sessions?

G. Hagn, US: I have both a comment and a question. The processing and presentation of radar images can greatly affect the ability of the system (including an operator) to detect targets. The computer assets for both real-time/near-real-time and off-line processing images have been rapidly increasing in both the civil sector as well as in the military sector. For example, computers developed in the civil sector to analyze high-definition television (HDTV), such as the Princeton engine developed by the David Sarnoff Research Center, can be used for off-line processing and image enhancement of radar data. This processing power opens new areas for research in clutter mitigation.

Regarding the paper by Baker, the data show a dramatic change from 4 degrees down to 3 degrees grazing angle. You evidently had located the critical angle below which shadowing greatly reduced the backscatter. Your results were at one frequency. A logical extension would be a multi-spectral system with variable incidence angle near the critical angle (which probably is a function of frequency). Have you considered this type of approach for the next step?

C. J. Baker, UK: From the limited amount of imagery that we have analyzed, it is not clear where any so-called critical angle may exist and so at this stage it is premature to extend the range of illumination frequencies. This is something that could be considered in the future.

K. C. Yeh, US: Any more questions?

R. Klemm, GE: I'd like to join the discussion on the grazing angle. Dr. Baker, it seems from your results that the synthetic aperture radar is applicable mostly for airborne, standoff surveillance or something. What about space-borne SAR or other applications where you really have much

larger grazing angles? I am talking about penetrating unmanned platforms with a small SAR which normally would have much steeper grazing angles.

C. J. Baker, UK: Again the effects of slight changes in geometry may well be very significant. I'm thinking of examples where one might want to use space-based system perhaps to do NTI using a quasi-DPCA technique when using a sequential orbit and if the orbits are out by a large enough factor then its going to increase the error -- it is going to reduce your ability to remove clutter to detect moving targets if that were the application you wanted to make with your SAR. In the case of a short-range penetrating type application, I think it would be more difficult to maintain the accuracy with which you can image in a given area, particularly within a hostile environment, and again this can introduce the sort of errors we see. What I haven't done in our analysis to date is to look at images at various geometries and see if the degree to which you observe changes as exaggerated as in the examples that I showed at very low grazing angles. Obviously the effects of shadowing are not going to be as significant as in the cases I was looking at, but there may be other effects that would upset other potential processing algorithms.

K. C. Yeh, US: We have come to the conclusion of this round table discussion. I would like to thank all the session chairs who served on the round table discussion. They have done such a splendid job in summarizing the papers that have been presented here so I ask them to write up their summaries so they may be included in the final proceedings. Thank you very much. I would also like to thank the participants of the round table.

REPORT DOCUMENTATION PAGE									
1. Recipient's Reference	2. Originator's Reference	3. Further Reference	4. Security Classification of Document						
	AGARD-CP-501	ISBN 92-835-0633-2	UNCLASSIFIED						
5. Originator	Advisory Group for Aerospace Research and Development North Atlantic Treaty Organization 7 rue Ancelle, 92200 Neuilly sur Seine, France								
6. Title	TARGET AND CLUTTER SCATTERING AND THEIR EFFECTS ON MILITARY RADAR PERFORMANCE								
7. Presented at	the Electromagnetic Wave Propagation Panel Specialists' Meeting, held in Ottawa, Canada, 6th—9th May 1991.								
8. Author(s)/Editor(s)	Various		9. Date September 1991						
10. Author's/Editor's Address	Various		11. Pages 342						
12. Distribution Statement	This document is distributed in accordance with AGARD policies and regulations, which are outlined on the back covers of all AGARD publications.								
13. Keywords/Descriptors	<table border="0"> <tr> <td>Clutter modeling</td> <td>Polarimetrics</td> </tr> <tr> <td>Target scattering</td> <td>Radar</td> </tr> <tr> <td>Signal processing</td> <td>Synthetic aperture radar</td> </tr> </table>			Clutter modeling	Polarimetrics	Target scattering	Radar	Signal processing	Synthetic aperture radar
Clutter modeling	Polarimetrics								
Target scattering	Radar								
Signal processing	Synthetic aperture radar								
14. Abstract									
<p>Recent advances in radar engineering have brought radar systems performance in detection, tracking, identification and guidance, closer to the physical limitations due to scattering characteristics of targets and clutter.</p> <p>Both modeling and measurements aspects of the scattering characteristics are addressed and their effects on radar systems are emphasized through the following sessions:</p> <ul style="list-style-type: none"> <li>— Clutter models and measurements</li> <li>— Target scattering</li> <li>— Signal processing and SAR</li> <li>— Polarimetrics</li> <li>— Miscellaneous applications</li> <li>— Classified applications</li> </ul>									

<p>AGARD Conference Proceedings 501 Advisory Group for Aerospace Research and Development, NATO <b>TARGET AND CLUTTER SCATTERING AND THEIR EFFECTS ON MILITARY RADAR PERFORMANCE</b> Published September 1991 342 pages</p> <p>Recent advances in radar engineering have brought radar systems performance in detection, tracking, identification and guidance, closer to the physical limitations due to scattering characteristics of targets and clutter.</p> <p>Both modeling and measurements aspects of the scattering characteristics are addressed and their effects on radar</p> <p>P.T.O.</p>	<p>AGARD-CP-501</p> <p>Clutter modeling Target scattering Signal processing Polarimetrics Radar Synthetic aperture radar</p>	<p>AGARD Conference Proceedings 501 Advisory Group for Aerospace Research and Development, NATO <b>TARGET AND CLUTTER SCATTERING AND THEIR EFFECTS ON MILITARY RADAR PERFORMANCE</b> Published September 1991 342 pages</p> <p>Recent advances in radar engineering have brought radar systems performance in detection, tracking, identification and guidance, closer to the physical limitations due to scattering characteristics of targets and clutter.</p> <p>Both modeling and measurements aspects of the scattering characteristics are addressed and their effects on radar</p> <p>P.T.O.</p>
<p>AGARD Conference Proceedings 501 Advisory Group for Aerospace Research and Development, NATO <b>TARGET AND CLUTTER SCATTERING AND THEIR EFFECTS ON MILITARY RADAR PERFORMANCE</b> Published September 1991 342 pages</p> <p>Recent advances in radar engineering have brought radar systems performance in detection, tracking, identification and guidance, closer to the physical limitations due to scattering characteristics of targets and clutter.</p> <p>Both modeling and measurements aspects of the scattering characteristics are addressed and their effects on radar</p> <p>P.T.O.</p>	<p>AGARD-CP-501</p> <p>Clutter modeling Target scattering Signal processing Polarimetrics Radar Synthetic aperture radar</p>	<p>AGARD Conference Proceedings 501 Advisory Group for Aerospace Research and Development, NATO <b>TARGET AND CLUTTER SCATTERING AND THEIR EFFECTS ON MILITARY RADAR PERFORMANCE</b> Published September 1991 342 pages</p> <p>Recent advances in radar engineering have brought radar systems performance in detection, tracking, identification and guidance, closer to the physical limitations due to scattering characteristics of targets and clutter.</p> <p>Both modeling and measurements aspects of the scattering characteristics are addressed and their effects on radar</p> <p>P.T.O.</p>

<p>systems are emphasized through the following sessions:</p> <ul style="list-style-type: none"> <li>— Clutter models and measurements</li> <li>— Target scattering</li> <li>— Signal processing and SAR</li> <li>— Polarimetrics</li> <li>— Miscellaneous applications</li> <li>— Classified applications</li> </ul> <p>Papers presented at the Electromagnetic Wave Propagation Panel Specialists' Meeting, held in Ottawa, Canada, 6th—9th May 1991.</p> <p>ISBN 92-835-0633-2</p>	<p>systems are emphasized through the following sessions:</p> <ul style="list-style-type: none"> <li>— Clutter models and measurements</li> <li>— Target scattering</li> <li>— Signal processing and SAR</li> <li>— Polarimetrics</li> <li>— Miscellaneous applications</li> <li>— Classified applications</li> </ul> <p>Papers presented at the Electromagnetic Wave Propagation Panel Specialists' Meeting, held in Ottawa, Canada, 6th—9th May 1991.</p> <p>ISBN 92-835-0633-2</p>
<p>systems are emphasized through the following sessions:</p> <ul style="list-style-type: none"> <li>— Clutter models and measurements</li> <li>— Target scattering</li> <li>— Signal processing and SAR</li> <li>— Polarimetrics</li> <li>— Miscellaneous applications</li> <li>— Classified applications</li> </ul> <p>Papers presented at the Electromagnetic Wave Propagation Panel Specialists' Meeting, held in Ottawa, Canada, 6th—9th May 1991.</p> <p>ISBN 92-835-0633-2</p>	<p>systems are emphasized through the following sessions:</p> <ul style="list-style-type: none"> <li>— Clutter models and measurements</li> <li>— Target scattering</li> <li>— Signal processing and SAR</li> <li>— Polarimetrics</li> <li>— Miscellaneous applications</li> <li>— Classified applications</li> </ul> <p>Papers presented at the Electromagnetic Wave Propagation Panel Specialists' Meeting, held in Ottawa, Canada, 6th—9th May 1991.</p> <p>ISBN 92-835-0633-2</p>

AGARD

NATO OTAN

7 RUE ANCELLE · 92200 NEUILLY-SUR-SEINE  
FRANCE

Téléphone (1)47.38.57.00 · Téléc 610 176  
Télécopie (1)47.38.57.99

DIFFUSION DES PUBLICATIONS  
AGARD NON CLASSIFIEES

L'AGARD ne détient pas de stocks de ses publications, dans un but de distribution générale à l'adresse ci-dessus. La diffusion initiale des publications de l'AGARD est effectuée auprès des pays membres de cette organisation par l'intermédiaire des Centres Nationaux de Distribution suivants. A l'exception des Etats-Unis, ces centres disposent parfois d'exemplaires additionnels; dans les cas contraire, on peut se procurer ces exemplaires sous forme de microfiches ou de microcopies auprès des Agences de Vente dont la liste suit.

CENTRES DE DIFFUSION NATIONAUX

**ALLEMAGNE**

Fachinformationszentrum,  
Karlsruhe  
D-7514 Eggenstein-Leopoldshafen 2

**BELGIQUE**

Coordonnateur AGARD-VSL  
Etat-Major de la Force Aérienne  
Quartier Reine Elisabeth  
Rue d'Evere, 1140 Bruxelles

**CANADA**

Directeur du Service des Renseignements Scientifiques  
Ministère de la Défense Nationale  
Ottawa, Ontario K1A 0K2

**DANEMARK**

Danish Defence Research Board  
Ved Idrætsparken 4  
2100 Copenhagen Ø

**ESPAGNE**

INTA (AGARD Publications)  
Pintor Rosales 34  
28008 Madrid

**ETATS-UNIS**

National Aeronautics and Space Administration  
Langley Research Center  
M/S 180  
Hampton, Virginia 23665

**FRANCE**

O.N.E.R.A. (Direction)  
29, Avenue de la Division Leclerc  
92320, Châtillon sous Bagneux

**GRECE**

Hellenic Air Force  
Air War College  
Scientific and Technical Library  
Dekelia Air Force Base  
Dekelia, Athens TGA 1010

**ISLANDE**

Director of Aviation  
c/o Flugrad  
Reykjavik

**ITALIE**

Aeronautica Militare  
Ufficio del Delegato Nazionale all'AGARD  
Aeroporto Pratica di Mare  
00040 Pomezia (Roma)

**LUXEMBOURG**

Voir Belgique

**NORVEGE**

Norwegian Defence Research Establishment  
Attn: Biblioteket  
P.O. Box 25  
N-2007 Kjeller

**PAYS-BAS**

Netherlands Delegation to AGARD  
National Aerospace Laboratory NLR  
Kluyverweg 1  
2629 HS Delft

**PORTUGAL**

Portuguese National Coordinator to AGARD  
Gabinete de Estudos e Programas  
CLAF  
Base de Alfragide  
Alfragide  
2700 Amadora

**ROYAUME UNI**

Defence Research Information Centre  
Kentigern House  
65 Brown Street  
Glasgow G2 8EX

**TURQUIE**

Millî Savunma Başkanlığı (MSB)  
ARGE Daire Başkanlığı (ARGE)  
Ankara

LE CENTRE NATIONAL DE DISTRIBUTION DES ETATS-UNIS (NASA) NE DETIENT PAS DE STOCKS  
DES PUBLICATIONS AGARD ET LES DEMANDES D'EXEMPLAIRES DOIVENT ETRE ADRESSEES DIRECTEMENT  
AU SERVICE NATIONAL TECHNIQUE DE L'INFORMATION (NTIS) DONT L'ADRESSE SUIT.

AGENCES DE VENTE

National Technical Information Service  
(NTIS)  
5285 Port Royal Road  
Springfield, Virginia 22161  
Etats-Unis

ESA/Information Retrieval Service  
European Space Agency  
10, rue Mario Nikis  
75015 Paris  
France

The British Library  
Document Supply Division  
Boston Spa, Wetherby  
West Yorkshire LS23 7BQ  
Royaume Uni

Les demandes de microfiches ou de photocopies de documents AGARD (y compris les demandes faites auprès du NTIS) doivent comporter la dénomination AGARD, ainsi que le numéro de série de l'AGARD (par exemple AGARD-AG-315). Des informations analogues, telles que le titre et la date de publication sont souhaitables. Veuillez noter qu'il y a lieu de spécifier AGARD-R-*nnn* et AGARD-AR-*nnn* lors de la commande de rapports AGARD et des rapports consultatifs AGARD respectivement. Des références bibliographiques complètes ainsi que des résumés des publications AGARD figurent dans les journaux suivants:

Scientific and Technical Aerospace Reports (STAR)  
publié par la NASA Scientific and Technical  
Information Division  
NASA Headquarters (NTT)  
Washington D.C. 20546  
Etats-Unis

Government Reports Announcements and Index (GRA&I)  
publié par le National Technical Information Service  
Springfield  
Virginia 22161  
Etats-Unis  
(accessible également en mode interactif dans la base de  
données bibliographiques en ligne du NTIS, et sur CD-ROM)



Imprimé par Specialised Printing Services Limited  
40 Chigwell Lane, Loughon, Essex IG10 3TZ